VERLAG DER TECHNISCHEN UNIVERSITÄT GRAZ

Georg Flatscher

Evaluation and approximation of timber connection properties for displacement-based analysis of CLT wall systems

TET 6

MONOGRAPHIC SERIES TU GRAZ
TIMBER ENGINEERING & TECHNOLOGY

Georg Flatscher

Evaluation and approximation of timber connection properties for displacement-based analysis of CLT wall systems

Monographic Series TU Graz

Timber Engineering & Technology

Monographic Series TU Graz

Timber Engineering & Technology **Volume 6**

Georg Flatscher

Evaluation and approximation of timber connection properties for displacement-based analysis of CLT wall systems

---

The work is based on the dissertation "Evaluation and approximation of timber connection properties for displacement-based analysis of CLT wall systems", presented by Georg Flatscher at Graz University of Technology, Institute of Timber Engineering and Wood Technology in May 2017.

Supervisors: G. Schickhofer (Graz University of Technology),
W. Seim (University of Kassel)

Cover photo	Wenner Bridge at St. Georgen, Styria / A (source: Gerhard Schickhofer)
Layout	Christina Fraueneder, TU Graz Stefan Schleich, TU Graz
Printed	Printservice, TU Graz

Verlag der Technischen Universität Graz
www.ub.tugraz.at/Verlag

Print
ISBN 978-3-85125-557-7

E-Book
ISBN 978-3-85125-558-4
DOI 10.3217/978-3-85125-557-7

PREFACE OF THE MONOGRAPHIC SERIES

Composing a scientific work in terms of a dissertation constitutes a supremely personal concern of a cognition-oriented extension of knowledge. After having finalised and published such a work it is the aim to conduct a liberal, scientific discourse with an interested and objective scientific community. This circumstance together with the associated possibility to discuss this scientific work have to be accentuated especially in times were the amount of applied research is increasing. In this spirit: **The personal liberty in research starts at that point where the externally demanded applicability ends**.

With the monographic series **Timber Engineering & Technology (TET)** of the Institute of Timber Engineering and Wood Technology the publishers aim on providing the community with fundamental works of the area of expertise. With regards to content this is judged as a contribution for an outstanding and open-minded scientific discourse among experts. Citing **B. von Chartes** (freely translated): **"…we are like dwarfs on the shoulders of giants, so that we can see more than they, and things at a greater distance, not by virtue of any sharpness of sight on our part, or any physical distinction, but because we are carried high and raised up by their giant size."**. Following this, today's state-of-the-art together with the own scientific work counts as basis of the next generations, thereby providing those fundamentals what from innovations can be derived in succession.

Graz, February 2013, Univ.-Prof. Dipl.-Ing. Dr.techn. Gerhard Schickhofer

...meiner Familie

DANKSAGUNG

Ohne den Rückhalt, welchen ich in meinem Umfeld stets finden konnte, wäre die Fertigstellung der vorliegenden Arbeit wohl nicht möglich gewesen. Deshalb ist es mir ein Anliegen die ersten Zeilen all jenen zu widmen, die mich dabei unterstützt haben.

Besonders möchte ich mich bei Herrn Univ.-Prof. Dipl.-Ing. Dr. techn. Gerhard Schickhofer bedanken. Durch die freundliche Aufnahme an seinem Institut hat er mir die Möglichkeit gegeben, den Holzbau und das universitäre Leben mit all seinen Facetten kennen zu lernen.

Ein weiterer Dank gebührt Herrn Prof. Dr.-Ing. Werner Seim, welcher das Korreferat für meine Dissertation übernommen hat. Die Zusammenarbeit mit ihm und seinem Mitarbeiter Dr.-Ing. Johannes Hummel, hat die vorliegende Arbeit maßgebend geprägt. Darüber hinaus möchte ich mich für den unkomplizierten Zugang zu den hier verwendeten Prüfdaten bedanken. Ein weiterer Dank für die Zurverfügungstellung von Prüfdaten gebührt dem Trees and Timber Research Institute (IVALSA).

Herzlich bedanken möchte ich mich auch bei meinem Kollegen und Freund Andreas Ringhofer. Die vielen Diskussionen im Moxx (danke Gigi und Gerald!), die stets konstruktive Kritik und der sprühende Enthusiasmus haben mir eine Brücke über viele Gräben auf dem Weg zu dieser Arbeit geschlagen.

Auch allen weiteren Arbeitskollegen am Institut für Holzbau und Holztechnologie sowie der holz.bau forschungs gmbh möchte ich meinen aufrichtigen Dank ausdrücken. Insbesondere die teils unkonventionellen und mitunter auch kritischen Ansätze von Manfred Augustin, haben mich immer wieder dazu bewogen über den vielzitierten Tellerrand hinauszublicken.

Der größte Dank gilt jedoch meiner Familie. Allen voran meiner Mutter Notburga, ohne deren uneingeschränkten Unterstützung der von mir bis heute beschrittene Lebensweg so nicht möglich gewesen wäre. Auch bei meinen Geschwistern Elisabeth, Bernhard und Harald möchte ich mich herzlich für den gebotenen Rückhalt bedanken.

Für ihre unaussprechliche Geduld, das in mich gesetzte Vertrauen und die stets aufbauenden Worte möchte ich mich abschließend noch bei meiner Lebensgefährtin Bettina bedanken. Vielen Dank, das du an meiner Seite bist.

Teile der vorliegenden Arbeit wurden im Rahmen des Projektes ‚focus_sts' vom Kompetenzzentrum holz.bau forschungs gmbh finanziert und in Kooperation mit dem Institut für Holzbau und Holztechnologie der TU Graz bearbeitet.

Das Projekt wurde aus Mitteln des Bundesministeriums für Wissenschaft, Forschung und Wirtschaft (BMWFW), des Bundesministeriums für Verkehr, Innovation und Technologie (BMVIT), der Steirischen Wirtschaftsförderungs-gesellschaft mbH (SFG), des Landes Steiermark (A12), des Kärntner Wirtschaftsförderungs Fonds (KWF), des Landes Niederösterreich Abteilung Wirtschaft, Tourismus und Technologie und der Standortagentur Tirol gefördert.

ABSTRACT

Aiming a comprehensive analysis of laterally loaded cross laminated timber (CLT) wall systems, the present thesis discusses two core topics. Initially, due to their major influence, the evaluation and approximation of timber connection properties are spotted. In particular, basing on an extensive discussion of already available methods, alternatives for determining the initial stiffness and ductility of timber joints are proposed. Furthermore, a capable displacement-based approach, able to approximate the entire course of even complex load-displacement relationships, is developed.

Subsequently, the focus is set on CLT wall systems. Besides a brief summary of currently applied calculation models, a new displacement-based method for predicting the load-displacement behaviour of wall diaphragms is proposed. In order to consider the nonlinear behaviour of connections, the afore-developed continuous function is used. The actual quality of the suggested wall model is verified by experimental results gathered from full scale wall tests, conducted at three independent research facilities. The positive outcome of this validation process consequently permits the use of the proposed model for a comprehensive parameter study.

Within the last part of the present thesis it is examined how several factors as, e.g., the wall length, vertical joints, different connections or the vertical load may affect the behaviour of CLT wall systems. Moreover, different approaches for determining the lateral load distribution on CLT wall diaphragms within one floor are discussed.

KURZFASSUNG

Die vorliegende Dissertation befasst sich im Wesentlichen mit der umfassenden Beschreibung von horizontal beanspruchten Brettsperrholz (BSP) Wandsystemen. Um dieses Ziel zu erreichen, splittet sich die Arbeit in zwei Kernpunkte. Aufgrund ihres großen Einflusses, werden zunächst unterschiedliche Methoden für die Bewertung und Approximation von Holzverbindungen, bzw. deren Last-Verschiebungskurven, untersucht. Neben einer umfangreichen Literaturrecherche werden hier auch alternative Ansätze für die Bestimmung der Anfangssteifigkeit und Duktilität von Holzverbindungen vorschlagen. Des Weiteren wird ein verformungsbasiertes Kurvenmodell für die Approximation von Prüfkurven entwickelt.

Der zweite Teil der Arbeit befasst sich ausschließlich mit BSP Wandsystemen. Neben einer zusammenfassenden Darstellung von aktuellen Berechnungsmethoden, wird ein neues, ebenfalls verformungsbasiertes Berechnungsmodell für die Vorhersage der gesamten Last-Verschiebungskurve eines BSP Wandsystems vorgestellt. Hierbei wird das zuvor beschriebene Kurvenmodell für die Implementierung des nichtlinearen Verhaltens der eingesetzten Verbindungen verwendet. In weiterer Folge wird die Qualität des Wandmodells anhand von experimentellen Prüfergebnissen, welche von drei unabhängigen Forschungseinrichtungen stammen, verifiziert. Die guten Ergebnisse dieses Validierungsprozesses erlauben schlussendlich den Einsatz des vorgeschlagenen Modells für die Erstellung einer umfassenden Parameterstudie.

Im Rahmen des letzten Teils der Arbeit, wird der Einfluss unterschiedlicher Faktoren, wie z.B. der Wandlänge, vertikaler Fugen, unterschiedlicher Verbindungen oder der vertikalen Last auf das Tragverhalten von BSP Wandsystemen untersucht. Des Weiteren werden unterschiedliche Ansätze für die Verteilung von horizontalen Lasten auf die einzelnen Wandscheiben innerhalb eines Stockwerks diskutiert.

CONTENTS

CHAPTER 1
INTRODUCTION

1-1 MOTIVATION

The natural grown building recourse timber has limited geometric boundary conditions and exhibits widely linear elastic behaviour (except for compressive stresses) and brittle failure mechanisms. As a consequence, joints are not only responsible for simply connecting single timber pieces to a structure and transferring loads, but rather should exhibit high qualities in stiffness and ductility as well; compare Gehri (1993).

In the past, typical timber structures mainly consisted of several linear shaped elements with a relatively high slenderness, i.e., posts and beams. For designing such structures, static models assuming simply pinned or rigid joints led to proper results. However, their actual behaviour lies in between (semi-rigid); compare Haller (1998). Moreover, according to section 5 "*Basis of structural analysis*" of the current European design standard for timber structures ON EN 1995-1-1 (2014) (also referred to as Eurocode 5), the effect of deformations from connections has to be considered; particularly in statically overdetermined systems. For this purpose, Eurocode 5 offers simple equations for determining the slip modulus of various single fasteners. The property 'ductility', intended for assessing the plastic capacity of a joint, is mentioned only once in Eurocode 5. In particular, connections owning an "adequate ductility" are scheduled as requirement for applying an elastic-plastic calculation method. Unfortunately, no further specifications regarding 'adequate ductility' or elastic-plastic calculation methods are given. The European standard for earthquake design ON EN 1998-1 (2011) (also referred to as Eurocode 8) pays a bit more attention to this parameter and, at least, defines three ductility classes for connections (low, medium and high).

As a rule of thumb, it can be stated that as compact timber elements are, as important connections' stiffness and ductility for a well-tempered behaviour of the structure gets. This particularly applies to cross-laminated timber (CLT) structures exposed to lateral loads, i.e. earthquakes or heavy wind loads.

Developed about 20 years ago, meanwhile CLT is a well-known engineered timber product frequently used for, e.g., residential buildings, office buildings, schools or bridges; compare Brandner et al. (2016). Aiming to investigate the lateral (cyclic) behaviour of CLT structures, an extensive experimental campaign was conducted at Graz University of Technology, Institute of Timber Engineering and Wood Technology and the competence centre holz.bau forschungs gmbh. This campaign includes 215 single joint tests on commonly used connections and fasteners, 17 full scale wall tests and a full scale shaking

table test on a three-storey CLT structure within the frame of the European Union (EU) project SERIES (Seismic Engineering Research Infrastructures for European Synergies); compare Flatscher et al. (2015) and Flatscher and Schickhofer (2015). Since the main experimental results of this research project have already been published, they are only partially mentioned in the present thesis. The focus is set on experiences made during post-processing the single joint tests and the preparation for the wall and shaking table tests.

Spotting the single joint tests and considering the thoughts mentioned above, not only the load-carrying capacity, but also the stiffness and ductility properties are important qualities for an efficient CLT connection. Besides several different loading protocols, a huge amount of proposals for post-processing the test data (means the evaluation of yield load, initial stiffness, ductility, etc.) are available on the 'scientific market'; compare, e.g., Muñoz et al. (2008) and Flatscher (2010). Unfortunately, excepting the maximum load and the corresponding displacement, not even one further parameter is distinctively measurable. Consequently, the choice of the post-processing model may finally influence the resulting properties; this substantially complicates a comparison with further test results available in literature.

While preparing the wall and shaking table tests it gets obvious that only limited information regarding the design of CLT wall systems is available. Moreover, the bulk of already existing (analytical) models is force-based and hardly enables the consideration of local deformations beyond the peak load. This, however, may be important for designing structures for, e.g., earthquake prone areas.

1-2 OBJECTIVES

Basing on the described experiences, the present thesis primarily aims to develop and validate a practical applicable, but still sophisticated, model for determining the behaviour of CLT wall systems under lateral loads. Moreover, due to their distinct influence, initially the focus is set on determining connection properties and simulating their whole load-displacement behaviour.

Determining connection properties

In the scientific community, it is a matter of common knowledge that different post-processing methods widely prohibit an easy and fast comparison of test results gathered at different research facilities. Even if scientists around the world have learned to deal with this cumbersome and inefficient circumstance, it still includes a practical issue. Probably the best examples are the different ductility values. Processing one and the same set of test data, may lead to a 'low' ductility applying one method and a 'high' ductility for another post-processing method. From an academic point of view probably just

an issue to be discussed, this criterion finally rules the practical use of respective connections in the design process.

Hence, within the first part of this thesis, an extensive literature review concerning different post-processing methods is conducted and a comparison based on selected experimental results is presented. Furthermore, new thoughts regarding the properties initial stiffness and ductility are given.

Approximating experimental test curves

An analytical approximation of experimental test curves is seen as a proper method for solving some basic issues. Firstly, it enables to offer not only single parameters, but also shape information in publications without the necessity of too many figures or even data tables. This further would allow other researchers to apply their post-processing methods on the test curves and therefore reach a better comparability of their test results. Secondly, analytical approaches enable a proper and easy implementation of connections' behaviour in further calculation models.

For timber connections, however, an approximation model, being able to simulate even complex test curves, is required. Moreover, a consideration of the post maximum softening should be possible as well. As a consequence, basing on a further literature study, a new displacement-based model, able to widely fulfil the above mentioned requirements, is proposed.

CLT wall systems

Besides describing and discussing the currently available methods for determining the behaviour of CLT wall systems, a new displacement-based calculation model is proposed. After a detailed description, the qualities of the model are verified by comparing its outputs with experimental test results, gathered from three independent laboratories.

Aiming a deeper insight into the behaviour of CLT wall systems, the new approach is finally applied for preparing a comprehensive parameter study. Besides varying parameters as, e.g., the length of wall systems or the amount of acting vertical loads, also the influence of vertical joints is discussed. Moreover, some remarks regarding the lateral load distribution within one floor are included as well.

1-3 GENERAL NOTE ON NOTATIONS AND TERMS

Comparing different literary sources or standards, the absence of distinct terms, symbols and notations is a common issue. For example, in ASTM D5652 (2013) the term 'ultimate load' is equated with the maximum load reached within an experimental test, whereas ON EN 12512 (2005) defines it as the load at the point of failure (compare section 2-3).

Thus, aiming a good comparability and confirmability, herein the same notifications are used for equal contents in different sources. In this context, the word ‘content’ is selected consciously, because the same notation does not necessarily mean that the corresponding definition is completely equal. If required, a differentiation between such values will be realised through appropriate indexing. Although some formulas and definitions may look different compared with the original one, in favour for an easier reading, the author decided against showing all original terms too. In general, the letter symbols used are defined where they first appear. Additionally, the most important one are listed in ANNEX A.

Furthermore, equivalent to ISO 16670 (2003), the terms ‘load’ and ‘displacement’ are taken as generic designations. Especially in Chapter 2 and Chapter 3 they represent any load or moment and any displacement, deflection, deformation or rotation, respectively.

CHAPTER 2
LOAD-DISPLACEMENT CURVES

2-1 INTRODUCTION

A fundamental principle in all engineering professions is that the designed structures have to resist the effects of actions. Satisfying this key point, besides the knowledge of the actions, information regarding the properties of the used materials and structures are required. Of course, today several software packages allow suitable simulations in a broad range and enable to avoid time consuming and expensive tests. Nevertheless, experimental campaigns are still necessary for gathering the input parameter for such programs.

A major output of experimental tests examining mechanical properties like stiffness or load-carrying capacity, is the so called load-displacement diagram. It documents the behaviour of the investigated specimen and is a common tool for visualising the properties of materials or structures. Such load-displacement (or stress-strain) curves are used in other fields of science too, e.g. in biomechanics; compare Korhonen and Saarakkala (2011) and Figure 2.1. Nevertheless, within this thesis, the focus is set on the load-displacement relationships predominantly relevant for the field of timber engineering.

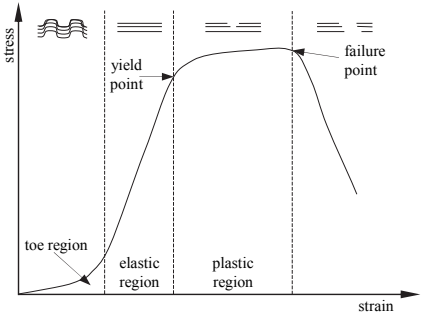

Figure 2.1: ***typical stress-strain curve for destructive tensile testing of skeletal soft tissues; Korhonen and Saarakkala (2011) – revised***

2-2 CHARACTERISTICS OF LOAD-DISPLACEMENT CURVES

To interpret and discuss load-displacement curves, some definitions and terms have to be presumed. Therefore, brief basic information regarding the areas and main points of typical load-displacement diagrams is given within the following sections.

When discussing the behaviour of materials or structures, the terms ‘elastic’ and ‘plastic’ are omnipresent. In this context, elastic means that displacements, occurring while applying a load, completely disappear upon the removal of the load; plastic deformations remain (see Figure 2.2).

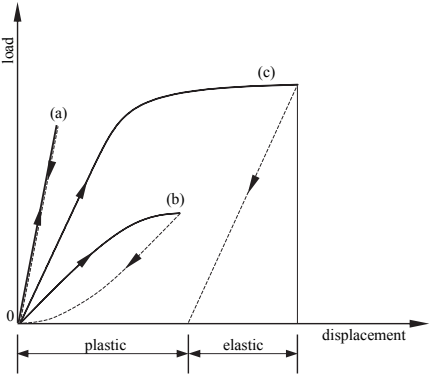

Figure 2.2: material properties ‘elastic’ and ‘plastic’ with loading and unloading path – (a) linear elastic; (b) nonlinear elastic; (c) elastic plastic; Issler et al. (1997) – revised

As mentioned before, and also given in several publications for engineering mechanics, basic mechanical properties can be extracted from experimental load-displacement curves; compare, e.g., Issler et al. (1997) or Boresi et al. (2011). The following explanations will refer to Figure 2.3, which illustrates a typical load-displacement relationship of a single nail loaded in tension.

Generally, load-displacement diagrams can be separated into a linear increasing (I), a nonlinear increasing (II) and a nonlinear decreasing (III) part. Furthermore, till the system tested is ‘well-rehearsed’, an initial sector (S), representing the initial slip, may occur. However, due to its limited influence on further discussions, this sector is not further considered in the following passages.

Region (I) is also known as elastic area and usually defined as the range between the origin 0 and the yield point Y; compare Figure 2.3 (a). A deeper insight into this part is given in Figure 2.3 (b). As illustrated, the elastic range includes the proportional limit (P), the elastic limit (E) and the plastic limit (Y); latter one is also known as yield point. Up to the proportional limit the test specimen behaves ideal linear elastic and the inclination of the line 0-P represents the initial stiffness (K_{ini}). For stress-strain diagrams, within this range Hook’s law applies and the inclination consequently represents the modulus

of elasticity (MOE; also termed as Young's modulus). Beyond the proportional limit, the curve starts to behave nonlinear, but up to the elastic limit, the deformations disappear upon removal of the load; compare line (b) in Figure 2.2.

A common model, defining the yield point Y, is the 0.2 % criterion; compare ASTM E6 (2003). In particular, this means that upon the removal of the load a strain of 0.2 % remains; see Figure 2.3 (b). However, several models and definitions concerning the yield point Y are given in literature and will be discussed in detail later on. Moreover, for timber connections, no distinction between the elastic and the plastic limit is made; usually all three points described above are summarised to the yield point as shown in Figure 2.3.

Region (II) represents the nonlinear increasing area between the yield point and the maximum value (M). After passing the peak, region (III) – the nonlinear decreasing area downward to fracture (U) – begins. The length of this region, in relation to the total displacement, indexes the specimen either as brittle or ductile for short or long distances, respectively.

Besides the mentioned core points of a load-displacement curve, Figure 2.3 also covers the corresponding load and displacement parameters. In particular, F_y and v_y for the yield point, F_{max} and v_{max} for the maximum and F_u and v_u for the ultimate point (point of failure). The load levels F_{pr} and F_{el} as well as the corresponding deformations v_{pr} and v_{el} for the proportional and elastic limit, respectively, are visualised in Figure 2.3 (b).

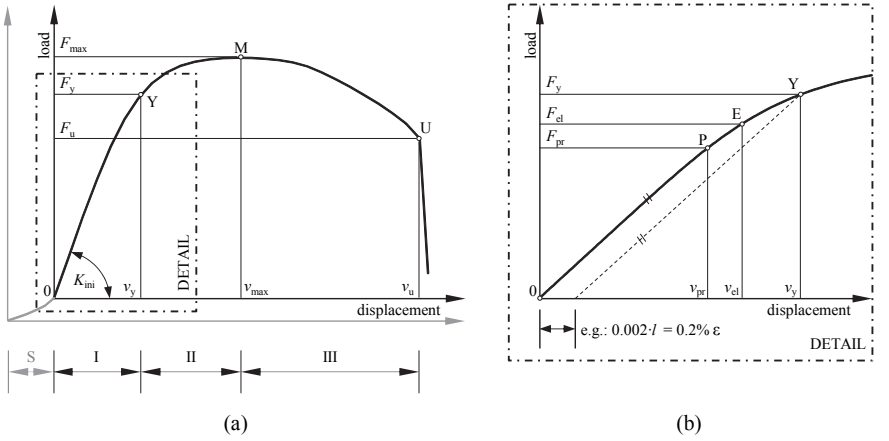

(a) (b)

Figure 2.3: definitions for discussing load-displacement relationships – (a) overview; (b) detail of elastic branch

2-3 ANALYSING LOAD-DISPLACEMENT CURVES

The shape of load-displacement curves received from experimental tests and consequently the resulting properties of the respective test specimens primarily depend on three core points: (i) the test configuration, (ii) the used equipment and (iii) the applied loading protocol. Needless to say, the more equal the mentioned influencing factors are, the easier the comparison of test results carried out in different laboratories is. Thus, usually test standards schedule the loading protocol, minimum criteria for test equipment and some further parameters as, e.g., the moisture content or minimum dimensions of timber specimens; compare, e.g., ON EN 1382 (1999). However, only limited regulations regarding test configurations are available; especially for timber connections.

Besides the mentioned boundary conditions influencing the shape of the load-displacement curve, the resulting properties of the considered specimen do further dependent on the models used for analysing the test data (post-processing); compare, e.g., Foliente (1996) or Muñoz et al. (2008).

The following sections give a brief description of widely accepted, yet different, methods for determining frequently used parameters. Here, of course, the main focus is set on definitions and suggestions applicable for load-displacement curves gathered from monotonic tests on fasteners, connections and wall systems used in timber engineering. Nevertheless, some selected models primarily intended for analysing envelope curves of quasi-static cyclic tests, structural timber members or steel specimens are included as well.

2-3.1 EN 26891

The ON EN 26891 (1991), which is identical to ISO 6891 (1983), represents the basic standard for experimental tests on joints made with mechanical fasteners in Europe and bases on Vermeyden (1963) and RILEM TC 3-TT (1977). The scheduled loading protocol is illustrated in Figure 2.4 (a) and the corresponding load-displacement diagram is given in Figure 2.4 (b). Latter one also exhibits parameters required as input parameters for Equations (2.1) to (2.6), defining the initial displacement v_{in}, the modified initial displacement $v_{i,mod}$, the joint settlement (or initial slip) v_s, the elastic displacement v_{el} and the stiffness values $K_{ini,1}$ and $K_{ini,2}$. The latter two parameters are originally entitled as slip modulus and initial slip modulus, respectively. Further aspects worth mentioning, are the absolute displacement limit of 15 mm and the circumstance that most properties rely on the estimated (F_{est}) instead of the actual peak load (F_{max}).

$$v_{in} = v_{04} \tag{2.1}$$

$$v_{i,mod} = \frac{4}{3} \cdot \left(v_{04} - v_{01} \right) \cdot v_{04} \tag{2.2}$$

$$v_s = v_{in} - v_{i,mod} \tag{2.3}$$

$$v_{el} = \frac{2}{3} \cdot \left(v_{14} + v_{24} - v_{11} - v_{21} \right) \tag{2.4}$$

$$K_{ini,1} = \frac{F_{04} - F_{01}}{v_{04} - v_{01}} = \frac{0.3 \cdot F_{est}}{v_{04} - v_{01}} = \frac{0.4 \cdot F_{est}}{v_{i,mod}} \tag{2.5}$$

$$K_{ini,2} = \frac{0.4 \cdot F_{est}}{v_{in}} \tag{2.6}$$

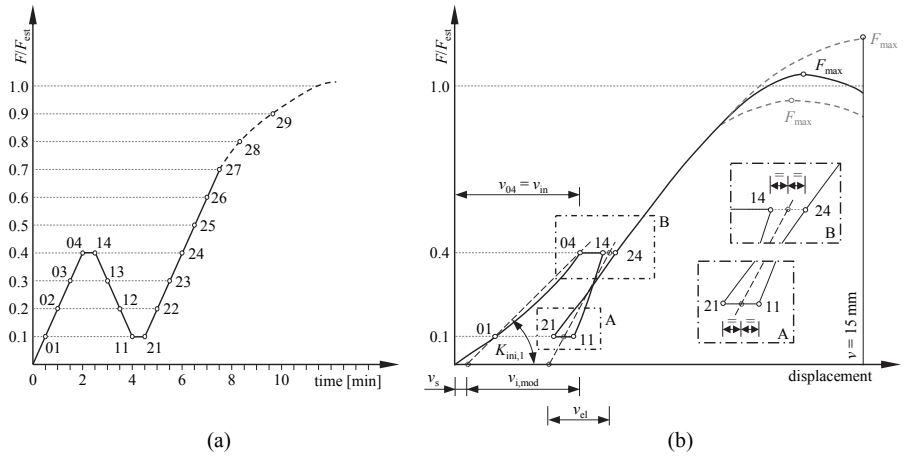

Figure 2.4: interpretation of the loading protocol as given in ON EN 26891 (1991) – (a) load-time protocol; (b) load-displacement diagram

2-3.2 ASTM D5652 AND ASTM D5764

The American standards ASTM D5652 (2013) and ASTM D5764 (2002) define the proportional limit and the yield limit as shown in Figure 2.5. For determining the yield point, they prescribe to horizontally offset the line representing the initial stiffness to 5 % of the fasteners' diameter. Thereby, it is not described in detail, how the initial stiffness has to be evaluated; ASTM D5764 (2002): *'(...) 11.1.1 Fit a straight line to the initial linear portion of the load-deformation curve. (...)'*. Similar to ON EN 26891 (1991), ASTM D5652 (2013) indicates 15 mm as the displacement where the test should be terminated. Since focussing on embedment strengths, ASTM D5764 (2002) limit this specific value to one half of the fasteners diameter. However, neither an initial hysteresis nor any further points or stiffness ratios are designated.

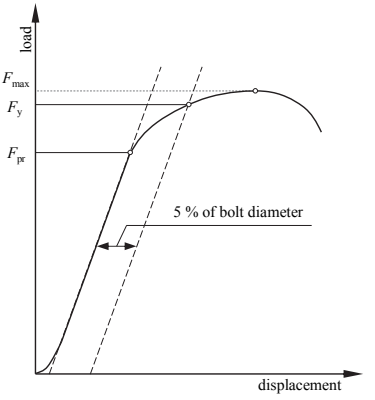

Figure 2.5: interpretation of a load-displacement graph according to ASTM D5764 (2002)

2-3.3 EN 12512

The European standard ON EN 12512 (2005) primarily regulates cyclic experiments of timber joints. The required input parameter for the cyclic loading protocol is the joint slip corresponding to the yield load. The preferred method for determining this value is the realisation of monotonic (pre)tests according to ON EN 26891 (1991) and the subsequent application of one of the two approaches described below.

If load-displacement curves cover two well defined linear parts, the yield values (load and displacement) are defined by the intersection between these two lines; compare Figure 2.6 (a). Elsewise, the yield point should be determined as illustrated in Figure 2.6 (b). Moreover, although not explicitly written, the inclination of the secant corresponding to 0.1 F_{max} and 0.4 F_{max}, i.e., tan(α), is frequently interpreted as the initial stiffness K_{ini}.

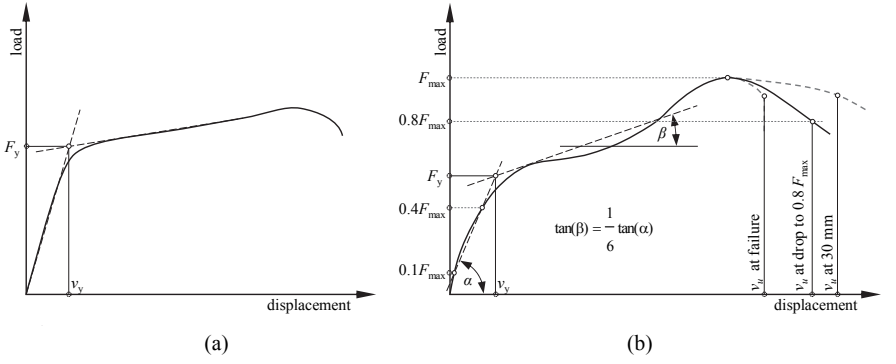

Figure 2.6: definition of the yield and the ultimate point according to ON EN 12512 (2005) – (a) definition for two well-defined linear parts; (b) definition if the test curve does not cover well-defined linear parts

The ON EN 12512 (2005) also schedules that the ultimate load F_u corresponds to the point of failure, 80 % of F_{max} or the load occurring at a displacement of 30 mm, whichever occurs first. Furthermore, as given in Equation (2.7), ductility D is defined as the ratio between the ultimate displacement (corresponding to F_u) and the yield displacement.

$$D = \frac{v_u}{v_y} \tag{2.7}$$

with

v_u ..... ultimate displacement

v_y ..... yield displacement

2-3.4 ISO 16670

The ISO 16670 (2003) is the international equivalent to the ON EN 12512 (2005). The biggest differences to the European standard, regarding the cyclic tests, are the higher test velocity and the loading protocol, which is based on the ultimate displacement v_u instead of the yield displacement v_y; compare Flatscher (2010). For the monotonic (pre)tests ISO 6891 (1983) is referred but with the remark to skip the preloading.

Regarding the determination of the ultimate displacement, it only contains two cases: (i) the displacement at failure or (ii) the displacement at $0.8 \cdot F_{max}$ in the descending portion of the load-displacement curve. A third case, restricting the maximum displacement, as given in ON EN 12512 (2005), is not included.

For determining the initial stiffness of the monotonic and the envelope curves of the cyclic tests, the annex of ISO 16670 (2003) proposes Equation (2.8).

$$K_{ini} = \frac{0.3 \cdot F_{max}}{v_{40} - v_{10}} \tag{2.8}$$

with

K_{ini} ..... initial stiffness

F_{max} ..... maximum load reached within the test

v_{10} ..... displacement obtained at 10 % of F_{max}

v_{40} ..... displacement obtained at 40 % of F_{max}

2-3.5 SIA 265

SIA 265 (2012) includes a similar definition for the yield point as the second method described in ON EN 12512 (2005). The difference is that the first line accords the secant, passing the origin and the point where $0.4 \cdot F_{max}$ is reached; see Figure 2.7. Moreover, in SIA 265 (2012) the initial stiffness is explicitly defined as given in Equation (2.9); the ductility is regulated equal to Equation (2.7).

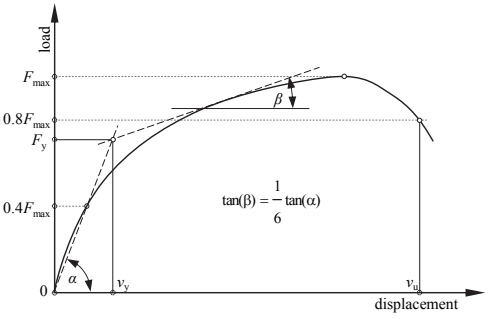

Figure 2.7: definitions of initial stiffness and yield point according to SIA 265 (2012)

$$K_{ini} = \frac{0.4 \cdot F_{max}}{v_{40}} = \frac{F_y}{v_y} \tag{2.9}$$

with

F_y..... yield load

2-3.6 EN 594

Between the test standards ON EN 594 (1996) and ON EN 594 (2011), considering the racking strength and stiffness of timber frame wall panels, the loading protocol and consequently the determination of the initial (racking) stiffness changes substantially. Furthermore, as described later on, the ISO 21581 (2010) refers to the loading protocol used in ON EN 594 (1996). Thus, both versions of this standard are summarised.

2-3.6.1 EN 594:1996

The loading protocol of ON EN 594 (1996) includes two initial cycles before the actual strength test starts; the stabilising and the stiffness load cycle. Only the second one is designated to be documented in the load-displacement plot; see Figure 2.8. Compared to ON EN 26891 (1991), this schedule stands out with much higher holding times (300 s and 600 s vs. 30 s) and a reduction of load within the stiffness cycle back to zero instead of 0.1 F_{est}. Moreover, it is scheduled to execute the whole test procedure displacement controlled with a displacement limit of 100 mm.

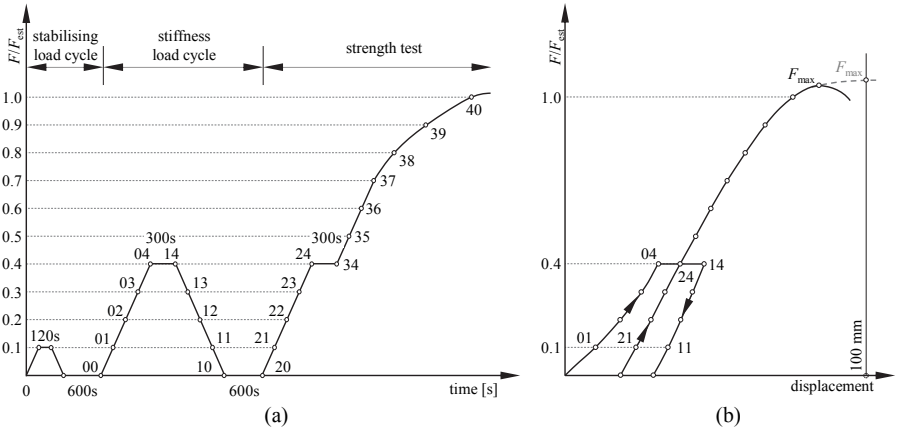

Figure 2.8: ***loading procedure according to ON EN 594 (1996) – (a) loading protocol; (b) corresponding load-displacement curve***

Further worth mentioning is the determination of the initial stiffness, which represents a mean value of the stiffness cycle and the actual strength test; compare Equation (2.10).

$$K_{ini} = \frac{1}{2} \cdot \left[\frac{F_{04} - F_{01}}{v_{04} - v_{01}} + \frac{F_{24} - F_{21}}{v_{24} - v_{21}} \right] \tag{2.10}$$

with

F_i ..... loads according to Figure 2.8

v_i ..... displacements according to Figure 2.8

2-3.6.2 EN 594:2011

The most distinct difference between ON EN 594 (1996) and ON EN 594 (2011) is that there are no more preloading cycles in the present version of this test standard. Consequently, the determination of the initial stiffness changes to the form already given in Equation (2.8), where the reference load for calculating the 10% and 40% limit is the actually reached peak load instead of the estimated one (see Figure 2.9).

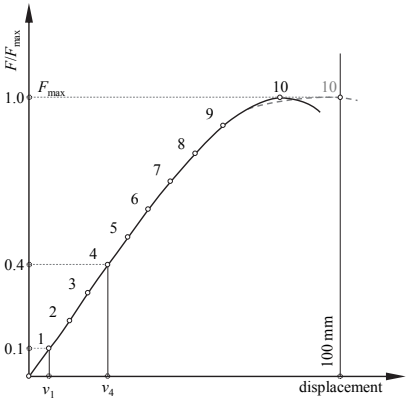

Figure 2.9: load-displacement graph according to ON EN 594 (2011)

2-3.7 ISO 21581

The international standard ISO 21581 (2010) describes boundary conditions for static and cyclic lateral load tests for shear walls used in timber structures. The schedule, considering the monotonic tests, is equal to the loading protocol presented in ON EN 594 (1996). For the cyclic tests, this standard contains regulations similar to the one in ISO 16670 (2003), which require the ultimate displacement v_u for preparing the cyclic loading protocol. The ISO 21581 (2010) distinguishes three cases to gather this parameter: (i) displacement at failure, displacement at $0.8 \cdot F_{max}$ in the descending part of the load-displacement curve and a displacement equal to $h/15$ (h = height of the wall specimen), whichever occurs first. The proposal regarding the initial stiffness accords with Equation (2.8).

2-3.8 EEEP MODEL

The equivalent energy elastic-plastic (EEEP) model is defined in ASTM E2126 (2011), whereat one of the first descriptions of this model is given in Park (1989). As the name suggests, the model searches an elastic-plastic approximation enveloping the same area (dissipating the same energy) as the original test curve does. Thereby, as given in Figure 2.10, the gradient of the elastic part (K_{ini}) and the failure limit is defined as already described in section 2-3.5.

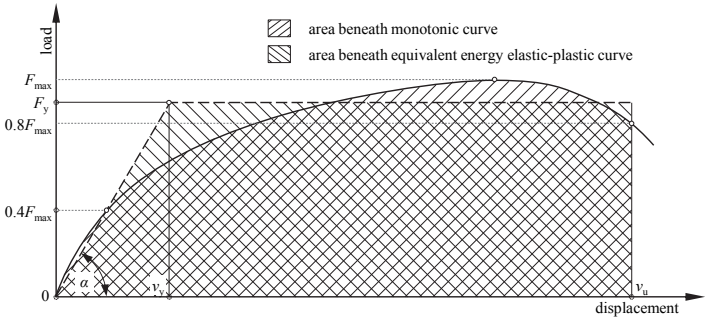

Figure 2.10: equivalent energy elastic-plastic (EEEP) curve according to ASTM E2126 (2011)

The boundary condition regarding the equivalence of dissipated energy is satisfied, if Equation (2.11) complies.

$$F_y = \left[v_u - \sqrt{(v_u)^2 - \frac{2 \cdot A}{K_{ini}}} \right] \cdot K_{ini} \tag{2.11}$$

with

A ..... area beneath the test curve from the origin to v_u

2-3.9 YASUMURA AND KAWAI

The method proposed in Yasumura and Kawai (1997) is not standardised, but yet frequently used. This model, originally developed for describing the behaviour of laterally loaded wood-framed shear walls, uses fragments of already existing methods in combination with a new idea for finding the yield parameters. As shown in Figure 2.11 (a) the yield point is once more identified by using two lines. The first line is again defined by the points on the original load-displacement curve where the load reaches 10 % and 40 % of F_{max}. The inclination of the second line (tangent) is defined by the points on the test curve where the load corresponds to $0.4 \cdot F_{max}$ and $0.9 \cdot F_{max}$. The intersection of these two lines notifies the yield load F_y. Deviating from other models, the yield displacement is defined on the original load-displacement curve where the load reaches F_y; compare Detail A in Figure 2.11 (a). Finally, the EEEP method is used for identifying the ultimate load F_u, whereby the elastic part is found to be the line going through the origin and the former determined yield point on the test curve. The ultimate displacement corresponds to the point, where the test curve falls the first time below a limit of $0.8 \cdot F_{max}$, compare Figure 2.11 (b).

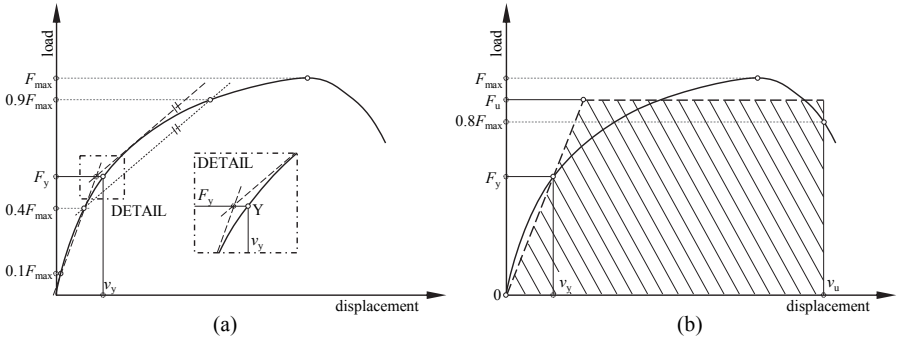

Figure 2.11: model as proposed in Yasumura and Kawai (1997) – (a) for determining the yield point; (b) for determining the ultimate load

2-3.10 EHLBECK

Ehlbeck (1979) proposes a model for describing the 'proportional limit'. However, following the used formulations in the original document as well as the explanations given in section 2-2, the term 'yield point' seems to be more convenient. As shown in Figure 2.12, the idea is to identify this point based on a small value of residual displacement. Consequently, the yield load F_y can be determined as given in Equation (2.12). The applied stiffness values $K_{ini,1}$ and $K_{ini,2}$, originally described as 'initial slip modulus' and 'slip modulus' (or 'secant slip modulus'), respectively, are defined as given in Equations (2.13) and (2.14).

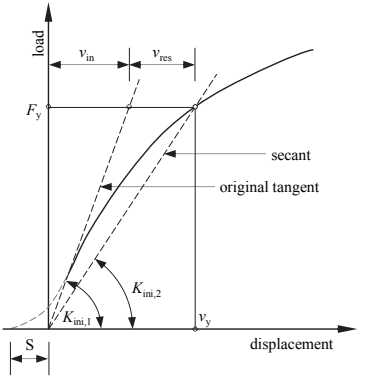

Figure 2.12: interpretation of the model given in Ehlbeck (1979)

$$F_y = \left[v_y - v_{res} \right] \cdot K_{ini,1} \tag{2.12}$$

$$K_{ini,1} = \frac{F_y}{v_{in}} \tag{2.13}$$

$$K_{\text{ini},2} = \frac{F_{\text{y}}}{v_{\text{y}}} = \frac{v_{\text{in}}}{v_{\text{in}} + v_{\text{res}}} \cdot K_{\text{ini},1} \tag{2.14}$$

with

v_{res} ..... residual displacement

Although some approaches have been discussed, a clear definition concerning the initial stiffness $K_{\text{ini},1}$ or the amount of residual displacement is missing. However, a diameter dependent offset, as for example given in ASTM D5652 (2013), is explicitly not recommended.

2-3.11 CUAP 06.03/08

CUAP 06.03/08 (2010), the "*Common Understanding of Assessment Procedure*" for self-tapping screws for use in timber constructions, includes an interesting approach for determining the characteristic yield strength as well. As illustrated in Figure 2.13, this method requires a hysteresis loop. In particular, after exceeding the estimated yield load ($F_{\text{y,est}}$), the test load is reduced to 10 % of $F_{\text{y,est}}$ and increased again till exceeding the original load afterwards. The first step while post-processing includes the construction of the midline through the hysteresis (line 1) and the parallel shifting of this line as a tangent to the original test curve (line 2). This second line, whose inclination may be interpreted as initial stiffness, is finally shifted to the prescribed percentage (here 0.2 % of elongation). The intersection of this third line with the original test curve defines the yield load.

It is also worth mentioning that the ON EN 10002-1 (2002), a standard for tensile testing of metallic materials, recommend the same procedure if the elastic branch of the load-displacement diagram is not clearly defined as a straight line.

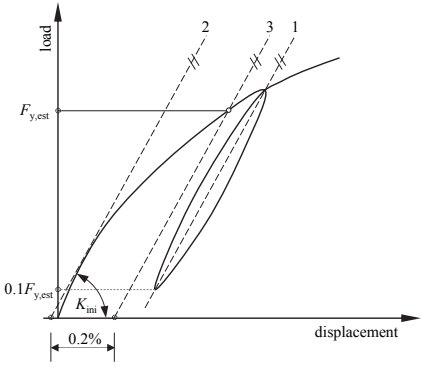

Figure 2.13: interpretation of the yield point definition according to CUAP 06.03/08 (2010) and ON EN 10002-1 (2002)

2-3.12 FURTHER MODELS

In ATC (1992) – a report dealing with cyclic testing of components of steel structures – an estimated yield load is used for determining the yield displacement and the elastic stiffness, which are subsequently used as control parameters for cyclic tests; compare Figure 2.14 (a).

Dolan (1993) presents a variation of the EEEP method where the energy equivalence for the elastic and the plastic part has to be satisfied separately; compare Figure 2.14 (b). Clear regulations according to the localization of the ultimate displacement or the determination of initial stiffness are missing. Hence, this approach has to be seen rather as a general idea than an unambiguous post-processing model.

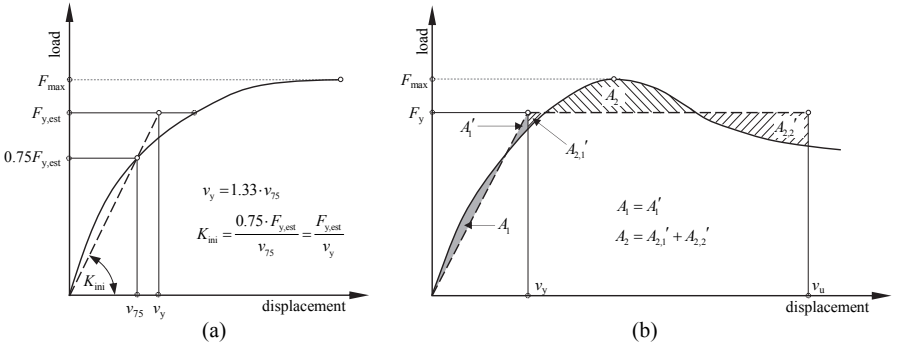

Figure 2.14: (a) determining control parameter for cyclic tests as given in ATC (1992); (b) interpretation of the EEEP approach proposed by Dolan (1993)

Focussing the yield point, in Dolan et al. (1994) two further variations of the EEEP model are shown, whereat the second one is quite similar to the method described in ASTM E2126 (2011); compare Figure 2.15 (a) and Figure 2.15 (b). Additionally, a variation of the model proposed by Ehlbeck (1979) is presented, which equalises the elastic and the residual displacement; see Figure 2.15 (c).

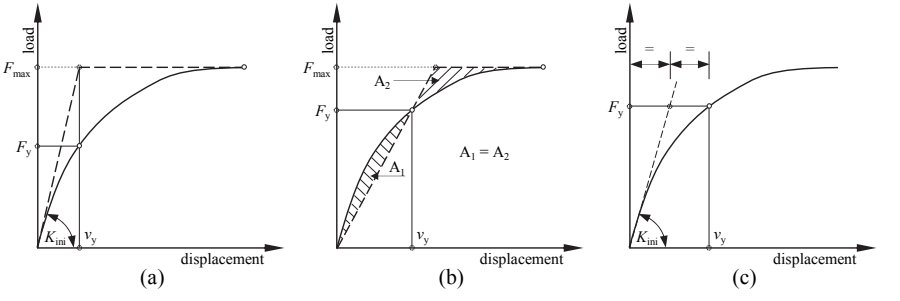

Figure 2.15: models shown in Dolan et al. (1994) – (a) equivalent elastic-plastic yield; (b) reduced stiffness; (c) ratio of yield to elastic displacement equal to 2.0

In Foliente (1996) and Karacabeyli and Ceccotti (1996), different methods for obtaining the yield load and displacement of a timber joint are discussed. Three of them are presented in Figure 2.16, whereat the model in Figure 2.16 (b) is illustrated in both publications. It is also worth mentioning that three of the four models investigated in Karacabeyli and Ceccotti (1996) further assume an ultimate displacement corresponding to the already mentioned $0.8 \cdot F_{max}$ border.

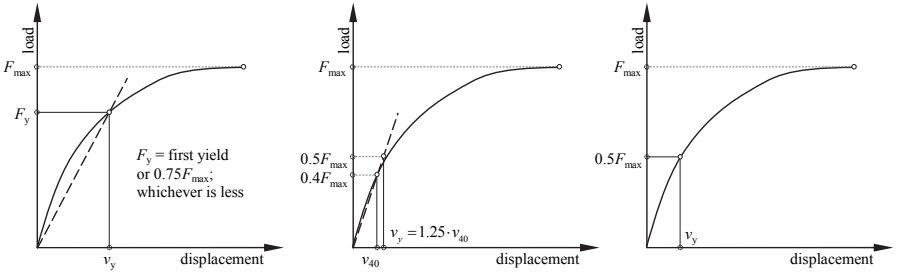

Figure 2.16: interpretation of the yield point as given in Foliente (1996) and Karacabeyli and Ceccotti (1996) – (a) model using a defined value of F_{max} or the first yield; (b) according to the Commonwealth Scientific and Industrial Research Organisation (CSIRO); (c) model used at Forintek (now FPInnovations, Canada)

Finally, an alternative method for determining the stiffness of a timber joint may be seen in the schedule for determining the Young's modulus of timber elements, given in ON EN 408 (2012). Thereby, a regression analysis of the load-displacement graph in between the 10 % and 40% borders of F_{est} have to be realised. The aim is to find the longest curve section with a correlation coefficient of 0.99 or higher. As long as this section, at least, includes the area between 20 % and 30 % of F_{est}, the initial stiffness could be calculated according to Equation (2.15); see also Figure 2.17.

$$K_{ini} = \frac{F_2 - F_1}{v_2 - v_1} \tag{2.15}$$

with

F_1 and F_2 ..... load borders of the linear branch satisfying the required correlation coefficient

v_1 and v_2..... associated displacement values

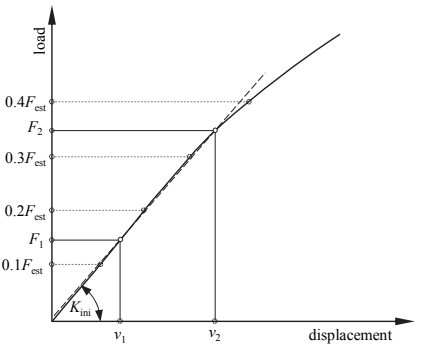

Figure 2.17: determining the initial stiffness by applying the regulations given in ON EN 408 (2012)

Note: The ON EN 408 (2012) prescribes a test data based evaluation of F_{est} and, hence, defines no limits for the deviation to the actual maximum load. This is not the case for tests with mechanical fasteners; compare ON EN 26891 (1991). Thus, for further investigations the actually reached peak load (F_{max}) is used as reference load for this model.

2-4 DISCUSSION OF SELECTED JOINT PROPERTIES

In timber engineering, the terms “load-bearing capacity”, “stiffness” and “ductility” are omnipresent within the design process. As discussed in Gehri (1993), these parameters are also the key to identify the potential and behaviour of fasteners and connections applied in timber structures. However, designing timber joints usually means to optimise the load-bearing capacity and/or the stiffness. In contrast, even if the parameter ductility is known as an important ratio, it rarely makes an appearance in practical design. Nevertheless, as a matter of common knowledge, timber itself exhibits a widely linear-elastic behaviour (except for compressive stress) and a tendency to brittle failure. Hence, if ductile behaviour in a timber structure is required (e.g., local in big area connections or global in earthquake engineering), it has to be realised by the applied fasteners and/or connections. As a consequence, due to the limited number of joints in solid timber structures using cross-laminated timber (CLT), this quality of a connection, especially here, is coming more and more to the fore; compare, e.g., Brandner et al. (2016).

As shown in section 2-3, not one, but several, approaches are available to distil the required parameters out of a load-displacement curve. To illustrate the possible range of results, a set of typical test curves is post-processed with some of these models within this section. In particular, the effect on the core parameters “initial stiffness”, “yield point”, “ultimate point” and “ductility” is investigated.

2-4.1 CONSIDERED TEST CURVES

All mentioned models use linear approximations to interpret the load-displacement behaviour. The ideal test curve for applying them would therefore possess an initial linear branch and a distinct yield point, but only few connections or fasteners in timber engineering show such characteristics. As a consequence, the accuracy of the methods does, not at least, rely on the shape of the processed load-displacement curves. For an objective assessment of the different post-processing approaches, hence, diverse curve types have to be considered.

Figure 2.18 (a) shows six different test curves, picked from research projects realised at TU Graz. Some basic information regarding the respective boundary conditions is listed in Table 2.1, but since here only the actual curve shapes are of interest, a further specification of test conditions is dispensed with.

***Table 2.1:** overview and legend for the discussed load-displacement curves*

ID	original test ID	connection or fastener	type of loading	notes
[T1]	S_V1_T41_M02	screw	tension	CLT/CLT fully threaded screw Ø 8.0x280 mm
[T2]	W_V1_T4_M03	angle bracket	tension	CLT/CLT | fixed with ringed shank nails Ø 4.0x60 mm
[S1]	W_V4_T3_M01	angle bracket	shear	CLT/CLT | fixed with ringed shank nails Ø 4.0x60 mm
[S2]	SH90_03	nail	shear	CLT/steel plate ringed shank nail, Ø 4.0x60 mm
[M1]	S_V1_T91_M04	screw	shear out of plane	CLT/CLT fully threaded screw Ø 8.0x280 mm
[M2]	S_V2_T82_M02	screw	shear orthogonal	CLT/CLT step joint fully threaded screw Ø 6.0x80 mm

As visible, the original scale of the chosen load-displacement relationships exhibit completely different courses. Enabling an assessment, based only on their shape, the test data have to be normalised. For this purpose, the curves are scaled to F_{max} and v_u for the axis of ordinates and axis of abscissae, respectively (v_u is assumed at 80 % of F_{max} in the descending branch of the test curve); compare Figure 2.18 (b).

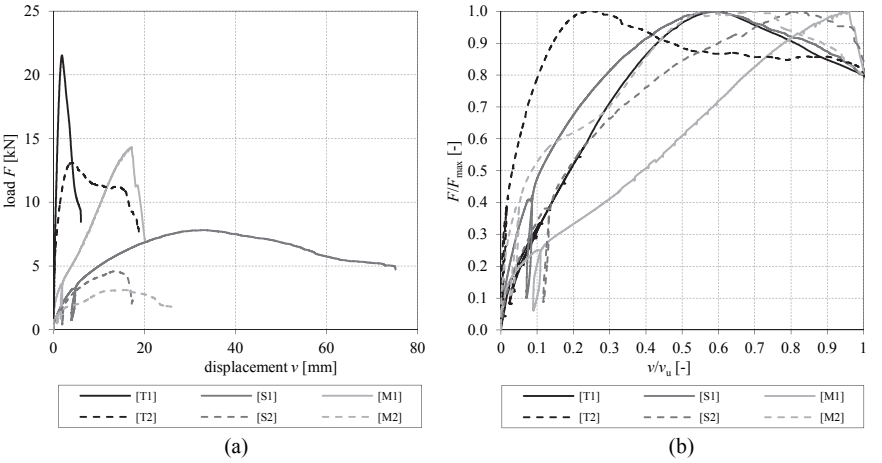

Figure 2.18: typical load-displacement curves for different fasteners and connections – (a) behaviour in original scale; (b) curves scaled to F_{max} and v_u

A first appraisal of the normalised curves in Figure 2.18 (b) shows a clear variation regarding the position where the ratio F/F_{max} reaches the value 1.0. Since this point can also be described by the ratio v_{max}/v_u, it consequently may be used for a rough classification regarding brittle or ductile behaviour; compare section 2-4.5.

As initially intended, the normalised form further allows distinguishing between the actual shapes of the test curves in a more certain way; especially in the area up to F_{max}. Figure 2.19 shows the chosen classification, using three groups.

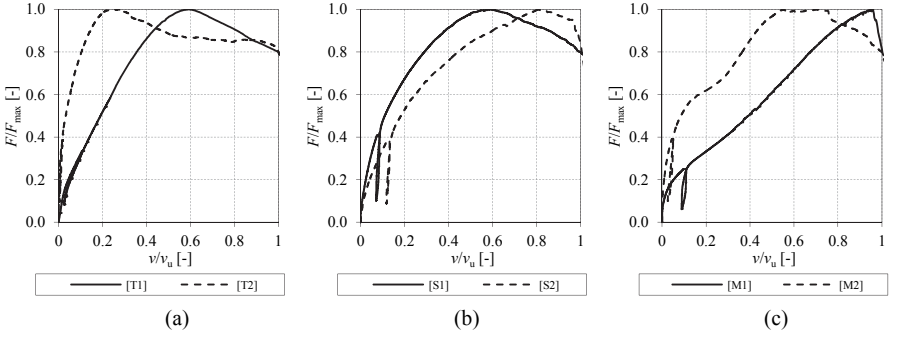

Figure 2.19: classification of load-displacement curves – (a) typical curve shapes for tension loaded timber joints; (b) typical curves shape for shear loaded timber joints; (c) possible other shapes appearing for load-displacement curves gathered from timber joints

The first group contains typical shapes for tension loaded joints [T] where the initial branch is often characterised by a nearly linear trend; compare Figure 2.19 (a). In contrast, Figure 2.19 (b) illustrates test

curves exhibiting an even round shape which is rife for shear [S] or moment loaded connections. Testing timber joints can also result in a mixture [M] of linear and round parts which markedly complicates their interpretation. Experimental diagrams, showing latter (sometimes local) behaviour, are collected in the third group; compare Figure 2.19 (c).

Since representing a good portion of possible load-displacement relationships appearing for timber joints equipped with mechanical fasteners, the following discussions regarding the already mentioned parameters primarily rely on these six test curves; occurring deviations are distinctively indicated.

2-4.2 INITIAL STIFFNESS

Besides the load-bearing capacity, the stiffness is actually the most important design parameter in constructive engineering. For materials, this property is generally given as the ratio between stress and strain in the linear elastic range (expressed as modulus of elasticity E). Similarly, the stiffness of a joint is defined by the ratio of load and displacement or moment and rotation. Although serving the same purpose, the available post-processing models do exhibit differences; compare section 2-3. Hence, the following passages comprise a general discussion regarding the determination of this parameter and its use in current standards.

2-4.2.1 The working load level

The bulk of methods, described in section 2-3, use the branch beneath 40 % of the achieved maximum load for determining the initial stiffness. This border has already been mentioned in Vermeyden (1963), labelled as ‘working load’. Furthermore, compared with the semi-probabilistic safety concept used in current European standards, the 40 % level nearly equates the resistance required for satisfying the ultimate limit state. Since it is important for the further discussions, this circumstance is derived within the current section.

Equation (2.16) exhibits the basic relationship between actions and resistances, as given in ON EN 1990 (2013).

$$E_d \leq R_d \tag{2.16}$$

with

E_d ..... design value of effect of actions

R_d ..... design value of the resistance

Applying the fundamental combination of actions, as given in ON EN 1990 (2013), in combination with the requirements for timber joints according to ON EN 1995-1-1 (2014), leads to the expression given in Equation (2.17)

$$\sum_{j\geq 1} \gamma_{G,j} \cdot G_{k,j} \text{ "+" } \gamma_{Q,1} \cdot Q_{k,1} \text{ "+" } \sum_{i>1} \gamma_{Q,i} \cdot \psi_{0,i} \cdot Q_{k,i} \leq \frac{R_k \cdot k_{mod}}{\gamma_M} \tag{2.17}$$

with

$G_{k,j}$ ..... characteristic value of permanent actions *j*
$Q_{k,1}$ ..... characteristic value of the leading variable action
$Q_{k,i}$ ..... characteristic value of the accompanying variable actions *i*
R_k ..... characteristic load-carrying capacity
k_{mod} ..... modification factor for duration of load and moisture content
γ_M ..... partial factor for material properties, also accounting for model uncertainties and dimensional variations
$\gamma_{G,j}$ | $\gamma_{Q,i}$ ..... partial factors for permanent actions *j* and variable actions *i*
$\psi_{0,i}$ ..... factor for combination value of a variable action *i*

For the ultimate limit state (ULS) the partial factors for permanent actions and variable actions are usually equal to 1.35 and 1.5, respectively. Furthermore, the partial factor for material properties, used for timber joints, is generally set to 1.3. Consequently, assuming a simple load situation with only one permanent as well as one variable action Equation (2.17) changes to Equation (2.18).

$$1.35 \cdot G_k + 1.5 \cdot Q_k \leq \frac{R_k \cdot k_{mod}}{1.3} \tag{2.18}$$

A further simplification is possible if the partial factors on the action side are summarised to a ‘global’ partial factor of 1.4. Furthermore, the modification factor k_{mod}, which actually receives values between 0.60 and 1.10, could roughly be set to 0.85 in average.

According to ON EN 14358 (2016), the characteristic value of the resistance is defined by the fifth percentile value of the resistance, means $R_k = R_{05}$. Assuming a logarithmic normal distribution (LND), similar to the regulations in ON EN 14358 (2016), Brandner (2012) schedules the following expression:

$$R_{05} = F_{max,mean} \cdot \frac{\exp\left[-1.645 \cdot \sqrt{\ln(CoV^2 + 1)}\right]}{\sqrt{CoV^2 + 1}} \tag{2.19}$$

with

R_{05} ..... 5 % percentile of the connections resistance
$F_{max,mean}$ ..... mean value of the connections resistance
CoV ..... coefficient of variation

Additionally, ON EN 14358 (2016) does not allow to use coefficients of variation lower than 5%. Entering this value in Equation (2.19) results in a ratio between R_k and $F_{max,mean}$ of 0.92. Basing on own experience, a CoV of 30 % is taken to generate a lower border for this factor, resulting in a ratio of 0.59.

However, for the following explanations an average *CoV* of 15 % and a resulting R_k-to-$F_{max,mean}$ value of 0.77 is assumed; compare Equation (2.20).

$$1.4 \cdot (G_k + Q_k) \leq \frac{F_{max,mean} \cdot 0.77 \cdot 0.85}{1.3} \tag{2.20}$$

Finally, the ratio between the mean value of resistance and the effect of actions, which could be seen as a kind of global safety factor, is identified to be approximately 2.8; see also Equation (2.21).

$$2.8 \leq \frac{F_{max,mean}}{(G_k + Q_k)} \tag{2.21}$$

The mentioned minimum and maximum borders for the *CoV* (5 % and 30 %) lead to factors between 2.3 and 3.6, respectively.

A similar illustration is possible if the safety concept given in SIA 164 (1992), used in Switzerland up to 2004, is applied. This concept was principally based on permissible forces and includes the possibility to determine the permissible reaction force by the mean value of maximum loads gathered from tests, divided by a safety factor equal to 3.0. The approach for calculating the effect of actions, which was regulated in SIA 160 (1989), uses a comparable concept as given in Equation (2.18). Linking this information, leads to a global safety factor of 2.8 too; compare Equation (2.22).

$$1.4 \cdot (G_k + Q_k) \leq 1.5 \cdot \frac{F_{max,mean}}{3.0} \quad \Rightarrow \quad 2.8 \leq \frac{F_{max,mean}}{G_k + Q_k} \tag{2.22}$$

As illustrated, both the semi-probabilistic safety concept, used in the current European standards, and the older safety concept, based on permissible forces, exhibit a global safety factor of about 2.8. In other words, the sum of characteristic actions may not exceed 36 % of the resistance' mean value. Using the mentioned variation of the *CoV*, the borders of the 'ultimate limit state area' can be indicated with 43 % (*CoV* = 5 %) as an upper and 28 % (*CoV* = 30 %) as a lower limit.

Discussing this context also raises the question about the borders for the serviceability limit state (SLS). Even if no conventional stress analysis is necessary for verifying this limit state, a maximum load level could be estimated as a consequence of the ULS constrains. Therefore, the ULS border of 36 % has to be divided by the assumed 'global' partial factor of 1.4. This, because according to the ON EN 1990 (2013), all partial factors for determining the design actions for the SLS are equal to 1.0. Consequently, the permitted loads in the serviceability limit state may not exceed about 26 % of the connections' resistance (31 % for *CoV* = 5 % and 20 % for *CoV* = 30 %). Both, the ULS and the SLS levels are illustrated in Figure 2.20.

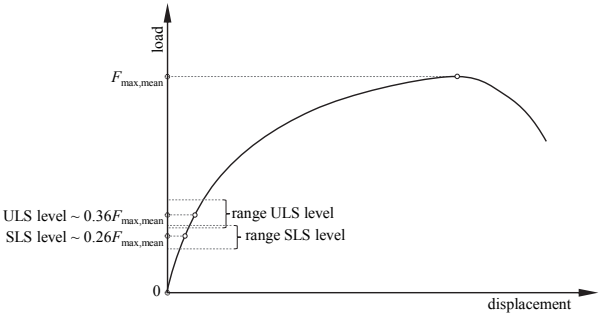

Figure 2.20: ultimate and serviceability limit state levels in relation to an original load-displacement curve

Although the presented calculations do base on several simplifications, they clearly identify the design-relevant area of a test curve beneath the mentioned 40 % level. Hence, the circumstance that post-processing models do concentrate on this area for determining the initial stiffness is comprehensible. Nevertheless, it may not be concealed that similar considerations for accidental load cases result in possible ranges of round 60 to 80 % of $F_{max,mean}$.

2-4.2.2 Comparing model results

As already mentioned, selected post-processing models will be applied to the six test curves visualised in Figure 2.18; the considered methods are summarised in Table 2.2.

Table 2.2: selected stiffness models used for comparison

source	K_{ini}	notes
EN 26891 ($K_{ini,1}$)	$\frac{0.3 \cdot F_{est}}{v_{04} - v_{01}}$	stiffness referenced in ON EN 1995-1-1 (2014)
EN 26891_2 ($K_{ini,2}$)	$\frac{0.4 \cdot F_{est}}{v_{04}}$	-
ASTM	tangent at origin	assumed between origin and 20 % of F_{max}
EN 12512	$\frac{0.3 \cdot F_{max}}{v_{40} - v_{10}}$	not explicit defined as stiffness in the source
SIA 265	$\frac{0.4 \cdot F_{max}}{v_{40}} = \frac{F_y}{v_y}$	-
EN 594	$\frac{1}{2} \cdot \left[\frac{F_{04} - F_{01}}{v_{04} - v_{01}} + \frac{F_{24} - F_{21}}{v_{24} - v_{21}} \right]$	version of 1996
Y & K	$\frac{F_y}{v_y}$	
CUAP	slope angle of hysteresis	not explicit defined as stiffness in the source
EN 408	0.99 correlation coefficient between 10% and 40% F_{max}	-

With respect to the circumstance that not all models offer distinct definitions for the initial stiffness, the following boundary conditions are applied:

(i) The 'initial linear portion' in the ASTM-model (compare section 2-3.2) is assumed to be the secant, passing the origin and the point where 20 % of F_{max} is reached.

(ii) For the model of Yasumura and Kawai (Y & K) the slope of the line connecting the origin with the yield point will be used as assigned stiffness. The 'first' initial stiffness of this model is equal to the regulations in the EN 12512 (compare section 2-3.9).

(iii) Although the inclination of the line, being necessary for devising the yield point according to the CUAP, is not explicit defined as a stiffness value (equal to the regulations in the EN 12512), it will be used for the following discussion too. Furthermore, in absence of an alternative, the slope angle is defined according to the actual hysteresis available from test data (reference points at 10 % and 40 % F_{est}).

The resulting stiffness parameters and some associated statistics are given in Table 2.3. Additionally, Figure 2.21 illustrates the different stiffness values in relation to the original test curve and the working load level.

Table 2.3: initial stiffness values according to different models and curve types

source	units	[T1]	[T2]	[S1]	[S2]	[M1]	[M2]
EN 26891 ($K_{ini,1}$)	[kN/mm]	18.135	16.114	0.610	0.714	-	0.988
EN 26891_2 ($K_{ini,2}$)	[kN/mm]	21.234	20.151	0.736	0.866	-	1.270
ASTM	[kN/mm]	30.445	57.445	1.185	1.348	3.027	2.990
EN 12512	[kN/mm]	16.140	14.974	0.648	0.655	0.862	0.828
SIA 265	[kN/mm]	19.114	18.819	0.779	0.795	1.117	1.068
EN 594	[kN/mm]	18.833	17.929	1.636	2.389	4.054	1.297
CUAP	[kN/mm]	19.530	19.744	2.662	4.064	6.596	1.607
Y & K	[kN/mm]	17.241	12.821	0.627	0.710	0.982	0.854
EN 408	[kN/mm]	15.036	11.611[1)]	0.652	0.705	1.012	0.838
median	[kN/mm]	18.83	17.93	0.74	0.79	1.12	1.07
max	[kN/mm]	30.45	57.44	2.66	4.06	6.60	2.99
min	[kN/mm]	15.04	11.61	0.61	0.65	0.86	0.83
ratio max/min	[-]	2.0	4.9	4.4	6.2	7.7	3.6

[1)] max. reached correlation 98 %

Note: The stiffness values according to ON EN 26891 (1991) for curve type [M1] are not considered. This, because the deviation between the chosen estimated load (F_{est}) and the reached maximum load (F_{max}) exceeds the permitted limit of 20 % (actually 37 % for this test). Despite this circumstance, the inclination of the corresponding hysteresis is considered for the CUAP stiffness; detailed justification is given later on – compare Figure 2.24.

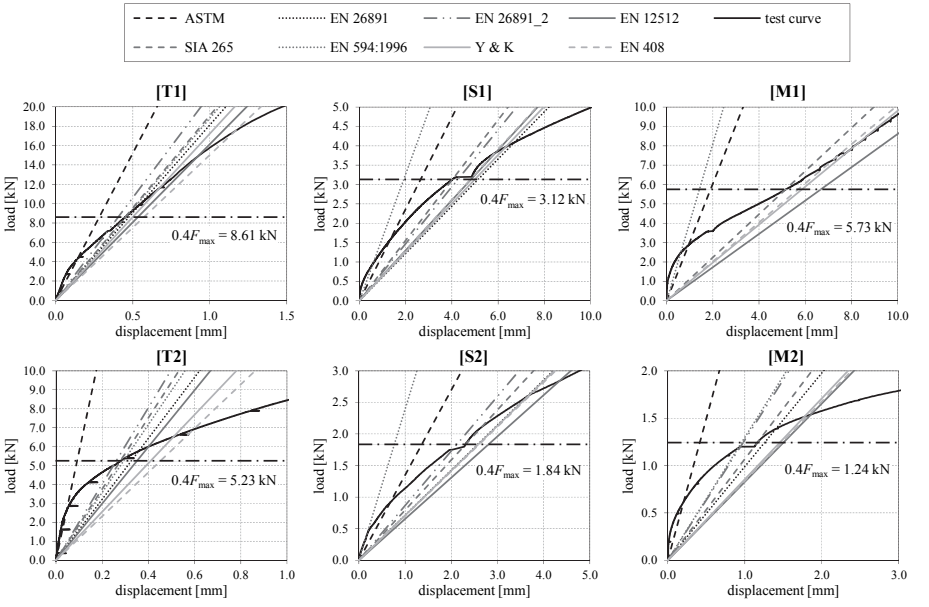

Figure 2.21: stiffness ratios for the considered test curves relating to the respective working load area

As expected, huge differences occur between the considered models. In particular, they are expressed through the respective max/min ratios (2.0 to 7.7). Furthermore, the maximum and minimum results are not always related to the same model. This confirms the hypothesis that the shape of a test curve also influences the accuracy of the models applied. Hence, mechanisms influencing the resulting stiffness values are discussed more in detail in the following sections.

Reference Points

Obviously, a clear difference exists between stiffness values using the origin (here termed as $K_{ini,0}$) or the 10 % level of the considered maximum load (F_{max} or F_{est}; here termed as $K_{ini,10}$) as initial reference point. The presented results in Table 2.3 always exhibit higher values for the first model (e.g. SIA 265 vs. EN 12512 or EN 26891_2 vs. EN 26891). This due to the concave shape in the very first branch of the respective test curves; compare Figure 2.22 (b). As illustrated in Figure 2.22 (a), a convex course would show higher stiffness values for $K_{ini,10}$.

In this context it has to be further mentioned that practical design usually starts at the origin. As a consequence, the linear branch corresponding to $K_{ini,10}$ has to be shifted to the origin and, hence, neglects any initial behaviour of the joint; see also Figure 2.22.

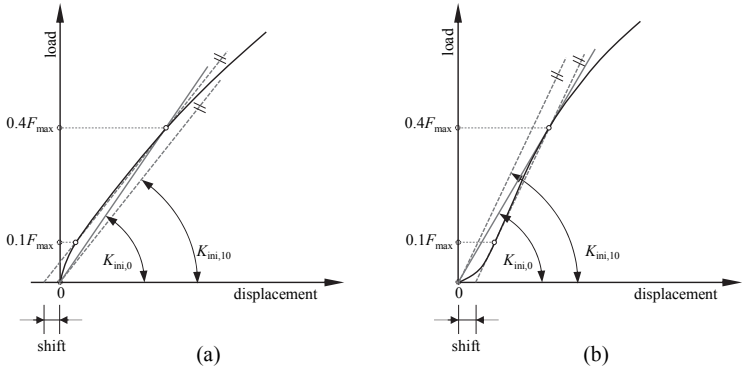

Figure 2.22: influence of reference points – (a) for concave initial curve shapes; (b) for convex initial curve shapes

Examining the stiffness ratios resulting from the ASTM model shows that this method leads to the highest values in three of the six considered cases. Here, the chosen low load level for the second reference point (20 % of F_{max}) is detected as the main reason. Nevertheless, even if a higher reference point would lead to a lower slope angle, it would contradict the basic intension of this model, i.e., stiffness at the origin.

Hysteretic stiffness

As described in sections 2-3.6.1 and 2-3.11, the regulations in ON EN 594 (1996) and CUAP 06.03/08 (2010) refer to the slope of the hysteresis. As a consequence, these models often result in distinctive higher stiffness properties compared to the one corresponding to the first loading branch; compare course of hystereses in Figure 2.18. An explanation regarding the high inclination of the un- and reloading paths of the hysteresis is given within the following passages.

While the initial consolidation, and especially at higher load levels, plastic deformations of the wood matrix, surrounding the single fasteners, occur. These deformations do not recede while unloading the connection, which results in a very fast loss of load within a short amount of displacement. When the load is increased again, the fastener perfectly fits the surrounding wood and therefore the accompanied deformations are smaller than during the first loading; compare Dorn et al. (2013). Both effects behave nearly linear and result in the mentioned high stiffness values.

At this point the question rises, if the slope of the hysteresis should not generally be used as the initial stiffness. An argument for this purpose is that in practical use connections are loaded and unloaded more than once. Consequently, the higher stiffness values actually appear. Furthermore, the main task of the initial stiffness ratios is to describe the elastic behaviour of a connection or fastener, which is, according

to the ON EN 26891 (1991), represented through this value too. Additionally, as published in Dorn et al. (2013), this stiffness keeps nearly constant over the whole loading period.

The reasons why the hysteretic stiffness should not be used anyway gets visible when a fully reversed cyclic test is compared with a corresponding monotonic one. For example, Figure 2.23 (a) illustrates the monotonic and the cyclic test curve of a shear loaded single nail (connection responsible for curve type [S2]). Confirming the observations described in Dorn et al. (2013), the slope angle according to the hysteretic branch of the monotonic test curve fits very well with the cyclic unloading paths.

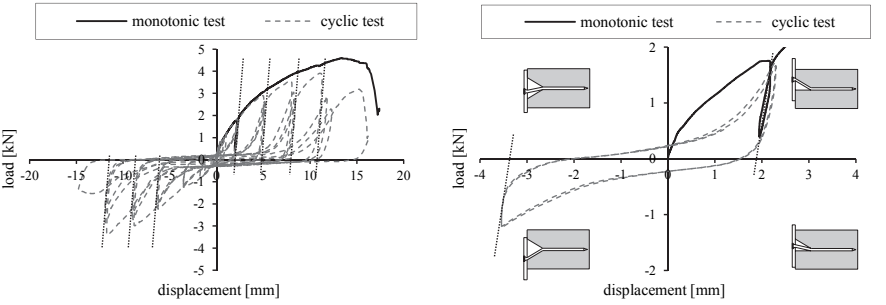

Figure 2.23: hysteretic stiffness of a single nail (configuration [S2]) – (a) comparison of monotonic and cyclic test; (b) single group of fully reversed cycles and associated nail deformations

However, the dramatically decrease of stiffness at the unloading path after passing a low load level is not covered by the single hysteresis. For a single fastener this reflects the point where it starts losing the contact to the surrounding (already plastically deformed) wood matrix. The load is not increasing anymore until the fastener gets contact with the ambient timber again. The low stiffness values between represent a mixture of the fasteners bending stiffness and friction. Furthermore, the reloading paths show a convex shape and therefore much lower grades over a long period, even lower than the initial stiffness of the monotonic test curve. Nevertheless, caused by the already compacted wood matrix, at the end of the cycles the inclination increases quite fast again. This also explains the typical pinched shape of load-displacement diagrams for cyclic loaded timber connections and is illustrated in Figure 2.23 (b).

Although the explained background bases on a single fastener, the same mechanisms occur for timber joints using multiple fasteners. Of course, here further parameters (e.g., cyclic behaviour of metal plates) are involved too but, as illustrated in Figure 2.24, the principles and the results are comparable.

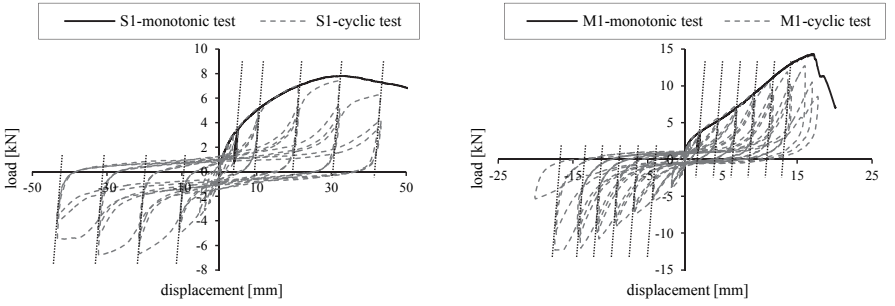

(a) (b)

Figure 2.24: comparison of hysteretic stiffness – (a) test curves of an angle bracket (curve type [S1]); (b) test curves of a shear loaded screw (curve type [M1])

Summarising, it can be stated that the hysteresis based stiffness values indeed represent a kind of elastic stiffness, but also neglect the plastic deformations occurring at even low load levels. Furthermore, the resulting stiffness values are usually used for calculations starting from the origin. Applying the high stiffness properties would therefore underestimate the appearing deformations or, the other way round, overestimate the occurring loads. Nevertheless, for investigating the deformation capacity of already erected structures, e.g., while restorations, information regarding the hysteretic stiffness might be quite useful.

F_{est} vs. F_{max}

Neglecting ON EN 594 (1996), which is not in force anymore, only ON EN 26891 (1991) and ON EN 408 (2012) include regulations using the estimated maximum load (F_{est}) for determining the reference points finally leading to the stiffness properties. Other standards and proposals usually use definitions basing on the actual peak load F_{max}; compare Table 2.2. Hence, some deliberations concerning this topic are given in the current section.

If F_{est} is chosen properly, the resulting stiffness parameters of the considered test series clearly refer to the already described (estimated) working load level. As illustrated in Figure 2.25 (a), this applies independently from specimens' behaviour beyond this point. However, ON EN 26891 (1991) allows deviations between F_{est} and the actual occurring mean peak load ($F_{max,mean}$) of up to 20 %. As a consequence, a pronounced over- or underestimation of the actual working load, and finally the corresponding stiffness, may appear; this especially if the variation of maximum loads is small.

In contrast, considering F_{max} perfectly fits the working load for each test specimen, but does not lead to the stiffness representing the (finally decisive) working load level of the test series (in this case a smaller variation of the reached maximum loads would be positive); compare Figure 2.25 (b).

Although currently not used, the consideration of test series' mean maximum load $F_{max,mean}$ for determining the stiffness properties, as illustrated in Figure 2.25 (c), would combine the advantages of both models and thus might lead to more convenient results.

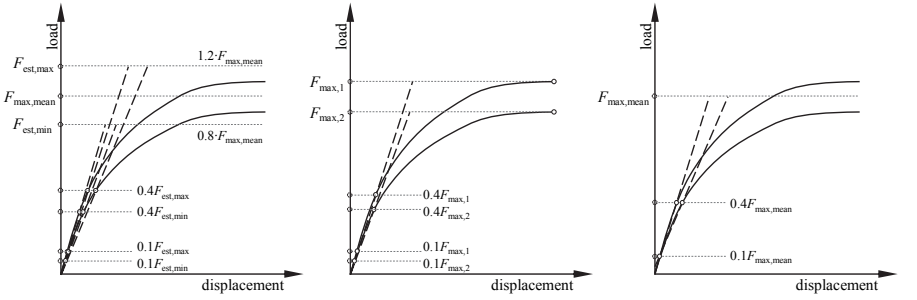

Figure 2.25: determining the stiffness of a test series based on estimated or actually reached maximum loads – (a) determination basing on F_{est}; (b) determination basing on F_{max}; (c) proposal with respect to $F_{max,mean}$

Of course, the herein discussed topic does not really concern test curves with a long linear elastic branch, but for load-displacement relationships with round shapes from the origin decisive deviations are possible. To illustrate this circumstance, Table 2.4 lists the stiffness properties for a small test series on shear loaded angle brackets connecting two CLT elements (further test details are given in section 5-2.2.3); Figure 2.26 illustrates the corresponding load-displacement graphs.

Table 2.4: comparison of different models for defining the stiffness ($F_{est,max}$ = 26.81 kN and $F_{est,min}$ = 17.87 kN)

ID	F_{max} [kN]	$K_{ini,Fest,max}$ [kN/mm]	$K_{ini,Fest,min}$ [kN/mm]	$K_{ini,Fmax}$ [kN/mm]	$K_{ini,Fmax,mean}$ [kN/mm]
W_V1_T3_M01	23.1	2.286	2.782	2.279	2.543
W_V1_T3_M02	21.2	1.917	2.593	2.295	2.209
W_V1_T3_M03	22.4	2.289	3.287	2.721	2.751
W_V1_T3_M04	22.7	2.101	2.741	2.082	2.364
mean values	22.3	2.148	2.851	2.344	2.467

The presented results clearly show the mentioned influence of small variations regarding the maximum load (here CoV = 3.6 %). In particular, the stiffness values based on $F_{est,max}$ and $F_{est,min}$ exhibit deviations of 25 % in average. Moreover it turns out that assuming low estimated loads tend to result in higher stiffness properties and vice versa.

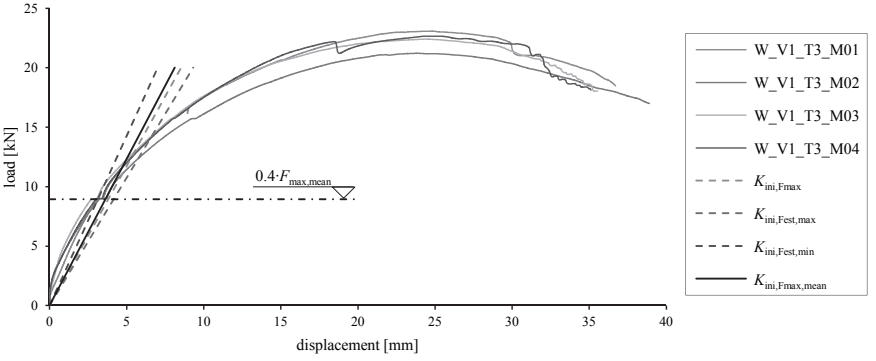

Figure 2.26: different stiffness values for a test series of shear loaded angle brackets (illustrated linear branches refer to respective mean values listed in Table 2.4)

2-4.2.3 Stiffness values in European standards

Since it is impossible to perform experimental tests for all joint variations, design standards often include proposals for determining the initial stiffness of single fasteners. Afterwards, the resulting values can be used to estimate the stiffness of connections consisting of more than one fastener.

Within this section, firstly, the background concerning regulations given in ON EN 1995-1-1 (2014) is reviewed. Secondly, the approaches currently scheduled in the Eurocode 5 and SIA 265 (2012) are briefly summarised and compared. In a final step, a comparison between the respective models and experimentally gathered stiffness properties is presented.

Background of stiffness regulations in Eurocode 5

The first presumptions regarding the deformation of shear loaded doweled and bolted joints with a single fastener at working load level are given in Johansen (1949); compare Equations (2.23) and (2.24). For these expressions it is assumed that the holes for dowels are predrilled with a slightly smaller diameter, the holes for bolts with the same diameter, as the tested fasteners. Furthermore, the working load per fastener and shear plane is defined as given in Equation (2.25). As a consequence, the elastic stiffness for doweled and bolted connections up to the working load level can be expressed as given in Equations (2.26) and (2.27)

$$v_{dowel}(F_w) = 0.04 \cdot d \tag{2.23}$$

$$v_{bolt}(F_w) = 0.1 \cdot d \tag{2.24}$$

$$F_w = 22.81 \cdot d^2 \tag{2.25}$$

$$K_{\text{ini,dowel}} = 570 \cdot d \tag{2.26}$$

$$K_{\text{ini,bolt}} = 228 \cdot d \tag{2.27}$$

with

d ..... diameter of the fastener [mm]

F_w ..... working load of a single fastener [N]

Based on the linear elastic solution given in Wilkinson (1972), Smith et al. (1984) and Whale and Smith (1986) described the initial stiffness for nailed joints and low loads as given in Equation (2.28). Thereby, for all timber members the same embedding strength and a tendency to failure mode 'f' (two plastic hinges per shear plane), are assumed.

$$K_{\text{ini}} = \frac{0.665668}{4} \cdot E_{\text{nail}}^{0.25} \cdot k_{01}^{0.75} \cdot d^{1.75} \tag{2.28}$$

with

E_{nail} ..... modulus of elasticity of nail [N/mm²]

k_{01} ..... elastic bearing constant of member 1 (stress per unit embedment) [N/mm³]

d ..... nail diameter [mm]

Note: According to Whale and Smith (1986), the elastic bearing constant describes the tangent to the initial portion of the load-embedment curve.

Based on experimental test results, Whale and Smith (1986) simplified Equation (2.28) for softwoods to Equation (2.29). The authors stated that this expression (for low loads) fits well to the results gathered from nonlinear Equation (2.30). The latter was given in draft Eurocode at this time and presumes that the characteristic load is reached at a displacement equal to 50 % of the nails' diameter.

$$K_{\text{ini}} = 5.15 \cdot \rho_m^{0.75} \cdot d^{0.95} \tag{2.29}$$

$$v_i = 0.5 \cdot d \cdot \left(\frac{F_i}{R_k} \right)^{1.5} \tag{2.30}$$

with

ρ_m ..... mean density [kg/m³]

v_i ..... displacement corresponding to F_i

F_i ..... actual force

Whale and Smith (1986) further confirmed the approximations then in force, determining the slip of doweled and bolted joints at about one third of the characteristic bearing capacity as given in Equations (2.31) and (2.32), respectively.

$$v_{\text{dowel}}\left(\sim\frac{R_{\text{k}}}{3}\right)=0.1\cdot d \tag{2.31}$$

$$v_{\text{bolt}}\left(\sim\frac{R_{\text{k}}}{3}\right)=0.1\cdot d+1\,\text{mm} \tag{2.32}$$

At this point it is worth mentioning that $R_k/3$ approximately equates the SLS load level. This gets obvious if the derivations, given in section 2-4.2.1, are applied on the characteristic instead of the mean load-carrying capacity. The resulting relations for the ultimate and service ability limit state are expressed in Equations (2.33) and (2.34), respectively.

$$\text{ULS}\le\frac{R_{\text{k}}\cdot 0.85}{1.3\cdot 1.4}\quad\Rightarrow\quad\text{ULS}\le\frac{R_{\text{k}}}{2.14} \tag{2.33}$$

$$\text{SLS}\le\frac{R_{\text{k}}}{2.14\cdot 1.4}\quad\Rightarrow\quad\text{SLS}\le\frac{R_{\text{k}}}{3.0} \tag{2.34}$$

A further interesting link appears if the actual force F_i in Equation (2.30) is set equal to $R_k/3$. Due to the resulting expression it seems that (on this load level) no real difference between the deformations of nailed or doweled joints was made; compare Equations (2.35) and (2.31).

$$v_{\text{nail}}\left(\frac{R_{\text{k}}}{3}\right)=0.096\cdot d \tag{2.35}$$

A model for estimating the load-bearing capacity of nailed joints is given in Whale et al. (1987); compare Equation (2.36). Thereby, again, an equal embedding strength of involved timber members and a slender nail provoking the failure mode ‘f’ are assumed. Furthermore, the accuracy of Equation (2.30), determining the slip of nailed joints at about one third of the characteristic load-carrying capacity (R_k), was confirmed by experimental results. The initial stiffness ratio could therefore be expressed as given in Equation (2.37).

$$R_{\text{k}}=5.7\cdot\rho_{\text{k}}^{0.5}\cdot d^{1.6} \tag{2.36}$$

$$K_{\text{ini}}=19.75\cdot\rho_{\text{k}}^{0.5}\cdot d^{0.6} \tag{2.37}$$

with

ρ_k ..... characteristic density [kg/m³]

The experimental campaigns presented in Whale et al. (1987) also include tests on bolted joints. Thereby it was found that the expected deformations, gathered from Equation (2.32), overestimate the joint slip at the SLS level by a factor of about 2.5. The massive deviation was explained by the test configuration which did not include the allowed tolerance of 1 mm for bolted connections. However, all test specimens consisted of three timber members and show mode ‘h’ failures according to Eurocode 5,

i.e., an embedding failure of the middle timber member without any plastic hinge in the bolt. Thus, a further possible reason for the low slip values has to be seen in the small thickness of involved timber members, leading to the mentioned failure mode and consequently to low deformations before failure; see also Figure 2.29 and relating explanations.

For determining the slip of doweled joints in softwoods at load levels less than $F_{max}/2.75$ (represents the permissible force according to the former German standard for timber constructions DIN 1052), Ehlbeck and Werner (1988b) proposed Equation (2.38). Thereby, K_{ini} and v_s represent the initial stiffness according to ISO 6891 (1983), which is approximated by Equation (2.39) and the initial slip, respectively.

$$v_i\left(F_i\right) = \frac{F_i}{K_{ini}} + v_s \tag{2.38}$$

$$K_{ini} = (1.2 \cdot d - 1.6) \cdot \rho_m \tag{2.39}$$

For the then prepared draft Eurocode 5, Ehlbeck and Werner (1988a) suggested the slightly simplified formulation given in Equation (2.40) for estimating the initial slip modulus of doweled joints at load levels less than 40 % of the characteristic load. Furthermore, for doweled and bolted softwood joints, the initial slip in v_s is indicated to be equal to 0.2 mm and 1.2 mm, respectively.

$$K_{ini} = d \cdot \rho_k \tag{2.40}$$

It is further worth mentioning that the original formulations also include a factor, appropriate for the possible influence of creep. However, since uniformly set equal to 1.0, it is not considered in the expressions given above.

The regulations regarding the stiffness of nailed and doweled joints in the current Eurocode 5 are mainly basing on the derivation given in Ehlbeck and Larsen (1993). In particular, in a first step the reference load level for determining the stiffness values, applicable in the service ability limit state, was defined to be equal to 40 % of the characteristic load. Furthermore it was assumed that there is no difference in stiffness between (thick) nails in predrilled holes and dowels driven into tight-fitting predrilled holes. Further necessary assumptions for the derivation were:

(i) a nailed timber-to-timber connection
(ii) no influence of the axial load-carrying capacity (‘rope effect’)
(iii) no influence of the load-to-grain direction
(iv) equal embedding strength ($f_{h,k}$) for all involved timber members expressed as

$$f_{h,k} = 0.00082 \cdot (100 - d) \cdot \rho_k \tag{2.41}$$

(v) a nail slenderness leading to failure mode ‘f’ (two plastic hinges) which is represented by Equation (2.42)

$$R_k = \sqrt{2 \cdot M_y \cdot f_{h,k} \cdot d} \tag{2.42}$$

(vi) and a yield moment (M_y) as given in Equation (2.43)

$$M_y = 180 \cdot d^{2.6} \tag{2.43}$$

For nailed joints with predrilled holes, satisfying the above mentioned boundary conditions, the characteristic load-carrying capacity can, hence, be expressed as given in Equation (2.44).

$$R_k = \sqrt{0.3 \cdot (100 - d) \cdot d^{3.6} \cdot \rho_k} \tag{2.44}$$

Based on *“(...) many tests available from various test laboratories (...)*” Ehlbeck and Larsen (1993) estimate the instantaneous slip at $0.4 \cdot R_k$ for the considered joint as given in Equation (2.45).

$$v_{40} = \frac{40 \cdot d^{0.8}}{\rho_k} \tag{2.45}$$

As a consequence, the initial stiffness value for the service ability limit state (K_{ser}) can be calculated as documented in Equation (2.46).

$$K_{ini} = K_{ser} = \frac{0.4 \cdot R_k}{v_{40}} = \frac{0.55 \cdot \sqrt{(100 - d)} \cdot d \cdot \rho_k^{1.5}}{100} \approx \frac{\rho_k^{1.5} \cdot d}{20} \tag{2.46}$$

For the ultimate limit state, a reference load level equal to 60 to 70 % of the characteristic load is assumed, which is obviously higher than the 47 % resulting from Equation (2.33). However, without any further information, Equation (2.47) was proposed for determining the ULS stiffness K_u.

$$K_u = \frac{2}{3} \cdot K_{ser} \tag{2.47}$$

Figure 2.27 finally depicts the serviceability limit state stiffness K_{ser} and the ultimate limit state stiffness K_u, according to the assumptions described in Ehlbeck and Larsen (1993).

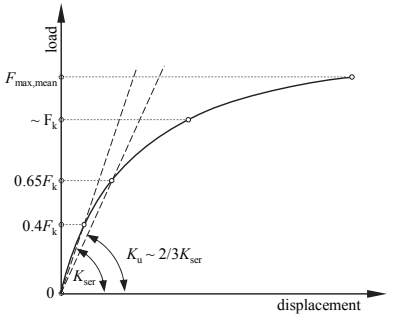

Figure 2.27: K_{ser} and K_u according to Ehlbeck and Larsen (1993); F_k is equivalent to R_k

Table 2.5 summarises the above described models for dowels and nails (with predrilled holes). Solely the listed Johansen model depicts the approach for bolts; this due to equal pre-drilling regulations. Moreover, for a better comparability, basing on assumptions documented in Whale et al. (1987), the mean density used in the original model of Whale and Smith (1986), is substituted by the characteristic density.

Table 2.5: overview stiffness models and associated reference loads

model	K_{ini} [N/mm]	**reference load**	**reference load basing on $F_{max,mean}$**	
			$CoV = 5\%$	$CoV = 15\%$
Johansen 1949	$228 \cdot d$	$22.81 \cdot d^2$	-	-
Whale 1986	$5.15 \cdot \rho_k^{0.75} \cdot d^{0.95}$	'low loads'	-	-
Whale 1987	$19.75 \cdot \rho_k^{0.5} \cdot d^{0.6}$	$R_k/3$	$0.31 \cdot F_{max,mean}$	$0.26 \cdot F_{max,mean}$
Ehlbeck 1988	$d \cdot \rho_k$	$R_k/2.5$	$0.37 \cdot F_{max,mean}$	$0.31 \cdot F_{max,mean}$
Ehlbeck 1993	$\rho_k^{1.5} \cdot d/20$	$R_k/2.5$	$0.37 \cdot F_{max,mean}$	$0.31 \cdot F_{max,mean}$

The diagrams, illustrated in Figure 2.28, show a comparison of the different stiffness models depending on the fasteners' diameter and the characteristic density of the timber members. As visible, the models proposed in Ehlbeck and Larsen (1993), Ehlbeck and Werner (1988a) and Whale and Smith (1986) lead to comparable results. Moreover, neglecting the density independent model of Johansen (1949), it is obvious that the model presented in Whale et al. (1987) always exhibits the lowest stiffness values.

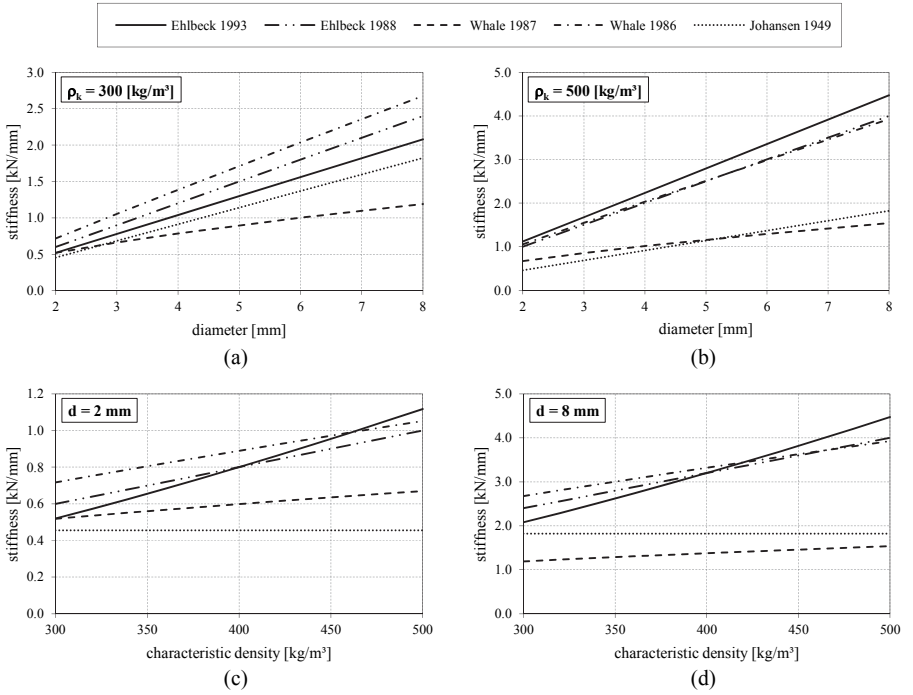

Figure 2.28: comparison of stiffness models – (a) stiffness over diameter for a characteristic density of 300 kg/m³; (b) stiffness over diameter for a characteristic density of 500 kg/m³; (c) stiffness over characteristic density for a diameter of 2 mm; (c) stiffness over characteristic density for a diameter of 8 mm

Focusing this circumstance, Figure 2.29 illustrates the test data and the corresponding prediction models published in Ehlbeck and Werner (1988b) and Whale et al. (1987). As can be seen, there are significant differences between the two experimental campaigns; especially for bigger diameters. A possible explanation is delivered by the used test configurations. In particular, while the main tests presented in Ehlbeck and Werner (1988b) had a slenderness ratio (ratio between the thickness of the middle timber member and the diameter of the fastener) between 6 and 8, the bolted specimens described in Whale et al. (1987) reached only a slenderness of 1 to 2.5. As already mentioned, this low slenderness provokes a dominant failure mode 'h', which obviously results in quite low stiffness values. The further considered nail tests owned slenderness ratios of approximately 6 to 11 and, hence, the corresponding stiffness properties are closer to the results presented in Ehlbeck and Werner (1988b).

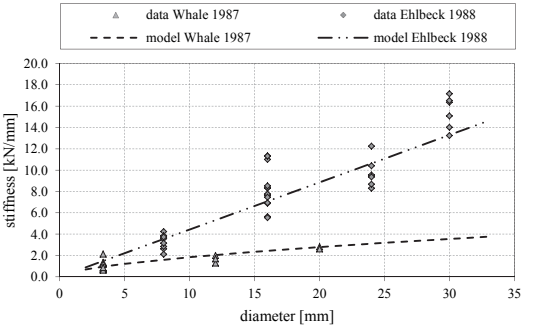

Figure 2.29: experimentally gathered stiffness values and corresponding prediction models as given in Whale et al. (1987) and Ehlbeck and Werner (1988b)

Eurocode 5 definitions

The current European design standard for timber structures ON EN 1995-1-1 (2014), distinguishes between stiffness values used in the serviceability limit state (K_{ser}) and the ultimate limit state (K_u). If test results are available, the stiffness K_{ser} is set equal to the initial stiffness $K_{ini,1}$ (originally k_s) as defined in ON EN 26891 (1991); see also section 2-3.1. An abridgement of the analytic formulas, offered in Eurocode 5 for determining the stiffness of shear loaded fasteners, is given in Table 2.6.

Table 2.6: slip modulus per shear plane per fastener under service load for shear loaded connections in timber-to-timber and wood-based panel-to-timber connections; abridgement according to ON EN 1995-1-1 (2014)

fastener type	K_{ser} [N/mm]
dowels, screws, and nails (with pre-drilling)	$\frac{\rho_m^{1.5}}{23}$
nails (without pre-drilling)	$\frac{\rho_m^{1.5} \cdot d^{0.8}}{30}$

Deviating from the expressions derived in Ehlbeck and Larsen (1993), these formulas use the mean density of the timber elements as input parameter instead of the characteristic one; this is compensated by inserting a higher divisor. Furthermore, if two connected timber elements possess different densities ($\rho_{m,1}$ and $\rho_{m,2}$), according to Eurocode 5, the density for calculating K_{ser} can be determined as given in Equation (2.48).

$$\rho_m = \sqrt{\rho_{m,1} \cdot \rho_{m,2}} \tag{2.48}$$

For steel-to-timber or concrete-to-timber connections, Eurocode 5 proposes to calculate the stiffness based on ρ_m of the timber member multiplied by the factor 2. This regulation can be explained as follows.

Assuming that the stiffness of one shear plane in a timber-to-timber joint consists of two equal springs working in a serial system, the stiffness regarding one of the adjacent timber elements can be expressed as shown in Equation (2.49).

$$\frac{1}{K_{\text{ser,timber}}} = \frac{1}{K_{\text{ser,1}}} + \frac{1}{K_{\text{ser,2}}} \quad \Rightarrow \quad K_{\text{ser,1}} = K_{\text{ser,2}} = 2 \cdot K_{\text{ser,timber}} \tag{2.49}$$

If one timber element is substituted by a steel member, and the stiffness of a dowel in a steel member is assumed to be infinite, the serial combination of the two springs lead to the formulation given in Equation (2.50).

$$\frac{1}{K_{\text{ser,steel}}} = \frac{1}{2 \cdot K_{\text{ser,timber}}} + \frac{1}{\infty} \quad \Rightarrow \quad K_{\text{ser,steel}} = 2 \cdot K_{\text{ser,timber}} \tag{2.50}$$

Note: Although this opportunity is comprehensible, the former German standard for timber structures did not include this factor up to its last valid version DIN 1052 (2008).

For designing structures with materials having different time-dependent properties, according to Eurocode 5, the final mean value of the stiffness, as defined in Equation (2.51), has to be applied for the serviceability limit state. Moreover, if the distribution of member forces and moments in the ultimate limit state is affected by the stiffness of the used connections, the slip modulus according to Equation (2.52) is scheduled for a first order linear elastic analysis.

$$K_{\text{ser,fin}} = \frac{K_{ser}}{1 + k_{def}} \tag{2.51}$$

$$K_{\text{ser,fin}} = \frac{K_{ser}}{1 + \psi_2 \cdot k_{def}} \tag{2.52}$$

with

$K_{\text{ser,fin}}$ ..... final mean value of slip modulus

k_{def} ..... deformation factor, used for the evaluation of creep deformation taking into account the relevant service class

ψ_2 ..... factor for the quasi-permanent value of the action causing the largest stress ($\psi_2 = 1.0$ for permanent actions)

Finally, the stiffness of a connection for the ultimate limit state (K_u) is defined as 2/3 of K_{ser}; compare Ehlbeck and Larsen (1993).

Further influencing factors as, e.g., the load-to-grain angle or the thickness of involved timber elements in relation to the fasteners' diameter (slenderness), are not considered in the current version of Eurocode 5.

SIA 265 definitions

As already described in section 2-3.5, the SIA 265 (2012) comprises instructions how to determine the stiffness of a test specimen with respect to its load-displacement curve. Additionally, equal to Eurocode 5, analytical approaches for some fasteners are offered; compare Table 2.7. Thereby, the SIA 265 (2012) uses the characteristic rather than the mean density as input parameter. Furthermore, it schedules different approaches for parallel and perpendicular loaded fasteners and intends a linear interpolation for other load-to-grain angles; see also Figure 2.30 (a) and (b).

Table 2.7: ***K_{ser} per shear plane per fastener for short term shear loaded fasteners in timber-to-timber and steel-to-timber connections according to SIA 265 (2012)***

fastener type	**force to grain**	**K_{ser} [N/mm] timber-to-timber**	**K_{ser} [N/mm] steel-to-timber**
dowels, bolts, nails and screws	parallel	$3 \cdot \rho_k^{0.5} \cdot d^{1.7}$	$6 \cdot \rho_k^{0.5} \cdot d^{1.7}$
	perpendicular	$1.5 \cdot \rho_k^{0.5} \cdot d^{1.7}$	$3 \cdot \rho_k^{0.5} \cdot d^{1.7}$
nails and screws (without pre-drilling)	parallel	$60 \cdot d^{1.7}$	$120 \cdot d^{1.7}$
	perpendicular	$30 \cdot d^{1.7}$	$60 \cdot d^{1.7}$

No remarks are given how to deal with mixed systems as, e.g., a timber-to-timber connection where the outer elements are oriented perpendicular to the inner one; compare Figure 2.30 (c). Nevertheless, assuming, once more, a system of serial springs, the stiffness of such a joint may be determined as given in Equation (2.53); here exemplary for a doweled connection.

$$\frac{1}{K_{ser}} = \frac{1}{2 \cdot \left(3 \cdot \rho_k^{0.5} \cdot d^{1.7}\right)} + \frac{1}{2 \cdot \left(1.5 \cdot \rho_k^{0.5} \cdot d^{1.7}\right)} \quad \Rightarrow \quad K_{ser} = 2 \cdot \rho_k^{0.5} \cdot d^{1.7} \tag{2.53}$$

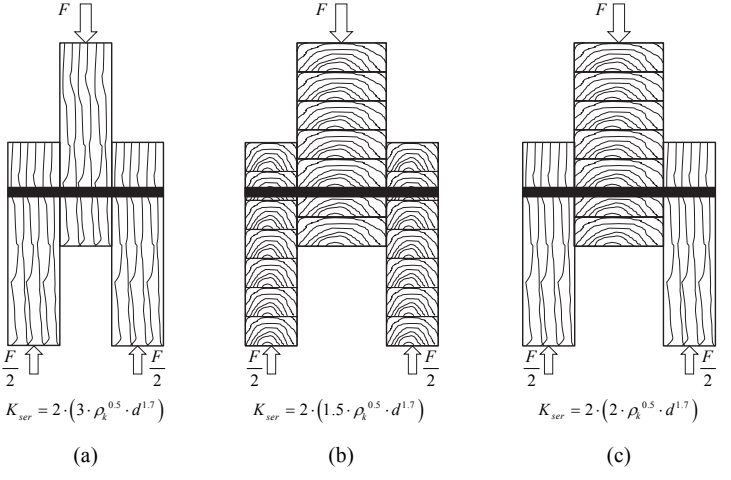

Figure 2.30: stiffness ratios depending on the load-to-grain direction – (a) parallel; (b) perpendicular; (c) mixed

Similar to Eurocode 5, the SIA 265 (2012) schedules a ratio of 2/3 between the stiffness for the ultimate limit state (K_u) and the serviceability limit state (K_{ser}). Nonetheless, a figure in the original source suggests that K_u represents the inclination between the origin and the point of maximum load, which is not consistent with the assumptions described in Ehlbeck and Larsen (1993); compare Figure 2.27 and Figure 2.31 (a).

For calculations applying the 2nd order theory and for the design of stabilising systems (e.g., bracing systems), the SIA 265 (2012) further schedules to reduce the stiffness values as given in the following expressions:

$$K = \frac{K_u}{1.7} \quad \text{for} \quad D < 3 \tag{2.54}$$

$$K = \frac{K_u}{1.5} \quad \text{for} \quad D \geq 3 \tag{2.55}$$

with

K ..... stiffness to be used in the calculation

K_u ..... ultimate limit state stiffness according to the regulations in SIA 265 (2012)

D ..... ductility ratio according to the regulations in SIA 265 (2012)

This standard also comprises a picture, illustrating a reduced SLS and ULS stiffness considering the slip of a connection; see Figure 2.31 (b) and compare Figure 2.22. Unfortunately, no further remarks concerning this illustration, or a note how to deal with the corresponding information, are given.

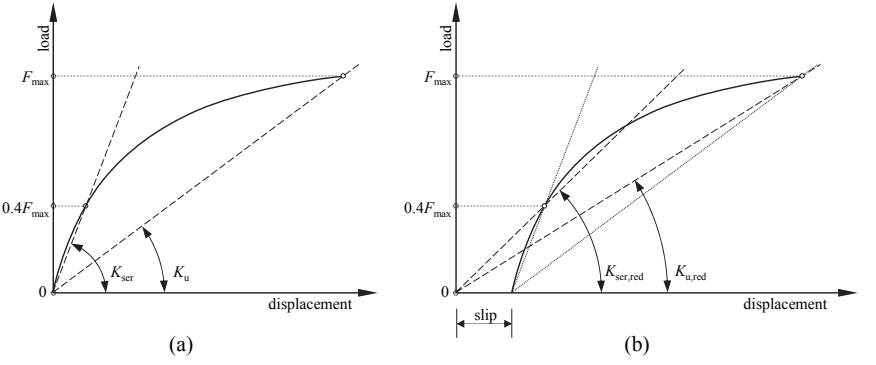

Figure 2.31: stiffness ratios according to SIA 265 (2012) – (a) standard regulations; (b) reduced stiffness values

Comparing Eurocode 5 and SIA 265

Figure 2.32 shows a comparison of the analytical stiffness models for dowels in the two considered standards (parallel loaded, timber-to-timber, characteristic and mean values of densities for C-classes and GL-classes according to ON EN 338 (2009) and ON EN 14080 (2013), respectively). Here, the tendency of Eurocode 5 regulations to reach higher results is clearly visible; this especially for higher densities. Even more pronounced is the difference in case of perpendicular loading (not illustrated). This, due to the required bisection of stiffness values scheduled in SIA 265 (2012); compare Table 2.7.

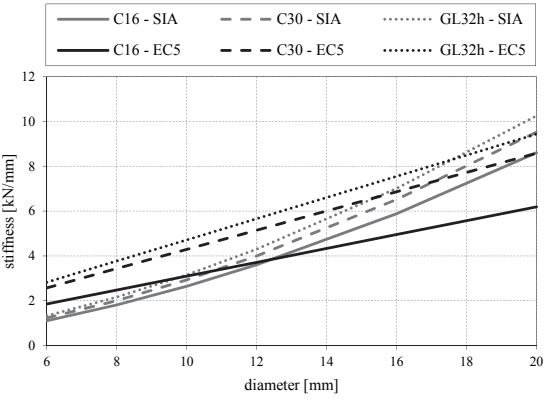

Figure 2.32: comparison of stiffness values for parallel loaded dowel connections (timber-to-timber) according to definitions given in SIA 265 and EC 5

Comparing analytical regulations with test results

Several studies compared their experimental test results with the models scheduled by Eurocode 5 or its drafts. Dorn et al. (2013), for example, performed tests on doweled steel-to-timber joints (slotted in steel plate; two shear planes; dowel diameter 12 mm) and documented the already mentioned influence of the dowel slenderness on the initial stiffness. Particularly, for slenderness ratios equal to 3.75 a good accuracy of the Eurocode 5 suggestion was found; for slenderness values lower or higher, the stiffness was under- or overestimated, respectively. This also confirms the interpretation of the low stiffness values published in Whale et al. (1987); compare Figure 2.29 and associated remarks.

Significant differences between the Eurocode 5 regulations and experimental results are also documented in Izzi et al. (2015). Besides others, investigations on shear loaded steel-to-timber joints (side members in steel, middle member in CLT, loaded parallel and perpendicular to the grain), using ringed shank nails (diameter equal to 4.0 mm) as fasteners, lead to approximately four times lower stiffness values as expected; compare Table 2.8. The load-displacement curves of the experimental tests and the linear slopes, representing the stiffness values of interest, are depicted in Figure 2.33.

Table 2.8: initial stiffness per shear plane per fastener basing on tests presented in Izzi et al. (2015) – mean densities for calculating the $K_{ser,EC5}$ properties are equal to 477 kg/m³ and 455 kg/m³ for SH00 and SH90, respectively; $K_{ini,exp}$ is determined according to ON EN 12512 (2005)

ID	load-to-grain	$K_{ini,exp}$ [kN/mm]	$K_{ser,EC5}$ [kN/mm]	$K_{ser,SIA}$ [kN/mm]
SH00	parallel	0.514	2.105	1.267
SH90	perpendicular	0.550	1.961	0.633

At first glance, the use of CLT, instead of solid wood members, may be seen as a possible explanation for the low experimental stiffness values compared to the analytical one. However, based on the lay-up of the used CLT panels as well as the documented position of the plastic hinges (all specimens show a type 'f' failure mode), it seems to be unlikely that the used timber product was influencing the test results in a relevant range. Thus, considering the already described background of the analytical formulations, two possible explanations remain.

Firstly, as already described, the regulations for steel-to-timber connections presume an infinite stiff fixation of the nail in the steel member. However, especially for low loads and small deformations, it is hardly possible to completely lock the rotation of a nail in a pre-drilled steel member. The second reason for the low stiffness values can be seen in the test configuration, using small gaps between the steel plates and the CLT member. This minimises the initial friction, which finally may have reduced the achievable initial stiffness.

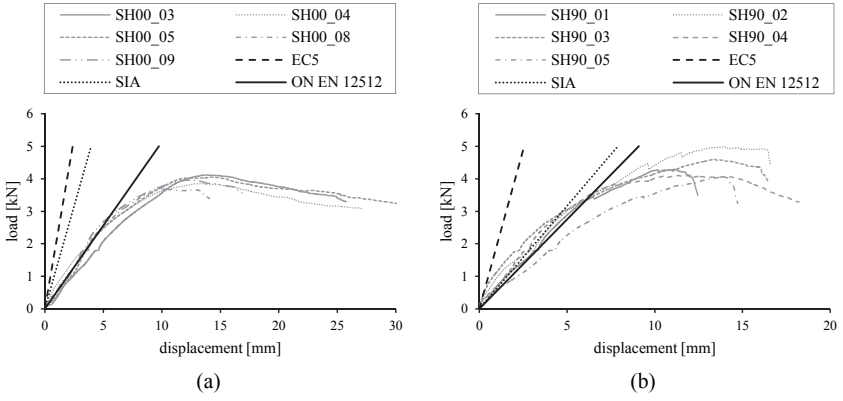

Figure 2.33: load-displacement curves and corresponding initial stiffness (mean value – scaled for one shear plane) of shear loaded steel-to-timber joints using ringed shank nails as fasteners in comparison with the stiffness values determined according to Eurocode 5 and SIA 265 – (a) load-to-grain angle equal to 0°; (b) load-to-grain angle equal to 90°

Figure 2.33 and Table 2.8 also contain the expected initial stiffness values following the regulations given in SIA 265 (2012). Comparing them with the experimental results show again the tendency of the Swiss standard resulting in lower stiffness values compared to Eurocode 5. Moreover, although also

distinctively overestimating the parallel loaded joints, due to the assumed factor of 0.5, the expected initial stiffness for the perpendicular loaded one fits quite good to the experimental results. However, since the test results show (i) only a small difference between the two stiffness values and (ii) a slightly higher stiffness for perpendicular loaded specimens, the good fit have to be seen critically anyway.

In contrast to the initial stiffness K_{ser}, a comparison of test results with the analytical predictions for the ULS stiffness K_u is not available in literature. Nevertheless, to allow a verification of the 2/3-regulation, a comparison for both the SIA 265 (2012) and the Eurocode 5 definition is presented in Table 2.9 and Table 2.10, respectively. For this purpose, the test curves described in section 2-4.1 are used again.

Table 2.9: comparison of theoretical and experimental ULS stiffness according to SIA 265 (2012)

ID	units	[T1]	[T2]	[S1]	[S2]	[M1]	[M2]
$K_{ser,exp}$	[kN/mm]	19.114	18.819	0.779	0.795	1.117	1.068
$K_{u,exp}$	[kN/mm]	11.276	3.123	0.234	0.342	0.832	0.198
$K_u = 2/3K_{ser,exp}$	[kN/mm]	12.743	12.546	0.519	0.530	0.744	0.712
diff $K_{u,exp}/K_u$	[%]	-12 %	-75 %	-55 %	-35 %	12 %	-72 %

Note: $K_{u,exp}$ represents the ULS stiffness based on test results as shown in SIA 265 (2012) and Figure 2.31 (a); means F_{max}/v_{max}

Table 2.10: comparison of theoretical and experimental ULS stiffness according to Eurocode 5

ID	units	[T1]	[T2]	[S1]	[S2]	[M1]	[M2]
$K_{ser,exp}$	[kN/mm]	16.140	14.974	0.648	0.655	0.862	0.828
$K_{u,exp}$	[kN/mm]	10.760	9.982	0.432	0.436	0.575	0.552
$K_u = 2/3K_{ser,exp}$	[kN/mm]	17.456	11.916	0.614	0.743	1.013	0.755
diff $K_{u,exp}/K_u$	[%]	62%	19%	42%	70%	76%	37%

Note: $K_{ser,exp}$ represents the initial stiffness properties according to ON EN 12512 (2005) and $K_{u,exp}$ represents the ULS stiffness based on test results as shown in Figure 2.27; means $(0.52 \cdot F_{max})/v_{52}$, assuming $F_k \sim 0.8 \cdot F_{max,mean}$, which is true for $CoV = 13\%$

As can be seen, the 2/3-regulation for K_u does not fit for both the SIA 265 (2012) and the Eurocode 5 definition of $K_{u,exp}$. Latter one is assumed to base on the 65 % criterion illustrated in Figure 2.27. Consequently, it has to be concluded that the current regulation for calculating K_u is hardly able to reflect the joint behaviour as it is intended to do.

2-4.2.4 Concluding remarks

The present investigations clearly show the difficulties in determining, comparing and discussing the stiffness properties of timber joints.

Firstly, the variations within the available methods for the analysis of experimental test data do complicate a serious assessment between different research projects. Of course, the presented comparison in Table 2.3 includes some 'exotic' models, but even if only the commonly used ON EN 12512 (2005) and SIA 265 (2012) regulations are considered, differences of up to 30 % occur. Furthermore, how high the differences are, does not at least depend on the shape of the test curve – especially within the first loading branch (compare Figure 2.22). This is also underlined by the fact that the highest or lowest ratios do not always result from the same models.

Secondly, analysing the analytical models scheduled in Eurocode 5 show that they are only valid for defined boundary conditions and important influencing factors as, e.g., the thickness of timber members and, hence, the occurring failure modes, are not considered. Furthermore, spotting the discussion regarding the working load level, it is debatable if the current regulations for K_{ser} and K_u do represent the intended stiffness properties.

Condensing the discussed points, the following method for determining stiffness properties out of experimentally gathered load-displacement diagrams is put up for discussion:

(i) performing a series of monotonic tests according to ON EN 26891 (1991) (or a comparable test standard; a hysteresis is not mandatory)
(ii) defining the mean value of documented maximum loads ($F_{max,mean}$)
(iii) determining the SLS stiffness (K_{SLS}) using the origin and $0.25 \cdot F_{max,mean}$ as reference points
(iv) determining the ULS stiffness (K_{ULS}) using the origin and $0.40 \cdot F_{max,mean}$ as reference points

Note: A potentially appearing slip area, caused by the test configuration, shall be cropped; slip caused by the connection itself should be considered.

In this context it is further worth to be discussed if an optional ratio K_{peak} equal to F_{max}/v_{max} should be determined as a reference for the deformation capability up to the actual load-carrying capacity.

Exemplary, Figure 2.34 visualises the alternative stiffness values for an angle bracket connection (a) and a shear loaded ringed shank nail (b). Additionally, the relevant load limits are plotted; information regarding the corresponding tests can be found in section 5-2.2.3 and Izzi et al. (2016), respectively.

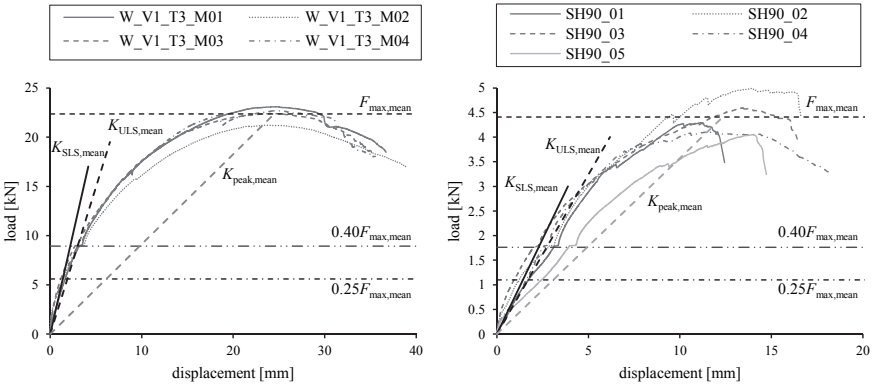

Figure 2.34: alternative stiffness values K_{SLS}, K_{ULS} and K_{peak} for – (a) an angle bracket connection; (b) a ringed shank nail

2-4.3 YIELD POINT

In common understanding, the yield point assigns the transition from the elastic branch of a load-displacement curve to the plastic one. Deformations occurring in the elastic part will disappear upon the removal of the load; deformations in consequence of loads higher than the yield load will remain (compare Figure 2.2). However, since timber connections usually do not develop a distinctive yield point, in many cases the described clear separation is hardly possible. A good summary and comparison of some conventional models is given in Muñoz et al. (2008), where six different models are applied for determining the yield limit of three different timber connections. Thereby, distinct differences in resulting yield displacements are documented; in some cases up to 80 % for the same connection. Moreover, it is stated that the suitability of the different models do, not at least, depend on the shape of considered load-displacement curves.

Within this section a similar comparison is performed, but besides conventional, also analytically based methods for defining the yield point are discussed.

2-4.3.1 Comparing conventional yield point models

The ten methods listed in Table 2.11 are used to determine the yield point parameters F_y and v_y for the test curves [T1] to [M1]. The boundary conditions, necessary for applying some of the models, are given in the following itemisation:

(i) The ASTM standard schedules to horizontally offset the line, representing the initial stiffness, equal to 5 % of the fasteners' diameter. Consequently, this method may only be applied for test curves describing the behaviour of single fasteners. However, to enable its use for the current comparison, the shift is modified to be equal to 5 % of the deformation measured at F_{max} (v_{max}); this alternative model is termed as ASTM*.

(ii) The CUAP based approach comprises a similar issue as the ASTM model does. It requires a horizontal offset equal to 0.2 % of the specimens' elongation (compare Figure 2.13). Since it is hardly possible to define the elongation of a timber connection, the already described shift equal to $0.05 \cdot v_{max}$ is applied for this method too (termed as CUAP*).

(iii) Both, the equivalent elastic-plastic yield model (compare Figure 2.15 (a); termed as EEPY) and the modified Ehlbeck model as given in Dolan et al. (1994) (compare Figure 2.15 (c); termed as EQUDIST), do not offer a distinct definition for the initial stiffness. Hence, for these models the ASTM stiffness (inclination at origin) is applied.

(iv) The CSIRO and the FORINTEK model do not explicit define the yield load. Hence, similar to Muñoz et al. (2008), for both models, F_y is defined as the load appearing at the yield displacement; in particular: $F_{y,CISRO} = F(1.25 \cdot v_{40})$ and $F_{y,FORINTEK} = 0.5 \cdot F_{max}$.

Table 2.11: investigated yield point models

source	F_y / v_y	notes
EN 12512	intersection of line 10/40 and tangent with inclination of 1/6 of line 10/40	-
SIA 265	intersection of line 0/40 and tangent with inclination of 1/6 of line 0/40	-
ASTM*	compare Figure 2.5	offset equal to 5 % v_{max}
CUAP*	compare Figure 2.13	offset equal to 5 % v_{max}
EEPY	compare Figure 2.15 (a)	$K_{ini} = K_{ini,ASTM}$
EQUDIST	compare Figure 2.15 (c)	$K_{ini} = K_{ini,ASTM}$
CSIRO	$v_y = 1.25 \cdot v_{40}$ compare Figure 2.16 (b)	F_y assumed to be the actual load at v_y; compare Muñoz et al. (2008)
FORINTEK	compare Figure 2.16 (c)	F_y assumed to be equal to $0.5F_{max}$; compare Muñoz et al. (2008)
EEEP	$F_y = \left[v_u - \sqrt{(v_u)^2 - \frac{2 \cdot A}{K_{ini}}} \right] \cdot K_{ini}$	-
Y & K	compare Figure 2.11 (a)	-

The resulting yield loads (F_y) and displacements (v_y) are documented in Table 2.12 and confirm the expected differences between the considered models. Since the absolute values are only of limited suitability for a comparison, some relative parameters are added too.

In a first step, the relations between the occurring model differences and the documented peak parameters (i.e., $\Delta F_y/F_{max}$ and $\Delta v_y/v_{max}$) are determined. The resulting percentages do fluctuate between 50 % to 76 % for yield loads and 11 % to 78 % for yield displacements and provide a first indication for actually huge differences between the considered approaches. Moreover, the further listed proportions between the lowest and highest yield displacements directly cover, in which range the chosen post-processing model may affect the subsequently determined ductility ratio (see also section 2-4.5).

Table 2.12: comparison of yield points – F_y in [kN]; v_y in [mm]

source	[T1]		[T2]		[S1]		[S2]		[M1]		[M2]	
	F_y	v_y	F_y	v_y	F_y	v_y	F_y	v_y	F_y	v_y	F_y	v_y
EN 12512	19.7	1.13	7.4	0.42	5.6	7.80	3.7	5.18	14.0	14.68	1.6	1.60
SIA 265	19.0	0.99	6.5	0.35	5.1	6.56	3.4	4.30	13.4	11.98	1.5	1.42
ASTM*	6.4	0.31	5.4	0.30	3.2	4.34	1.7	1.97	3.7	2.09	1.3	1.21
CUAP*	8.7	0.46	6.1	0.43	2.4	2.49	1.1	0.94	3.1	1.23	1.4	1.47
EEPY	12.0	0.71	4.9	0.23	4.1	6.59	2.5	3.41	5.5	4.73	1.2	1.04
EQUDIST	17.1	1.12	4.1	0.14	4.2	7.10	2.7	4.08	4.3	2.85	1.1	0.72
CSIRO	10.1	0.56	5.7	0.35	3.4	5.02	2.2	2.89	6.7	6.41	1.4	1.45
FORINTEK	10.7	0.61	6.5	0.51	3.9	6.13	2.3	3.02	7.2	7.02	1.5	1.90
EEEP	19.2	1.01	11.5	0.61	6.8	8.78	4.0	5.05	12.7	11.35	2.6	2.46
Y & K	11.6	0.67	6.5	0.51	4.0	6.33	2.6	3.67	7.7	7.84	1.5	1.77
$\Delta F_y \mid \Delta v_y$	13.3	0.82	7.4	0.47	4.4	6.29	2.9	4.24	10.9	13.45	1.5	1.74
$\Delta F_y/F_{max} \mid \Delta v_y/v_{max}$	62 %	43 %	56 %	11 %	57 %	19 %	63 %	32 %	76 %	78 %	50 %	11 %
ratio max/min	3.1	3.6	2.8	4.4	2.8	3.5	3.6	5.5	4.5	11.9	2.4	3.4

For supporting the discussion, Figure 2.35 illustrates the various yield points and the corresponding load-displacement diagrams. Initially, the points off the curve, according to the frequently used models EN 12512, SIA 265 and EEEP, attract attention. Excepting curve [M2], these three models always provide the highest yield loads and also the corresponding yield displacements are usually quite high. Besides this, a distinctive accumulation of yield points for curve types [T2], [S1] and especially [M2] is visible. A less clear, but still recognisable, tendency of accumulation occurs for curve types [T1] and [S2]. Finally, the wide spread yield points for curve type [M1] have to be highlighted.

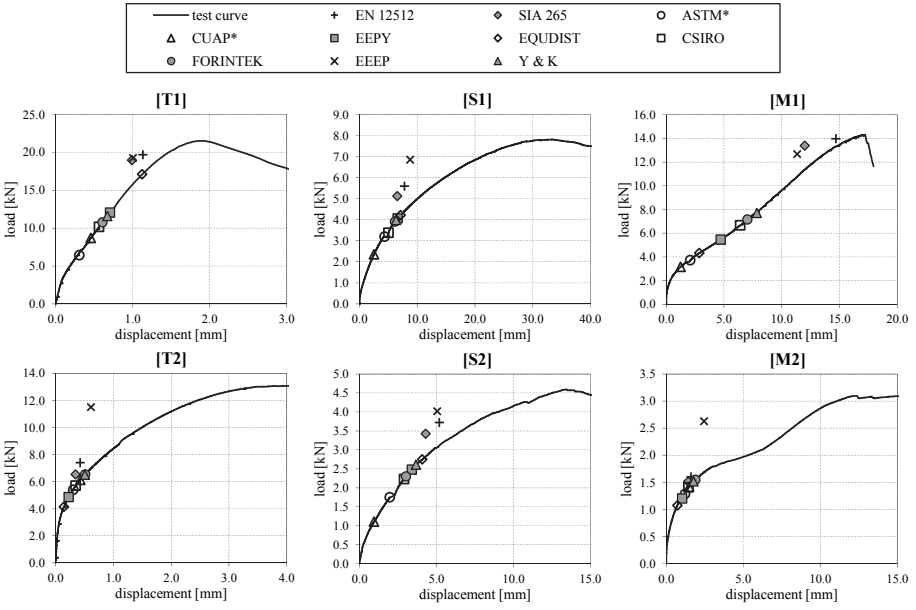

Figure 2.35: illustration of different yield points for curve shapes [T1] to [M2]

Despite the huge differences in results and visual tendencies, not even one of the considered methods has distinctive weaknesses or strengths. Good examples for this statement are the results related to curve type [M1]. The specific shape of this test curve leads to the highest differences in the current comparison – absolute and relative. Nevertheless, it is hardly possible to judge which method describes the (not existing) yield point in a more accurate way. Even the models defining the yield point off the load-displacement curve are not generally unqualified. Especially for calculating the ductility ratio these points have their eligibility.

Summarising, it has to be stated that due to the absence of distinct yield points, an objective assessment regarding the accuracy of the considered models is hardly possible. However, a feasible alternative appears if the yield point is defined by applying analytical methods. Hence, this topic is discussed more in detail within the following section.

2-4.3.2 Alternative methods for defining the yield point

A common analytical model for approximating the load-displacement curve of timber joints is proposed in Foschi (1974); detailed information regarding this and further analytical approaches are offered in Chapter 3. Based on this model, Jorissen and Fragiacomo (2011) derived Equation (2.56) for determining the yield displacement (see also Figure 2.36).

$$v_y = \frac{F_t}{K_{ini} - K_p} \tag{2.56}$$

with

K_p ..... inclination of the plastic branch

F_t ..... intersection of the asymptote (inclination K_p) and the ordinate

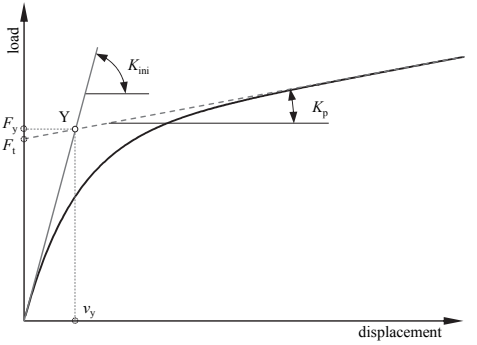

Figure 2.36: yield point (Y) according to Jorissen and Fragiacomo (2011)

A more detailed examination, including a mathematical definition for the yield point, is given in Christensen (2008). He deduced that the displacement, at which the second derivative of the load-displacement curve (d^2F/dv^2) achieves an extreme value, represents the yield limit (v_y). Furthermore, the associated load is identified as the yield load F_y; compare Figure 2.39 (a). Consequently, the yield point can be localised by setting the third derivative equal to zero; see Equation (2.57).

$$\frac{d^3F}{dv^3} = 0 \tag{2.57}$$

Applying the difference method, allows a numerical derivation of test data. If, for example, F_i is the load at step i and v_i is the corresponding displacement, the first and second derivations can be determined, e.g., using Newton's difference quotient as shown in Equations (2.58) and (2.59).

$$\frac{dF}{dv} = K_{T,i} = \frac{F_{i+1} - F_i}{v_{i+1} - v_i} \tag{2.58}$$

$$\frac{d^2F}{dv^2} = \Delta K_{T,i} = \frac{K_{T,i+1} - K_{T,i}}{v_{i+1} - v_i} \tag{2.59}$$

with

K_T ..... tangent stiffness

The load-displacement curve illustrated in Figure 2.37 (a) represents a withdrawal test of a self-tapping screw up to its load-carrying capacity (test according to ON EN 1382 (1999); screw: Ø 8mm; threaded part in timber (spruce): 40 mm; angle between screw axis and grain direction: 90°). As can be seen, although the load-displacement diagram appears smooth, the numerical derivations exhibit strong noise; compare Figure 2.37 (b) and (c). Especially the very high amplitudes of the second derivation (ΔK_T) prohibit a sufficient analysis.

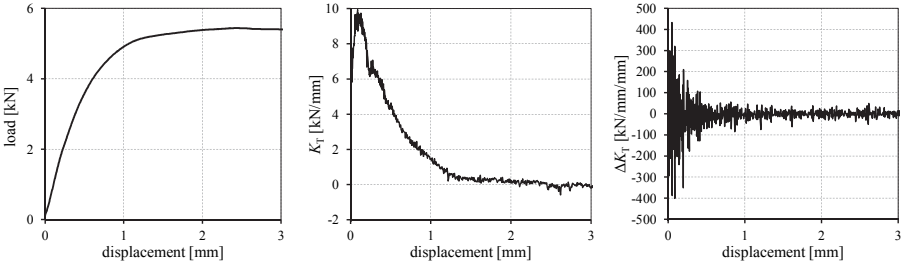

(a) (b) (c)

Figure 2.37: withdrawal tests of a single self-tapping screw – (a) load-displacement curve up to F_{max}; (b) first numerical derivation (Newton's difference quotient) of the load-displacement curve, representing the tangent stiffness K_T; (c) second numerical derivation (Newton's difference quotient) of the load-displacement curve, representing the changing of the tangent stiffness ΔK_T

A smoother trend can be reached if the symmetric difference quotient, as given in Equations (2.60) and (2.61), is used for determining the derivations. Furthermore, enlarging the increment via, e.g., considering only each second data couple also supports reducing the peaks. Although it is possible to lift the first derivation to an acceptable level, the second one still keeps hardly assessable (compare Figure 2.38).

$$\frac{\mathrm{d}F}{\mathrm{d}v} = K_{\mathrm{T,i}} = \frac{F_{\mathrm{i+1}} - F_{\mathrm{i-1}}}{v_{\mathrm{i+1}} - v_{\mathrm{i-1}}} \tag{2.60}$$

$$\frac{\mathrm{d}^2F}{\mathrm{d}v^2} = \Delta K_{\mathrm{T,i}} = \frac{K_{\mathrm{T,i+1}} - K_{\mathrm{T,i-1}}}{v_{\mathrm{i+1}} - v_{\mathrm{i-1}}} \tag{2.61}$$

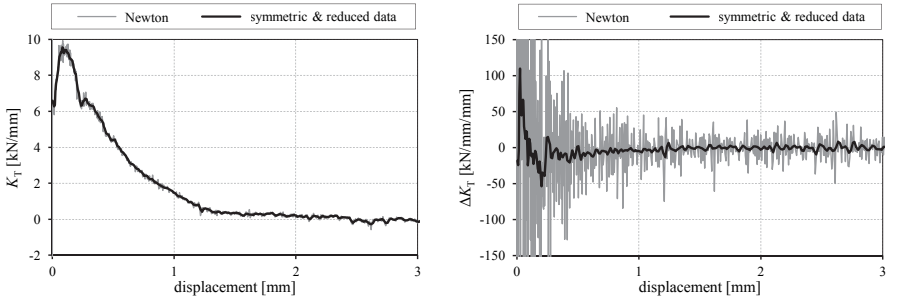

Figure 2.38: comparison of numerical derivations based on the withdrawal test presented in Figure 2.37: Newton's difference quotient using the full data set vs. symmetric differece qouotient in consequence of a reduced data set (only each second data couple considered) – (a) first derivation; (b) second derivation

Consequently, a continuous and differentiable function would be advantageous for determining the yield point according to this theory. Here, to give an example, the analytical approach proposed in Christensen (2008) is applied; detailed information regarding this model is given in Chapter 3. As illustrated in Figure 2.39, up to F_{max}, this model approximates the original test curve quite well and also the first derivation shows similarities to the numerical result. The benefit of the analytical model can especially be seen at the second derivation. This, due to the fact that deviating from the numerical output, the analytical one exhibits a distinctive extreme value for defining the yield displacement.

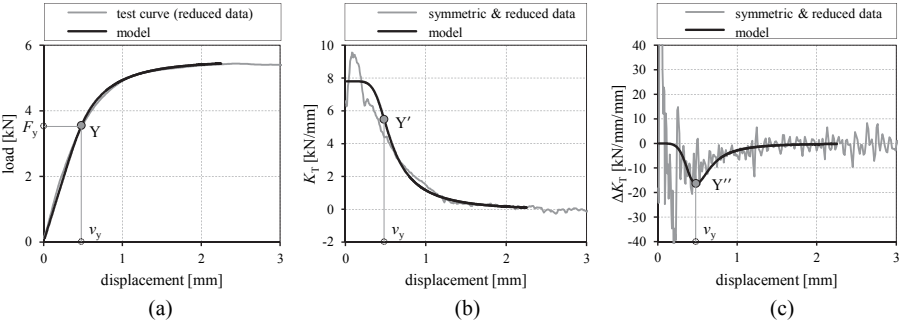

Figure 2.39: comparison of original test data and analytical model applied for determining the yield displacement – (a) load-displacement curve; (b) first derivation; (c) second derivation

A further field, where the derivations of a load-displacement curve can be applied, is the localisation of the linear elastic branch. Since this part requires a constant tangent stiffness, it is represented by the range where the second derivation is equal to zero and the first derivation exhibits a horizontal plateau; see also section 3-4 and Brandner et al. (2017).

2-4.3.3 Concluding remarks

In timber engineering, neither the yield load nor the yield displacement is a parameter directly used in practical design. However, since the yield displacement is required for several models describing the ductile capacity of a joint, defining the yield point is still an essential factor in post-processing. Nevertheless, the presented comparison of selected models exhibits huge differences between the resulting parameters. Especially for timber joints owning complex load-displacement behaviours not only the relative, but also the absolute deviations are quite high. This circumstance finally complicates – if not prohibits – a serious analysis of international test results. A possible solution for this issue is seen in the application of analytical models in the evaluation process.

2-4.4 ULTIMATE POINT

For assessing the capacity of a connection, it is further mandatory to define the final available (ultimate) load and/or displacement (i.e., for determining the corresponding ductility – compare section 2-4.5). Thereby, similar to the yield point, the focus of interest is set on the ultimate displacement v_u, whereas the associated load F_u is only of limited relevance for (standard) post-processing.

Besides a limiting compression strain criteria – which is not in practical use for mechanical timber connections – Park (1989) suggests three possible definitions for determining the ultimate point; see Figure 2.40.

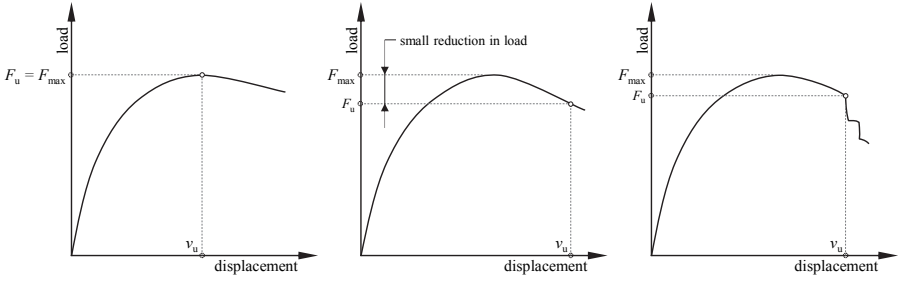

Figure 2.40: possible definitions for the ultimate displacement v_u according to Park (1989) – (a) based on peak load; (b) based on significant load capacity after maximum load; (c) at failure

Since most timber fasteners and connections exhibit some deformation capacity after reaching the maximum load F_{max}, the criteria shown in Figure 2.40 (a) may lead to rather conservative values. Consequently, as proposed in Park (1989), the criteria given in Figure 2.40 (b) and (c) should be preferred. However, some current standards include a further criterion, limiting the permitted absolute displacement for an experimental test; compare ON EN 12512 (2005) or ON EN 26891 (1991).

For the 'small reduction in load', stated in Figure 2.40 (b), Park (1989) proposes a value equal to 20 % of F_{max}. Unfortunately, no remarks which assumption has been used for electing this ratio were found. However, for determining the curvature ductility factor of concrete buildings, a similar post-ultimate strength limit is scheduled, i.e., 85 % of the moment of resistance; compare ON EN 1998-1 (2011). Moreover, as mentioned in Jorissen and Fragiacomo (2011), the 20 % limit is also used by the Italian regulation for masonry buildings. Along with several test standards (compare section 2-3), the 20 % border is further adopted in the timber part of ON EN 1998-1 (2011). In particular, it limits the accepted reduction of resistance for timber joints, within three fully reversed cycles, at a specific rate of displacement (see also section 2-4.5).

Summarising, the ultimate point can be detected either at (i) the point of failure, (ii) 20 % loss of resistance or (iii) a pre-defined deformation limit, whichever occurs first.

Differing from the regulations concerning the initial stiffness or the yield point, determining the ultimate point as described above, is widely accepted in international standards and literature (compare SIA 265 (2012), ON EN 12512 (2005), ASTM E2126 (2011), Yasumura and Kawai (1997), Jorissen and Fragiacomo (2011), etc.).

Nevertheless, similar to the yield point, analytical approaches are available for determining the ultimate point too; compare Jorissen and Fragiacomo (2011) or Christensen (2011). They mainly focus on load-displacement curves which do not show a distinct failure or at least a reduction of load after reaching F_{max}. Hence, no further remarks regarding these models are given at this point.

2-4.5 DUCTILITY

In general, the ductility of a material, a connection, a structural element or a whole structure is describing its capability to attain large displacements (or rotations) without losing too much strength (as mentioned above, 20 % seems to be acceptable). In structural engineering, this quality is highly appreciated because (i) it allows statically overdetermined structures to redistribute forces and ensures a robust behaviour, (ii) enables energy dissipation in case of seismic loading and (iii) ensures large displacements in case of unexpected loadings so as to warn occupants before a collapse occurs; compare Jorissen and Fragiacomo (2010).

As a matter of common knowledge, timber widely behaves linear elastic and tends to brittle failure (exempt for compressive stresses). Thus, the ductility of timber structures (global ductility) is mainly influenced by the quality of the joints connecting the single timber members. Furthermore, since mechanical connections in timber engineering are usually equipped with fasteners (nails, dowels, bolts, screws, etc.), the ductility of a connection system, not at least, depend on their ductile capacity. Additionally, the ductile behaviour of single fasteners affects if and how they act as a group (local

ductility); compare Mischler (1997). As a consequence, not only high strength and stiffness, but also a proper ductility is necessary for an effective timber connection; compare Haller (1998) and Figure 2.41.

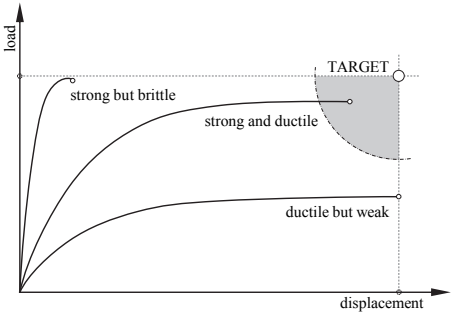

Figure 2.41: different load-displacement curves; Haller (1998) – revised

2-4.5.1 Ductility in practical design

As described in several literature sources, ductile joints enable to implement the elastic-plastic calculation method to the static design of timber structures; compare, e.g., Brühl et al. (2011) or Jorissen and Fragiacomo (2011). Furthermore, Eurocode 5 provides this design method in its section 5 "*Basis of structural analysis*" as follows:

> *"5.1 (3): For structures able to redistribute the internal forces via connections of adequate ductility, elastic-plastic methods may be used for the calculation of the internal forces in the members"*

Note: Translation according to EN 1995-1-1 (2004).

Unfortunately, this standard does not offer any further information about 'adequate ductility'.

The SIA 265 (2012) includes some more information. In particular, besides a clear definition of the ductility ratio, latter standard schedules a reduction of the safety factor from 1.7 to 1.5 as soon as the ductility measure is higher than 3.0.

Even more than for static design, the ductile capacity of a structure is highly appreciated for structures exposed to dynamic loads, i.e., earthquakes. This, because it usually results in reduced affecting loads; compare, e.g., Fragiacomo et al. (2011), Sustersic et al. (2011) or Smith et al. (2015).

The European standard for earthquake design ON EN 1998-1 (2011), for instance, describes the three ductility classes low, medium and high (*DCL*, *DCM* and *DCH*, respectively). They are used to define the relevant behaviour factor (q-factor), applicable for force-based design methods. In particular, Eurocode 8 offers the following definition to verify the ductility classes *M* and *H* for timber structures:

"8.3 (3)P: In order to ensure that the given values of the behaviour factor may be used, the dissipative zones shall be able to deform plastically for at least three fully reversed cycles at a static ductility ratio of 4 for ductility class M structures and at a static ductility ratio of 6 for ductility class H structures, without more than 20 % reduction of their resistance."

Notes: Translation according to EN 1998-1 (2004).
For determining the properties of dissipative zones in timber structures, Eurocode 8 refers to the pre-version of ON EN 12512 (2005) where the ductility is defined as given in Equation (2.7).

SIA 265 (2012) uses a similar classification for selecting the q-factor; unfortunately, a clear definition of the four available ductility classes (no, low, medium and high ductility) is missing. Nevertheless, the context enables the conclusion that ductility measures higher than 3.0 are assessed as 'high'.

Smith et al. (2006) also presented a method classifying the ductile capacity and Brühl (2013) extended this regulation by requirements for absolute deformations. A classification similar to the regulations given in SIA 265 (2012) is described in Smith et al. (2015).

Although deviating terms are used, more or less every source resorts to four classifications groups, i.e., brittle, low ductility, moderate ductility and high ductility. The required ductility values for achieving a defined classification, however, exhibit significant differences. In particular, as visible in Table 2.13, the regulations according to Eurocode 8 and Smith et al. (2006) require approximately twice as high ductility values for the respective classification levels as they are scheduled in SIA 265 (2012) or Smith et al. (2015).

Table 2.13: classification of ductility levels

classification	Eurocode 8	Smith et al. (2006)	ext. Brühl (2013) $\Delta v = v_u - v_y$ [mm]	SIA 265 (assumed)	Smith et al. (2015)
brittle	-	$D \leq 2$	$\Delta v \leq 1$	$1 \leq D$	$D = 1$
low ductility	$D < 4$	$2 < D \leq 4$	$1 < \Delta v \leq 3$	$1 < D \leq 2$	$D = 1.25$
moderate ductility	$4 \leq D < 6$	$4 < D \leq 6$	$3 < \Delta v \leq 6$	$2 < D \leq 3$	$1.25 < D \leq 3$
high ductility	$D \geq 6$	$D > 6$	$\Delta v > 6$	$D > 3$	$D > 3$

Nevertheless, the described method for determining the ductility (ultimate divided by yield displacement), in combination with one of the classification methods summarised in Table 2.13, finally enables an expedient comparison of similar fasteners or connections. Its relative quality, however, hinders a serious assessment of different joining systems. To underline this predication, Figure 2.42 exemplarily illustrates two test curves ([T1] and [S2], tension loaded fully threaded screw and shear loaded ringed shank nail, respectively) and the corresponding ductility values according to Equation (2.7). As can be seen, although the two fasteners exhibit totally different load-displacement relationships, the ductility measures are nearly equal; similar observations are discussed in Piazza et al. (2011).

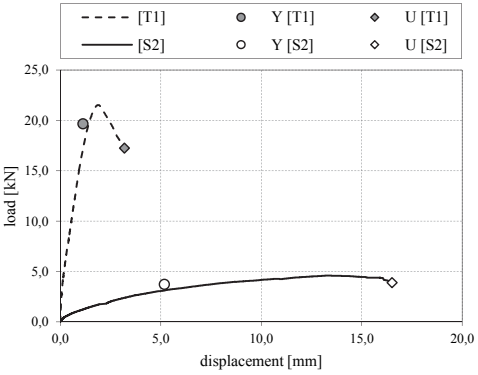

ID	v_y [mm]	v_u [mm]	D [-]
[T1]	1.13	3.20	2.8
[S2]	5.18	16.51	3.2

$$D = \frac{v_u}{v_y}$$

Figure 2.42: two different test curves with the same magnitude of ductility – all properties according to ON EN 12512 (2005)

The already discussed differences in the determination of the yield point do additionally complicate this topic; compare Muñoz et al. (2008). Especially for load-displacement relationships exhibiting yield displacements close to or even smaller than one, the sensitivity against this parameter increases. Figure 2.43, where the development of the ductility is plotted against the yield displacement for test curve [T1] (v_u = 3.2 mm), illustrates this circumstance. In particular, the variation of the yield displacement between 0.31 mm and 1.13 mm (compare Table 2.12), leads to a variation of the ductility measure between 2.8 and 10.3.

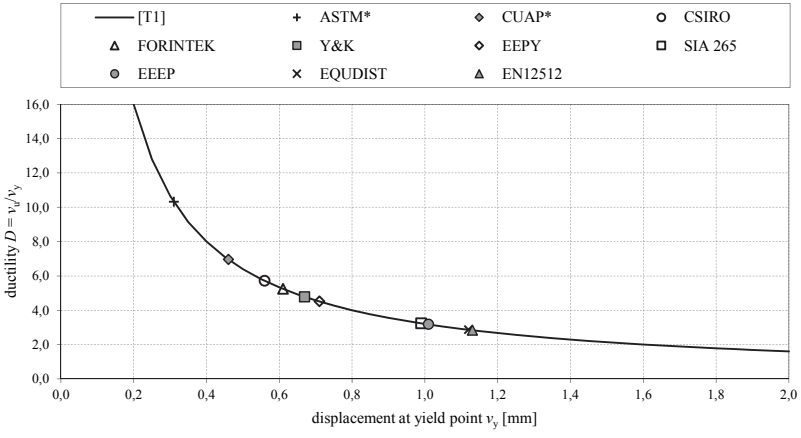

Figure 2.43: development of the parameter ductility in dependency of the yield displacement, including ductility measures according to the yield values given in Table 2.12

2-4.5.2 Alternative ductility measures

Stehn and Björnfot (2002) conducted a literature survey regarding models applicable for determining the ductility of timber joints. An assortment of these models (including some variations) is given in Figure 2.44.

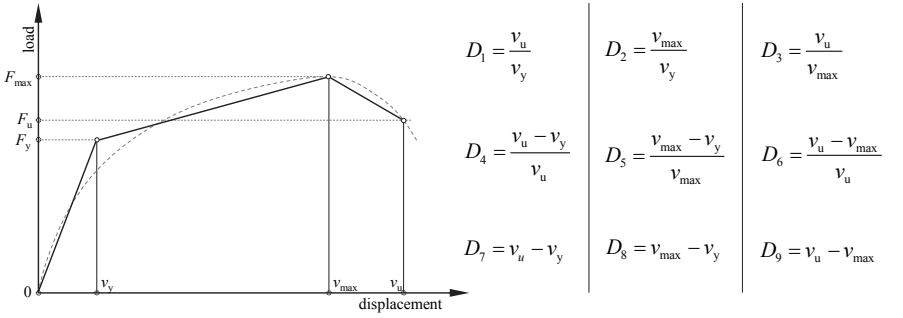

Figure 2.44: different models for determining the parameter 'ductility', Stehn and Björnfot (2002) - revised

Besides relative ductility measures (D_1-D_6), Stehn and Björnfot (2002) also considered absolute alternatives (D_7-D_9). Furthermore, the dissipated energy up to F_{max} (D_{10}) or F_u (D_{11}), expressed in Equations (2.62) and (2.63), respectively, is shown as a possible measure. Additionally, the authors suggested a model, describing how 'close' the shape of a load-displacement curve follows a perfect plastic behaviour up to F_{max}; see Equation (2.64).

$$D_{10} = E_{D,max} = \int_0^{v_{max}} f(F,v)dv \tag{2.62}$$

$$D_{11} = E_{D,u} = \int_0^{v_u} f(F,v)dv \tag{2.63}$$

$$D_{12} = \frac{E_{D,max}}{F_{max} \cdot v_{max}} \tag{2.64}$$

Furthermore, experimental test results of tension loaded nailed joints with slotted-in steel plates are presented. The data gathered from these tests are used to evaluate the different ductility models; this by comparing their results with the actual occurred failure modes (visually determined by x-ray scanning). Besides the statement that it is better to use the models related to the maximum point (v_{max}) rather than the ultimate point (v_u), the authors conclude that the best measure for ductility is given by the dissipated energy ($E_{D,max}$).

A further investigation regarding this topic is presented in Jorissen and Fragiacomo (2010), where the ductility models discussed in Stehn and Björnfot (2002) are applied on data, gathered from parallel to the

grain loaded single bolted connections. This comparison shows that the models D_1, D_7 and D_{11} fit very well. Furthermore, the energy based model given in Equation (2.65) is suggested.

$$D_{13} = \frac{E_{D,u}}{0.5 \cdot F_y \cdot v_y} \tag{2.65}$$

The authors stated that ductility measures have to be consistent, i.e., the ductility parameter of obviously brittle connections should clearly differ from connections able to develop large displacements. As a consequence, based on the comparison shown in Figure 2.42, the ductility measure D_1 has to be seen critical.

Adapting a ductility model originally presented in Stehn and Björnfot (2002) (not included in Figure 2.44), Brühl et al. (2011) suggests Equations (2.66) and (2.67) as alternative ductility measures. Furthermore, based on two different behaving load-displacement curves exhibiting equal areas underneath the graph, Brühl et al. (2011) disproves the general judgment regarding the good fit of energy based models, mentioned in Stehn and Björnfot (2002).

$$D_{14} = \frac{v_{max}}{\frac{F_{max}}{K_{ini}}} = \frac{K_{ini}}{F_{max}} \cdot v_{max} \tag{2.66}$$

$$D_{15} = \frac{v_u}{\frac{F_u}{K_{ini}}} = \frac{K_{ini}}{F_u} \cdot v_u \tag{2.67}$$

Malo et al. (2011) proposed three additional models, one displacement-based, as given in Equation (2.68), and two energy-based, expressed in Equations (2.69) and (2.70); see also Figure 2.45. Additionally, it is recommended to apply different ductility measures for static and dynamic (or impact) loads; in particular, ductility relating to F_{max} (D_{16} and D_{17}) for static loads and ductility relating to the ultimate capacity (D_{18}) for dynamic or impact loads. Due to the lack of uniqueness, Malo et al. (2011) further stated that ductility measures related to the yield point should be avoided.

$$D_{16} = \frac{v_{max} - \frac{F_{max}}{K_{ini}}}{\frac{F_{max}}{K_{ini}}} = \frac{v_{max} \cdot K_{ini} - F_{max}}{F_{max}} \tag{2.68}$$

$$D_{17} = \frac{E_{D,max} - \frac{F_{max}^2}{2 \cdot K_{ini}}}{\frac{F_{max}^2}{2 \cdot K_{ini}}} = \frac{2 \cdot K_{ini} \cdot E_{D,max} - F_{max}^2}{F_{max}^2} \tag{2.69}$$

$$D_{18} = \frac{E_{D,u} - \frac{F_u^2}{2 \cdot K_{ini}}}{\frac{F_{max}^2}{2 \cdot K_{ini}}} = \frac{2 \cdot K_{ini} \cdot E_{D,u} - F_u^2}{F_{max}^2} \tag{2.70}$$

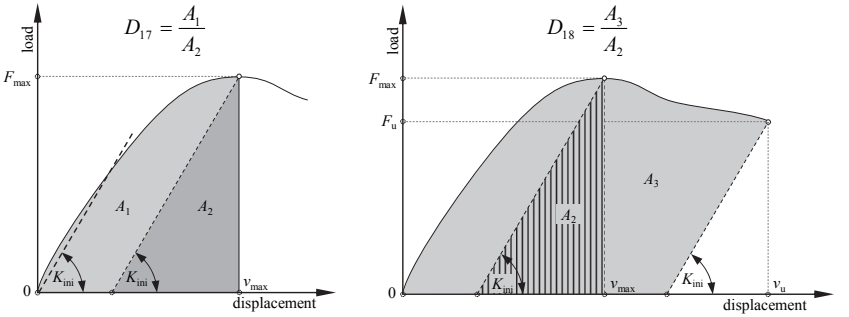

Figure 2.45: energy based models according to Malo et al. (2011) – (a) up to v_{max} for static loads; (b) up to v_u for dynamic and impact loads

Aiming a quantitative comparison, the mentioned models are applied on the six test curves described in section 2-4.1. The required basic parameters for this purpose, determined as scheduled in ON EN 12512 (2005), are summarised in Table 2.14. For the sake of clearness, further approaches available for determining, e.g., the yield displacement, are neglected for this study. The resulting ductility measurements are listed in Table 2.15.

Table 2.14: basic parameter for determining the diverse ductility values

source	units	[T1]	[T2]	[S1]	[S2]	[M1]	[M2]
v_y	[mm]	1.13	0.42	7.80	5.18	14.68	1.60
v_{max}	[mm]	1.91	4.19	33.35	13.43	17.22	15.70
v_u	[mm]	3.20	16.17	55.89	16.51	17.95	22.19
F_y	[kN]	19.7	7.4	5.6	3.7	14.0	1.6
F_{max}	[kN]	21.5	13.1	7.8	4.6	14.3	3.1
F_u	[kN]	17.2	10.5	6.2	3.9	11.6	2.5
K_{ini}	[kN/mm]	16.140	14.974	0.648	0.655	0.862	0.828
$E_{D,max}$	[kNmm]	26.71	43.45	190.69	42.55	146.05	36.73
$E_{D,u}$	[kNmm]	51.85	182.32	352.24	56.15	155.50	55.07

The high variability of both magnitude and type of the calculated ductility measures hardly enable a ‘direct’ comparison of the single values. As a consequence, the discussion is focused on the hierarchical order of the different curve types resulting from the output of every single model. However, as there is no method showing the ‘true’ ductility, the reference order for further discussions is scheduled by the author

as objective as possible. For this purpose, besides the relative and absolute displacement capacities, also the shape of the test curves is incorporated via visual judgement.

Table 2.15: ductility values according to different models and curve types

ID	units	[T1]	[T2]	[S1]	[S2]	[M1]	[M2]
D_1	[-]	2.82	38.20	7.16	3.19	1.22	13.90
D_2	[-]	1.68	9.89	4.27	2.59	1.17	9.83
D_3	[-]	1.68	3.86	1.68	1.23	1.04	1.41
D_4	[-]	0.65	0.97	0.86	0.69	0.18	0.93
D_5	[-]	0.41	0.90	0.77	0.61	0.15	0.90
D_6	[-]	0.40	0.74	0.40	0.19	0.04	0.29
D_7	[mm]	2.06	15.75	48.09	11.33	3.27	20.59
D_8	[mm]	0.77	3.76	25.55	8.25	2.54	14.10
D_9	[mm]	1.29	11.98	22.54	3.08	0.73	6.49
D_{10}	[kNmm]	26.71	43.45	190.69	42.55	146.05	36.73
D_{11}	[kNmm]	51.85	182.32	352.24	56.15	155.50	55.07
D_{12}	[mm]	0.65	0.79	0.73	0.69	0.59	0.75
D_{13}	[-]	4.65	116.32	16.17	5.83	1.52	43.12
D_{14}	[-]	1.43	4.79	2.77	1.91	1.04	4.19
D_{15}	[-]	3.00	23.15	5.80	2.79	1.33	7.40
D_{16}	[-]	0.43	3.79	1.77	0.91	0.04	3.19
D_{17}	[-]	0.86	6.61	3.05	1.64	0.23	5.33
D_{18}	[-]	2.97	31.31	6.85	2.77	0.65	8.85

The assessment of the different models is finally realised by means of a point-based method applying the following rules: if the considered ductility model provides the same position for a curve type as the reference order, five points are allocated; for every single deviating rank one point is subtracted. The chosen reference order and the resulting weightings for every single model are presented in Table 2.16.

The summed-up points show that displacement-based absolute ductility measures provide an equal (D_7) or a quite similar (D_8 and D_9) ranking as the reference order does. The models relating to the (absolute) dissipated energy, (D_{10} and D_{11}) also do result in an acceptable order (24 of 30 points). Nevertheless, the underestimation of test curves exhibiting low load-carrying capacities is obvious too. 18 points, and consequently the 'worst fit', show the ductility values D_3 and D_6, describing the post-peak behaviour of the test curves. The further relative measurements – independent if displacement or energy based – lead to an acceptable correlation as well (24 and 22 of 30 points).

Table 2.16: weighting of ductility models for evaluating the accordance to the reference order; belonging points for every model are parenthesised

models / reference order	high →					low	**sum**
	[S1]	**[M2]**	**[T2]**	**[S2]**	**[M1]**	**[T1]**	
D_7	[S1] (5)	[M2] (5)	[T2] (5)	[S2] (5)	[M1] (5)	[T1] (5)	**30**
D_8	[S1] (5)	[M2] (5)	[S2] (4)	[T2] (4)	[M1] (5)	[T1] (5)	**28**
D_9	[S1] (5)	[T2] (4)	[M2] (4)	[S2] (5)	[T1] (4)	[M1] (4)	**26**
D_1, D_2, D_4, D_5, D_{12}, D_{13}, D_{14}, D_{16}, D_{17}	[T2] (3)	[M2] (5)	[S1] (3)	[S2] (5)	[T1] (4)	[M1] (4)	**24**
D_{10}	[S1] (5)	[M1] (2)	[T2] (5)	[S2] (5)	[M2] (2)	[T1] (5)	**24**
D_{11}	[S1] (5)	[T2] (4)	[M1] (3)	[S2] (5)	[M2] (2)	[T1] (5)	**24**
D_{15}, D_{18}	[T2] (3)	[M2] (5)	[S1] (3)	[T1] (3)	[S2] (4)	[M1] (4)	**22**
D_3, D_6	[T2] (3)	[T1] (1)	[S1] (3)	[M2] (3)	[S2] (4)	[M1] (4)	**18**

The good agreement of the absolute ductility measures, coupled with the additional information provided by the dissipated energy, facilitate a further expression for the ductile capacity of a connection; see Equation (2.71).

$$v_{ip} = \frac{E_{D,u}}{F_{max}} \tag{2.71}$$

with

v_{ip} ..... ultimate displacement in case of ideal plasticity

$E_{D,u}$ ..... dissipated energy up to ultimate point

The resulting parameter v_{ip} corresponds to the theoretical displacement capacity of an equivalent ideal plastic behaving connection. Furthermore, similar to Equation (2.64), the relation between the new parameter and the actual ultimate displacement v_u provides the information how 'close' the shape of the whole test curve describes the (theoretical) ideal plastic equivalent; compare Equations (2.72) and (2.73) and Figure 2.46.

$$\phi_{ip} = \frac{E_{D,u}}{F_{max} \cdot v_u} = \frac{v_{ip}}{v_u} \quad \begin{cases} 1 & \dots \text{ ideal plastic} \\ 0.5 & \dots \text{ ideal elastic} \end{cases} \tag{2.72}$$

$$\Phi_{ip} = \frac{\phi_{ip} - 0.5}{0.5} \cdot 100 \quad \begin{cases} 100\,\% & \dots \text{ ideal plastic} \\ 0\,\% & \dots \text{ ideal elastic} \end{cases} \tag{2.73}$$

with

ϕ_{ip} ..... shape parameter [-]

Φ_{ip} ..... shape parameter [%]

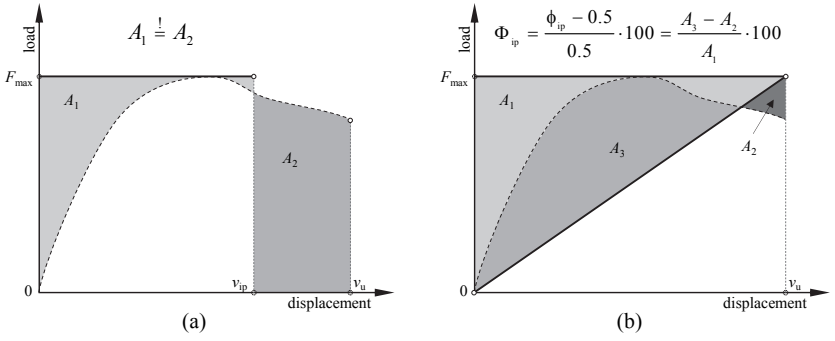

Figure 2.46: ratio of areas for the alternative ductility parameters – (a) determining the ultimate displacement in case of ideal plasticity; (b) determining the shape parameter

Applying this new proposal to the six test curves, leads to the same hierarchical order as the reference; corresponding results are presented in Table 2.17. Additional benefits of this method are the independency of the yield displacement and the 'tangible' quality of the resulting parameters. Moreover, a high v_{ip} value, in combination with a high shape parameter, expresses the properties for an effective connection as suggested by Haller (1998); see also Figure 2.41.

Table 2.17: ductility values according to the proposed approach

ID	units	[T1]	[T2]	[S1]	[S2]	[M1]	[M2]
v_{ip}	[mm]	2.41	13.95	45.10	12.22	10.86	17.77
ϕ_{ip}	[-]	0.75	0.86	0.81	0.74	0.61	0.80
Φ_{ip}	[%]	51	72	61	48	21	60

Finally, in dependence on Table 2.13, the classification for the new approach may look as shown in Table 2.18.

Table 2.18: possible classification of ductility levels relying on the new parameters

classification	equivalent plastic displacement v_{ip} [mm]	shape parameter Φ_{ip}
low ductility	$v_{ip} < 3$	$\Phi_{ip} < 40$ %
moderate ductility	$3 \le v_{ip} < 6$	$\Phi_{ip} \ge 40$ %
high ductility	$v_{ip} \ge 6$	$\Phi_{ip} \ge 60$ %

Note: Different borders for the equivalent plastic displacement may be contemplated; i.e., for assessing bigger structural elements as, e.g., walls.

2-5 INTERMEDIATE CONCLUSIONS

Applying fasteners, connections or single structural elements in civil engineering, requires knowledge regarding the load-displacement relationship of the respective elements. The common manner to obtain this information is the realization of experimental tests, followed by a qualified analysis of the gathered data. The resulting properties, i.e., loadbearing capacity, initial stiffness, yield point, ultimate point and ductility are important characteristics, enabling an assessment and finally the design of examined products.

The challenge in analysing timber joints can be seen in the plurality of load-displacement relationships. Most of them do not show a distinctive yield point or, at least, an initial linear branch which finally complicates the evaluation process. Moreover, although partwise leading to pronounced different properties, the various curve shapes hardly enable an objective assessment of the different post-processing methods available in literature. Latter aspect further hinders, if not prohibits, a clear comparison of international test results.

A possible way to handle this issue can be seen in the application of analytical approaches, being able to transport the information regarding the curve shape. Besides additional possibilities for post-processing, as, e.g., described in Christensen (2008) or Malo et al. (2011), it further allows a direct comparison of gathered load-displacement curves and the application of any post-processing model favoured; compare Pellicane et al. (1991). Additionally, suitable (continuous) mathematical models can be applied for improving more complex calculation models.

CHAPTER 3
ANALYTICAL APPROXIMATION

3-1 INTRODUCTION

In many instances, the load-bearing capacity and the initial stiffness of a timber joint represent sufficient information for practical design. However, if plastic displacement capacities (or rotations) are required, e.g., for applying the elastic-plastic or another nonlinear design method, detailed information regarding the whole load-displacement relationship is preferred. Furthermore, for the investigation of joints equipped with multiple fasteners, the nonlinear behaviour of every single fastener is an appreciated information for determining the actual load-distribution; compare, e.g., Smith (1987), Blaß (1990), Jorissen (1999) or Brühl and Kuhlmann (2012). Moreover, since the same principle may improve the evaluation of CLT wall systems, a closer look on approximating load-displacement curves will follow within this chapter.

In principle, there are two possibilities for describing the progress of a monotonic test graph: (i) piecewise or (ii) continuous. Typical examples for category (i) and (ii) are piecewise linear approximations and continuous mathematical functions, respectively, whereat mixed models can be found in literature as well; compare, e.g., Brandner et al. (2017). Moreover, since not all functions are invertible, it also has to be distinguished between displacement- and force-based models. Force-based models have the advantage that they are closer to practical design, i.e., the engineer can directly calculate the displacement corresponding to the actual force. However, only displacement controlled approaches allow an adequate consideration of the post maximum softening branch.

To give an overview, some of the models available in literature are introduced in this chapter. In a further step, four of them are used for approximating the six test curves described in section 2-4.1. Finally, basing on the collected information, a new displacement-based model is suggested and validated.

3-2 PIECEWISE LINEAR MODELS

Probably the most popular approximation of a load-displacement relationship is the elastic-(ideal) plastic one, where the initial stiffness is usually used as the slope of the elastic branch. Subsequently, the plastic part can be determined, e.g., via energy equilibrium as suggested in Yasumura and Kawai (1997) or as given in Youssef-Agha et al. (1989). Latter applies a strain-hardening factor of 0.15 to describe the moment-rotation relationship of steel joints. This assumption is quite similar to the scheduled slope of the

tangent-stiffness as mentioned in ON EN 12512 (2005), which equals 1/6 of K_{ini}. Piazza and Turrini (1986), show a bilinear approximation for glued in steel pins, where the slope of the second line was much lower (1/500 of K_{ini}).

For simulating the load-displacement relationship of shear loaded steel dowels, Brühl and Kuhlmann (2012) proposed a trilinear method in dependence on the component model given in the European design standard for steel structures ON EN 1993-1-8 (2012), also referred to as Eurocode 3; see also section 3-4. Thereby the slope of the initial branch is defined to be equal to K_{ini}. The second branch is characterized by an inclination of one third of K_{ini} and the last section assumes an ideal plastic behaviour; compare Equations (3.1) to (3.4) and Figure 3.1 (a).

$$F_1 = \frac{2}{3} \cdot F_{max} \tag{3.1}$$

$$v_1 = \frac{F_1}{K_{ini}} = \frac{2 \cdot F_{max}}{3 \cdot K_{ini}} \tag{3.2}$$

$$F_2 = F_{max} \tag{3.3}$$

$$v_2 = v_1 + \frac{\Delta F}{\frac{1}{3} \cdot K_{ini}} = v_1 + \frac{F_{max}}{K_{ini}} = \frac{5 \cdot F_{max}}{3 \cdot K_{ini}} \tag{3.4}$$

Aiming to estimate the behaviour of a reverse channel connection (RCC) to tubular columns, AlHendi and Celikag (2015) also apply – among others – the Eurocode 3 model. Depending on the considered type of connection, their investigations show that a trilinear simplification of the original method lead to an inclination of the second branch which is equal to 1/7 or 1/8.5 of K_{ini}; compare Figure 3.1 (b).

A further possibility to approximate the shape of a test curve with three lines can be seen in simply connecting the yield, maximum and ultimate point; compare, e.g., Izzi et al. (2015), Gavric et al. (2015a) and Figure 3.1 (c).

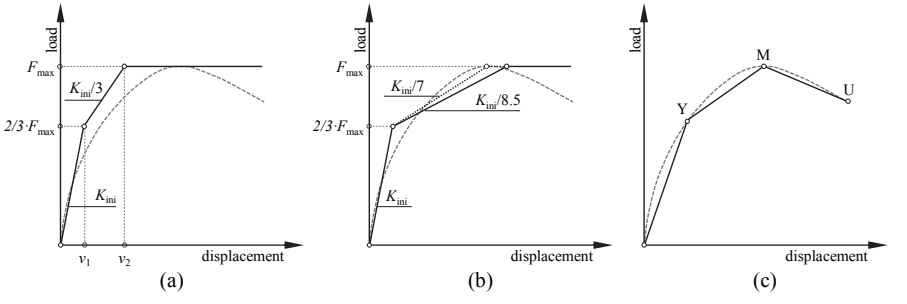

***Figure 3.1:** trilinear models for approximating the load-displacement curve – (a) variation of Eurocode 3 model as described in Brühl and Kuhlmann (2012); (b) Eurocode 3 model as explained in AlHendi and Celikag (2015); (c) connection of yield-, maximum- and ultimate point*

An example for a multi linear approximation (chain line) is presented in Razzaq (1983); its generalized form is given in Equation (3.5) and the corresponding graph is illustrated in Figure 3.2.

$$F(v) = \left[\sum_{i=1}^{j} v_i \cdot \left(K_i - K_{i+1}\right)\right] + K_{j+1} \cdot v \; ; v_j \le v \le v_{j+1} \tag{3.5}$$

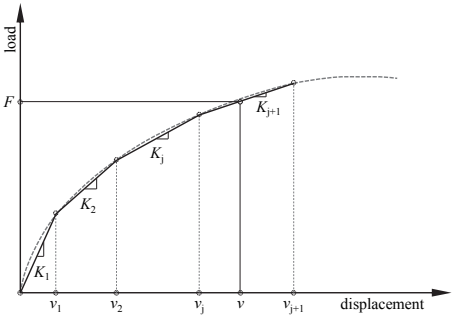

Figure 3.2: multilinear approximation according to Razzaq (1983)

Depending on the 'fineness' of the single segments, multi linear descriptions do have the potential to reflect the load-displacement behaviour of timber joints in a high quality. Therefore, software applications able to perform nonlinear calculations do willingly resort to this type of approximation; compare, e.g., RFEM 5 (2015).

However, the discontinuities in the transient points of the different line segments may lead to singularities in calculations and are, hence, an essential issue of such piecewise linear models. Furthermore, to get an adequate approximation of a curve, it has to be separated in a huge number of single pieces, which further complicates the handover of information – especially in printed publications.

3-3 CONTINUOUS FUNCTIONS

Several mathematical functions describing the load-displacement relationship of different joints are available in literature. Corresponding reviews for joints in timber and steel structures are given in, e.g., McLain (1975), Abdulrahman (2002), Judd (2005), Diaz et al. (2011) or AlHendi and Celikag (2015).

The following sections will give a further overview, whereby no separation between models applied for different materials or connection types is made; the chosen classifications only consider the (mathematical) type of function.

3-3.1 POWER AND POLYNOMIAL FUNCTIONS

Power and polynomial functions are quite easy to use and, in general, one direct and unique solution exists. Furthermore, the Weierstrass approximation theorem states that every continuous function (in a defined interval) can be approximated by a polynomial function; compare Glos (1978). Consequently it can be assumed that every arbitrary (continuous) test curve can be described by a polynomial function as given in Equation (3.6).

$$F(v) = \sum_{i=1}^{n} C_i \cdot v^i \tag{3.6}$$

with

C_i ..... constant values

Probably one of the first power models describing the behaviour of steel joints has been developed by Ramberg and Osgood (1943); the revised version of the proposed three-parameter model is given in Equation (3.7).

$$v(F) = \frac{F}{K_{ini}} + C_1 \cdot \left(\frac{F}{K_{ini}}\right)^{C_2} \tag{3.7}$$

with

C_1, C_2 ..... curve fitting parameters

An example for a power function, applicable for timber structures, is given in Mack (1977). The author uses the function expressed in Equation (3.8) to describe the relation between load and the displacement of a nailed joint up to 0.5 mm.

$$F(v) = C_1 \cdot d^{C_2} \cdot \rho \cdot v^{C_3} \tag{3.8}$$

with

ρ ..... density

d ..... nail diameter

C_1-C_3 ..... curve fitting parameters

A further power model is shown in Tissell and Elliott (2004) where Equation (3.9) is applied to calculate the fasteners slip depending on its actual load.

$$v(F) = \left(\frac{F}{C_1}\right)^{C_2} \tag{3.9}$$

with

C_1, C_2 ..... curve fitting parameters

As described in Tomasi et al. (2009) and Malo et al. (2011), O'Halloran (1973) also uses a power function for approximating the stress-strain curve for wood in compression. Thereby, the fitting parameters C_1 and C_2 allow describing the post-maximum softening branch; compare adapted Equation (3.10).

$$F(v) = K_{\text{ini}} \cdot v - C_1 \cdot v^{C_2} \tag{3.10}$$

Frye and Morris (1975) used 'standardised' polynomial functions for describing the moment-rotation characteristics of connections in steel structures. Allocating their model to load-displacement relationships, results in the following (general) expression.

$$v(F) = \sum_{i=1}^{n} C_i (C_s \cdot F)^i \tag{3.11}$$

with

C_i ..... curve fitting parameters

C_s ..... standardisation factor (dimensionless factor depending on the size parameters for the particular connection considered)

However, a disadvantage of polynomial functions can be seen in the high number of necessary terms for describing more complex curve shapes with sufficient accuracy. Additionally, as explained in Glos (1978), polynomial functions with several terms tend to produce 'wavy' shapes and the possible occurrence of negative stiffness values is physically unacceptable; compare also Wu and Chen (1990).

3-3.2 EXPONENTIAL AND LOGARITHMIC FUNCTIONS

Based on experimental tests on joints equipped with short bolts as fasteners, Teichmann and Borkmann (1930) assumed a linear context between embedment stress and the bedding modulus. Allocating their approach to the currently spotted question, leads to the expression given in Equation (3.12), showing a linear context between load and stiffness. As visible, this expression yields to K_{ini} for $F = 0$ and to a stiffness value equal to zero for $F = F_{\max}$. Solving the inhomogeneous linear differential equation by applying the boundary condition $F(v = 0) = 0$, finally leads to the exponential and logarithmic expressions given in Equations (3.13) and (3.14).

$$\frac{dF}{dv} = -\frac{K_{\text{ini}}}{F_{\max}} \cdot F + K_{\text{ini}} \tag{3.12}$$

$$F(v) = F_{\max} \cdot \left(1 - e^{-\frac{K_{\text{ini}}}{F_{\max}} v}\right) \tag{3.13}$$

$$v(F) = -\frac{F_{\max}}{K_{\text{ini}}} \cdot \ln\left(1 - \frac{F}{F_{\max}}\right) \tag{3.14}$$

Probably this was the first time an exponential function has been used for describing an experimental test curve in timber engineering. However, also other models in literature use this mathematical tool.

As described in Mack (1977), Mack (1966) shows that the load-displacement relationship of nailed joints up to a displacement of 2.54 mm (0.1 inch) can be properly described by Equation (3.15).

$$F(v) = C_1(C_2 \cdot v + C_3) \cdot (1 - e^{-C_4 \cdot v})^{C_5} \tag{3.15}$$

with

C_1-C_5 ..... constant values accounting for species, nail diameter and moisture condition

The most common load-displacement approximation in timber engineering is proposed by Foschi (1974); compare Equation (3.16). In particular, this model enables to consider a defined post-elastic stiffness K_p, whose inclination theoretically intersect the vertical axis of the load-displacement diagram at F_t; see also Figure 3.3. As a consequence, assuming K_p to be equal to zero finally results in the exponential model of Teichmann and Borkmann (1930) as expressed in Equation (3.13).

$$F(v) = (F_t + K_p \cdot v) \cdot \left[1 - e^{\left(-\frac{K_{ini}}{F_t} \cdot v\right)}\right] \tag{3.16}$$

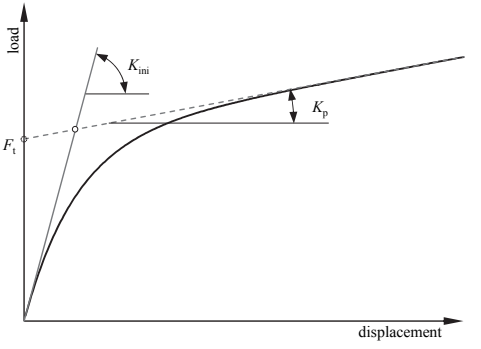

Figure 3.3: exponential approximation model proposed by Foschi (1974)

Even if the original expression was 'only' intended to describe the embedment behaviour of a single nail, i.e. of a 'Glulam Rivet', this approach is applied for approximating the load-displacement relationship of many different types of fasteners and connections. This, not only for timber, but also for steel structures; compare Chisala (1999). Furthermore, several modifications of the original expression can be found in literature.

For example, Smith (1987) uses ($v - v_{in}$) instead of v as control variable; this for considering the initial slip v_{in}, relating to the tolerance in a bolt hole. Furthermore, since the original formulation does not include a limit for the resulting load, for the determination of the load-carrying capacity of joints with

multiple nails, Blaß (1991) implements a limit at F_{max}. Pursuing the same goal, Jorissen (1999) combined both modifications, which finally leads to the expression given in Equation (3.17); see also Figure 3.4.

$$F(v) = \left[F_t + K_p \cdot (v - v_{in})\right] \cdot \left[1 - e^{\left(-\frac{K_{ini} \cdot (v - v_{in})}{F_t}\right)}\right] \leq F_{max} \tag{3.17}$$

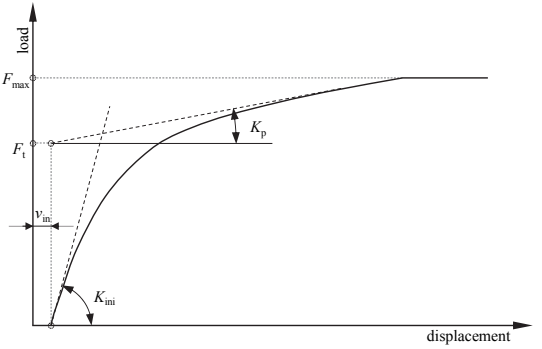

Figure 3.4: modified model of Foschi (1974) as described in Jorissen (1999)

A further variation is shown in Girhammar et al. (2004), where the authors extended the original expression of Foschi (1974) to a five parameter model; compare Equation (3.18). This modification enables the consideration of the softening branch and was used to describe load-displacement relationships of sheathing-to-timber joints for wood-framed shear walls.

$$F(v) = \left(F_t + K_p \cdot v\right) \cdot \left[1 - e^{\left(-\frac{K_{ini} \cdot v}{F_t}\right)}\right] \cdot e^{\left(-\frac{v^{C_1}}{C_2}\right)} \tag{3.18}$$

with

C_1, C_2..... curve fitting parameters

Yee and Melchers (1986) applied the exponential model given in Equation (3.19) for approximating the semi-rigid behaviour of steel joints. Thereby, the additional factor C allows fitting the radius of the transition region between the elastic stiffness K_{ini} and the plastic stiffness K_p. For small values of K_p, and a parameter C equal to zero, the model of Yee and Melchers (1986) yields to similar results as the model of Foschi (1974) does.

$$F(v) = F_t \cdot \left[1 - e^{\left(-\frac{(K_{ini} - K_p + C \cdot v) \cdot v}{F_t}\right)}\right] + K_p \cdot v \tag{3.19}$$

with

C..... parameter to control the rate of decay of the slope of the curve, obtained from test data

Analysing the behaviour of flexibly-jointed frames in steel structures, Lui and Chen (1986) proposed the exponential function given in Equation (3.20).

$$F(v) = F_{in} + \sum_{j=1}^{n} C_j \cdot \left[1 - e^{\left(-\frac{|v|}{2 \cdot j \cdot C_s} \right)} \right] + K_p \cdot |v| \tag{3.20}$$

with

F_{in} ..... initial load

C_j ..... curve fitting parameters

C_s ..... scaling factor

The tangent stiffness of this model can be expressed as given in Equation (3.21); the initial stiffness K_{ini} (at $v = 0$) results from Equation (3.22). It is also worth mentioning that the authors schedule to apply the tangent stiffness $K_T(v)$ for the loading, and the initial stiffness K_{ini} for the unloading case.

$$K_T(v) = \sum_{j=1}^{n} \frac{C_j}{2 \cdot j \cdot C_s} \cdot e^{\left(-\frac{|v|}{2 \cdot j \cdot C_s} \right)} + K_p \tag{3.21}$$

$$K_{ini} = \sum_{j=1}^{n} \frac{C_j}{2 \cdot j \cdot C_s} + K_p \tag{3.22}$$

Aiming to accommodate linear components in the hardening branch, according to Chen and Kishi (1989), Kishi and Chen (1986) modified this model as given in Equation (3.23).

$$F(v) = F_{in} + \sum_{j=1}^{n} C_j \cdot \left[1 - e^{\left(-\frac{|v|}{2 \cdot j \cdot C_s} \right)} \right] + \sum_{k=1}^{m} D_k \cdot \left(|v| - |v_k| \right) \cdot H\left[|v| - |v_k| \right] \tag{3.23}$$

with

v_k ..... starting displacement of k^{th} linear component (taken from experimental tests)

$H[|v|-|v_k|]$..... Heaviside's step function (1 for $[|v|-|v_k|] \geq 0$; 0 for $[|v|-|v_k|] < 0$)

C_j, D_k ..... curve fitting parameters

A three parameter exponential model, simulating the moment-rotation behaviour of steel joints, is proposed in Chenaghlou (1997). The adapted displacement- and force-based versions are given in Equations (3.24) and (3.25), respectively.

$$F(v) = F_{max} \cdot C_3 \cdot \left(e^{\frac{-1}{10^{C_1} \cdot v + C_2}} - C_4 \right) \tag{3.24}$$

$$v(F) = \frac{1}{10^{C_1}} \cdot \left(\frac{-1}{\ln\left(\frac{F}{F_{max} \cdot C_3} + C_4 \right)} - C_2 \right) \tag{3.25}$$

with

C_1..... connection parameter (function of F_{max} and K_{ini})

C_2..... shift parameter

C_3..... $1 + e^{-\frac{1}{C_2}}$

C_4..... $C_3 - 1 = e^{-\frac{1}{C_2}}$

Studying the nonlinear properties of Japanese conventional wooden structures, Gao and Kajikawa (2010) proposed three further exponential functions. The function given in Equation (3.26) is suggested for simulating the backbone curve of experimental cyclic tests. Furthermore, Equations (3.27) and (3.28) are scheduled for approximating the single loading and unloading paths of the hysteresis, respectively.

$$F(v) = C_1 \cdot \left(e^{C_2 \cdot v} - e^{C_3 \cdot v} \right) \tag{3.26}$$

$$F_{loading}(v) = C_1 \cdot e^{C_2 \cdot \sin(C_3 \cdot v)} + C_4 \tag{3.27}$$

$$F_{unloading}(v) = C_1 \cdot e^{C_2 \cdot v} + C_3 \cdot e^{C_4 \cdot v} \tag{3.28}$$

with

C_1-C_4 ..... curve fitting parameters

Investigating the load-slip relations in laterally loaded nailed joints, McLain (1975) proposed the two parameter logarithmic function as given in Equation (3.29). Thereby, it seems that variable C_1 mainly influences the initial portion of the curve and C_2 the later one.

$$F(v) = C_1 \cdot \log_{10}\left(1 + C_2 \cdot v\right) \tag{3.29}$$

with

C_1, C_2..... curve fitting parameters

In order to evaluate the behaviour of semi-rigid steel joints, Wu and Chen (1990) suggested the mathematical function given in Equation (3.30). This, especially for test curves exhibiting "*(...) an elastic-plastic hardening behaviour and do not flatten out near the final loading (...)*"; Wu and Chen (1990). Furthermore, the authors offer two linear functions predicting the shape parameter C for some practical steel joints. However, not being relevant for timber structures, they are not discussed within this thesis.

$$F(v) = C \cdot \ln\left(1 + \frac{v}{C \cdot \frac{F_{max}}{K_{ini}}}\right) \cdot F_{max} \tag{3.30}$$

with

C..... shape parameter (function of F_{max} and K_{ini})

Lee and Moon (2002) proposed a two parameter logarithmic model for describing the nonlinear moment-rotation behaviour of semi-rigid steel connections; compare Equations (3.31) and (3.32). As described, the model is applicable for several load-displacement relationships, but the included shape parameters C_1 and C_2 do not have a distinct physical meaning. Hence, some additional (joint-specific) functions, gathered from statistical regression analysis on experimental data sets, using the initial and plastic stiffness as well as the Young's modulus as variables, are offered for predicting these parameters.

$$F(v) = C_1 \cdot \left[\ln\left(C_2 \cdot 10^3 \cdot v + 1\right)\right]^{C_2} \tag{3.31}$$

$$K_T(v) = C_1 \cdot C_2 \cdot \left[\ln\left(C_2 \cdot 10^3 \cdot v + 1\right)\right]^{C_2 - 1} \cdot \frac{C_2 \cdot 10^3}{C_2 \cdot 10^3 + 1} \tag{3.32}$$

with

C_1, C_2..... shape parameters (functions of K_{ini} K_p, and E)

Note: The original paper depicts Equation (3.31) as a partial floor function.

Primarily aiming to discuss the topic 'yield stress' (compare section 2-4.3.2) rather than the best fit for a defined test curve, Christensen (2008) uses Equation (3.33) for simulating a load-displacement (original: stress-strain) relationship.

$$v(F) = \frac{F}{K_{ini}} - C_1 \cdot \ln\left[1 - \left(\frac{F}{F_{max}}\right)^{C_2}\right] \tag{3.33}$$

with

C_1 ..... fitting parameter (has to be positive)

C_2 ..... fitting parameter (usually ≥ 1.0)

For this model, two limit cases have to be considered. In particular, (i) the second part disappears for very small loads, which leads to a linear elastic branch, and (ii) for loads close to F_{max} the model exhibits high plastic deformations; compare Equations (3.34) and (3.35), respectively. Furthermore, if C_2 becomes very large, the model tends to the elastic-perfectly plastic form.

$$\left(\frac{F}{F_{max}}\right)^{C_2} \ll 1.0 \quad \Rightarrow \quad \ln(1) \cong 0 \quad \Rightarrow \quad v = \frac{F}{K_{ini}} \tag{3.34}$$

$$\left(\frac{F}{F_{max}}\right)^{C_2} \rightarrow 1.0 \quad \Rightarrow \quad \ln(0) = -\infty \quad \Rightarrow \quad v \rightarrow \infty \tag{3.35}$$

For evaluating the yield point in consequence of this analytical approach, the yield criterion in Equation (2.57) has to be expressed by the derivatives of displacement with respect to the load. Following Christensen (2008), it could be shown that Equations (3.36) to (3.38) are true. Furthermore, Equation (3.38) reduces to Equation (3.39) if the yield criterion of Equation (2.57) is considered.

$$K_T(v) = \frac{dF}{dv} = \frac{1}{\frac{dv}{dF}} \tag{3.36}$$

$$\Delta K_T(v) = \frac{d^2F}{dv^2} = -\left(\frac{d^2v}{dF^2}\right) \Big/ \left(\frac{dv}{dF}\right)^3 \tag{3.37}$$

$$\frac{d^3F}{dv^3} = 3 \cdot \left(\frac{d^2v}{dF^2}\right)^2 \Big/ \left(\frac{dv}{dF}\right)^5 - \left(\frac{d^3v}{dF^3}\right) \Big/ \left(\frac{dv}{dF}\right)^4 \tag{3.38}$$

$$\frac{d^3F}{dv^3} = 0 \quad \Rightarrow \quad 3 \cdot \left(\frac{d^2v}{dF^2}\right)^2 - \left(\frac{d^3v}{dF^3}\right) \cdot \left(\frac{dv}{dF}\right) = 0 \tag{3.39}$$

Note: The solved equations for the tangent stiffness $K_T(v)$ and the changing of the tangent stiffness $\Delta K_T(v)$ are documented in ANNEX D.

3-3.3 RATIONAL FUNCTIONS

Besides their already described exponential model, Teichmann and Borkmann (1930) also offered a rational function for approximating the deformation of wood in dependence on the allocated embedment stress; compare Equations (3.40) and (3.41). However, since the exponential form yields to more accurate results, the rational model was neglected within their further investigations.

$$F(v) = \frac{F_{max} \cdot K_{ini} \cdot v}{F_{max} + K_{ini} \cdot v} = \frac{K_{ini} \cdot v}{1 + \left(\frac{K_{ini} \cdot v}{F_{max}}\right)} \tag{3.40}$$

$$v(F) = \frac{F}{K_{ini} \cdot \left(1 - \frac{F}{F_{max}}\right)} \tag{3.41}$$

Aiming to compute nonlinear structures, Goldberg and Richard (1963) proposed Equation (3.42) for describing load-displacement, moment-rotation and stress-strain relationships. As clearly visible, this model is quite similar to the one proposed in Teichmann and Borkmann (1930), but contains one further parameter C defining the general nonlinear behaviour. Additionally, according to Richard and Abbott

(1975), Equation (3.42) may be inverted to Equation (3.43), enabling to calculate the displacement in terms of the actual load.

$$F(v) = \frac{K_{ini} \cdot v}{\left(1 + \left(\frac{K_{ini} \cdot v}{F_{max}}\right)^{C}\right)^{\frac{1}{C}}} \tag{3.42}$$

$$v(F) = \frac{F}{K_{ini} \cdot \left(1 - \left(\frac{F}{F_{max}}\right)^{C}\right)^{\frac{1}{C}}} \tag{3.43}$$

with

C..... shape parameter

As described in Bosco et al. (2014), Giuffre and Pinto (1970) modified the model of Goldberg and Richard (1963) to describe the behaviour of steel under reversed cyclic loading. In a further step Menegotto and Pinto (1973) enriched this modification, considering the kinematic hardening, and applied it for computing the behaviour of steel rebars embedded in reinforced concrete beams. Revised according to the notations used in the present thesis, the resulting mathematical function is expressed in Equation (3.44).

$$F(v) = v \cdot \frac{F_y}{v_y} \cdot \left(\frac{1 - \frac{K_p}{K_{ini}}}{\left(1 + \left(\frac{v}{v_y}\right)^{C}\right)^{\frac{1}{C}}} + \frac{K_p}{K_{ini}} \right) \tag{3.44}$$

For this model it is worth mentioning that the considered yield point represents the intersection of the two asymptotes owning the inclinations K_{ini} and K_p; compare Figure 3.5.

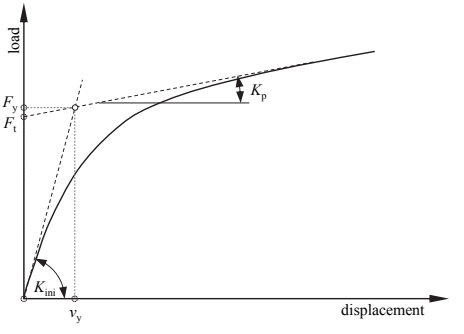

Figure 3.5: model proposed by Menegotto and Pinto (1973) and Richard and Abbott (1975)

Assuming the start of computation at the origin, consequently enables to substitute the parameter v_y as given in Equation (3.45). If, additionally, the yield load F_y is replaced by the expression in Equation (3.46), Equation (3.44) finally yields to the model proposed by Richard and Abbott (1975); compare Equation (3.47) and Figure 3.5. Furthermore, for a plastic stiffness equal to zero (elastic-perfectly plastic model), Equation (3.47) again reduces to the model presented by Goldberg and Richard (1963); compare Equation (3.42).

$$v_y = \frac{F_y}{K_{ini}} \tag{3.45}$$

$$F_y = \frac{F_t}{1 - \frac{K_p}{K_{ini}}} \tag{3.46}$$

$$F(v) = \frac{\left(K_{ini} - K_p\right) \cdot v}{\left(1 + \left(\frac{\left(K_{ini} - K_p\right) \cdot v}{F_t}\right)^C\right)^{\frac{1}{C}}} + K_p \cdot v \tag{3.47}$$

According to Richard and Abbott (1975), their model leads to similar results as the Ramberg and Osgood (1943) function, but with one major advantage: it enables to simulate test curves exhibiting strain (or force) softening as well. Furthermore, in this context the application of F_t instead of F_y is reasonable since, otherwise, a yield load higher than the reached maximum load would occur; compare Figure 3.6 (a). Additionally, this model offers the opportunity to continuously compute the tangent modulus as it is expressed in Equation (3.48) and depicted in Figure 3.6 (b).

$$K_T(v) = \frac{\left(K_{ini} - K_p\right)}{\left(1 + \left(\frac{\left(K_{ini} - K_p\right) \cdot v}{F_t}\right)^C\right)^{\frac{(C+1)}{C}}} + K_p \tag{3.48}$$

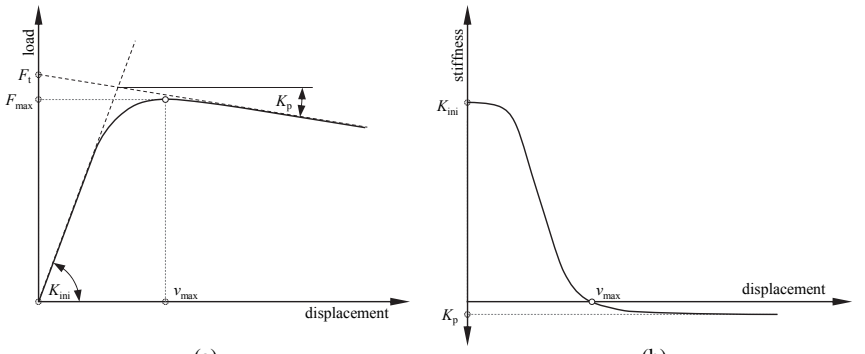

Figure 3.6: ***applying the Richard and Abbott (1975) model for approximating a curve shape exhibiting a softening branch – (a) load-displacement relationship; (b) stiffness-displacement diagram***

Finally, the authors explain how the shape parameter C may be determined by forcing the analytical expression through two actual points on the experimental test-curve. Nowadays, this step may be replaced by, e.g., an automated least squares fit and, hence, it is not further described.

In order to simulate the behaviour of timber in compression along the grain, Glos (1978) proposed the mathematical function given in Equation (3.49).

$$F(v) = \frac{v + C_1 \cdot v^{C_5}}{C_2 + C_3 \cdot v + C_4 \cdot v^{C_5}} \tag{3.49}$$

For determining the constant values C_1 to C_4, the boundary conditions listed below are applied. In particular, Equations (3.50) and (3.51) regulate the tangent modulus at the origin and the maximum point, Equation (3.52) forces the model curve through the maximum point and Equation (3.53) defines the asymptotic load level (F_a) of the softening branch; compare Figure 3.7 (a). The resulting functions for computing the constant values are documented in ANNEX D.

$$\frac{dF}{dv}(v = 0) = K_{ini} \tag{3.50}$$

$$\frac{dF}{dv}(v = v_{max}) = K_{max} = 0 \tag{3.51}$$

$$F(v = v_{max}) = F_{max} \tag{3.52}$$

$$F(v \gg v_{max}) = F_a \tag{3.53}$$

The shape affecting parameter C_5 is defined as a positive integer; for the originally investigated topic ‘strength along the grain’, Glos (1978) suggested to use $C_5 = 7$.

Besides the possibility to describe the post-peak behaviour, the differentiability and, hence, the continuous description of the tangent stiffness as given in Equation (3.54), is a major advantage of this model; see also Figure 3.7 (b).

$$K_T(v) = \frac{C_2 + C_1 \cdot C_2 \cdot C_5 \cdot v^{(C_5-1)} + (C_5 - 1) \cdot (C_1 \cdot C_3 - C_4) \cdot v^{C_5}}{\left(C_2 + C_3 \cdot v + C_4 \cdot v^{C_5}\right)^2} \tag{3.54}$$

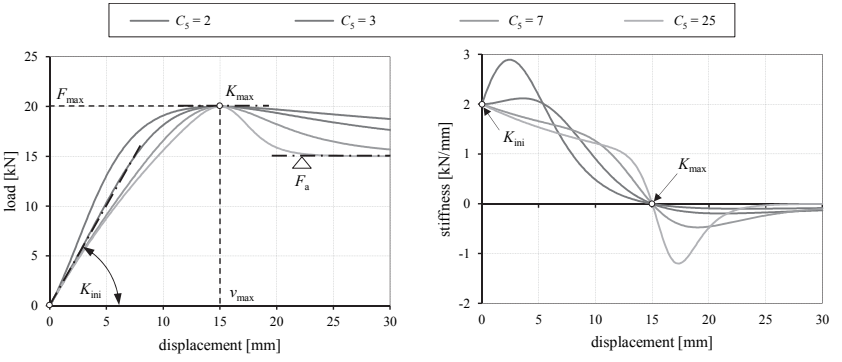

(a) (b)

Figure 3.7: analytical model according to Glos (1978) – (a) influencing parameters (F_{max} = 20 kN; v_{max} = 15 mm; K_{ini} = 2 kN/mm; F_a = 15 kN) and effect of shape parameter C_5; (b) trend of continuously defined tangent stiffness

Piazza and Turrini (1986) uses the hyperbolic law shown in Equation (3.55) for describing the behaviour of timber-to-timber connections realised by glued in steel pins.

$$(F - K_{ini} \cdot v) \cdot (F - F_{max}) - C \cdot F^2 = 0 \tag{3.55}$$

Note: The original paper uses a (+) instead of a (–) in front of the constant parameter C. However, applying the expression above permits the use of a positive value for the parameter C.

A rearrangement of Equation (3.55) finally enables to express the displacement in dependency of the actual load and vice versa; compare Equations (3.56) and (3.57), respectively.

$$v(F) = \frac{(F - C \cdot F - F_{max}) \cdot F}{(F - F_{max}) \cdot K_{ini}} \tag{3.56}$$

$$F(v) = \frac{\sqrt{v^2 \cdot K_{ini}^2 + 2 \cdot (2 \cdot C - 1) \cdot v \cdot F_{max} \cdot K_{ini} + F_{max}^2} - v \cdot K_{ini} - F_{max}}{2 \cdot (C - 1)} \tag{3.57}$$

3-4 SEGMENTED MODELS

In contrast to the approximation of load-displacement relationships via peace wise linear or continuous nonlinear models, segmented approaches, as understood herein, do combine both methods. Furthermore, the combination of different piecewise continuous models is disposed to this approximation method as well. Although not further considered in this thesis, models using B-splines (piecewise polynomial functions) are an example for such a combination.

For describing the stress-strain behaviour of wood loaded parallel to the grain (compression or tension), Conners (1989) proposed an approach consisting of two linear branches and a nonlinear (polynomial) one in between; compare Figure 3.8.

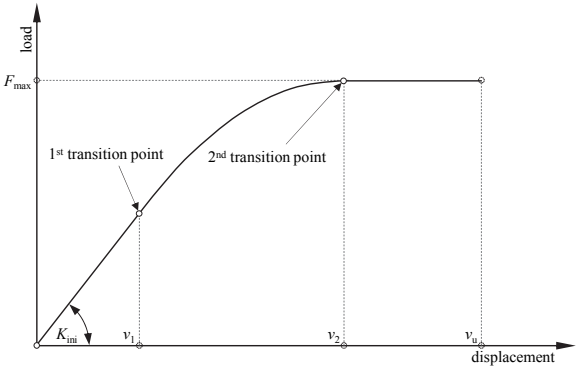

Figure 3.8: segmented model according to Conners (1989)

The general conditions scheduled by the author are given in Equations (3.58) to (3.60).

$$F(v) = C_1 + C_2 \cdot v, \quad v \le v_1 \tag{3.58}$$

$$F(v) = C_3 + C_4 \cdot v + C_5 \cdot v^2, \quad v_1 < v \le v_2 \tag{3.59}$$

$$F(v) = C_6 + C_7 \cdot v, \quad v > v_2 \tag{3.60}$$

with

$C_{1\text{-}7}$ ..... fitting parameters

$v_{1,2}$ ..... displacement at transition points

Assuming an equal tangent stiffness for the linear and the nonlinear parts at the transition points, enables to express the displacement borders (v_1 and v_2) as follows:

$$v_1 = \frac{C_2 - C_4}{2 \cdot C_5} \tag{3.61}$$

$$v_2 = \frac{C_7 - C_4}{2 \cdot C_5} \tag{3.62}$$

Furthermore, it can be shown that the following conditions are true:

$$C_3 = \frac{\left(C_2 - C_4\right)^2}{4 \cdot C_5} = C_5 \cdot v_1^2 \tag{3.63}$$

$$C_6 = \frac{C_2^2 - 2 \cdot C_2 \cdot C_4}{4 \cdot C_5} = C_5 \cdot \left(v_1^2 - v_2^2\right) \tag{3.64}$$

This, in combination with the additional assumptions listed below, enables to transform the approach as given in Equations (3.65) to (3.67), where not even one single fitting parameter remains:

(i) the approximation starts at the origin
(ii) the slope of the first linear branch represents the initial stiffness K_{ini}
(iii) an ideal plastic behaviour occurs after reaching the peak load $F_{\max}$

$$F(v) = K_{\text{ini}} \cdot v, \quad v \le v_1 \tag{3.65}$$

$$F(v) = \frac{4 \cdot F_{\max}^2 + K_{\text{ini}}^2 \cdot \left(v - v_{\max}\right)^2 - 4 \cdot F_{\max} \cdot K_{\text{ini}} \cdot v_{\max}}{4 \cdot \left(F_{\max} - K_{\text{ini}} \cdot v_{\max}\right)}, \quad v_1 < v \le v_2 \tag{3.66}$$

$$F(v) = F_{\max}, \quad v > v_2 \tag{3.67}$$

The corresponding transition points are defined as follows:

$$v_1 = \frac{2 \cdot F_{\max}}{K_{\text{ini}}} - v_{\max} \tag{3.68}$$

$$v_2 = v_{\max} \tag{3.69}$$

A segmented model approximating the stress-strain relationship of concrete under uniaxial compression is presented in CEB (1993). Equations (3.70) to (3.73) and Figure 3.9 explain this model, consisting of two curvilinear branches, adjusted to the herein used notations.

$$F(v) = F_{\max} \cdot \frac{\frac{K_{\text{ini}}}{K_{\text{peak}}} \cdot \frac{v}{v_{\max}} - \left(\frac{v}{v_{\max}}\right)^2}{1 + \left(\frac{K_{\text{ini}}}{K_{\text{peak}}} - 2\right) \cdot \frac{v}{v_{\max}}}, \quad v \le v_{\text{lim}} \tag{3.70}$$

$$F(v) = -F_{max} \cdot \left[\left(\frac{C}{v_{max}} - \frac{2}{v_{lim}} \right) \cdot \frac{v^2}{v_{lim}} + \left(\frac{4 \cdot v_{max}}{v_{lim}} - C \right) \cdot \frac{v}{v_{max}} \right]^{-1}, \quad v > v_{lim} \tag{3.71}$$

$$C = \frac{4 \cdot \left[\left(\frac{v_{lim}}{v_{max}} \right)^2 \cdot \left(\frac{K_{ini}}{K_{peak}} - 2 \right) + 2 \cdot \frac{v_{lim}}{v_{max}} - \frac{K_{ini}}{K_{peak}} \right]}{\left[\frac{v_{lim}}{v_{max}} \cdot \left(\frac{K_{ini}}{K_{peak}} - 2 \right) + 1 \right]^2} \tag{3.72}$$

$$v_{lim} = v_{max} \cdot \sqrt{\frac{1}{2} \cdot \left(\frac{K_{ini}}{2 \cdot K_{peak}} + 1 \right) + \left[\frac{1}{4} \cdot \left(\frac{K_{ini}}{2 \cdot K_{peak}} + 1 \right)^2 - \frac{1}{2} \right]} \tag{3.73}$$

with

K_{peak} ..... secant stiffness from the origin to the maximum point

v_{lim} ..... limiting displacement (at $0.5 \cdot F_{max}$; compare Figure 3.9)

Note: The displacement value v_{lim} has no distinct meaning; it only limits the applicability of the curve described by Equation (3.70); see also Figure 3.9.

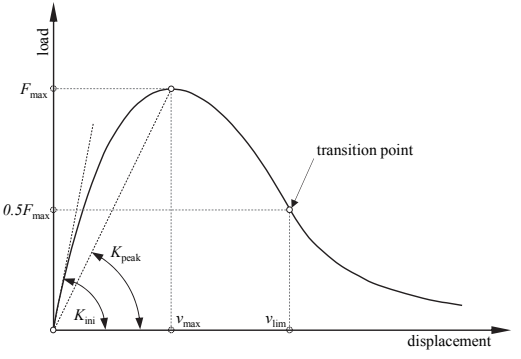

Figure 3.9: segmented model for concrete under uniaxial compression according to CEB (1993)

Aiming to simulate the hysteretic response of mechanical connections, Foschi (2000) applied the model defined in Equations (3.74) and (3.75) for determining the embedment response parameters; see also Foschi et al. (2000) and Figure 3.10. Thereby, the first part is equal to the exponential model originally described in Foschi (1974). The second one also exhibits an exponential shape, but is regulated by the parameter C, forcing the softening branch through the ultimate point; compare Equation (3.76). Here, the maximum point is used as transition point and can be determined as expressed in Equation (3.77). Furthermore, a linear behaviour is scheduled in case of reversal; detailed information regarding the latter point is given in section 3-6.4.

$$F(v) = (F_t + K_p \cdot v) \cdot \left[1 - e^{\left(-\frac{K_{ini}}{F_t} \cdot v \right)} \right], \quad v \le v_{max} \tag{3.74}$$

$$F(v) = F_{max} \cdot e^{C \cdot (v - v_{max})^2}, \quad v_{max} < v \tag{3.75}$$

$$C = \frac{\ln\left(\frac{F_u}{F_{max}} \right)}{\left(v_{max} \cdot \left(\frac{v_u}{v_{max}} - 1 \right) \right)^2} \tag{3.76}$$

$$F_{max} = \left(F_t + K_p \cdot v_{max} \right) \cdot \left(1 - e^{\left(-\frac{K_{ini}}{F_t} \cdot v_{max} \right)} \right) \tag{3.77}$$

with

C ..... parameter regulating the decay in load after passing v_{max}

Note: Equations (3.74) to (3.77) are slightly adapted according to the terms used in the present thesis.

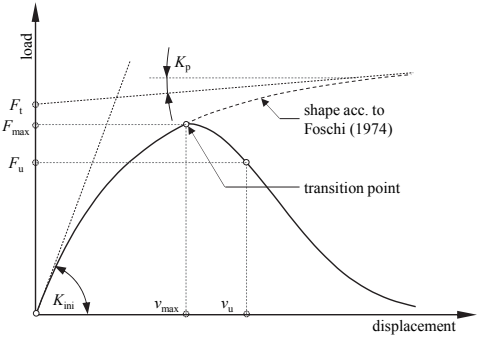

Figure 3.10: segmented model according to Foschi et al. (2000)

In the course of investigating the cyclic behaviour of wooden platform-frame shear walls, Folz and Filiatrault (2001) proposed to separate the envelope curve of sheathing-to-framing connectors into three phases: (i) a nonlinear increase of load up to the maximum load-carrying capacity F_{max} (corresponding to v_{max}) by applying the model of Foschi (1974), (ii) a linear decrease of load for displacements beyond v_{max} and (iii) failure at ultimate displacement v_u; see also Equations (3.78) to (3.80) and Figure 3.11 (a).

$$F(v) = (F_t + C_1 \cdot K_{ini} \cdot v) \cdot \left[1 - e^{\left(-\frac{K_{ini} \cdot v}{F_t} \right)} \right], \quad v \le v_{max} \tag{3.78}$$

$$F(v) = F_{max} + C_2 \cdot K_{ini} \cdot (v - v_{max}), \quad v_{max} < v \le v_u \tag{3.79}$$

$$F(v) = 0, \quad v > v_u \tag{3.80}$$

with

C_1 ..... parameter regulating the plastic stiffness ($C_1 \cdot K_{ini} = K_p$)

C_2 ..... parameter regulating the inclination of the softening branch

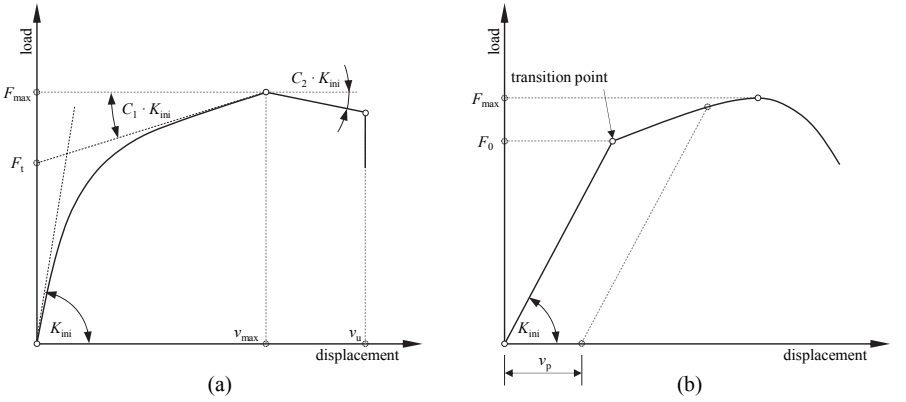

Figure 3.11: segmented models according to – (a) Folz and Filiatrault (2001); (b) Malo et al. (2011)

To optimize the data (post-) processing, a curve fitting method, combining a linear part for the elastic zone with either a polynomial or an exponential function for the plastic one, is suggested in Malo et al. (2011). The applied polynomial and exponential approaches are given in Equations (3.81) and (3.82), respectively.

$$F(v) = F_0 + C_1 \cdot v_p + C_2 \cdot v_p^2 + C_3 \cdot v_p^3, \quad v \ge \frac{F_0}{K_{ini}} \tag{3.81}$$

$$F(v) = F_0 + C_1 \cdot \left(1 - e^{-C_2 \cdot v_p}\right) + C_3 \cdot \left(1 - e^{-C_4 \cdot v_p}\right), \quad v \ge \frac{F_0}{K_{ini}} \tag{3.82}$$

$$v_p = v - \frac{F(v)}{K_{ini}} \tag{3.83}$$

with

F_0, C_1-C_4 ..... fitting parameters

v_p ..... permanent (plastic) deformation

Note: According to Malo et al. (2011), opposite signs for C_1 and C_3 are required for ensuring a maximum point in the exponential approach.

However, since both the linear and the nonlinear segments are fitted independently to the experimental test curves, a distinct kink may occur at the transition point; compare Figure 3.11 (b).

An established segmented model is given in Eurocode 3, i.e., ON EN 1993-1-8 (2012). The therein described method, determining the rotational stiffness of steel joints (component model), schedules the following conditions:

$$K_S(F) = K_{ini}, \quad F \le \frac{2}{3} \cdot F_{max} \tag{3.84}$$

$$K_S(F) = \frac{K_{ini}}{\left(1.5 \cdot \frac{F}{F_{max}}\right)^C}, \quad \frac{2}{3} \cdot F_{max} < F \le F_{max} \tag{3.85}$$

with

K_S ..... secant stiffness from the origin; compare Figure 3.12

C ..... fitting parameter

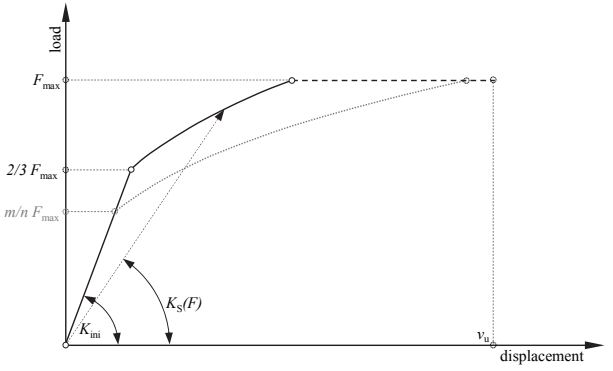

Figure 3.12: segmented model as scheduled in Eurocode 3 (the further visualised variation of the linear branch (grey dashed line) is originally not intended)

For calculating the displacement instead of the secant stiffness, Equations (3.86) and (3.87) can be applied. Furthermore, an ideal plastic behaviour may be assumed after reaching F_{max} and up to the ultimate displacement (in Eurocode 3: rotation capacity).

$$v(F) = \frac{F}{K_{ini}}, \quad F \le \frac{2}{3} \cdot F_{max} \tag{3.86}$$

$$v(F) = \frac{F \cdot \left(1.5 \cdot \frac{F}{F_{max}}\right)^C}{K_{ini}}, \quad \frac{2}{3} \cdot F_{max} < F \le F_{max} \tag{3.87}$$

Although not intended in Eurocode 3, this model, in principle, also offers the option to arbitrarily change the load level, regulating the linear branch. For this purpose it is necessary, to adapt Equation (3.87) as given in Equation (3.88); this in order to achieve a continuous crossover between the linear and the nonlinear segments; compare Figure 3.12.

$$v(F) = \frac{F \cdot \left(\frac{n}{m} \cdot \frac{F}{F_{max}} \right)^{C}}{K_{ini}}, \quad \frac{m}{n} \cdot F_{max} < F \leq F_{max} \tag{3.88}$$

with

m, n..... parameters regulating the length of the linear branch

For the simulation of the withdrawal behaviour of single self-tapping screws positioned in the narrow-face of CLT elements, Brandner et al. (2017) modified the model proposed in Glos (1978) by adding an initial linear branch; compare Equations (3.89) and (3.90). Furthermore, Brandner et al. (2017) offered the possibility to consider the initial slip (v_{in}) by shifting the simulated load-displacement curve horizontally to the extent of v_{in}; see Equation (3.91).

$$F(v) = 0, \quad v \leq v_{ini} \tag{3.89}$$

$$F(v) = K_{ini} \cdot (v - v_{in}), \quad v_{in} < v \leq v_{lin} \tag{3.90}$$

$$F(v) = \frac{v - v_{lin}}{\left[C_1 + C_2 \cdot (v - v_{lin}) + C_3 \cdot (v - v_{lin})^{C_4} \right]} + K_{ini} \cdot (v_{lin} - v_{in}), \quad v > v_{lin} \tag{3.91}$$

with

C_1-C_3 ..... constant parameters determined by boundary conditions

C_4 ..... shape parameter

v_{in}..... initial slip; start of linear branch

v_{lin} ..... end of linear branch

To ensure a smooth transition between the linear elastic and nonlinear plastic part, the slope of the initial linear branch is used as the initial stiffness for the nonlinear part. Additionally, since a residual resistance is not applicable for the considered case, the asymptotic load level of the softening branch is set equal to zero ($F_a = 0$). Thus, one constant value of the original model, presented in Glos (1978), disappears; the modified terms for calculating the constant values C_1 to C_3 of Equation (3.91) are documented in ANNEX D.

For localising the linear elastic area, wherein the initial stiffness K_{ini} is determined by a linear regression, Brandner et al. (2017) applied a variation of the method indicated in section 2-4.3.2. In particular, the authors define the horizontal plateau in the plot of the first derivation of the load-displacement curve as the relevant area. However, instead of a numerical derivation, a ‘load increment

per data row' versus displacement plot is used for identifying this section. Since this procedure is only applicable in case of displacement controlled tests, herein the more general tangent stiffness instead of the load-increment is used for further investigations.

The graphs depicted in Figure 3.13 illustrate the withdrawal behaviour of a single self-tapping screw, placed in an end-grain butt joint at the narrow face of a five-layered CLT element (screw: Ø 8 mm; threaded part in timber (spruce): 80 mm; angle between screw axis and grain direction: 0°). As visible, the application of the above described model enables a quite good approximation of this load-displacement curve.

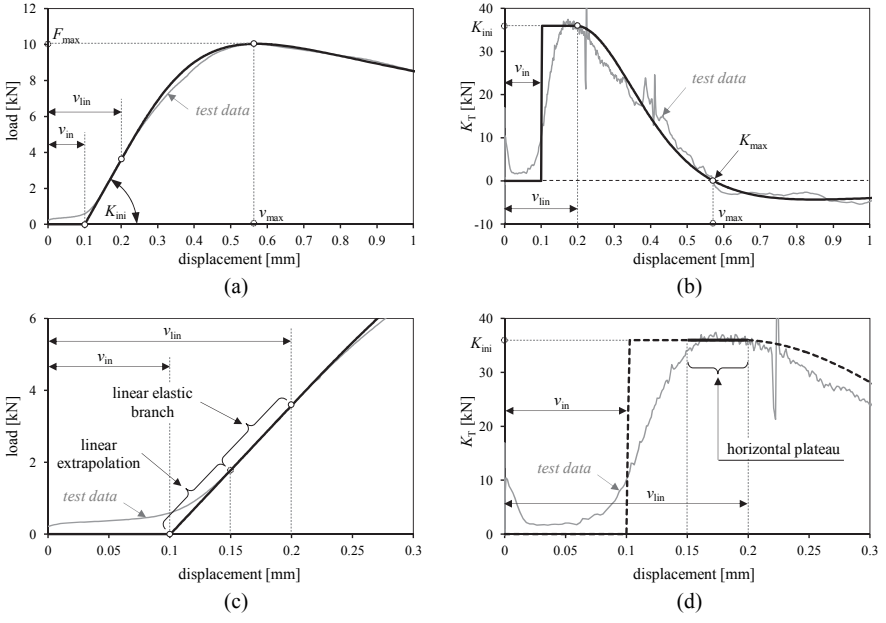

Figure 3.13: segmented model proposed in Brandner et al. (2017), applied to approximate the test curve of an axially loaded single self-tapping screw – (a) overview load-displacement diagram; (b) overview tangent stiffness-displacement diagram; (c) detail load-displacement diagram; (d) detail tangent stiffness-displacement diagram

3-5 COMPARISON OF SELECTED MODELS

Functions using the actual load as control variable are hardly able to describe the post peak behaviour. Hence, a comprehensive (continuous) approximation of experimentally received load-displacement curves requires a displacement controlled application. As a consequence, only displacement-based models are considered in the present section. However, since the consideration of all displacement controlled

models described before would go beyond the scope of the present thesis, basing on preliminary investigations, four capable models have been selected for the following discussion. The chosen approaches are (i) the piecewise linear model connecting yield, maximum and ultimate point (Y-M-U model), (ii) the exponential function proposed by Yee and Melchers (1986), (iii) the rational function developed by Glos (1978) and (iv) the segmented model described in Brandner et al. (2017). For assessing their qualities, the considered models are applied for approximating the six test curves introduced in section 2-4.1. Thereby, the alignment of the models is realised in two steps.

Firstly, the already identified parameters for the yield, maximum and ultimate points and the initial stiffness values are used to get the model curves into a rough shape. For this purpose, the initial stiffness and the yield point are determined according to ON EN 12512 (2005) and Yasumura and Kawai (1997), respectively.

Secondly, the least-squares method is applied to find the best possible fit of the respective models. This, by means of varying the available parameters, excluded the maximum load F_{max} and the corresponding displacement v_{max}. In this context it further has to be mentioned that all investigations are performed in the spreadsheet software program Microsoft ® Excel (2010) and the implemented 'Solver' is applied to process the least-squares fit.

The final input parameters for each single curve are documented in ANNEX D, Figure 3.14 illustrates the resulting approximation curves. Additionally, as a first objective criterion, Table 3.1 lists the differences in dissipated energies related to the original test curves.

Table 3.1: differences in dissipated energy related to the experimental test curve

model	[T1]	[T2]	[S1]	[S2]	[M1]	[M2]
Y-M-U	4.55 %	0.79 %	2.86 %	2.89 %	3.04 %	3.49 %
Yee and Melchers (1986)	1.18 %	0.09 %	0.05 %	0.15 %	0.24 %	0.77 %
Glos (1978)	0.62 %	0.55 %	0.42 %	0.59 %	1.25 %	3.07 %
Brandner et al. (2017)	0.27 %	1.60 %	0.78 %	0.81 %	0.01 %	1.75 %

At first glance both the acceptable shape and the small differences in dissipated energies, attest a good alignment for all considered approximation models. Nevertheless, a more detailed visual judgement and the analysis of the sums of least-squares, as an additional objective assessing criterion (compare Table 3.2), lead to the following observations.

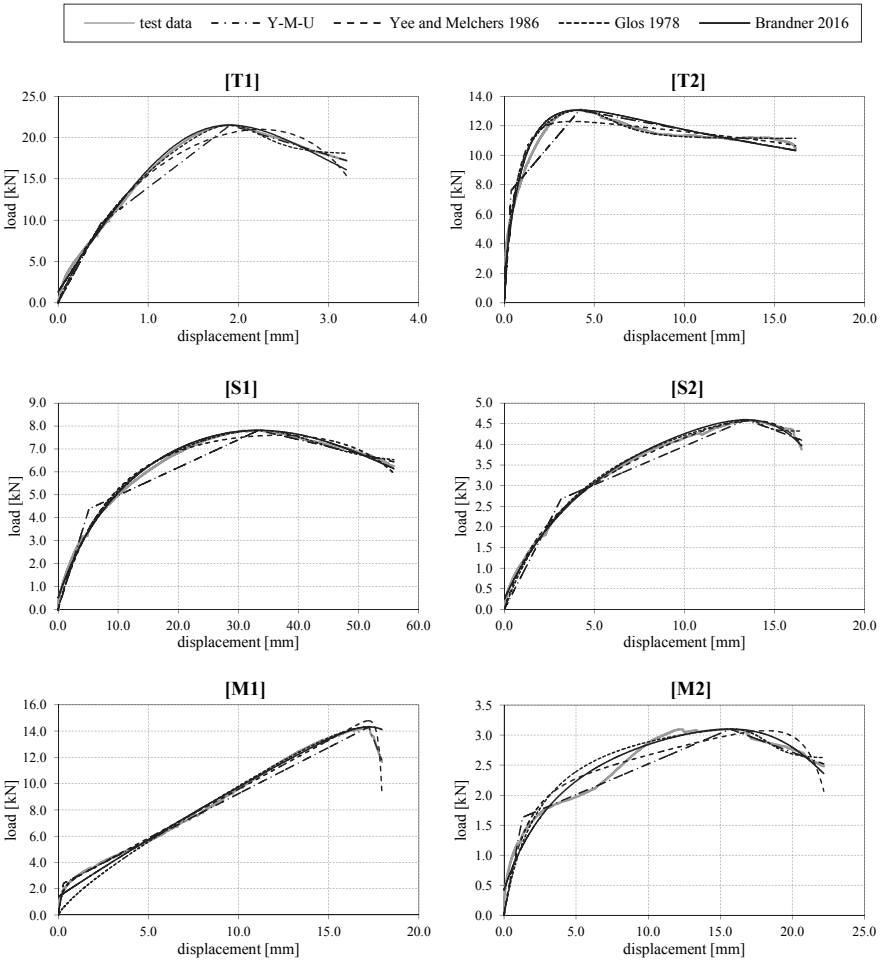

Figure 3.14: load-displacement diagrams of test curves [T1] to [M2] and respective approximations according to discussed models

The piecewise linear model mostly exhibits the 'worst' fit, but offers a good approximation of curve [M1]. A better performance is shown by the model of Yee and Melchers (1986). Especially for the test curves [S2] and [M1] this approach results in a very good alignment. A mentionable disadvantage of this model is the inadequate description of the maximum point; compare, e.g., curves [T1] and [T2].

The function developed in Glos (1978) shows a good fit to the tension and shear test curves ([T1], [T2], [S1] and [S2]) but stumbles when describing the more complex shapes of [M1] and [M2]. Especially the initial and final part of test curve [M1] cannot be approximated in a satisfying way.

A generally good performance is shown by the model of Brandner et al. (2017). In particular it exhibits the lowest least-squares ratio (1.0) for five of the six considered test curves; compare Table 3.2. Nevertheless, fitting this model to the original test data (here) results in negative initial displacements which finally prohibits a start at the origin; compare, e.g., diagram [M1] and input parameters in ANNEX D. Furthermore, this approximation method is also not able to simulate the experimental test curve [M2] in a satisfying way. However, summarising, this approach shows the best skills of the four considered approaches.

***Table 3.2:** relative least-squares related to the minimum for each considered test curve*

model	[T1]	[T2]	[S1]	[S2]	[M1]	[M2]
Y-M-U	4.2	2.1	7.5	8.1	2.7	1.8
Yee and Melchers (1986)	2.2	1.9	2.5	1.1	1.0	1.7
Glos (1978)	1.8	1.2	1.5	2.1	6.9	2.0
Brandner et al. (2017)	1.0	1.0	1.0	1.0	2.6	1.0

Note: Since the sum of least-squares depends on absolute values, for enabling an easy comparison, Table 3.2 solely contains relative least-squares related to the minimum for each considered test curve; i.e., the value 1.0 signifies the best fit.

Finally, to get a further indicator regarding the quality of the single models, the resulting (tangential) stiffness-displacement relationships are investigated. Since not explicit given in the previous section, Equation (3.92) and Equations (3.93) to (3.95) show the formulas applied for determining the tangential stiffness corresponding to the models of Yee and Melchers (1986) and Brandner et al. (2017), respectively.

$$K_{\mathrm{T}}(v) = \left(K_{\mathrm{ini}} - K_{\mathrm{p}} + 2 \cdot C \cdot v\right) \cdot e^{\left(-\frac{\left(K_{\mathrm{ini}} - K_{\mathrm{p}} + C \cdot v\right) \cdot v}{F_{\mathrm{t}}}\right)} + K_{\mathrm{p}} \tag{3.92}$$

$$K_{\mathrm{T}}(v) = 0, \quad v \le v_{\mathrm{in}} \tag{3.93}$$

$$K_{\mathrm{T}}(v) = K_{\mathrm{ini}}, \quad v_{\mathrm{in}} < v \le v_{\mathrm{lin}} \tag{3.94}$$

$$K_{\mathrm{T}}(v) = \frac{C_1 - C_3 \cdot (C_4 - 1) \cdot (v - v_{\mathrm{lin}})^{C_4}}{\left[C_1 + C_2 \cdot \left(v - v_{\mathrm{lin}}\right) + C_3 \cdot \left(v - v_{\mathrm{lin}}\right)^{C_4}\right]^2}, \quad v > v_{\mathrm{lin}} \tag{3.95}$$

Figure 3.15 illustrates the stiffness diagrams determined by calculating the symmetric difference quotient as given in Equation (2.60) and the corresponding approximations. Furthermore, the initial stiffness K_{ini} according to ON EN 12512 (2005) is visualised for all considered test curves.

Assessing the trends of the approximation models, lead to a similar judgement as described afore. Firstly, it is obvious that the Heaviside step function of the piecewise linear model can hardly exceed the fit of the nonlinear approaches. Focusing on the latter one, a good fit to the ‘standard’ curves ([T1] to [S2]) and problems when approximating the more complex curves ([M1] and [M2]), are visible.

Nevertheless, especially test curve [T1] indicates the partwise distinct differences between the considered models.

A further point worth mentioning is the deviation between the tangential stiffness in the origin and the secant stiffness K_{ini} according to ON EN 12512 (2005). As expected, the latter parameter generally underestimates the experimentally gathered tangential stiffness at the origin. This clearly visualises, why the corresponding input parameter for the bulk of approximation models is in most cases distinctively higher than the stiffness properties applied for linear elastic calculations; compare input parameters in ANNEX D and stiffness parameters in Table 2.3.

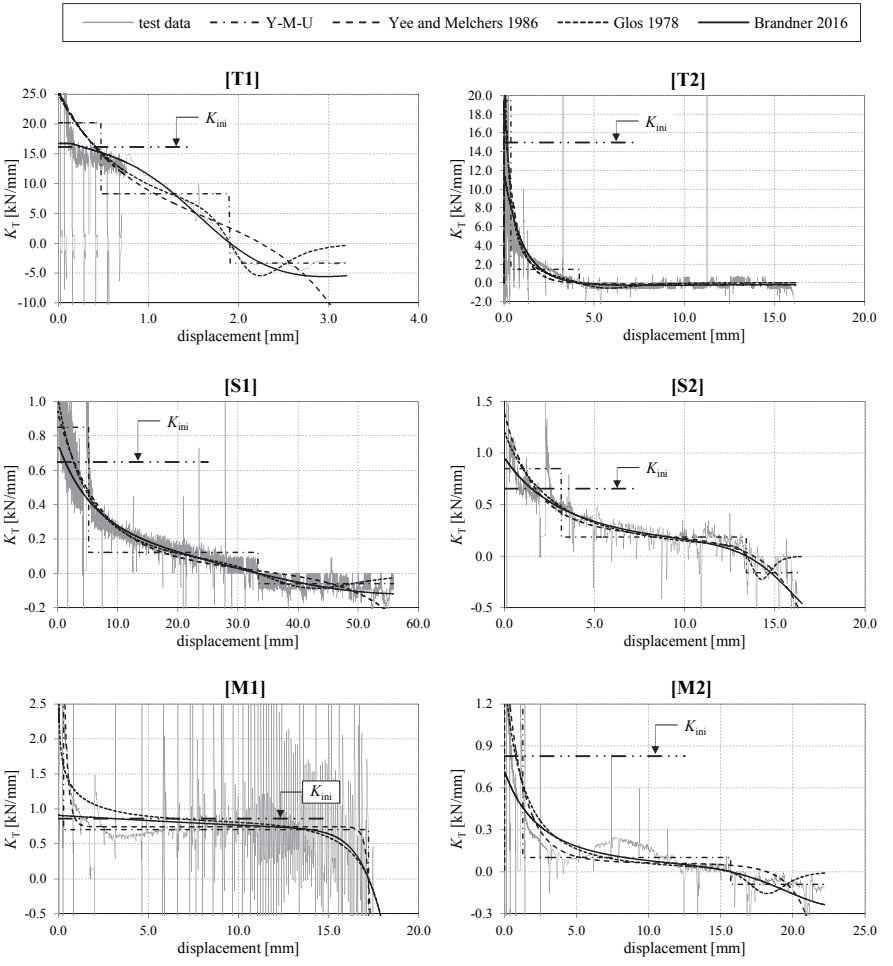

Figure 3.15: tangential stiffness-displacement diagrams of test curves [T1] to [M2] and corresponding courses of considered approximation models

3-6 NEW ANALYTICAL MODEL

The sum of experience collected within the last sections, combined with advisements found in literature, lead to the following requirements for an efficient approximation model; see also Yee and Melchers (1986) or Malo et al. (2011):

(i) the function is displacement controlled, continuous and differentiable

(ii) the expression is of simple form and contains only few parameters

(iii) the necessary parameters are physically meaningful and easy to determine

(iv) the resulting curve passes through the origin and has the ability to represent diverse curve shapes, including the post maximum softening

Several methods described herein comply with points (i) to (iii) but only few satisfy requirement (iv). Especially the continuous description of complex curve types seems challenging. However, in the opinion of the author, Glos (1978) proposed the most promising approach for solving this issue; the good fit of the modified version discussed in Brandner et al. (2017), further confirms this assessment.

A further approximation model basing on the ideas presented in Glos (1978) is suggested in Flatscher and Schickhofer (2014). A slightly enhanced version of this analytical approach is described and discussed within the following sections.

3-6.1 BASIC MODEL AND PARAMETERS

In principle, the here proposed model adapts the one given in Glos (1978), implementing two additional points where the resulting graph is forced to go through; compare points A and B in Figure 3.16. Furthermore, since not physically meaningful for the bulk of load-displacement relationships, the boundary condition relating to the asymptotic load is replaced by a condition regulating the tangential stiffness in point B; see also Figure 3.16.

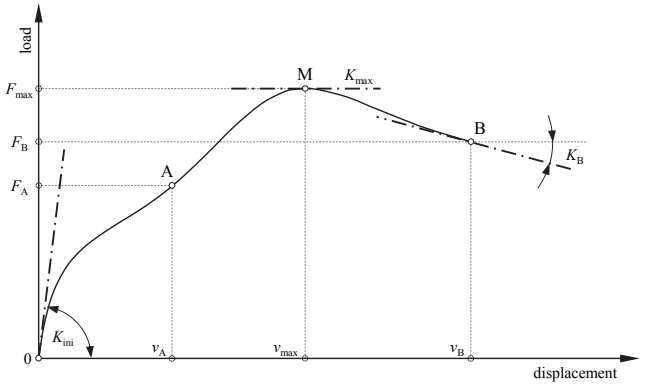

Figure 3.16: proposed analytical model and corresponding parameters

Additionally, since more parameters are involved, the mathematical function itself has to be modified as well; this by inserting two further coefficients as expressed in Equation (3.96).

$$F(v) = \frac{v + C_1 \cdot v^m + C_2 \cdot v^n}{C_3 + C_4 \cdot v + C_5 \cdot v^m + C_6 \cdot v^n} \tag{3.96}$$

with

C_1-C_6 ..... coefficients to be determined by boundary conditions

n, m ..... fitting parameters (1 < m < n)

The boundary conditions, necessary for determining the coefficients C_1 to C_6, are given in Equations (3.97) to (3.102), whereat the first three conditions are identical to Equations (3.50) to (3.52).

$$\frac{dF}{dv}\left(v = 0\right) = K_{\text{ini}} \tag{3.97}$$

$$\frac{dF}{dv}\left(v = v_{\max}\right) = K_{\max} = 0 \tag{3.98}$$

$$F\left(v = v_{\max}\right) = F_{\max} \tag{3.99}$$

$$F\left(v = v_{\text{A}}\right) = F_{\text{A}} \tag{3.100}$$

$$F\left(v = v_{\text{B}}\right) = F_{\text{B}} \tag{3.101}$$

$$\frac{dF}{dv}\left(v = v_{\text{B}}\right) = K_{\text{B}} \tag{3.102}$$

with

F_{A} ..... load at v_{A} ($v_{\text{A}} < v_{\max}$)

F_{B} ..... load at v_{B} ($v_{\text{B}} > v_{\max}$)

K_{B} ..... tangential stiffness at point B

Due to the extended function, solving the boundary conditions becomes relatively complex. Hence, this is performed with the software application Wolfram Mathematica 7 (2008); the corresponding solutions for C_1 to C_6 are documented in ANNEX D (section D-3.1).

Unfortunately, the resulting formulations are quite long and require a high number of available digits for further analysis, which finally leads to the circumstance that common software packages may have problems while executing the – in principle ordinary – numerical computations. Microsoft ® Excel (2010), for example, enables calculations with 15 digits in maximum, which is not enough for the present task. Hence, some simplifications are necessary to enable the application of this approach not only in high sophisticated software programs.

3-6.2 SIMPLIFICATIONS

Since primarily responsible for the long solutions, the relevance of the variable fitting parameters *n* and *m* is investigated in a first step. As illustrated in Figure 3.17, varying power values can highly influence the shape of the simulated curves, but varying the tangential stiffness in point B leads to similar results; compare Figure 3.18.

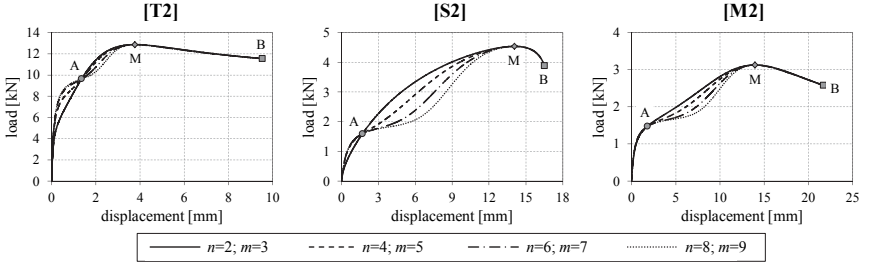

Figure 3.17: variation of fitting parameters n and m for the new analytical approach

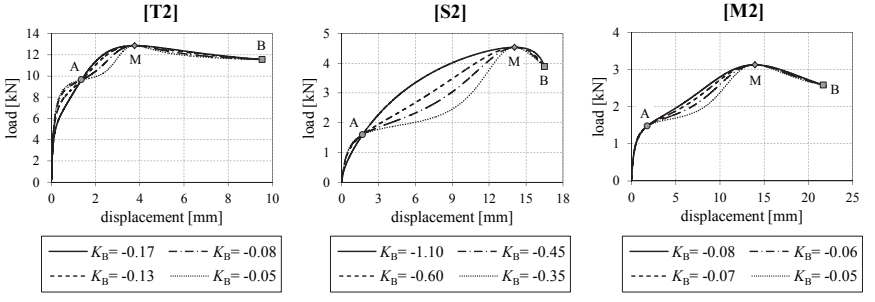

Figure 3.18: defined power values (m = 2 and n = 3) and varying tangential stiffness in point B

Although limiting the possibility of vernier adjustments, the parameters *n* and *m* are scheduled with the integers 2 and 3 for further investigations. The resulting expression and its first derivation are given in Equations (3.103) and (3.104), respectively.

$$F(v) = \frac{v + C_1 \cdot v^2 + C_2 \cdot v^3}{C_3 + C_4 \cdot v + C_5 \cdot v^2 + C_6 \cdot v^3} \tag{3.103}$$

$$K_T(v) = \frac{dF}{dv} = \frac{1 + 2 \cdot C_1 \cdot v + 3 \cdot C_2 \cdot v^2}{C_3 + C_4 \cdot v + C_5 \cdot v^2 + C_6 \cdot v^3} - \frac{(C_4 + 2 \cdot C_5 \cdot v + 3 \cdot C_6 \cdot v^2) \cdot (v + C_1 \cdot v^2 + C_2 \cdot v^3)}{(C_3 + C_4 \cdot v + C_5 \cdot v^2 + C_6 \cdot v^3)^2} \tag{3.104}$$

Defining the position of the points A and B enable a further simplification of the model without touching its good fit in a huge extent. Thus, point A is fixed at a displacement equal to 50 % of v_{max} and point B is defined as the ultimate point with a corresponding load equal to 80 % of F_{max}; compare Equations (3.105) and (3.106).

$$F\left(v = \frac{v_{max}}{2}\right) = F_A \tag{3.105}$$

$$F\left(v = v_B\right) = \frac{4 \cdot F_{max}}{5} \tag{3.106}$$

Even if the described modifications distinctively reduce their complexity, the resulting formulas, leading to the coefficients C_1 to C_6, are still noticeable longer compared to the one found in Glos (1978). Nevertheless, the current form allows their application in common spreadsheet programs and once implemented, the simplified approach can be used efficiently.

Note: The simplified formulas for determining the coefficients C_1 to C_6 are also documented in ANNEX D.

3-6.3 APPROXIMATION QUALITIES

In order to allow a comparison with the models discussed in section 3-5, the here proposed model is used to approximate the test curves described in section 2-4.1 as well. The already commented process using the 'Solver' in Microsoft ® Excel (2010), finally leads to the least-squares listed in Table 3.3. The same table contains the best results obtained from the other models discussed in section 3-5. As can be seen, the new approach leads to an improved result for every single test curve.

Table 3.3: least-squares – comparing new approach and 'best other' models

model	units	[T1]	[T2]	[S1]	[S2]	[M1]	[M2]
best other	[kN^2]	256.1	2060.8	116.3	8.7	139.3	51.9
new approach	[kN^2]	16.1	352.0	31.3	6.4	59.6	14.2
factor	[-]	15.9	5.9	3.7	1.4	2.3	3.6

Note: Excluding [M1], whose least-square result is taken from the approximation following the model of Yee and Melchers (1986), all 'best other' results are gathered from the model of Brandner et al. (2017).

A good opportunity for documenting the benefits of the new approach is shape [M2]; Figure 3.19 (a) illustrates the original test curve as well as both the approximations according to Brandner et al. (2017) and the new model. Obviously, the new model enables a slightly better fit of the initial branch and the local pinch in the middle of the test graph. However, especially sudden load drops, as one occurs for curve [M1], are quite challenging to describe, and in this special case the model of Yee and Melchers (1986) shows a better performance; compare Figure 3.19 (b).

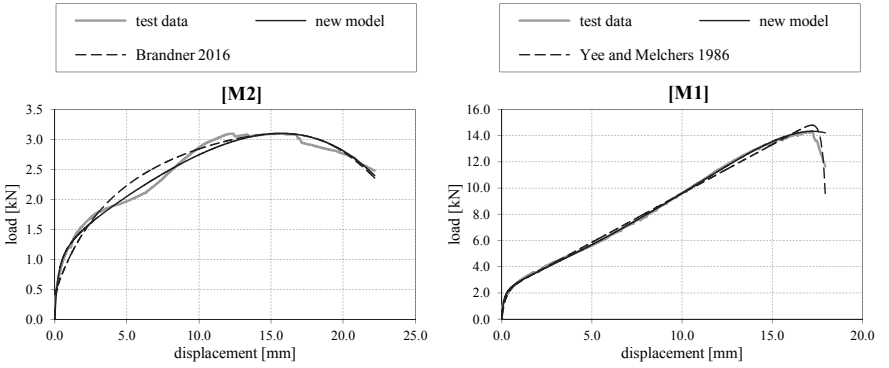

Figure 3.19: comparing new and best fitting other model with experimental test curves – (a) [M2] and model of Brandner et al. (2017); (b) [M1] and model of Yee and Melchers (1986)

A reason for this difference is that the model of Yee and Melchers (1986) is not forced to pass the original maximum point. Hence, for a better alignment of local effects close to the maximum point, the parameters F_{max} and v_{max} are varied in a new computation too; the resulting graphs are given in Figure 3.20.

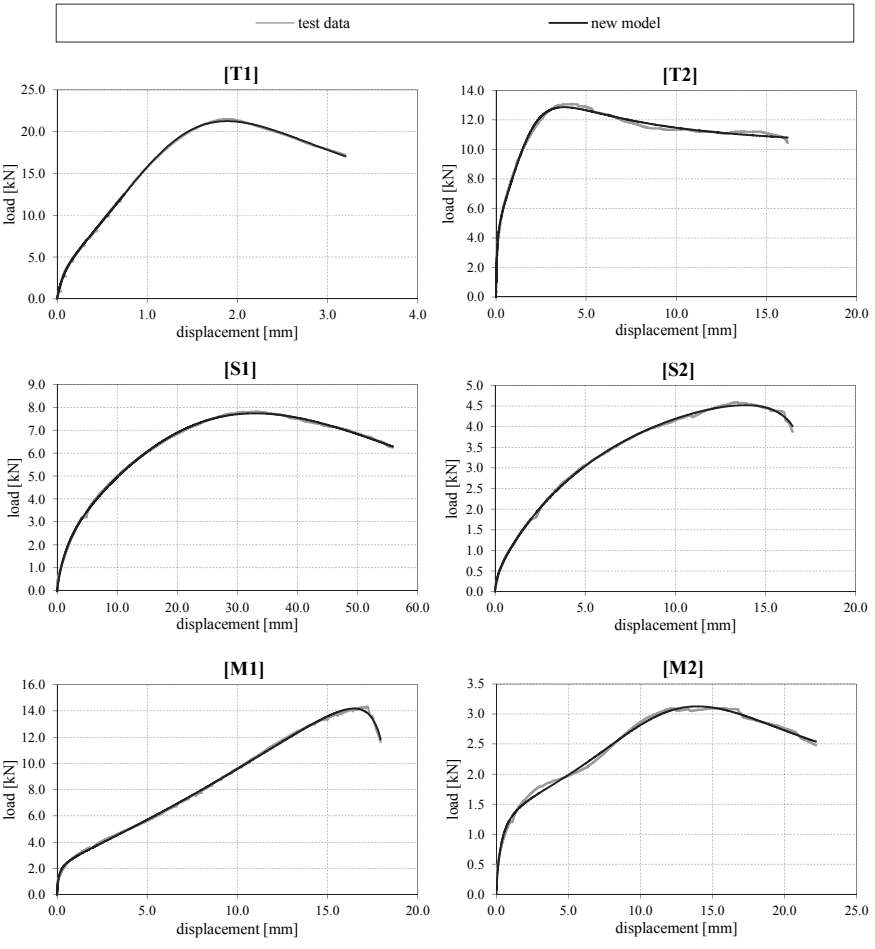

Figure 3.20: new model used for approximating the test curves [T1] to [M2]

The input parameters, being necessary for plotting these curves, are listed Table 3.4; here again the quite high initial stiffness values are outstanding. It is further worth mentioning that the 'optimised' peak loads only deviate 1.6 % in maximum from the measured one; the corresponding displacement values show slightly higher deviations (up to 11 % for [M2]).

Table 3.4: input parameters for the proposed analytical approach

parameter	units	[T1]	[T2]	[S1]	[S2]	[M1]	[M2]
F_{max}	[kN]	21.27	12.87	7.73	4.52	14.18	3.13
v_{max}	[mm]	1.89	3.78	32.92	13.88	16.47	13.97
K_{ini}	[kN/mm]	59.220	93.253	1.952	4.649	27.086	4.695
F_A	[kN]	15.07	11.16	6.33	3.60	8.16	2.31
v_B	[mm]	3.21	29.14	56.92	16.96	18.03	22.67
K_B	[kN/mm]	-3.797	-0.022	-0.096	-1.194	-6.528	-0.078

Of course, an additional degree of freedom may also improve the fit of the other models. Hence, to allow an objective comparison, the modified alignment process, where all available parameters are varied, is conducted for the further models too. The resulting (again relative) least-squares are listed in Table 3.5 and indicate that, even in this case, the new approach leads to an improved fit.

Table 3.5: relative least-squares related to the minimum for each considered test curve; every model is fitted by varying all available parameters

model	[T1]	[T2]	[S1]	[S2]	[M1]	[M2]
Y-M-U	67.0	23.0	19.1	32.4	5.0	8.5
Yee and Melchers (1986)	49.0	21.7	13.7	5.6	4.9	11.5
Glos (1978)	38.1	11.8	7.0	7.9	30.9	11.4
Brandner et al. (2017)	17.4	8.3	3.6	2.3	11.3	6.1
new model	1.0	1.0	1.0	1.0	1.0	1.0

Although the proposed model is able to simulate several different test curves, its rational form contains the disadvantage to produce singular points. Their location can be detected by solving Equation (3.107), representing the divisor of the model function.

$$C_3 + C_4 \cdot v + C_5 \cdot v^2 + C_6 \cdot v^3 = 0 \tag{3.107}$$

However, the smooth shape in between the typical range of interest ($v = 0$ to $v = v_u$) is usually not affected.

3-6.4 ADDITIONAL FEATURE

Besides transferring the information regarding the shape of an experimental test graph, or using the simulated curve for further post-processing, analytical models do further enable a nonlinear consideration of connections, e.g., in pushover analyses. Sometimes such computations may require a reversal of displacement in single joints, but most of the discussed models – including the new one – would exactly follow the loading path back to the origin without considering any plastic deformation. A proper solution for this unsatisfying fact offers an approach proposed in Foschi (2000), pretending a linear decreasing behaviour in case of reversal; the necessary algorithm is shortly reflected within the following passage.

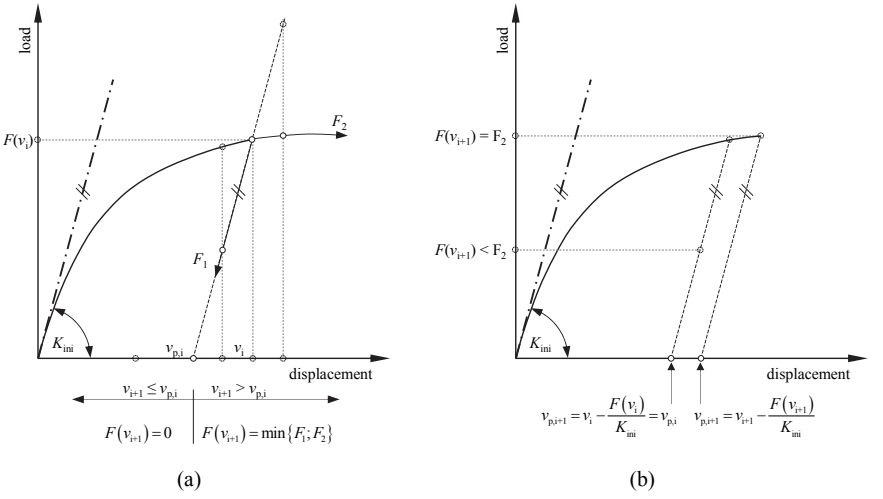

(a) (b)

Figure 3.21: algorithm for considering plastic deformations in case of displacement reversal – (a) determining the load $F(v_{i+1})$; (b) determining plastic deformation $v_{p,i+1}$

As illustrated in Figure 3.21, this 'add-on' requires one additional parameter for every single displacement step *i*; in particular, the plastic deformation v_p. For this purpose, a linear decreasing load path, owning an inclination equal to the initial stiffness K_{ini}, is assumed and leads to the expression

$$v_{p,i} = v_i - \frac{F(v_i)}{K_{ini}} \tag{3.108}$$

with

$v_{p,i}$ ..... plastic deformation according to displacement step v_i

Calculating the corresponding load for the next displacement $F(v_{i+1})$, thus, requires the consideration of the conditions given in Equations (3.109) and (3.110); see also Figure 3.21 (a).

$$F(v_{i+1}) = 0, \quad v_{i+1} \le v_{p,i} \tag{3.109}$$

$$F(v_{i+1}) = \min \begin{cases} F_1 = K_{ini} \cdot (v_{i+1} - v_{p,i}) \\ F_2 = F_{model}(v_{i+1}) \end{cases}, \quad v_{i+1} > v_{p,i} \tag{3.110}$$

with

F_{model} ..... load determined according to the applied approximation model

Note: Equation (3.110) is only valid as long as the tangential stiffness at v_{i+1} is lower than K_{ini}. More general would be a separate definition for the linear and the nonlinear part considering also the displacement *v* where the parameter v_p is calculated. However, since this procedure would require the storage of an additional parameter, the given one is preferred.

Finally, for determining the plastic deformation belonging to the displacement v_{i+1} ($v_{p,i+1}$), Equations (3.111) and (3.112) have to be respected; see also Figure 3.21 (b).

$$v_{p,i+1} = v_{i+1} - \frac{F(v_{i+1})}{K_{ini}}, \quad F(v_{i+1}) = F_2 \tag{3.111}$$

$$v_{p,i+1} = v_{p,i}, \quad F(v_{i+1}) < F_2 \tag{3.112}$$

To demonstrate the functionality of this model extension, the alternating displacement schedules of two cyclic tests (configurations responsible for curve types [S1] and [M1]) are used for the data input. To calculate the necessary coefficients for the respective analytical functions, the parameters given in Table 3.4 are used. As illustrated in Figure 3.22, this 'add-on' works quite efficient and enables, at least, a rough consideration of the cyclic behaviour. However, further discussions will only focus on monotonic investigations.

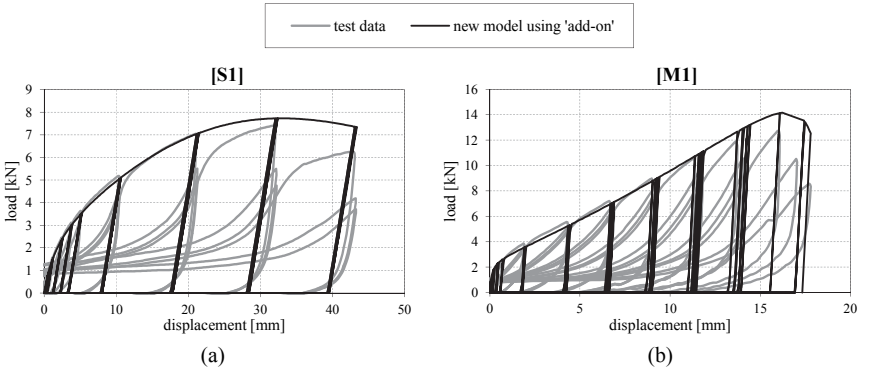

Figure 3.22: example of use for the model extension considering plastic deformations in case of displacement reversal – (a) applying input data of [S1]; (b) applying input data of [M1]

3-7 INTERMEDIATE CONCLUSIONS

This chapter examines about 35 methods enabling the approximation of a monotonic load-displacement curve. Besides the very common piecewise linear alignments, several continuous models basing on power, polynomial, exponential, logarithmic or rational functions are described.

Most of these models simply use the two parameters 'initial stiffness' and 'load-carrying capacity' (K_{ini} and F_{max}, respectively), combined with some 'shape parameters', to simulate the test curve of interest. This yields to the circumstance that almost every model is able to approximate smooth 'standard' load-displacement curves, but stumbles if an alignment of more complex shapes is required. Furthermore, since most of these models only aim the description up to the maximum load, besides displacement- also

force controlled methods are available. However, only displacement controlled models are able to simulate continuously the whole shape of an experimental test diagram including the post maximum softening.

Within all considered models found in literature, the rational approach originally proposed in Glos (1978) shows the most promising potential. In principle, it supposes that the basic form of the function fits to the experimental load-displacement curve and computes the unknown values based on defined boundary conditions. Nevertheless, this method also focuses on classical round shapes.

As a consequence, a new analytical model, basing on the ideas of Glos (1978), but using additional and modified boundary conditions, is developed. The proposed approach, enables the simulation of several different curve types with high accuracy and, hence, its application for different fields.

Firstly, once aligned to the original test curve, the information regarding the shape of the curve can be easily transferred by disclosing the necessary input parameters or even the resulting coefficients. Secondly, its accuracy allows using the model curve for further post-processing, as suggested, e.g., in Malo et al. (2011) or Piazza et al. (2011), and may consequently support the exchange and communication in the scientific community, helping to reduce barriers caused by the diversity of standards.

Another broad field for the new model are nonlinear analytical calculations, especially those where the displacement-based character and the possibility to accurately describe the softening branch are seen as useful qualities. In this context, the model extension, considering plastic deformations in case of displacement reversal, further improves the proposed approach.

CHAPTER 4
MODELLING CLT WALL SYSTEMS

4-1 INTRODUCTION

As already mentioned, timber exhibits a widely linear elastic behaviour (except for compressive stresses) and brittle failure mechanisms. The same, of course, applies for cross laminated timber (CLT) in its common form. This plate-like engineered timber product is composed of an uneven number of layers, bonded perpendicular to each other; compare Figure 4.1.

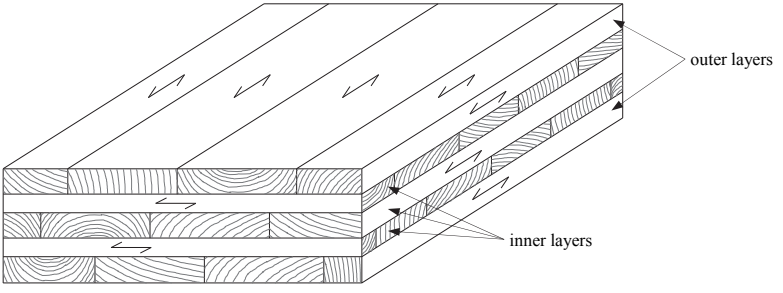

Figure 4.1: cross laminated timber (CLT)

Mechanically laminated alternatives using screws, staples or timber-to-timber dove-tail joints, as, e.g., discussed in Pozza et al. (2014) or Kuklik (2015), may have different properties. However, the following discussion solely focusses on the 'classical' bonded version of CLT. An up-to-date report, summarising detailed information and references regarding history, production and properties of CLT, is published in Brandner et al. (2016). Therefore, and since not mandatory for the present thesis, further information regarding the building material CLT is reduced to essential notes in the respective parts.

Due to the high in-plane stiffness of CLT, for investigating CLT wall systems a special attention has to be turned on the applied connection systems. Especially in case of huge lateral loads, e.g., as a result of earthquakes or heavy winds, they are not only reliable for the load-carrying capacity but rather for the stiffness and deformation properties. Hence, achieving a well-tempered behaviour of CLT structures requires an adequate consideration of connections' load-bearing performance.

Besides the characteristics of the connections and the CLT element(s), the behaviour of a CLT wall system is further influenced by wall geometry (height, length and openings), the acting vertical load, friction and the surrounding building components. Specific notes regarding the single points are given in the respective sections of the present thesis.

Several experimental campaigns on single and coupled walls, as well as whole buildings, confirm the mentioned conditions and further show huge plastic deformations in single connections – prior at the edges of the tested systems; compare e.g. Seim and Hummel (2013). As a consequence, discussing CLT wall systems further requires the consideration of the connections' plastic and post peak behaviour.

The current chapter focuses on the wall-level and particularly on current calculation models applicable for determining the behaviour of CLT wall systems. Furthermore, a new displacement-based model considering the nonlinear behaviour of the applied connections via the continuous approximation method introduced in Chapter 3 is proposed. Finally, some notes concerning the implementation of CLT wall systems in a finite element (FE) software are offered.

4-2 CLT WALL SYSTEMS – GENERAL COMMENTS

Within the present thesis, in accordance with current calculation models, a CLT wall system consists of one CLT element and connections joining it to the foundation and – if explicitly mentioned – the ceiling (or roof) element above. Furthermore, if vertical joints are used for connecting adjacent CLT elements, even more than one CLT element attends the system and the additional joint has to be considered as well. Figure 4.2 visualises the described main elements and includes some specific notations which are used in the following sections.

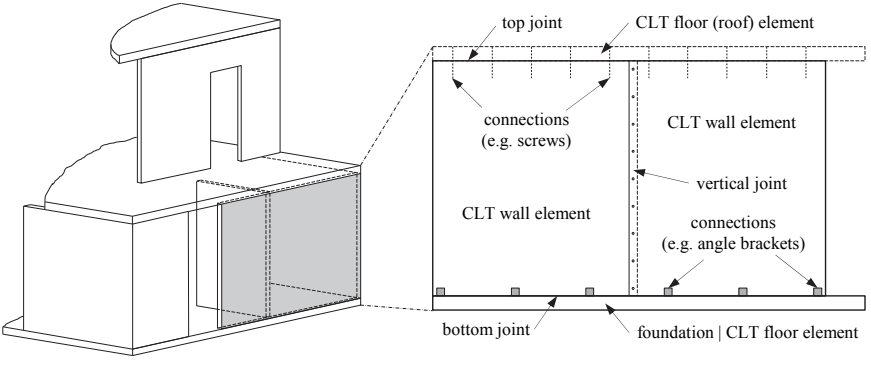

Figure 4.2: elements defining a CLT wall system

As described in Girhammar and Källsner (2006), Girhammar and Källsner (2007) or Popovski et al. (2014), transverse walls may also influence the wall behaviour and therefore should be seen as a possible part of a wall system. If necessary, they may be considered by applying additional vertical point loads acting at the respective positions of perpendicular walls. However, the present thesis primarily analyses two dimensional systems and, hence, neglects this aspect for further discussions.

4-2.1 APPLIED FASTENERS AND CONNECTIONS

As described in Brandner et al. (2016), joints within a CLT structure may be separated as depicted in Figure 4.3, i.e., (i) wall-to-wall or floor-to-floor joints, (ii) wall-to-floor joints and (iii) wall-to-foundation joints. At present, they are mainly equipped with angle-brackets, hold-downs (using nails, screws and bolts as fasteners) and fully or partially threaded self-tapping timber screws. Due to this circumstance, several experimental campaigns regarding these connections have been published; compare, e.g., Uibel and Blaß (2007), Follesa et al. (2010), Flatscher and Schickhofer (2011), Gavric et al. (2011), Bratulic et al. (2014a), Tomasi and Smith (2014) and Izzi et al. (2016).

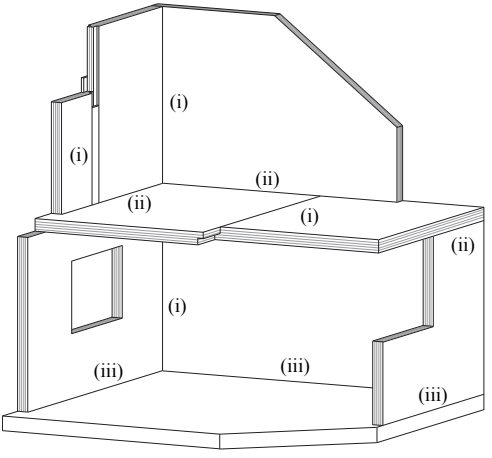

Figure 4.3: joints in a CLT structure – (i) wall-to-wall or floor-to-floor joints, (ii) wall-to-floor joints and (iii) wall-to-foundation joints; from Brandner et al. (2016)

However, the mentioned connections have not primarily been developed for CLT structures. Especially angle brackets and hold-downs are adapted from wood-framed shear wall systems and hardly reach the stiffness and load-carrying capacity of CLT walls. As a consequence, they can be termed as 'the weakest link' in the system. Although, positive for a so called 'capacity based design', the partially huge differences in utilizations and the – sometimes – cumbersome mounting situations, recommend a distinctive development in this field. First examples concerning this topic can be found in Latour et al. (2012), Nakashima et al. (2014), Polastri and Angeli (2014), Stecher et al. (2014), Kraler et al. (2014), Scotta et al. (2015) or Flatscher and Augustin (2016).

Despite these arguments, focusing on a general description of CLT wall systems as well as the access to original test data, the present thesis solely considers angle-brackets, hold-downs and screws. Anyway, the discussed and suggested approaches can be adapted for any other connection system too.

4-2.2 CONTRIBUTIONS TO LATERAL DEFLECTION

When applying a lateral load on the top of a CLT wall system, four contributions to the occurring total lateral top (or head) deflection can be identified: (i) sliding (translation), (ii) rocking (rotation), (iii) shear and (iv) bending; compare Figure 4.4 and Equation (4.1). Although mainly influenced by the characteristics and position of the applied connections, contributions (i) and (ii) are heavily dependent on friction and the acting vertical load as well. Contributions (iii) and (iv), however, do only depend on the characteristics of the used CLT element and are often summarised as v_{CLT}.

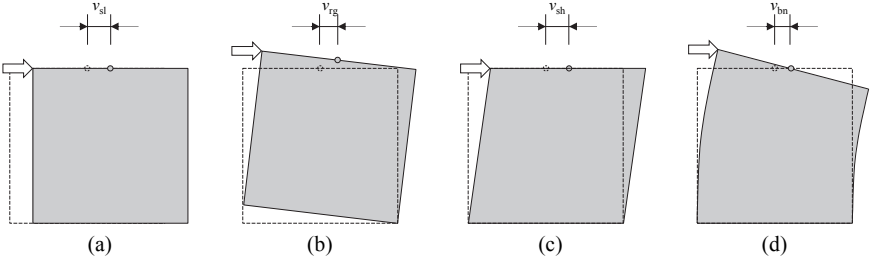

Figure 4.4: ***contributions to total lateral top (or head) deflection of a CLT wall system – (a) sliding (rigid body translation); (b) rocking (rigid body rotation); (c) shear deformation of the CLT element; (d) bending deformation of the CLT element***

$$v_{tot} = v_{sl} + v_{rg} + v_{sh} + v_{bn} = v_{sl} + v_{rg} + v_{CLT} \tag{4.1}$$

with

v_{tot} ..... total lateral head deflection of the CLT wall system
v_{sl} ..... contribution according to sliding (rigid body translation)
v_{rg} ..... contribution according to rocking (rigid body rotation)
v_{sh} ..... contribution according to the shear deformation of the CLT element
v_{bn} ..... contribution according to the bending deformation of the CLT element
v_{CLT} ..... contribution according to the (summarised) deformations of the CLT element

Experimental tests on squared CLT wall systems, equipped with different types of connections, show that the CLT deformation usually contributes less than 10 % to the total head deflection. Although influenced by the wall geometry, assuming a practical relevant use of currently available connections, this percentage might not distinctively be exceeded for other wall configurations (except in case of present openings).

Due to the substantial influence of applied connections, the geometry of walls and the acting vertical loads, a similar estimation for the contributions ‘sliding’ and ‘rocking’ is hardly possible. However, simulations show that CLT wall systems (without vertical joints) owning a length-to-height ratio below 1.5, primarily exhibit rocking deflections and, consequently, predominant sliding for longer walls; compare parameter study in Chapter 6.

4-3 MODELS IN LITERATURE

Although not considered in the current basic document of Eurocode 5, the normative annex K "Cross laminated timber" (originally "Brettsperrholz") of ON B 1995-1-1 (2015) (national supplements of Austria), provides some information concerning the design with CLT. Therein, not only regulations regarding the building material, but also the use of fasteners and even the maximum distances for fasteners and connections are scheduled. However, no model for evaluating CLT wall systems is given and adopting the existing model for wood-framed wall diaphragms is not possible. This, due to the fact that both provided methods (in particular Method A and Method B) do focus on the capacity of the wall element itself; the connection to the surrounding building components is mentioned only rudimentary. Approaches for determining the load-carrying capacity and stiffness of CLT wall systems are only available in literature. To get an overview, currently published models are summarised in the following section.

4-3.1 GENERAL ASSUMPTIONS AND NOTATIONS

The following assumptions and notations are valid for the whole section:

- While focusing on connections, the CLT wall elements are assumed to behave rigidly.
- Since not all models consider the influence of stiffness, only one version per connection type (i.e., hold-down or angle bracket) is taken into account. In other words: if a CLT wall is equipped with angle brackets, it is assumed that all these connections exhibit the same properties.
- The designations given in Figure 4.5 are used for all following descriptions – independent from the variables used in the original documents.

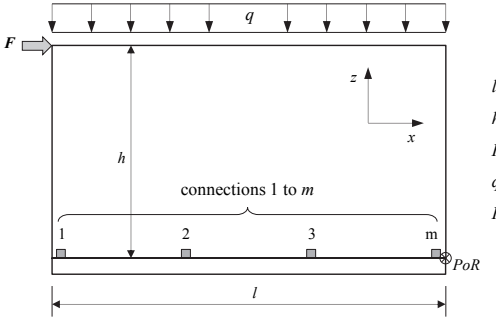

l ..... length of the CLT wall element
h ..... height of the CLT wall element
F ..... lateral load acting on wall-system
q ..... vertical line load acting on wall-system
PoR ..... point of rotation

Figure 4.5: designations used for further discussion on CLT wall systems

- Due to geometric boundary conditions, every point on the top of a CLT wall system exhibits slightly different horizontal displacements in case of rocking. However, since the rotation angle φ usually keeps small, the differences are minimal and therefore are neglected herein. The horizontal displacement resulting from rocking is determined according to Equation (4.2); see also Figure 4.6.

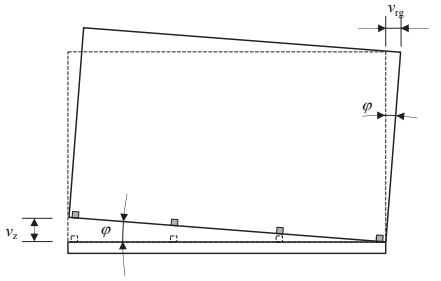

Figure 4.6: definition of lateral displacement according to rocking

$$v_{rg} = h \cdot \frac{v_z}{l} = h \cdot \varphi \tag{4.2}$$

4-3.2 CONSIDERATION OF CONNECTIONS

This section solely focuses on the influence of connection systems. Information regarding the consideration of CLT properties is offered in section 4-3.3.

4-3.2.1 Ceccotti 2006

As far as the author knows, the first scientific investigation on connections applied at CLT structures is documented in Ceccotti et al. (2006a). A first advice how connections may be considered in the design of a CLT building can be found in Ceccotti et al. (2006). Therein the authors propose to use only hold-downs for resisting the overturning moment of a CLT structure. Accordingly it can be concluded that the further applied angle brackets are seen as being responsible for transmitting the resulting shear forces.

When focussing on a single CLT wall system loaded by a lateral load *F* as shown in Figure 4.7, these assumptions consequently lead to Equations (4.3) and (4.4) for determining the acting loads per angle bracket and hold-down, respectively.

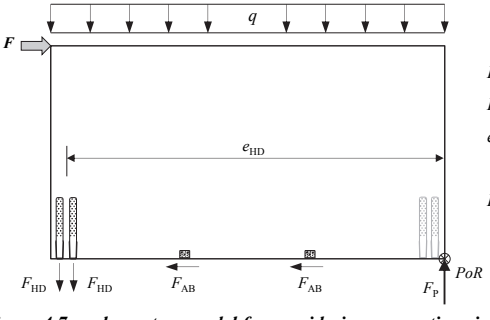

Figure 4.7: elementary model for considering connections in CLT structures according to Ceccotti et al. (2006)

$$F_{AB} = \frac{F}{n_{AB}} \tag{4.3}$$

$$F_{HD} = \frac{2 \cdot F \cdot h - q \cdot l^2}{2 \cdot e_{HD} \cdot n_{HD}} \tag{4.4}$$

with

n_{AB} ..... number of considered angle brackets

n_{HD} ..... number of considered hold downs

Consequently, the load-carrying capacity of a CLT wall system may be expressed as given in Equation (4.5).

$$R_{ges} = \min \begin{cases} R_{sliding} = & R_{AB} \cdot n_{AB} \\ R_{rocking} = & \dfrac{q \cdot l^2 + 2 \cdot R_{HD} \cdot e_{HD} \cdot n_{HD}}{2 \cdot h} \end{cases} \tag{4.5}$$

with

R_{ges} ..... lateral load-carrying capacity of CLT wall system

$R_{sliding}$ ..... lateral load-carrying capacity against sliding

$R_{rocking}$ ..... lateral load-carrying capacity against rocking

R_{AB} ..... lateral (horizontal) load-carrying capacity per angle bracket

R_{HD} ..... axial (vertical) load-carrying capacity per hold-down

Note: In the following discussion, the illustration based on an acting load F is preferred.

Although, or perhaps because this approach is quite simple, it is still often used in practical design with minor adaptions; compare, e.g., Wallner-Novak et al. (2013). However, no remarks regarding the determination of the wall systems' stiffness are mentioned herein.

4-3.2.2 BSP-Handbuch 2010

Schickhofer et al. (2010) does also not include a distinct wall model, but offers some parts being necessary for determining the distribution of loads within a wall system. However, similar to Ceccotti et al. (2006), the uplift forces are solely allocated to hold-downs and the shear loads to angle brackets.

Regarding the transmission of shear loads, an even distribution over the wall length is assumed, leading to an equal force in every angle bracket. Furthermore, the authors mention that in practical cases a huge part of the acting shear load may be transmitted by friction. Nevertheless, this effect is not considered in further calculations. Thus, the load per angle bracket F_{AB} can be determined as given in Equation (4.3).

For investigating the reaction against an overturning moment, three different models are described, i.e., (i) rigid continuous bearing (elastic solution), (ii) open gap without tension bracing and (iii) open gap with tension bracing.

Model I – elastic solution

This – more theoretical – model assumes a linear elastic and continuous behaviour of the bottom joint. Consequently, an acting lateral load, combined with a vertical one, leads to a load distribution in the joint as depicted in Figure 4.8.

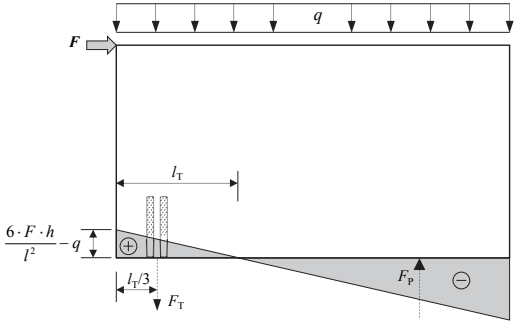

Figure 4.8: depiction of Model I according to Schickhofer et al. (2010)

Furthermore, expecting hold-downs' position in the balance point of the 'tension triangle', the resulting tension load can be determined by Equations (4.6) and (4.7).

$$l_T = \frac{l}{2} - \frac{q \cdot l^3}{12 \cdot F \cdot h} \tag{4.6}$$

$$F_{HD} \cdot n_{HD} = F_T = \left(\frac{6 \cdot F \cdot h}{l^2} - q \right) \cdot \frac{l_T}{2} = \frac{3 \cdot F \cdot h - q \cdot l^2}{2 \cdot l} + \frac{q^2 \cdot l^3}{24 \cdot F \cdot h} \tag{4.7}$$

Model II – open gap without tension bracing

Model II represents a scenario where the bottom joint is not under compression over the whole length, but the vertical load is still able to counter the acting overturning moment without requiring a tensile bracing. Equation (4.8) describes this situation under the assumption of a triangular load distribution in the bottom joint; see also Figure 4.9. The two limiting values for this model can be determined by setting the compression zone either equal to the wall length or zero. The corresponding lateral loads can be calculated as given in Equations (4.9) and (4.10). As soon as the lateral load exceeds $F_{lim,max}$, a tensile bracing is mandatory. Between $F_{lim,max}$ and $F_{lim,min}$ it is optional and beneath $F_{lim,min}$ no tension bracing is necessary anyway.

$$F \cdot h + F_P \cdot \frac{l_P}{3} - \frac{q \cdot l^2}{2} = F \cdot h + q \cdot l \cdot \left(\frac{l_P}{3} - \frac{l}{2} \right) = 0 \tag{4.8}$$

$$F_{lim,min} = \frac{q \cdot l^2}{6 \cdot h} \tag{4.9}$$

$$F_{lim,max} = \frac{q \cdot l^2}{2 \cdot h} \tag{4.10}$$

with

$F_{lim,max|min}$ ..... limiting or 'extreme' values complying Equation (4.8)

Note: Setting the length of the compression zone equal to zero leads to infinite compressive stresses in the bottom joint (i.e. the point of rotation).

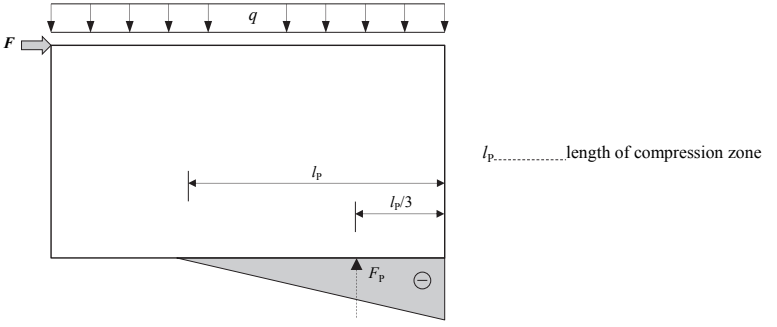

Figure 4.9: depiction of Model II according to Schickhofer et al. (2010)

Model III – open gap with tension bracing

The third model considers a compression zone and a defined tension bracing at the end of the CLT wall element; compare Figure 4.10 and the equilibrium condition given in Equation (4.11). A possible way for solving this equation is to estimate the length of the compression zone l_P (e.g., as 20 % of the walls' length) or setting the tension bracing equal to the load-carrying capacity of the applied hold-downs. Another solution is obtained if the edge pressure is assumed to equalise the compression capacity of the CLT element; for the latter case, l_P may be expressed as given in Equation (4.12). Afterwards the load in the hold-downs can be determined as given in Equation (4.13).

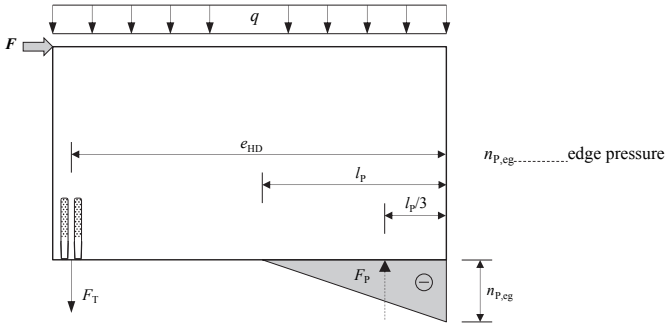

Figure 4.10: depiction of Model III according to Schickhofer et al. (2010)

$$F \cdot h + F_P \cdot \frac{l_P}{3} - \frac{q \cdot l^2}{2} - F_T \cdot e_{HD} = 0 \tag{4.11}$$

$$l_P = \frac{3 \cdot e_{HD} \cdot n_{P,eg} - \sqrt{3} \cdot \sqrt{-8 \cdot F \cdot h \cdot n_{P,eg} + 3 \cdot e_{HD}^2 \cdot n_{P,eg}^2 - 8 \cdot e_{HD} \cdot l \cdot n_{P,eg} \cdot q + 4 \cdot l^2 \cdot n_{P,eg} \cdot q}}{2 \cdot n_{P,eg}} \tag{4.12}$$

$$F_{HD} \cdot n_{HD} = F_T = \frac{6 \cdot F \cdot h - q \cdot l \cdot (3 \cdot l - 2 \cdot l_P)}{2 \cdot (3 \cdot e_{HD} - l_P)} \tag{4.13}$$

4-3.2.3 Ringhofer 2010/2011

A detailed description concerning the seismic design of a CLT structure is documented in Ringhofer (2010) and is further developed in Schickhofer and Ringhofer (2011). Besides others, here the stiffness properties of the applied connections (angle brackets, hold-downs and screws) and the CLT element itself are considered for the first time; at least for determining the centre of stiffness.

However, angle brackets are again solely considered for transmitting shear loads, and the assumption of parallel acting angle brackets once more enables the application of Equation (4.3) for determining the respective loads.

The resistance against overturning is calculated by means of an approach primarily used in the design of reinforced concrete. This method assumes a rectangular stress block instead of a triangular one, being responsible for bearing the compression loads, and a point load positioned in the centre of the applied hold-downs for bracing the resulting uplift forces; compare Figure 4.11 and Equation (4.14). The width of the stress block, calculated as given in Equation (4.15), and consequently the position of the reacting compression load, depends on the compression strength of CLT. The formulas used to determine this parameter are given in Equations (4.16) and (4.17) for a wall-to-foundation and a wall-to-floor joint, respectively.

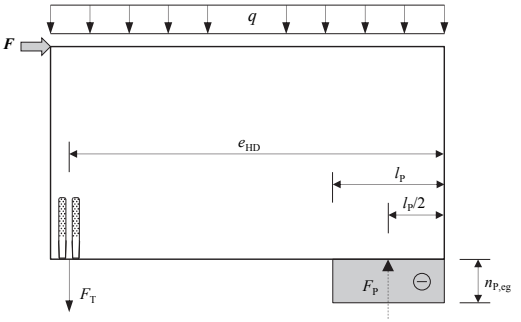

Figure 4.11: illustration of stress-block model according to Ringhofer (2010)

$$F \cdot h + F_P \cdot \frac{l_P}{2} - \frac{q \cdot l^2}{2} - F_T \cdot e_{HD} = 0 \tag{4.14}$$

$$l_P = \frac{e_{HD} \cdot n_{P,eg} - \sqrt{n_{P,eg} \cdot \left(-2 \cdot F \cdot h + e_{HD}^2 \cdot n_{P,eg} - 2 \cdot e_{HD} \cdot l \cdot q + l \cdot q^2\right)}}{n_{P,eg}} \tag{4.15}$$

$$n_{P,eg,found} = t_{eff} \cdot f_{c,0} \tag{4.16}$$

$$n_{P,eg,floor} = t_{CLT} \cdot f_{c,90} \tag{4.17}$$

with

$n_{P,eg,found}$ ..... compression strength for a wall-to-foundation joint
$n_{P,eg,floor}$ ..... compression strength for a wall-to-floor joint
t_{eff} ..... effective thickness of CLT element (sum of vertical layer thickness)
t_{CLT} ..... total thickness of CLT wall element
$f_{c,0}$ ..... compression strength parallel to the grain
$f_{c,90}$ ..... compression strength perpendicular to the grain

For performing the modal analysis of an example building, in Schickhofer and Ringhofer (2011) the walls are modelled as bars and the connections are considered with equivalent springs. In particular, the lateral stiffness of the angle brackets is summarised in a linear spring; compare Equation (4.18). The rotational spring, representing the rocking behaviour of the CLT wall system, is determined by considering the uplift (vertical) stiffness of the hold-downs and the deformations (indentations) in the compression zone; compare Equations (4.19) to (4.21) and Figure 4.12. Finally, the stiffness of the CLT element is implemented by adapting the properties of the respective bars. Hence, this approach may be seen as a kind of 'component model' as scheduled in Eurocode 3.

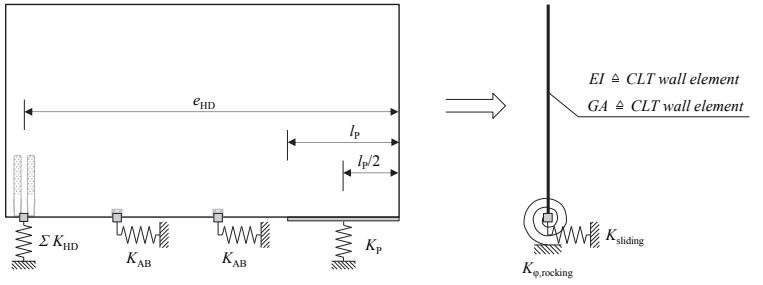

Figure 4.12: defining an equivalent rotational and linear spring for simplified calculations as described in Schickhofer and Ringhofer (2011)

$$K_{sliding} = n_{AB} \cdot K_{AB} \tag{4.18}$$

$$K_{\varphi,rocking} = \frac{\left(e_{HD} - l_P/2\right)^2}{\frac{1}{n_{HD} \cdot K_{HD}} + \frac{1}{K_P}} \tag{4.19}$$

$$K_{P,found} = \frac{2 \cdot E_{0,CLT} \cdot l_P \cdot t_{eff,wall}}{h_{wall}} \tag{4.20}$$

$$K_{P,floor} = \frac{2 \cdot E_{90,CLT} \cdot l_P \cdot t_{CLT,wall}}{t_{CLT,floor}} \tag{4.21}$$

with

$K_{sliding}$ ..... stiffness of lateral spring representing displacement according to sliding

K_{AB} ..... stiffness per angle bracket

$K_{\varphi,rocking}$ ..... stiffness of rotational spring representing displacement according to rocking

K_{HD} ..... stiffness per hold-down

K_P ..... stiffness representing the deformations (indentations) in the compression zone, either for a wall-to-foundation or a wall-to-floor joint

$E_{0,CLT}$ ..... MOE of CLT parallel to the grain

$E_{90,CLT}$ ..... MOE of CLT perpendicular to the grain

Note: Equation (4.21) bases on an assumption met in Meisel (2009). Furthermore, Equation (4.20) is slightly modified compared to the original document.

4-3.2.4 Gavric 2011/2015

Gavric et al. (2011) presented the first detailed analytical model, principally being able to simulate the entire load-displacement relationship of a CLT wall system. Besides taking shear and uplift capacity of applied connections into account, a further developed version of this model additionally enables the consideration of vertical joints; compare Gavric et al. (2015a). The content of the latter publication is

discussed in detail whereby, due to the models' force-based character, the descriptions are focused on the appearing displacements.

For determining the sliding deformation, Equation (4.23) is derived from Equation (4.22). As can be seen, this expression even considers the influence of friction.

$$F = \sum\left(K_{\mathrm{C,x,m}}\right)\cdot v_{\mathrm{sl}} + \mu_{\mathrm{f}}\cdot q\cdot l \tag{4.22}$$

$$v_{\mathrm{sl}} = \frac{F - \mu_{\mathrm{f}}\cdot q\cdot l}{\sum\left(K_{\mathrm{C,x,m}}\right)} \tag{4.23}$$

with

v_{sl} ..... lateral displacement according to sliding

μ_{f} ..... coefficient of friction

$K_{\mathrm{C,x,m}}$ ..... lateral stiffness of connections

Determining rocking deformations as described in Gavric et al. (2015a), exhibits distinct differences if compared to the models discussed afore. Firstly, the uplift resistance of all connections may be considered. In particular, similar to the determination of the sliding displacement, the stiffness of each connection is considered in the calculation process. Moreover, as already mentioned, the publication further provides an approach to account for the influence of vertical joints. Finally, no compression zone is defined and it is assumed that the wall element(s) rotate around their lower corner(s). Hence, the bearing load F_{P} is concentrated in the respective point(s); compare Figure 4.13 and Figure 4.14 (a).

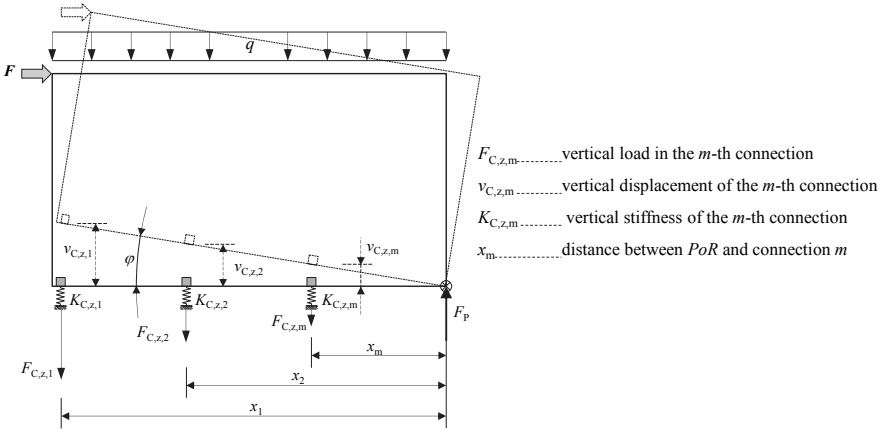

Figure 4.13: notations for determining the rocking behaviour of a single wall element according to Gavric et al. (2015a)

Assuming a single CLT wall without any vertical joint is leading to the basic formulations for this approach. Equation (4.24) shows the equilibrium condition of the system depicted in Figure 4.13; the

reacting loads per connection are determined as given in Equation (4.25). The rocking deformation at an actual load F can finally be expressed as given in Equation (4.26).

$$F \cdot h - \frac{q \cdot l^2}{2} - \sum\left(F_{C,z,m} \cdot x_m\right) = F \cdot h - \frac{q \cdot l^2}{2} - \frac{v_{rg}}{h} \cdot \sum\left(K_{C,z,m} \cdot x_m^2\right) = 0 \tag{4.24}$$

$$F_{C,z,m} = K_{C,z,m} \cdot v_{C,z,m} = K_{C,z,m} \cdot x_m \cdot \varphi = K_{C,z,m} \cdot x_m \cdot \frac{v_{rg}}{h} \tag{4.25}$$

$$v_{rg} = v_{rg,single} = \frac{\left(F \cdot h - \frac{q \cdot l^2}{2}\right) \cdot h}{\sum\left(K_{C,z,m} \cdot x_m^2\right)} \tag{4.26}$$

When considering vertical joints, according to Gavric et al. (2015a), two cases are possible: (i) coupled behaviour and (ii) single-coupled behaviour. Case (i) occurs if the displacement in the vertical joint is equal to the vertical displacement (v_z) of the adjacent CLT element; as a consequence, two compressional bearing loads ($F_{P,I}$ and $F_{P,II}$) appear. Case (ii) describes the scenario where the displacement in the vertical joint is too small to close the gap and only causes a 'step' in the wall system. Both cases, (i) and (ii), are depicted in Figure 4.14 (a) and (b), respectively. In this context it is important to point out that solely displacements parallel to the vertical joint (v_{vj}) are considered, which finally causes an unaffected rotation angle φ.

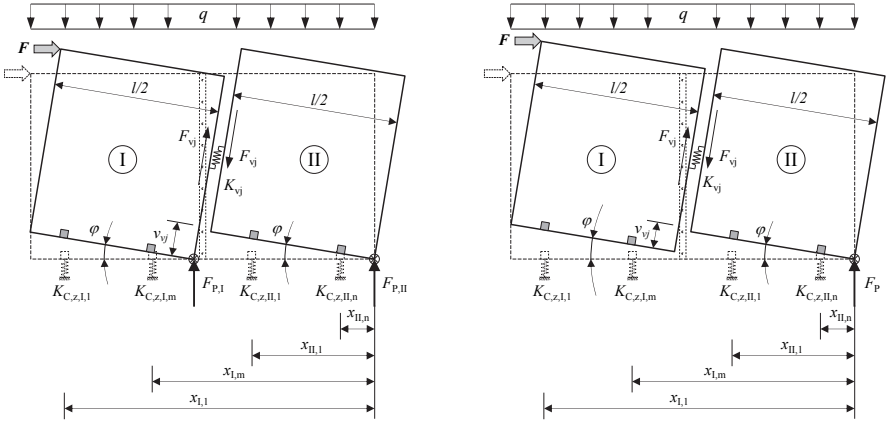

Figure 4.14: CLT wall system including a vertical joint – (a) coupled behaviour; (b) single-coupled behaviour

For the sake of simplicity, and in line with the original paper, in the following description only one vertical joint is considered and further assumed to exactly halve the CLT wall element. Consequently, in combination with Equation (4.2), the vertical displacement for case (i) can be described as given in

Equation (4.27). These simplifications finally lead to the expressions for rocking displacement of a coupled and a single-coupled wall system as shown in Equations (4.28) and (4.29), respectively. More detailed information regarding the derivation of these formulations can be found in Gavric et al. (2015a).

$$v_{\mathrm{vj}} = \varphi \cdot \frac{l}{2} = \frac{v_{\mathrm{rg}} \cdot l}{2 \cdot h} \tag{4.27}$$

$$v_{\mathrm{rg,coupled}} = \frac{\left(F \cdot h - q \cdot \frac{l^2}{4}\right) \cdot h}{\sum\left(K_{\mathrm{C,z,I,m}} \cdot \left(x_{\mathrm{I,m}} - \frac{l}{2}\right)^2\right) + \sum\left(K_{\mathrm{C,z,II,n}} \cdot x_{\mathrm{II,n}}^2\right) + K_{\mathrm{vj}} \cdot \left(\frac{l}{2}\right)^2} \tag{4.28}$$

$$v_{\mathrm{rg,single\text{-}coupled}} = \frac{\left(F \cdot h - q \cdot \frac{l^2}{2} + \frac{q \cdot \frac{l}{2} \cdot \sum\left(K_{\mathrm{C,z,I,m}} \cdot x_{\mathrm{I,m}}\right)}{\sum\left(K_{\mathrm{C,z,I,m}}\right) + K_{\mathrm{vj}}}\right) \cdot h}{\sum\left(K_{\mathrm{C,z,I,m}} \cdot x_{\mathrm{I,m}}^2\right) + \sum\left(K_{\mathrm{C,z,II,n}} \cdot x_{\mathrm{II,n}}^2\right) - \frac{\left(\sum\left(K_{\mathrm{C,z,I,m}} \cdot x_{\mathrm{I,m}}\right)\right)^2}{\sum\left(K_{\mathrm{C,z,I,m}}\right) + K_{\mathrm{vj}}}} \tag{4.29}$$

with

v_{vj} ..... displacement of vertical joint along its main direction; compare Figure 4.14

K_{vj} ..... stiffness of the vertical joint along its main direction

$K_{\mathrm{C,z,I,m}}$ ..... axial (vertical) stiffness of *m*-th connection joining wall element I

$K_{\mathrm{C,z,II,n}}$ ..... axial (vertical) stiffness of *n*-th connection joining wall element II

Note: Equation (4.29) slightly differs from the corresponding expression in the original paper.

Although valid for investigating CLT wall systems with linear-elastic springs, it has to be mention that Equations (4.23), (4.26), (4.28) and (4.29) cannot be used unadapted for simulating a nonlinear behaviour. Due to this, in Gavric et al. (2015a) it is suggested to use an incremental loading procedure with a load step ΔF, leading to an increase in rocking and sliding displacement (Δv_{rg} and Δv_{sl}, respectively). The actual load and displacement shares may therefore be determined by means of Equations (4.30) and (4.31), respectively.

$$F_{\mathrm{i}} = F_{\mathrm{i-1}} + \Delta F_{\mathrm{i}} \tag{4.30}$$

$$v_{\mathrm{i}} = v_{\mathrm{i-1}} + \Delta v_{\mathrm{i}} \tag{4.31}$$

with

F_{i} ..... load at incremental step *i*

ΔF_{i} ..... *i*-th incremental load step

v_{i} ..... corresponding displacement to load F_{i}

Δv_{i} ..... corresponding incremental displacement step to ΔF_{i}

In order to consider the nonlinear behaviour of connections, Gavric et al. (2015a) applied a trilinear approximation of experimental test curves, i.e., the Y-M-U model with data points according to ON EN 12512 (2005); compare section 3-2 and Figure 4.15.

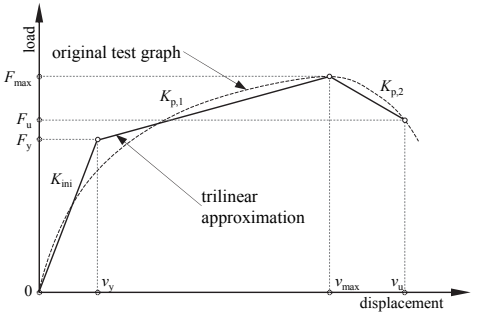

Figure 4.15: trilinear test curve approximation as used in Gavric et al. (2015a)

Due to the bi-directional loading of the connections, the authors further applied the quadratic interaction given in Equation (4.32). Thereby, the load-carrying capacity (R) is defined as the respective 'yield strength' F_y; compare Figure 4.15. Moreover, as soon as the condition in Equation (4.32) is exceeded, plastification is assumed to occur in both directions (lateral and vertical) simultaneously.

$$\left(\frac{F_{C,x}}{R_{C,x}}\right)^2 + \left(\frac{F_{C,z}}{R_{C,z}}\right)^2 \leq 1.0 \tag{4.32}$$

with

$F_{C,x}$ ..... lateral load in connection
$R_{C,x}$ ..... lateral load-carrying capacity of the connection
$F_{C,z}$..... vertical load in the connection
$R_{C,z}$..... vertical load-carrying capacity of the connection

Since force-based models are usually inapplicable for illustrating a softening branch, Gavric et al. (2015a) assume the incremental load step to become negative as soon as (i) the most outer connection reaches its maximum load-carrying capacity against uplift or (ii) any connector reaches its load-carrying capacity against sliding – whatever occurs first. In this context, load-carrying capacity means the respective maximum load (F_{max}); compare Figure 4.15.

Note: Information regarding negative load step is not included in the original paper and was part of a personal conversation between I. Gavric and the author of this thesis.

Finally it has to be mentioned that, according to Gavric et al. (2015a), no sliding is possible as long as friction is higher than the acting lateral load. Similar, no rocking displacement occurs as long as the vertical load prohibits a rotation of the CLT panel. Consequently, Equation (4.33) for sliding and

Equations (4.34) to (4.36) for single, coupled and single-coupled rocking behaviour, respectively, have to be attained before any connection based displacement occurs.

$$F - \mu_f \cdot q \cdot l > 0 \tag{4.33}$$

$$F \cdot h - \frac{q \cdot l^2}{2} > 0 \tag{4.34}$$

$$F \cdot h - q \cdot \frac{l^2}{4} > 0 \tag{4.35}$$

$$F \cdot h - q \cdot \frac{l^2}{2} + \frac{q \cdot \frac{l}{2} \cdot \sum\left(K_{C,z,I,m} \cdot x_{I,m}\right)}{\sum\left(K_{C,z,I,m}\right) + K_{vj}} > 0 \tag{4.36}$$

After reaching these load levels, the increment of growth for the respective contributions to total head deflection may be determined as expressed in Equations (4.37) to (4.40).

$$\Delta v_{sl} = \frac{\Delta F}{\sum\left(K_{C,x,m}\right)} \tag{4.37}$$

$$\Delta v_{rg,single} = \frac{\Delta F \cdot h^2}{\sum\left(K_{C,z,m} \cdot x_m^2\right)} \tag{4.38}$$

$$\Delta v_{rg,coupled} = \frac{\Delta F \cdot h^2}{\sum\left(K_{C,z,I,m} \cdot \left(x_{I,m} - \frac{l}{2}\right)^2\right) + \sum\left(K_{C,z,II,n} \cdot x_{II,n}^2\right) + K_{vj} \cdot \left(\frac{l}{2}\right)^2} \tag{4.39}$$

$$\Delta v_{rg,single\text{-}coupled,i} = \frac{\Delta F_i \cdot h^2 + \frac{q \cdot l}{2} \cdot h \cdot \left(\left(\frac{\sum\left(K_{C,z,I,m} \cdot x_{I,m}\right)}{\sum\left(K_{C,z,I,m}\right) + K_{vj}}\right)_i - \left(\frac{\sum\left(K_{C,z,I,m} \cdot x_{I,m}\right)}{\sum\left(K_{C,z,I,m}\right) + K_{vj}}\right)_{i-1}\right)}{\sum\left(K_{C,z,I,m} \cdot x_{I,m}^2\right) + \sum\left(K_{C,z,II,n} \cdot x_{II,n}^2\right) - \frac{\left(\sum\left(K_{C,z,I,m} \cdot x_{I,m}\right)\right)^2}{\sum\left(K_{C,z,I,m}\right) + K_{vj}}} \tag{4.40}$$

Regarding Equation (4.40) it is worth mentioning that the load step dependant subtraction term (in dividend) usually results to very small values. Hence, if the chosen load step is small enough, the incremental rocking displacement for the single-coupled wall behaviour may also be determined as given in Equation (4.41). Besides an easier and step-independent formulation, this simplification further prohibits discontinuity effects at the transition points from one stiffness area to the next.

$$\Delta v_{rg,single\text{-}coupled} = \frac{\Delta F \cdot h^2}{\sum\left(K_{C,z,I,m} \cdot x_{I,m}^2\right) + \sum\left(K_{C,z,II,n} \cdot x_{II,n}^2\right) - \frac{\left(\sum\left(K_{C,z,I,m} \cdot x_{I,m}\right)\right)^2}{\sum\left(K_{C,z,I,m}\right) + K_{vj}}} \tag{4.41}$$

As depicted in Gavric et al. (2015a), this method enables a good simulation of diverse experimentally gathered load-displacement curves. However, the necessary assumption for finding the start of negative load increments, leads to the circumstance that a weak connection in the 'wrong' position may control the behaviour of the wall system. In particular, the consideration of weak connections at the most outer corners may distinctively underestimate the properties of systems where rocking is the controlling mechanism. For wall configurations where the sliding capacity is decisive, single connections with low shear properties may lead to a similar effect. Nevertheless, neglecting the inelastic area, this model is mechanically consistent and therefore applicable for many practical cases.

4-3.2.5 Felicetti 2012

A first step towards the displacement-based modelling is undertaken in Felicetti (2012) by developing a semi-displacement-based approach. Similar to Pei et al. (2012), this model assumes that every CLT wall system exhibits some rocking deflection. However, Felicetti (2012) also takes the contributions basing on sliding and CLT deformation into account. A short step-by step explanation of this approach is given below.

- Step 1: Applying a lateral displacement and assuming that it is only carried by rocking.
- Step 2: Determine the load, responsible for creating this displacement.
- Step 3: Determine the corresponding sliding and CLT deformations (basing on the actual load).
- Step 4: Repeat steps 1 to 3 till either uplift or shear capacity of considered connections is reached.

For performing the single calculations, Felicetti (2012) applied a mixture of the models described in Schickhofer et al. (2010), Schickhofer and Ringhofer (2011) and Gavric et al. (2011); the connections' load-displacement behaviour is also approximated by a trilinear model.

However, a comparison with experimental tests, discussed in Flatscher (2012), turned out that the 'rocking assumption' partially leads to outlying results and therefore limits the practical use. Hence, this model is not considered for further discussions.

4-3.2.6 Flatscher 2014

In Flatscher et al. (2014) the first fully displacement-based approach for investigating the behaviour of CLT wall systems is presented. Basing on the shear block model described in section 4-3.2.3, it continuously considers the nonlinear behaviour of connections (in this case screws) via an analytical approach similar to the one described in section 3-6. Nevertheless, since the input parameter is a lateral displacement instead of a lateral load, a direct and independent determination of respective sliding and rocking contributions is not possible. Hence, the relation between these two shares was fitted by comparing model and test results. Although not practicable at this stage of development, in principle it demonstrates the applicability of displacement-based approaches. The basic assumptions of this 'first

trial' are further developed and finally lead to the proposal described in section 4-4. The similarity of the two methods is further the reason why additional remarks are omitted at this point.

4-3.2.7 Further models

Further models with varying itemisations and aims, but principally dealing with the design of CLT wall systems, are discussed, e.g., in Sustersic and Dujic (2012), Casagrande et al. (2012), Wallner-Novak et al. (2013), Gavric and Popovski (2014) and Casagrande et al. (2016). However, all models are force-based and rely, more or less, on the mechanical relations described in the sections above. As a consequence, no further detailed discussions are included in the present thesis.

4-3.3 CONSIDERATION OF CLT ELEMENTS

As already mentioned, compared to the commonly applied connections, the stiffness and load-carrying capacity of CLT elements are relatively high. Hence, this part probably may be neglected in many cases. Nevertheless, assuming situations with short walls or openings, the stiffness of a CLT element may significantly decrease. Hence and further for the sake of completeness, the following part discusses how CLT may be considered in CLT wall systems.

4-3.3.1 Bending

A simple approach for considering the bending behaviour of a CLT element is applied in Ringhofer (2010). Here, the total thickness of a CLT element (t_{CLT}) and the modulus of elasticity (MOE) of the raw material parallel to the grain are used to determine the bending stiffness of the considered wall element. Consequently, assuming a cantilever bearing system, the share of bending deformation may be determined as given in Equation (4.42).

$$v_{bn} = \frac{4 \cdot F \cdot h^3}{E_0 \cdot l^3 \cdot t_{CLT}} \tag{4.42}$$

with

E_0..... MOE of raw material parallel to the grain

Relying on the composite theory, Blaß and Fellmoser (2004) investigate strength and stiffness capacities of solid wood panels. Adapted to the behaviour of laterally loaded CLT wall elements, their findings regarding the effective bending stiffness may be expressed as given in Equations (4.43) and (4.44).

$$K_{\mathrm{CLT,bn,eff}} = E_0 \cdot \frac{l^3 \cdot t_{\mathrm{CLT}}}{12} \cdot k_{\mathrm{comp}} \tag{4.43}$$

$$k_{\mathrm{comp}} = 1 - \left(1 - \frac{E_{90}}{E_0}\right) \cdot \frac{t_{\mathrm{eff}}}{t_{\mathrm{CLT}}} \tag{4.44}$$

with

$K_{\mathrm{CLT,bn,eff}}$ ..... effective bending stiffness of CLT wall element

k_{comp} ..... composite factor for solid wood panels with cross layers

E_{90} ..... MOE of raw material perpendicular to the grain

According to ON EN 338 (2009), the MOE for softwood parallel to the grain is approximately thirty times higher than perpendicular to the grain. Hence, considering the usual small influence of CLT deformations on the total head deflection of a CLT wall system, as a conservative assumption, the MOE perpendicular to the grain may be set equal to zero. This finally leads to the model applied in Sustersic and Dujic (2012) and Gavric et al. (2015a), considering only vertical layers for the bending stiffness. Due to this, Equation (4.45) may be used for determining the actual bending deformations.

$$v_{\mathrm{bn}} = \frac{4 \cdot F \cdot h^3}{E_0 \cdot l^3 \cdot t_{\mathrm{eff}}} \tag{4.45}$$

4-3.3.2 Shear

According to Sustersic and Dujic (2012), the shear deformation of a CLT wall element may be determined as given in Equation (4.46). The authors further stated that the effective shear cross section may be set equal to the full cross section of the wall element as long as the adjacent lamellas in a layer are glued together on their narrow sides. For other cases a reduction is recommended and appropriate sources are linked.

$$v_{\mathrm{sh}} \approx \frac{F \cdot h}{G \cdot t_{\mathrm{CLT}} \cdot l} \tag{4.46}$$

with

G ..... shear modulus of timber

Gavric et al. (2015a) use a similar approach, but consider only the cross sectional area of vertical layers and additionally include the shear correction factor for rectangular profiles (originally termed as ‘shape reduction factor’); compare Equation (4.47).

$$v_{\mathrm{sh}} = \frac{1.2 \cdot F \cdot h}{G \cdot A_{\mathrm{eff}}} = \frac{1.2 \cdot F \cdot h}{G \cdot t_{\mathrm{eff}} \cdot l} \tag{4.47}$$

According to Moosbrugger et al. (2006), three fundamental mechanisms have to be considered when determining shear deformations in CLT wall elements: (i) pure shear, (ii) torsional shear and (iii) the effect of finite in-layer board spacings.

Basing on a representative volume sub-element (RVSE) and assuming an infinite number of layers, the authors derive Equation (4.48) for determining an effective shear modulus G^*. As can be seen, this formulation includes a supplemental parameter (α_{FIT}), introduced for fitting the simplified mechanical model to results of further conducted FEM-simulations.

$$G^* = \frac{G}{1+\frac{u}{a}\cdot\left(1+2\cdot\frac{G}{G_R}\right)+\alpha_{FIT}\cdot 3\cdot\frac{G}{G_T}\cdot\left(1+\frac{u}{a}\right)^2\cdot\left(\frac{t_i}{a}\right)^2+2\cdot\frac{G}{E}\cdot\left(\frac{u}{a}\right)^3} \tag{4.48}$$

with

G^* ..... effective shear modulus for CLT wall element
G_R ..... rolling shear modulus of timber
G_T ..... torsional shear modulus of timber assumed to equal $(G + G_R)/2$
a ..... single board width or mean distance between cracks
u ..... gap/crack width
α_{FIT} ..... fitting parameter basing on FEM-simulations

Schickhofer et al. (2010) use the same approach but postulate a gap width to board width ratio (u/a) equal to zero. Furthermore, due to the low rolling shear modulus, the effective torsional shear modulus is taken to be the half of the shear modulus in direction of the grain. Assuming an even layer thickness and relying on FEM-simulations, finally Equations (4.49) and (4.50) are suggested for determining the effective shear modulus of three and five-layered CLT elements, respectively.

$$G_3^* = G_{mean}\cdot 0.65 \tag{4.49}$$

$$G_5^* = G_{mean}\cdot 0.70 \tag{4.50}$$

with

G_{mean} ..... mean shear modulus of raw material

In Bogensperger et al. (2010) and Silly (2010), the so called boundary effect, considering a finite number of layers, is investigated more in detail. Using the same assumptions as described in Schickhofer et al. (2010), finally leads to Equation (4.51) whereby the fitting parameter α_{FIT} is proposed to be determined for three and five-layered CLT elements as expressed in Equations (4.52) and (4.53), respectively.

$$G^* = \frac{G_{mean}}{1+\alpha_{FIT}\cdot 6\cdot\left(\frac{t_{mean}}{a}\right)^2} \tag{4.51}$$

$$\alpha_{FIT,3} = 0.53 \cdot \left(\frac{t_{mean}}{a} \right)^{-0.79} \tag{4.52}$$

$$\alpha_{FIT,5} = 0.43 \cdot \left(\frac{t_{mean}}{a} \right)^{-0.79} \tag{4.53}$$

with

t_{mean} ..... mean layer thickness

The ON B 1995-1-1 (2015) picked up this model and schedules the slightly adapted version, valid for CLT elements with gap widths smaller than 2 mm, expressed in Equation (4.54).

$$G^* = \frac{G_{mean}}{1 + 6 \cdot p_S \left(\frac{t_{max}}{a} \right)^{q_S}} \tag{4.54}$$

with

t_{max} ..... maximum layer thickness in CLT element

p_S, q_S ..... parameters according to Table 4.1.

Table 4.1: parameters for calculating the effective shear stiffness according to ON B 1995-1-1 (2015)

parameter	3 layers	5 and more layers
p_S	0.53	0.43
q_S	1.21	

Silly (2010) also performed a study where the influence of 2 mm gaps are investigated. Compared to the results where the thickness of a gap/crack is set equal to zero, Equations (4.55) to (4.57) lead to approximately 13 % lower stiffness values; for determining α_{FIT}, again, Equations (4.52) and (4.53) may be used for the respective number of layers.

$$G^* = \frac{G_{mean}}{1 + 3.4 \cdot \alpha_u \cdot \frac{u}{a} + \alpha_{FIT} \cdot 6 \cdot \left(1 + 2 \cdot \frac{u}{a} \right) \cdot \left(\frac{t_{mean}}{a} \right)^2} \tag{4.55}$$

$$\alpha_{u,3} = 12.97 \cdot \left(\frac{t_{mean}}{a} \right)^{0.59} \tag{4.56}$$

$$\alpha_{u,5} = 10.67 \cdot \left(\frac{t_{mean}}{a} \right)^{0.57} \tag{4.57}$$

with

α_u ..... fitting parameter basing on FEM-simulations considering 2 mm gaps/cracks

Note: In the original document, the more general notation t_i instead of t_{mean} is used.

Using an effective shear modulus G^* as described above, enables to calculate the shear deformation of a CLT element by means of Equation (4.58).

$$v_{sh} = \frac{F \cdot h}{G^* \cdot t_{CLT} \cdot l} \tag{4.58}$$

Table 4.2 depicts reduction factors, representing the ratio between the effective shear modulus for CLT and the shear modulus of solid timber (G^*/G) according to the discussed models. For the model applied in Gavric et al. (2015a) it is assumed that the outer layers are vertical; compare Figure 4.1. As can be seen, the reduction is between 30 to 50 % of G and should therefore not be neglected.

Table 4.2: ***reduction factors for CLT shear modulus; basic assumptions are: an even layer thickness of 30 mm, a board width of 150 mm and a gap/crack width of 2 mm (if necessary)***

model	**3 layers (t_{CLT} = 90 mm)**	**5 layers (t_{CLT} = 150 mm)**
Gavric et al. (2015a)	0.56	0.50
Schickhofer et al. (2010)	0.65	0.70
Silly (2010) without gaps	0.69	0.73
Silly (2010) with gaps	0.59	0.64
ON B 1995-1-1 (2015)	0.69	0.73

4-3.3.3 Openings

Besides investigating full CLT elements, Moosbrugger et al. (2006) further describe the possible influence of an opening on the effective shear modulus. As a first (rough) estimation, a simple area based approach, as expressed in Equation (4.59), is used. Moreover, relying on an additional FEM-simulation examining the behaviour of a CLT wall including a centred and quadratic opening, Equation (4.60) is introduced.

$$G_{op} = G^* \cdot \left(1 - \frac{A_{op}}{l \cdot h}\right) \tag{4.59}$$

$$G_{op} = G^* \cdot \left(e^{-6 \cdot \left(\frac{l_{op}}{l}\right)^{2.5}}\right) \tag{4.60}$$

with

G_{op} ..... reduced shear modulus for a CLT wall element including an opening

A_{op} ..... area of the wall opening

l_{op} ..... length (= width) of the wall opening

Based on experimental test results and several numerical simulations, Dujic et al. (2007) propose a more general model for considering the presence of openings in CLT wall elements. It considers not only the opening area, but also the length of remaining full height wall segments. The corresponding formulas

are given in Equations (4.61) and (4.62), for the geometric notations see Figure 4.16. It is further worth mentioning that this method is used to reduce bending and shear stiffness simultaneously; compare Sustersic and Dujic (2012).

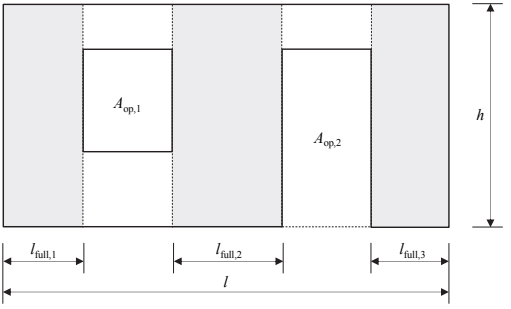

Figure 4.16: geometric boundary conditions and notations for a CLT wall element including various openings according to Dujic et al. (2007)

$$K_{CLT,op} = K_{CLT} \cdot \frac{r_{CLT}}{2 - r_{CLT}} \tag{4.61}$$

$$r_{CLT} = \frac{h \cdot \sum l_{full,i}}{h \cdot \sum l_{full,i} + \sum A_{op,j}} \tag{4.62}$$

with

$K_{CLT,op}$ ..... stiffness of a CLT wall element including openings

K_{CLT} ..... stiffness of a CLT wall element without openings

r_{CLT} ..... panel area ratio

$l_{full,i}$ ..... length of full height wall segments

Comparing the three approaches, Figure 4.17 illustrates a diagram, where the ratio between the shear modulus of a quadratic wall, with and without a centred quadratic opening, depending on the width of the opening, is illustrated. If Equation (4.60), representing the FEM-simulation conducted in Moosbrugger et al. (2006), is assumed to represent the 'real' behaviour, the model proposed in Dujic et al. (2007) leads to an acceptable approximation, but the area based model given in Equation (4.59) seems to be too progressive. Experimental results for the verification of one of these models are widely missing; single experimental results can be found in Dujic et al. (2007), Kawai et al. (2014) and Flatscher et al. (2015). The latest findings concerning openings in CLT walls, including a FE-based parameter study and an additional prediction model, are discussed in Shahnewaz et al. (2016).

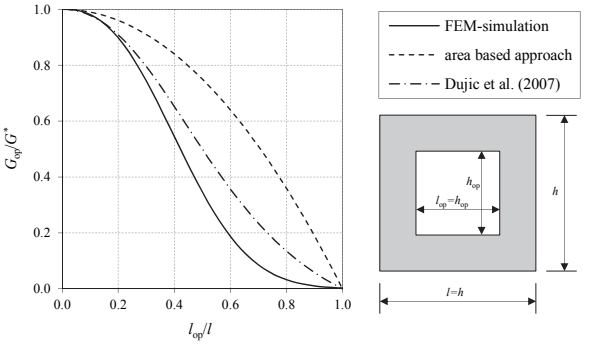

Figure 4.17: comparison of shear stiffness reduction models in case of a centred quadratic opening in a quadratic CLT wall element

4-3.4 CONCLUDING REMARKS

Within this section, some analytical approaches for considering the influence of connections, CLT elements and openings in CLT elements are summarised. The most advanced model is proposed in Gavric et al. (2015a). Therein, the vertical and lateral stiffness of every single connection as well as vertical joints are considered. Thus, for the increasing branch of the load-displacement relationship, this model enables a proper prediction. Unfortunately, its force-based character leads to some issues in defining the maximum load-carrying capacity of the wall system.

A possible improvement of describing the peak load and, especially, the subsequent softening area, is seen in the application of displacement-based approaches. A first trial is presented in Flatscher et al. (2014), but detailed descriptions, or a solution concerning the determination of the contributions to total head deflection, are still missing.

Regarding the consideration of CLT deformations, applicable elastic solutions are already available. Since plastic deformations are not relevant for the spotted topic, further discussions base on the present models without further adaptions. In particular, for bending deformations Equation (4.45) and for shear deformations Equation (4.58) – in combination with the definitions for the effective shear modulus as given in ON B 1995-1-1 (2015) and Equation (4.54) – are applied. Finally, for considering openings in CLT wall elements, the model developed in Dujic et al. (2007) is used.

4-4 NEW DISPLACEMENT-BASED MODEL

In this section, a new displacement-based calculation model for predicting the load-displacement behaviour of various CLT wall systems is presented. In a first step, the basic mechanisms are described and afterwards further aspects are discussed in detail.

Note: Some parts of the present section are preliminary published in Flatscher and Schickhofer (2016).

4-4.1 PRINCIPLE MODE OF OPERATION

Similar to the model described in Gavric et al. (2015a), while investigating the connections' behaviour a rigid CLT body is assumed. The contributions to total head deflection concerning CLT are determined in a separate step. Furthermore, the point of rotation is again defined in the lower corner of the wall element.

Probably the biggest difference to force-based models is that the sliding and rocking behaviour cannot be analysed separately. A possible solution for this issue is already offered in Flatscher et al. (2014), where experimental results are used to fit the respective ratio. For enabling wall analyses independent from test results, an iterative process basing on equilibrium conditions is developed. Within the following passage, this approach is described step by step and Figure 4.18 visualises the therefore most important elements and notations.

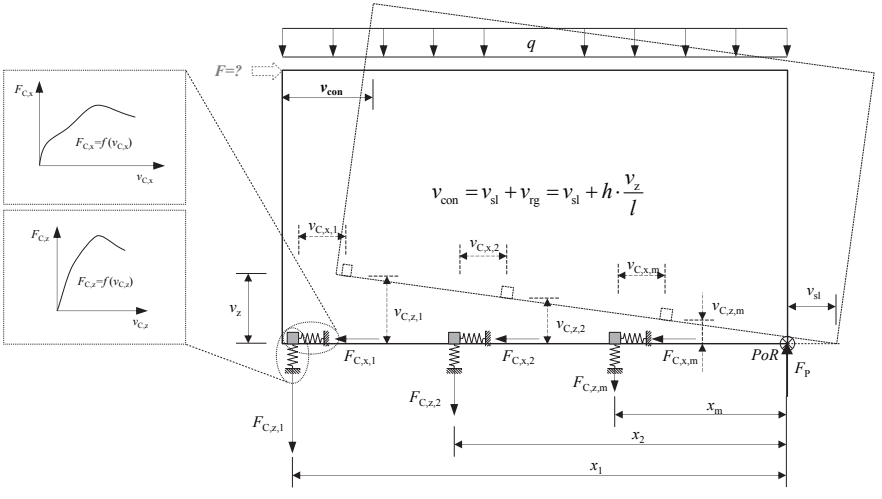

Figure 4.18: displacement-based model – overview and applied notations

- **Step 1:**

  In the first instance, the sliding and rocking contributions to the applied (connection based) lateral displacement are estimated. For this purpose the share parameter p, attending values between 0 and 1, is introduced; compare Equations (4.63) and (4.64).

$$v_{sl} = p \cdot v_{con} \tag{4.63}$$

$$v_{rg} = (1 - p) \cdot v_{con} \tag{4.64}$$

  with

  p ..... share parameter; $0 \leq p \leq 1$ (e.g., $p = 0.5$)

  v_{con} ..... connection based lateral deflection of CLT wall system

- **Step 2:**

  Next, lateral and vertical displacements for every considered connection are computed as expressed in Equations (4.65) and (4.66).

$$v_{C,x,m} = v_{sl} = v_{con} \cdot p \tag{4.65}$$

$$v_{C,z,m} = x_m \cdot \frac{v_{rg}}{h} = x_m \cdot \frac{(1-p) \cdot v_{con}}{h} \tag{4.66}$$

  with

  $v_{C,x,m}$ ..... lateral (horizontal) displacement of a connection

  $v_{C,z,m}$ ..... uplift (vertical) displacement of a connection

- **Step 3:**

  Afterwards, depending on the respective displacements, appearing loads for every considered connection are determined; compare Equations (4.67) and (4.68). For this purpose, linear elastic, multi linear or any other method may be applied. However, due to its already explained advantages, here the displacement-based model suggested in Chapter 3 is preferred; compare Equation (3.103) in section 3-6.

$$F_{C,x,m} = f\left(v_{C,x,m}\right) \tag{4.67}$$

$$F_{C,z,m} = f\left(v_{C,z,m}\right) \tag{4.68}$$

- **Step 4:**

  Now the lateral loads acting on the CLT wall system, causal for the assumed displacements, are computed as given in Equations (4.69) and (4.70). In order to consider the possible influence of friction as intended in Equation (4.69), it is necessary to determine the actual bearing load F_P. Due to equilibrium conditions, this parameter depends on both the external vertical load q and the actual acting uplift loads in the connections; compare Equation (4.71).

$$F_{sl} = \underbrace{\sum\left(F_{C,x,m}\right)}_{\text{connections}} + \underbrace{F_P \cdot \mu_f}_{\text{friction}} \tag{4.69}$$

$$F_{rg} = \underbrace{\frac{\sum\left(F_{C,z,m} \cdot x_m\right)}{h}}_{\text{connections}} + \underbrace{\frac{q \cdot l^2}{2 \cdot h}}_{\text{vertical load}} \tag{4.70}$$

$$F_P = \sum\left(F_{C,z,m}\right) + q \cdot l \tag{4.71}$$

with

F_{sl} ..... load responsible for sliding

F_{rg} ..... load responsible for rocking

- **Step 5:**

  So far, loads responsible for sliding and rocking deflections are determined independently. However, since physically only one lateral load F can act at the same time, the constraint given in Equation (4.72) shall be complied.

$$F \overset{!}{=} F_{sl} \overset{!}{=} F_{rg} \tag{4.72}$$

  If this condition is satisfied, the share parameter p assumed in step 1 is correct and the calculation process can go further to step 6. Elsewise, steps 1 to 5 have to be repeated with a varying parameter p until the equilibrium is reached. In particular, if F_{sl} is greater than F_{rg}, p has to be decreased; otherwise p has to be increased.

  However, it is also possible that the share parameter reaches its limit (either 1 or 0) before Equation (4.72) is fulfilled. This case frequently (but not only) occurs at small deformations, where one contribution to the total head deflection may be prohibited by the boundary conditions (e.g. rocking by high vertical loads or sliding via a high influence of friction). If so, the minimum of F_{sl} and F_{rg} is taken as the relevant load value.

- **Step 6:**

  Knowing the actual load F finally enables to determine the elastic CLT deformations. As already mentioned, for this purpose Equations (4.45) and (4.58) for bending and shear, respectively, are applied. Furthermore, the model described in Dujic et al. (2007) is suggested for considering the presence of openings; compare Equations (4.61) and (4.62).

4-4.2 SPECIFICS AND ADDITIONAL EFFECTS

Basing on the described mode of operation, the current section spots some specifics and additional effects, which may be considered when applying the new approach.

4-4.2.1 Constant displacement in case of load decrease

In principle, the described process enables a direct determination of the corresponding lateral load at any displacement level. Nevertheless, since the calculation requires iteration, in spite of the continuous definition of connections' load-bearing behaviour, an equivalent definition for the load-displacement relationship of a CLT wall system is not possible. Hence, it is necessary to determine the appearing load for several displacement levels separately. The distinct number solely depends on the demands on accuracy of the final piecewise linear load-displacement curve.

However, using the absolute displacement values as input parameters may lead, in some cases, to an issue when reaching the softening branch. In particular, due to fulfilling the condition given in Equation (4.72), the iterative process may result in *p*-values, leading to a reduction of either sliding or rocking deflections. This especially occurs if one of the respective resistances is distinctively higher than the other one. Although the applied approximation model for connections enables to simulate this case (compare section 3-6.4), and the effects on resulting load-displacement curves are usually small, measurements on experimental tests have shown that such a behaviour is unlikely while the total head displacement increases; compare test graphs documented in ANNEX C.

Thus, for preventing this effect, the approach expressed in Equations (4.73) and (4.74) is suggested. Here, the share parameter regulates the incremental instead of the absolute displacement. Consequently, since p cannot attend negative values, a decrease of actual sliding or rocking deflection, in case of increasing total deflection, is prohibited; the further calculations are unaffected.

$$v_{\mathrm{sl,i}} = v_{\mathrm{sl,i\text{-}1}} + p \cdot \Delta v_{\mathrm{con,i}} \tag{4.73}$$

$$v_{\mathrm{rg,i}} = v_{\mathrm{rg,i\text{-}1}} + (1 - p) \cdot \Delta v_{\mathrm{con,i}} \tag{4.74}$$

with

$v_{\mathrm{sl|rg,i}}$ ..... actual (estimated) contribution to total displacement
$v_{\mathrm{sl|rg,i\text{-}1}}$ ..... contribution to total displacement of previous calculation step
$\Delta v_{\mathrm{con,i}}$ ..... actual (estimated) increment of connection based lateral deflection

In other words, as long as the applied total head deflection is beneath $v_{\max}$ (corresponding displacement to the peak load) of the examined CLT wall system, the suggested modification leads to equal results as if sliding and rocking shares are determined from absolute displacement values. However, as soon as a reduction of either sliding or rocking deflection is required for fulfilling Equation (4.72), the modified approach forces the respective share to keep constant. As a consequence, the parameter p for

this scenario is either zero or one and the claim for equal loads cannot be fulfilled anymore. Hence, as described in step five of section 4-4.1, the minimum of the two determined loads is assumed to be the relevant one.

For illustrating the effects described afore, Figure 4.19 depicts the load-displacement relationship of a wall system, consisting of a single CLT element with 2.4 m in length and 3.0 m in height (assumed to be totally rigid), two hold-downs (one at each corner at the bottom joint) and one single angle bracket in the centre of the bottom joint. Moreover, a rigid foundation as well as a coefficient of friction and a vertical line load equal to zero are assumed. Detailed information concerning the implementation of connections can be found in Chapter 5.

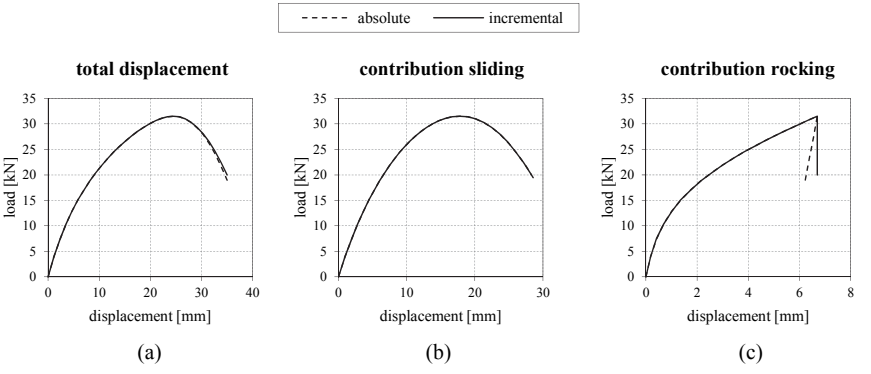

Figure 4.19: absolute and incremental determination of displacement shares for a CLT wall system – (a) total head deflection; (b) contribution sliding; (c) contribution rocking

The load vs. total displacement diagram given in Figure 4.19 (a), illustrates that the modified approach leads to equal results up to the peak load and to a similar one afterwards. Same occurs for sliding, but not for rocking. In particular, due to the low shear potential of only one angle bracket, sliding is the limiting behaviour and reaches its descending part earlier. As a consequence, the bearing capacity of the wall system decreases and for complying the required load equilibrium, the approach using absolute displacement values results in a decreasing rocking displacement; compare dashed line in Figure 4.19 (c). The incremental method, however, enforces a constant rocking displacement in case of a decreasing load. For further investigations solely the incremental procedure is used.

4-4.2.2 Interaction of shear and tension loads in connections

It is of common knowledge that an interaction of load-carrying capacities exists if a connection or a fastener is loaded in two different directions at the same time. A simple way to consider this effect is a linear combination of capacity utilisation as, e.g., scheduled in Eurocode 5 for smooth nails subjected to a combination of axial and lateral loads. A more frequently used model is the quadratic interaction as

scheduled in Eurocode 5 for other than smooth nails and screws. The latter approach is further provided for angle brackets, i.e., in the technical assessment ETA-06/00106 (2014).

A first experimental series, investigating combined axial and lateral loads on a hold-down, is presented in Pozza et al. (2016). Although no distinct interaction model is suggested, the published results show a loss of axial load-carrying capacity of approximately 10 % for lateral deformations up to 15 mm. A slightly higher impairment of maximum load is found at lateral deformation levels equal to 30 mm and 45 mm (22 % in maximum). Moreover, only a minor effect of combined loading on the initial (uplift) stiffness is stated.

Liu and Lam (2016) confirm that the shear and tension behaviour of hold-downs is relatively independent. However, they also offer some results of bi-directional loaded angle brackets (simulating a wall-to-foundation joint) and summarise that for such connections the interaction may not be neglected.

Another experimental campaign focussing on steel-to-timber joints, including one fully threaded self-tapping timber screw as fastener, show that for verifying the load-carrying capacity of such joints, the quadratic interaction model leads to quite conservative results and even higher power values may be possible; compare Laggner et al. (2016). The same study further investigates the effect of bi-directional loading on the initial stiffness of screwed steel-to-timber joints, but only a minor influence was found.

Summarising it can be stated that only minor research is done on combined loading of connections and implementing this effect in analytical and numerical models is not distinctively solved. Nevertheless, a possible solution is given in Gavric et al. (2015a), where the yield criterion for combined axial and lateral loads is determined by means of a quadratic interaction; compare Equation (4.32). Unfortunately, this way of combination is hardly applicable for a continuous approximation model as used in the present displacement-based approach. Hence, for considering the interaction an alternative method, scaling the original load-displacement curve, is applied.

In particular, it is assumed that if the available potential for the maximum load is reduced to, e.g., 70 %, the same reduction takes place for any other point at the loading path. Additionally, in the incremental determination process (see section 4-4.2.1) the reduction factor for the *i*-th step is forced to be equal or smaller than the same parameter in the step before. Finally, if the connector fails in one direction, the bearing capacity of the other one is assumed to be zero as well. The described approach, for determining the actual potential and the resulting scaled loads, is expressed in Equations (4.75) to (4.77).

$$\left(\frac{F_{C,x,m}}{F_{max,C,x,m}}\right)^k + \left(\frac{F_{C,z,m}}{F_{max,C,z,m}}\right)^k \leq 1.0 \quad \rightarrow \quad \begin{cases} \delta_{x,m} = \left(1 - \left(\frac{F_{C,z,m}}{F_{max,C,z,m}}\right)^k\right)^{\frac{1}{k}} \\ \delta_{z,m} = \left(1 - \left(\frac{F_{C,x,m}}{F_{max,C,x,m}}\right)^k\right)^{\frac{1}{k}} \end{cases} \tag{4.75}$$

$$F^*_{C,x,m} = F_{C,x,m} \cdot \delta_{x,m} \tag{4.76}$$

$$F^*_{C,z,m} = F_{C,z,m} \cdot \delta_{z,m} \tag{4.77}$$

with

$F_{max,C,x|z}$ ..... maximum load-carrying capacity of connection in the respective direction

k ..... parameter for interaction (e.g., two for quadratic interaction as scheduled in Eurocode 5)

$\delta_{x|z}$ ..... reduction factor

$F^*_{C,x|z}$ ..... scaled load in connection at defined displacement level

The effect of the suggested interaction approach on the actual load-bearing behaviour of an angle bracket (i.e., AE116; compare section 5-2.2) is illustrated in Table 4.3 and Figure 4.20. In particular, Table 4.3 lists five specific curve points and Figure 4.20 depicts the corresponding (scaled) load-displacement relationships for shear and uplift. For this example the interaction parameter k is set equal to two, resulting in a quadratic interaction.

Table 4.3: effect of interaction model on load-carrying behaviour of an angle bracket at defined levels of displacement

step *i*	shear | $F_{max,C,x}$ = 31.50 kN				tension (uplift) | $F_{max,C,z}$ = 36.30 kN			
	$v_{C,x,i}$ [mm]	$F_{C,x,i}(v_{C,x,i})$ [kN]	$\delta_{x,i}$ [-]	$F^*_{C,x,i}$ [kN]	$v_{C,z,i}$ [mm]	$F_{C,z,i}(v_{C,z,i})$ [kN]	$\delta_{z,i}$ [-]	$F^*_{C,z,i}$ [kN]
1	2.00	7.67	88%	**6.75**	3.00	17.21	97%	**16.69**
2	4.00	13.80	79%	**10.91**	6.00	22.24	90%	**19.99**
3	8.00	22.77	58%	**13.11**	12.00	29.68	69%	**20.51**
4	13.50	29.79	33%	**9.76**	16.50	34.29	33%	**11.16**
5	21.15	30.38	27%	**8.13**	23.85	34.98	26%	**9.25**

Note: The input parameters for these curve simulations are documented in section 5-2.2.

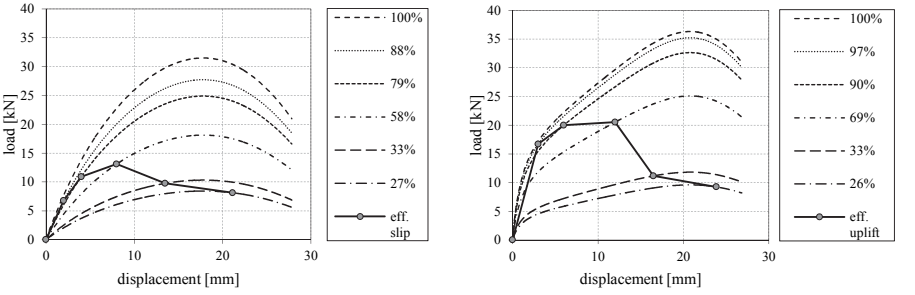

***Figure 4.20:** effect of interaction model on load-displacement behaviour for an angle bracket AE116 in case of bi-directional loading – (a) in lateral direction (shear); (b) in vertical direction (uplift)*

4-4.2.3 Shift of compression load F_P

So far, the resulting compression load F_P is concentrated in the assumed point of rotation, i.e., one of the corners at the bottom joint. Thus, this parameter does not appear in the formula used to determine the actual rocking load F_{rg}; compare Equation (4.70). However, actually the compressional stress is distributed over a specific length, which finally leads to a horizontal shift of F_P; compare, e.g., Schickhofer et al. (2010) or Ringhofer (2010). Moreover, in this area, compressional deformations (indentations), further influencing the actual lateral displacement, occur.

In order to consider the shift of the bearing load, Equation (4.70) is adapted to Equation (4.78). As depicted in Figure 4.21, and further visible in Equations (4.79) to (4.81), the implemented term bases on the assumption of a triangular stress-distribution in the compression zone. Since rather consistent with the displacement-based approach than the stress-block model suggested in Ringhofer (2010), this approach is preferred herein. Furthermore, it can be shown that the applied lever arm is approximately 30 % longer compared to the one resulting for the stress-block model. As a consequence, the assumption of a triangular stress-distribution finally leads to slightly more conservative results.

$$F_{rg} = \underbrace{\frac{\sum\left(F_{C,z,m} \cdot x_m\right)}{h}}_{\text{connections}} + \underbrace{\frac{q \cdot l^2}{2 \cdot h}}_{\text{vertical load}} - \underbrace{\frac{F_P \cdot l_P}{3 \cdot h}}_{\substack{\text{shift of} \\ \text{bearing load}}} \tag{4.78}$$

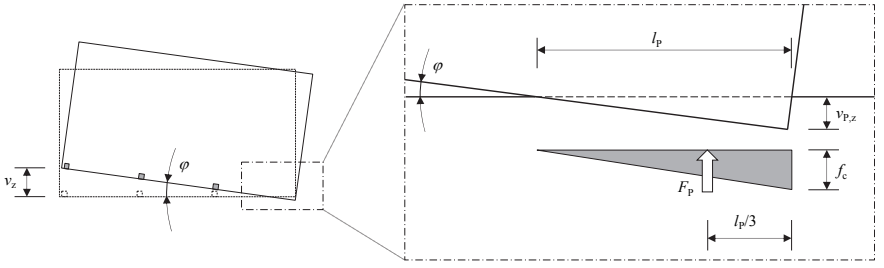

Figure 4.21: illustration of how compressional stress and indentations are considered in the new model

$$l_P = \frac{2 \cdot F_P}{t_P \cdot f_c} \tag{4.79}$$

$$t_P = \begin{cases} t_{eff} & \text{for rigid foundation} \\ t_{CLT} & \text{for CLT foundation} \end{cases} \tag{4.80}$$

$$f_c = \begin{cases} f_{c,0} & \text{for rigid foundation} \\ f_{c,90} & \text{for CLT foundation} \end{cases} \tag{4.81}$$

with

t_P ..... relevant thickness for stress distribution

f_c ..... relevant compression strength for stress distribution

The resulting indentation $v_{P,z}$ can be determined as expressed in Equation (4.82), but, for including this additional (negative) vertical displacement in the general calculation process, a further iteration is necessary; this, because it is affected by v_z and influences this parameter at the same time. However, compared to the displacements occurring in the currently applied connections, resulting $v_{P,z}$ values are usually small and have a minor influence on the primary outcome. Consequently, it would also be possible to use the indentation of the former step for determining the reduced vertical displacements per connection in the actual one; compare Equation (4.83).

$$v_{P,z} = \sin(\varphi) \cdot l_P = \sin\left(\frac{v_z}{l}\right) \cdot l_P \tag{4.82}$$

$$v_{C,z,m,i} = x_m \cdot \frac{v_{rg,i}}{h} - v_{P,z,i} \approx x_m \cdot \frac{v_{rg,i}}{h} - v_{P,z,i-1} \tag{4.83}$$

with

$v_{P,z}$ ..... indentation

4-4.2.4 Vertical joints

The basic version of the proposed model does not include the possibility for considering vertical joints. This, because the production of CLT elements up to 18 m (or even 30 m) is possible and a segmentation in principle is not necessary; compare Brandner et al. (2016). Furthermore, applying full CLT wall elements, instead of segmented ones, enables a reduction of assembling time and is therefore often used in practical design. Nevertheless, since shorter wall elements are available on the market as well, vertical joints are partially inevitable. Moreover, as discussed more in detail later on, some literature sources even demand a segmentation of CLT wall elements in seismic zones; compare discussions in Chapter 6. Hence, in order to consider vertical joints in the displacement-based approach too, the process described in Gavric et al. (2015a) is adapted as follows.

Similar to section 4-3.2.4, the following formulas are limited to only one vertical joint, exactly halve the CLT element. Moreover, CLT based bending deformation is considered in a simplified manner; compare Equation (4.84). A simultaneously consideration of indentations and openings is not possible.

$$v_{\mathrm{bn,vj}} = \frac{2 \cdot F \cdot h^3}{E_0 \cdot \left(\frac{l}{2}\right)^3 \cdot t_{\mathrm{eff}}} \tag{4.84}$$

with

$v_{\mathrm{bn,vj}}$ ..... CLT bending deformation in case of a vertical joint

Applying Equation (4.85) enables to determine the rocking displacement in case of a coupled behaviour. Alternatively, Equation (4.86) can be used as well; compare Figure 4.14. The required displacement parameters for determining the corresponding loads in the connections are given in Equations (4.87) to (4.89).

$$F_{\mathrm{rg,coupled}} = \frac{1}{h} \cdot \left[\sum \left(F_{\mathrm{C,z,I,m}} \cdot \left(x_{\mathrm{I,m}} - \frac{l}{2} \right) \right) + \sum \left(F_{\mathrm{C,z,II,n}} \cdot x_{\mathrm{II,n}} \right) + F_{\mathrm{vj}} \cdot \frac{l}{2} + \frac{q \cdot l^2}{4} \right] \tag{4.85}$$

$$F_{\mathrm{rg,coupled}} = \frac{1}{h} \cdot \left[\sum \left(F_{\mathrm{C,z,I,m}} \cdot x_{\mathrm{I,m}} \right) + \sum \left(F_{\mathrm{C,z,II,n}} \cdot x_{\mathrm{II,n}} \right) - F_{\mathrm{P,I}} \cdot \frac{l}{2} + \frac{q \cdot l^2}{2} \right] \tag{4.86}$$

$$v_{\mathrm{vj}} = \frac{v_{\mathrm{rg}} \cdot l}{2 \cdot h} \tag{4.87}$$

$$v_{\mathrm{C,z,I,m}} = x_{\mathrm{I,m}} \cdot \frac{v_{\mathrm{rg}}}{h} - v_{\mathrm{vj}} = x_{\mathrm{I,m}} \cdot \frac{v_{\mathrm{rg}}}{h} - \frac{v_{\mathrm{rg}} \cdot l}{2 \cdot h} \tag{4.88}$$

$$v_{\mathrm{C,z,II,n}} = x_{\mathrm{II,n}} \cdot \frac{v_{\mathrm{rg}}}{h} \tag{4.89}$$

Note: Notations are equal to the one described in section 4-3.2.4.

For simulating single-coupled behaviour it can be shown that the basic formulas, presented in Flatscher and Schickhofer (2016), may be simplified to Equation (4.90). Although the parameter v_{vj} disappears in this formulation, the forces in the connections of the first CLT segment (denoted by 'I' in Figure 4.14) still depend on both the rocking deformation v_{rg} and the displacement in the vertical joint v_{vj}. Consequently, a further iteration has to be included in the calculation process anyway. As the criterion for this approach, the actual load in the vertical joint is used; compare Equation (4.91).

$$F_{\text{rg,single-coupled}} = \frac{1}{h} \cdot \left[\sum \left(F_{\text{C,z,I,m}} \cdot x_{\text{I,m}} \right) + \sum \left(F_{\text{C,z,II,n}} \cdot x_{\text{II,n}} \right) + \frac{q \cdot l^2}{2} \right] \tag{4.90}$$

$$F_{\text{vj}}(v_{\text{vj}}) = \frac{q \cdot l}{2} + \sum \left(F_{\text{C,z,I,m}} \right) \tag{4.91}$$

In particular, it is suggested to firstly calculate the actual uplift loads for a distinct displacement by means of the principle mode of operation (without considering the vertical joint). Afterwards, the required displacement in the vertical joint for complying Equation (4.91) may be determined by an iterative process. During this step, the uplift (v_z) of the first CLT segment and, consequently, the vertical displacements of the connections (i.e. $v_{C,z,I,m}$), are reduced. Since this decrease of displacement influences the actual load in the respective connections, the two iterations have to be repeated till equilibrium is reached.

4-4.3 LIMITATIONS

Although the presented model enables to simulate the behaviour of various configurations, not all effects occurring in a CLT wall system can be described. The following itemisation gives an overview to not considered effects and limitations. Some of these points are discussed more in detail in Chapter 5.

- Consideration of a top joint

  As described in section 4-2, a CLT wall system also contains a top joint. The possible influence of this joint on the lateral behaviour of the CLT wall system is basically not considered in the proposed model. Solely the influence on a vertical joints' stiffness may be implemented in a simplified way; e.g., by enlarging the connections' stiffness or adding a supplemental stiffness parameter; compare section 5-5.1.1.

- Bending of the floor element

  The current model schedules a bending resistant foundation or floor element. Due to the circumstance that load-carrying wall elements are usually placed one upon the other (separated by the floor element), this is an acceptable assumption; especially if the top joint is designed stiffer than the bottom joint above. However, if a wall system is situated on a CLT floor not underpinned by another wall, bending effects may prohibit simultaneous acting of connections, which cancels a basic assumption of the suggested approach and, hence, may lead to unrepresentative results; see also section 5-5.1.1.

- Vertical bending of CLT wall element(s)

  As already mentioned, the presented approach assumes a rigid CLT wall element while examining the behaviour of applied connections. As a consequence, the actual occurring vertical bending deformation of CLT, leading to a curved rather than straight bottom edge and therefore an additional uplift deflection for applied connections, is not considered. For configurations where rocking becomes the decisive wall behaviour, the expectable deformations in this direction are quite small; see also section 5-5.2. In case of big wall openings (especially doors) such deformations, however, may distinctively influence the action of connections.

- Eccentricity of lateral and/or vertical loads

  Although the vertical position of load application can be defined independently from the walls' height, possible shifts of lateral and/or vertical loads due to rocking displacement, are not considered in the current version of the model.

4-4.4 SPREAD SHEET TOOL FOR COMPUTING CLT WALL SYSTEMS

Since the new model requires several computations and, at least, one iterative process, a calculation 'by hand' is not feasible. Nevertheless, one of the major aims of the herein presented approach is to enable a high quality calculation in a spread sheet program, prohibiting the necessity of high sophisticated software tools. To proof if this aim has been achieved, the basic calculation steps and the additional features, are implemented in a Microsoft ® Excel (2010) sheet, computing up to 31 points of the wall systems' load-displacement graph. This tool is further applied to prepare the later described model validation and parameter study.

4-4.5 CONCLUDING REMARKS

Within this section, a displacement-based calculation method for predicting the lateral load-displacement behaviour of CLT wall systems is developed. The benefit, compared to the force-based alternatives, can be seen in the improved consideration of connections' behaviour and the possibility to simulate also the post peak behaviour without further assumptions. This, by means of applying the approximation method described in section 3-6, which enables the continuous and accurate simulation of the whole load-displacement relationship of the used connections.

Besides the principle mode of operation, a new method for considering interactions and indentations is suggested as well. Moreover, the possibility to consider openings and vertical joints is implemented. Nevertheless, compared to the force-based methods, as, e.g., proposed in Gavric et al. (2015a), the herein proposed procedure is a bit more complex and requires, at least, one iterative process. However, due to its analytical quality, the required calculation processes may be implemented in a common spread sheet based tool for enabling a fast and easy use of the suggested model. For proofing this statement, an appropriate application is programmed in Microsoft ® Excel (2010). This tool is further used for

validating the quality of the new approach and to perform a study, investigating the influence of different parameters on the behaviour of CLT wall systems; compare Chapter 5 and Chapter 6.

4-5 FINITE ELEMENT SOLUTION

Besides analytical approaches, detailed numerical calculations, using finite element (FE) software tools, enable to simulate the behaviour of CLT wall systems with high accuracy. Although such investigations are usually time-consuming and therefore seldom used in practical design, they are frequently applied in research projects; this, for preventing expensive experimental campaigns. Moreover, besides single wall systems, even dynamic time history analysis on whole buildings can be modelled in programs using FE. Nevertheless, some calibrations on experimental test results are necessary anyway. Examples, where FE-simulations are applied, can be found in, e.g., Dujic et al. (2007), Dujic et al. (2010), Ceccotti (2008), Rinaldin et al. (2011), Pozza et al. (2013), Shen et al. (2013) and Izzi et al. (2015).

Modelling CLT wall systems can be realised with different levels of detail; starting with a simple linear elastic spring, up to a high sophisticated volume-model, considering nonlinearities of the used materials, single fasteners and steel parts. However, the level of detail correlates with the effort for compilation and calculation. Hence – from an economic point of view – it has to be adapted on the scaling level and the estimated output.

The present thesis focusses on the analytical description of load-displacement curves and a detailed description of complex FE models would go beyond its scope. Nevertheless, for verifying the fit of analytical approaches, FE models are of avail; particular for configurations where no experimental results are available. Thus, no general discussion on FE modelling, but rather a limited description of applicable and applied FE solutions, is given within this section.

All FE simulations used in the present thesis, are realised in RFEM 5 (2015). This program enables fast compilation and detailed modelling of diverse issues (i.e. nonlinear effects including the softening branch and orthotropic behaviour of CLT elements). Furthermore, since it is commonly used in engineering bureaus, every calculation, which is performed in this context, may be reproduced and verified.

4-5.1 MODELLING CONNECTIONS

Following the above defined aspects, a detailed modelling of every single connection, including fasteners and steel parts, is not feasible; it is quite time consuming and would require an enormous memory space. Furthermore, for investigating wall systems, such a level of detail is not necessary. Nevertheless, in order to show that it is basically possible, a tension loaded AE116 angle bracket in a wall-to-floor joint, using nonlinear springs for every nail, is modelled; required information is gathered

from experimental tests presented in Izzi et al. (2015). Moreover, nonlinear material properties for the steel bracket itself are used; timber is not modelled in detail.

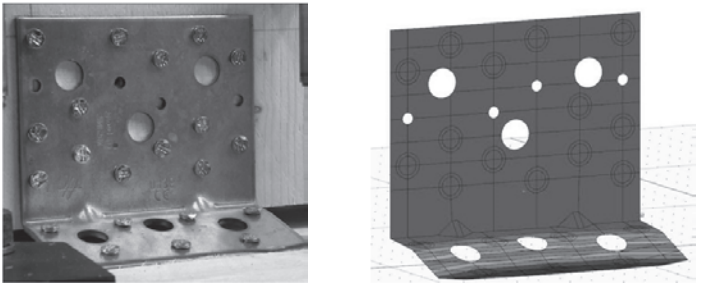

(a) (b)

Figure 4.22: visual comparison of angle bracket deformations – (a) experimental test; (b) FE model

As shown in Figure 4.22, the deformations of the angle bracket can be properly simulated. The computed loads at different displacement levels are also in good agreement with the experimentally gathered results; compare Figure 4.23. However, for this single connection the file (including the results) has a size of close to 1 GB and computing 14 different displacement levels requires approximately two hours if the iterations per load case are limited to 100 in maximum.

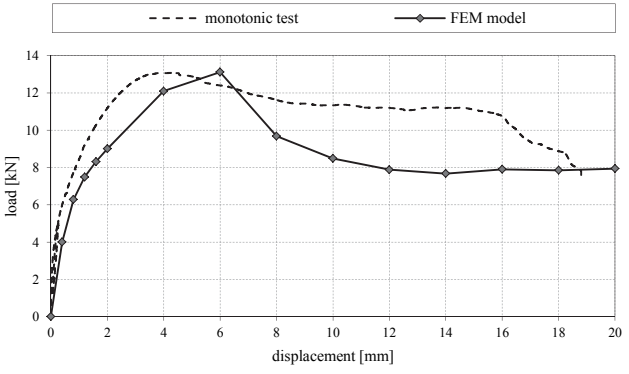

Figure 4.23: experimental and FEM simulated load displacement curves of tension loaded angle bracket AE116; detailed information regarding experimental results are given in Chapter 5

A more feasible approach for considering single connections is described in Vogt (2015). In particular, there the author applies 1D (beam) elements to simulate the behaviour of nails, joining the sheeting element of a wood-framed diaphragm to the studs and rails. The vertical and lateral resistance of such an element can be controlled by its length, cross section and material properties. Vogt (2015) further shows how the necessary cross section and the length of the element may be derived mechanically. Besides others, a distinct advantage of this model is the possibility to consider a kind of interaction between axial

and lateral loading; this, by means of stress interaction, resulting from the fact that shear and tension (uplift) loads are carried by the same element.

Such a beam-model is in principle also applicable for simulating connection systems consisting of several fasteners and steel elements. However, their load-bearing behaviour usually depends on various conditions (i.e., material properties, geometry and number of applied fasteners) and, hence, the necessary input parameters can hardly be derived from mechanical conditions. As a consequence, approximating the load-displacement behaviour of a connection requires a kind of 'trial-and-error' fitting.

In general, the shape of the load-displacement curves to be simulated can be adjusted by adapting the stress-strain path of the used material. For this purpose, RFEM 5 (2015) enables a piecewise linear definition for positive and negative stresses with up to 20 coordinates deviating from zero. Nevertheless, since modelling 1D elements – at least in RFEM 5 (2015) – can only be realised with isotropic materials, the different behaviour, while vertical (uplift) and lateral (shear) loading, has to be regulated by varying the cross section.

For illustrating the quality of such a model, the behaviour of an AE116 angle bracket in a wall-to-foundation joint (compare Chapter 5) is simulated. Therefore, the beam element is modelled as a 650 mm long cantilever with a rotated OVAL_M cross section (10/63 mm | rotation 90°) and an 'Isotropic Plastic 1D' material model. The loading is applied via nodal deformations on the cantilevers' end. Figure 4.24 shows a screenshot of the model, illustrating the distribution of normal stresses while loaded under 45° (equal lateral and vertical displacement) as well as the parameters used for defining the materials' stress-strain diagram.

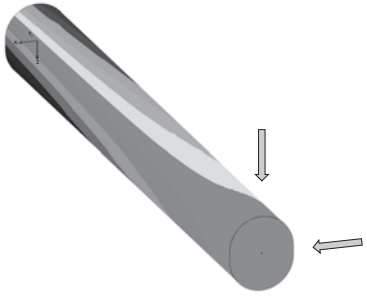

(a)

ID	ε_x [-]	σ_x [N/mm²]
1	0.00000000	0
2	0.00071429	230
3	0.00142390	260
4	0.00213820	290
5	0.00284780	310
6	0.00356210	330
7	0.00427170	350
8	0.00498600	370
9	0.00569560	390
10	0.00640990	400
11	0.00711960	410
12	0.00783380	420

ID	ε_x [-]	σ_x [N/mm²]
13	0.00854350	420
14	0.00925780	420
15	0.00996740	420
16	0.01068200	415
17	0.01139100	400
18	0.01210600	370
19	0.01281500	320
20	0.01352900	240
21	0.01423900	130

E = 321998 N/mm²

(b)

Figure 4.24: FE beam model for an AE116 angle bracket realised in RFEM 5 (2015) – (a) screenshot showing cross section and normal stresses; (b) parameters for defining materials' stress-strain diagram

A comparison between the FE simulation, using the described 1D element, and the approximated load-displacement curves of the angle bracket loaded in shear and tension (average curves as defined in Chapter 5), is illustrated in Figure 4.25. As can be seen, due to the isotropic material definition, the shape of the FE graphs for vertical and lateral loading are similar and only scaled by the cross sections' form. However, the results show that this approach is in principle applicable and enables acceptable results. Moreover, it needs only few processing power compared to the detailed modelling of a whole connection described afore. Finally, once more, the benefit of considering a kind of interaction has to be highlighted; compare black dashed lines in Figure 4.25, representing a loading under 45°, i.e., equal lateral and vertical displacement. However, though supported in the material definition, the post peak behaviour of the connection is obviously not considered in the FE calculation. For comparison, grey dashed lines in Figure 4.25 show the result of combined loading when applying the interaction model as suggested in section 4-4.2.2.

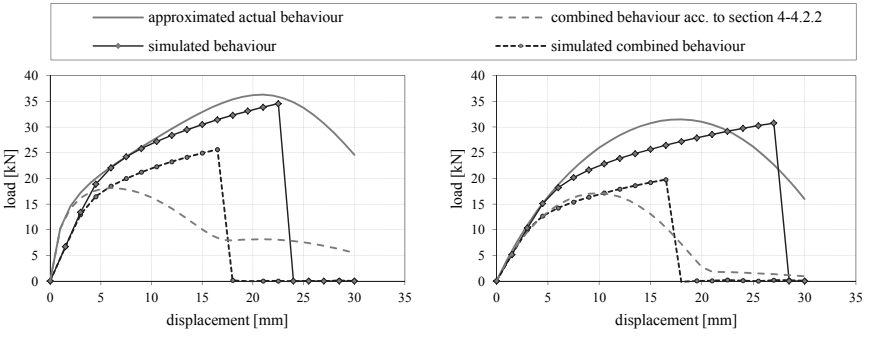

(a) (b)

Figure 4.25: FE beam-model suggested in Vogt (2015) applied for simulating shear, uplift and combined shear/uplift behaviour of an AE116 angle bracket in a wall-to-foundation joint – (a) behaviour in z-direction (uplift); (b) behaviour in x-direction (shear)

A further method applicable for considering the nonlinear behaviour of connections in RFEM 5 (2015), is the implementation of single supports and defining their behaviour over a piecewise linear load-displacement diagram. Moreover, if a displacement controlled load input (imposed nodal deformations) is used, the consideration of the softening branch is also possible. A disadvantage of this approach is that no interaction between shear (lateral) and uplift (vertical) bearing loads is possible. In particular, no degradation of load-carrying capacity or stiffness can be considered in the simulation. Nevertheless, modelling the connections in this way is quite simple, requires no fitting, enables to simulate the post peak area of every connection and finally leads to feasible results for the aimed task. Due to this, the latter mentioned method is preferred for all further investigations.

4-5.2 MODELLING CLT ELEMENTS

As already described, CLT elements are usually quite stiff and contribute only little to the overall behaviour of a CLT wall system. Modelling the wall element as a rigid diaphragm would therefore be an easy and, in principle, acceptable solution. This, however, is not evident for short or very long wall elements, where bending might play a role, or in case if the influence of openings is investigated.

For considering CLT and its orthotropic nature – at least elastically – RFEM 5 (2015) offers the possibility to implement a user defined stiffness matrix, ruling the behaviour of the surface element. Basically, 21 matrix elements have to be defined, considering bending, torsion, shear, membrane and eccentric effects. For an orthotropic CLT diaphragm, where a Poisson ratio equal to zero is assumed, as, e.g., suggested in Silly (2010), solely eight elements remain; all others are zero. These parameters may finally be determined according to the models developed in Schickhofer et al. (2010), Silly (2010) and partwise given in ON B 1995-1-1 (2015); the applied equations, as well as some further information, are documented in ANNEX D.

4-6 INTERMEDIATE CONCLUSIONS

Besides some general definitions, currently available models for predicting the behaviour of laterally loaded CLT wall systems are summarised and discussed in this chapter. As documented, nearly all models are force-based and the described approaches using the walls' deflection as input parameter are not generally feasible. However, displacement-based methods do exhibit the distinct advantage that they enable an enhanced consideration of connections; especially after passing their maximum load-carrying capacity.

Thus, a new displacement basted concept is proposed and described in detail. Thereby, not only the general mode of operation, but also new approaches concerning the load-interaction in connections and the indentations close to the point of rotation, are offered. In addition, adapting the model proposed in Gavric et al. (2015a), the implementation of a vertical joint is possible as well.

Since state of the art, and used later on for validating the suggested analytical approach, finally some options concerning the implementation of connection systems and CLT wall elements in a FE-program are briefly discussed.

CHAPTER 5
EXPERIMENTAL PROGRAM AND MODEL VALIDATION

5-1 INTRODUCTION

In the last decade, several experimental tests, dealing with the lateral behaviour of CLT structures, are conducted in the scientific community. In principle, these investigations may be separated in (i) single joint tests, (ii) tests on CLT wall systems and (iii) investigations on whole structures. Examples for (i) and (ii) can be found in Dujic et al. (2005), Ceccotti et al. (2006a), Flatscher and Schickhofer (2011), Popovski and Karacabeyli (2011), Flatscher (2012), Okabe et al. (2012), Hummel et al. (2013), Gavric et al. (2014), Kawai et al. (2014), Pozza et al. (2014), Flatscher et al. (2015), Gavric et al. (2015a), Gavric et al. (2015b), Malaga-Chuquitaype et al. (2016) and Pozza et al. (2016). Tests on CLT structures are documented in Ceccotti et al. (2006), Ceccotti et al. (2013), Popovski et al. (2014), Flatscher and Schickhofer (2015) and Yasumura et al. (2015).

In 2010, an extensive experimental campaign, including all three areas (single joints, walls and structures), was started at Graz University of Technology, Institute of Timber Engineering and Wood Technology (TU Graz) and the competence centre holz.bau forschungs gmbh (hbf). In particular, the behaviour of connection systems currently applied in Europe, i.e., angle brackets, hold-downs and screws, was investigated. Basing on these results, full scale CLT wall systems were tested within a second step; compare, Flatscher et al. (2015). Finally, within the framework of the European Union (EU) Seismic Engineering Research Infrastructures for European Synergies (SERIES) project, a full scale shaking table test on a three-storey CLT structure was realised; see Flatscher and Schickhofer (2015).

In the present chapter, relevant information regarding conducted single joint and wall tests is collected. Especially the parameters required for simulating the connections and further validating the proposed displacement-based wall model are documented. Moreover, basing on the suggestions given in Chapter 2, the alternative stiffness and ductility parameters are listed. Although the primary focus is set on TU Graz investigations, for expanding the data basis, results of independent research projects, as documented in Gavric (2013), Seim and Hummel (2013) and Seim et al. (2013), are partially summarised as well.

The data sets are then used for simulating the behaviour of 25, already tested, wall configurations. Afterwards, the resulting load-displacement relationships are compared with the actual test curves, gathered from corresponding experiments. Finally, the load-displacement behaviour of nine additional

wall configurations, not yet tested, is estimated with the proposed model and the results are compared to FE-based simulations.

5-2 CONNECTIONS

Within the program conducted at TU Graz, 215 monotonic and cyclic single joint tests, including various types and configurations for angle brackets, hold-downs and screws, were realised. For the present thesis, solely tests on connections and fasteners used for both single joint and wall tests are of interest. Hence, this section focusses in particular on the properties of angle bracket AE116, hold-down HTT22 and some selected screws; basic information regarding these connections and fasteners are summarised in Table 5.1. A comprehensive documentation of the conducted test program is published in Flatscher et al. (2013) and Bratulic et al. (2014b).

***Table 5.1:** selected connections and fasteners examined in the course of TU Graz tests*

type	name	dimensions	producer	notes
angle bracket	AE116	116×90×48×3 mm	Simpson Strong-Tie	14 | 7 nails (2 bolts)
hold-down	HTT22	559×64×62×3 mm	Simpson Strong-Tie	15 nails and 1 bolt
nail	CNA	Ø 4.0×60 mm	Simpson Strong-Tie	annular-ringed shank
bolt I	FBN II 12/10	Ø 12×106 mm	Fischer	
bolt II	threaded rod	M 16	-	
screw I	Stardrive	Ø 8.0×280 mm	Schmid Schrauben Hainfeld	fully threaded
screw II	ASSY PLUS VG	Ø 6.0×80 mm	Würth	fully threaded
screw III	ASSY PLUS VG	Ø 6.0×120 mm	Würth	fully threaded

5-2.1 GENERAL INFORMATION

5-2.1.1 Material and methods

For angle brackets and hold-downs both wall-to-floor and wall-to-foundation joints were tested. The configurations used to examine the behaviour of screwed joints include wall-to-floor and wall-to-wall joints. For the wall elements three-layered CLT panels with a total thickness of 98 mm and a lay-up of 32-34-32 mm were used. Floor elements had five layers and a lay-up of 26-27-28-27-26 mm, leading to a total thickness of 134 mm. All CLT panels are produced out of C 24 spruce, owning a mean density of 423 kg/m³ (CoV = 6 %); mean densities of CLT elements involved in the single experiments are given in ANNEX B. Moreover, according to ON EN 26891 (1991) and ON ISO 554 (1994), all timber elements were conditioned at the standard environment of 20 ± 2 °C temperature and 65 ± 5 % relative humidity, aiming a balanced moisture content of 12 ± 2 %.

For investigating wall-to-foundation joints equipped with angle brackets, concrete specimens with a total thickness of 190 mm were produced out of a C25/30 concrete with plastic fibres; reinforcement was realised with a steel mesh AQ60. For experiments focusing on the behaviour of hold-downs, the same configuration was designated. However, due to occurring issues in a preliminary test, it was decided to substitute the concrete element by a steel foundation; compare Flatscher et al. (2013).

All single joint tests were realised with the universal testing device 'lignum_uni_275' (Z-250, ZWICK company, Germany) at the lignum test centre (LTC), which is associated to the Institute of Timber Engineering and Wood Technology. For measuring the occurring displacements, linear variable displacement transducers (LVDTs) were used in various positions. Detailed illustrations of the single configurations are documented in ANNEX B.

The loading procedure for monotonic tests was performed as scheduled in ON EN 26891 (1991). Basing on Flatscher (2010), for the cyclic tests it was decided to follow the instructions given in ISO 16670 (2003) instead of those in ON EN 12512 (2005). The loading rate for most cyclic tests was kept constant with 2 mm/s; solely two tests of configuration S_V1_T41 and all tests of configuration XS_VG2_T72 were loaded with 0.8 mm/s and 0.5 mm/s, respectively. The reason for this variation was the relatively small displacement of these connections when reaching the peak load (3.1 mm in maximum).

5-2.1.2 Post-processing

The post-processing of the here considered tests, contains the following four steps:

(i) determining relevant connection properties as defined in ON EN 12512 (2005)
(ii) determining additional stiffness and ductility measures as proposed in Chapter 2
(iii) approximating the load-displacement curves (backbone curves for cyclic tests) by applying the displacement-based model proposed in Chapter 3
(iv) determining average, maximum and minimum load-displacement curves applicable as input for the analytical wall model

Since it is not in common use, this procedure is shown more in detail for one configuration. For the sake of shortness, further test documentation is only summarised and detailed results are shifted to ANNEX B. Finally it is important to mention that the documented properties and load-displacement diagrams (if not explicitly described in another way) are referred to one single connection (or fastener).

5-2.2 ANGLE BRACKETS

The present section comprises information about tests on shear and tension (uplift) loaded wall-to-foundation and wall-to-floor joints equipped with angle brackets; Figure 5.1 illustrates a sketch of the two applied test configurations.

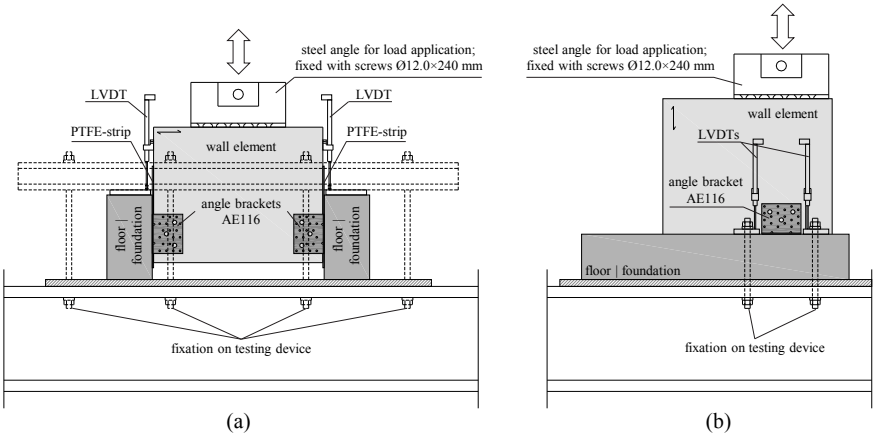

Figure 5.1: test configurations for angle bracket AE116 – (a) shear loaded angle brackets; (b) tension (uplift) loaded angle brackets

The investigated connection is an angle bracket, designated as AE116 and produced by Simpson Strong-Tie; compare Simpson Strong-Tie (2012) and ETA-06/00106 (2014). Depending on the configuration, solely CNA annular-ringed shank nails according to ETA-04/0013 (2015) or a combination of nails and FBN II 12/10 anchor bolts are used as fasteners. The pattern of the fasteners as depicted in Figure 5.2, relies on Simpson Strong-Tie (2012) and was kept constant for all tests.

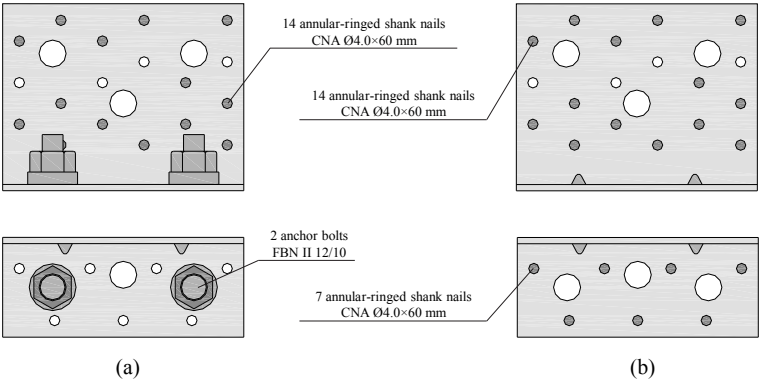

Figure 5.2: pattern of fasteners for angle bracket AE116 – (a) applied for wall-to-foundation joints; (b) applied for wall-to-floor joints

5-2.2.1 Shear loaded wall-to-foundation joint

For these tests, the angle brackets were used for joining a CLT wall element to two concrete blocks. Due to minimising the influence of friction, PTFE (Polytetrafluoroethylene) strips were located between the concrete and CLT elements. Some impressions of the test configuration are depicted in Figure 5.3.

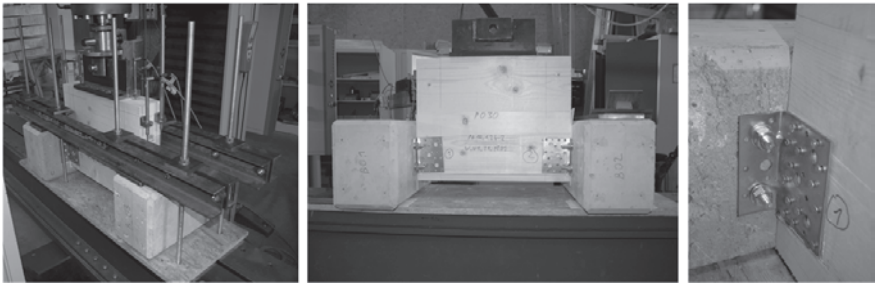

***Figure 5.3:** test configuration applied for shear loaded angle brackets in a wall-to-foundation joint (internal designation W_V1_T1)*

The gathered (mean) properties of the monotonic and cyclic tests are listed in Table 5.2; detailed single and some additional results are listed in ANNEX B. Here, the values according to ON EN 12512 (2005) are given in the first columns (indexed with 'EN'), whereas the alternative measures are listed behind. Regarding the determination of the parameter 'ductility' it is important to mention that the required ultimate point (F_u and v_u) is determined as either the point of failure or 20 % loss of resistance, whichever occurs first. The 30 mm limit, as scheduled in ON EN 12512 (2005), is generally neglected.

As visible, the cyclic tests show slightly lower properties for this configuration if compared to the monotonic one. Regarding the ductility, the alternative parameters classify this connection as 'moderate', whereas the corresponding property according to ON EN 12512 (2005), combined with the regulations given in Eurocode 8, lead to ductility class 'low' (DCL). The differences between the common and alternative stiffness properties are also clearly visible. In particular, compared to $K_{ser,EN}$ the parameter K_{SLS} gives approximately 38 % higher values and even the K_{ULS} parameters are 23 % higher in average.

***Table 5.2:** mean parameters of a shear loaded angle bracket in a wall-to-foundation joint*

notations	***n***	F_{max}	$K_{ser,EN}$	D_{EN}	**D-class**	K_{SLS}	K_{ULS}	v_{ip}	Φ_{ip}	**D-class**
units	[-]	[kN]	[kN/mm]	[-]	[-]	[kN/mm]	[kN/mm]	[mm]	[-]	[-]
monotonic	3	34.88	2.894	3.0	low	3.986	3.537	23.2	56%	moderate
cyclic	4	29.98	2.625	2.4	low	3.605	3.236	16.9	48%	moderate
comp.	-	-14.0%	-9.3%	-20.0%	-	-9.6%	-8.5%	-27.2%	-14.3%	-

Within the next step of post-processing, the load-displacement relationships are approximated by applying the analytical model proposed in Chapter 3. Both, original load-displacement curves of

monotonic experiments and the corresponding simulations are given in Figure 5.4. As can be seen, the approximated curves fit the original one with high accuracy.

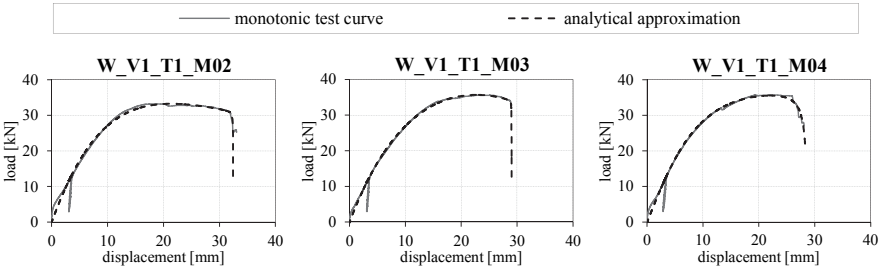

Figure 5.4: monotonic test curves of a shear loaded angle bracket in a wall-to-foundation joint

Figure 5.5 exhibits the positive part of the hysteresis gathered from cyclic tests as well as the corresponding approximations of the first, second and third envelope curves. For further discussions only the first envelope curves are of interest.

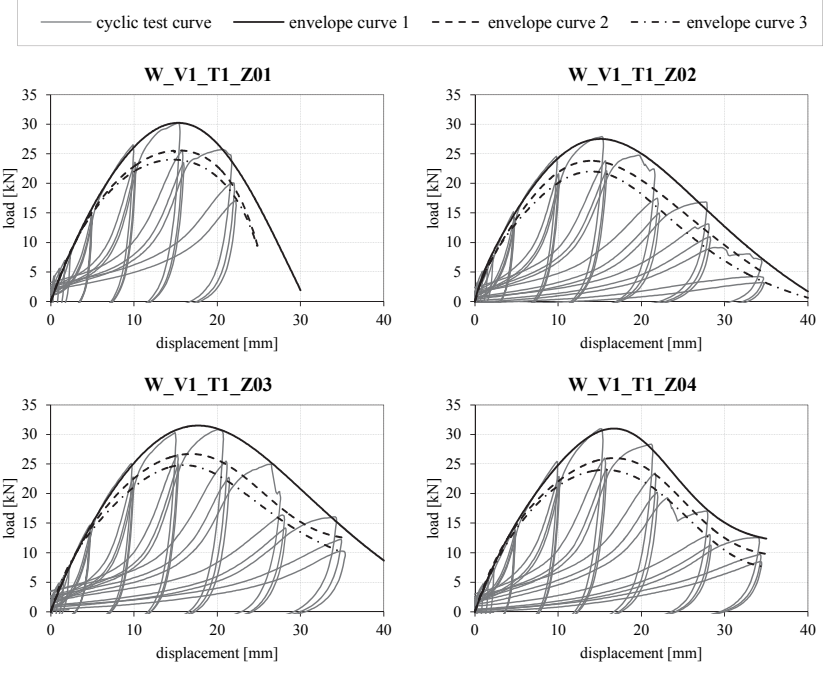

Figure 5.5: hysteresis of a shear loaded angle bracket in a wall-to-foundation joint

The parameters, being necessary for realising the simulations of monotonic and first cyclic envelope curves, are listed in Table 5.3; parameters for second and third envelope curves are given in ANNEX B.

Table 5.3: input parameters for simulating monotonic and cyclic test curves of a shear loaded angle bracket in a wall-to-foundation joint

notations	F_{max}	v_{max}	K_{ini}	F_A	v_B	K_B
units	[kN]	[mm]	[kN/mm]	[kN]	[mm]	[kN]
M02	33.25	21.40	4.30	28.00	32.40	-100.00
M03	35.70	22.70	4.14	28.90	29.00	-280.00
M04	35.55	22.00	3.90	29.70	27.80	-8.20
Z01	30.22	15.30	3.90	22.00	21.50	-1.90
Z02	27.50	15.10	6.00	20.50	22.80	-1.20
Z03	31.50	17.70	3.90	23.20	26.50	-1.20
Z04	31.00	16.70	4.00	22.00	23.00	-1.65

Now, the displacement-based and continuous quality of the applied approximation model enables to determine an 'average' load-displacement relationship. In particular, it is possible to calculate the corresponding load values for every single test at exact the same level of displacement. Plotting the average of these load values against the applied displacement input consequently yields to the wanted 'average' curve. Maximum and minimum load-displacement relationships can be determined in a similar way.

Demonstrating the explained procedure, the above listed parameters are used to determine the load values for ten exemplary displacement levels; compare Table 5.4. Figure 5.6 illustrates the resulting load-displacement points for every considered experiment, as well as the corresponding average, maximum and minimum curves. Obviously, monotonic and cyclic test data are mixed. This, because the wall model which is finally used, does not distinct between monotonic and cyclic loadings.

Table 5.4: corresponding as well as average, maximum and minimum loads for defined displacement points

v [mm]	$F_{M02}(v)$ [kN]	$F_{M03}(v)$ [kN]	$F_{M04}(v)$ [kN]	$F_{Z01}(v)$ [kN]	$F_{Z02}(v)$ [kN]	$F_{Z03}(v)$ [kN]	$F_{Z04}(v)$ [kN]	$F_{mean}(v)$ [kN]	$F_{max}(v)$ [kN]	$F_{min}(v)$ [kN]
0	0.0	0.0	0.0	0.0	0.0	0.0	0.0	0.0	0.0	0.0
3	11.4	10.9	11.3	10.3	10.6	9.8	10.0	10.6	11.4	9.8
6	19.8	19.1	20.4	18.4	17.5	17.4	17.3	18.6	20.4	17.3
9	25.6	25.3	26.8	24.5	22.9	23.5	23.2	24.5	26.8	22.9
12	29.4	29.7	30.9	28.6	26.3	28.0	27.7	28.7	30.9	26.3
15	31.7	32.8	33.4	30.2	27.5	30.7	30.5	31.0	33.4	27.5
18	32.9	34.7	34.8	29.1	26.6	31.5	30.7	31.5	34.8	26.6
21	33.2	35.6	35.5	25.1	24.0	30.4	27.9	30.3	35.6	24.0
24	33.1	35.6	35.3	18.7	20.5	28.0	23.1	27.8	35.6	18.7
28	32.3	34.5	26.4	7.7	15.3	23.3	17.2	22.4	34.5	7.7

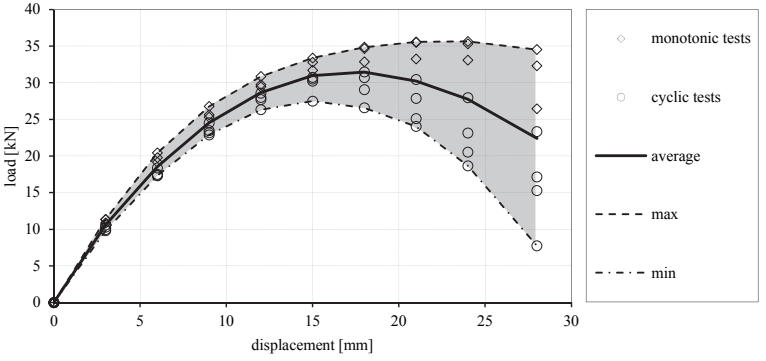

Figure 5.6: ***mean, maximum and minimum load-displacement relationships out of a set of approximated test curves***

Of course, ten reference points may be not enough for determining accurate mean curves. Hence, finally about 500 displacement points are used for these computations. This also simplifies the last step in post-processing, i.e., the fit of the (continuous) approximation model to the produced (piecewise linear) mean, maximum and minimum curvatures. The resulting model parameters for the presently discussed connection are listed in Table 5.5.

Table 5.5: ***input parameters for simulating average, maximum and minimum test curves of a shear loaded AE116 angle bracket in a wall-to-foundation joint***

	notations	F_{max}	v_{max}	K_{ini}	F_A	v_B	K_B	**valid range**
	units	[kN]	[mm]	[kN/mm]	[kN]	[mm]	[kN]	[mm]
W_V1_T1	**average curve**	31.50	17.80	4.30	24.30	25.60	-1.65	$0 \le v \le 35$ mm
	maximum curve	35.60	22.00	4.10	30.00	33.00	-3.00	$0 \le v \le 35$ mm
	minimum curve	27.60	15.50	3.70	20.80	22.20	-1.70	$0 \le v \le 28$ mm

Note: The valid range of the approximation curves indicates the region, wherein their use is reasonable, i.e., leads to positive load values and no singular points.

Figure 5.7 finally illustrates the original monotonic and the first envelope curves of cyclic tests, as well as the simulated mean, maximum and minimum curvatures.

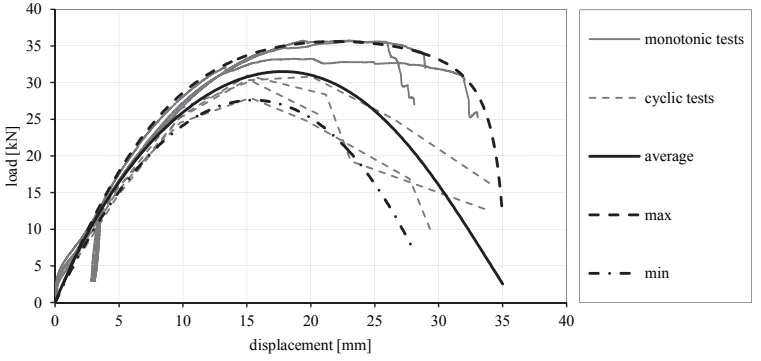

Figure 5.7: ***comparison of original test curves and average, maximum and minimum simulations for a shear loaded angle bracket in a wall-to-foundation joint***

5-2.2.2 Tension (uplift) loaded wall-to-foundation joint

Similar to the shear loaded wall-to-foundation joint, the angle brackets in these tests were fixed with 14 CNA nails on the wall element and two FBN II 12/10 bolts on the concrete foundation. For this and also for the other 'tension' configurations it is further important to mention that the cyclic loading protocol was slightly modified. In particular, for defining the negative (compression) cycles, not a defined percentage of the mean ultimate displacement, but the same percentage of the mean maximum load, gathered from the monotonic tests, was applied; the respective loading rate (here 2 mm/s) was kept constant anyway. The set-up for the monotonic and cyclic tests is depicted in Figure 5.8.

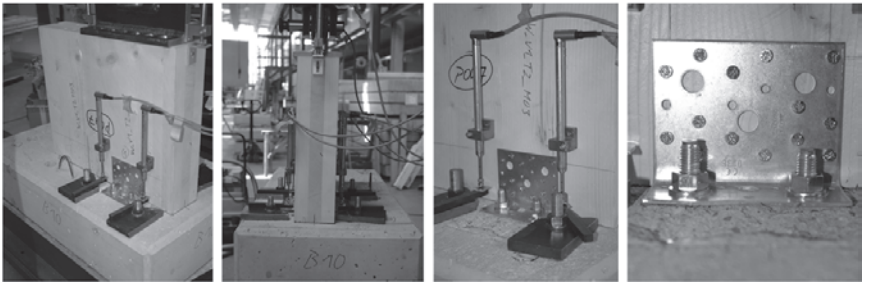

Figure 5.8: ***test configuration applied for tension (uplift) loaded angle brackets in a wall-to-foundation joint (internal designation W_V1_T2)***

As can be seen in Table 5.6, the monotonic and the cyclic tests exhibit a quite similar behaviour; solely K_{SLS} increases mentionable in cyclic tests. Moreover, this parameter exhibits much higher values compared to the commonly applied $K_{ser,EN}$ (factor 2.3 and 2.9 for monotonic and cyclic tests, respectively).

A further point attracting the attention, when using the common (EN) model as a reference, is the distinctively higher ductility in relation to the shear loaded configuration; the new proposal leads to only slightly higher values and an equal classification. Moreover, compared with the shear based properties, it can be noticed that the tension loaded angle brackets exhibit a comparable load-carrying capacity and even higher stiffness values.

Table 5.6: mean parameters of a tension (uplift) loaded angle bracket in a wall-to-foundation joint

notations	n	F_{max}	$K_{ser,EN}$	D_{EN}	**D-class**	K_{SLS}	K_{ULS}	v_{ip}	Φ_{ip}	**D-class**
units	[-]	[kN]	[kN/mm]	[-]	[-]	[kN/mm]	[kN/mm]	[mm]	[-]	[-]
monotonic	3	36.10	5.989	9.5	high	13.833	7.260	22.3	56%	moderate
cyclic	3	37.26	5.812	8.8	high	17.094	7.303	20.9	52%	moderate
comp.	-	3.2%	-3.0%	-7.4%	-	23.6%	0.6%	-6.4%	-7.1%	-

Table 5.7 finally contains the parameters being necessary for simulating the average, maximum and minimum curvatures illustrated in Figure 5.9.

Table 5.7: input parameters for simulating average, maximum and minimum test curves of a tension (uplift) loaded AE116 angle bracket in a wall-to-foundation joint

	notations	F_{max}	v_{max}	K_{ini}	F_A	v_B	K_B	**valid range**
	units	[kN]	[mm]	[kN/mm]	[kN]	[mm]	[kN]	[mm]
	average curve	36.30	20.80	18.40	27.80	27.90	-1.96	$0 \le v \le 35$ mm
W_V1_T2	**maximum curve**	40.10	24.70	20.00	31.60	32.00	-2.40	$0 \le v \le 35$ mm
	minimum curve	32.30	21.70	23.00	27.00	25.57	-9.80	$0 \le v \le 26$ mm

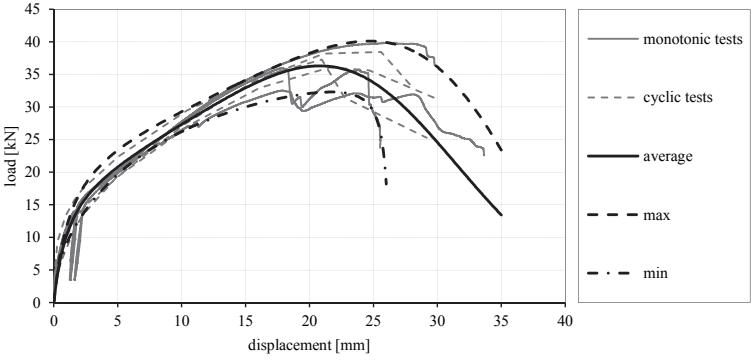

Figure 5.9: comparison of original test curves and average, maximum and minimum simulations for a tension (uplift) loaded angle bracket in a wall-to-foundation joint

5-2.2.3 Shear loaded wall-to-floor joint

To fix the shear loaded angle brackets on the wall element, again 14 CNA annular-ringed shank nails were used. However, differing from the wall-to-foundation tests, here the connection between the floor element and the steel bracket is realised by inserting 7 CNA nails; compare Figure 5.2. Some pictures of the set-up, which again includes PTFE strips between the wall and floor elements, are illustrated in Figure 5.10.

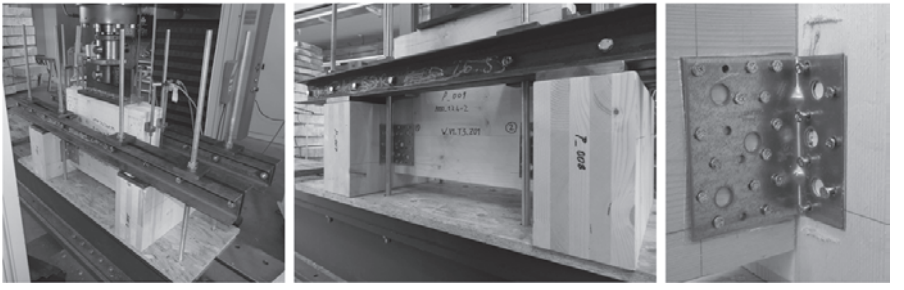

Figure 5.10: test configuration applied for shear loaded angle brackets in a wall-to-floor joint (internal designation W_V1_T3)

As documented in Table 5.8, these experiments show a distinctively lower load-carrying capacity compared to the wall-to-foundation tests (round 36 % less for monotonic and 27 % less for cyclic tests). Excepting the parameter K_{SLS}, which shows slightly higher results, the stiffness parameters also decrease for the current configuration (20 % in maximum). The biggest difference, however, occurs for the commonly determined ductility ratios, which nearly doubled. The corresponding alternative properties also show an increase, but not in that extent. Nevertheless, latter approach classifies the ductile capacity of the monotonic tests as high.

When comparing monotonic and cyclic tests, besides the decrease in ductility in case of cyclic loading, no mentionable differences appear. Finally, also here the clearly higher K_{SLS} parameters, in relation to the $K_{ser,EN}$ values, have to be noticed.

Table 5.8: mean parameters of a shear loaded angle bracket in a wall-to-floor joint

notations	***n***	F_{max}	$K_{ser,EN}$	D_{EN}	**D-class**	K_{SLS}	K_{ULS}	v_{ip}	Φ_{ip}	**D-class**
units	[-]	[kN]	[kN/mm]	[-]	[-]	[kN/mm]	[kN/mm]	[mm]	[-]	[-]
monotonic	4	22.34	2.344	5.6	moderate	4.091	2.987	29.5	62%	high
cyclic	6	21.94	2.572	4.3	moderate	3.874	3.050	19.2	51%	moderate
comp.	-	-1.8%	9.7%	-23.2%	-	-5.3%	2.1%	-34.9%	-17.7%	-

The input parameters for simulating the determined average, maximum and minimum curvatures are listed in Table 5.9; the corresponding graphs are visualised in Figure 5.11.

Table 5.9: input parameters for simulating average, maximum and minimum test curves of a shear loaded AE116 angle bracket in a wall-to-floor joint

	notations	F_{max}	v_{max}	K_{ini}	F_A	v_B	K_B	valid range
	units	[kN]	[mm]	[kN/mm]	[kN]	[mm]	[kN]	[mm]
W_V1_T3	average curve	21.90	20.30	4.90	17.40	28.70	-0.98	$0 \le v \le 40$ mm
	maximum curve	23.70	20.70	16.40	19.90	35.40	-0.57	$0 \le v \le 45$ mm
	minimum curve	20.70	20.30	4.20	16.30	25.80	-1.85	$0 \le v \le 30$ mm

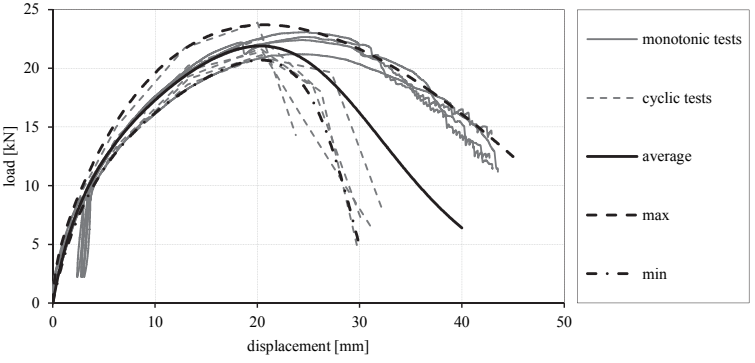

Figure 5.11: comparison of original test curves and average, maximum and minimum simulations for a shear loaded angle bracket in a wall-to-floor joint

5-2.2.4 Tension (uplift) loaded wall-to-floor joint

The last considered configuration with angle brackets represents a tension loaded wall-to-floor joint. Figure 5.12 illustrates the test set-up of these experiments, where the same number and position of nails as for the corresponding shear tests was used.

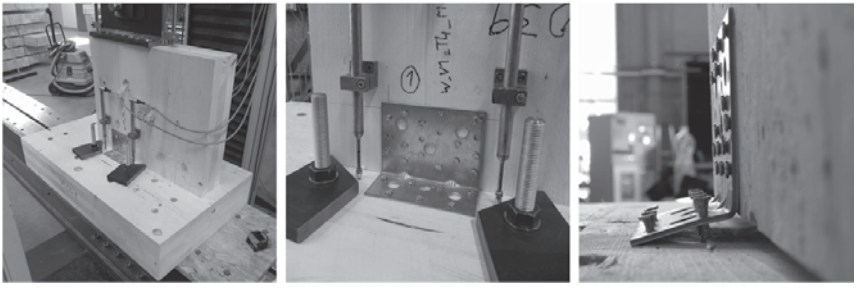

Figure 5.12: test configuration applied for tension loaded angle brackets in a wall-to-floor joint (internal designation W_V1_T4)

As documented in Table 5.10, in case of cyclic loading, here the load-carrying capacity, the stiffness and ductility properties decrease. Moreover, relying on the relatively small deformations before reaching the peak load, the stiffness ratios K_{SLS} and $K_{ser,EN}$ again show distinct differences.

Table 5.10: mean parameters of a tension loaded angle bracket in a wall-to-floor joint

notations	n	F_{max}	$K_{ser,EN}$	D_{EN}	D-class	K_{SLS}	K_{ULS}	v_{ip}	Φ_{ip}	D-class
units	[-]	[kN]	[kN/mm]	[-]	[-]	[kN/mm]	[kN/mm]	[mm]	[-]	[-]
monotonic	4	12.83	13.161	30.8	high	35.358	20.551	14.2	79%	high
cyclic	8	11.63	9.769	16.7	high	16.897	11.378	10.9	73%	high
comp.	-	-9.4%	-25.8%	-45.8%	-	-52.2%	-44.6%	-23.2%	-7.6%	-

Concerning the ductility it can be stated that the parameters according to both the ON EN 12512 (2005) and the alternative ductility measures lead to the classification 'high', but the difference between monotonic and cyclic results, provided by the common model, suggests a distinct deviation in the respective load-displacement relationships. However, as visible in Figure 5.13, where the original and simulated test curves are illustrated, this actually is not the case (required curve parameters are listed in Table 5.11). The alternative ductility values lead to more stable results and additionally indicate the reduced displacement capacity in relation to the wall-to-foundation joints; compare parameter v_{ip}.

Table 5.11: input parameters for simulating average, maximum and minimum test curves of a tension loaded AE116 angle bracket in a wall-to-floor joint

	notations	F_{max}	v_{max}	K_{ini}	F_A	v_B	K_B	valid range
	units	[kN]	[mm]	[kN/mm]	[kN]	[mm]	[kN]	[mm]
W_V1_T4	**average curve**	12.00	5.00	20.00	11.10	12.70	-0.46	$0 \le v \le 20$ mm
	maximum curve	13.86	4.48	36.60	11.97	16.37	-0.09	$0 \le v \le 18$ mm
	minimum curve	10.80	4.53	9.00	9.92	10.48	-0.62	$0 \le v \le 18$ mm

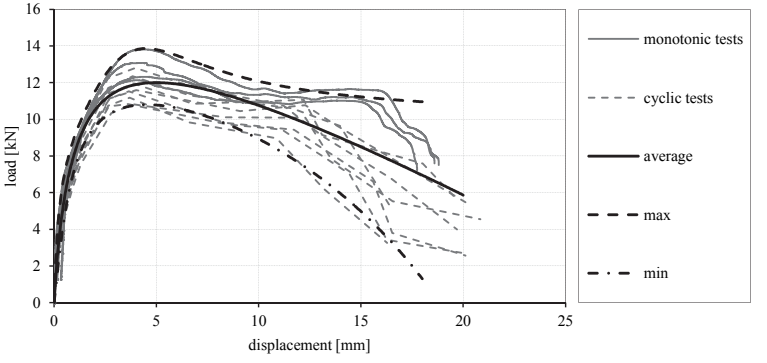

Figure 5.13: comparison of original test curves and average, maximum and minimum simulations for a tension loaded angle bracket in a wall-to-floor joint

A further comparison of this configuration to the one representing a wall-to-foundation joint shows the much lower load-carrying capacity, i.e., a reduction to approximately one-third occurs. Nevertheless, since all tests fail due to nail withdrawal in the floor section, the uplift capacity may be increased with replacing these nails by screws. Regarding the stiffness parameters it can be stated that, apart from the

parameter K_{SLS} determined from the cyclic tests, all stiffness parameters distinctively increase if compared to the results on a rigid foundation.

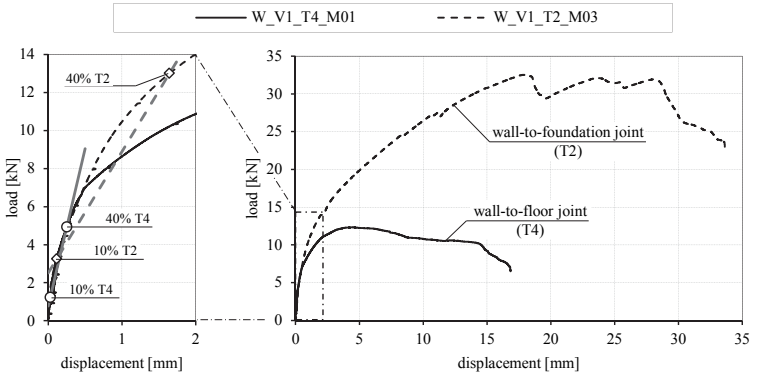

Figure 5.14: comparison between the 'elastic branch' of a tension loaded angle bracket located on either a concrete foundation or a CLT floor

This circumstance mainly bases on the lower peak load, leading to reference points (i.e. 10 % and 40 % of F_{max} for $K_{ser,EN}$) located closer to the origin. Figure 5.14 illustrates this by facing the original load-displacement relationships of two representative experiments; one for a wall-to-floor joint and another for a wall-to-foundation joint. As visible, the actual initial behaviour of both configurations is quite similar and only the already mentioned reference points vary. Hence, fastening the metal connector with screws to the floor element, which forces the nails in the wall segment to be decisive, might probably also fit the stiffness parameters to the one gathered from the wall-to-foundation joints.

5-2.3 HOLD-DOWNS

For investigating the load-bearing behaviour of hold-downs, a product designated as HTT22 and produced by Simpson Strong-Tie was chosen; compare Simpson Strong-Tie (2012) and ETA-07/0285 (2015). Although this connector possesses a specific amount of lateral load-carrying capacity and stiffness, according to the producers' specification, this type of connection is solely considerable for bearing tension loads. Hence, it was decided to perform only tension tests for wall-to-foundation and wall-to-floor joints. A sketch of the applied test configuration is illustrated in Figure 5.15 (a).

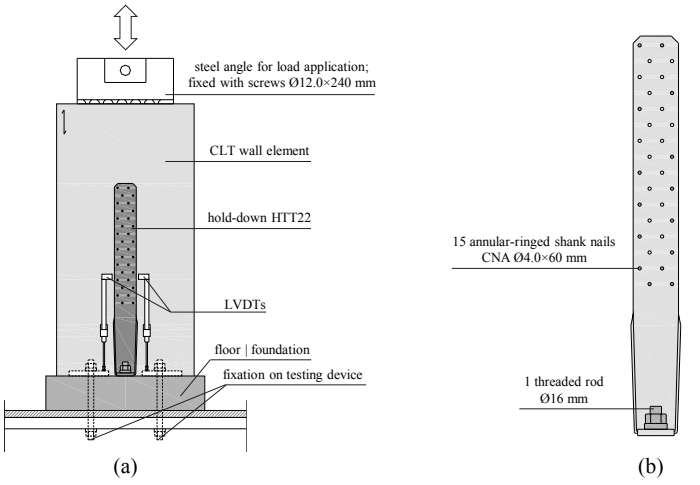

Figure 5.15: hold-down HTT22 – (a) test configuration; (b) type and pattern of fasteners

For all considered tests, 15 CNA annular-ringed shank nails were used for fastening the metal connector to the CLT wall element. The connection to the steel foundation or the CLT floor element was realised by a threaded rod with a diameter of 16 mm. Equal to the tests performed on angle brackets, the pattern of the applied fasteners, as illustrated in Figure 5.15 (b), was kept constant for all experiments.

5-2.3.1 Tension loaded wall-to-foundation joint

As already mentioned, when performing tension loaded wall-to-foundation tests with hold-downs, the originally planned configuration (with a concrete foundation) leads to some issues. In particular, the used anchor bolt fails in withdrawal before any mentionable failure of the nails occur. Since not the connection to the concrete, but rather to the timber, was of primary interest, an alternative substructure made of steel was constructed. As a consequence, the compression part in the loading protocol was totally rejected, means that the cycles start and end at a displacement level of 0 mm. The finally applied test set-up is illustrated in Figure 5.16.

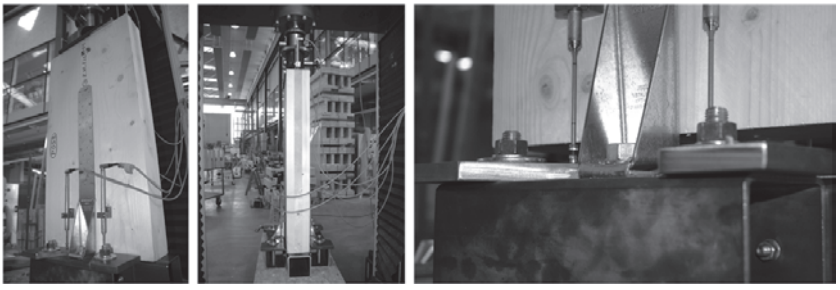

Figure 5.16: test configuration applied for tension loaded hold-downs in a wall-to-foundation joint (internal designation Z_V2_T21)

Table 5.12 lists the experimentally gathered parameters for the investigated hold-down connection. As visible, no distinct difference for monotonic and cyclic tests appears. Nevertheless, the ductility and stiffness parameters, corresponding to the common and alternative post-processing models, again differ distinctively from each other.

Table 5.12: mean parameters of a tension loaded HTT22 hold-down in a wall-to-foundation joint

notations	n	F_{max}	$K_{ser,EN}$	D_{EN}	**D-class**	K_{SLS}	K_{ULS}	v_{ip}	Φ_{ip}	**D-class**
units	[-]	[kN]	[kN/mm]	[-]	[-]	[kN/mm]	[kN/mm]	[mm]	[-]	[-]
monotonic	1	48.82	8.061	7.4	high	15.315	10.326	20.4	57%	moderate
cyclic	3	51.13	7.698	6.5	high	16.000	9.571	19.8	56%	moderate
comp.	-	4.7%	-4.5%	-12.2%	-	4.5%	-7.3%	-2.9%	-1.8%	-

Comparing the hold-down properties with the results gathered from wall-to-foundation joints equipped with angle brackets, as expected, an increase in load-carrying capacity and stiffness, as well as a slightly decrease in ductility, can be noticed. However, the absolute differences are quite small and not further mentionable.

For implementing hold-downs' behaviour to the analytical wall model, the parameters listed in Table 5.13 can be used. The simulations resulting from these input values and the original test curves are illustrated in Figure 5.17.

Table 5.13: input parameters for simulating average, maximum and minimum test curves of a tension loaded HTT22 hold-down in a wall-to-foundation joint

	notations	F_{max}	v_{max}	K_{ini}	F_A	v_B	K_B	**valid range**
	units	[kN]	[mm]	[kN/mm]	[kN]	[mm]	[kN]	[mm]
Z_V2_T21	**average curve**	49.80	18.30	36.70	40.10	27.00	-2.30	$0 \le v \le 35$ mm
	maximum curve	53.60	20.20	23.00	42.20	27.90	-2.50	$0 \le v \le 35$ mm
	minimum curve	47.70	17.50	36.50	38.60	25.90	-2.40	$0 \le v \le 33$ mm

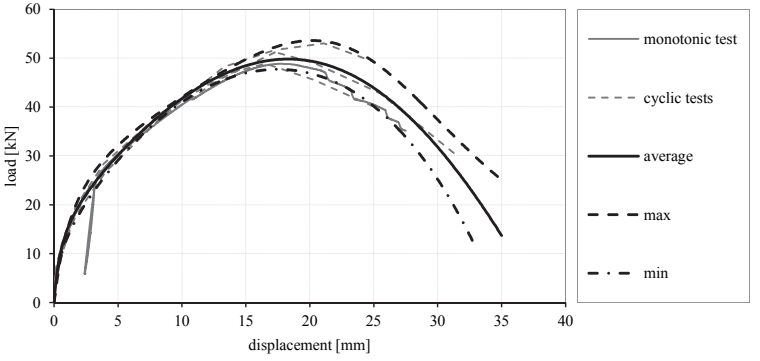

Figure 5.17: comparison of original test curves and average, maximum and minimum simulations for a tension loaded hold-down in a wall-to-foundation joint

5-2.3.2 Tension loaded wall-to-floor joint

Differing to the latter described configuration, the present one uses a CLT floor element instead of the steel foundation. For anchoring the still necessary threaded rod, a rigid counter-plate was used; compare set-up illustrations in Figure 5.18 and ANNEX B.

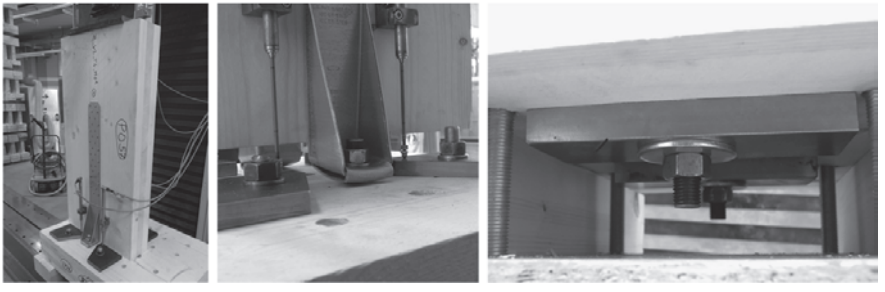

Figure 5.18: test configuration applied for tension loaded hold-downs in a wall-to-floor joint (internal designation Z_V2_T4)

As documented in Table 5.14, the monotonic and cyclic experiments on wall-to-floor joints led to quite similar results. Furthermore, when comparing these results with the one gathered from the wall-to-foundation tests, no significant differences occur as well. Nevertheless, the absence of a distinct linear elastic branch again provokes clearly higher stiffness parameters when considering the alternative post-processing models.

Table 5.14: mean parameters of a tension loaded HTT22 hold-down in a wall-to-floor joint

notations	n	F_{max}	$K_{ser,EN}$	D_{EN}	D-class	K_{SLS}	K_{ULS}	v_{ip}	Φ_{ip}	D-class
units	[-]	[kN]	[kN/mm]	[-]	[-]	[kN/mm]	[kN/mm]	[mm]	[-]	[-]
monotonic	2	51.53	7.183	8.9	high	15.743	9.292	27.9	60%	high
cyclic	4	52.34	6.948	6.5	high	20.298	8.938	21.9	55%	moderate
comp.	-	1.6%	-3.3%	-27.0%	-	28.9%	-3.8%	-21.5%	-8.3%	-

The input parameters for simulating the behaviour of this connection are listed in Table 5.15, the corresponding load-displacement curves are given in Figure 5.19.

Table 5.15: input parameters for simulating average, maximum and minimum test curves of a tension loaded HTT22 hold-down in a wall-to-floor joint

	notations	F_{max}	v_{max}	K_{ini}	F_A	v_B	K_B	valid range
	units	[kN]	[mm]	[kN/mm]	[kN]	[mm]	[kN]	[mm]
Z_V2_T4	average curve	51.80	21.50	33.00	40.70	31.10	-2.02	$0 \le v \le 45$ mm
	maximum curve	56.10	21.40	31.00	43.00	32.80	-1.38	$0 \le v \le 45$ mm
	minimum curve	48.40	21.20	22.00	38.00	29.60	-2.24	$0 \le v \le 40$ mm

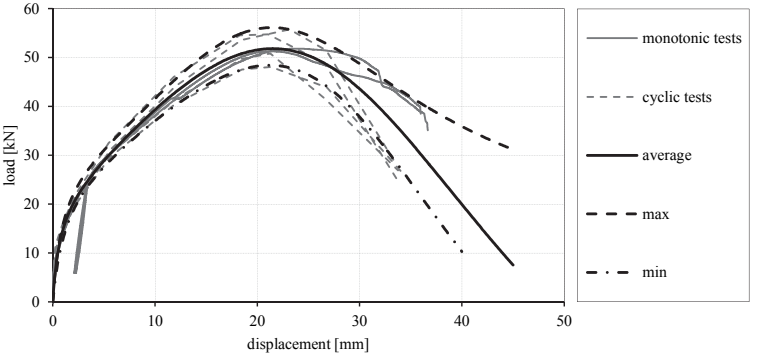

Figure 5.19: comparison of original test curves and average, maximum and minimum simulations for a tension loaded hold-down in a wall-to-floor joint

5-2.4 SCREWS

For joining CLT floor elements to the walls beneath (wall-to-floor joints), or wall elements to each other (wall-to-wall joints), usually fully or partially threaded self-tapping timber screws are used. Even though this type of fastener is optimised to bear axial loads, especially in CLT structures, shear loads have to be carried in some cases as well. Within the following sections two joint types are considered: (i) a tension and shear loaded wall-to-floor joint and (ii) a shear loaded wall-to-wall joint. Moreover, for the latter one, which represents a vertical joint between adjacent wall panels, two different screw configurations (parallel and inclined) are investigated. The test configurations used for examining the

wall-to-floor joint are shown in Figure 5.20, whereas Figure 5.21 illustrates the wall-to-wall configurations. Finally it has to be mentioned that here solely fully threaded screws are considered.

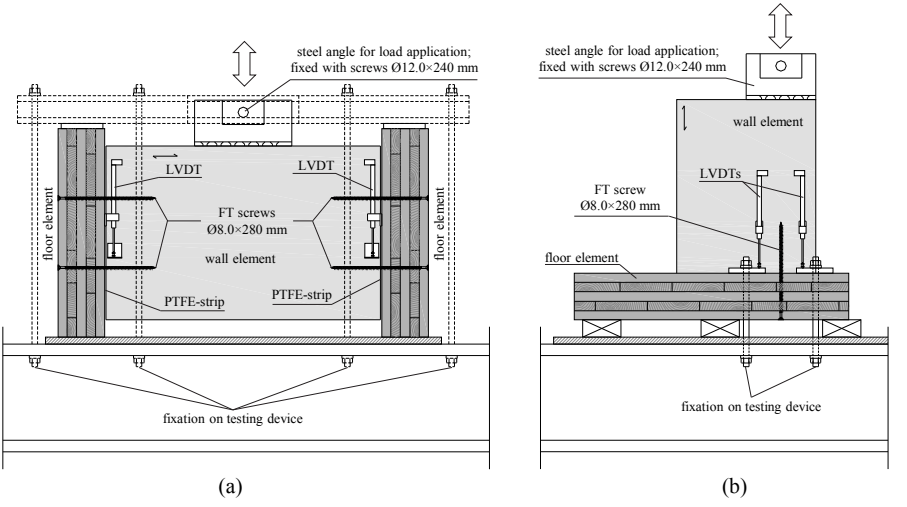

Figure 5.20: screws applied in a wall-to-floor joint – (a) test configuration for shear loads; (b) test configuration for tension loads

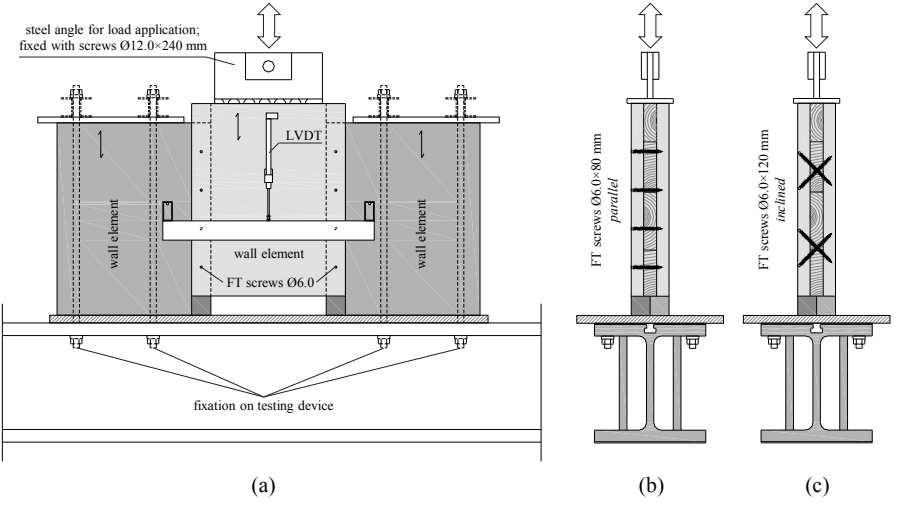

Figure 5.21: screwed joints connecting adjacent wall panels (vertical joint) – (a) general test set-up; (b) configuration with parallel screws; (c) configuration with inclined screws

5-2.4.1 Shear loaded wall-to-floor joint

For these tests, fully threaded screws from the company Schmid Schrauben Hainfeld GmbH (product class 'Stardrive') with a diameter of 8 mm, a total length of 280 mm and a countersunk-head were used to join the CLT elements; compare ETA-12/0373 (2012). In particular, as illustrated in Figure 5.20 (a), two screws per side were applied parallel to each other, whereat the angle between the grain direction of the wall elements' middle layer and the screw axis was equal to 90°. Moreover, as can be seen in Figure 5.22, again PTFE-strips were located in the joint for reducing the influence of friction.

Figure 5.22: test configuration applied for shear loaded fully threaded screws in a wall-to-floor joint (internal designation S_V1_T61)

The mean test results gathered from this configuration are documented in Table 5.16. Here it can be seen that load-carrying and stiffness parameters for cyclic tests exhibit higher values compared to the monotonic one. The ductility, however, decreases at the same time. Furthermore, this type of connection is able to reach high levels of displacement, i.e., the peak load is reached at approximately 28 mm and the ultimate load at round 40 mm. Nevertheless, due to also high values of yield displacement (circa 19 mm in average), the ductility parameters according to ON EN 12512 (2005) are quite low. Differing from that, the alternative model designates a 'moderate' ductility for this type of connection.

Table 5.16: mean parameters of a shear loaded screw (Ø 8.0×280 mm) in a wall-to-floor joint

notations	n	F_{max}	$K_{ser,EN}$	D_{EN}	**D-class**	K_{SLS}	K_{ULS}	v_{ip}	Φ_{ip}	**D-class**
units	[-]	[kN]	[kN/mm]	[-]	[-]	[kN/mm]	[kN/mm]	[mm]	[-]	[-]
monotonic	3	10.64	0.462	2.2	low	0.969	0.593	34.3	54%	moderate
cyclic	6	12.40	0.584	2.0	low	1.168	0.740	25.6	41%	moderate
comp.	-	16.5%	26.3%	-9.1%	-	20.5%	24.7%	-25.4%	-24.1%	

For this type of connection, maximum, minimum and average load-displacement curves can be simulated with the parameters given in Table 5.17; a comparison with the corresponding original test curves is illustrated in Figure 5.23.

Table 5.17: input parameters for simulating average, maximum and minimum test curves of a shear loaded screw (Ø 8.0×280 mm) in a wall-to-floor joint

	notations	F_{max}	v_{max}	K_{ini}	F_A	v_B	K_B	valid range
	units	[kN]	[mm]	[kN/mm]	[kN]	[mm]	[kN]	[mm]
S_V1_T61	average curve	11.60	28.55	7.60	8.45	40.60	-0.36	$0 \le v \le 45$ mm
	maximum curve	13.70	25.00	26.70	10.60	42.40	-0.23	$0 \le v \le 45$ mm
	minimum curve	10.10	28.20	12.00	7.30	37.20	-0.52	$0 \le v \le 42$ mm

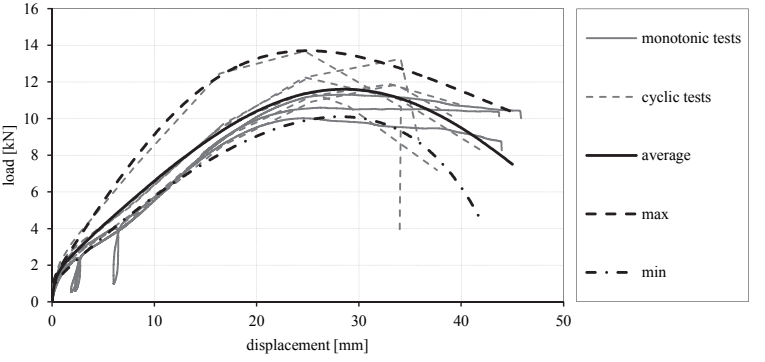

Figure 5.23: comparison of original test curves and average, maximum and minimum simulations for a shear loaded screw in a wall-to-floor joint

5-2.4.2 Tension loaded wall-to-floor joint

As illustrated in Figure 5.20 (b), the layup of the test configuration is more or less similar to the one used for tension tests on angle brackets and hold-downs. In this case, only one single screw is used to connect the two CLT elements. The applied screw, and the angle between its axis and the grain direction of the wall elements' middle layer, was equal to the shear tests described afore (screw axis-to-grain angle equal to 90°). Some impressions of the test set-up are illustrated in Figure 5.24.

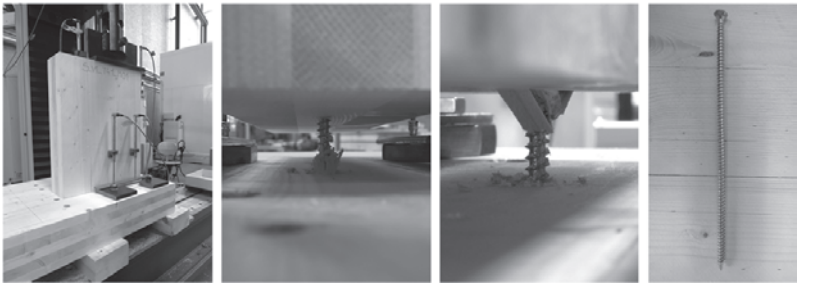

Figure 5.24: test configuration applied for a tension loaded fully threaded screw in a wall-to-floor joint (internal designation S_V1_T41)

The results listed in Table 5.18 show the expected high load-carrying capacity and stiffness, and the low ductility. Moreover, even if the gathered parameters mostly exhibit higher values for the cyclic tests, the differences between the two loading procedures are quite small. However, the parameters $K_{ser,EN}$ and K_{SLS} again show a distinct deviation.

Table 5.18: mean parameters of an axially (tension) loaded screw (Ø 8.0×280 mm) in a wall-to-floor joint

notations	***n***	F_{max}	$K_{ser,EN}$	D_{EN}	**D-class**	K_{SLS}	K_{ULS}	v_{ip}	Φ_{ip}	**D-class**
units	[-]	[kN]	[kN/mm]	[-]	[-]	[kN/mm]	[kN/mm]	[mm]	[-]	[-]
monotonic	3	20.84	17.603	3.5	low	27.409	20.408	2.6	55%	low
cyclic	6	23.09	18.338	3.7	low	25.491	20.971	2.9	57%	low
comp.	-	10.8%	4.2%	5.7%	-	-7.0%	2.8%	11.5%	3.6%	-

For simulating the behaviour of the applied screw, the parameters given in Table 5.19 can be used; the resulting load-displacement relationships and the corresponding original test curves are compared in Figure 5.25.

Table 5.19: input parameters for simulating average, maximum and minimum test curves of an axially (tension) loaded screw (Ø 8.0×280 mm) in a wall-to-floor joint

	notations	F_{max}	v_{max}	K_{ini}	F_A	v_B	K_B	**valid range**
	units	[kN]	[mm]	[kN/mm]	[kN]	[mm]	[kN]	[mm]
S_V1_T41	**average curve**	21.95	2.28	25.00	17.86	3.86	-4.76	$0 \le v \le 5$ mm
	maximum curve	27.00	2.81	58.00	21.76	4.30	-7.32	$0 \le v \le 5$ mm
	minimum curve	18.28	2.05	23.70	14.83	3.41	-4.52	$0 \le v \le 4.5$ mm

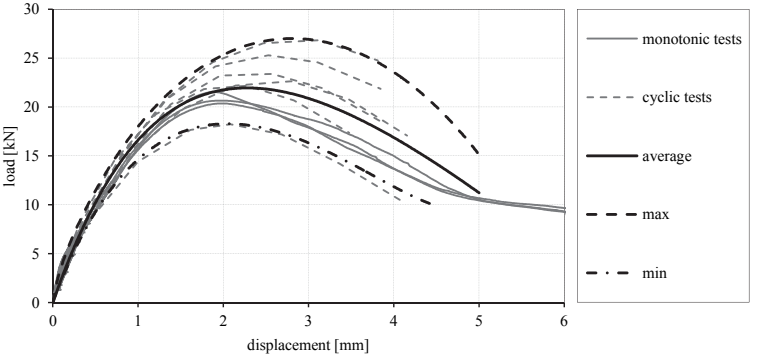

Figure 5.25: comparison of original test curves and average, maximum and minimum simulations for a tension loaded screw in a wall-to-floor joint

5-2.4.3 Shear loaded wall-to-wall joint with parallel screws

For connecting adjacent CLT panels, butt joints, half-lap joints and spline joints (see Figure 5.26) are frequently used in practical design. The experimental investigations conducted at TU Graz solely consider half-lap joints (also known as step joints).

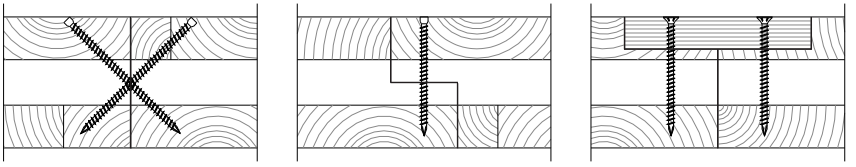

Figure 5.26: variants of vertical joints – (a) butt joint; (b) half-lap joint; (c) spline joint (one-sided)

Here, fully threaded self-tapping screws from the company Würth Handelsges. m.b.H. (i.e., 'ASSY PLUS VG' screws) with a diameter of 6 mm and a cylinder head were used as fasteners; compare ETA-11/0190 (2013). The length of the screws for the parallel screw pattern was equal to 80 mm; some impressions of this test set-up are given in Figure 5.27.

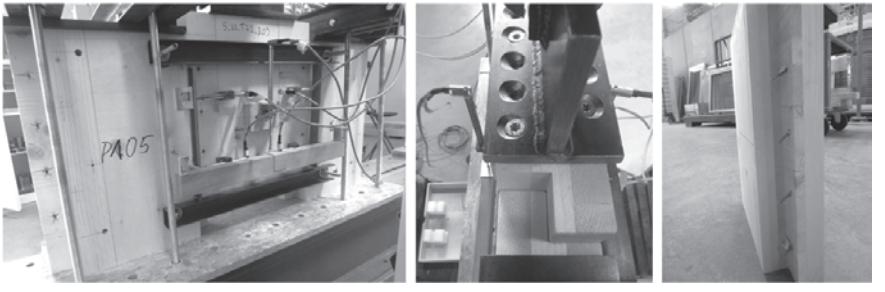

Figure 5.27: test configuration applied for a shear loaded wall-to-wall joint equipped with parallel screws (internal designation S_V2_T72)

The properties gathered from these tests are documented in Table 5.20. Here it can be seen that cyclic tests lead to higher stiffness parameters and (considering the common model) a higher ductility. Moreover, since laterally loaded, the screwed connection exhibits pronounced displacement capacities; compare parameter v_{ip}.

Table 5.20: mean parameters of a shear loaded wall-to-wall joint equipped with one screw

notations	***n***	F_{max}	$K_{ser,EN}$	D_{EN}	**D-class**	K_{SLS}	K_{ULS}	v_{ip}	Φ_{ip}	**D-class**
units	[-]	[kN]	[kN/mm]	[-]	[-]	[kN/mm]	[kN/mm]	[mm]	[-]	[-]
monotonic	2	3.02	0.463	5.5	moderate	0.985	0.567	15.8	41%	moderate
cyclic	3	2.89	0.706	8.8	high	1.229	0.837	13.8	51%	moderate
comp.	-	-4.2%	52.4%	60.0%	-	24.8%	47.5%	-12.7%	24.4%	-

The input parameters for simulating the behaviour of this connection are given in Table 5.21 and the actual shapes of the approximated and original test curves are illustrated in Figure 5.28.

Table 5.21: input parameters for simulating average, maximum and minimum test curves of a shear loaded wall-to-wall joint equipped with one Ø 6.0×80 mm screw

	notations	F_{max}	v_{max}	K_{ini}	F_A	v_B	K_B	valid range
	units	[kN]	[mm]	[kN/mm]	[kN]	[mm]	[kN]	[mm]
S_V2_T72	average curve	2.86	15.35	2.05	2.12	20.27	-0.22	$0 \le v \le 25$ mm
	maximum curve	3.12	16.79	2.19	2.45	22.23	-0.25	$0 \le v \le 25$ mm
	minimum curve	2.62	13.69	1.71	1.81	18.24	-0.18	$0 \le v \le 23$ mm

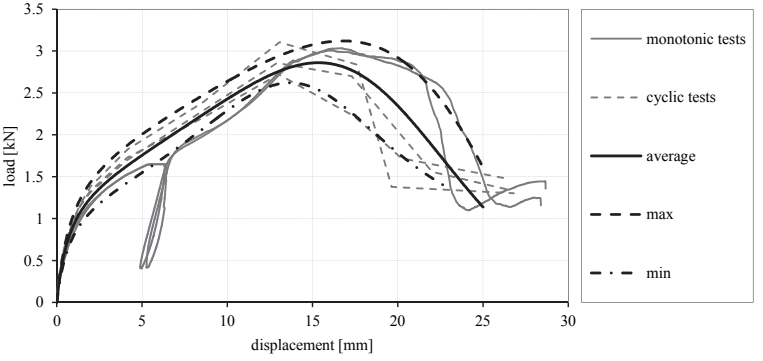

Figure 5.28: comparison of original test curves and average, maximum and minimum simulations for a shear loaded wall-to-wall joint equipped with one screw

5-2.4.4 Shear loaded wall-to-wall joint with inclined screws

The last experimental single joint test examined herein in detail, is a variation of the latter one. As an alternative to the parallel application, the screws were inserted crosswise with an inclination of 45°. Moreover, the length of the screws was increased to 120 mm; all other specifications were kept constant; compare Figure 5.29.

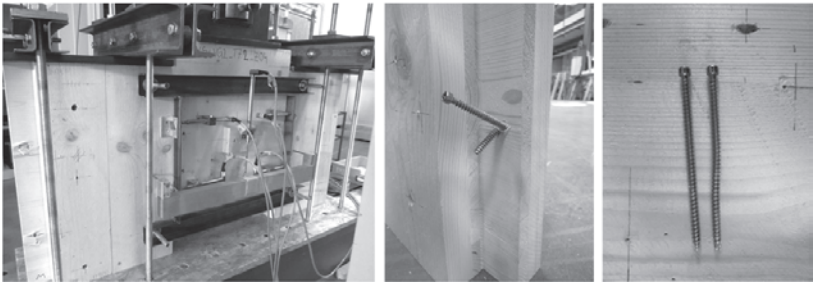

Figure 5.29: test configuration applied for a shear loaded wall-to-wall joint equipped with inclined (45°) screws (internal designation XS_VG2_T72)

As documented in Table 5.22, inclining the screws leads to clearly higher load-carrying and stiffness properties. However, the displacement capacity and the ductility distinctively decrease if compared to the parallel insertion of the screws.

Table 5.22: mean parameters of a shear loaded wall-to-wall joint equipped with a pair of inclined screws

notations	n	F_{max}	$K_{ser,EN}$	D_{EN}	**D-class**	K_{SLS}	K_{ULS}	v_{ip}	Φ_{ip}	**D-class**
units	[-]	[kN]	[kN/mm]	[-]	[-]	[kN/mm]	[kN/mm]	[mm]	[-]	[-]
monotonic	2	8.79	7.224	3.2	low	10.505	7.632	2.9	58%	low
cyclic	4	8.32	8.405	4.0	low	10.882	9.386	2.6	57%	low
comp.	-	-5.3%	16.4%	25.0%	-	3.6%	23.0%	-10.3%	-1.7%	-

Note: Due to the crosswise application of the fasteners, the parameters offered in Table 5.22 and Table 5.23 relate to a pair of screws instead of a single screw.

If comparing the shapes of the test curves, the difference in behaviour can be seen as well. In particular, the wall-to-wall joint with inclined screws shows rather the load-displacement behaviour of an axially loaded screw than of a laterally loaded one; compare Figure 5.30 and Figure 5.25. The model parameters, needed to simulate the load-displacement relationship of the here described type of connection, are listed in Table 5.23.

Table 5.23: input parameters for simulating average, maximum and minimum test curves of a shear loaded wall-to-wall joint equipped with a pair of inclined Ø 6.0×120 mm screws

	notations	F_{max}	v_{max}	K_{ini}	F_A	v_B	K_B	**valid range**
	units	[kN]	[mm]	[kN/mm]	[kN]	[mm]	[kN]	[mm]
XS_VG2_T72	**average curve**	8.43	1.83	10.84	6.55	3.34	-1.35	$0 \le v \le 6$ mm
	maximum curve	10.31	2.00	13.86	8.00	3.41	-1.82	$0 \le v \le 6$ mm
	minimum curve	7.55	1.67	9.34	5.50	2.83	-1.59	$0 \le v \le 6$ mm

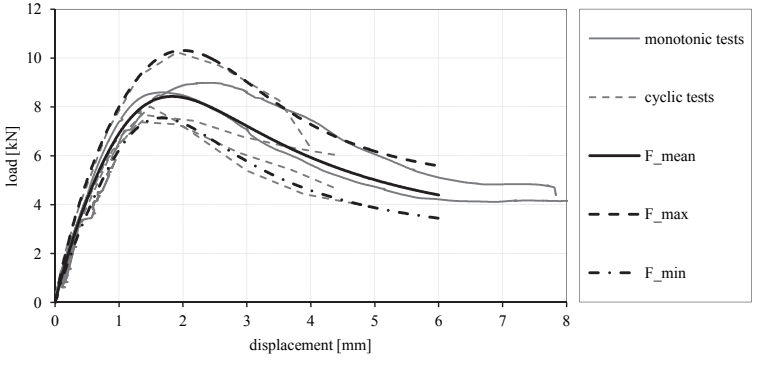

Figure 5.30: comparison of original test curves and average, maximum and minimum simulations for a shear loaded wall-to-wall joint equipped with inclined screws

5-3 WALL SYSTEMS

For investigating the influence of different connections, vertical joints, wall openings and vertical loads, a series of 17 experimental tests on CLT wall systems was prepared. Due to missing testing devices at TU Graz, these experiments were realised at the University of Kassel (Germany). The main experiences, gathered out of this campaign, are already discussed in several publications; compare Flatscher (2012), Flatscher et al. (2013), Hummel et al. (2013), Flatscher et al. (2014), Flatscher et al. (2015). Hence, the following sections solely include a rough description of the test set-up, the configurations and gathered main results.

5-3.1 CONFIGURATIONS AND TEST SET-UP

Five different configurations were used to investigate the influence of the above mentioned parameters. An overview, including the most important dimensions as well as some information about the applied connections, is illustrated in Figure 5.31. For each configuration monotonic and cyclic tests were conducted. Moreover, two monotonic tests were realised with different loading rates. For the sake of completeness and an easier comparison in further sections, Table 5.24 summarises the relevant conditions for every tested specimen and further includes the corresponding internal designations.

Table 5.24: listing of performed CLT wall tests including fundamental boundary conditions (M = monotonic | Z = cyclic)

ID	vertical load [kN/m]	loading rate [mm/s]	applied connections (bottom joint)	notes
WA_A_M01	20.8	0.5 | 1.0	4 AB	-
WA_A_M02	20.8	0.033 | 0.067	4 AB	-
WA_A_Z01	20.8	2.0	4 AB	test interrupted by testing machine
WA_A_Z02	0	2.0	4 AB	-
WA_A_Z03	20.8	2.0	4 AB	-
WA_B_M01	20.8	0.033 | 0.067	2 AB | 2 HD	-
WA_B_Z01	20.8	2.0	2 AB | 2 HD	-
WA_B_Z02	5.0	2.0	2 AB | 2 HD	-
WA_C_M01	20.8	0.5 | 1.0	4 AB	vert. joint with 24 screws
WA_C_M02	20.8	0.033 | 0.067	4 AB	vert. joint with 24 screws
WA_C_Z01	20.8	2.0	4 AB	vert. joint with 24 screws
WA_D_M01	20.8	0.033 | 0.067	12 screws	-
WA_D_Z01	20.8	2.0	12 screws	-
WA_D_Z02	5.0	2.0	12 screws	-
WA_E_M01	20.8	0.033 | 0.067	2 AB | 2 HD	opening 0.9/2.1 m
WA_E_Z01	20.8	2.0	2 AB | 2 HD	opening 0.9/2.1 m
WA_E_Z02	5.0	2.0	2 AB | 2 HD	opening 0.9/2.1 m

Note: AB = angle bracket AE116 | HD = hold down HTT22 | screws in vertical joint: fully threaded Ø 6.0×100 mm (inserted parallel) | screws in bottom joint: fully threaded Ø 8.0×280 mm (inserted parallel)

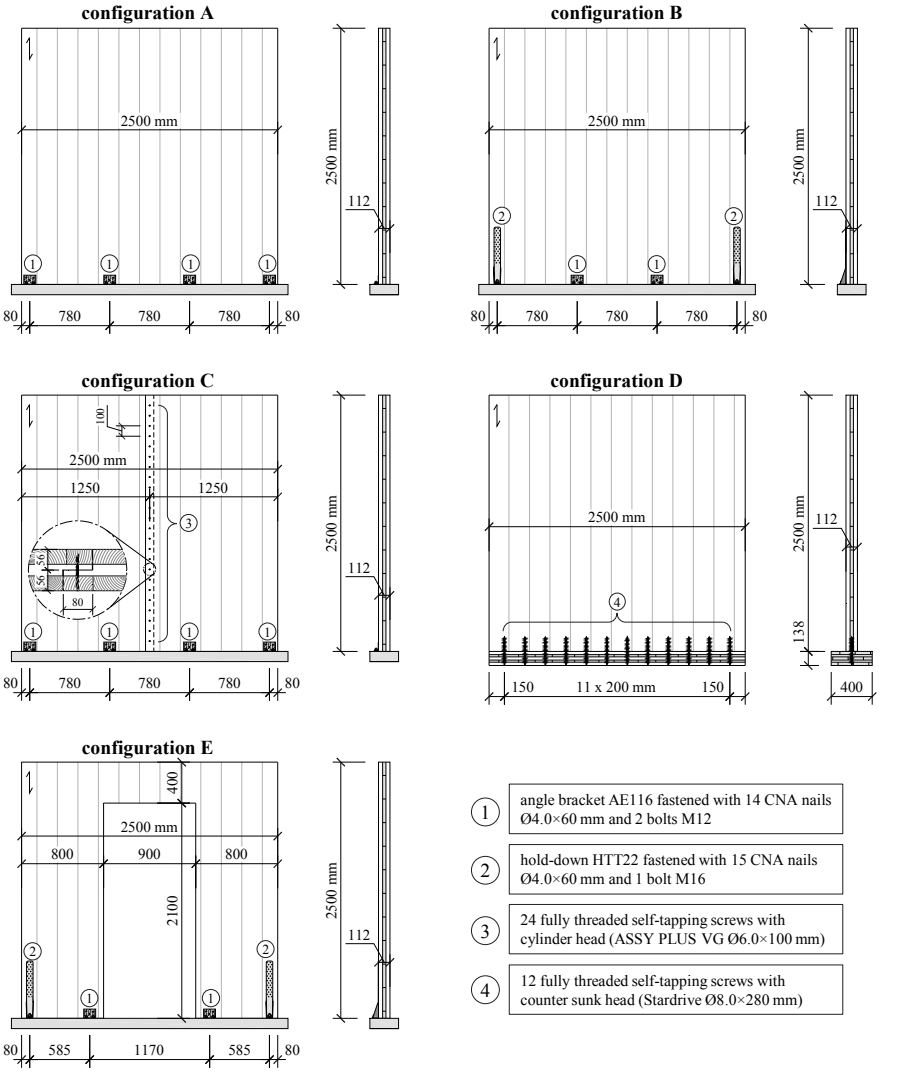

Figure 5.31: overview to the experimentally investigated wall configurations

5-3.1.1 Test set-up

The testing device, used for performing the CLT wall experiments, is illustrated in Figure 5.32. The two vertical (force controlled) hydraulic jacks (1) were used to apply the vertical loads on the massive 'load-distribution' beam (2). The horizontal hydraulic jack (3) was responsible for inducing the lateral loads (displacements). For preventing constraint forces, a hinge (4), only able to transfer lateral loads, was used to link this (displacement controlled) cylinder to the load-distribution beam. The load transfer to the CLT wall system was realised by a further steel girder (5), which was fastened to the CLT element with 24 (20 for configuration C) partially threaded and double-inclined screws (a). For transferring lateral loads between the two steel girders, welded block shear connectors and eccentric bolts (b) were used; the vertical loads were transmitted via contact, i.e., with elastomer bearings (c) between the upper and the lower girder. The additionally placed steel brackets (d) were mounted for safety reasons only, i.e., for preventing huge out of plane movements. Finally, a further steel beam (6), rigidly connected to the concrete floor of the laboratory, represents the foundation for the wall tests.

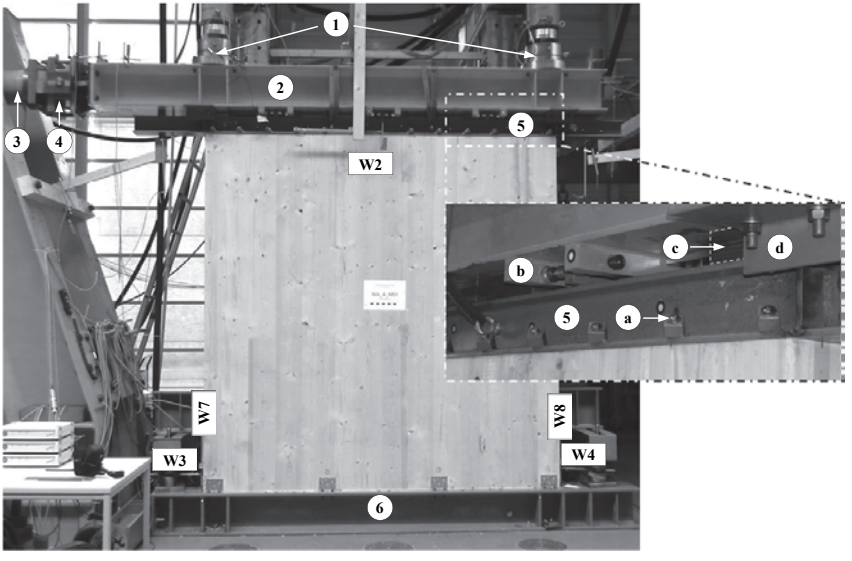

***Figure 5.32:** test set-up for performing CLT wall tests – (1) vertical hydraulic jacks; (2) load-distribution beam (HEB 300); (3) horizontal hydraulic jack; (4) hinge; (5) load-transfer beam (HEB 120); (a) partially threaded screws for lateral load transfer (Ø 8.0×160 mm); (b) welded block shear connectors with eccentric bolts; (c) elastomer bearings; (d) steel bracket; (6) steel foundation (HEB 280); [W2-W8] LVDT's*

For measuring the occurring displacements and deformations, the test specimens were equipped with several LVDT's (min. 10; max. 12). Figure 5.32 depicts the position and designation of the most important one; in particular, W2 for total lateral head deflection, W7 and W8 for uplift at the corners and W3 and W4 for measuring the sliding of the wall system. The CLT deformations were gathered from two

potentiometers, mounted on the back of the wall specimens. Further information regarding the test set-up can be found in ANNEX B as well as in Seim and Hummel (2013) and Flatscher et al. (2013).

The loading protocol for all tests follows the schedule given in ISO 21581 (2010) with only minor adaptions. In particular, the duration between loading and unloading paths for the monotonic tests was fixed with 120 s; see also Seim and Hummel (2013).

5-3.1.2 Materials

Three-layered CLT elements with a total thickness of 112 mm (40-32-40 mm) and 2.5 m in length and height were used as wall specimens (outer layers oriented vertically). The floor elements for configuration D consisted of five-layered CLT panels with a layup of 32-21-32-21-32 mm (total thickness equal to 138 mm; outer layers oriented parallel to the wall element). Equal to the single joint tests, the base material, used for producing the CLT wall elements, was spruce of the strength class C24. Punctual measurements on four wall elements with a 'FMD Moisture Meter' show a moisture content of 10.3 % in average (CoV = 7 %). Due to the given boundary conditions, it was not possible to determine the local densities of the wall and floor elements.

The applied connections and fasteners were equivalent to the one investigated in the single joint tests; compare Figure 5.31 and Table 5.24. Also the number and position of nails was kept constant. Although the impact is regarded as low, two differences concerning the used connections have to be mentioned anyway:

(i) the vertical joint in configuration C was equipped with Ø 6.0×100 mm screws and had a width of 80 mm; the corresponding single joint tests exhibited a half-lap width of 50 mm and Ø 6.0×80 mm screws were used as fasteners

(ii) the foundation for the wall tests was a steel beam; single joint tests, spotting wall-to-foundation joints equipped with angle brackets, were realised on concrete blocks

Finally it is important to mention that the angle brackets and hold-downs were solely mounted on one side of the wall specimens.

5-3.2 RESULTS

Selected properties of the conducted wall tests, including the stiffness and ductility parameters as suggested in Chapter 2, and the corresponding contributions to the total head deflection at the peak load (v_{max}) are listed in Table 5.25. Some more results, load-displacement graphs and the respective model parameters for simulating the test curves (envelope curves for cyclic tests), are documented in ANNEX B.

Table 5.25: primary results of performed CLT wall tests including contributions to deflection when reaching v_{max} (M = monotonic | Z = cyclic)

ID	F_{max} [kN]	v_{max} [mm]	$K_{ser,EN}$ [kN/mm]	D_{EN} [kN]	K_{SLS} [kN/mm]	K_{ULS} [kN/mm]	v_{ip} [-]	Φ_{ip} [%]	$v_{sl,max}$ [%]	$v_{rg,max}$ [%]	$v_{CLT,max}$ [%]
WA_A_M01	74.30	33.7	8.414	10.2	18.484	10.256	33.4	56	19.8	76.6	3.6
WA_A_M02	62.77	30.6	11.349	22.5	63.020	15.365	40.2	66	20.3	78.0	1.8
WA_A_Z01	62.98	26.3	10.943	16.0	21.816	12.906	33.4	64	20.8	77.0	2.2
WA_A_Z02	53.86	29.9	3.452	4.6	6.846	4.196	41.1	58	16.3	80.9	2.8
WA_A_Z03	61.18	25.4	9.745	16.5	21.613	12.727	35.8	66	19.5	77.8	2.8
WA_B_M01	77.36	34.6	6.052	5.5	24.481	8.000	29.0	49	38.4	58.2	3.5
WA_B_Z01	71.73	42.4	4.688	4.9	12.491	5.817	38.3	54	48.0	49.2	2.8
WA_B_Z02	69.98	40.8	3.064	2.8	7.481	3.900	33.2	39	23.9	71.7	4.5
WA_C_M01	71.82	39.2	8.779	11.8	13.480	10.648	36.7	60	19.1	78.2	2.7
WA_C_M02	64.80	34.1	8.265	15.1	21.571	10.460	43.4	65	18.2	79.9	1.9
WA_C_Z01	62.75	28.7	14.465	25.0	28.893	17.363	36.4	65	17.3	80.7	2.0
WA_D_M01	51.07	9.7	17.778	20.7	110.069	23.672	33.2	78	9.2	84.0	6.9
WA_D_Z01	60.42	11.3	14.573	15.1	31.026	21.169	27.9	70	8.7	80.0	11.3
WA_D_Z02	46.80	11.8	8.208	7.0	13.820	10.390	22.8	64	11.0	81.3	7.8
WA_E_M01	74.62	47.3	3.917	4.7	7.935	4.714	40.8	46	33.2	46.8	19.9
WA_E_Z01	75.76	51.1	3.813	5.0	8.508	4.705	48.1	51	31.4	48.4	20.2
WA_E_Z02	57.79	40.2	2.678	3.1	4.870	3.195	36.3	45	22.5	57.7	19.8

Note: $v_{sl,max}$, $v_{rg,max}$ and $v_{CLT,max}$, represent the sliding, rocking and CLT contributions to total head deflection v_{max}, respectively

Since documented elsewhere and not required for the aimed topic, a detailed analysis of the single test results is not designated in the present thesis. Nevertheless, supporting further discussions and for the sake of completeness, the following passage will summarise the major findings.

5-3.2.1 General behaviour

All tested wall systems exhibit a well-tempered load-carrying capacity, stiffness and ductility; no brittle timber failure occurs for any specimen. Nevertheless, the amplitude of vertical load, the type of connections and the presence of an opening distinctively influence their behaviour. Regarding the effect of the vertical load it can be stated that all tests with a reduced amplitude exhibit lower load, stiffness and ductility parameters. Moreover, aside from configuration D, the share of rocking deformation increases while, at the same time, the contribution of sliding decreases. It is further worth mentioning that a higher loading rate for monotonic tests led to higher peak loads; compare Table 5.25 and Figure 5.33.

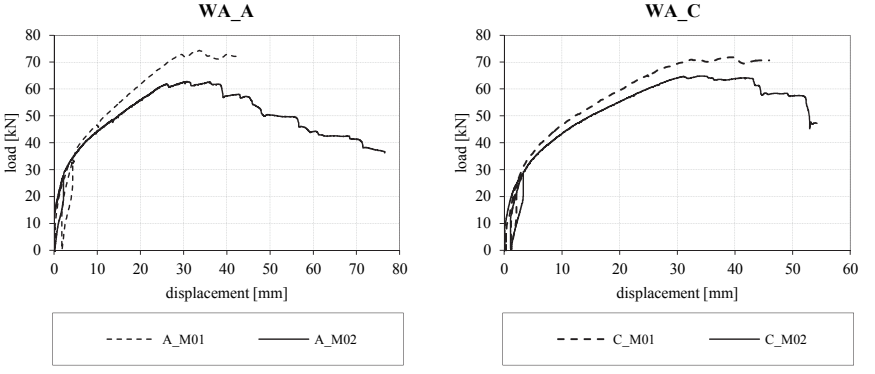

(a) (b)

Figure 5.33: influence of a varying loading rate on the load-displacement relationship of CLT wall systems – (a) configuration A; (b) configuration C

5-3.2.2 Influence of connections

As expected, the absence of hold-downs in configuration A yielded to lower maximum loads compared to configuration B. Interestingly enough, stiffness and ductility parameters are higher. One reason for this circumstance can be seen in the high sliding contribution of configuration B, where only two angle brackets have been applied. This probably limits the effect of the higher rocking resistance (stiffness) caused by the hold-downs. However, as visible in Figure 5.34 (a), the initial part of the load-displacement curves, for equal vertical loads, is similar. Hence, the main reason for the lower initial stiffness values can be seen in the higher maximum load of configuration B and the resulting shift of reference points, used for determining the secant stiffness; compare discussions in Chapter 2 or section 5-2.2.4. Moreover, this comparison also illustrates that classical hold-downs are not necessarily required for all CLT wall systems.

Finally, a remark regarding the outstanding K_{SLS} value of configuration A_M02: when considering the corresponding test graph in Figure 5.34 (a) it gets obvious that this high value solely relies on the sensitivity of the stiffness model at low load and displacement levels and not on a divergent behaviour; the same applies to test D_M01, illustrated in Figure 5.34 (b).

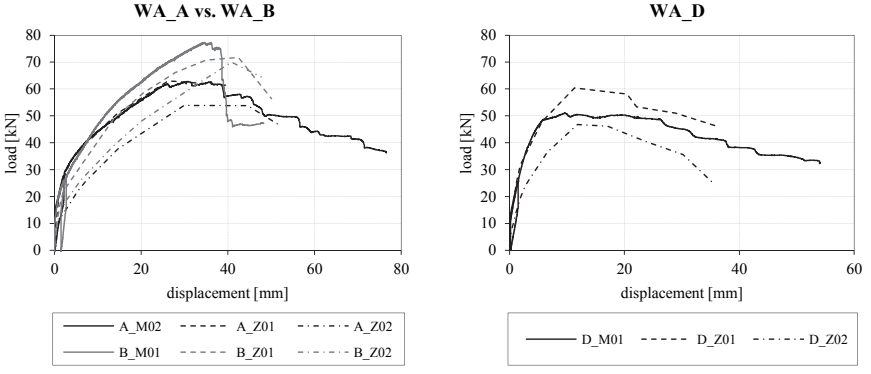

(a) (b)

Figure 5.34: influence of connections – (a) load-displacement behaviour of configurations A and B; (b) behaviour of a screwed top joint (configuration D)

Configuration D, where fully threaded self-tapping screws were used to fasten the CLT wall and floor elements, represents a typical top joint (compare Figure 4.2). As illustrated in Figure 5.34 (b), these tests exhibit a specific load-displacement relationship. As expected, the initial stiffness is distinctively high, but the relative low peak load and the pronounced plastic branch, in combination with the high share of rocking, seems astonishing at a first glance. However, a detailed analysis of the collected video material reveals a slight bending of the CLT floor element, which was not continuously connected to the steel foundation; compare Figure B.41 in ANNEX B. Due to this, a simultaneous acting of screws against uplift was prohibited, which consequently leads to the above described characteristics of this configuration. Some further remarks regarding this topic are given in section 5-5.1.1.

5-3.2.3 Influence of an opening

As shown in Figure 5.35 (a), the load-displacement relationships of configurations B and E are quite similar. Nevertheless, the opening in configuration E causes lower stiffness values as well as higher absolute (total) and CLT related deflections; the load-carrying capacity is not affected in this extent. The bulk of additional deformations are related to the reduced stiffness of the CLT elements. This circumstance is illustrated in Figure 5.35 (b), where the shares of CLT deformation are subtracted from the total head displacements. Of course, the discontinuous bottom line (in combination with the reduced CLT stiffness) further enables a somehow independent acting of the two CLT flanks. Consequently, the resulting time-delayed reaction of the connections might also influence the behaviour of the wall system. Moreover, the position of the angle brackets were not exactly the same for configurations B and E; compare Figure 5.31. However, in this case, the connection based differences are quite small and quantitative hardly ascertainable.

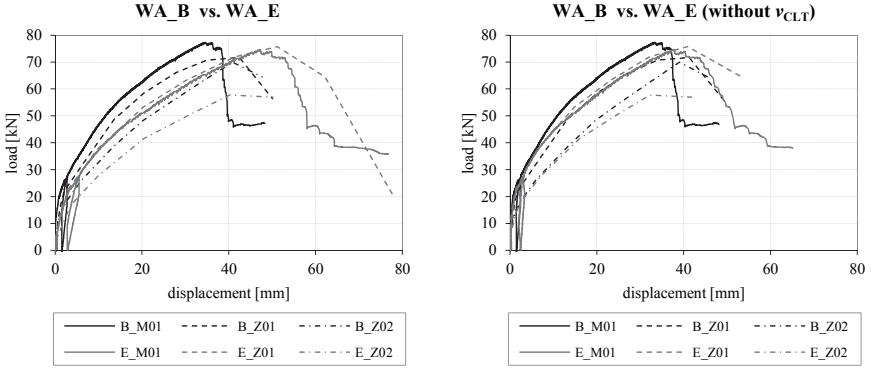

Figure 5.35: influence of an opening – (a) load-displacement behaviour of configurations B and E; (b) behaviour of configurations B and E without considering the CLT deformations

5-3.2.4 Influence of a vertical joint

Comparing the results of configurations A and C shows that the vertical joint in configuration C does not have a distinct influence on the load-displacement behaviour. This is confirmed in Figure 5.36 (a), where the corresponding test graphs are compared. Moreover, the results listed in Table 5.25 show that the higher loading rate of tests A_M01 and C_M01 and the lower vertical load of configuration A_Z02 have much higher influence on the wall properties than the vertical joint.

Nevertheless, in this context it is important to mention that the deflection in the vertical joint was not only regulated by the applied fasteners (i.e. 24 screws), but also the load-transfer beam screwed on the top of the wall; compare Figure 5.32. As a consequence, the walls exhibited pronounced single-coupled behaviour with a deflection in the vertical joint of only 4 mm in average when reaching the peak load; see Figure 5.36 (b). Similar situations may also arise in buildings where the CLT floor (or roof) is fastened to the wall elements beneath; compare further discussions in section 5-5 and Chapter 6.

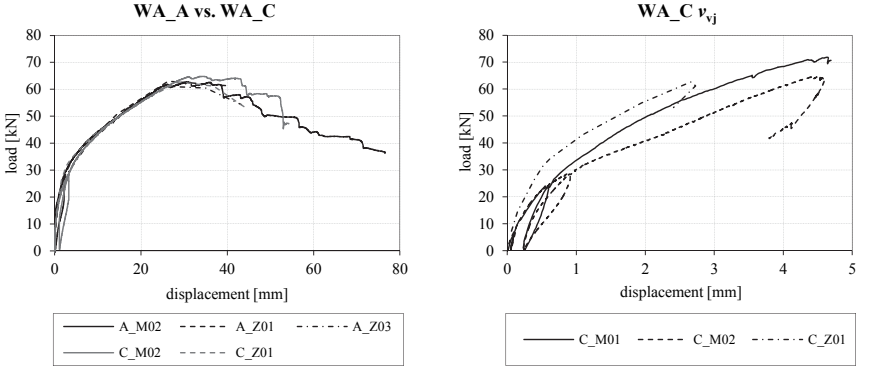

(a) (b)

Figure 5.36: influence of a vertical joint – (a) load-displacement behaviour of configurations A and C; (b) evolution of vertical joint displacement (configuration C)

5-4 CONSIDERED EXTERNAL TEST RESULTS

To expand the data set applicable for validating the suggested wall model, independently performed experimental investigations, documented in Gavric (2013), Seim et al. (2013) and Seim and Hummel (2013), are considered. Since well documented in the mentioned publications, the information herein is limited to a brief summary of the test outputs required for further discussion. In particular, besides the curve parameters for simulating the behaviour of the applied connections, solely the boundary conditions of the tested wall systems are listed.

5-4.1 UNIVERSITY OF TRIESTE | IVALSA

To continue the investigations started in the Sistema Costruttivo Fiemme (SOFIE) research project, an extensive testing program was initiated at the IVALSA Trees and Timber Research Institute (Italy) in 2010. As documented in Gavric (2013), approximately 200 single joint tests on 20 different configurations were realised. However, for simulating the further conducted 16 tests on CLT wall systems, only the six single joint tests listed in Table 5.26 are needed.

Table 5.26: considered tests on single joints conducted at IVALSA

ID	*n*	connection	loading	applied fasteners	type
TEST 1	5	hold-down (WHT540)	uplift	12 nails and 1 bolt Ø 16 mm	wall-to-foundation
TEST 3	6	hold-down (WHT540)	shear	12 nails and 1 bolt Ø 16 mm	wall-to-foundation
TEST 5	6	angle bracket (AE116)	uplift	11 nails and 1 bolt Ø 12 mm	wall-to-foundation
TEST 7	5	angle bracket (AE116)	shear	11 nails and 1 bolt Ø 12 mm	wall-to-foundation
TEST 9	6	half-lap joint	shear	HBS Ø 8.0×80 mm	wall-to-wall
TEST 10	6	spline joint	shear	2×HBS Ø 8.0×80 mm + LVL	wall-to-wall

Note: nails = annular-ringed shank nails Ø 4.0×60 mm; HBS screws were inserted orthogonal to the surface of the CLT elements

The parameters required for simulating the load-displacement relationship of the considered connections are listed in Table 5.27. The corresponding comparison between the actual backbone curves and the simulated ones are illustrated in Figure 5.37.

Table 5.27: input parameters for simulating load-displacement curves of selected connections tested at IVALSA

	notations	F_{max}	v_{max}	K_{ini}	F_A	v_B	K_B	valid range
	units	[kN]	[mm]	[kN/mm]	[kN]	[mm]	[kN]	[mm]
TEST 1	**average curve**	46.00	17.30	7.10	32.50	21.60	-4.50	$0 \le v \le 28$ mm
	maximum curve	51.60	21.40	8.80	40.00	28.00	-3.25	$0 \le v \le 35$ mm
	minimum curve	41.30	16.80	4.10	27.10	19.30	-10.40	$0 \le v \le 19.8$ mm
TEST 3	**average curve**	11.00	100.00	0.95	7.15	123.00	-0.18	$0 \le v \le 140$ mm
	maximum curve	14.9	127.30	1.40	9.60	155.50	-0.21	$0 \le v \le 170$ mm
	minimum curve	8.25	86.90	0.65	5.85	118.20	-0.09	$0 \le v \le 100$ mm
TEST 5	**average curve**	23.30	18.20	5.60	17.60	25.40	-1.35	$0 \le v \le 30$ mm
	maximum curve	26.30	20.20	4.60	19.90	25.60	-1.75	$0 \le v \le 30$ mm
	minimum curve	21.80	17.70	4.00	16.10	24.20	-1.10	$0 \le v \le 26$ mm
TEST 7	**average curve**	26.70	26.20	3.20	21.40	40.70	-0.57	$0 \le v \le 50$ mm
	maximum curve	29.80	31.20	4.30	24.00	49.30	-0.46	$0 \le v \le 55$mm
	minimum curve	24.60	23.30	3.00	18.90	33.00	-0.90	$0 \le v \le 45$ mm
TEST 9	**average curve**	5.16	25.36	3.70	4.16	34.52	-0.24	$0 \le v \le 40$ mm
	maximum curve	6.45	25.69	5.14	5.14	35.23	-0.28	$0 \le v \le 40$ mm
	minimum curve	4.50	24.60	2.60	3.00	32.10	-0.23	$0 \le v \le 40$ mm
TEST 10	**average curve**	7.25	34.50	1.60	6.20	43.00	-0.53	$0 \le v \le 47$ mm
	maximum curve	9.00	52.00	2.70	7.80	80.00	-0.15	$0 \le v \le 80$mm
	minimum curve	6.20	25.00	1.50	5.10	38.00	-0.11	$0 \le v \le 40$ mm

Note: TEST 10 parameters simulate the behaviour of two HBS screws in combination with a 28 mm thick LVL strip; compare Gavric (2013).

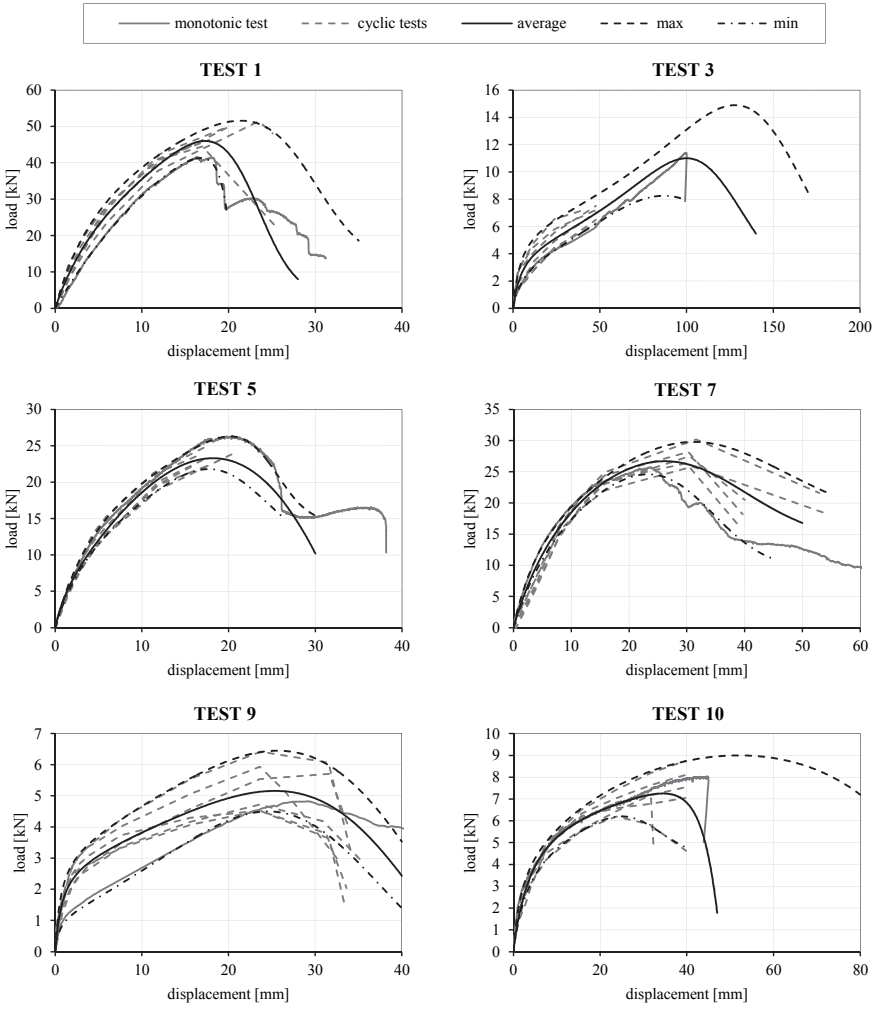

Figure 5.37: comparison of original test (backbone) curves and average, maximum and minimum simulations for connections tested at IVALSA

The wall systems investigated at IVALSA and their most important boundary conditions are listed in Table 5.28. For all wall tests five-layered CLT panels with an equal layer thickness of 17 mm (total wall thickness of 85 mm) were used. The outer layers were oriented vertically and the specimens consisted of one 2.95×2.95 m (single) or two 2.95×1.48 m (coupled) CLT elements. For realising the coupled tests using a spline joint, a 175 mm wide LVL strip was applied.

Table 5.28: listing of IVALSA wall tests including fundamental boundary conditions

ID	vertical load [kN/m]	applied connections (bottom joint)	applied fasteners (vertical joint)	notes
1.1	18.5	2 AB | 2 HD	-	-
1.2	18.5	4 AB | 2 HD	-	-
1.3	9.25	4 AB | 2 HD	-	
1.4	18.5	4 AB | 2 HD	-	-
2.1	18.5	4 AB | 2 HD	20 HBS Ø 8.0×100 mm	half-lap joint
2.2	18.5	4 AB | 2 HD	20 HBS Ø 8.0×100 mm	half-lap joint
2.3	18.5	4 AB | 2 HD	10 HBS Ø 8.0×100 mm	half-lap joint
2.4	18.5	4 AB | 4 HD	5 HBS Ø 8.0×100 mm	half-lap joint
3.1	18.5	4 AB | 2 HD	2×20 HBS Ø 8.0×100 mm	spline joint
3.2	18.5	4 AB | 2 HD	2×10 HBS Ø 8.0×100 mm	spline joint
3.3	18.5	4 AB | 4 HD	2×5 HBS Ø 8.0×100 mm	spline joint
3.4	18.5	4 AB | 2 HD	2×10 HBS Ø 8.0×100 mm	spline joint
3.5	18.5	4 AB | 2 HD	2×10 HBS Ø 8.0×100 mm	spline joint
3.6	0	4 AB | 2 HD	2×10 HBS Ø 8.0×100 mm	spline joint
4.1	18.5	4 AB | 2 HD	2×10 Würth ASSY Ø 8.0×200 mm	spline joint
4.2	18.5	4 AB | 2 HD	2×10 Würth ASSY Ø 8.0×200 mm	spline joint

Note: AB = angle bracket AE116 | HD = hold down WHT540 | all screws in vertical joint were inclined with 35° | Würth ASSY screws were fully threaded and double inclined for test 4.2 (35° in vertical and horizontal direction)

The basic geometry of the wall systems, including the position of the connections, is illustrated in Figure 5.38; for all experiments a steel girder was used as foundation. The tests were performed cyclically with a loading rate equal to 2.25 mm/s. The loading protocol was taken from ON EN 12512 (2005) and the therefor required yield displacement was predefined with v_y = 10 mm. More detailed information can be found in Gavric (2013).

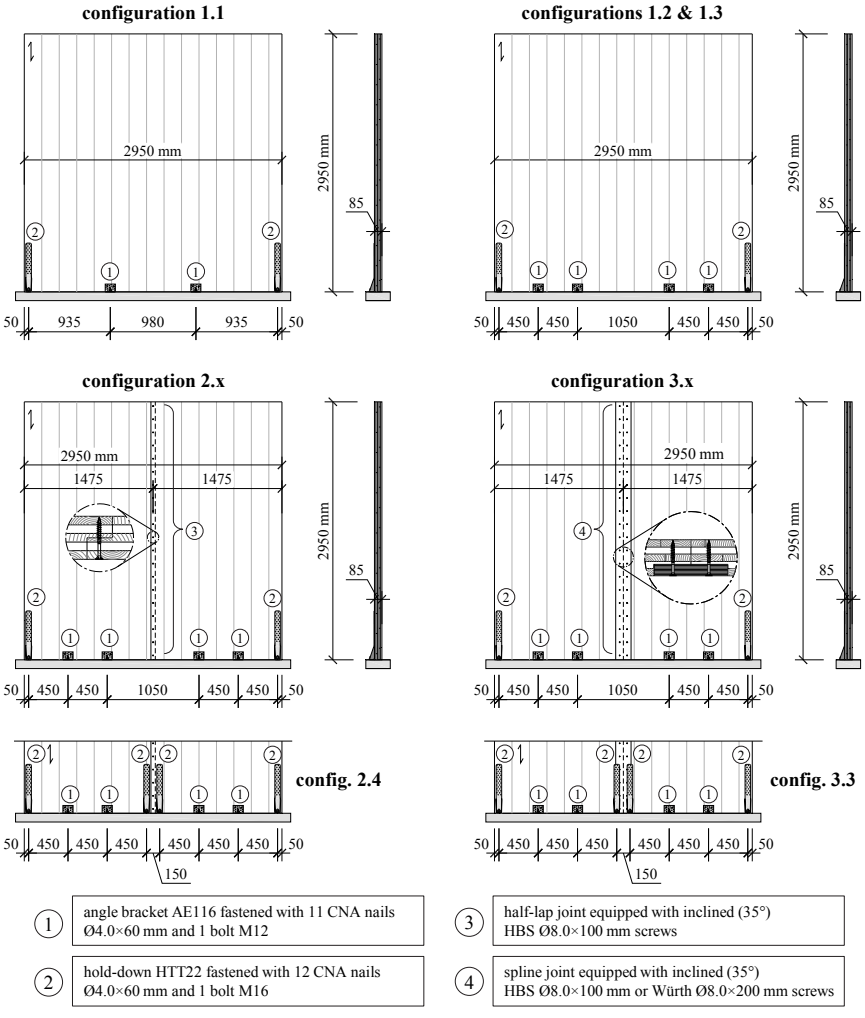

Figure 5.38: wall configurations used for experimental investigations at IVALSA

5-4.2 UNIVERSITY OF KASSEL

In the frame of the research project OPTIMBERQUAKE, several experimental investigations on timber connections and wall elements were conducted at the University of Kassel (Germany). In the present thesis, only tests on CLT single joints and wall systems are spotted.

Basing on Seim et al. (2013), Table 5.29 summarises the boundary conditions of the six configurations, used to examine the behaviour of angle brackets and hold-downs.

Table 5.29: selected connection tests conducted at the University of Kassel

ID	*n*	connection	loading	applied fasteners	type
AB-St-S	4	angle bracket (AE116)	shear	14 nails and 2 bolts Ø 12 mm	wall-to-foundation
AB-Ti-S	4	angle bracket (AE116)	shear	14 nails and 7 nails (wall | floor)	wall-to-floor
AB-St-T	1	angle bracket (AE116)	uplift	14 nails and 2 bolts Ø 12 mm	wall-to-foundation
HD-St-T	3	hold-down (HTT22)	uplift	17 nails and 1 bolt Ø 16 mm	wall-to-foundation
HD-Ti-T	4	hold-down (HTT22)	uplift	17 nails and 1 bolt Ø 16 mm (washer Ø 68 ×5mm)	wall-to-floor
HD-St-S	1	hold-down (HTT22)	shear	32 nails and 1 bolt Ø 16 mm	wall-to-foundation

Note: nails = annular-ringed shank nails Ø 4.0×60 mm

The model parameters, required for simulating the respective load-displacement relationships, are listed in Table 5.30. The actual load-displacement (backbone) curves, as well as the approximated ones, are illustrated in Figure 5.39.

Table 5.30: input parameters for simulating load-displacement curves of angle brackets and hold-downs tested at the University of Kassel

	notations	F_{max}	v_{max}	K_{ini}	F_A	v_B	K_B	valid range
	units	[kN]	[mm]	[kN/mm]	[kN]	[mm]	[kN]	[mm]
	average curve	35.90	16.40	9.70	28.90	22.50	-3.10	$0 \le v \le 25$ mm
AB-St-S	**maximum curve**	39.50	18.50	9.00	34.00	27.00	-2.90	$0 \le v \le 29$ mm
	minimum curve	34.50	16.40	7.40	25.80	20.70	-3.20	$0 \le v \le 24$ mm
	average curve	21.60	14.80	3.50	14.30	18.68	-1.75	$0 \le v \le 20$ mm
AB-Ti-S	**maximum curve**	26.30	25.00	3.30	21.80	31.00	-4.20	$0 \le v \le 32$ mm
	minimum curve	19.80	15.30	2.50	12.30	18.10	-3.10	$0 \le v \le 20$ mm
AB-St-T	-	35.20	17.20	28.30	23.00	22.80	-2.00	$0 \le v \le 35$ mm
	average curve	63.10	25.00	21.40	47.00	29.07	-12.20	$0 \le v \le 30$ mm
HD-St-T	**maximum curve**	67.00	28.10	20.00	51.00	33.00	-10.00	$0 \le v \le 34$ mm
	minimum curve	62.40	24.60	11.40	45.70	28.20	-12.30	$0 \le v \le 29$ mm
	average curve	61.60	49.00	15.00	45.50	56.50	-4.50	$0 \le v \le 60$ mm
HD-Ti-T	**maximum curve**	67.80	61.00	27.60	52.40	67.40	-12.00	$0 \le v \le 68$ mm
	minimum curve	59.90	47.70	16.70	44.20	51.90	-15.50	$0 \le v \le 52$ mm
HD-St-S	-	10.20	29.60	3.50	7.40	35.50	-0.95	$0 \le v \le 37$ mm

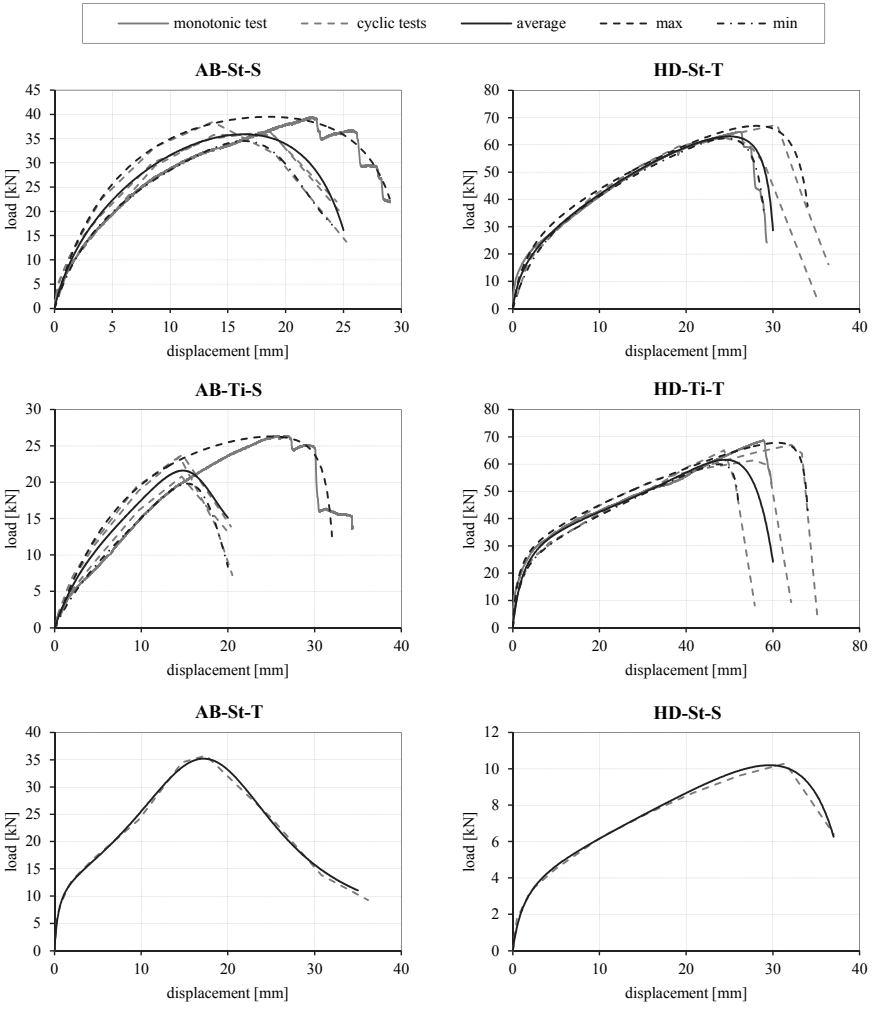

Figure 5.39: comparison of original test curves and average, maximum and minimum simulations for connections tested at the University of Kassel

Within the experimental program at the University of Kassel, 15 tests on CLT wall systems were realised. However, since some investigated points cannot be simulated with the current version of the analytical model, only 11 data sets are considered in the present thesis. In particular, experiments using a Sylodyn® strip as interlayer (between wall and floor elements) and tests with eccentric vertical loads are excluded. The considered tests, including some boundary conditions, are listed in Table 5.31.

Table 5.31: selected boundary conditions for wall tests performed at the University of Kassel

ID	vertical load [kN/m]	support conditions	loading protocol	loading rate
W-CLT-1.1	10	rigid (steel)	monotone	1.0 mm/s
W-CLT-1.2	10	rigid (steel)	ISO	1.0 mm/s
W-CLT-1.3	10	rigid (steel)	CUREE	0.025 Hz
W-CLT-2.1	50	rigid (steel)	monotone	1.0 mm/s
W-CLT-2.2	50	rigid (steel)	ISO	1.0 mm/s
W-CLT-2.3	50	rigid (steel)	CUREE	0.025 Hz
W-CLT-3.1	10	CLT floor element	monotone	1.0 mm/s
W-CLT-3.2	10	CLT floor element	ISO	1.0 mm/s
W-CLT-3.3	50	CLT floor element	ISO	1.0 mm/s
W-CLT-3.5	50	rigid (steel)+2×PE interlayer	ISO	1.0 mm/s
W-CLT-4.3	100	rigid (steel)	ISO	1.0 mm/s

Note: 'monotone' and 'ISO' according to ISO 21581 (2010); 'CUREE' according to Krawinkler et al. (2001)

Figure 5.40 illustrates the basic geometry of the tested walls; all configurations were equipped with two hold-downs and three angle brackets. The five-layered wall elements consisted of 2.5×2.5 m CLT panels with a total thickness of 105 mm (equal layer thickness of 21 mm). For those tests where CLT was used as foundation, a five-layered floor element with a layup of 32-21-32-21-32 mm and a total thickness of 138 mm was used. The orientation of the outer layers was vertical for the wall elements and parallel to the wall surface for the floor panels. More in-depth information, regarding the wall tests conducted at the University of Kassel, is given in Seim and Hummel (2013).

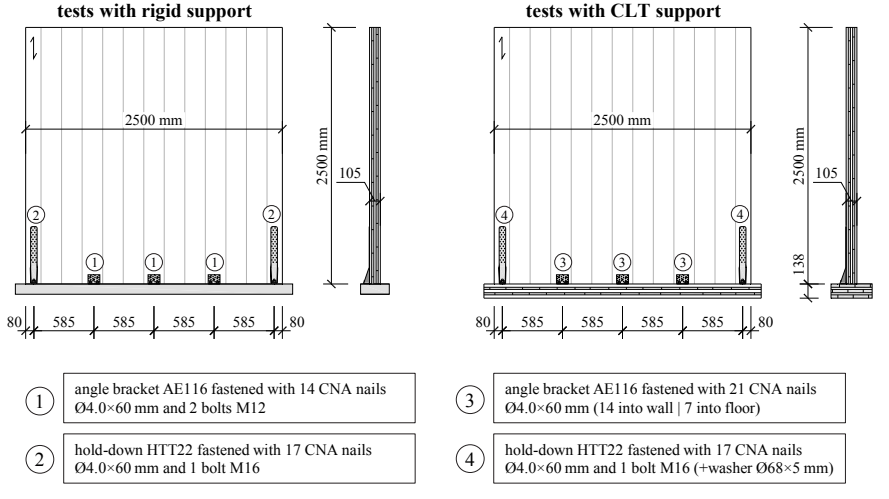

Figure 5.40: wall configurations used for experimental investigations at the University of Kassel

5-5 MODEL VALIDATION

For validating its quality, the documented wall tests are simulated with the displacement-based model proposed in section 4-4. Moreover, some selected tests are further simulated with the FE model described in section 4-5. Besides showing its possibilities, this step prepares and legitimates a subsequent FE-based model validation on configurations, where no experimental results do exist (i.e., long and short wall segments).

5-5.1 VALIDATION ON EXPERIMENTAL RESULTS

For all following simulations, the material properties listed in Table 5.32 are kept constant. The chosen parameters for $E_{0,mean}$ and $G_{0,mean}$ are basing on the suggestions given in Brandner et al. (2016). The mean compressive strengths parallel and perpendicular to the grain are chosen according to the results presented in Poussa et al. (2007) and Brandner and Schickhofer (2014), respectively. Due to expected high (local) indentations and the characteristic behaviour of timber loaded in compression perpendicular to the grain, here the original strength value for this load direction is doubled (i.e., $k_{c,90} = 2.0$); compare, e.g., Brandner and Schickhofer (2014). Since the coefficient of friction can highly influence the simulated results, this parameter is kept constant for all simulations as well. In particular, for rigid (steel) foundations 0.2 is used as an average value of the parameters assumed in Hummel and Seim (2016) and Gavric et al. (2015a), i.e., 0.1 and 0.3, respectively. In case of wall-to-floor tests, the coefficient of friction is assumed to be equal to 0.35, which is close to 0.38, determined in Hummel and Seim (2016). Finally, the parameter a, representing the board width, refers to the assumptions made in Silly (2010).

Table 5.32: chosen material parameters for further wall simulations

parameters	values
$E_{0,mean}$	11600 N/mm²
G_{mean}	650 N/mm²
$f_{c,0,mean}$	35.0 N/mm²
$f_{c,90,mean}$	7.0 N/mm²
a	150 mm
$\mu_{f,rigid}$	0.2
$\mu_{f,CLT}$	0.35

The required parameters for implementing the respective connections are taken from sections 5-2 and 5-4. Here it is important to mention that each considered wall system is simulated three times, i.e., with the average, maximum and minimum approximations of the applied connections. This procedure offers the opportunity to illustrate (at least simplified) the influence of varying connection properties on the simulated wall behaviour.

Since the analytical model enables to consider the bi-directional loading of the connections (i.e. shear and uplift), another important point is the type of interaction. For angle brackets, placed in wall-to-foundation tests, and the screws in configuration D of TU Graz tests, a quadratic interaction is applied. For hold-downs, an interaction is generally neglected; compare section 4-4.2.2. A further exception is made for angle brackets in wall-to-floor joints (configurations 3.1 to 3.3 conducted at the University of Kassel). A preliminary comparison of simulated and experimental wall tests show that in this case an interaction powered by six, instead of two, leads to much better results; compare Figure 5.41. The higher power value represents a less pronounced interaction for shear and tension (uplift) strengths, which may be explained by the occurring failure mode. In particular, differing to wall-to-foundation tests, here the nails in the floor segment are decisive; compare Seim and Hummel (2013) and explanations in section 5-2.2. Although the chosen interaction leads to proper results, further research regarding this topic is highly recommended.

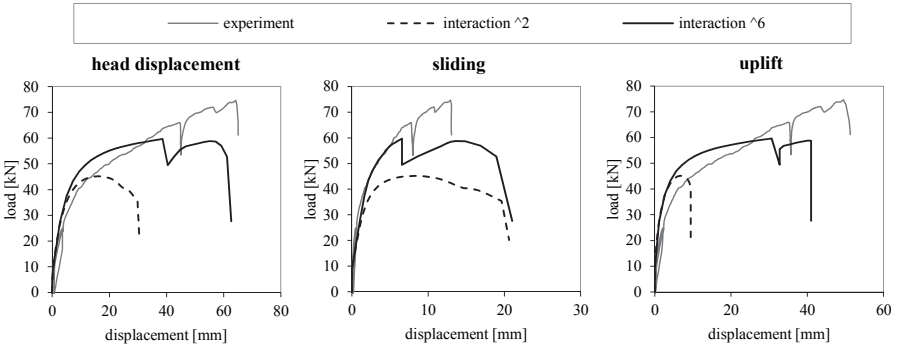

Figure 5.41: comparison of interaction models for angle brackets located in a wall-to-floor joint; here test W-CLT-3.1

Since not all aspects investigated in experimental tests are able to be simulated by the proposed model (e.g. loading rate or cyclic behaviour), the available data sets are regrouped concerning boundary conditions, which can be considered (detailed classification is given in respective sections). It is further worth mentioning that here cyclic test results are solely represented by their first positive envelope curve.

Besides a short summary, some selected configurations are discussed more in detail in the subsequent sections. An entire documentation of original and simulated load-displacement diagrams, together with some selected curve properties, is given in ANNEX C.

5-5.1.1 TU Graz

The groups formed for validating the wall model on TU Graz tests are listed in Table 5.33. The position of connections and the geometry of wall specimens may be taken from section 5-3.1, i.e., Figure 5.31.

Table 5.33: validation groups formed for TU Graz tests

ID	vertical load [kN/m]	applied connections (bottom joint)	included experimental tests	note
VAL_01	20.8	4 AB	A_M01 | A_M02 | A_Z01 | A_Z03	
VAL_02	0	4 AB	A_Z02	
VAL_03	20.8	2 AB | 2 HD	B_M01 | B_Z01	
VAL_04	5.0	2 AB | 2 HD	B_Z02	
VAL_05	20.8	4 AB	C_M01 | C_M02 | C_Z01	vert. joint
VAL_06	20.8	12 screws	D_M01 | D_Z01	
VAL_07	5.0	12 screws	D_Z02	
VAL_08	20.8	2 AB | 2 HD	E_M01 | E_Z01	opening 0.9/2.1 m
VAL_09	5.0	2 AB | 2 HD	E_Z02	opening 0.9/2.1 m

Due to the characteristics of the testing devise described in section 5-3.1.1, simulating the experimental tests further requires to differ between the height of the wall segment and the height of load introduction. In particular, the horizontal hydraulic jack was approximately 300 mm above the top joint; compare Figure B.31 in ANNEX B. As a consequence, the applied load had a 'height' of 2.8 m, whereas the wall exhibits a height equal to 2.5 m.

Moreover it is conceivable that the 'load-transfer beam' somehow influences the acting of the vertical joint in configuration C. Hence, this effect is considered by implementing an additional linear elastic-plastic spring; for further information compare Figure 5.47 and the corresponding passage.

Figure 5.42 shows a comparison between experimentally gathered and simulated properties. If more than one experimental test is considered in a validation group, the mean value of the respective test results is shown. Properties computed with the analytical model, are illustrated with average, maximum and minimum values.

For validations 01 to 05, as well as 08 and 09, it can be seen that the peak load is accurately described. For validations 06 and 07, representing the screwed wall-to-floor joint, this parameter is highly overestimated. Regarding the displacement associated to the peak load (v_{max}), the simulated results show an underestimation for configurations where hold-downs are applied; all other configurations match well with the test results. The stiffness parameter $K_{ser,EN}$, however, shows bigger differences. In particular, most simulations overestimate the actual initial stiffness determined according to ON EN 12512 (2005); this especially for validations 06 and 07. The contributions to the total head deflection exhibit good accordance for validations 01 to 05. Here, the biggest deviations again occur for validations 06 and 07, where the share of rocking is distinctively underestimated, whereas both sliding and CLT contributions are overestimated. Furthermore, the CLT deformation for validations 08 and 09 is clearly underestimated in the corresponding the simulations.

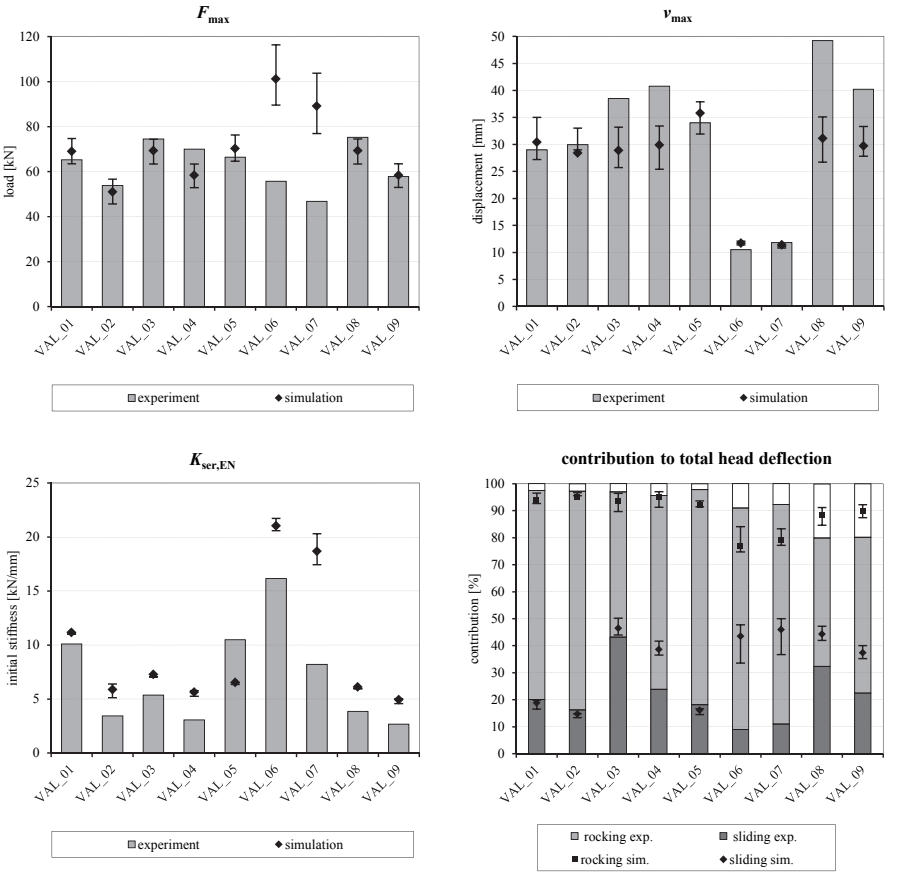

Figure 5.42 model validation basing on tests conducted by TU Graz

Summarising, the biggest differences occur for validations 06 and 07. The reason for this deviating behaviour is already addressed in section 5-3.2.2. In particular, excluding the 'indentation area', the analytical model assumes that all (not failed) connections act simultaneously. This requires a straight bottom edge of the wall segment and an even floor element. However, due to a non-continuous bearing, a slight bending of the floor element occurs during these experiments. In combination with the small displacement capacity of axially loaded screws, a sequential loading of applied fasteners occurs; compare Figure 5.43 (a). As a consequence, the simulated wall behaviour distinctively overestimates the actual capacity of such a joint; see Figure 5.43 (b).

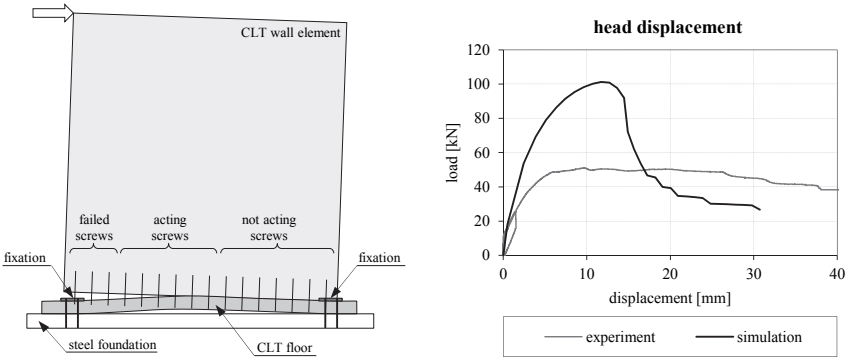

Figure 5.43: screwed wall-to-floor joint (configuration D) – (a) superelevated sketch of the deformed wall systems' shape; (b) comparison between actual and simulated load-displacement behaviour (test WA_D_M01)

Excursion: cyclic behaviour

The herein validated model does not allow considering any cyclic effects. Nevertheless, it is conceivable that using the 3rd envelope curves of single joint tests may enable simulating the 3rd envelope curve of wall tests. To give an example, this procedure is performed for test WA_A_Z03; the output is illustrated in Figure 5.44. Although both (1st and 3rd) actual envelope curves are overestimated with the applied (average) input parameters, the reduced capacity, in principle, is displayed in a correct manner. However, since actually not aimed in the present thesis, no further remarks about this topic will follow.

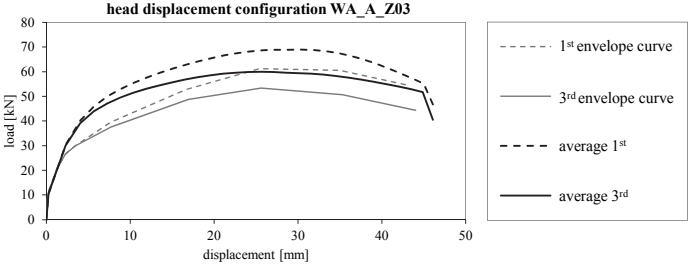

Figure 5.44: example for simulating 3rd envelope curve of a wall system (WA_A_Z03)

Validation of the FE-model

As already noted, selected configurations are additionally simulated by applying the FE-Model described in section 4-5; i.e., validations 01, 03, 04 and 05. The input parameters, used for modelling the CLT surface element and the connections, are documented in ANNEX D. It further has to be mentioned that the main parts of the test set up are also modelled for these simulations. In particular, the load-distribution beam and the load-transfer beam, including the welded block shear connectors and the elastomer bearings, are considered (compare Figure 5.45). Moreover, equal to the analytical simulations, a coefficient of friction equal to 0.2 is considered in the compression bearings of the bottom joint.

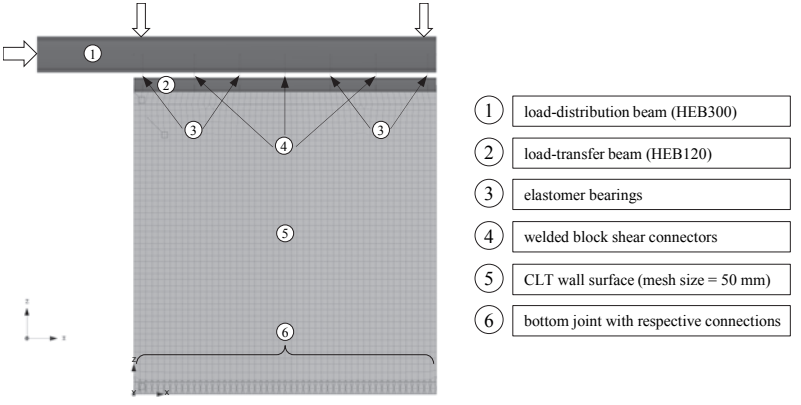

Figure 5.45: overview finite element model

- Validations 01, 03 and 04

Figure 5.46 illustrates a comparison between the actual load-displacement curves of the considered tests and the FE-simulations. Additionally, the average simulations of the analytical model are shown.

As can be seen, similar to the analytical approach, the FE-model leads to proper simulations of the global wall behaviour. Nevertheless, as already mentioned in section 4-5.1, a consideration of interaction effects for bi-directional loaded connections in the applied FE-model, is not possible. This also explains the raised load values at higher displacement levels. Moreover, it can be shown that the load-displacement curves, basing on FE- and analytical computations, are nearly congruent as soon as the interaction is deactivated in the analytical calculation; see also discussion in section 5-5.2.

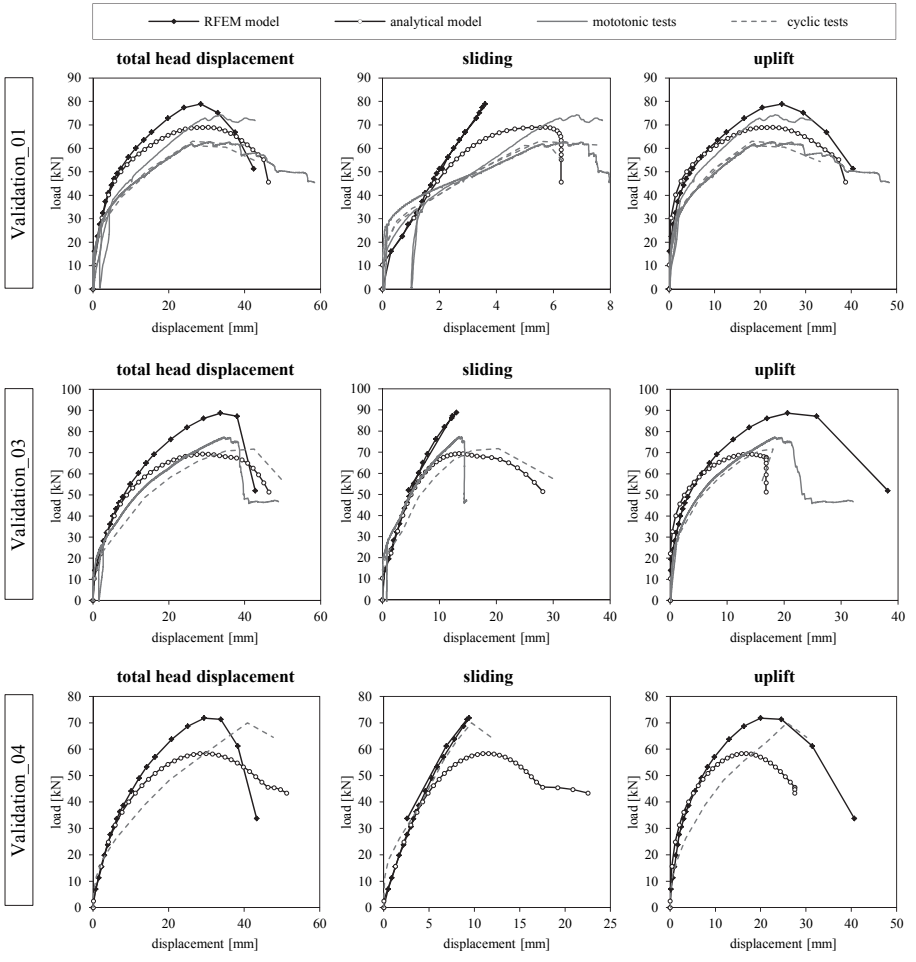

Figure 5.46: FE- and analytical simulations compared to actual behaviour of experimental tests (validations 01, 03 and 04)

- Validation 05

As already mentioned, for experiments in which the influence of a vertical joint was investigated, the load-transfer beam might has limited its displacement. Hence, to enable an accurate simulation of this configuration, the screws, connecting the load-transfer beam to the CLT panels, are modelled as well; this by implementing horizontally rigid, but vertically flexible, elements. However, since test results for an appropriate connection with inclined screws are not available, their behaviour has to be estimated. For this purpose, the load-displacement relationship of a tension loaded and crosswise screwed wall-to-floor connection, as documented in Bratulic et al. (2014b), is scaled. In particular, since the diameter was equal

(8 mm), the ratio of the decisive (effective) screw lengths is used as scaling parameter, i.e., 152 mm/80 mm = 1.9. The resulting input parameters for the finally applied springs are documented in ANNEX D.

The consideration of this 'top joint effect' in the analytical model requires information about the actual resistance imposed by the steel beam. Due to this, an additional FE-simulation is performed in which the vertical joint is modelled without screws. Moreover, left and right CLT panels are supported independently by rigid line bearings. Then, the left CLT panel is loaded by a series of imposed line displacements, i.e., six different levels between 1 mm and 15 mm; compare Figure 5.47 (a). The resulting bearing loads allow illustrating the vertical load-carrying behaviour caused by the steel beam. For implementing this additional resistance in the analytical computation, a linear elastic-plastic approximation is applied; compare Figure 5.47 (b). Thereby, the required parameters K^+, F_{lim} and v_{lim} are chosen in a way that the multilinear approximation equalizes the dissipated energy (enveloped area) of the simulated behaviour.

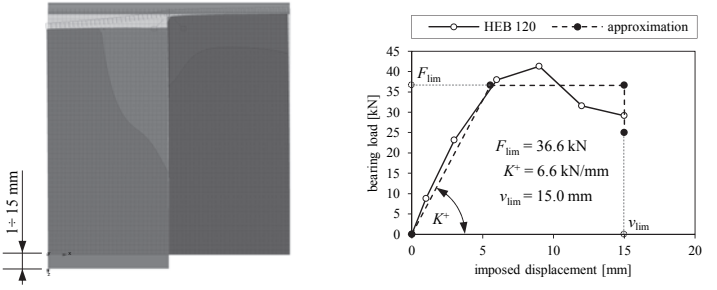

(a) (b)

Figure 5.47: investigating the 'top joint effect' – (a) RFEM model; (b) diagram illustrating bearing loads at defined imposed displacement levels and the chosen multilinear approximation

Figure 5.48 compares experimentally gathered and simulated load-displacement curves. As can be seen, not only the simulated head-displacements, but also the vertical joint displacements fit well with the test results.

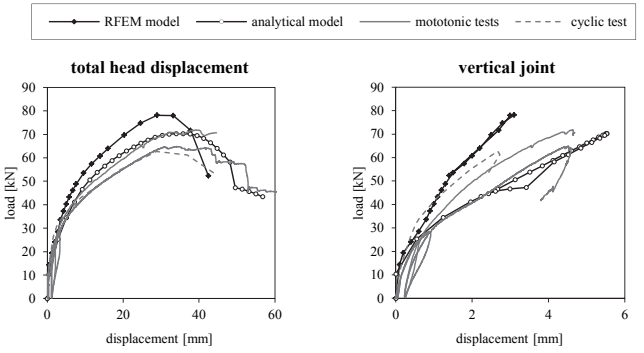

Figure 5.48: FE- and analytical simulations compared to actual behaviour of experimental tests (total head and vertical joint behaviour of VAL_05)

For comparison, Figure 5.49 finally shows load-displacement curves of simulations in which the load-transfer beam is not considered. For this purpose, in the analytical simulation K^{+}, F_{lim} and ν_{lim} are set equal to zero and in the FE-model the steel beam is cut. As expected, the FE-model and the analytical model lead to slightly lower maximum loads but higher displacement levels. However, both overestimate the experimentally gathered vertical joint displacements by far.

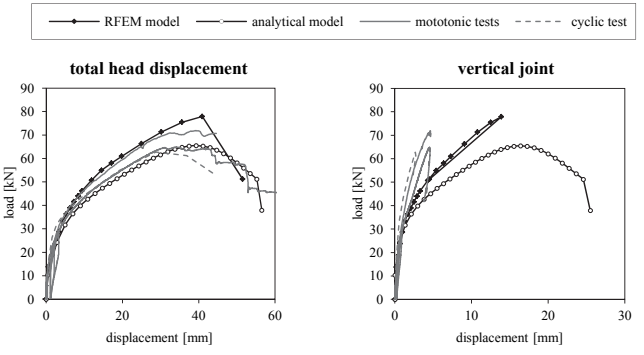

Figure 5.49: comparison between simulated and experimental results in which the influence of load-transfer beam is neglected

Summarising, it can be stated that the FE-based model enables to approximate the actual wall behaviour in an acceptable way. Nevertheless, the disability for considering interaction effects limits its applicability.

5-5.1.2 University of Trieste | IVALSA

Table 5.34 gives an overview of the groups formed for validating the analytical wall model on tests conducted at IVALSA. The position of connections and the geometry of wall specimens may be taken from section 5-4.1.

Table 5.34: validation groups formed for IVALSA tests

ID	vertical load [kN/m]	applied connections (bottom joint)	included experimental tests	note
VAL_10	18.5	2 AB | 2 HD	1.1	
VAL_11	18.5	4 AB | 2 HD	1.2 | 1.4	
VAL_12	9.25	4 AB | 2 HD	1.3	
VAL_13	18.5	4 AB | 2 HD	2.1 | 2.2	half-lap joint with 20 screws
VAL_14	18.5	4 AB | 2 HD	2.3	half-lap joint with 10 screws
VAL_15	18.5	4 AB | 4 HD	2.4	half-lap joint with 5 screws
VAL_16	18.5	4 AB | 2 HD	3.1	spline joint with 2×20 screws
VAL_17	18.5	4 AB | 2 HD	3.2 | 3.4 | 3.5 | 4.1 | 4.2	spline joint with 2×10 screws
VAL_18	18.5	4 AB | 4 HD	3.3	spline joint with 2×5 screws
VAL_19	0	4 AB | 2 HD	3.6	spline joint with 2×10 screws

Before starting the analytical simulations, again a brief look is taken at the specifications of the test set-up. Following the documentation in Gavric (2013), the horizontal hydraulic jack seems to have the same height as the tested wall segments. As a consequence, the load eccentricity, as used for simulating TU Graz tests, is not needed for the present validation.

As further described in Gavric (2013), for all tests a steel girder was fixed on the top of the tested wall systems. Although not used for load introduction, but rather for simulating a CLT floor, a consideration of this element is mandatory when simulating coupled wall systems. Since detailed information regarding the steel beam and the applied fasteners is missing, basing on some photographs, a UPN100 profile and twelve partially threaded and vertically inserted screws (HBS Ø8.0×160 mm) are assumed. Applying the FE based procedure described afore, finally enables determining the linear elastic-plastic spring required for analytical simulations; compare Figure 5.50.

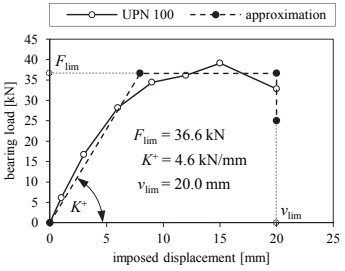

Figure 5.50: additional resistance in vertical joint caused by UPN100 profile on the top of CLT wall systems tested at IVALSA

Note: For FE simulation, the behaviour of HBS screws is estimated by scaling the average curve described in section 5-2.4.2. As scaling factor the ratio of effective lengths (134 mm/80 mm = 1.675) is used; resulting input parameters are documented in ANNEX D.

A further point to keep in mind is that half-lap and spline joints in wall tests were equipped with inclined screws; compare Table 5.28 and Figure 5.51. Consequently, the results from corresponding single joint tests, realised with orthogonal inserted screws, are usually not applicable for wall simulations.

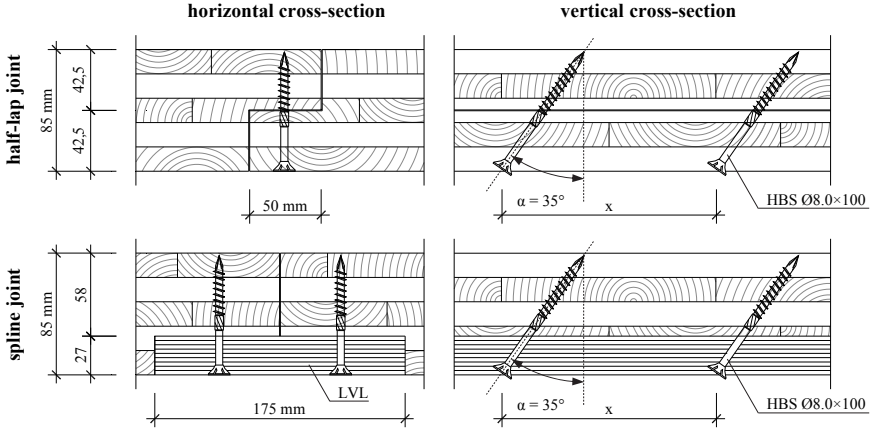

Figure 5.51: inclination of screws in half-lap and spline joints used for IVALSA tests

However, since the used partially threaded screws had countersunk heads and were inclined in only one direction (not crosswise), higher load-carrying capacities are not expected. Increased resistances are also not expected for tests 4.1 and 4.2, in which the spline joints were equipped with fully threaded screws. This, because the threaded part in the LVL strip was too short (~20 mm) to become decisive, compared to the head pull-through capacity. As a consequence, and in the absence of alternatives, the original single joint data are used for further simulations anyway.

In Figure 5.52 experimentally gathered and simulated results are compared; contributions to total head deflection are taken from Gavric et al. (2015a).

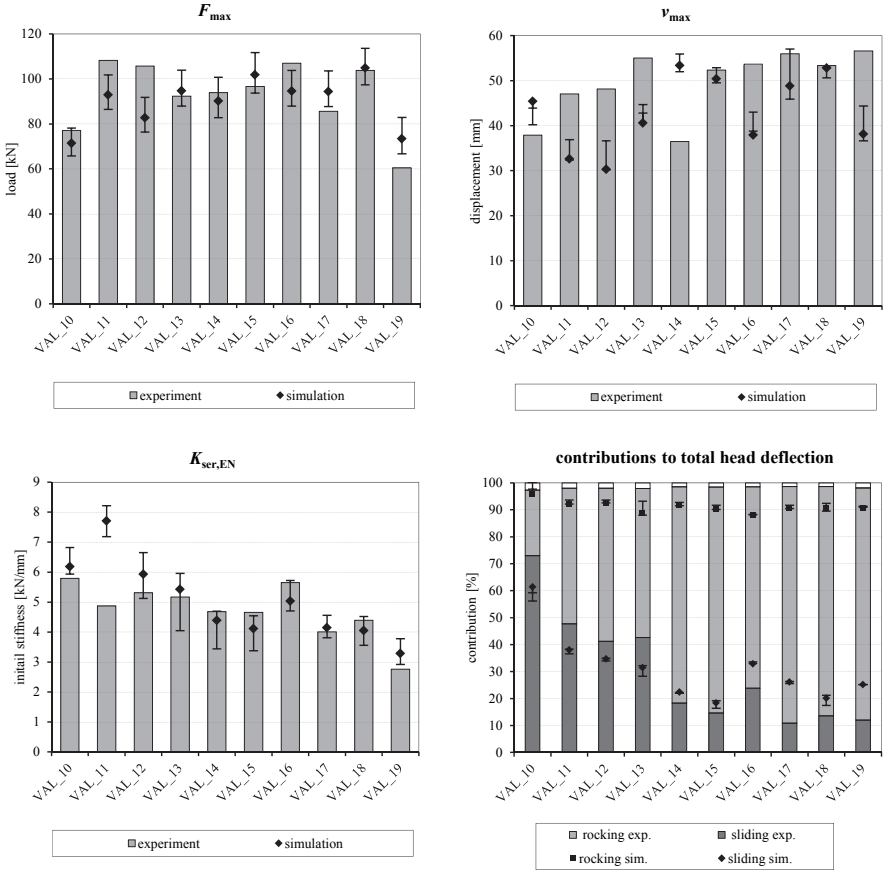

Figure 5.52: model validation basing on tests conducted at IVALSA

The majority of the simulated parameters are close to the one documented in the experiments. Moreover, the vertical joint behaviour (coupled or single-coupled), as documented in Gavric et al. (2015a), fits well with the model output (except for validation 19). Nevertheless, for tests in which coupling was realised with spline joints (VAL_16 to VAL_19), the vertical joint displacement is underestimated; compare detailed results in ANNEX C. It consequently seems that the inclination of screws actually reduces the spline joint capacities compared to the orthogonal arrangement in single joint tests. Only the simulation of configuration 3.3 (VAL_18), where two additional hold downs were placed close to the vertical joint, does not show this effect. Nevertheless, it is also conceivable that the additional

stiffness, representing the top joint, effect is overestimated. Anyway, since both vertical joint behaviour and top joint effect are based on assumptions, a more detailed discussion seems not productive at the moment.

Finally, it should not be concealed that the analytical simulation results in too high maximum translation (sliding) for validations 17 and 19; see also ANNEX C. However, it can be shown that this may be remediated by increasing the coefficient of friction from 0.2 to 0.3. Moreover, reducing the vertical joint capacity also influences this parameter in a positive way.

5-5.1.3 University of Kassel

Finally the tests conducted at the University of Kassel are simulated with the analytical model too. The corresponding groups are listed in Table 5.35.

Table 5.35: validation groups formed for tests performed at the University of Kassel

ID	vertical load [kN/m]	applied connections (bottom joint)	included experimental tests	note
VAL_20	10	3 AB | 2 HD	W-CLT-1.1 | W-CLT-1.2 | W-CLT-1.3	
VAL_21	50	3 AB | 2 HD	W-CLT-2.1 | W-CLT-2.2 | W-CLT-2.3	
VAL_22	10	3 AB | 2 HD	W-CLT-3.1 | W-CLT-3.2	CLT floor
VAL_23	50	3 AB | 2 HD	W-CLT-3.3	CLT floor
VAL_24	50	3 AB | 2 HD	W-CLT-3.5	PE interlayer
VAL_25	100	3 AB | 2 HD	W-CLT-4.3	

These experiments were conducted with the same testing devise and set-up as the one discussed in section 5-5.1.1. Consequently, for simulating them, the load has to be applied at a height of 2.8 m (eccentricity of 300 mm). A consideration of the load-transfer beam is not necessary, because no vertical joints are included. Instead of that, the influence of CLT floors and high vertical loads are the outstanding criterions of these tests. In this context it has to be mentioned that the parameters describing the uplift behaviour of angle brackets for validations 22 and 23 are taken from TU Graz tests (equal configuration; compare section 5-2.2.4). The shear resistance of hold-downs in wall-to-floor joints is set equal to zero. Moreover, due to the limited influence, the circumstance that the shear behaviour of hold-downs for wall-to-foundation joints was examined with 32 instead of 17 nails is neglected. Finally, in order to consider the PE interlayer in configuration W-CLT-4.3 (VAL_24), the coefficient of friction is set equal to zero in this case.

Figure 5.53 summarises and compares experimentally gathered and simulated wall properties in the familiar manner; contributions to total head deflection are taken from Seim and Hummel (2013). In principle, here the displacement-based model, once more, enables an accurate simulation of the actual wall behaviours; see also detailed comparison in ANNEX C. Nevertheless, the outstanding

overestimation of the initial stiffness for validation 23 and the arising high F_{max} parameter for validation 25 are worth to be discussed in detail.

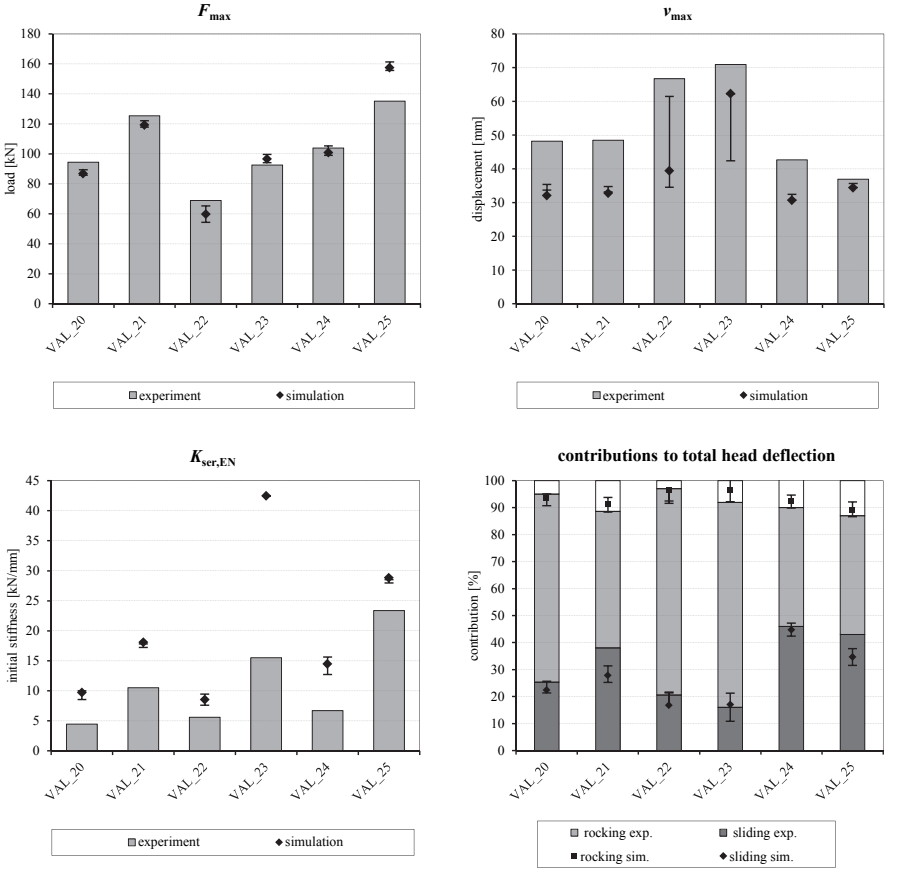

Figure 5.53: model validation basing on tests conducted at the University of Kassel

A comparison of original and simulated wall behaviour for validation 23 is given in Figure 5.54 (a). As visible, the analytical model is able to simulate the general behaviour in a proper way. However, the detail in Figure 5.54 (b) illustrates that the analytical model only considers a linear elastic deflection in the first branch of the load-displacement relationship. In particular, rotation and translation is prohibited by the applied vertical load up to 55.8 kN and 43.8 kN, respectively. As a consequence, here only the deformation of the CLT wall element is displayed; compare Equations (4.69) and (4.70). A probably arising wall rotation, basing on indentations, is not considered until the restoring influence of the vertical load against rocking is overcome. Even if the occurring differences, compared to the total displacement

capacity of the wall, are small, this effect obviously influences the initial wall behaviour and consequently its stiffness parameter.

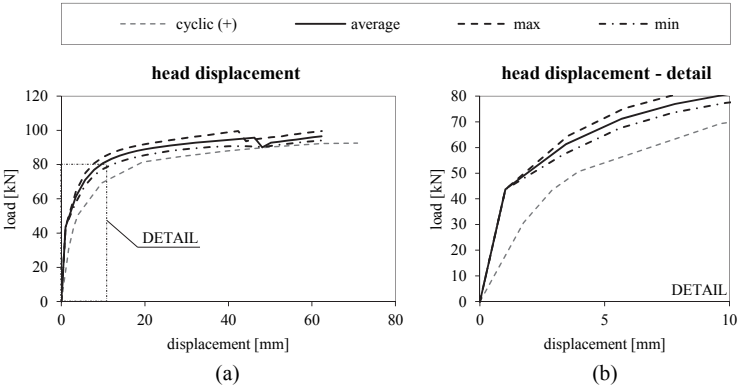

Figure 5.54: validation 23 – (a) load versus head displacement; (b) detail of initial branch

The vertical load is also seen as the decisive parameter for validation 25. As illustrated in Figure 5.55, the actual load is overestimated at any point of the load-displacement diagram. As also visible, the sliding contribution is starting at the correct load level whereas the uplift deformations occur too late in the simulation. Hence, it seems that the model overestimates the restoring effect of the vertical load against rocking, which, of course, especially affects the simulations where high vertical loads are applied. Additionally, similar to validations 20 and 21, the distinct kink at approximately 30 % to 40 % of the peak load and the subsequent linear branch of the sliding contribution is not simulated. Unfortunately, a clear reason for this behaviour has not been detected so far and, hence, cannot be considered in the analytical model.

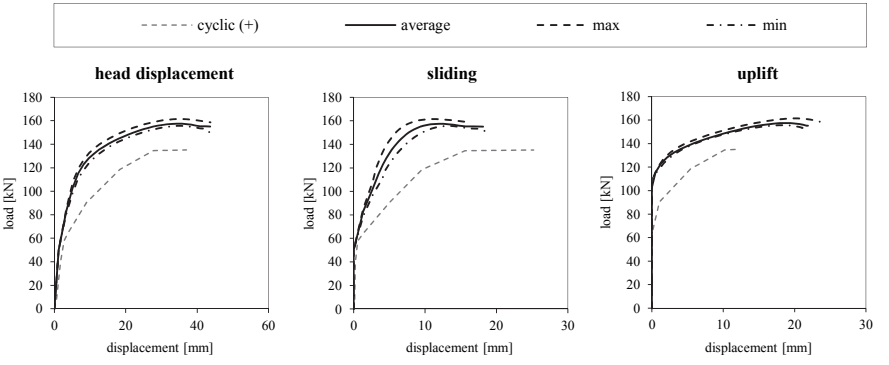

Figure 5.55: selected load-displacement diagrams of validation 25

Finally, the reduced difference between maximum and minimum curvatures can be regarded as an indication for the limited influence of varying connection properties in case of high vertical loads.

5-5.2 FINITE ELEMENT SIMULATIONS

As demonstrated in section 5-5.1.1, the FE model described in section 4-5 enables an acceptable simulation of CLT wall systems. Therefore, here it is applied to validate the quality of the analytical model for not yet tested wall systems. In particular, three different wall lengths (1.0 m, 4.0 m and 6.0 m) under three different vertical loads (10 kN/m, 25 kN/m and 50 kN/m) are simulated. The bottom joint is equipped with angle brackets (AB) basing on TU Graz tests (wall-to-foundation average parameters according to section 5-2.2) and the spacing between them is kept constant with a_{con} = 1 m; compare Figure 5.56. All further parameters are equal to the one described in section 5-5.1.1.

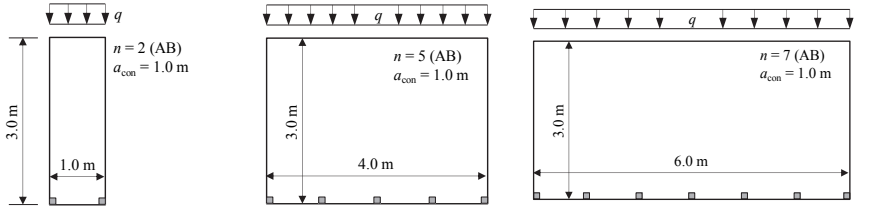

VAL_26: q = 10 kN/m
VAL_27: q = 25 kN/m
VAL_28: q = 50 kN/m

VAL_29: q = 10 kN/m
VAL_30: q = 25 kN/m
VAL_31: q = 50 kN/m

VAL_32: q = 10 kN/m
VAL_33: q = 25 kN/m
VAL_34: q = 50 kN/m

Figure 5.56: boundary conditions for FE based model validation

Figure 5.57 illustrates a comparison of load-displacement curves (total head deflection) gathered from FE-based and analytical simulations. Furthermore, since the applied FE model is not able to consider interaction effects of bi-directional loaded connections, two analytically determined curves are given: (i) with and (ii) without interaction. Additional illustrations, including a comparison of sliding and uplift deflections, are documented in ANNEX C.

Generally, analytical results neglecting the interaction effects are quite close to the FE simulations. Moreover, for validations 26, 27, 28 and 34 interactions do not have an influence on the global wall behaviour. This, because the analytical simulation of wall systems with l = 1.0 m and VAL_34 only show rotation and translation, respectively. All further validations are distinctively affected as soon as the interaction is considered.

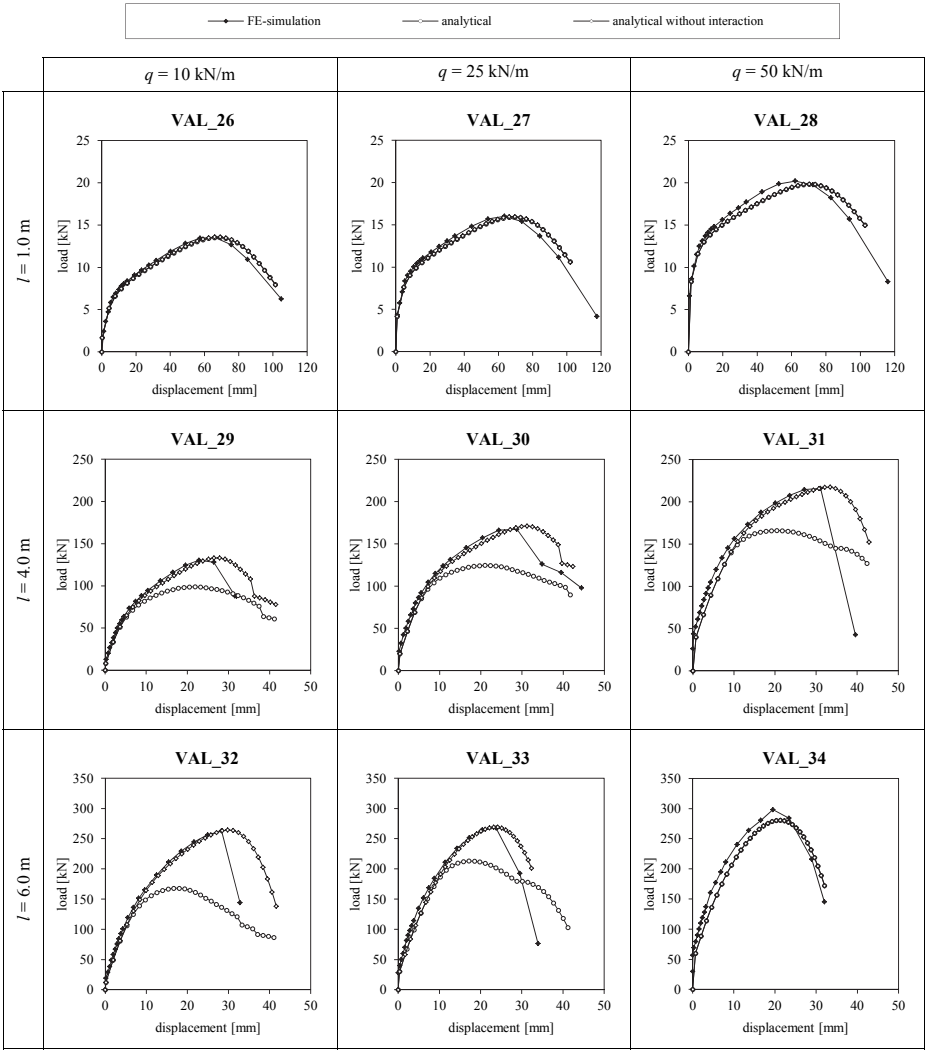

Figure 5.57: comparison of FE-based and analytically determined load-displacement curves

The FE study further enables to visualise the vertical bending of CLT wall elements (not considered in the analytical model). Due to the occurring high lateral loads and the geometric boundary conditions, this effect especially gets visible when simulating long (uncoupled) wall systems. The highest CLT-based uplift deformation is, hence, determined for validation 34 (5.8 mm at the peak load of 298 kN; compare Figure 5.58).

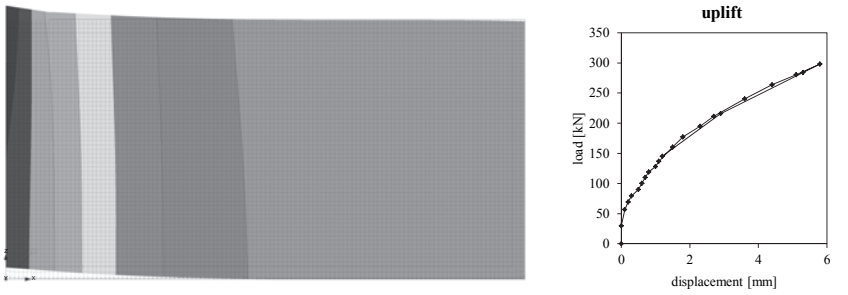

(a) (b)

Figure 5.58: vertical deformation of CLT wall element – (a) screenshot of vertical deformations at peak load; (b) vertical deformation at different load levels

However, in such cases, (usually) sliding becomes the controlling mechanism and the actual influence on the global wall behaviour is limited; compare Figure 5.57. Moreover, it can be shown that applying a line- instead of a single load on the walls' top reduces the additional uplift for this wall to approximately 3.0 mm.

5-6 INTERMEDIATE CONCLUSIONS

For enabling a well-founded validation of the displacement-based wall model suggested in Chapter 4, experimental results of three independent research projects are appropriately edited in a first step. In particular, single joint and wall tests, performed at the Universities of Graz, Trieste and Kassel are considered. In a second step, the data of single joint tests are used as input parameters for simulating the load-displacement relationships of the experimental wall tests. Moreover, some selected configurations are also simulated with a FE-based model.

Although generally leading to accurate results, some occurring limitations of the model may not be concealed. Probably the most important one is the disability to consider the bending behaviour of CLT floor elements. This distinctively turned out when simulating the screwed connection of configuration C (VAL_05). Moreover, the underestimation of CLT deformations for configuration E (VAL_08 and VAL_09) attracts attention and leads to the recommendation for further research on the influence of openings. Other points worth mentioning are the incomplete consideration of indentations (compare VAL_23) and the overestimation of rocking capacity in case of high vertical loads (e.g., for VAL_25). Furthermore, due to missing appropriate test results of single joints, a detailed validation of the proposed interaction model is recommended for further studies.

However, the majority of the considered configurations are simulated with high accuracy and also the further conducted FE based simulations confirm the qualities of the proposed model.

CHAPTER 6
PARAMETER STUDY AND APPLICATION

6-1 INTRODUCTION

Within the present chapter, the displacement based wall model is applied to investigate the influence of selected factors on the behaviour of CLT wall systems. For this purpose, in total 96 CLT wall systems are simulated and evaluated. Moreover, some further investigations, spotting the behaviour and influence of a vertical joint, are conducted. Finally, some aspects regarding the behaviour of a whole structure, including the load distribution on wall diaphragms within one floor, are discussed.

For the sake of simplicity, if not explicitly described in another way, all wall simulations do base on the same boundary conditions. In particular, the properties defined in section 5-5.1 are applied and wall elements are assumed as five-layered CLT panels with an equal layer thickness of 20 mm (t_{CLT} = 100 mm) and a height of 3.0 m. Required connection properties are mainly taken from section 5-2 (TU Graz tests) and refer to the respective average approximations.

Note: Some aspects of the present section have already been addressed in Flatscher and Schickhofer (2016).

6-2 VARIATION OF SELECTED PARAMETERS

The present section briefly illustrates how the factors (i) wall length l, (ii) spacing between applied connections a_{con}, (iii) acting vertical load q and (iv) friction μ_f may influence the behaviour of CLT wall systems. In particular, the respective effect on the load-carrying capacity, the corresponding total head displacement, the initial stiffness and the sliding contribution are discussed. All herein used simulations do refer to a rigid foundation.

6-2.1 WALL LENGTH AND NUMBER OF CONNECTIONS

The length of a CLT wall system and the number of applied connections can be seen as the most important factors affecting its load-bearing behaviour. Hence, 30 simulations with varying wall lengths (0.5 m to 6.0 m) and connection spacings (0.25 m to 2.0 m) are realised. Thereby, the vertical load and the applied coefficient of friction are kept constant with 15.0 kN/m and 0.2, respectively. Moreover, only angle brackets are used as connections.

Figure 6.1 illustrates the effect of this variationw on the attainable load-carrying capacity (F_{max}), the initial stiffness (here K_{ULS} as described in Chapter 2), the sliding contribution when reaching the peak load ($v_{sl,max}$) and the total head displacement corresponding to F_{max} (v_{max}).

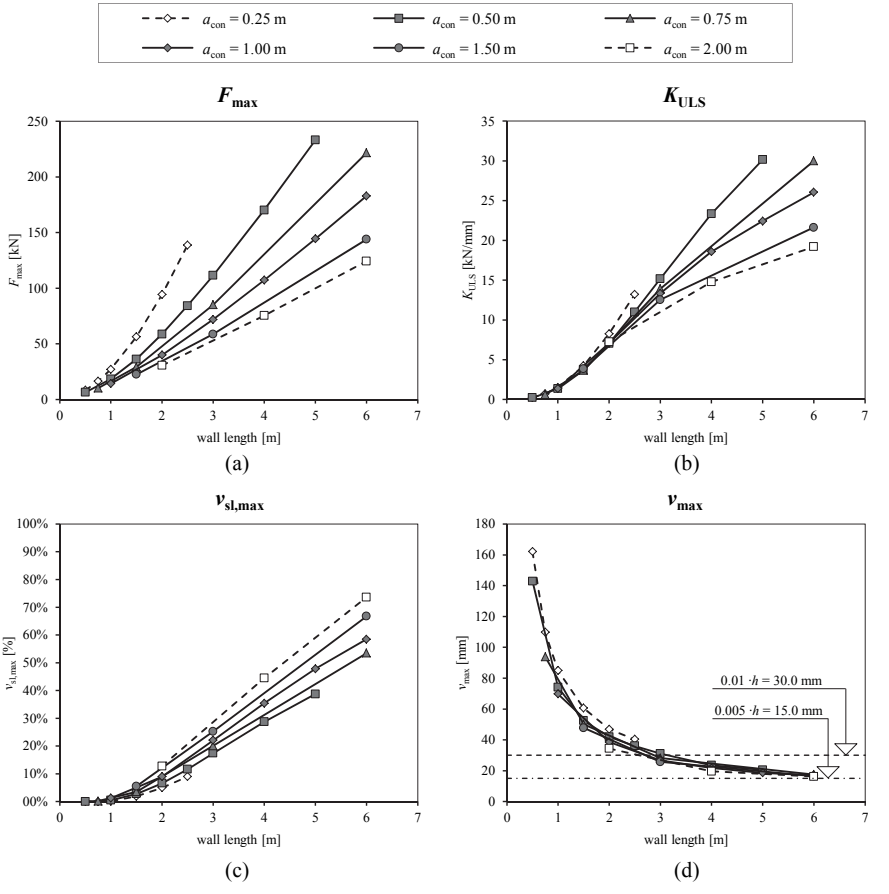

Figure 6.1: influence of wall length and connections' spacing on selected CLT wall parameters – (a) peak load; (b) initial stiffness; (c) sliding contribution to total head deflection; (d) head deflection when reaching F_{max}

As expected, Figure 6.1 (a) clearly visualises that the load-carrying capacity of a CLT wall system distinctively depends on its length and the number of applied connections. In particular, as longer the wall and as shorter the distances between the connections, the higher the resulting peak load is. A similar relationship can be observed for the initial stiffness; compare Figure 6.1 (b). The sliding contribution also increases with the wall length but decreases with smaller spacings between the connections; compare

Figure 6.1 (c). Focussing the sliding contribution further shows that from a length-to-height ratio greater than two ($l/h > 2.0$) sliding becomes the decisive mechanism.

The course of the parameter v_{max}, visualised in Figure 6.1 (d), primarily depends on the walls' length whereas the number of connections show only a minor influence. This diagram further indicates that the interstorey drift levels, scheduled for damage limitation in ON EN 1998-1 (2011) and Follesa et al. (2011), i.e., 0.5% and 1.0% of storeys' height, might be too progressive for CLT structures. In particular, although considering nonlinear effects and mean values, an interstorey drift of 1.0 % forces walls longer than 3.0 m to go beyond v_{max}, which necessarily leads to damages. Some further thoughts, concerning the displacement capacity of CLT wall systems when reaching the peak load, are given in Sommerlade et al. (2016).

For an additional impression, Figure 6.2 illustrates head deflections corresponding to $0.25 \cdot F_{max}$ (~ SLS), $0.40 \cdot F_{max}$ (~ ULS) and $0.70 \cdot F_{max}$ (~ accidental load level); compare discussion in Chapter 2. As visualised, the displacement values for loads, satisfying the SLS and ULS level, are approximately 2.0 mm and 4.0 mm on average, respectively. For a load level equating a seismic event, the average of corresponding displacement values reach slightly more than a 0.5 % interstorey drift, whereat walls longer than 2.5 m still show lower deflections. Of course, these results only correspond to the chosen boundary conditions and do not consider additional deflections between the wall and the floor above. Nevertheless, aiming an effective damage limitation, interstorey drifts for CLT structures should be restricted to 0.5 % of storeys' height in maximum. Probably even lower limits (e.g., 0.25 % of h) may be considered for structures primarily using long CLT walls ($l/h > 1.0$) for the building stiffening.

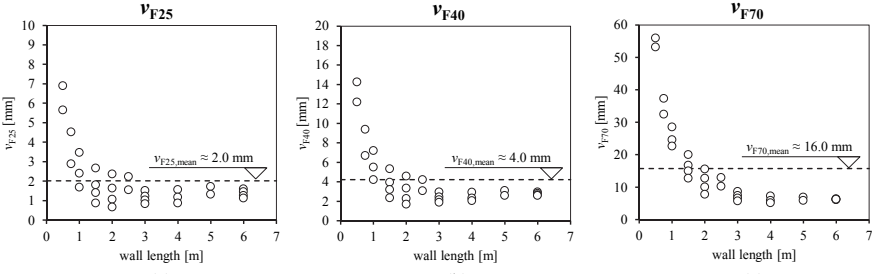

Figure 6.2: head displacement for different load levels – (a) 25 % of F_{max}; (b) 40 % of F_{max}; (c) 70 % of F_{max}

6-2.2 MAGNITUDE OF VERTICAL LOAD

For investigating the influence of vertical loads, 30 further CLT walls with a varying length (1.0 m to 6.0 m) and vertical load (0 kN/m to 50 kN/m), but a constant spacing between the connections ($a_{con} = 1.0$ m) and coefficient of friction ($\mu_f = 0.2$), are analysed. Figure 6.3 illustrates the resulting course

of peak load, initial stiffness and sliding contribution over the walls' length. Since no distinct influences occur, v_{max} is not considered at this juncture.

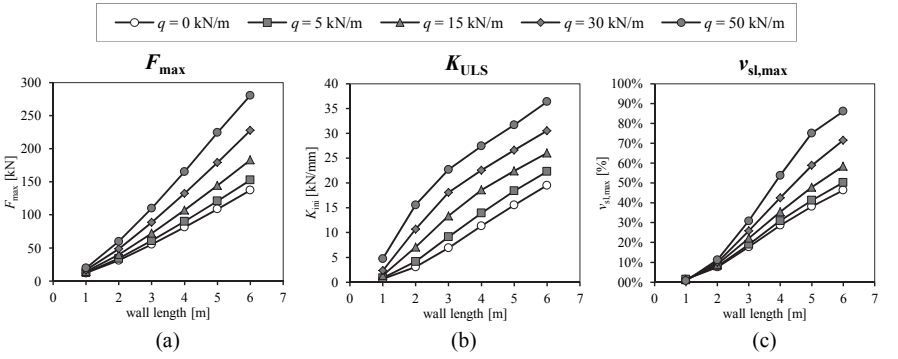

Figure 6.3: influence of vertical load on selected CLT wall parameters – (a) peak load; (b) initial stiffness; (c) sliding contribution to total head deflection

Obviously, increased vertical load results in increased load-carrying capacities and stiffness properties. In particular, a vertical load of 50 kN/m nearly doubles the attainable peak loads compared to the same configurations without a vertical load. Concerning the initial stiffness, an even higher influence is given, whereat this effect decreases for longer walls. Nevertheless, this parameter is still doubled for wall lengths of 6.0 m. A distinct influence of vertical loads is also detected on the contributions to the total head deflection. As a consequence, the *l*/*h* ratio indicating when sliding becomes the controlling mechanism as described afore, has to be reduced for higher vertical loads (e.g. round 1.5 for a vertical load equal to 50 kN/m).

6-2.3 COEFFICIENT OF FRICTION

Friction is a physical reality but, due to its hardly assessable character, it is reluctantly used in design. Nevertheless, to show its possible effect on an analysis, results of in total 48 wall simulations are compared herein. In particular, configurations with varying wall lengths (1.0 m to 6.0 m) and coefficients of friction (0 to 0.3) are simulated. Moreover, two different vertical loads are considered (10 kN/m and 50 kN/m). The distance between the connections is kept constant with 1.0 m.

Figure 6.4 illustrates diagrams, comparing the parameters F_{max}, K_{ULS} and $v_{sl,max}$, depending on the varied boundary conditions; due to minor influence, v_{max} is again neglected. Although friction (in the observed range) does not show an as pronounced influence as the vertical load, it still enables a distinct increase of load-carrying capacity and stiffness. If, as an example, the coefficient of friction is changed from 0.1 to 0.3, walls with a vertical load equal to 10 kN/m show approximately 10 % higher maximum loads. For walls where 50 kN/m are present, even 15 % higher load-carrying capacities occur; compare

Figure 6.4 (a). Concerning the initial stiffness, the same parameter variation leads to approximately 15 % higher results for a vertical load of 10 kN/m. For a vertical load equal to 50 kN/mm, the raise comes close to the factor two; compare Figure 6.4 (b). A varying coefficient of friction also influences the contributions to total head deflection. As expected, the sliding contribution is reduced when a higher coefficient of friction is considered in the calculation. Nevertheless, the influence distinctively decreases with an increasing wall length; see Figure 6.4 (c).

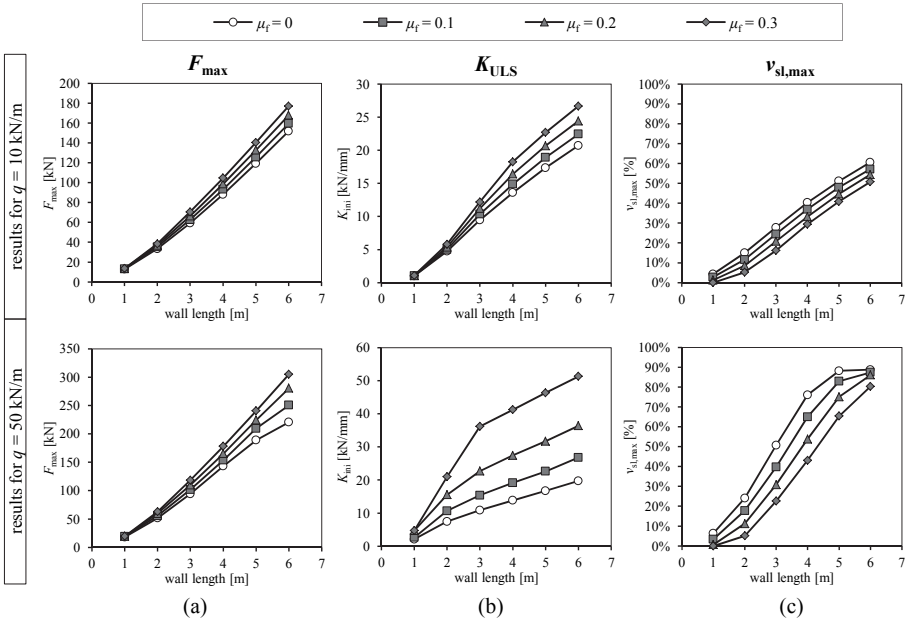

***Figure 6.4:** influence of friction on selected CLT wall parameters under different amounts of vertical load – (a) peak load; (b) initial stiffness; (c) sliding contribution to total head deflection*

6-2.4 CONCLUDING REMARKS

Basing on several wall simulations, the present section briefly discusses the dependency of selected CLT wall properties on diverse boundary conditions. Primarily, it is shown that not only the wall length and number of connections, but also the acting vertical load and friction distinctively influence the behaviour of laterally loaded wall diaphragms. Moreover, it is indicated that the current regulations regarding the acceptable interstorey drift levels might not be valid for CLT structures. Concerning the contributions to total head deflection it turned out that as soon as the wall length exceeds approximately two times the wall height, sliding becomes the controlling mechanism. A further interesting effect is briefly addressed in the following passage.

As already described, the initiation of connection based deflections (i.e., sliding and rocking) is affected by vertical load and friction. Due to this, CLT based deformations (although still small) are predominant at low lateral load levels. Figure 6.5 visualises this circumstance for four different loading levels, considering the results of all herein simulated walls. Focusing on the average values, it can be seen that for loads, satisfying the SLS and ULS conditions (assumed as 25 % and 40 % of F_{max}, respectively), the relative CLT contribution yields to 45 % and 34 % whereat averaged absolute deformations are only 0.6 mm and 1.0 mm. Higher load levels, relevant for accidental load cases, again show more familiar dimensions for this parameter (19 % and 1.8 mm for 70 % of F_{max}; 8 % and 2.6 mm when reaching F_{max}). Nevertheless, this observation shows that a consideration of CLT properties is reasonable if analysing deformations of wall systems. This especially at lower load levels and, at least, as soon as the enhancing effects of vertical load and friction are considered.

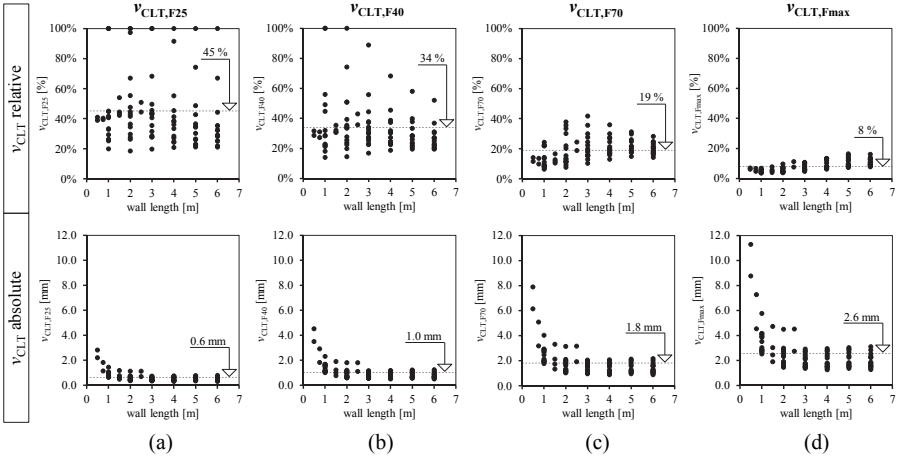

Figure 6.5: ***absolute and relative CLT deformations for different load levels – (a) 25 % of F_{max}; (b) 40 % of F_{max}; (c) 70 % of F_{max}; (d) 100 % of F_{max}***

6-3 VERTICAL JOINTS

Especially for the load case 'earthquake', currently the implementation of vertical joints is seen as an option for enhancing the ductile capacity of CLT structures. This particularly comes out in the proposals for revising Section 8 of Eurocode 8 (*"Specific rules for Timber Buildings"*) as given in Follesa et al. (2011) and Follesa et al. (2015). Following them, for reaching the ductility classification 'high' (DCH), the use of segmented walls is required. Although this approach is in principle comprehensible, the further requirement for connecting the floor elements and the walls underneath with sufficient overstrength has to be seen critically. In particular, due to the stiffness of the floor element and the applied fasteners in the

top joint, an unobstructed displacement of the vertical joints is prevented; compare illustration in Figure 6.6. Hence, neglecting this effect may overestimate the influence of vertical joints on the global behaviour of CLT structures.

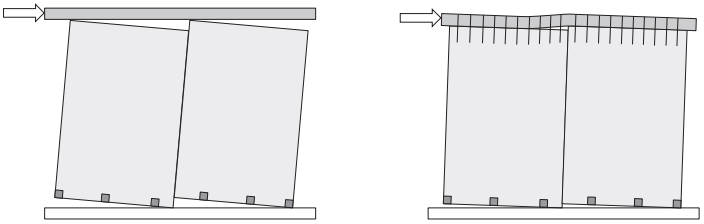

(a) (b)

Figure 6.6: behaviour of a vertical joint – (a) without limitation; (b) reduced deflection due to the influence of the top joint

As a consequence, besides showing the general influence of a vertical joint on a CLT wall system, the top joint effect is spotted as well within the present section.

The basic configuration for the following investigations consists of a segmented CLT wall with 4.0 m in length (two coupled CLT elements with l = 2.0 m each), equipped with 6 equally spaced angle brackets (a_{con} = 0.8 m). As fasteners for the vertical (half-lap) joint are either fully threaded parallel or inclined screws, as documented in sections 5-2.4.3 and 5-2.4.4, respectively, considered. The applied vertical load (20 kN/m) and the coefficient of friction (0.2) are kept constant for all simulations.

Regarding the top joint, two different configurations are considered. Fully and partially threaded screws are used with an equal spacing of 200 mm and 500 mm, respectively. The fully threaded screws are chosen to simulate a top joint with ‘sufficient overstrength’. The partially threaded screws with counter sunk heads, applied with the maximum spacing according to the normative annex K of ON B 1995-1-1 (2015), should represent a lower practical limit. The corresponding floor element is assumed to consist of a five-layered CLT element, owning an equal layer thickness of 30 mm (t_{CLT} = 150 mm); the orientation of the outer layers is assumed to be parallel to the walls surface.

As reference, two additional CLT wall systems are simulated, i.e., an uncoupled (full) CLT wall with 4.0 m in length and a segmented CLT wall without fasteners in both the vertical and the top joint. Table 6.1 gives an overview concerning the finally analysed wall systems and Figure 6.7 visualises the geometric boundary conditions.

Table 6.1: configurations simulated for investigating the influence of vertical joints and the 'top joint effect'

ID	wall	screws in vertical joint		screws in top joint	
		orientation	number	type	spacing
01	uncoupled	-	-	-	-
02	segmented	-	-	-	-
03	segmented	parallel	10	-	-
04	segmented	parallel	20	-	-
05	segmented	parallel	30	-	-
06	segmented	inclined	15 (pairs)	-	-
07	segmented	parallel	20	fully threaded	200 mm
08	segmented	parallel	20	partially threaded	500 mm

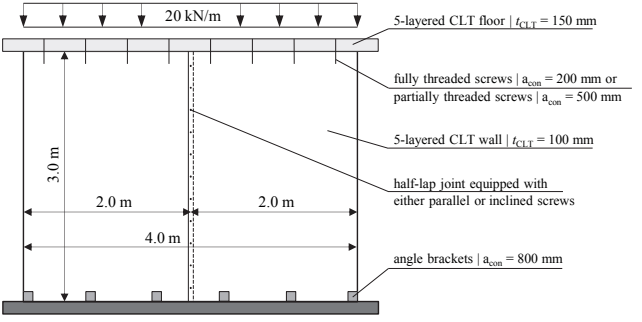

Figure 6.7: geometric boundary conditions for parameter study on vertical joints

Before starting actual wall simulations, the additional stiffness, corresponding to the respective top joint configuration, has to be determined by applying the FE-based procedure already described in section 5-5.1.1. For this purpose, the required input parameters for fully threaded screws are deduced from tests documented in section 5-2.4.2. The behaviour of partially threaded screws is estimated basing on experimental tests published in Gavric (2013). The finally applied input data for the considered fasteners and CLT elements are documented in ANNEX D. In this context it further has to be mentioned that for the FE-simulation a 1.0 m wide CLT floor element is used. Figure 6.8 illustrates the resulting load-displacement curves and the multilinear approximations for the analytical wall model.

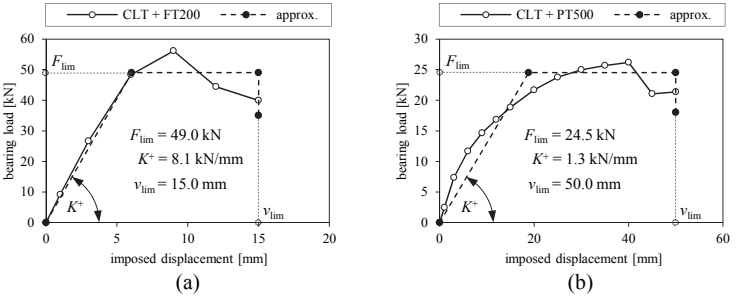

Figure 6.8: multilinear approximation of the ‚top joint effect' – (a) 200 mm spaced fully threaded screws; (b) 500 mm spaced partially threaded screws

Figure 6.9 visualises how a vertical joint (without consideration of the top joint) affects the behaviour of a CLT wall system and principally confirms the declarations described in Follesa et al. (2015). In particular, except the wall, where inclined screws are used to join the two CLT elements, all segmented wall systems exhibit a higher displacement capacity compared to the uncoupled one. Nevertheless, basing on the number of fasteners in the vertical joint, a more or less distinct reduction in load-carrying capacity occurs as well.

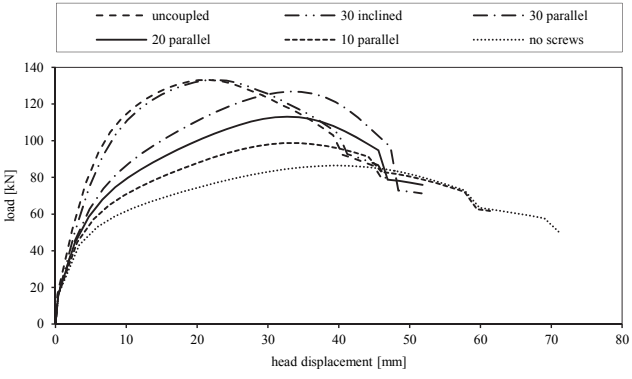

Figure 6.9: general influence of a vertical joint on the load-displacement relationship of a CLT wall system

For illustrating the influence of the top joint, the wall system, in which 20 parallel screws are used for connecting the two wall segments, is spotted. As shown in Figure 6.10, fixing the floor element with partially threaded screws shows a slight increase of load-carrying capacity and exhibits similar capacities for head and vertical joint displacement. However, once boundary conditions for a sufficient overstrength are applied, vertical joint behaviour changes from coupled to single-coupled and distinctively limits its deflection; compare Figure 6.10 (b). As a consequence, although still higher than for the uncoupled wall system, the displacement capacity is reduced in a noticeable way.

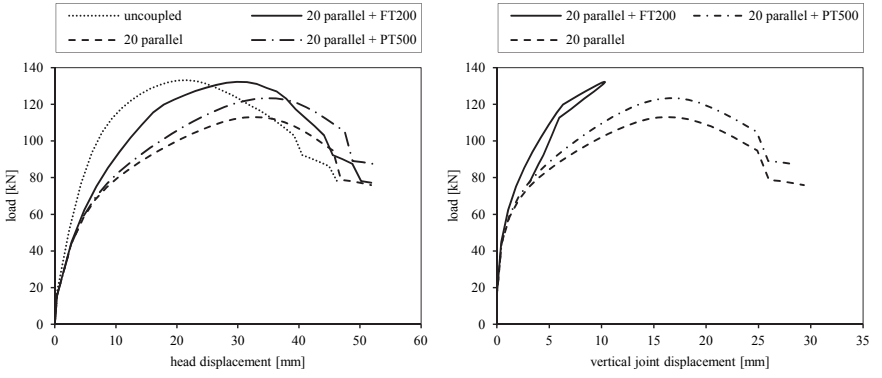

Figure 6.10: top joint effect – (a) change of system behaviour; (b) reduced displacement in vertical joint

Summarising, it can be stated that the implementation of vertical joints indeed has the potential to improve the displacement capacity of long CLT wall systems. However, depending on the design of the vertical as well as the top joint, this effect may be distinctively reduced. Moreover, it has to be considered that the vertical joint can only act as long as rocking occurs. In other words, as soon as rocking is prevented (e.g. by choosing to long segments or in case of high vertical loads), the influence of the vertical joint disappears. As a consequence, solely implementing vertical joints without considering the boundary conditions may lead to a misinterpretation of the actual wall behaviour.

6-4 MODELLING STRUCTURES

So far, the present thesis solely spots single CLT wall systems. Within this section, the presented analytical model is further applied to simulate (i) the load-displacement behaviour of a single-storey structure, including a discussion about the lateral load distribution on considered wall diaphragms, and (ii) the behaviour of a two-storey building, originally examined in Hummel (2016).

6-4.1 SINGLE STOREY STRUCTURE

The present section aims to investigate the influence of connections and wall foundations on the load-displacement behaviour of a single-storey structure. Moreover, the lateral load distribution on wall diaphragms is discussed. For this purpose, the floor plan in Figure 6.11 is used as a reference (storey height is assumed to be equal to 3.0 m). The additionally illustrated columns, and the beam in the middle of the structure, are only responsible for carrying vertical loads and are not considered for lateral load-bearing.

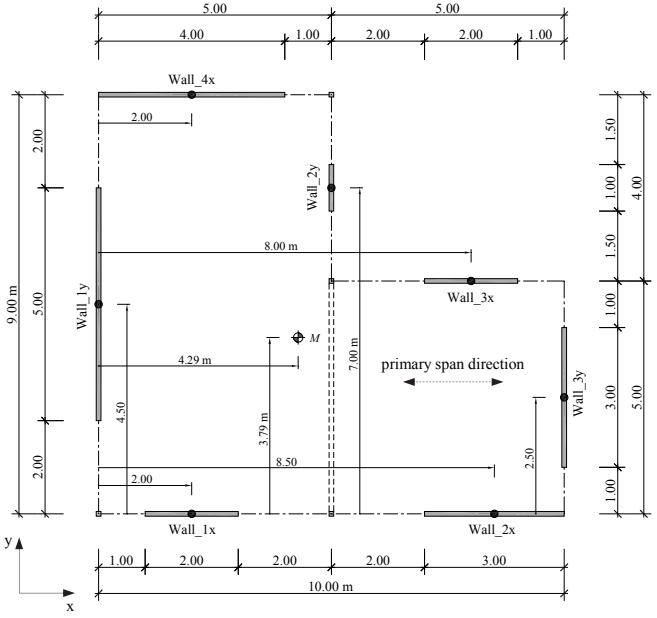

Figure 6.11: floor plan of investigated single-storey structure (assuming an equal distribution of gravity loads, the centre of mass (M) is set equal to the centre of floor area)

Again, five-layered CLT wall elements and the connection properties defined in section 5-2 are used; the vertical loads per wall are listed in Table 6.2. For the sake of simplicity, these values were determined in a FE-study, in which a five-layered CLT ceiling element (primary span in x-direction) was used to distribute the applied vertical surface load of 4.0 kN/m². As additional information, depending on the spacing between them, Table 6.2 lists the number of applied connections per wall.

Table 6.2: length, vertical load and number of applied connections for walls responsible for lateral load transfer

ID	**length** [m]	**vertical load** [kN/m]	**number of applied connections**	
			a_{con} = 1.0 m	a_{con} = 0.5 m
Wall_1x	2.0	9.34	3	5
Wall_2x	3.0	5.87	4	7
Wall_3x	2.0	9.16	3	5
Wall_4x	4.0	4.72	5	9
Wall_1y	5.0	13.39	6	11
Wall_2y	1.0	20.16	2	3
Wall_3y	3.0	10.44	4	7

Table 6.3 summarises the performed simulations and the therein varied parameters, i.e., the spacing between the connections, the type of applied connections and the foundation where the CLT walls are mounted on.

Table 6.3: performed simulations and varied parameters

ID	spacing between connections (a_{con})	type of connections	foundation
SIM_01	1.0 m	HD + AB	
SIM_02	1.0 m	AB	rigid
SIM_03	0.5 m	AB	
SIM_04	1.0 m	HD + AB	
SIM_05	1.0 m	AB	CLT
SIM_06	0.5 m	AB	

Note: If considered, in maximum two hold-downs (HD) are used per wall (one at each corner).

6-4.1.1 Generating and comparing pushover curves

The herein compared load-displacement curves of the single-storey structure (also referred to as capacity or pushover curves), are all generated with the same procedure. In particular, assuming a rigid floor element, all wall systems (in the respective direction) are forced to exhibit the same lateral deflection. As a consequence, determining the corresponding load for a defined 'storey deflection', the reacting forces of the involved wall systems, at the same deflection level, have to be summed-up. Repeating this analysis several times, finally leads to the achieved load-displacement relationship of the structure; compare schematic illustration in Figure 6.12. It is important to mention that pushover curves, determined by means of this simplified approach, do not consider any torsional effects.

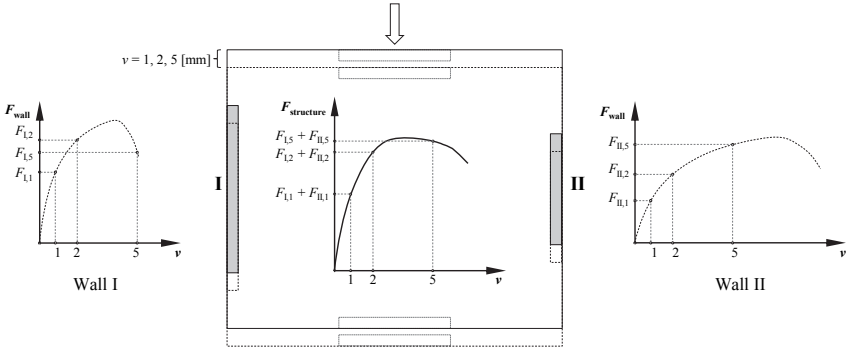

Figure 6.12: schematic illustration of how pushover curves may be determined in a simplified manner; torsional effects are neglected

Figure 6.13 illustrates the resulting pushover curves in x-direction for the single-storey structure shown in Figure 6.11. The behaviour for simulations 01, 02 and 03 (rigid foundation) are plotted in

Figure 6.13 (a), whereas Figure 6.13 (b) shows a comparison between simulations 04, 05 and 06 (CLT foundation).

As can be seen, assuming a rigid (concrete) foundation, where angle brackets are able to carry an essential amount of uplift loads, the implementation of hold-downs do not show a major influence; compare SIM_01 and SIM_02. However, reducing the distance between the connections (without hold-downs), distinctively increases the load-carrying capacity and stiffness of the structure (SIM_03).

As expectable, increasing the number of connections also improves the load-carrying capacity and stiffness when CLT is used as foundation; compare SIM_05 and SIM_06 in Figure 6.13 (b). Moreover, due to the low vertical load-bearing capacity of angle brackets fixed with nails on the CLT floor, in this case, a consideration of hold-downs is more efficient. This is illustrated by SIM_04, which exhibits distinctively higher load-carrying and displacement capacities and actually shows a similar behaviour as resulting from simulations 01 and 02 (rigid foundation). Nevertheless, it is conceivable that the use of screws, instead of nails, for fixing the angle brackets on the CLT floor element, may result in an improved wall behaviour as well; compare remarks in section 5-2.2.4. Hence, it may be stated that classical hold-downs are not necessary as soon as connection systems with an adequate capacity against both shear and uplift are applied.

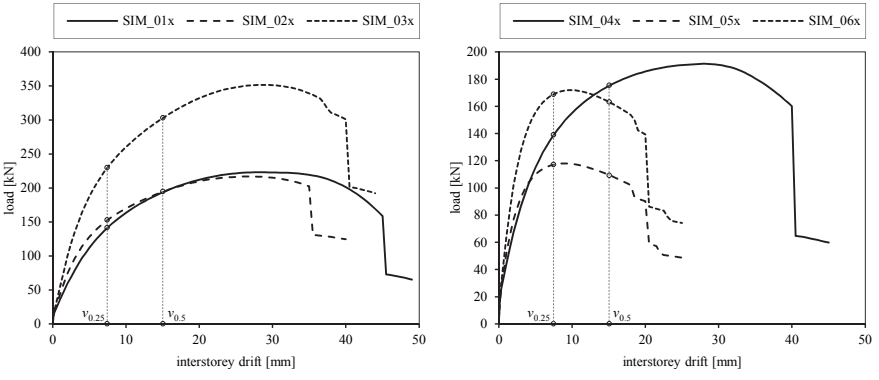

Figure 6.13: load-displacement behaviour of the single-storey structure in x-direction – (a) for simulations 01, 02 and 03; (b) for simulations 04, 05 and 06

Besides the global load-bearing behaviour, Figure 6.13 also includes interstorey drift borders equal to 0.25 % and 0.50 % of walls' height (7.5 mm and 15.0 mm, respectively). As can be seen, the occurring loads at the considered displacement levels are already quite high, i.e., 64 % to 99 % of respective peak load when reaching the 0.25 % level. This confirms the doubts concerning the damage limitation criteria for CLT structures exceeding an interstorey drift of 0.5 %; compare discussion in section 6-2.1.

6-4.1.2 Lateral load distribution on single wall diaphragms

In general, the distribution of lateral loads primary depends on the stiffness of single wall diaphragms and the geometry of the analysed structure. Considering only the structural eccentricity and taking the lower left corner of the reference structure as the origin, actual wall loads, basing on an applied external force $F_{x(y)}$, may be determined as given in Equations (6.1) to (6.6); see also ON B 1998-1 (2011), Schickhofer and Ringhofer (2011) or Bachmann (2002).

$$x_S = \frac{\sum\left(K_{y,i} \cdot x_i\right)}{\sum\left(K_{y,i}\right)} \tag{6.1}$$

$$y_S = \frac{\sum\left(K_{x,i} \cdot y_i\right)}{\sum\left(K_{x,i}\right)} \tag{6.2}$$

$$e_{0,x} = x_M - x_S \tag{6.3}$$

$$e_{0,y} = y_M - y_S \tag{6.4}$$

$$F_{x,r} = F_x \cdot \frac{K_{x,r}}{\sum\left(K_{x,i}\right)} + \frac{K_{x,r} \cdot y'_r}{\sum\left(K_{y,i} \cdot x'^2_i\right) + \sum\left(K_{x,i} \cdot y'^2_i\right)} \cdot \left(F_x \cdot e_{0,y} - F_y \cdot e_{0,x}\right) \tag{6.5}$$

$$F_{y,k} = F_y \cdot \frac{K_{y,k}}{\sum\left(K_{y,i}\right)} + \frac{K_{y,k} \cdot x'_k}{\sum\left(K_{y,i} \cdot x'^2_i\right) + \sum\left(K_{x,i} \cdot y'^2_i\right)} \cdot \left(F_y \cdot e_{0,x} - F_x \cdot e_{0,y}\right) \tag{6.6}$$

with

x, y ..... coordinates for the centre of a single wall system
x_M, y_M ..... coordinates for the centre of mass (x_M = 4.29 m, y_M = 3.79 m; compare Figure 6.11)
x_S, y_S ..... coordinates for the centre of stiffness
x', y' ..... coordinates for the centre of a single wall system in relation to the centre of stiffness
$e_{0,x(y)}$ ..... distance between the centre of stiffness and the centre of mass (structural eccentricity)
$F_{x(y)}$ ..... applied later load in $x(y)$-direction
$F_{x(y),r(k)}$ ..... lateral load to be transmitted by wall $r(k)$ in $x(y)$-direction
$K_{x(y)}$ ..... respective wall stiffness in $x(y)$-direction

A widely accepted (simplified) method for distributing lateral loads in concrete structures bases on the bending stiffness of the wall diaphragms, assuming them as a cantilever; compare Bachmann (2002). Hence, neglecting the shear stiffness and assuming an equal wall thickness, the stiffness of wall diaphragms can be estimated proportional to their length powered by three (l^3). Nevertheless, due to the high influence of connection technique, it can be shown that this approach is not sufficient for CLT wall systems and consequently not considered in further discussions.

A simplified method for CLT structures is given in Wallner-Novak et al. (2013). Basing on comparative calculations on CLT walls equipped with angle brackets and hold downs, the authors propose to estimate walls' stiffness proportional to their length powered by 1.5 ($l^{1.5}$). However, this approach does also not consider the number of connections, or any other influencing factor described in section 6-2.

More complex, but probably the most reliable access for predicting lateral load distribution, is the consideration of effective wall stiffness at the relevant lateral deflection level ($F(v)/v$). As an alternative, of course, the initial wall stiffness can be used as well. Although the latter approach enables a consideration of several influencing factors, it also postulates that all wall systems remain in their (quasi) linear elastic branch and nonlinear effects are neglected.

To compare the capability of the described approaches, the distribution of lateral loads in the reference structure is determined for two different configurations. Case (i) considers the boundary conditions of SIM_02, i.e., a rigid foundation and equally spaced angle brackets (a_{con} = 1.0 m). Case (ii) also assumes a rigid foundation and uses only angle brackets, but the distance between the connections is reduced to 0.5 m for Walls 2x, 1y and 3y. For both scenarios, the lateral loads to be distributed do base on an assumed interstorey drift equal to 0.25 % of walls' height (7.5 mm) and are determined as described in section 6-4.1.1. The resulting loads in x- and y-direction can, hence, be detected as F_x = 153 kN and F_y = 167 kN for case (i) and F_x = 175 kN and F_y = 245 kN for case (ii).

The resulting lateral loads per wall and the respective centres of stiffness for the compared distribution models (effective stiffness at 0.25 % interstorey drift $K_{0.25}$, initial stiffness K_{ULS} and proportional stiffness $l^{1.5}$) are visualised in Figure 6.14.

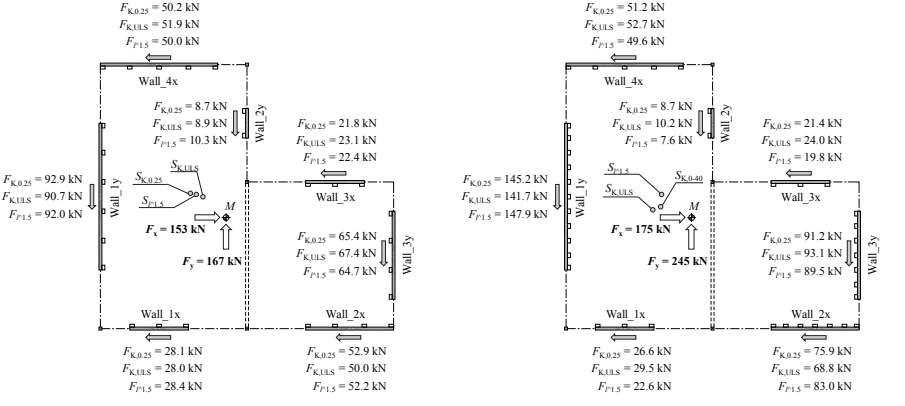

Figure 6.14: distribution of lateral loads on shear walls – (a) case (i): equal distance between connections; (b) case (ii): reduced distance between connections for Wall_2x, Wall_1y and Wall_3y

As can be seen, differences between lateral loads at case (i) are marginal. Assuming that the displacement-based procedure offers the 'real' occurring loads, only Wall_2y exhibits a mentionable overestimation by the simplified ($l^{1.5}$) approach. For case (ii), however, the application of initial stiffness and the length based model lead to deviations up to approximately 18 %; interestingly enough, in opposite directions. Due to this, and further considering the findings in section 6-2, it is suggested to limit the use of simplified models to predesigns and CLT structures, where connections with comparable properties and spacings, as well as similar vertical loads within one floor are ensured; see also Flatscher and Schickhofer (2016). A more detailed analysis is recommended for complex systems.

One point which shall be kept in mind in any case, is the distinct reduction of effective stiffness at higher lateral load (or displacement) levels. This effect is documented in Table 6.4 for the present example, where differences between the initial (K_{ULS}) and the effective ($K_{0.25}$) stiffness of up to 44 % occur (averaged reduction from initial to effective stiffness ~ 37 %).

Table 6.4: reduction of effective stiffness for higher load (or displacement) levels

ID	case (i)			case (ii)		
	K_{ULS} [kN/mm]	$K_{0.25}$ [kN/mm]	Δ [-]	K_{ULS} [kN/mm]	$K_{0.25}$ [kN/mm]	Δ [-]
Wall_1x	5.181	2.986	-42%	5.181	2.986	-42%
Wall_2x	9.247	5.619	-39%	12.079	8.518	-29%
Wall_3x	5.128	2.972	-42%	5.128	2.972	-42%
Wall_4x	13.696	8.808	-36%	13.696	8.808	-36%
Wall_1y	21.741	14.910	-31%	29.450	22.375	-24%
Wall_2y	1.751	1.054	-40%	1.751	1.054	-40%
Wall_3y	11.292	6.321	-44%	13.567	9.177	-32%

6-4.2 TWO-STOREY STRUCTURE

Even though primarily not intended, in a simplified manner, the current wall model may also be used for determining the capacity curve of a multi-storey structure. For this purpose, in principle two steps are necessary. Firstly, the load-displacement relationship of every single floor has to be computed. This can be realised by applying the procedure described in section 6-4.1.1. In this case, it is imported to apply the load eccentricities, matched for considering the moments being generated from the floors above; see effective heights of load application (h_{load}) in Figure 6.15.

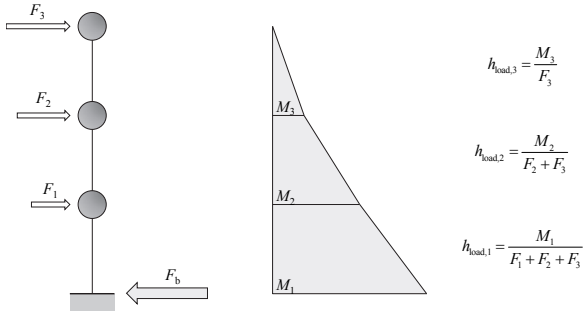

Figure 6.15: determining effective heights of load application

Secondly, the lateral loads are applied and the corresponding displacements per floor can be readout from 'local' pushover diagrams processed before. The sum of these displacements results in the top displacement of the structure, which finally can be plotted against the base-shear (F_b). It has to be noted that the force-based nature of the second step restricts this approach to the increasing branch of the capacity curve, i.e., post peak building behaviour cannot be simulated.

For the demonstration of the described procedure, the two-storey structure, investigated in Hummel (2016), is used as a reference. In particular, the 'shear wall type' (SWT) building with 'single wall elements' (SWE), is remodelled.

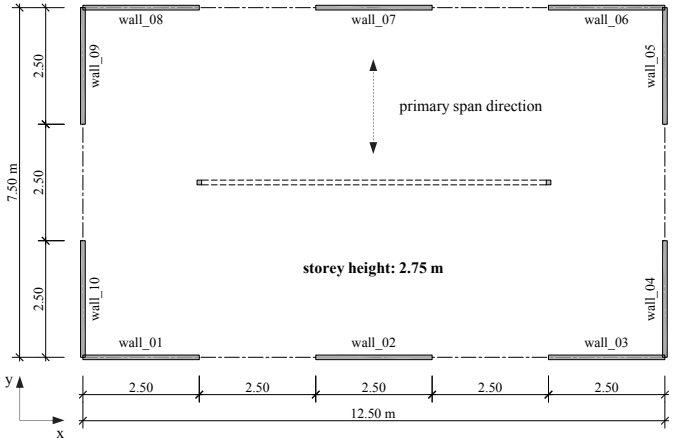

Figure 6.16: floor plan of two-storey structure, Hummel (2016) – revised

Figure 6.16 illustrates the floor plan of the considered structure (storey height equal to 2.75 m) and Table 6.5 lists the applied connections. For simulating them, the connection properties determined from the single joint tests performed at the University of Kassel (compare section 5-4.2), are used. Since angle brackets are only partially scheduled in the second floor, here the lateral load-carrying capacity of hold-

downs is set equal to the corresponding behaviour in the wall-to-foundation joint. For simulating the screws, respective parameters are taken from TU Graz data sets as documented in 5-2.4.

Table 6.5: connections per wall according to Hummel (2016)

	walls in x-direction		**walls in y-direction**	
	bottom joint	top joint	bottom joint	top joint
1st floor	2 HD + 1 AB	9 screws	4 HD + 1 AB	11 screws
2nd floor	2 HD	3 screws	2 HD + 1 AB	7 screws

Note: If four hold-downs (HD) are used, two are located at each corner. All screws are applied without inclinations.

The vertical loads acting on the walls were, once more, determined in a preliminary FE-study, using the layups and loads documented in Hummel (2016). Particularly, a roof load of 1.0 kN/m², a load on the floor slab of 3.36 kN/m² and a gravity load per wall equal to 4.13 kN/m is considered. The resulting vertical loads per wall are summarised in Table 6.6.

Table 6.6: vertical load on considered shear walls taken from the FE-study

	1st floor [kN/m]	**2nd floor** [kN/m]
wall_01; wall_03; wall_06; wall_08	16.76	6.08
wall_02; wall_07	25.39	8.06
wall_04; wall_05; wall_09; wall_10	13.06	5.23

For determining the external forces to be applied on the structure, according to Hummel (2016), lumped masses of 14.8 t and 42.6 t at the roof and floor slab level are assumed, respectively. Moreover, a linear load pattern is applied. The resulting load relations and eccentricities are given in Figure 6.17.

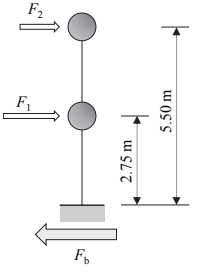

$$F_2 = F_b \cdot \frac{z_2 \cdot m_2}{\sum(z_i \cdot m_i)} = F_b \cdot \frac{5.5 \cdot 14.8}{5.5 \cdot 14.8 + 2.75 \cdot 42.6} = F_b \cdot 0.41$$

$$h_{load,2} = \frac{M_2}{F_2} = \frac{F_b \cdot 0.41 \cdot 2.75}{F_b \cdot 0.41} = 2.75\,\text{m}$$

$$F_1 = F_b \cdot \frac{z_1 \cdot m_1}{\sum(z_i \cdot m_i)} = F_b \cdot \frac{2.75 \cdot 42.6}{5.5 \cdot 14.8 + 2.75 \cdot 42.6} = F_b \cdot 0.59$$

$$h_{load,1} = \frac{M_1}{F_1 + F_2} = \frac{F_b \cdot 0.41 \cdot 5.5 + F_b \cdot 0.59 \cdot 2.75}{F_b \cdot 0.41 + F_b \cdot 0.59} = 3.88\,\text{m}$$

Figure 6.17: load relations and eccentricities for a linear load pattern

For enabling a direct comparison with the original capacity curves published in Hummel (2016), two further conditions are considered while performing the simulations. In particular, the influence of friction is neglected and due to an assumed (sufficient) overstrength against uplift, deflections of top joints (equipped with screws) are limited to sliding. The latter condition also excludes the described issues when simulating screwed joints; compare section 5-5.1.1.

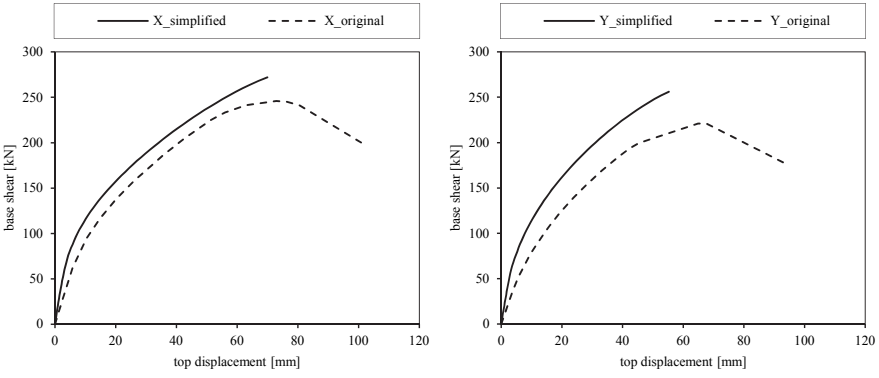

(a) (b)

Figure 6.18: comparison of simplified and original capacity curves of the two-storey structure (SWT | SWE) described in Hummel (2016) – (a) in x-direction; (b) in y-direction

Although similar in shape, the here simulated pushover curves for the x- and y-direction exhibit a stiffer structural behaviour compared to the original one; compare Figure 6.18. The reason can be seen in the inability of the simplified procedure to consider 'global' effects as, e.g., the bending stiffness of floor diaphragms between the wall segments, or the influence of the overturning moment on vertical load distributions. Especially the latter point is supported by the higher deviations in y-direction, where the external lever arm is shorter. Moreover, an additionally performed simulation of the four-storey structure documented in Hummel (2016), further confirms this assumption with exhibiting unacceptable differences compared to the original capacity curves.

As a consequence, it has to be stated that the simplified wall-based approach in its present form, is not applicable for extensive structural modelling; this, especially for buildings, where the structural height-to-length (or width) ratio becomes higher than 0.5. In such cases, either additional calculation steps (e.g., reduction of vertical load – even to the negative range – according to the respective position of the wall and the acting overturning moment) or a finite element analysis is recommended.

6-5 INTERMEDIATE CONCLUSIONS

Within this chapter, the displacement-based wall model is initially applied to investigate how different influencing factors may affect the main properties of a CLT wall system. In particular, the effects of wall length, the distance between the applied connections, acting of vertical loads and friction are spotted. According to this parameter study, it can be concluded that especially the first three aspects exhibit a distinct influence on the load-carrying capacity and the initial stiffness of the wall systems. Moreover, it is shown that current regulations regarding acceptable interstorey drift levels may not be valid for CLT

structures. As a consequence, achieving an effective damage limitation, it is recommended to limit the corresponding deflections to an amount not higher than 0.5 % of the interstorey height.

A further section focuses on the possible effect of vertical joints on the load-displacement relationship of CLT wall systems. Regarding this topic, it can be stated that an implementation of vertical joints principally enables a higher displacement capacity with a concurrent loss of load-carrying capacity and stiffness. It is also shown that this behaviour is distinctively affected by the applied connections (fasteners) in the vertical and top joint. Especially the implementation of inclined (fully threaded) screws in the vertical joint, or a top joint designed with overstrength, may reduce the achieved effect in a distinct manner.

The third part of this chapter primarily deals with the behaviour of a single storey structure. Thereby, it is shown that classical hold-downs are not necessarily required for CLT buildings as soon as connections able to carry shear and uplift loads are applied. Moreover, investigations concerning the lateral load distribution on single wall diaphragms have shown that simplified approaches are applicable for predesigns and structures where vertical loads and the type as well as the spacing of connections, do not exhibit higher variations within one floor. Elsewise, a more detailed analysis is recommended.

Finally the quality of the analytical model for computing the capacity curve of a multi-storey structure is examined. Although, it is generally working, due to a missing possibility of the wall-based analysis to consider global effects, this approach is not recommended to be applied for extensive structural modelling.

CHAPTER 7
CONCLUSIONS

7-1 SUMMARY

The present thesis deals with two core topics, finally achieving a comprehensive description of CLT wall systems. In particular, due to their major influence, initially the evaluation and approximation of timber connection properties are spotted. Subsequently, the focus is set on modelling and discussing the load-displacement relationship of entire CLT wall systems. The following passages offer a brief summary of the presented contents and major findings.

At the beginning, an extensive literature review concerning international post-processing models is conducted. Here, approximately ten methods for defining the initial stiffness and the yield point, and about 20 approaches to convey the ductile capacity of timber joints are compared and discussed. As documented, partially huge differences between the investigated methods are recognized. Moreover, the circumstance that most ductility models relate to the yield point, and some approaches describing the yield point rely on the initial stiffness, illustrates the appearing issues when comparing connection parameters, gathered from different research facilities. Hence, basing on an analysis of pros and cons of the various models, alternative approaches for defining the initial stiffness (basing on the relevant load levels) and the ductility (independent from initial stiffness and yield point) are suggested.

Although satisfying the requirements for a linear elastic analysis, single properties do hardly enable a proper consideration of connections' behaviour in more sophisticated calculation models. Thus, a further literature survey on analytical models, applicable for approximating the load-displacement relationship of timber joints, is conducted. As it turned out, most of the round 35 considered curve models primarily focus on describing the section up to the peak load and neglect the post maximum softening branch. Moreover, a satisfying approximation of load-displacement curves, deviating from conventional round shapes, is hardly possible with these models. Hence, basing on an already existing rational function, a new displacement-based approach is developed. The resulting six-parameter model enables to simulate the entire course of even complex load-displacement relationships with high accuracy. Consequently, besides enabling a proper consideration of connections' behaviour in nonlinear calculation models, this method further allows an effective documentation of load-displacement graphs (even in printed publications). To exemplify this quality, all experimental tests, discussed in the present thesis, are documented in this way.

To start the discussion on CLT wall systems, a summary concerning currently applied calculation models is presented. Here, it turns out that the corresponding offer is limited and mainly force-based methods are available. Due to this, subsequently a new displacement-based approach, using the approximation model suggested afore to implement the connections' behaviour, is introduced. For proofing its actual qualities, in a further step, the output of the proposed wall model is compared to experimental test results, gathered from three independent research facilities and some FE simulations. In total, 34 wall systems with varying geometries, connections and vertical loads are investigated. The outcome of this validation process is generally positive and, hence, permits the use of the suggested model for the subsequently performed parameter study.

Within this final part of the present thesis, the influence of several factors on the behaviour of CLT wall systems is examined. In particular, it is shown that the wall length, the distance between applied connections and the acting vertical load do play an important role, when evaluating the load-carrying capacity and the initial stiffness. Concerning the contributions to total head deflection, it is found that for walls with an l/h ratio higher than two, sliding becomes the controlling mechanism. Moreover, due to the gathered results it is recommended to limit the acceptable (damage limiting) interstorey drift for CLT structures to an amount not higher than 0.5 % of the respective storey height. A further performed study spots the possible influence of vertical joints. Here, it is shown that such joints indeed have the potential to increase the displacement capacity of CLT wall systems. Nevertheless, for a reliable analysis of their actual benefit, the consideration of the top joint effect, the geometry and the acting vertical loads is required.

The proposed wall model is also applied for analysing whole structures. In this context, is illustrated that classical hold-downs may be omitted in CLT structures, where connections with an adequate bearing-capacity against both shear and uplift loads are applied. An additional discussion concerning the lateral load distribution on wall diaphragms shows that for defined boundary conditions even simplified methods may lead to an acceptable result – for more complex situations, a detailed analysis is recommended.

For testing the limits of the wall-based analysis, finally the capacity curve of a two-storey structure is generated. Although generally working, it gets obvious that global effects may hardly be considered by this simplified approach. Hence, for structures with a height-to-length (or width) ratio higher than 0.5, more detailed analyses are necessary.

7-2 OUTLOOK

The presented investigations on post-processing methods clearly demonstrate the occurring issues for data exchange between international research facilities. Moreover, also practical questions concerning the applicability of connections for defined purposes (keyword: ductility), may be affected. Especially nowadays, where international collaborations are rather usual than unusual, in the opinion of the author a widely accepted consensus regarding data post-processing and interpretation is desirable. The herein proposed approaches regarding initial stiffness, ductility and test curve approximation may represent a possible basis, but a further broad discussion concerning this topic is highly recommended.

Spotting the discussion on CLT wall systems, the suggested displacement-based model offers a capable tool for analysing the general behaviour of various wall configurations. Nevertheless, further research regarding the influence of openings, flexible foundations and – in the first instance – surrounding structural elements is recommended. In particular, the effects of perpendicular walls, as well as the interaction between separated wall elements and the floor structure, on the global behaviour of CLT buildings, are still open questions. Answering them, may enable to define simplified rules for designing even mid-rise structures without applying sophisticated (i.e., FE-based) calculation models.

Finally, rather a practical than a scientific issue can be seen in the circumstance that rarely information is available regarding the stiffness of frequently applied connection systems. Since quite important for designing CLT structures, it is suggested to implement this parameter in prospective approvals; at least as soon as the respective connections are designated to be applied in CLT structures.

ANNEX A REGISTER

A-1 References

Abdulrahman, N. (2002), Load transfer mechanism in punched metal plate timber connections, Doctoral thesis, Napier University, Edinburgh, U.K.

AlHendi, H. and Celikag, M. (2015), 'Finite element prediction of reverse channel connections to tubular columns behavior', *Engineering Structures* **100**, 599–609.

ASTM D5652 (2013), 'Standard test methods for bolted connections in wood and wood-based products'.

ASTM D5764 (2002), 'Standard test method for evaluating dowel-bearing strength of wood and wood-based products'.

ASTM E2126 (2011), 'Standard test methods for cyclic (reversed) load test for shear resistance of vertical elements of the lateral force resisting systems for buildings'.

ASTM E6 (2003), 'Standard terminology relating to methods of mechanical testing'.

ATC (1992), Guidelines for cyclic seismic testing of components of steel structures, Technical Report ATC-24, Applied Technology Council, Redwood City, California, U.S.A.

Bachmann, H. (2002), *Erdbebensicherung von Bauwerken*, 2 edn, Birkhäuser Verlag, Zürich, Switzerland. ISBN: 3-7643-6941-8; (in German).

Blaß, H. J. (1990), Load distribution in nailed joints, *in* 'Proceedings of the 23th CIB W18 Meeting - CIB-W18/23-7-2', Lisbon, Portugal.

Blaß, H. J. (1991), 'Traglastberechnung von Nagelverbindungen', *Holz als Roh- und Werkstoff* **49**(3), 91–98. (in German).

Blaß, H. J. and Fellmoser, P. (2004), Design of solid wood panels with cross layers, *in* 'Proceedings of the 8th World Conference on Timber Engineering WCTE2004', Lahti, Finland.

Bogensperger, T., Moosbrugger, T. and Silly, G. (2010), Verification of CLT-plates under loads in plane, *in* 'Proceedings of the 11th World Conference on Timber Engineering WCTE2010', Riva del Garda, Italy.

Bogensperger, T. and Silly, G. (2014), 'Zweiachsige Lastabtragung von Brettsperrholzplatten', *Bautechnik* **91**(10), 742–752. (in German).

Boresi, A. P., Chong, K. P. and Lee, J. D. (2011), *Elasticity in engineering mechanics*, Vol. 3, John Wiley and Sons, Inc., U.S.A.

Bosco, M., Ferrara, E., Ghersi, A., Marino, E. M. and Rossi, P. P. (2014), Improvement of the model proposed by Menegotto and Pinto for steel, *in* 'Proceedings of the 2nd European conference on earthquake engineering and seismology', Istanbul, Turkey.

Brandner, R. (2012), Stochastic system actions and effects in engineered timber products and structures, Doctoral thesis, Graz University of Technology, Graz, Austria.

Brandner, R., Flatscher, G., Ringhofer, A., Schickhofer, G. and Thiel, A. (2016), 'Cross laminated timber (CLT) - overview and development', *European Journal of Wood and Wood Products* **74**(3), 331–351.

Brandner, R., Ringhofer, A. and Grabner, M. (2017), 'Probabilistic models for the withdrawal behaviour of single self-tapping screws in the narrow face of cross laminated timber (CLT)', *European Journal of Wood and Wood Products* . (accepted).

Brandner, R. and Schickhofer, G. (2014), Properties of cross laminated timber (CLT) in compression perpendicular to grain, *in* 'Proceedings of the 1st INTER Meeting - INTER/47-12-5', Bath, United Kingdom.

Bratulic, K., Flatscher, G. and Brandner, R. (2014a), Monotonic and cyclic behaviour of joints with self-tapping screws in CLT structures, *in* K.-U. Schober, ed., 'COST Action FP1004, Experimental Research with Timber', University of Bath, Prague, Czech Republic, pp. 1–8.

Bratulic, K., Flatscher, G., Brandner, R., Augustin, M. and Schickhofer, G. (2014b), Monotones und zyklisches Verhalten von Schraubenverbindungen in BSP-Strukturen, technical report SGSC 3.1.1_2, holz.bau forschungs gmbh, Graz, Austria. unpublished, (in German).

Brühl, F. (2013), Duktile Verbindungen im Holzbau, *in* '19. Internationales Holzbau-Forum 2013', Vol. I Prolog IV, Garmisch-Partenkirchen. (in German).

Brühl, F. and Kuhlmann, U. (2012), Requirements on ductility in timber structures, *in* 'Proceedings of the 45th CIB W18 Meeting - CIB-W18/45-7-5', Växjö, Sweden.

Brühl, F., Kuhlmann, U. and Jorissen, A. (2011), 'Consideration of plasticity within the design of timber structures due to connection ductility', *Engineering Structures* **33**(11), 3007–3017.

Casagrande, D., Rossi, S., Sartori, T. and Tomasi, R. (2012), Analytical and numerical analysis of timber framed shear walls, *in* 'Proceedings of the 12th World Conference on Timber Engineering WCTE2012', Auckland, New Zealand.

Casagrande, D., Rossi, S., Sartori, T. and Tomasi, R. (2016), 'Proposal of an analytical procedure and a simplified numerical model for elastic response of single-storey timber shear-walls', *Construction and Building Materials* **102**, 1101–1112.

CEB (1993), *CEB-FIP Model Code 1990: Design Code*, number 213/214, T. Telford. Comite Euro International Du Beton (CEB).

Ceccotti, A. (2008), 'New technologies for construction of medium-rise buildings in seismic regions: The XLAM case', *Structural Engineering International: Journal of the International Association for Bridge and Structural Engineering (IABSE)* **18**(2), 156–165.

Ceccotti, A., Follesa, M., Lauriola, M. P., Sandhaas, C., Minowa, C., Kawai, N. and Yasumura, M. (2006), Which Seismic Behaviour Factor for Multi-Storey Buildings made of Cross-Laminated Wooden Panels?, *in* 'Proceedings of the 39th CIB W18 Meeting - CIB-W18/39-15-4', Florence, Italy.

Ceccotti, A., Lauriola, M. P., Pinna, M. and Sandhaas, C. (2006a), SOFIE Project - Cyclic tests on cross-laminated wooden panels, *in* D. A. Bender, D. S. Gromala and D. V. Rosowsky, eds, 'Proceedings of the 9th World Conference on Timber Engineering WCTE2006', Portland, OR, USA.

Ceccotti, A., Sandhaas, C., Okabe, M., Yasumura, M., Minowa, C. and Kawai, N. (2013), 'SOFIE project - 3D shaking table test on a seven-storey full-scale cross-laminated timber building', *Earthquake Engineering & Structural Dynamics* **42**, 2003–2021.

Chen, W.-F. and Kishi, N. (1989), 'Semirigid steel beam-to-column connections: data base and modeling', *Journal of Structural Engineering* **115**(1), 105–119.

Chenaghlou, M. R. (1997), Semi-Rigidity of Connections in Space Structures, Doctoral thesis, University of Surrey - Department of Civil Engineering, Surrey, United Kingdom.

Chisala, M. L. (1999), 'Modelling M-R curves for standard beam-to-column connections', *Engineering Structures* **21**, 1066–1075.

Christensen, R. M. (2008), 'Observations on the definition of yield stress', *Acta Mechanica* **196**(3-4), 239–244.

Christensen, R. M. (2011), 'X. Defining yield stress and failure stress (strength)'. read online 26.May 2015. www.failurecriteria.com

Conners, T. E. (1989), 'Segmented models for stress-strain diagrams', *Wood Science and Technology* **23**, 65–73.

CUAP 06.03/08 (2010), 'Self-tapping screws for use in timber constructions'.

Diaz, C., Marti, P., Victoria, M. and Querin, O. M. (2011), 'Review on the modelling of joint behaviour in steel frames', *Journal of Constructional Steel Research* **67**, 741–758.

DIN 1052 (2008), 'DIN 1052: Design of timber structures - General rules and rules for buildings'. (in German).

Dolan, D. J. (1993), Proposed test method for dynamic properties of connections assembled with mechanical fasteners, *in* 'Proceedings of the 26th CIB W18 Meeting - CIB-W18/26-7-1', Athens, Georgia, USA.

Dolan, D. J., Blaß, H. J., Ceccotti, A., Dyrbye, C., Gnuschke, M., Hansen, K. F., Nielsen, J., Ohlsson, S., Parche, M., Reyer, E., Stieda, C. K. A., Vergne, A., Vignoli, A. and Yasumura, M. (1994), 'Timber structures in seismic regions - RILEM State-of-the-art Report', *Materials and Structures* **27**, 157–184.

Dorn, M., de Borst, K. and Eberhardsteiner, J. (2013), 'Experiments on dowel-type timber connections', *Engineering Structures* **47**, 67–80.

Dujic, B., Aicher, S. and Zarnic, R. (2005), Racking of Wooden Walls exposed to Different Boundary Conditions, *in* 'Proceedings of the 38th CIB W18 Meeting - CIB-W18/38-15-6', Stuttgart, Germany.

Dujic, B., Klobcar, S. and Zarnic, R. (2007), Influence of Openings on Shear Capacity of Wooden Walls, *in* 'Proceedings of the 40th CIB W18 Meeting - CIB-W18/40-15-6', Bled, Slovenia.

Dujic, B., Strus, K., Zarnic, R. and Ceccotti, A. (2010), Prediction of dynamic response of a 7-storey massive XLam wooden building tested on a shaking table, *in* 'Proceedings of the 11th World Conference on Timber Engineering WCTE2010', Vol. 4, Trentino, pp. 3450–3457.

Ehlbeck, J. (1979), Nailed joints in wood structures, Technical Report 166, Virginia Polytechnic Institute and State University, Blacksburg, Virginia, USA.

Ehlbeck, J. and Larsen, H. J. (1993), Eurocode 5 - Design of Timber Structures: Joints, *in* 'International workshop on wood connectors', Forest Products Society, Madison, USA, pp. 9–23. ISBN (print): 0935018565, 978-0935018561.

Ehlbeck, J. and Werner, H. (1988*a*), Design of joints with laterally loaded dowels - Proposals for improving the design rules in the CIB-Code and the draft Eurocode 5, *in* 'Proceedings of the 21th CIB W18 Meeting - CIB-W18A/21-7-4', Parksville, Canada.

Ehlbeck, J. and Werner, H. (1988*b*), 'Untersuchungen über die Tragfähigkeit von Stabdübelverbindungen', *Holz als Roh- und Werkstoff* **46**, 281–288. (in German).

EN 1995-1-1 (2004), 'Eurocode 5: Design of timber structures - Part 1-1: General - Common rules and rules for buildings'.

EN 1998-1 (2004), 'Eurocode 8: Design of structures for earthquake resistance - Part 1: General rules, seismic actions and rules for buildings'.

ETA-04/0013 (2015), SIMPSON STRONG-TIE Manufacturing facilities | CNA Connector nails, PCR Connector nails and CSA Connector screws, European Technical Assessment ETA-04/0013, ETA-Danmark A/S, Denmark.

ETA-06/00106 (2014), SIMPSON STRONG-TIE A/S | Three-dimensional nailing plate (timber-to-timber/timber-to-concrete angle bracket), European Technical Assessment ETA-06/00106, ETA-Danmark A/S, Denmark.

ETA-07/0285 (2015), SIMPSON STRONG-TIE A/S | Three-dimensional nailing plate (timber to timber and timber to concrete/steel hold downs and post bases), European Technical Assessment ETA-07/0285, ETA-Danmark A/S, Denmark.

ETA-11/0190 (2013), Würth Schrauben, Europäische technische Zulassung ETA-11/0190, Deutsches Institut für Bautechnik (DIBt), Deutschland. (in German).

ETA-12/0373 (2012), Schmid Schrauben RAPID, STARDRIVE und SP, Europäische technische Zulassung ETA-12/0373, Österreichisches Institut für Bautechnik (OIB), Österreich. (in German).

Felicetti, M. (2012), Pareti in legno a tavole incrociate con differenti collegamenti Proposta e implementazione di un modello analitico, Master thesis, Universita degli studi di Trento, Italy. (in Italian).

Flatscher, G. (2010), Außergewöhnliche Einwirkung „Erdbeben“ - Überlegungen zur versuchstechnischen Erfassung der Verbindungstechnik im Holz-Massivbau, Master thesis, Technische Universität Graz, Austria. (in German).

Flatscher, G. (2012), Versuchstechnische Betrachtung zyklisch beanspruchter Wandelemente in der Holz-Massivbauweise, *in* ‘18. Internationales Holzbau-Forum 2012’, Vol. I Prolog IV, Garmisch-Partenkirchen. (in German).

Flatscher, G. and Augustin, M. (2016), Machbarkeitsstudie - BSP-Verbindung mit Aluminiumprofil und Bohrstabdübeln, technical report SGSC 3.2.3, holz.bau forschungs gmbh, Graz, Austria. unpublished, (in German).

Flatscher, G., Bratulic, K., Brandner, R. and Schickhofer, G. (2013), Zusammenfassende und weiterführende Arbeiten zum Verhalten von BSP-Tragwerken bei der Beanspruchungssituation Erdbeben, technical report SGSC 3.1.1_1, holz.bau forschungs gmbh, Graz, Austria. unpublished, (in German).

Flatscher, G., Bratulic, K. and Schickhofer, G. (2014), Screwed joints in cross-laminated timber structures, *in* ‘Proceedings of the 13th World Conference on Timber Engineering WCTE2014’, Quebec City, Canada.

Flatscher, G., Bratulic, K. and Schickhofer, G. (2015), ‘Experimental tests on cross-laminated timber joints and walls’, *ICE Journal Structures and Buildings* **168**(11), 868–877.

Flatscher, G. and Schickhofer, G. (2011), Verbindungstechnik in BSP bei monotoner und zyklischer Beanspruchung - Statusbericht TU Graz, *in* ‘9. Grazer Holzbau-Fachtagung’, Graz, pp. G1–G22. (in German).

Flatscher, G. and Schickhofer, G. (2014), Beschreibung der Last-Verschiebungskurven von Verbindungen im Holzbau, *in* U. Kuhlmann and K. Stephan, eds, ‘Holzbau Forschung + Praxis’, Stuttgart, Germany. (in German).

Flatscher, G. and Schickhofer, G. (2015), ‘Shaking-table test of a cross-laminated timber structure’, *ICE Journal Structures and Buildings* **168**(11), 878–888.

Flatscher, G. and Schickhofer, G. (2016), Displacement-based determination of laterally loaded cross laminated timber (CLT) wall systems, *in* ‘Proceedings of the 3rd INTER Meeting - INTER/49-12-1’, Graz, Austria.

Foliente, G. C. (1996), Issues in seismic performance testing and evaluation of timber structural systems, *in* ‘Proceedings of the International Wood Engineering Conference’, Vol. 1, New Orleans, Louisiana, pp. 29–36.

Follesa, M., Brunetti, M., Cornacchini, R. and Grasso, S. (2010), Mechanical in-plane joints between cross laminated timber panels, *in* ‘Proceedings of the 11th World Conference on Timber Engineering WCTE2010’, Riva del Garda, Italy.

Follesa, M., Fragiacomo, M. and Lauriola, M. P. (2011), A proposal for revision of the current timber part (Section 8) of Eurocode 8 Part 1, *in* 'Proceedings of the 44th CIB W18 Meeting - CIB-W18/44-15-1', Alghero, Italy.

Follesa, M., Fragiacomo, M., Vassallo, D., Piazza, M., Tomasi, R., Rossi, S. and Casagrande, D. (2015), A proposal for a new background document of chapter 8 of Eurocode 8, *in* 'Proceedings of the 2nd INTER Meeting - INTER/48-15-1', Sibenik, Croatia.

Folz, B. and Filiatrault, A. (2001), 'Cyclic analysis of wood shear walls', *Journal of Structural Engineering* **127**(4), 433–441.

Foschi, R. O. (1974), 'Load-slip characteristics of nails', *Wood Science* **7**(1), 69–76.

Foschi, R. O. (2000), Modeling the hysteretic response of mechanical connections for wood structures, *in* 'Proceedings of the 6th World Conference on Timber Engineering WCTE2000', Whistler Resort, Canada.

Foschi, R. O., Yao, F. and Rogerson, D. (2000), Determining embedment response parameters from connector tests, *in* 'Proceedings of the 6th World Conference on Timber Engineering WCTE2000', Whistler Resort, Canada.

Fragiacomo, M., Dujic, B. and Sustersic, I. (2011), 'Elastic and ductile design of multi-storey crosslam massive wooden buildings under seismic actions', *Engineering Structures* **33**(11), 3043–3053.

Frye, M. J. and Morris, G. A. (1975), 'Analysis of flexibly connected steel frames', *Canadian Journal of Civil Engineering* **2**, 280–291.

Gao, Y. and Kajikawa, H. (2010), Exponential hysteretic characteristics of wooden structures: model development and experiment validation, *in* 'Proceedings of the 11th World Conference on Timber Engineering WCTE2010', Trentino, Italy.

Gavric, I. (2013), Seismic Behaviour of Cross-Laminated Timber Buildings, Doctoral thesis, Universita degli Studi di Trieste, Trieste.

Gavric, I., Ceccotti, A. and Fragiacomo, M. (2011), Experimental cyclic tests on cross-laminated timber panels and typical connections, *in* 'Proceedings of the 14th ANIDIS Conference', Bari, Italy.

Gavric, I., Fragiacomo, M. and Ceccotti, A. (2014), 'Cyclic behaviour of typical metal connectors for cross-laminated (CLT) structures', *Materials and Structures* pp. 1–17. Article in Press.

Gavric, I., Fragiacomo, M. and Ceccotti, A. (2015*a*), 'Cyclic behaviour of CLT wall systems: Experimental tests and analytical prediction models', *Journal of Structural Engineering* **141**(11).

Gavric, I., Fragiacomo, M. and Ceccotti, A. (2015*b*), 'Cyclic behaviour of typical screwed connections for cross-laminated (CLT) structures', *European Journal of Wood and Wood Products* .

Gavric, I. and Popovski, M. (2014), Design models for CLT shearwalls and assemblies based on connection properties, *in* 'Proceedings of the 1st INTER Meeting - INTER/47-15-4', Bath, United Kingdom.

Gehri, E. (1993), Grundlagen der Verbindungstechnik, *in* 'Proceedings of the 25. Fortbildungskurs Schweizerische Arbeitsgemeinschaft für Holzforschung (SAH) 'Holzwerkstoffe auf Furnierbasis", Weinfelden, Schweiz. (in German).

Girhammar, U. A., Bovim, Nils, I. and Källsner, B. (2004), Characteristics of sheathing-to-timber joints in wood shear walls, *in* 'Proceedings of the 8th World Conference on Timber Engineering WCTE2004', Lahti, Finland.

Girhammar, U. A. and Källsner, B. (2006), Effect of transverse walls on capacity of wood-framed wall diaphragms, *in* 'Proceedings of the 39th CIB W18 Meeting - CIB-W18/39-15-1', Florence, Italy.

Girhammar, U. A. and Källsner, B. (2007), Effect of transverse walls on capacity of wood-framed wall diaphragms - part 2, *in* 'Proceedings of the 40th CIB W18 Meeting - CIB-W18/40-15-2', Bled, Slovenia.

Giuffre, A. and Pinto, P. E. (1970), 'Il comportamento del cemento armato per sollecitazioni cicliche di forte intensita', *Giornale del Genio Civile* **5**, 391–408.

Glos, P. (1978), Zur Bestimmung des Festigkeitsverhaltens von Brettschichtholz bei Druckbeanspruchung aus Werkstoff- und Einwirkungskenngrößen, Berichte zur Zuverlässigkeitstheorie der Bauwerke Heft 35, Laboratorium für den Konstruktiven Ingenieurbau (LKI), Technische Universität München. (in German).

Goldberg, J. E. and Richard, R. M. (1963), 'Analysis of nonlinear structures', *Journal of Structural Division (ASCE)* **89**(4), 333–351.

Haller, P. (1998), Progress in timber joint development and modelling, *in* J. Natterer and J. L. Sandoz, eds, 'Proceedings of the 5th World Conference on Timber Engineering WCTE1998', Vol. 1, Montreux, Switzerland, pp. 337–344.

Hummel, J. (2016), Displacement-based seismic design for multi-storey cross laminated timber buildings, Doctoral thesis, Universität Kassel, Kassel, Germany.

Hummel, J., Flatscher, G., Seim, W. and Schickhofer, G. (2013), CLT Wall Elements Under Cyclic Loading – Details for Anchorage and Connection, *in* R. Harris, A. Ringhofer and G. Schickhofer, eds, 'COST Action FP1004, Focus Solid Timber Solutions – European Conference on Cross Laminated Timber (CLT)', The University of Bath, Graz, pp. 152–165.

Hummel, J. and Seim, W. (2016), Performance-based design as a tool to evaluate behavior factors for multi-storey timber buildings, *in* 'Proceedings of the 14th World Conference on Timber Engineering WCTE2016', Vienna, Austria.

ISO 16670 (2003), 'Timber structures - Joints made with mechanical fasteners - Quasi-static reversed-cyclic test method'.

ISO 21581 (2010), 'Timber structures - Static and cyclic lateral load test methods for shear walls'.

ISO 6891 (1983), 'Timber structures - Joints made with mechanical fasteners - General principles for the determination of strength and deformation characteristics'. identical with ON EN 26891.

Issler, L., Ruoß, H. and Häfele, P. (1997), *Festigkeitslehre - Grundlagen*, Vol. 2, Springer-Verlag Berlin, Deutschland. (in German).

Izzi, M., Flatscher, G., Fragiacomo, M. and Schickhofer, G. (2016), 'Experimental investigations and design provisions of steel-to-timber joints with annular-ringed shank nails for Cross-Laminated Timber structures', *Construction and Building Materials* **122**, 446–457.

Izzi, M., Flatscher, G., Rinaldin, G., Fragiacomo, M. and Schickhofer, G. (2015), Experimental tests on annular ringed shank nails for seismic resistant cross-laminated timber (CLT) structures, *in* 'Proceedings of the 16th ANIDIS Conference', L'Aquila, Italy.

Johansen, K. W. (1949), Theory of timber connection, *in* 'Publication 9 - International Association of Bridge and Structural Engineering', Bern.

Jorissen, A. (1999), 'Double shear timber connections with dowel type fasteners', *Heron* **44**(3), 163–186.

Jorissen, A. and Fragiacomo, M. (2010), Ductility in Timber Structures, *in* 'Proceedings of the 43th CIB W18 Meeting - CIB-W18/43-7-2', Nelson, New Zealand.

Jorissen, A. and Fragiacomo, M. (2011), 'General notes on ductility in timber structures', *Engineering Structures* **33**(11), 2987–2997.

Judd, J. P. (2005), Analytical modeling of wood-frame shear walls and diaphragms, Master thesis, Brigham Young University, Utah, U.S.A.

Karacabeyli, E. and Ceccotti, A. (1996), Quasi-static reversed-cyclic testing of nailed joints, *in* 'Proceedings of the 29th CIB W18 Meeting - CIB-W18/29-7-7', Bordeaux, France.

Kawai, N., Tsuchimoto, T., Tsuda, C., Murakami, S., Miura, S., Isoda, H. and Miyake, T. (2014), Lateral loading tests on CLT shear walls by assembly of narrow panels and by a large panel with an opening, *in* 'Proceedings of the 13th World Conference on Timber Engineering WCTE2014'.

Kishi, N. and Chen, W. F. (1986), Data base of steel beam-to-column connections, Technical Report CE-STR-86-26, School of Civil Engineering, Purdue University, West Lafayette, Indiana, U.S.A.

Korhonen, R. K. and Saarakkala, S. (2011), *Biomechanics and modeling of skeletal soft tissues, Theoretical Biomechanics*, InTech, chapter 6, pp. 113–132.

Kraler, A., Kögl, J. and Maderebner, R. (2014), Sherpa-CLT-Connector for cross laminated timber (CLT) elements, *in* 'Proceedings of the 13th World Conference on Timber Engineering WCTE2014', Quebec City, Canada.

Krawinkler, H., Parisi, F., Ibarra, L., Ayoub, A. and Medina, R. (2001), Development of a testing protocol for woodframe structures, Technical Report W-02, Department of Civil and Environmental Engineering, Standford University, Richmond, California, U.S.A. CUREE Publication.

Kuklik, P. (2015), Behaviour of mechanically laminated CLT members, *in* 'Proceedings of the 2nd International Conference on Innovative Materials, Structures and Technologies; IOP Conf. Series: Materials Science and Engineering', Vol. 96, Riga, Latvia.

Laggner, T. M., Flatscher, G. and Schickhofer, G. (2016), Combined loading of self-tapping screws, *in* 'Proceedings of the 14th World Conference on Timber Engineering WCTE2016', Vienna, Austria.

Latour, M., Rizzano, G. and Torello, G. (2012), Seismic Performance of Cross-Laminated Timber Panel Buildings with Dissipative Connections, *in* 'Proceedings of the 15th World Conference on Earthquake Engineering WCEE2012', Lisbon, Portugal.

Lee, S.-S. and Moon, T.-S. (2002), 'Moment-rotation model of semi-rigid connections with angles', *Engineering Structures* **24**, 227–237.

Liu, J. and Lam, F. (2016), Experimental test of cross laminated timber connections under bi-directional loading, *in* 'Proceedings of the 14th World Conference on Timber Engineering WCTE2016', Vienna, Austria.

Lui, E. M. and Chen, W.-F. (1986), 'Analysis and behaviour of flexibly-jointed frames', *Engineering Structures* **8**, 107–118.

Mack, J. J. (1966), *The strength and stiffness of nailed joints under short-duration loading*, Commonwealth Scientific and Industrial Research Organization (CISRO), Division of Forest Products, Melbourne, Australia. Paper No. 40.

Mack, J. J. (1977), 'The load-displacement curve for nailed joints', *Journal of the Institute of Wood Science* **7**(6), 34–36.

Malaga-Chuquitaype, C., Skinner, J., Dowdall, A. and Kernohan, J. (2016), Response of CLT shear walls under cyclic loads, *in* 'Proceedings of the 14th World Conference on Timber Engineering WCTE2016', Vienna, Austria.

Malo, K. A., Seim, J. and Ellingsbø, P. (2011), 'Quantifying ductility in timber structures', *Engineering Structures* **33**(11), 2998–3006.

McLain, T. E. (1975), Curvilinear load-slip relations in laterally-loaded nailed joints, Doctoral thesis, Colorado State University, Fort Collins, Colorado.

Meisel, A. (2009), Historische Dachstühle | Tragsysteme, Bestandserfassung, statische Analyse und Sanierung mit flächenhaften Holzwerkstoffen, Master thesis, Technische Universität Graz, Austria. (in German).

Menegotto, M. and Pinto, P. E. (1973), 'Method of analysis for cyclically loaded reinforced concrete plane frames including changes in geometry and non-elastic behaviour of elements under combined normal force and bending', *IABSE reports of the working commissions* **13**, 15–22.

Microsoft ® Excel (2010). Part of Microsoft Office Professional Plus 2010, Version 14.0.xx (64-Bit).

Mischler, A. (1997), Influence of ductility on the load-carrying capacity of joints with dowel-type fasteners, *in* 'Proceedings of the 30th CIB W18 Meeting - CIB-W18/30-7-6', Vancouver, Canada.

Moosbrugger, T., Guggenberger, W. and Bogensperger, T. (2006), Cross-Laminated Timber Wall Segments under homogeneous Shear - with and without Openings, *in* D. A. Bender, D. S. Gromala and D. V. Rosowsky, eds, 'Proceedings of the 9th World Conference on Timber Engineering WCTE2006', Portland, OR, USA.

Muñoz, W., Mohammad, M., Salenikovich, A. and Quenneville, P. (2008), Need for a Harmonised Approach for Calculations of Ductility of Timber Assemblies, *in* 'Proceedings of the 41th CIB W18 Meeting - CIB-W18/41-15-1', St. Andrews, Canada.

Nakashima, S., Kitamori, A., Komatsu, K., Que, Z. and Isoda, H. (2014), Development and evaluation of CLT shear walls using drift pinned joint, *in* 'Proceedings of the 13th World Conference on Timber Engineering WCTE2014', Quebec City, Canada.

O'Halloran, M. R. (1973), A curvilinear stress-strain model for wood in compression, Doctoral thesis, Colorado State University, Fort Collins, Colorado, U.S.A.

Okabe, M., Yasumura, M., Kobayashi, K., Haramiishi, T., Nakashima, Y. and Fujita, K. (2012), Effecto of vertical load under cyclic lateral load tests for evaluating Sugi CLT wall panel, *in* 'Proceedings of the 12th World Conference on Timber Engineering WCTE2012', Auckland, New Zealand.

ON B 1995-1-1 (2015), 'Eurocode 5: Design of timber structures - Part 1-1: General - Common rules and rules for buildings (National specifications for the implementation of ON EN 1995-1-1, national comments and national supplements)'. (in German).

ON B 1998-1 (2011), 'Eurocode 8: Design of structures for earthquake resistance - Part 1: General rules, seismic actions and rules for buildings - National specifications concerning ON EN 1998-1 and national comments'. (in German).

ON EN 10002-1 (2002), 'Metallic materials - Tensile testing - Part 1: Method of test at ambient temperature'. (in German).

ON EN 12512 (2005), 'Timber structures - Test methods - Cyclic testing of joints made with mechanical fasteners (consolidated version)'. (in German).

ON EN 1382 (1999), 'Timber structures - Test methods - Withdrawal capacity of timber fasteners'. (in German).

ON EN 14080 (2013), 'Timber structures - Glued laminated timber and glued solid timber - Requirements'. (in German).

ON EN 14358 (2016), 'Timber structures - Calculation and verification of characteristic values'. (in German).

ON EN 1990 (2013), 'Eurocode - Basis of structural design (consolidated version)'. (in German).

ON EN 1993-1-8 (2012), 'Eurocode 3: Design of steel structures - Part 1-8: Design of joints (consolidated version)'. (in German).

ON EN 1995-1-1 (2014), 'Eurocode 5: Design of timber structures - Part 1-1: General - Common rules and rules for buildings (consolidated version)'. (in German).

ON EN 1998-1 (2011), 'Eurocode 8: Design of structures for earthquake resistance - Part 1: General rules, seismic actions and rules for buildings (consolidated version)'. (in German).

ON EN 26891 (1991), 'Timber structures - Joints made with mechanical fasteners - General principles for the determination of strength and deformation characteristics'. identical with ISO 6891, (in German).

ON EN 338 (2009), 'Structural timber - Strength classes'. (in German).

ON EN 408 (2012), 'Timber structures - Structural timber and glued laminated timber - Determination of some physical and mechanical properties'. (in German).

ON EN 594 (1996), 'Timber structures - Test methods - Racking strength and stiffness of timber frame wall panels'. (in German).

ON EN 594 (2011), 'Timber structures - Test methods - Racking strength and stiffness of timber frame wall panels'. (in German).

ON ISO 554 (1994), 'Normklimate für die Konditionierung und/oder Prüfung - Zahlenangaben'. identical with ISO 554:1976 - (in German).

Park, R. (1989), 'Evaluation of ductility of structures and structural assemblages from laboratory testing', *Bulletin of the New Zealand National Society for Earthquake Engineering* **22**(3), 155–166.

Pei, S., Popovski, M. and van de Lindt, John, W. (2012), Seismic design of a multi-story cross laminated timber building based on component level testing, *in* 'Proceedings of the 12th World Conference on Timber Engineering WCTE2012', Auckland, New Zealand.

Pellicane, P. J., Stone, J. L. and Vanderbilt, M. (1991), 'Generalized model for lateral load slip of nailed joints', *Journal of Materials in Civil Engineering* **3**(1), 60–77. cited By 6.

Piazza, M., Polastri, A. and Tomasi, R. (2011), 'Ductility of timber joints under static and cyclic loads', *ICE Journal Structures and Buildings* **164**(SB2), 79–90.

Piazza, M. and Turrini, G. (1986), Advances in technology of joints for laminated timber - Analyses of the structural behaviour, *in* 'Proceedings of the 19th CIB W18 Meeting - CIB-W18/19-7-9', Florence, Italy.

Polastri, A. and Angeli, A. (2014), An innovative connection system for CLT structures: experimental - numerical analysis, *in* 'Proceedings of the 13th World Conference on Timber Engineering WCTE2014', Quebec City, Canada.

Popovski, M., Gavric, I. and Schneider, J. (2014), Performance of two-storey CLT house subjected to lateral loads, *in* 'Proceedings of the 13th World Conference on Timber Engineering WCTE2014', Quebec City, Canada.

Popovski, M. and Karacabeyli, E. (2011), Seismic performance of cross-laminated wood panels, *in* 'Proceedings of the 44th CIB W18 Meeting - CIB-W18/44-15-7', Alghero, Italy.

Poussa, M., Tukiainen, P. and Ranta-Maunus, A. (2007), Experimental study of compression and shear strength of spruce timber, *in* 'Proceedings of the 40th CIB W18 Meeting - CIB-W18/40-6-2', Bled, Slovenia.

Pozza, L., Massari, M., Savoia, M. and Ferracuti, B. (2016), Experimental campaign of mechanical CLT connections subjected to a combination of shear and tension forces, *in* 'Proceedings of the 3nd International Conference on Structures and Architecture ICSA2016', Guimaraes, Portugal.

Pozza, L., Scotta, R., Trutalli, D., Ceccotti, A. and Polastri, A. (2013), Analytical formulation based on extensive numerical simulations of behavior factor q for CLT buildings, *in* 'Proceedings of the 46th CIB W18 Meeting - CIB-W18/46-15-5', Vancouver, Canada.

Pozza, L., Scotta, R., Trutalli, D., Pinna, M., Polastri, A. and Bertoni, P. (2014), 'Experimental and numerical analyses of new massive wooden shear-wall systems', *Buildings* **4**(3), 355–374.

Ramberg, W. and Osgood, W. R. (1943), Description of stress-strain curves by three parameters, Technical note 902, National Advisory Committee for Aeronautics, Washington.

Razzaq, Z. (1983), 'End restraint effect on steel column strength', *Journal of Structural Engineering* **109**(2), 314–334.

RFEM 5 (2015). Structural Analysis and Design Software, Dlubal Software GmbH, Version 5.05.xx. www.dlubal.com

Richard, R. M. and Abbott, B. (1975), 'Versatile elastic-plastic stress-strain formula', *Journal of the Engineering Mechanics Division* **101**(EM4), 511–515.

RILEM TC 3-TT (1977), 'Testing methods for joints with mechanical fasteners in load-bearing timber structures', *Materials and Structures* **10**(56), 99–101.

Rinaldin, G., Amadio, C. and Fragiacomo, M. (2011), A component approach for non-linear behavior of cross-laminated solid timber panels, *in* 'Proceedings of the ANIDIS Conference', Bari, Italy.

Ringhofer, A. (2010), Erdbebennormung in Europa und deren Anwendung auf Wohnbauten in Holz-Massivbauweise, Master thesis, Technische Universität Graz, Austria. (in German).

Schickhofer, G., Bogensperger, T., Moosbrugger, T., Augustin, M., Blaß, H. J., Ebner, H., Ferk, H., Fontana, M., Frangi, A., Hamm, P., Jöbstl, R. A., Richter, A., Thiel, A., Traetta, G. and Uibel, T. (2010), *BSPhandbuch Holz-Massivbauweise in Brettsperrholz Nachweise auf Basis des neuen europäischen Normenkonzepts*, 2. edn, Verlag der Technischen Universität Graz, Graz. (in German).

Schickhofer, G. and Ringhofer, A. (2011), *The seimic behaviour of buildings erected in solid timber construction | Seismic design according to EN 1998 for a 5-storey reference building in CLT*, Vol. 1, TU Graz, Graz, Austria.

Scotta, R., Pozza, L., Trutalli, D., Marchi, L. and Ceccotti, A. (2015), Dissipative connections for squat or scarcely jointed CLT buildings. Experimental tests and numerical validation, *in* 'Proceedings of the 2nd INTER Meeting - INTER/48-15-6', Sibenik, Croatia.

Seim, W. and Hummel, J. (2013), CLT-wall elements - monotonic and cyclic testing, technical report 2D, Universität Kassel, Kassel, Germany. project: optimberquake (optimberquake.eu).

Seim, W., Hummel, J. and Vogt, T. (2013), Anchoring units - monotonic and cyclic testing, technical report 2C, Universität Kassel, Kassel, Germany. project: optimberquake (optimberquake.eu).

Shahnewaz, M., Tannert, T., Alam, M. S. and Popovski, M. (2016), In-plane stiffness of CLT panels with and without openings, *in* 'Proceedings of the 14th World Conference on Timber Engineering WCTE2016', Vienna, Austria.

Shen, Y.-L., Schneider, J., Tesfamariam, S., Stiemer, S. F. and Mu, Z.-G. (2013), 'Hysteresis behavior of bracket connection in cross-laminated-timber shear walls', *Construction and Building Materials* **48**, 980–991.

SIA 160 (1989), 'Einwirkungen auf Tragwerke'. (in German).

SIA 164 (1992), 'Holzbau'. (in German).

SIA 265 (2012), 'Timber Structures'. (in German).

Silly, G. (2010), Nummerische Studie zur Drill- und Schubsteifigkeit von Brettsperrholz (BSP), Master thesis, Technische Universität Graz, Austria. (in German).

Simpson Strong-Tie (2012), *Qualitätsverbinder für Holzkonstruktionen - Charakteristische Werte nach EC5 und DIN 1052.*, Simpson Strong-Tie GmbH, Bad Nauheim, Germany. C-DE-2012/13 (in German).

Smith, I. (1987), Modelling the load-deformation behaviour of connections with pin-type fasteners under combined moment, thrust and shear forces, *in* 'Proceedings of the 20th CIB W18 Meeting - CIB-W18/20-7-4', Dublin, Ireland.

Smith, I., Asiz, A., Snow, M. and Chui, Y. H. (2006), Possible Canadian / ISO approach to deriving design values from test data, *in* 'Proceedings of the 39th CIB W18 Meeting - CIB-W18/39-17-1', Florence, Italy.

Smith, I., Whale, L. R. J., Anderson, C. and Held, L. (1984), Mechanical properties of nails and their influence on mechanical properties of nailed timber joints subjected to lateral loads, *in* 'Proceedings of the 17th CIB W18 Meeting - CIB-W18/17-7-1', Rapperswil, Switzerland.

Smith, T., Moroder, D., Sarti, F., Pampanin, S. and Buchanan, A. H. (2015), The reality of seismic engineering in a modern timber world, *in* 'Proceedings of the 2nd INTER Meeting - INTER/48-102-3', Sibenik, Croatia.

Sommerlade, K., Hummel, J. and Seim, W. (2016), Mean and characteristic values for deformation capacity of light-frame and cross-laminated timber walls, *in* 'Proceedings of the 14th World Conference on Timber Engineering WCTE2016', Vienna, Austria.

Stecher, G., Kögl, J. and Beikircher, W. (2014), Mechanical behaviour of dovetail connections for cross laminated timber wall elements, *in* 'Proceedings of the 13th World Conference on Timber Engineering WCTE2014', Quebec City, Canada.

Stehn, L. and Björnfot, A. (2002), Comparison of different ductility measures for a nailed steel-to-timber connection, *in* 'Proceedings of the 7th World Conference on Timber Engineering WCTE2002', Vol. 2, Shah Alam, Malaysia, pp. 155–163.

Sustersic, I. and Dujic, B. (2012), Simplified cross-laminated timber wall modelling for linear-elastic seismic analysis, *in* 'Proceedings of the 45th CIB W18 Meeting - CIB-W18/45-15-6', Växjö, Sweden.

Sustersic, I., Dujic, B. and Fragiacomo, M. (2011), Influence of connection properties on the ductility and seismic resistance of multi-storey cross-lam buildings, *in* 'Proceedings of the 44th CIB W18 Meeting - CIB-W18/44-15-9', Alghero, Italy.

Teichmann, A. and Borkmann, K. (1930), Versuche mit kurzen Bolzen in Holzbauteilen, 179. Bericht der Deutschen Versuchsanstalt für Luftfahrt, E.V. Berlin-Adlershof, *in* 'Luftfahrtforschung, Berichte der Deutschen Versuchsanstalt für Luftfahrt, E.V., Berlin-Adlershof (DVL), der Aerodynamischen Versuchsanstalt zu Göttingen (AVA), des Aerodynamischen Institutes der Techn. Hochschule Aachen (AIA) und anderer Stätten der Luftfahrtforschung. Gesammelt als Beihefte zur Zeitschrift für Flugtechnik und Motorluftschiffahrt (ZFM) von der Wissenschaftlichen Gesellschaft für Luftfahrt E.V. (WGL)', Vol. 8, Verlag von R. Oldenbourg, München und Berlin, pp. 18–38. (in German).

Tissell, J. R. and Elliott, J. R. (2004), Plywood diaphragms, Research Report 138, APA - The Engineered wood association.

Tomasi, R., Parisi, M. A. and Piazza, M. (2009), 'Ductile design of glued-laminated timber beams', *Practice Periodical on Structural Design and Construction* **14**(3), 113–122.

Tomasi, R. and Smith, I. (2014), 'Experimental characterization of monotonic and cyclic loading responses of CLT panel-to-foundation angle bracket connections', *Journal of Materials in Civil Engineering* .

Uibel, T. and Blaß, H. J. (2007), Edge joints with dowel type fasteners in cross laminated timber, *in* 'Proceedings of the 40th CIB W18 Meeting - CIB-W18/40-7-2', Bled, Slovenia.

Vermeyden, P. (1963), 'A loading procedure for testing timber joints', *Heron* **11**(2), 41–51.

Vogt, T. (2015), Entwicklung eines Berechnungsmodells zur Beschreibung des Trag- und Verformungsverhaltens von Holzrahmenwänden unter Berücksichtigung lokaler Effekte, Doctoral thesis, Universität Kassel, Kassel, Germany. (in German).

Wallner-Novak, M., Koppelhuber, J. and Pock, K. (2013), *Brettsperrholz Bemessung - Grundlagen für Statik und Konstruktion nach Eurocode*, 1. edn, proHolz Austria. ISBN: 978-3-902320-96-4; (in German).

Whale, L. R. J. and Smith, I. (1986), The derivation of design clauses for nailed and bolted joints in Eurocode 5, *in* 'Proceedings of the 19th CIB W18 Meeting - CIB-W18/19-7-6', Florence, Italy.

Whale, L. R. J., Smith, I. and Larsen, J. H. (1987), Design of nailed and bolted joints - proposals for the revision of existing formulae in draft Eurocode 5 and the CIB code, *in* 'Proceedings of the 20th CIB W18 Meeting - CIB-W18/20-7-1', Dublin, Ireland.

Wilkinson, T. L. (1972), 'Analysis of nailed joints with dissimilar members', *Journal of the Structural Division, Proceedings of the American Society of Civil Engineers* **98**(ST9), 2005–2013.

Wolfram Mathematica 7 (2008), 'Mathematica'. Version: 7.0.1.0.

Wu, F.-H. and Chen, W.-F. (1990), 'A design model for semi-rigid connections', *Engineering Structures* **12**, 88–97.

Yasumura, M. and Kawai, N. (1997), Evaluation of wood framed shear walls subjected to lateral load, *in* 'Proceedings of the 30th CIB W18 Meeting - CIB-W18/30-15-4', Vancouver, Canada.

Yasumura, M., Kobayashi, K., Okabe, M., Miyake, T. and Matsumoto, K. (2015), 'Full-scale tests and numerical analysis of low-rise CLT structures under lateral loading', *Journal of Structural Engineering* **142**(4), 12.

Yee, Y. L. and Melchers, R. E. (1986), 'Moment-rotation curves for bolted connections', *Journal of Structural Engineering* **112**(3), 615–635.

Youssef-Agha, W., Aktan, H. M. and Olowokere, O. (1989), 'Seismic response of low-rise steel frames', *Journal of Structural Engineering* **115**(3), 594–607.

A-2 List of notations

Latin upper case letters

A ..... area

C ..... constant value; curve fitting parameters

D ..... ductility ratio

E_D ..... dissipated energy

$E_{0|90}$ ..... modulus of elasticity (*MOE*) or Young's modulus of timber parallel (0) or perpendicular (90) to the grain

F ..... load

F_A ..... load at displacement v_A

F_B ..... load at displacement v_B

$F_{C,x}$ ..... lateral load in connection

$F_{C,z}$ ..... vertical load in connection

F_{est} ..... estimated maximum load

F_k ..... characteristic load (equivalent to R_k)

F_{lim} ..... 'limiting' or 'extreme' value for load applications

F_{max} ..... maximum load

F_P ..... compression (bearing) load

F_{rg} ..... load responsible for rocking

F_{sl} ..... load responsible for sliding

F_u ..... ultimate load

F_{vj} ..... load in vertical joint

F_y ..... yield load

ΔF ..... incremental load step

G ..... shear modulus of timber

G^* ..... effective shear modulus for CLT wall element

G_R ..... rolling shear modulus of timber

G_T ..... torsional shear modulus of timber

$I_{x|y}$ ..... moment of inertia in $x|y$-direction

K ..... stiffness

K_B ..... tangential stiffness at point B

K_{CLT} ..... stiffness of a CLT wall element without openings

$K_{C,x}$ ..... lateral (horizontal) stiffness of connection in a wall system

$K_{C,z}$ ..... axial (vertical) stiffness of connection in a wall system

K_{ini} ..... initial stiffness

K_p ..... inclination of the plastic branch

K_{ser} ..... stiffness (slip modulus) according to ON EN 1995-1-1 (2014)

K_{SLS} ..... stiffness applicable in the SLS

K_T ..... tangent stiffness

K_u ..... instantaneous stiffness (slip modulus) according to ON EN 1995-1-1 (2014)

K_{ULS} ..... stiffness applicable in the ULS

K_{vj} ..... stiffness of vertical joint in its main direction

PoR ..... point of rotation

R_k ..... characteristic load-carrying capacity

Latin lower case letters

a ..... single board width or mean distance between cracks

a_{con} ..... distance between connections in a wall system

d ..... diameter

$f_{c,0}$ ..... compression strength parallel to the grain

$f_{c,90}$ ..... compression strength perpendicular to the grain

h ..... height of a CLT wall element

l ..... length of a CLT wall element

l_{full} ..... length of full height wall segments

l_p ..... length of compression zone

p_S, q_S ..... parameters for determining shear stiffness of CLT elements

q ..... vertical line load acting on a wall system

r_{CLT} ..... panel area ratio

t_{CLT} ..... total thickness of CLT wall element

t_{eff} ..... effective thickness of CLT element (sum of vertical layer thickness)

t_{max} ..... maximum layer thickness in CLT element

t_{mean} ..... mean layer thickness

u ..... gap/crack width

v ..... displacement

v_{bn} ..... lateral bending deformation of CLT wall element

v_{CLT} ..... lateral deformations of CLT wall element ($v_{sh} + v_{bn}$)

$v_{CLT,max}$ ..... CLT contribution to head deflection v_{max}

v_{con} ..... connection based lateral displacement of a wall system

$v_{C,x}$ ..... lateral (horizontal) displacement of a connection

$v_{C,z}$ ..... axial (vertical) displacement of a connection

v_{in} ..... initial slip/displacement

v_{ip} ..... ultimate displacement in case of ideal plasticity

v_{lim} ..... limiting displacement

v_{max} ..... displacement corresponding to F_{max}

$v_{P,z}$ ..... indentation

v_{rg} ..... lateral displacement of a wall system according to rocking

$v_{rg,max}$ ..... rocking contribution to head deflection v_{max}

v_{sh} ..... lateral shear deformation of CLT wall element

v_{sl} ..... lateral displacement of a wall system according to sliding

$v_{sl,max}$ ..... sliding contribution to head deflection v_{max}

v_{tot} ..... total lateral head deflection of a CLT wall system

v_{u} ..... ultimate displacement

v_{vj} ..... displacement of vertical joint along its main direction

v_{y} ..... yield displacement

v_{z} ..... vertical displacement according to rocking

Δv ..... incremental displacement step

x_{m} ..... distance between *PoR* and connection m

Greek letters

α, β ..... angles

α_{FIT} ..... fitting parameter basing on FEM-simulations

α_{u} ..... fitting parameter basing on FEM-simulations considering gaps/cracks

ϕ_{ip} ..... shape parameter [-]

Φ_{ip} ..... shape parameter [%]

φ ..... rotation angle of CLT wall element

κ ..... shear correction factor

μ_{f} ..... coefficient of friction

ρ ..... density

ρ_{k} ..... characteristic density

ρ_{m} ..... mean density

ANNEX B TEST DOCUMENTATION

B-1 Single joint tests Graz

B-1.1 Angle brackets

Shear loaded wall-to-foundation joint (W_V1_T1)

Table B.1: basic information for configuration W_V1_T1

parts	materials	specifications
wall segment	CLT	C24 | 98 mm (32-34-32)
floor segments	concrete	C25/30 | 190 mm
connection	angle bracket	AE116
fasteners wall	annular-ringed shank nails	14 × CNA Ø 4.0×60 mm
fasteners floor	bolts	2 × FBN II 12/10

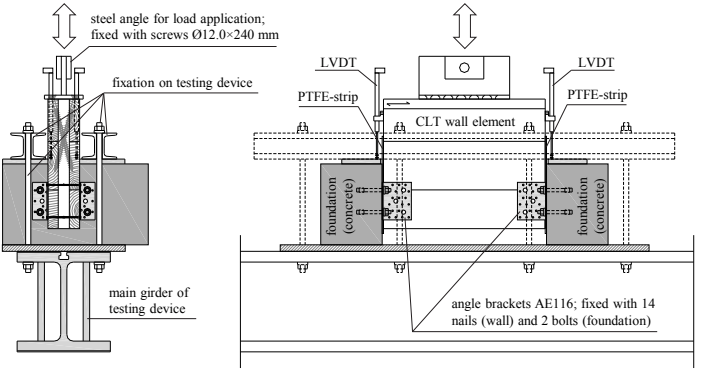

Figure B.1: test set-up for monotonic and cyclic experiments on configuration W_V1_W1 – (a) sheer plan; (b) front view

Table B.2: results of monotonic tests on configuration W_V1_T1

notations		units	M02	M03	M04	mean	*CoV*
ρ_{mean}		[kg/m³]	420	423	423	**422**	0.4%
F_{max}		[kN]	33.25	35.66	35.73	**34.88**	4.0%
v_{max}		[mm]	18.7	23.2	23.1	**21.7**	11.8%
$K_{ser,EN}$		[kN/mm]	2.722	2.963	2.998	**2.894**	5.2%
$F_{y,EN}$		[kN]	30.23	30.94	30.99	**30.72**	1.4%
$v_{y,EN}$		[mm]	10.0	9.7	9.5	**9.8**	2.8%
F_u		[kN]	27.55	32.00	28.71	**29.42**	7.9%
v_u		[mm]	32.4	29.0	27.7	**29.7**	8.2%
D_{EN}		[-]	3.2	3.0	2.9	**3.0**	5.1%
***D*-class**		[-]	low	low	low	**low**	
K_{SLS}		[kN/mm]	4.258	3.752	3.950	**3.986**	6.4%
K_{ULS}		[kN/mm]	3.477	3.477	3.658	**3.537**	3.0%
v_{ip}		[mm]	26.3	22.2	21.2	**23.2**	11.6%
Φ_{ip}		[-]	63%	53%	53%	**56%**	10.3%
***D*-class**		[-]	high	moderate	moderate	**moderate**	
approximation curves	F_{max}	[kN]	33.25	35.70	35.55		
	v_{max}	[mm]	21.40	22.70	22.00		
	K_{ini}	[kN/mm]	4.30	4.14	3.90		
	F_A	[kN]	28.00	28.90	29.70		
	v_B	[mm]	32.40	29.00	27.80		
	K_B	[kN/mm]	-100.00	-280.00	-8.20		

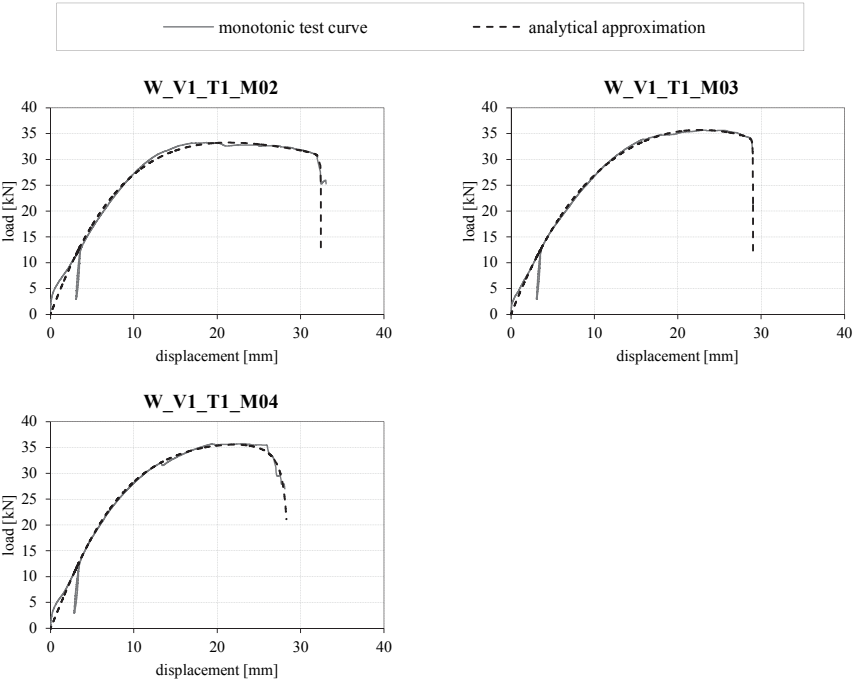

Figure B.2: actual and approximated load-displacement curves of monotonic tests on configuration W_V1_T1

Table B.3: results of cyclic tests on configuration W_V1_T1

notations		units	Z01	Z02	Z03	Z04	mean	*CoV*
ρ_{mean}		[kg/m³]	438	401	413	411	**416**	3.8%
F_{max}		[kN]	30.22	27.92	30.82	30.96	**29.98**	4.7%
v_{max}		[mm]	15.3	15.3	20.1	15.0	**16.4**	14.7%
$K_{ser,EN}$		[kN/mm]	2.690	2.723	2.613	2.475	**2.625**	4.2%
$F_{y,EN}$		[kN]	27.59	24.91	28.19	29.25	**27.49**	6.7%
$v_{y,EN}$		[mm]	9.4	8.3	9.9	10.9	**9.6**	11.0%
F_u		[kN]	25.69	22.33	24.65	24.77	**24.36**	5.9%
v_u		[mm]	20.6	22.2	26.8	22.0	**22.9**	11.8%
D_{EN}		[-]	2.2	2.7	2.7	2.0	**2.4**	14.8%
***D*-class**		[-]	low	low	low	low	**low**	
K_{SLS}		[kN/mm]	3.919	3.668	3.602	3.229	**3.605**	7.9%
K_{ULS}		[kN/mm]	3.319	3.358	3.230	3.038	**3.236**	4.4%
v_{ip}		[mm]	14.9	16.5	20.4	15.8	**16.9**	14.3%
Φ_{ip}		[-]	45%	49%	52%	44%	**48%**	7.7%
***D*-class**		[-]	moderate	moderate	moderate	moderate	**moderate**	
appr. envelope curves 1	F_{max}	[kN]	30.22	27.50	31.50	31.00		
	v_{max}	[mm]	15.30	15.10	17.70	16.70		
	K_{ini}	[kN/mm]	3.90	6.00	3.90	4.00		
	F_A	[kN]	22.00	20.50	23.20	22.00		
	v_B	[mm]	21.50	22.80	26.50	23.00		
	K_B	[kN/mm]	-1.90	-1.20	-1.20	-1.65		
appr. envelope curves 2	F_{max}	[kN]	25.50	23.80	26.70	26.00		
	v_{max}	[mm]	14.70	14.00	16.80	16.70		
	K_{ini}	[kN/mm]	4.20	6.00	4.00	4.50		
	F_A	[kN]	19.50	17.80	20.50	20.10		
	v_B	[mm]	21.50	21.50	24.50	23.60		
	K_B	[kN/mm]	-2.00	-1.05	-1.20	-1.38		
appr. envelope curves 3	F_{max}	[kN]	24.00	22.00	24.80	24.00		
	v_{max}	[mm]	14.70	14.00	16.00	15.60		
	K_{ini}	[kN/mm]	4.20	5.00	5.00	3.90		
	F_A	[kN]	19.00	16.50	18.60	18.70		
	v_B	[mm]	21.30	20.50	23.50	23.00		
	K_B	[kN/mm]	-1.70	-1.15	-1.05	-1.21		

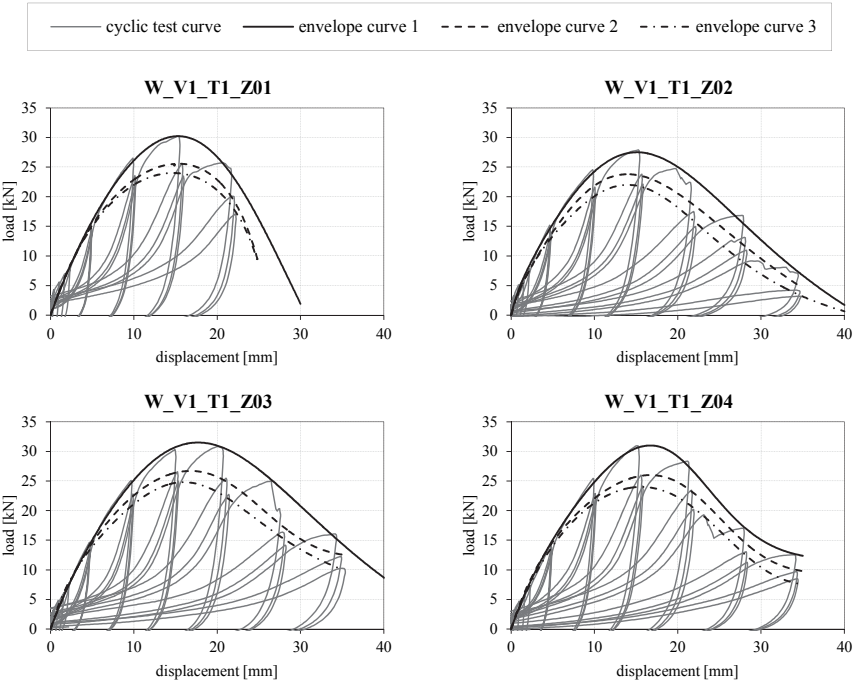

Figure B.3: actual and approximated load-displacement curves of cyclic tests on configuration W_V1_T1

Tension loaded wall-to-foundation joint (W_V1_T2)

Table B.4: basic information for configuration W_V1_T2

parts	materials	specifications
wall segment	CLT	C24 | 98 mm (32-34-32)
floor segment	concrete	C25/30 | 190 mm
connection	angle bracket	AE116
fasteners wall	annular-ringed shank nails	14 × CNA Ø 4.0×60 mm
fasteners floor	bolts	2 × FBN II 12/10

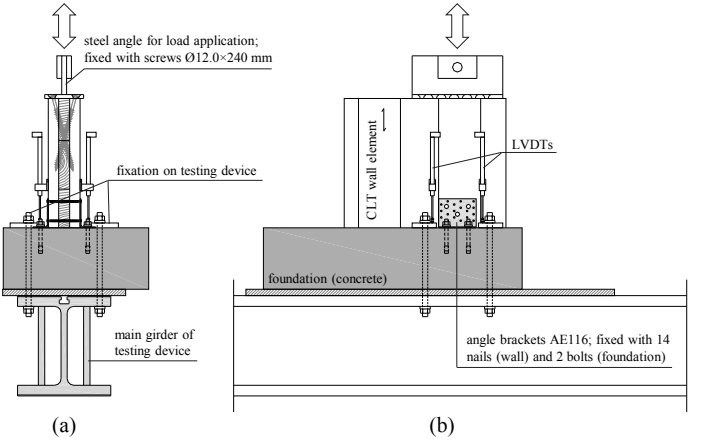

Figure B.4: test set-up for monotonic and cyclic experiments on configuration W_V1_W2 – (a) sheer plan; (b) front view

Table B.5: results of monotonic tests on configuration W_V1_T2

notations		units	M01	M02	M03	mean	*CoV*
ρ_{mean}		[kg/m³]	450	450	414	**438**	4.7%
F_{max}		[kN]	35.97	39.81	32.53	**36.10**	10.1%
v_{max}		[mm]	17.9	26.1	17.9	**20.6**	23.0%
$K_{ser,EN}$		[kN/mm]	6.189	5.397	6.379	**5.989**	8.7%
$F_{y,EN}$		[kN]	21.31	24.18	18.70	**21.39**	12.8%
$v_{y,EN}$		[mm]	2.9	3.9	2.5	**3.1**	22.0%
F_u		[kN]	28.78	36.45	26.02	**30.42**	17.8%
v_u		[mm]	25.1	29.8	30.7	**28.5**	10.5%
D_{EN}		[-]	8.6	7.7	12.1	**9.5**	24.5%
***D*-class**		[-]	high	high	high	**high**	
K_{SLS}		[kN/mm]	15.317	14.105	12.077	**13.833**	11.8%
K_{ULS}		[kN/mm]	8.000	7.572	6.208	**7.260**	12.9%
v_{ip}		[mm]	19.1	22.9	25.0	**22.3**	13.4%
Φ_{ip}		[-]	52%	54%	63%	**56%**	10.5%
***D*-class**		[-]	moderate	moderate	high	**moderate**	
approximation curves	F_{max}	[kN]	36.00	40.00	31.90		
	v_{max}	[mm]	21.20	27.00	21.80		
	K_{ini}	[kN/mm]	30.00	36.80	33.00		
	F_A	[kN]	28.60	32.20	27.30		
	v_B	[mm]	25.20	31.00	32.20		
	K_B	[kN/mm]	-7.50	-11.50	-1.60		

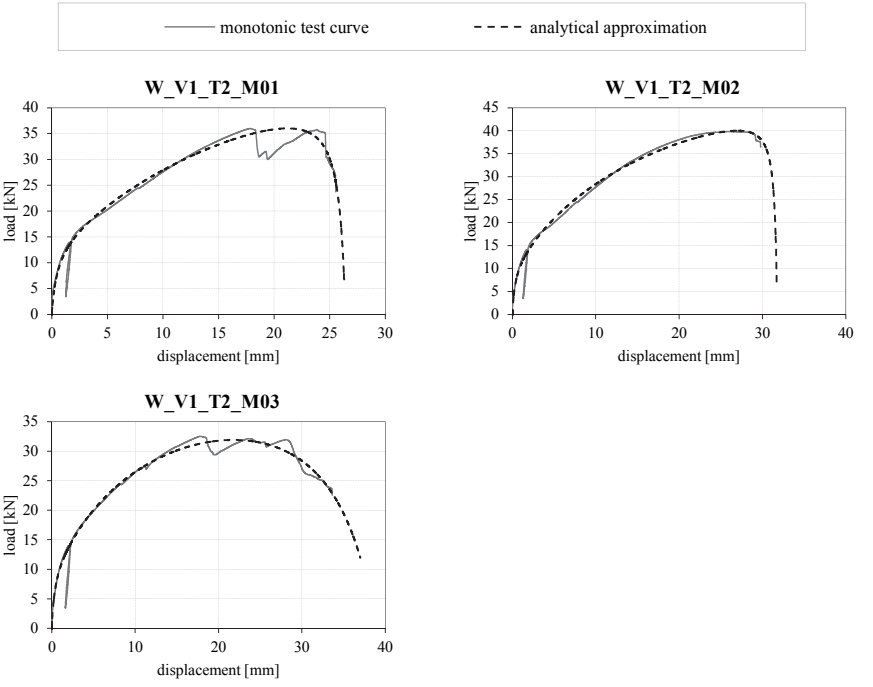

Figure B.5: actual and approximated load-displacement curves of monotonic tests on configuration W_V1_T2

Table B.6: results of cyclic tests on configuration W_V1_T2

notations		units	Z01	Z02	Z03	mean	*CoV*
ρ_{mean}		[kg/m³]	414	404	404	**407**	1.4%
F_{max}		[kN]	37.26	36.09	38.44	**37.26**	3.2%
v_{max}		[mm]	21.0	21.6	25.6	**22.7**	11.0%
$K_{ser,EN}$		[kN/mm]	8.443	5.078	3.914	**5.812**	40.5%
$F_{y,EN}$		[kN]	17.65	22.66	28.78	**23.03**	24.2%
$v_{y,EN}$		[mm]	1.7	3.9	6.6	**4.1**	60.0%
F_u		[kN]	29.81	31.40	33.34	**31.52**	5.6%
v_u		[mm]	24.4	29.8	27.9	**27.4**	9.9%
D_{EN}		[-]	14.4	7.6	4.3	**8.8**	58.5%
***D*-class**		[-]	high	high	moderate	**high**	
K_{SLS}		[kN/mm]	32.960	10.537	7.786	**17.094**	80.8%
K_{ULS}		[kN/mm]	10.815	5.994	5.101	**7.303**	42.1%
v_{ip}		[mm]	18.6	23.1	20.9	**20.9**	10.8%
Φ_{ip}		[-]	52%	55%	50%	**52%**	4.8%
***D*-class**		[-]	moderate	moderate	moderate	**moderate**	
appr. envelope curves 1	F_{max}	[kN]	37.50	36.10	39.00		
	v_{max}	[mm]	19.80	22.20	23.50		
	K_{ini}	[kN/mm]	20.00	20.00	18.00		
	F_A	[kN]	29.00	27.70	29.30		
	v_B	[mm]	27.00	32.00	31.80		
	K_B	[kN/mm]	-1.70	-1.20	-1.90		
appr. envelope curves 2	F_{max}	[kN]	32.00	32.60	35.00		
	v_{max}	[mm]	19.00	21.80	24.30		
	K_{ini}	[kN/mm]	28.00	18.00	13.00		
	F_A	[kN]	26.00	25.00	26.90		
	v_B	[mm]	27.00	31.20	32.20		
	K_B	[kN/mm]	-1.35	-1.10	-1.80		
appr. envelope curves 3	F_{max}	[kN]	30.40	31.20	33.00		
	v_{max}	[mm]	18.70	21.80	24.30		
	K_{ini}	[kN/mm]	40.00	15.00	12.00		
	F_A	[kN]	24.50	24.00	26.00		
	v_B	[mm]	27.00	30.50	32.20		
	K_B	[kN/mm]	-1.25	-1.10	-1.90		

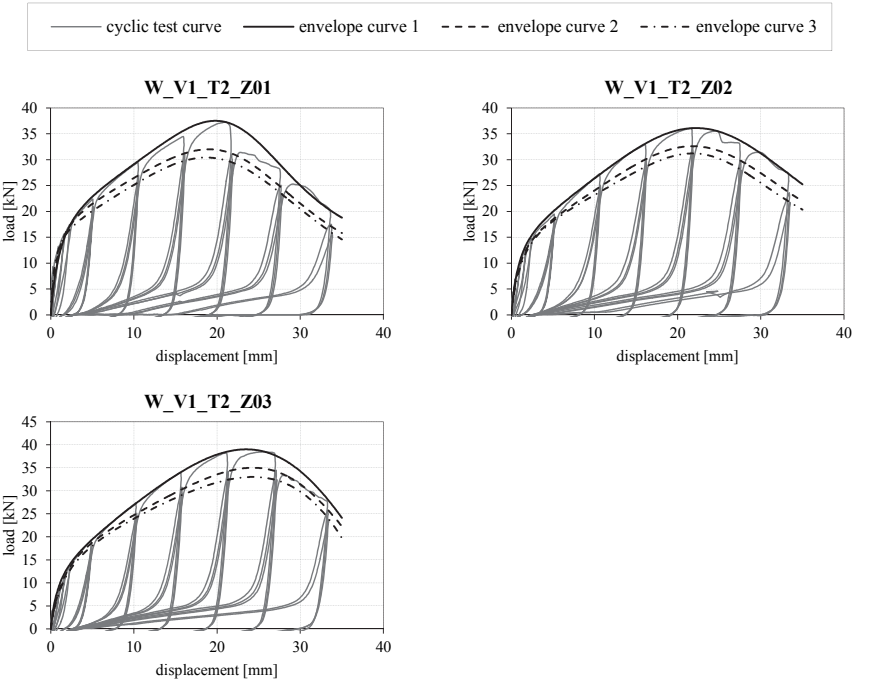

Figure B.6: actual and approximated load-displacement curves of cyclic tests on configuration W_V1_T2

Shear loaded wall-to-floor joint (W_V1_T3)

Table B.7: basic information for configuration W_V1_T3

parts	materials	specifications
wall segment	CLT	C24 | 98 mm (32-34-32)
floor segments	CLT	C24 | 138 mm (26-27-28-27-26)
connection	angle bracket	AE116
fasteners wall	annular-ringed shank nails	14 × CNA Ø 4.0×60 mm
fasteners floor	annular-ringed shank nails	7 × CNA Ø 4.0×60 mm

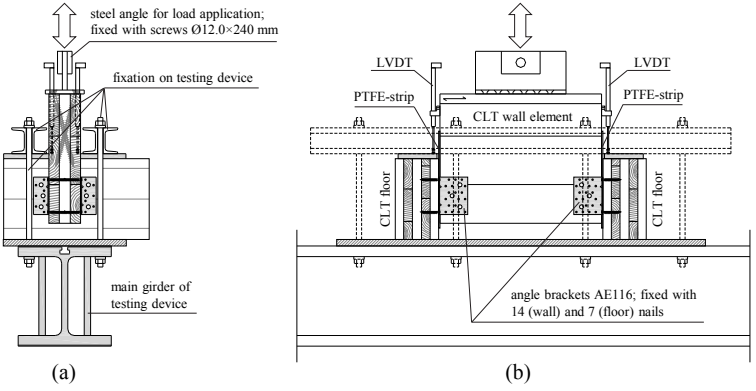

Figure B.7: test set-up for monotonic and cyclic experiments on configuration W_V1_W3 – (a) sheer plan; (b) front view

Table B.8: results of monotonic tests on configuration W_V1_T3

notations		**units**	**M01**	**M02**	**M03**	**M04**	**mean**	***CoV***
ρ_{mean}		[kg/m³]	450	438	450	438	**444**	1.6%
F_{max}		[kN]	23.08	21.21	22.41	22.66	**22.34**	3.6%
v_{max}		[mm]	24.8	24.0	24.4	24.7	**24.5**	1.5%
$K_{ser,EN}$		[kN/mm]	2.279	2.295	2.721	2.082	**2.344**	11.5%
$F_{y,EN}$		[kN]	17.86	15.85	16.28	18.76	**17.19**	7.9%
$v_{y,EN}$		[mm]	7.3	6.1	5.4	8.1	**6.7**	17.8%
F_u		[kN]	18.47	16.99	18.04	18.13	**17.91**	3.6%
v_u		[mm]	36.7	38.9	35.5	35.1	**36.6**	4.6%
D_{EN}		[-]	5.0	6.3	6.6	4.3	**5.6**	19.4%
***D*-class**		[-]	moderate	high	high	moderate	**moderate**	
K_{SLS}		[kN/mm]	3.444	3.980	4.851	4.088	**4.091**	14.2%
K_{ULS}		[kN/mm]	2.870	2.783	3.320	2.975	**2.987**	7.9%
v_{ip}		[mm]	29.3	31.5	28.9	28.3	**29.5**	4.7%
Φ_{ip}		[-]	60%	62%	63%	61%	**62%**	2.1%
***D*-class**		[-]	high	high	high	high	**high**	
approximation curves	F_{max}	[kN]	23.00	21.10	22.40	22.55		
	v_{max}	[mm]	24.10	24.40	23.00	22.30		
	K_{ini}	[kN/mm]	4.50	10.00	11.80	10.00		
	F_A	[kN]	19.00	17.75	18.60	18.50		
	v_B	[mm]	36.30	38.40	35.80	36.50		
	K_B	[kN/mm]	-0.80	-0.65	-0.71	-0.57		

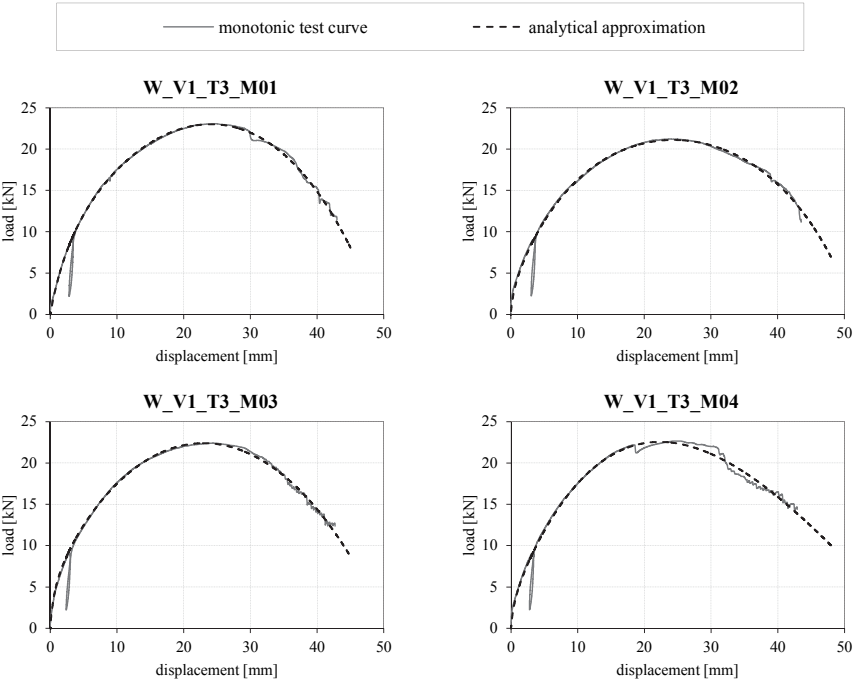

Figure B.8: actual and approximated load-displacement curves of monotonic tests on configuration W_V1_T3

Table B.9: results of cyclic tests on configuration W_V1_T3

notations		units	Z02	Z04	Z05	Z06	Z07	Z08	mean	*CoV*
ρ_{mean}		[kg/m³]	437	437	429	429	425	425	**430**	1.3%
F_{max}		[kN]	22.54	23.89	21.14	21.67	20.96	21.43	**21.94**	5.0%
v_{max}		[mm]	20.4	20.0	20.4	20.3	20.4	20.5	**20.3**	0.8%
$K_{ser,EN}$		[kN/mm]	2.503	2.786	2.422	2.527	2.544	2.647	**2.572**	5.0%
$F_{y,EN}$		[kN]	17.48	18.60	16.23	16.28	15.39	16.50	**16.75**	6.7%
$v_{y,EN}$		[mm]	6.4	6.1	6.1	6.0	5.5	5.7	**6.0**	5.3%
F_u		[kN]	18.29	19.11	16.91	17.34	16.77	17.15	**17.59**	5.2%
v_u		[mm]	25.8	21.9	26.1	26.4	28.5	23.5	**25.4**	9.2%
D_{EN}		[-]	4.1	3.6	4.2	4.4	5.1	4.1	**4.3**	11.5%
***D*-class**		[-]	moderate	low	moderate	moderate	moderate	moderate	**moderate**	
K_{SLS}		[kN/mm]	4.017	4.297	3.670	3.479	3.718	4.067	**3.874**	7.8%
K_{ULS}		[kN/mm]	3.080	3.450	2.807	2.854	2.944	3.164	**3.050**	7.8%
v_{ip}		[mm]	19.4	16.0	19.8	19.9	22.2	17.8	**19.2**	10.9%
Φ_{ip}		[-]	50%	46%	52%	51%	56%	52%	**51%**	6.4%
***D*-class**		[-]	moderate	moderate	moderate	moderate	moderate	moderate	**moderate**	
appr. envelope curves 1	F_{max}	[kN]	22.40	23.80	20.80	21.60	21.00	21.40		
	v_{max}	[mm]	20.00	18.50	19.80	19.80	22.00	19.00		
	K_{ini}	[kN/mm]	5.00	5.00	5.00	5.00	5.00	5.00		
	F_A	[kN]	17.50	18.80	16.50	16.90	17.00	17.10		
	v_B	[mm]	28.00	24.70	28.00	28.00	31.00	25.70		
	K_B	[kN/mm]	-1.20	-1.75	-1.00	-1.08	-1.10	-1.29		
appr. envelope curves 2	F_{max}	[kN]	18.10	19.20	17.00	17.40	17.00	17.50		
	v_{max}	[mm]	17.70	17.60	17.50	17.70	18.00	17.50		
	K_{ini}	[kN/mm]	5.00	6.00	6.00	5.50	6.00	6.50		
	F_A	[kN]	14.50	15.70	14.00	13.80	13.80	14.40		
	v_B	[mm]	25.00	23.60	25.00	25.00	26.00	23.80		
	K_B	[kN/mm]	-1.00	-1.40	-0.88	-0.91	-0.78	-1.13		
appr. envelope curves 3	F_{max}	[kN]	16.90	18.00	15.80	16.80	15.90	16.30		
	v_{max}	[mm]	17.30	17.20	17.50	17.50	18.20	17.00		
	K_{ini}	[kN/mm]	5.00	6.00	6.00	6.00	6.00	6.80		
	F_A	[kN]	14.00	14.90	13.00	13.20	13.20	13.50		
	v_B	[mm]	24.50	23.00	24.50	23.50	24.70	23.50		
	K_B	[kN/mm]	-1.00	-1.40	-0.88	-1.09	-1.00	-1.01		

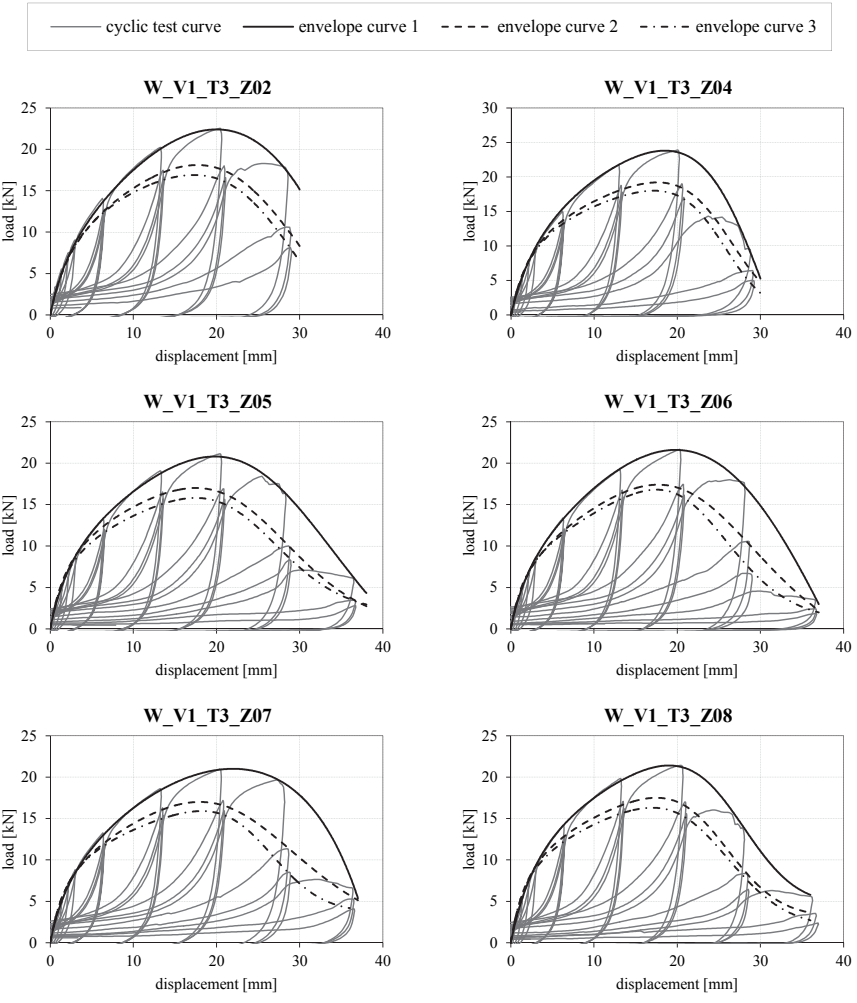

Figure B.9: actual and approximated load-displacement curves of cyclic tests on configuration W_V1_T3

Tension loaded wall-to-floor joint (W_V1_T4)

Table B.10: basic information for configuration W_V1_T4

parts	materials	specifications
wall segment	CLT	C24 | 98 mm (32-34-32)
floor segment	CLT	C24 | 138 mm (26-27-28-27-26)
connection	angle bracket	AE116
fasteners wall	annular-ringed shank nails	14 × CNA Ø 4.0×60 mm
fasteners floor	annular-ringed shank nails	7 × CNA Ø 4.0×60 mm

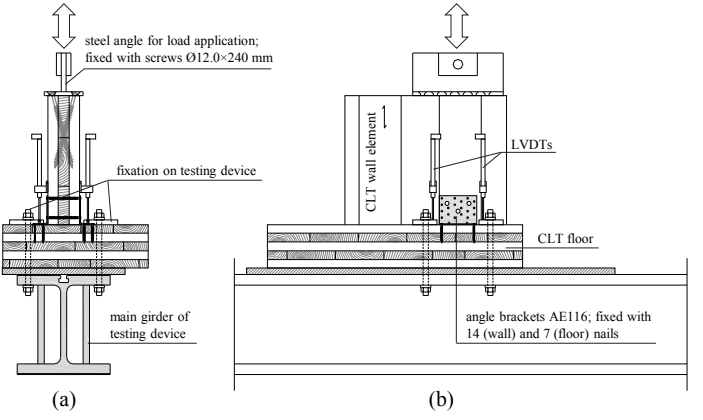

Figure B.10: test set-up for monotonic and cyclic experiments on configuration W_V1_W4 – (a) sheer plan; (b) front view

Table B.11: results of monotonic tests on configuration W_V1_T4

notations		units	M01	M02	M03[1)]	M04	mean	*CoV*
ρ_{mean}		[kg/m³]	441	441	439	439	**440**	0.3%
F_{max}		[kN]	12.32	12.13	13.07	13.81	**12.83**	6.0%
v_{max}		[mm]	4.4	4.0	4.2	4.5	**4.3**	5.1%
$K_{ser,EN}$		[kN/mm]	16.541	13.493	14.974	7.637	**13.161**	29.5%
$F_{y,EN}$		[kN]	6.99	7.39	7.41	10.91	**8.17**	22.4%
$v_{y,EN}$		[mm]	0.4	0.5	0.4	1.3	**0.6**	67.9%
F_u		[kN]	9.86	9.71	10.46	11.05	**10.27**	6.0%
v_u		[mm]	14.6	16.1	16.2	16.5	**15.8**	5.3%
D_{EN}		[-]	38.9	33.2	38.2	12.7	**30.8**	39.9%
***D*-class**		[-]	high	high	high	high	**high**	
K_{SLS}		[kN/mm]	34.043	32.651	58.511	16.228	**35.358**	49.3%
K_{ULS}		[kN/mm]	23.202	20.267	27.089	11.646	**20.551**	31.9%
v_{ip}		[mm]	12.9	14.3	15.8	13.8	**14.2**	8.5%
Φ_{ip}		[-]	76%	78%	95%	67%	**79%**	14.8%
***D*-class**		[-]	high	high	high	high	**high**	
approximation curves	F_{max}	[kN]	12.30	12.10	13.00	13.90		
	v_{max}	[mm]	5.10	4.30	3.90	4.30		
	K_{ini}	[kN/mm]	40.00	30.00	50.00	30.00		
	F_A	[kN]	11.45	11.07	11.20	11.30		
	v_B	[mm]	13.05	16.00	16.00	16.00		
	K_B	[kN/mm]	-0.45	-0.16	-0.09	-0.10		

[1)] Due to a differing 'valid range', here approximation parameters deviate from [T2] approximation in Chapter 3; however, the resulting load-displacement curve is similar.

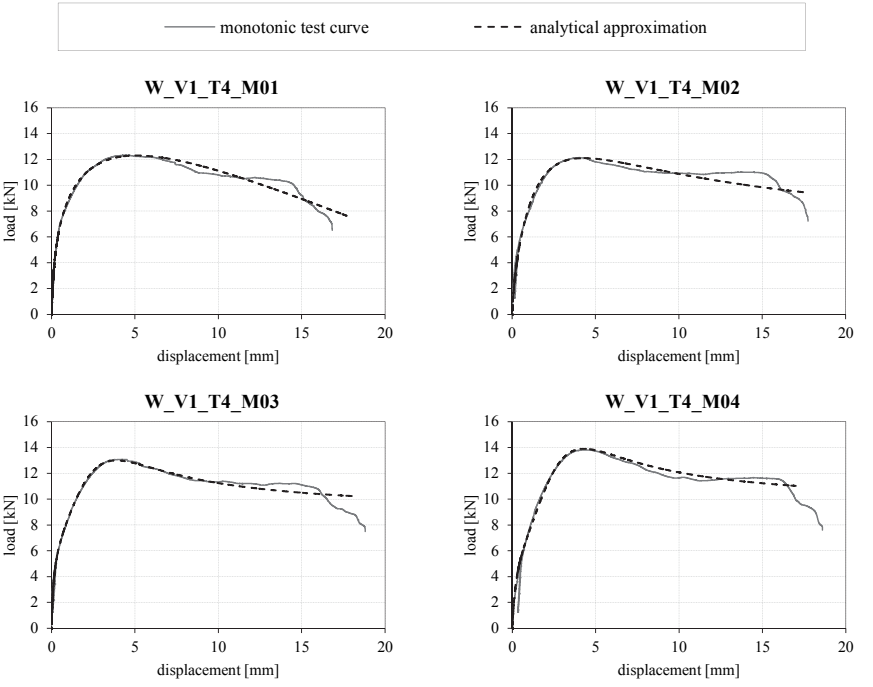

Figure B.11: actual and approximated load-displacement curves of monotonic tests on configuration W_V1_T4

Table B.12: results of cyclic tests on configuration W_V1_T4

notations		units	Z01	Z02	Z03	Z04	Z05	Z06	Z07	Z08	mean	*CoV*
ρ_{mean}		[kg/m³]	443	443	432	432	444	444	445	445	**441**	1.3%
F_{max}		[kN]	12.35	12.80	11.17	11.59	10.83	10.82	11.95	11.52	**11.63**	6.1%
v_{max}		[mm]	3.8	4.0	3.7	4.0	3.6	3.9	3.9	3.6	**3.8**	4.1%
$K_{ser,EN}$		[kN/mm]	10.087	12.106	8.448	8.085	10.992	8.256	9.265	10.917	**9.769**	15.2%
$F_{y,EN}$		[kN]	8.56	8.20	8.25	8.87	6.90	7.69	8.60	7.40	**8.06**	8.3%
$v_{y,EN}$		[mm]	0.8	0.6	0.9	1.0	0.6	0.9	0.8	0.6	**0.8**	19.9%
F_u		[kN]	9.88	10.24	8.94	9.27	8.66	8.66	9.56	9.22	**9.30**	6.1%
v_u		[mm]	13.4	11.8	10.9	14.4	12.2	13.1	12.9	12.0	**12.6**	8.6%
D_{EN}		[-]	17.2	19.1	12.3	14.2	21.2	15.2	15.4	19.0	**16.7**	17.7%
***D*-class**		[-]	high	high	high	high	high	high	high	high	**high**	
K_{SLS}		[kN/mm]	18.092	20.690	16.015	13.470	19.431	13.272	16.631	17.577	**16.897**	15.6%
K_{ULS}		[kN/mm]	12.313	15.003	9.950	9.413	11.816	9.048	11.348	12.131	**11.378**	17.0%
v_{ip}		[mm]	11.5	10.2	9.1	12.6	10.6	11.6	11.3	10.2	**10.9**	9.9%
Φ_{ip}		[-]	72%	73%	67%	75%	74%	77%	75%	70%	**73%**	4.4%
***D*-class**		[-]	high	high	high	high	high	high	high	high	**high**	
appr. envelope curves 1	F_{max}	[kN]	12.20	12.80	11.10	11.50	10.80	10.80	11.90	11.40		
	v_{max}	[mm]	5.10	5.10	4.20	5.00	4.70	5.00	5.50	4.40		
	K_{ini}	[kN/mm]	20.00	25.00	12.00	10.00	15.00	14.00	20.00	14.00		
	F_A	[kN]	11.45	12.00	10.00	10.80	10.10	10.10	11.10	10.40		
	v_B	[mm]	13.50	12.20	10.00	15.00	12.50	13.50	13.50	11.20		
	K_B	[kN/mm]	-0.51	-0.61	-0.59	-0.40	-0.50	-0.40	-0.45	-0.49		
appr. envelope curves 2	F_{max}	[kN]	11.00	11.50	9.90	10.30	9.60	9.55	10.60	10.30		
	v_{max}	[mm]	5.10	5.10	4.00	6.00	3.50	4.90	4.50	3.00		
	K_{ini}	[kN/mm]	20.00	21.00	13.00	21.00	13.00	15.00	14.00	15.00		
	F_A	[kN]	10.50	11.00	9.10	9.70	8.80	8.90	9.80	9.40		
	v_B	[mm]	12.00	12.50	10.00	14.00	10.50	13.00	13.50	9.50		
	K_B	[kN/mm]	-0.50	-0.46	-0.54	-0.43	-0.38	-0.35	-0.32	-0.39		
appr. envelope curves 3	F_{max}	[kN]	10.50	11.00	9.50	10.00	9.40	9.20	10.30	9.90		
	v_{max}	[mm]	4.90	4.90	3.70	4.90	4.30	4.40	4.50	3.00		
	K_{ini}	[kN/mm]	20.00	20.00	14.00	14.00	16.00	14.00	14.00	15.00		
	F_A	[kN]	10.00	10.50	8.70	9.20	8.70	8.50	9.50	9.00		
	v_B	[mm]	12.00	12.00	9.50	12.00	10.00	11.50	12.00	8.50		
	K_B	[kN/mm]	-0.47	-0.44	-0.50	-0.41	-0.54	-0.36	-0.38	-0.46		

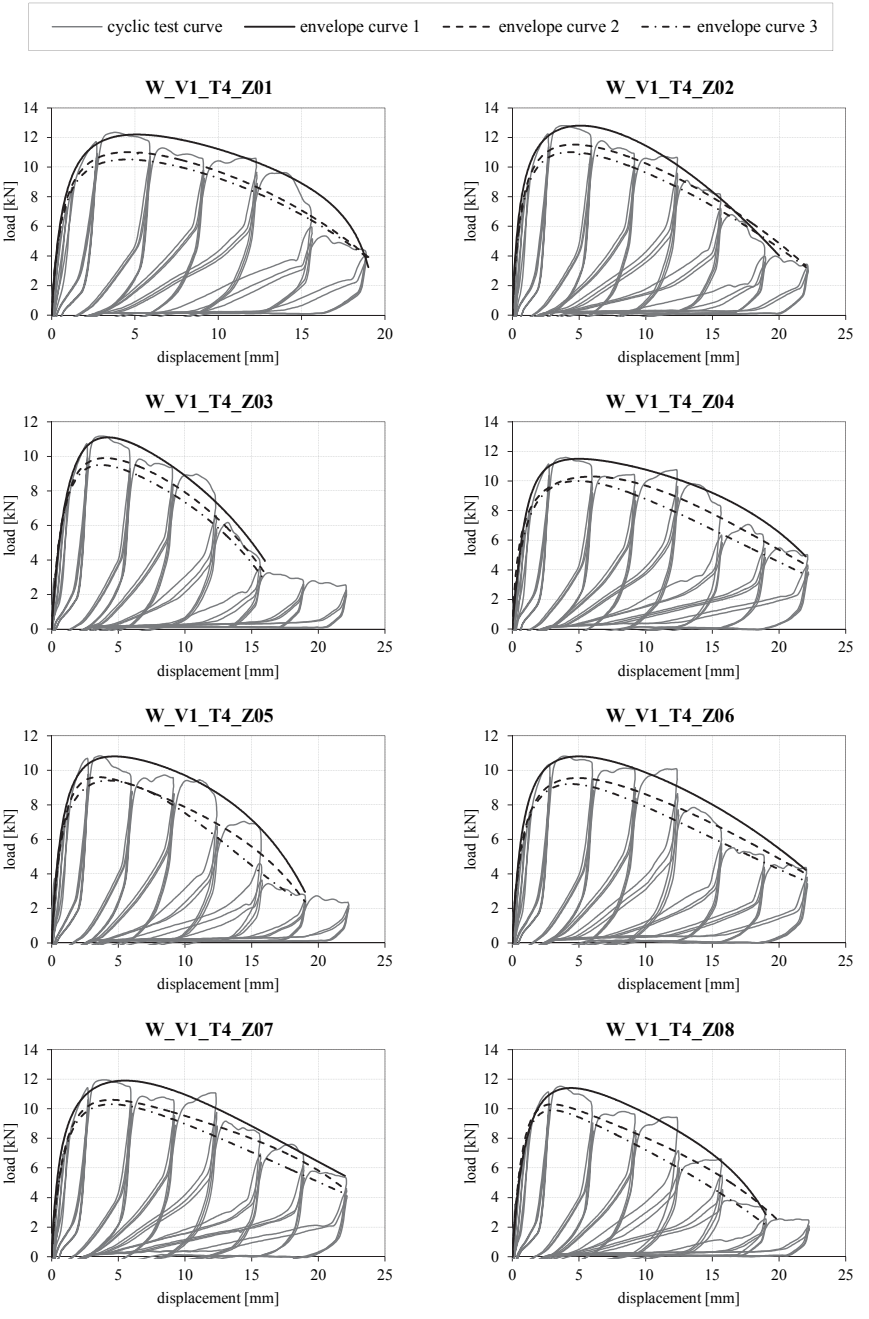

Figure B.12: actual and approximated load-displacement curves of cyclic tests on configuration W_V1_T4

B-1.2 Hold-downs

Tension loaded wall-to-foundation joint (Z_V2_T21)

Table B.13: basic information for configuration Z_V2_T21

parts	materials	specifications
wall segment	CLT	C24 | 98 mm (32-34-32)
floor segment	steel	-
connection	hold-down	HTT22
fasteners wall	annular-ringed shank nails	15 × CNA Ø 4.0×60 mm
fastener floor	threaded rod	Ø 16.0mm

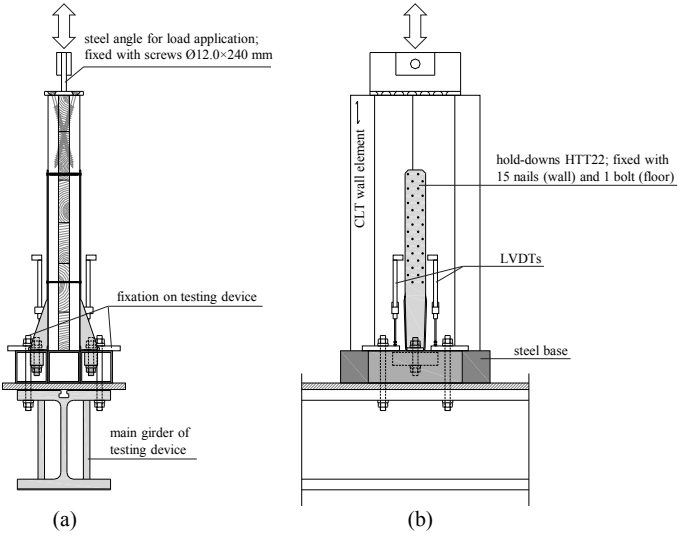

Figure B.13: test set-up for monotonic and cyclic experiments on configuration Z_V2_T21 – (a) sheer plan; (b) front view

Table B.14: results of monotonic test on configuration Z_V2_T21

notations		units	M03
ρ_{mean}		[kg/m³]	393
F_{max}		[kN]	48.82
v_{max}		[mm]	17.7
$K_{ser,EN}$		[kN/mm]	8.061
$F_{y,EN}$		[kN]	32.33
$v_{y,EN}$		[mm]	3.5
F_u		[kN]	39.12
v_u		[mm]	25.9
D_{EN}		[-]	7.4
***D*-class**		[-]	high
K_{SLS}		[kN/mm]	15.315
K_{ULS}		[kN/mm]	10.326
v_{ip}		[mm]	20.4
Φ_{ip}		[-]	57%
***D*-class**		[-]	moderate
approximation curve	F_{max}	[kN]	48.40
	v_{max}	[mm]	17.70
	K_{ini}	[kN/mm]	32.00
	F_A	[kN]	38.50
	v_B	[mm]	25.60
	K_B	[kN/mm]	-2.40

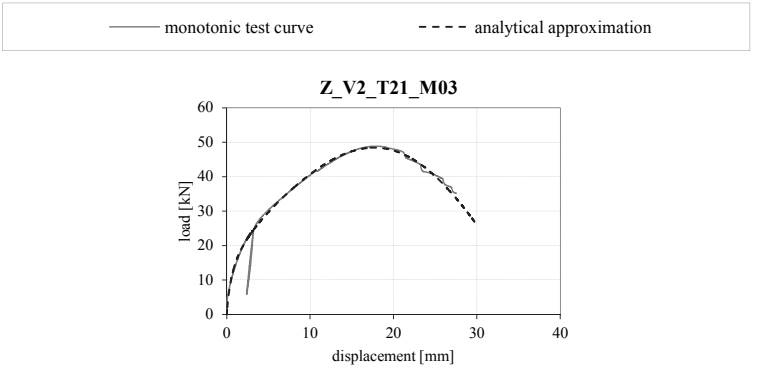

Figure B.14: actual and approximated load-displacement curve of monotonic test on configuration Z_V2_T21

Table B.15: results of cyclic tests on configuration Z_V2_T21

notations		units	Z01	Z02	Z03	mean	*CoV*
ρ_{mean}		[kg/m³]	397	411	428	**412**	3.8%
F_{max}		[kN]	48.90	51.45	53.04	**51.13**	4.1%
v_{max}		[mm]	16.5	17.0	21.1	**18.2**	13.8%
$K_{ser,EN}$		[kN/mm]	9.119	6.917	7.059	**7.698**	16.0%
$F_{y,EN}$		[kN]	30.79	38.82	36.28	**35.29**	11.6%
$v_{y,EN}$		[mm]	2.9	5.0	4.5	**4.2**	26.5%
F_u		[kN]	39.56	41.16	49.41	**43.38**	12.2%
v_u		[mm]	25.4	26.3	24.8	**25.5**	2.8%
D_{EN}		[-]	8.7	5.2	5.5	**6.5**	29.8%
***D*-class**		[-]	high	moderate	moderate	**high**	
K_{SLS}		[kN/mm]	17.680	13.025	17.295	**16.000**	16.1%
K_{ULS}		[kN/mm]	10.702	8.603	9.409	**9.571**	11.1%
v_{ip}		[mm]	20.2	20.3	19.0	**19.8**	3.7%
Φ_{ip}		[-]	59%	55%	53%	**56%**	5.5%
***D*-class**		[-]	moderate	moderate	moderate	**moderate**	
appr. envelope curves 1	F_{max}	[kN]	48.50	51.00	53.00		
	v_{max}	[mm]	16.50	17.50	21.00		
	K_{ini}	[kN/mm]	30.00	30.00	40.00		
	F_A	[kN]	39.00	39.50	42.00		
	v_B	[mm]	26.00	27.00	28.20		
	K_B	[kN/mm]	-1.55	-1.75	-3.70		
appr. envelope curves 2	F_{max}	[kN]	44.00	46.20	48.30		
	v_{max}	[mm]	16.50	17.00	20.00		
	K_{ini}	[kN/mm]	30.00	30.00	25.00		
	F_A	[kN]	36.50	36.80	39.00		
	v_B	[mm]	26.50	26.50	28.00		
	K_B	[kN/mm]	-1.50	-1.70	-2.80		
appr. envelope curves 3	F_{max}	[kN]	43.00	45.00	46.30		
	v_{max}	[mm]	16.50	16.50	20.00		
	K_{ini}	[kN/mm]	30.00	30.00	30.00		
	F_A	[kN]	35.50	36.80	38.00		
	v_B	[mm]	26.00	26.00	28.00		
	K_B	[kN/mm]	-1.60	-1.75	-2.90		

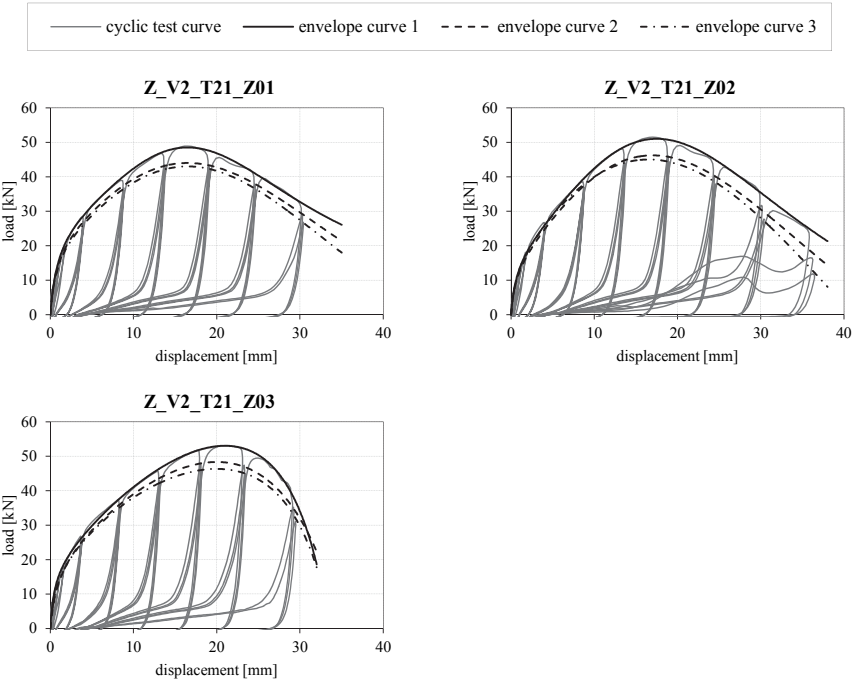

Figure B.15: actual and approximated load-displacement curves of cyclic tests on configuration Z_V2_T21

Tension loaded wall-to-floor joint (Z_V2_T4)

Table B.16: basic information for configuration Z_V2_T4

parts	materials	specifications
wall segment	CLT	C24 | 98 mm (32-34-32)
floor segment	CLT	C24 | 138 mm (26-27-28-27-26)
connection	hold-down	HTT22
fasteners wall	annular-ringed shank nails	15 × CNA Ø 4.0×60 mm
fasteners floor	threaded rod	Ø 16.0mm (+ counter-plate)

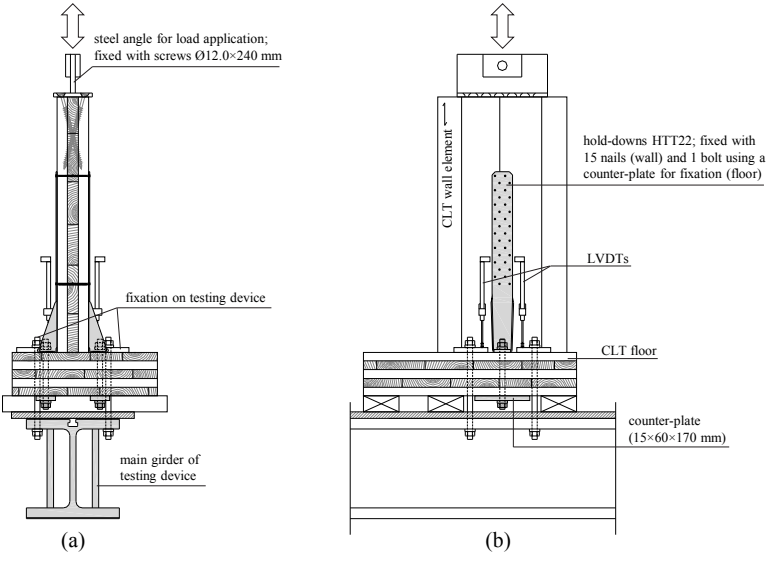

Figure B.16: test set-up for monotonic and cyclic experiments on configuration Z_V2_T4 – (a) sheer plan; (b) front view

Table B.17: results of monotonic tests on configuration Z_V2_T4

notations		units	M01	M02	mean	*CoV*
ρ_{mean}		[kg/m³]	423	423	**423**	0.0%
F_{max}		[kN]	51.80	51.27	**51.53**	0.7%
v_{max}		[mm]	24.1	21.3	**22.7**	8.7%
$K_{ser,EN}$		[kN/mm]	7.009	7.356	**7.183**	3.4%
$F_{y,EN}$		[kN]	32.79	32.90	**32.85**	0.2%
$v_{y,EN}$		[mm]	4.0	3.8	**3.9**	3.3%
F_u		[kN]	41.45	41.02	**41.24**	0.7%
v_u		[mm]	34.4	35.3	**34.8**	1.8%
D_{EN}		[-]	8.6	9.2	**8.9**	4.8%
***D*-class**		[-]	high	high	**high**	
K_{SLS}		[kN/mm]	14.780	16.707	**15.743**	8.7%
K_{ULS}		[kN/mm]	9.099	9.485	**9.292**	2.9%
v_{ip}		[mm]	27.5	28.3	**27.9**	2.0%
Φ_{ip}		[-]	60%	60%	**60%**	0.0%
***D*-class**		[-]	high	high	**high**	
approximation curves	F_{max}	[kN]	51.70	51.30		
	v_{max}	[mm]	24.50	21.50		
	K_{ini}	[kN/mm]	48.00	40.00		
	F_A	[kN]	42.00	40.20		
	v_B	[mm]	34.60	35.00		
	K_B	[kN/mm]	-2.40	-1.05		

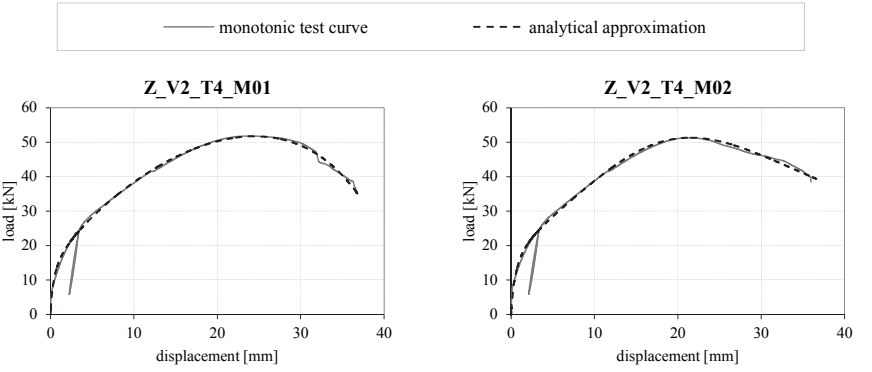

Figure B.17: actual and approximated load-displacement curves of monotonic tests on configuration Z_V2_T4

Table B.18: results of cyclic tests on configuration Z_V2_T4

notations		units	Z01	Z02	Z03	Z04[1)]	mean	*CoV*
ρ_{mean}		[kg/m³]	429	412	449	445	**434**	3.9%
F_{max}		[kN]	55.76	50.83	54.71	48.06	**52.34**	6.8%
v_{max}		[mm]	23.2	21.3	21.1	21.3	**21.7**	4.5%
$K_{ser,EN}$		[kN/mm]	6.163	6.980	7.537	7.111	**6.948**	8.3%
$F_{y,EN}$		[kN]	40.71	33.15	36.98	30.79	**35.41**	12.3%
$v_{y,EN}$		[mm]	5.8	4.1	4.2	3.7	**4.5**	20.7%
F_u		[kN]	44.61	40.66	43.77	38.45	**41.87**	6.8%
v_u		[mm]	28.7	27.0	28.1	29.1	**28.2**	3.2%
D_{EN}		[-]	5.0	6.6	6.6	7.9	**6.5**	18.3%
***D*-class**		[-]	moderate	high	high	high	**high**	
K_{SLS}		[kN/mm]	14.342	21.446	25.893	19.511	**20.298**	23.6%
K_{ULS}		[kN/mm]	8.609	8.649	10.384	8.112	**8.938**	11.1%
v_{ip}		[mm]	21.9	20.6	22.0	23.0	**21.9**	4.5%
Φ_{ip}		[-]	52%	52%	57%	58%	**55%**	5.8%
***D*-class**		[-]	moderate	moderate	moderate	moderate	**moderate**	
appr. envelope curves 1	F_{max}	[kN]	55.60	51.00	55.50	48.10		
	v_{max}	[mm]	23.00	20.50	20.30	21.00		
	K_{ini}	[kN/mm]	20.00	30.00	30.00	30.00		
	F_A	[kN]	43.00	39.00	42.00	38.00		
	v_B	[mm]	31.50	28.80	28.30	30.50		
	K_B	[kN/mm]	-2.60	-2.30	-2.40	-1.86		
appr. envelope curves 2	F_{max}	[kN]	51.20	46.00	51.00	45.00		
	v_{max}	[mm]	22.60	20.00	20.40	21.80		
	K_{ini}	[kN/mm]	20.00	25.00	30.00	25.00		
	F_A	[kN]	40.00	36.50	40.00	36.00		
	v_B	[mm]	31.30	28.40	28.90	29.70		
	K_B	[kN/mm]	-2.35	-2.10	-2.25	-2.18		
appr. envelope curves 3	F_{max}	[kN]	49.00	44.50	49.00	43.00		
	v_{max}	[mm]	22.00	20.00	20.80	21.80		
	K_{ini}	[kN/mm]	20.00	30.00	30.00	20.00		
	F_A	[kN]	38.20	35.00	39.00	35.00		
	v_B	[mm]	29.90	28.00	28.90	29.50		
	K_B	[kN/mm]	-2.40	-2.13	-2.35	-2.18		

1) tested with a thinner counter-plate (6 mm instead of 15 mm)

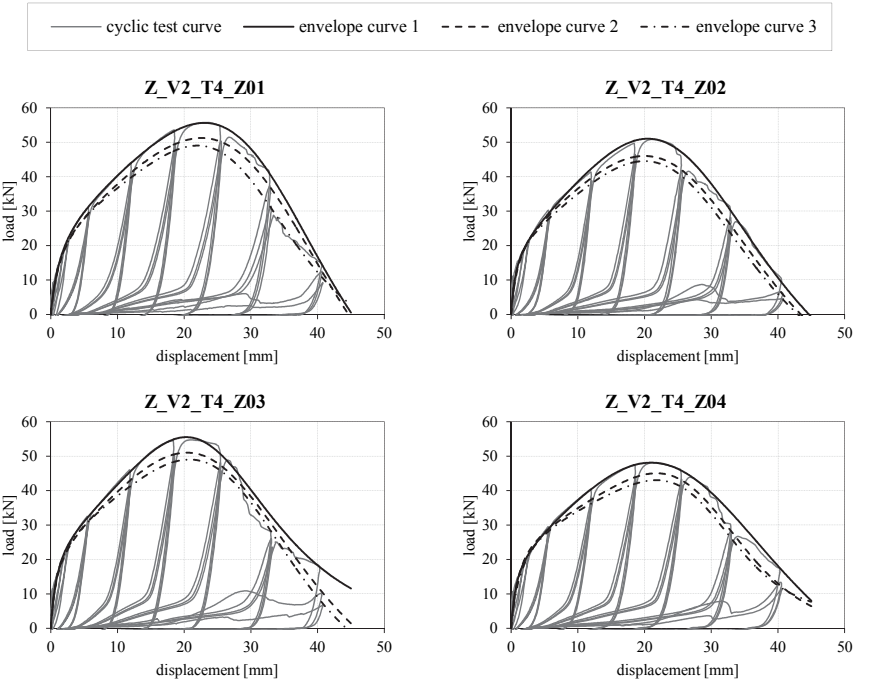

Figure B.18: actual and approximated load-displacement curves of cyclic tests on configuration Z_V2_T4

B-1.3 Screws

Shear loaded wall-to-floor joint (S_V1_T61)

Table B.19: basic information for configuration S_V1_T61

parts	materials	specifications
wall segment	CLT	C24 | 98 mm (32-34-32)
floor segments	CLT	C24 | 138 mm (26-27-28-27-26)
connection	screws	Stardrive Ø 8.0×280 mm

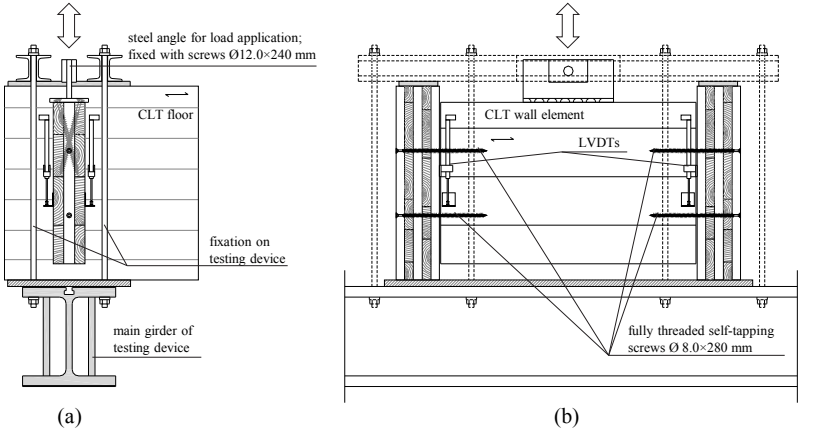

Figure B.19: test set-up for monotonic and cyclic experiments on configuration S_V1_T61 – (a) sheer plan; (b) front view

Table B.20: results of monotonic tests on configuration S_V1_T61

notations		units	M01	M02	M03	mean	*CoV*
ρ_{mean}		[kg/m³]	422	427	427	**425**	0.7%
F_{max}		[kN]	11.31	10.60	10.02	**10.64**	6.1%
v_{max}		[mm]	28.2	26.2	24.6	**26.3**	6.9%
$K_{ser,EN}$		[kN/mm]	0.448	0.474	0.466	**0.462**	2.9%
$F_{y,EN}$		[kN]	11.01	10.19	9.62	**10.28**	6.8%
$v_{y,EN}$		[mm]	22.5	19.8	18.7	**20.3**	9.7%
F_u		[kN]	10.03	10.12	8.27	**9.47**	11.0%
v_u		[mm]	45.8	43.7	44.0	**44.5**	2.6%
D_{EN}		[-]	2.0	2.2	2.4	**2.2**	9.1%
***D*-class**		[-]	low	low	low	**low**	
K_{SLS}		[kN/mm]	0.845	0.853	1.211	**0.969**	21.6%
K_{ULS}		[kN/mm]	0.575	0.584	0.621	**0.593**	4.1%
v_{ip}		[mm]	34.9	34.0	34.1	**34.3**	1.4%
Φ_{ip}		[-]	52%	56%	55%	**54%**	3.9%
***D*-class**		[-]	moderate	moderate	moderate	**moderate**	
approximation curves	F_{max}	[kN]	11.31	10.59	9.95		
	v_{max}	[mm]	29.40	28.60	26.30		
	K_{ini}	[kN/mm]	5.58	2.56	16.40		
	F_A	[kN]	7.96	7.84	7.23		
	v_B	[mm]	65.00	362.00	58.68		
	K_B	[kN/mm]	-0.05	0.00	-0.05		

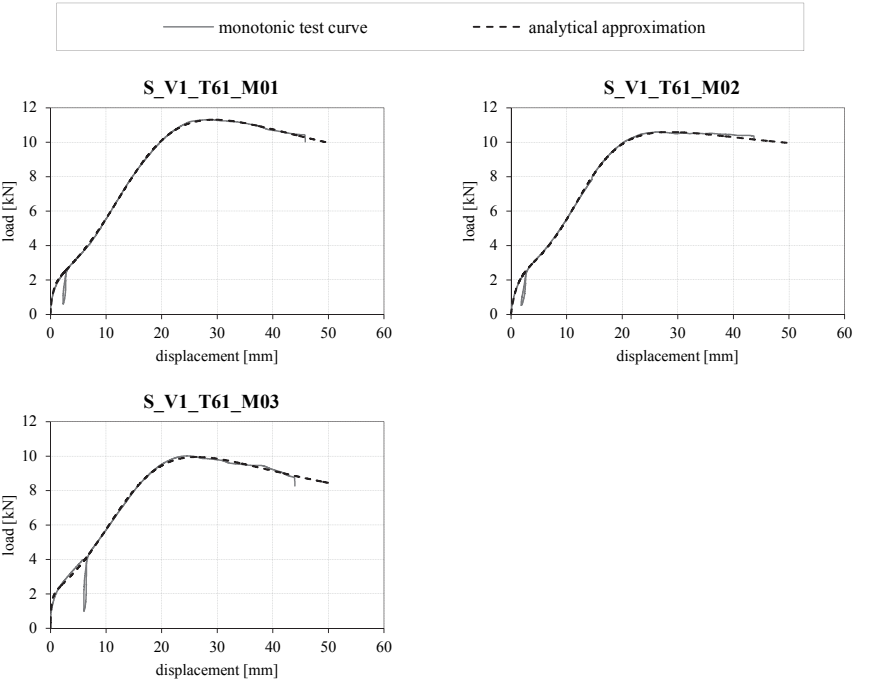

Figure B.20: actual and approximated load-displacement curves of monotonic tests on configuration S_V1_T61

Table B.21: results of cyclic tests on configuration S_V1_T61

notations		units	Z01	Z02	Z03	Z04	Z05	Z06	mean	*CoV*
ρ_{mean}		[kg/m³]	432	430	435	432	424	429	**430**	0.9%
F_{max}		[kN]	13.68	11.46	12.25	13.25	11.88	11.85	**12.40**	7.1%
v_{max}		[mm]	24.7	25.0	24.7	34.1	33.1	33.6	**29.2**	16.6%
$K_{ser,EN}$		[kN/mm]	0.826	0.622	0.554	0.544	0.493	0.466	**0.584**	22.3%
$F_{y,EN}$		[kN]	12.17	10.46	11.82	12.02	10.85	10.91	**11.37**	6.3%
$v_{y,EN}$		[mm]	13.4	15.3	19.4	20.0	20.1	21.3	**18.3**	17.3%
F_u		[kN]	10.95	9.17	9.80	10.60	10.66	10.15	**10.22**	6.4%
v_u		[mm]	33.1	32.7	37.5	35.1	40.4	39.0	**36.3**	8.7%
D_{EN}		[-]	2.5	2.1	1.9	1.8	2.0	1.8	**2.0**	13.2%
***D*-class**		[-]	low	low	low	low	low	low	**low**	
K_{SLS}		[kN/mm]	1.733	1.221	1.260	1.093	0.863	0.836	**1.168**	28.1%
K_{ULS}		[kN/mm]	1.098	0.744	0.701	0.714	0.605	0.576	**0.740**	25.3%
v_{ip}		[mm]	24.3	23.0	26.7	23.6	29.0	27.0	**25.6**	9.1%
Φ_{ip}		[-]	47%	41%	42%	34%	43%	38%	**41%**	10.8%
***D*-class**		[-]	moderate	moderate	moderate	low	moderate	low	**moderate**	
appr. envelope curves 1	F_{max}	[kN]	13.80	11.50	12.10	13.00	12.00	11.80		
	v_{max}	[mm]	23.80	25.00	27.30	33.00	32.80	34.20		
	K_{ini}	[kN/mm]	5.00	3.00	6.00	3.00	5.00	5.00		
	F_A	[kN]	10.20	7.70	8.30	9.70	8.70	8.50		
	v_B	[mm]	33.50	35.00	38.50	41.00	47.00	44.00		
	K_B	[kN/mm]	-0.57	-0.34	-0.36	-1.00	-0.31	-0.60		
appr. envelope curves 2	F_{max}	[kN]	9.50	9.10	9.00	10.00	9.80	9.30		
	v_{max}	[mm]	20.70	25.50	24.00	28.00	34.00	33.90		
	K_{ini}	[kN/mm]	5.00	3.00	2.50	3.00	3.00	3.00		
	F_A	[kN]	7.80	6.70	5.90	7.10	7.10	7.00		
	v_B	[mm]	32.00	37.50	35.00	37.60	49.00	44.70		
	K_B	[kN/mm]	-0.34	-0.23	-0.15	-0.40	-0.22	-0.42		
appr. envelope curves 3	F_{max}	[kN]	8.70	8.50	7.80	9.40	9.00	8.50		
	v_{max}	[mm]	20.70	25.50	25.30	27.90	30.00	33.90		
	K_{ini}	[kN/mm]	5.00	3.00	3.00	3.00	3.00	3.00		
	F_A	[kN]	7.00	6.20	5.90	6.50	6.00	6.40		
	v_B	[mm]	31.30	35.30	34.30	36.20	39.00	44.00		
	K_B	[kN/mm]	-0.32	-0.29	-0.35	-0.45	-0.36	-0.42		

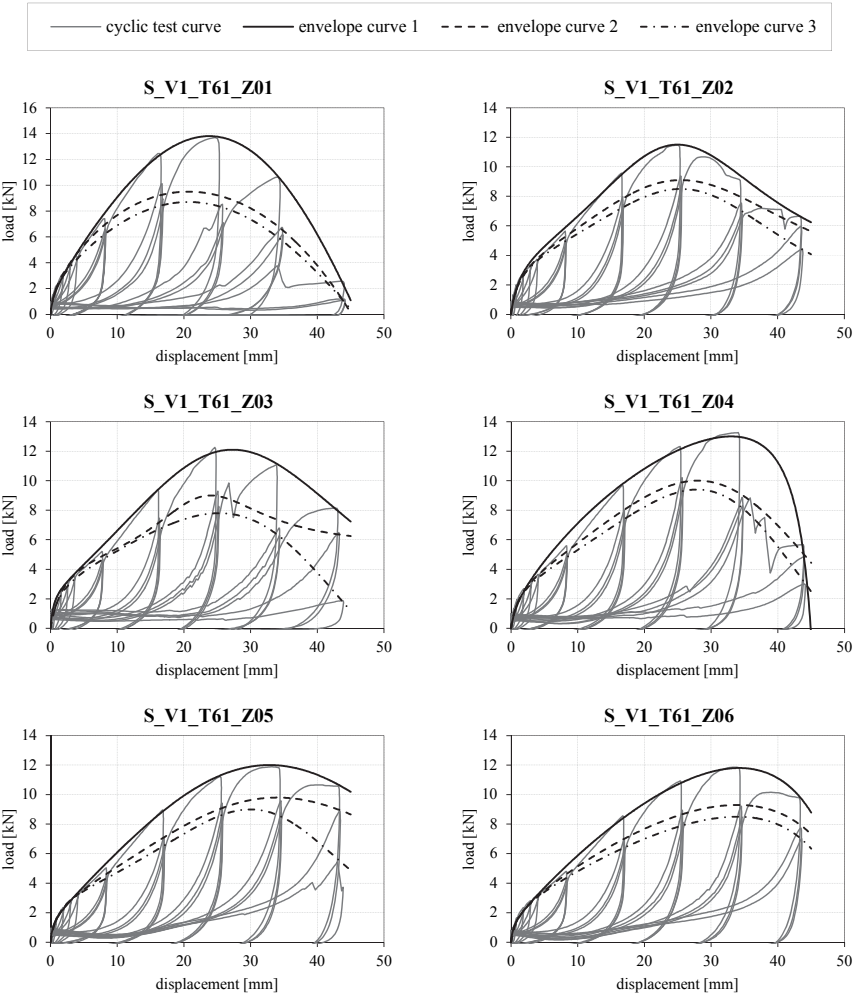

Figure B.21: actual and approximated load-displacement curves of cyclic tests on configuration S_V1_T61

Tension loaded wall-to-floor joint (S_V1_T41)

Table B.22: basic information for configuration S_V1_T41

parts	materials	specifications
wall segment	CLT	C24 | 98 mm (32-34-32)
floor segment	CLT	C24 | 138 mm (26-27-28-27-26)
connection	screws	Stardrive Ø 8.0×280 mm

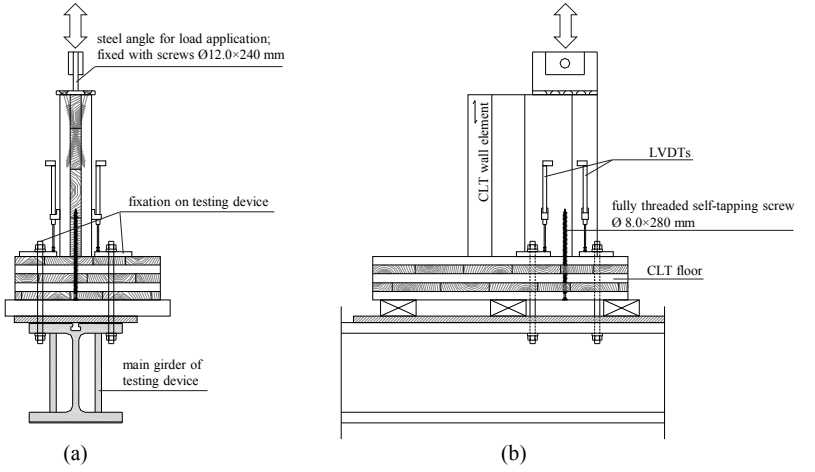

Figure B.22: test set-up for monotonic and cyclic experiments on configuration S_V1_T41 – (a) sheer plan; (b) front view

Table B.23: results of monotonic tests on configuration S_V1_T41

notations		units	M01	M02[1)]	M03	mean	*CoV*
ρ_{mean}		[kg/m³]	427	427	427	**427**	0.0%
F_{max}		[kN]	20.65	21.52	20.36	**20.84**	2.9%
v_{max}		[mm]	2.0	1.9	2.0	**2.0**	3.0%
$K_{ser,EN}$		[kN/mm]	18.509	16.143	18.157	**17.603**	7.3%
$F_{y,EN}$		[kN]	17.98	19.71	17.66	**18.45**	6.0%
$v_{y,EN}$		[mm]	0.9	1.1	0.9	**1.0**	13.1%
F_u		[kN]	16.57	17.22	16.29	**16.70**	2.9%
v_u		[mm]	3.6	3.2	3.4	**3.4**	6.6%
D_{EN}		[-]	4.0	2.8	3.6	**3.5**	17.5%
***D*-class**		[-]	moderate	low	low	**low**	
K_{SLS}		[kN/mm]	32.900	26.191	23.137	**27.409**	18.2%
K_{ULS}		[kN/mm]	21.968	19.350	19.905	**20.408**	6.8%
v_{ip}		[mm]	2.9	2.4	2.6	**2.6**	9.7%
Φ_{ip}		[-]	59%	50%	55%	**55%**	8.2%
***D*-class**		[-]	low	low	low	**low**	
approximation curves	F_{max}	[kN]	20.60	21.30	20.50		
	v_{max}	[mm]	2.00	1.93	2.03		
	K_{ini}	[kN/mm]	77.00	62.00	29.80		
	F_A	[kN]	15.90	15.28	15.38		
	v_B	[mm]	3.50	3.16	3.27		
	K_B	[kN/mm]	-3.63	-4.50	-4.38		

[1)] Due to a differing 'valid range', approximation parameters here do deviate from [T1] approximation in Chapter 3; however, the resulting load-displacement curve is similar.

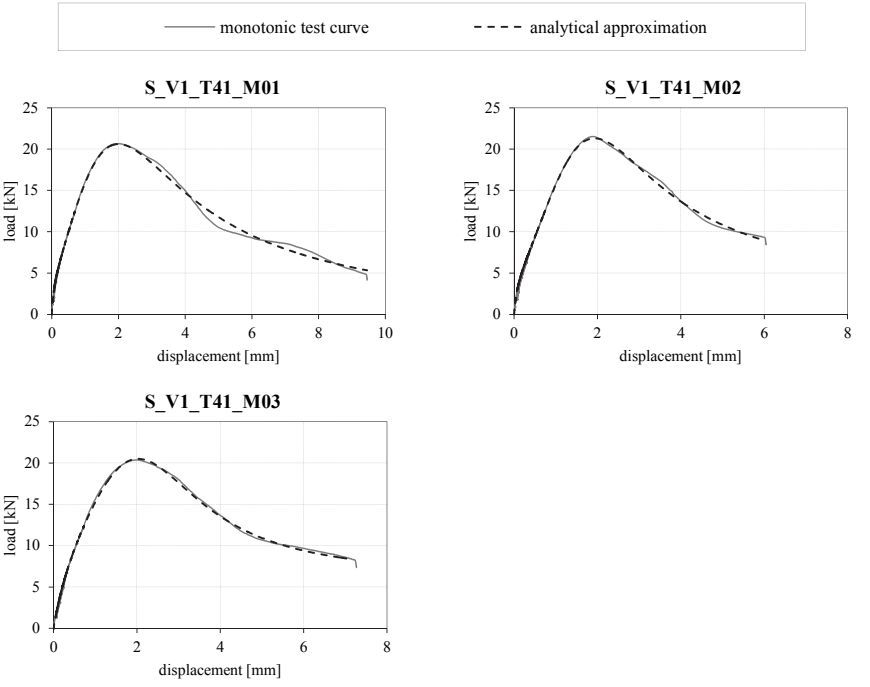

Figure B.23: actual and approximated load-displacement curves of monotonic tests on configuration S_V1_T41

Table B.24: results of cyclic tests on configuration S_V1_T41

notations		units	Z01	Z02	Z03	Z04	Z05	Z06	mean	*CoV*
ρ_{mean}		[kg/m³]	426	426	426	430	430	430	**428**	0.5%
F_{max}		[kN]	26.82	23.38	25.27	22.63	22.17	18.25	**23.09**	12.7%
v_{max}		[mm]	3.1	2.6	2.5	2.8	2.3	2.1	**2.6**	14.5%
$K_{ser,EN}$		[kN/mm]	17.326	16.790	18.282	17.444	22.911	17.275	**18.338**	12.5%
$F_{y,EN}$		[kN]	23.08	21.05	21.71	18.90	17.99	15.43	**19.69**	14.2%
$v_{y,EN}$		[mm]	1.2	1.2	1.1	1.0	0.8	0.8	**1.0**	19.3%
F_u		[kN]	24.76	18.71	21.85	18.11	17.73	14.60	**19.29**	18.4%
v_u		[mm]	3.8	3.8	3.8	4.0	3.4	3.3	**3.7**	7.5%
D_{EN}		[-]	3.1	3.2	3.5	4.0	4.5	4.0	**3.7**	14.6%
***D*-class**		[-]	low	low	low	moderate	moderate	moderate	**low**	
K_{SLS}		[kN/mm]	26.725	21.223	28.504	26.049	27.306	23.140	**25.491**	10.8%
K_{ULS}		[kN/mm]	21.579	18.769	22.628	20.603	24.175	18.074	**20.971**	11.0%
v_{ip}		[mm]	2.9	3.0	3.0	3.1	2.7	2.6	**2.9**	6.7%
Φ_{ip}		[-]	52%	58%	56%	56%	59%	59%	**57%**	4.7%
***D*-class**		[-]	low	moderate	moderate	moderate	low	low	**low**	
appr. envelope curves 1	F_{max}	[kN]	27.00	23.40	25.30	23.00	22.30	18.30		
	v_{max}	[mm]	2.80	2.30	2.73	2.60	2.20	2.10		
	K_{ini}	[kN/mm]	35.00	20.00	30.00	35.00	35.00	30.00		
	F_A	[kN]	21.70	18.50	21.00	18.50	18.30	15.00		
	v_B	[mm]	4.30	4.00	4.20	4.00	3.60	3.40		
	K_B	[kN/mm]	-7.30	-5.00	-8.00	-5.50	-5.50	-4.55		
appr. envelope curves 2	F_{max}	[kN]	25.00	22.10	24.00	21.00	20.90	17.20		
	v_{max}	[mm]	2.60	2.30	2.50	2.40	2.00	2.00		
	K_{ini}	[kN/mm]	35.00	25.00	30.00	35.00	30.00	30.00		
	F_A	[kN]	20.00	17.50	20.00	17.00	17.40	14.00		
	v_B	[mm]	4.30	3.85	4.10	3.85	3.50	3.40		
	K_B	[kN/mm]	-4.80	-4.50	-6.00	-4.80	-5.00	-4.00		
appr. envelope curves 3	F_{max}	[kN]	24.00	21.50	23.10	20.30	20.20	16.80		
	v_{max}	[mm]	2.60	2.10	2.40	2.30	1.90	2.00		
	K_{ini}	[kN/mm]	35.00	20.00	30.00	35.00	30.00	30.00		
	F_A	[kN]	19.50	16.90	18.90	16.50	16.90	14.00		
	v_B	[mm]	4.20	3.70	4.00	3.80	3.40	3.28		
	K_B	[kN/mm]	-5.50	-4.00	-4.50	-4.50	-4.50	-4.40		

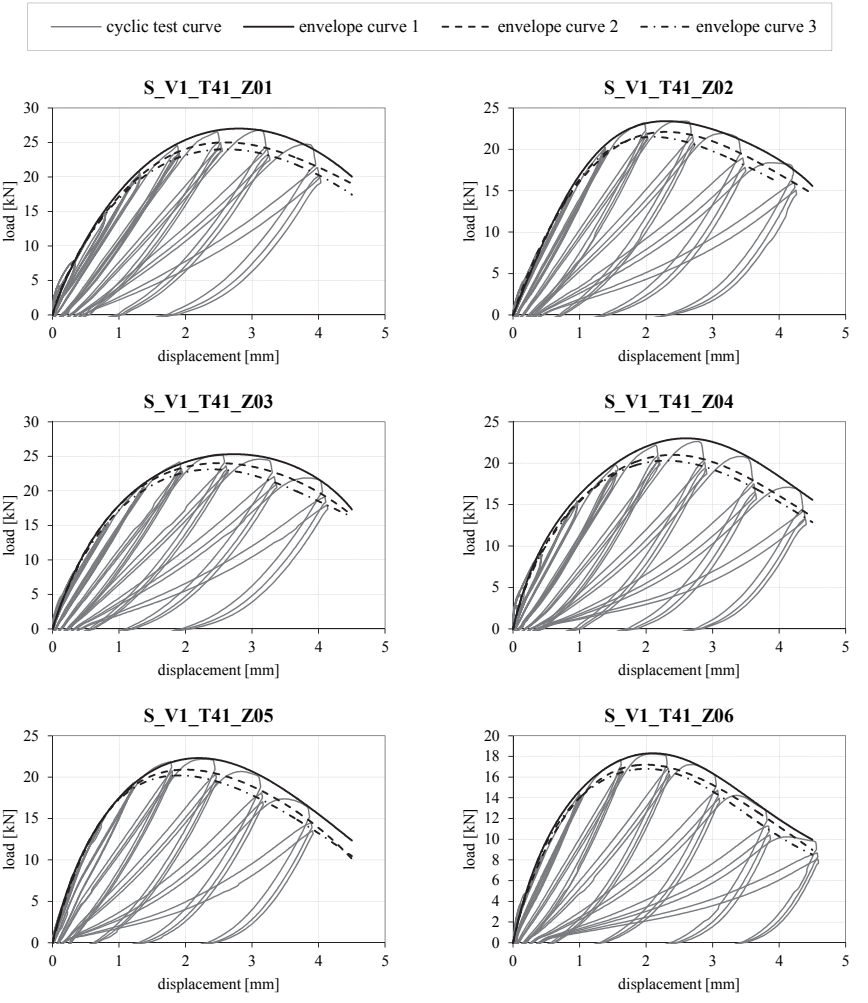

Figure B.24: actual and approximated load-displacement curves of cyclic tests on configuration S_V1_T41

Shear loaded wall-to-wall joint with parallel screws (S_V2_T72)

Table B.25: basic information for configuration S_V2_T72

parts	materials	specifications
wall segments	CLT	C24 | 98 mm (32-34-32)
connection	screws (half-lap joint)	ASSY PLUS VG Ø 6.0×80 mm

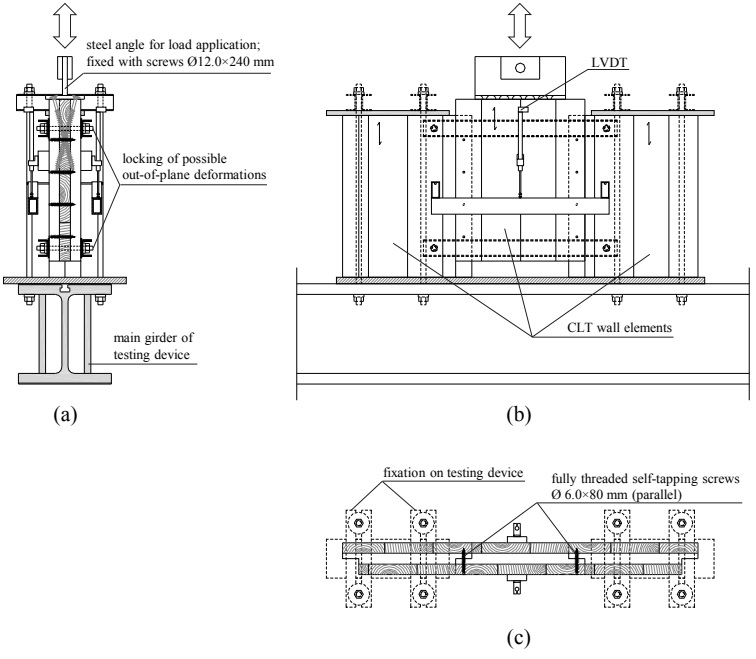

Figure B.25: test set-up for monotonic and cyclic experiments on configuration S_V2_T72 – (a) sheer plan; (b) front view; (c) plan view

Table B.26: results of monotonic tests on configuration S_V2_T72

notations		units	M01	M02	mean	*CoV*
ρ_{mean}		[kg/m³]	372	374	**373**	0.4%
F_{max}		[kN]	3.01	3.03	**3.02**	0.6%
v_{max}		[mm]	16.1	16.7	**16.4**	2.5%
$K_{ser,EN}$		[kN/mm]	0.469	0.457	**0.463**	1.9%
$F_{y,EN}$		[kN]	2.11	2.15	**2.13**	1.2%
$v_{y,EN}$		[mm]	4.0	4.2	**4.1**	4.2%
F_u		[kN]	2.42	2.43	**2.42**	0.4%
v_u		[mm]	21.9	23.0	**22.5**	3.7%
D_{EN}		[-]	5.5	5.4	**5.5**	1.3%
***D*-class**		[-]	moderate	moderate	**moderate**	
K_{SLS}		[kN/mm]	1.066	0.904	**0.985**	11.6%
K_{ULS}		[kN/mm]	0.579	0.556	**0.567**	2.9%
v_{ip}		[mm]	15.4	16.2	**15.8**	3.4%
Φ_{ip}		[-]	41%	41%	**41%**	0.0%
***D*-class**		[-]	moderate	moderate	**moderate**	
approximation curves	F_{max}	[kN]	3.05	3.02		
	v_{max}	[mm]	18.20	18.00		
	K_{ini}	[kN/mm]	2.80	2.00		
	F_A	[kN]	2.15	2.12		
	v_B	[mm]	21.80	22.60		
	K_B	[kN/mm]	-0.48	-0.28		

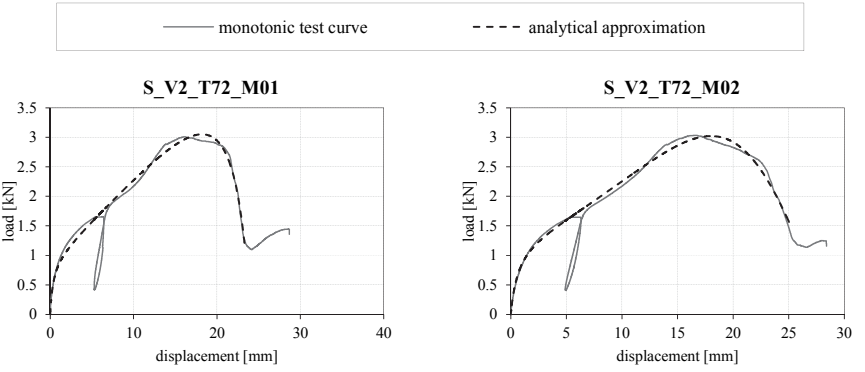

Figure B.26: actual and approximated load-displacement curves of monotonic tests on configuration S_V2_T72

Table B.27: results of cyclic tests on configuration S_V2_T72

notations		units	Z01	Z02	Z03	mean	*CoV*
ρ_{mean}		[kg/m³]	372	382	371	**375**	1.6%
F_{max}		[kN]	2.72	3.10	2.86	**2.89**	6.7%
v_{max}		[mm]	13.0	13.1	12.9	**13.0**	0.5%
$K_{ser,EN}$		[kN/mm]	0.772	0.651	0.695	**0.706**	8.7%
$F_{y,EN}$		[kN]	1.41	2.00	1.61	**1.67**	17.7%
$v_{y,EN}$		[mm]	1.7	2.7	2.0	**2.1**	25.1%
F_u		[kN]	2.18	2.48	2.28	**2.32**	6.7%
v_u		[mm]	17.7	18.1	19.0	**18.3**	3.7%
D_{EN}		[-]	10.6	6.6	9.3	**8.8**	23.2%
***D*-class**		[-]	high	high	high	**high**	
K_{SLS}		[kN/mm]	1.100	1.328	1.260	**1.229**	9.5%
K_{ULS}		[kN/mm]	0.833	0.854	0.823	**0.837**	1.9%
v_{ip}		[mm]	13.3	13.5	14.5	**13.8**	4.7%
Φ_{ip}		[-]	50%	49%	53%	**51%**	4.1%
***D*-class**		[-]	moderate	moderate	moderate	**moderate**	
appr. envelope curves 1	F_{max}	[kN]	2.70	3.15	3.00		
	v_{max}	[mm]	13.00	15.00	15.00		
	K_{ini}	[kN/mm]	2.00	1.80	1.50		
	F_A	[kN]	2.00	2.30	2.15		
	v_B	[mm]	17.70	18.20	18.30		
	K_B	[kN/mm]	-0.15	-0.35	-0.30		
appr. envelope curves 2	F_{max}	[kN]	2.00	2.30	2.20		
	v_{max}	[mm]	10.00	12.00	12.00		
	K_{ini}	[kN/mm]	2.00	1.80	1.80		
	F_A	[kN]	1.70	1.86	1.76		
	v_B	[mm]	18.00	15.30	15.30		
	K_B	[kN/mm]	-0.05	-0.25	-0.21		
appr. envelope curves 3	F_{max}	[kN]	1.85	2.10	2.00		
	v_{max}	[mm]	8.80	11.00	11.50		
	K_{ini}	[kN/mm]	2.00	2.00	2.00		
	F_A	[kN]	1.65	1.75	1.66		
	v_B	[mm]	16.50	15.20	15.50		
	K_B	[kN/mm]	-0.05	-0.16	-0.15		

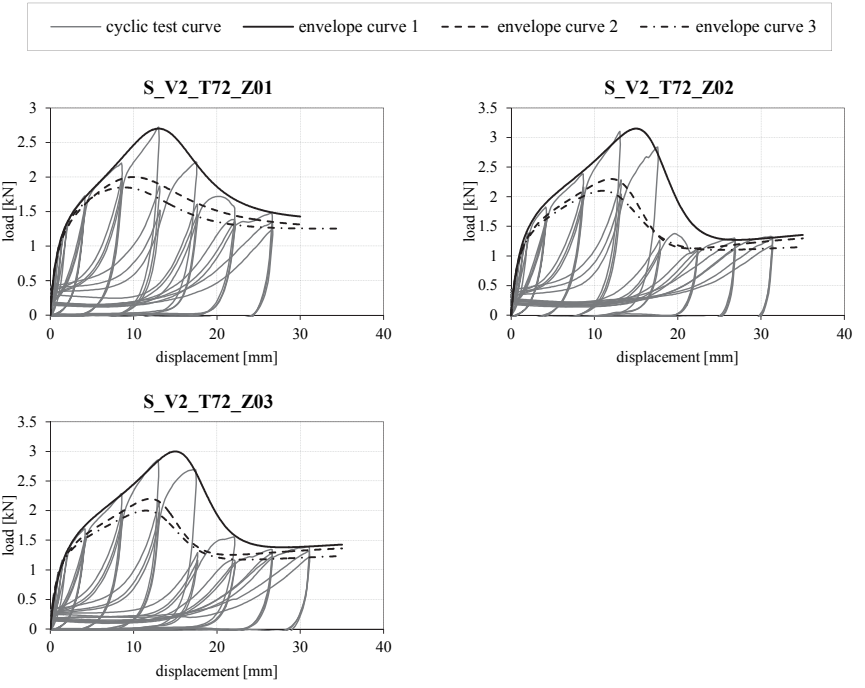

Figure B.27: actual and approximated load-displacement curves of cyclic tests on configuration S_V2_T72

Shear loaded wall-to-wall joint with inclined screws (XS_VG2_T72)

Table B.28: basic information for configuration XS_VG2_T72

parts	materials	specifications
wall segments	CLT	C24 | 98 mm (32-34-32)
connection	screws (half-lap joint)	ASSY PLUS VG Ø 6.0×120 mm

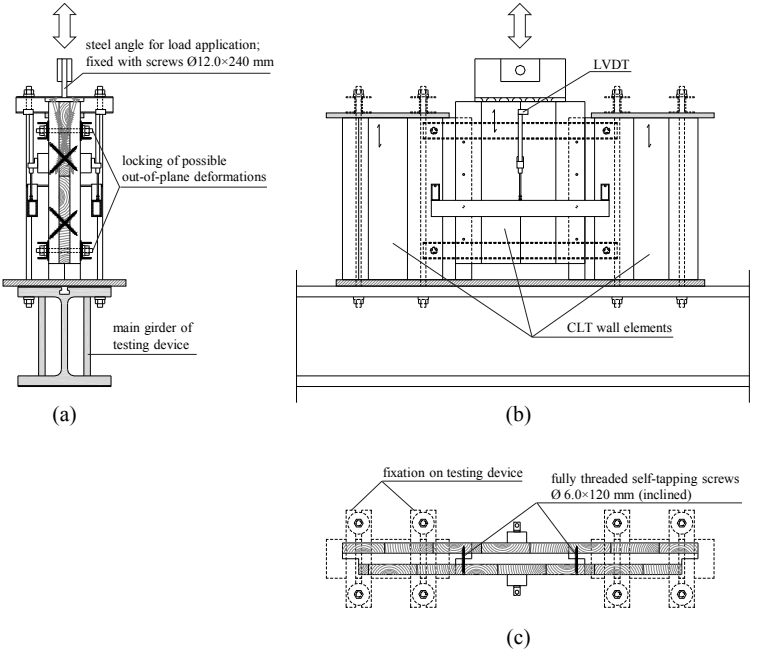

Figure B.28: test set-up for monotonic and cyclic experiments on configuration XS_VG2_T72 – (a) sheer plan; (b) front view; (c) plan view

Table B.29: results of monotonic tests on configuration XS_VG2_T72

notations		units	M01	M02	mean	*CoV*
ρ_{mean}		[kg/m³]	446	446	**446**	0.0%
F_{max}		[kN]	8.60	8.99	**8.79**	3.1%
v_{max}		[mm]	1.7	2.3	**2.0**	21.6%
$K_{ser,EN}$		[kN/mm]	9.321	5.127	**7.224**	41.1%
$F_{y,EN}$		[kN]	7.58	8.50	**8.04**	8.0%
$v_{y,EN}$		[mm]	0.8	1.5	**1.2**	43.6%
F_u		[kN]	6.89	7.19	**7.04**	3.0%
v_u		[mm]	3.1	4.2	**3.6**	22.1%
D_{EN}		[-]	3.7	2.7	**3.2**	22.1%
***D*-class**		[-]	low	low	**low**	
K_{SLS}		[kN/mm]	10.450	10.560	**10.505**	0.7%
K_{ULS}		[kN/mm]	9.198	6.066	**7.632**	29.0%
v_{ip}		[mm]	2.4	3.3	**2.9**	21.9%
Φ_{ip}		[-]	57%	58%	**58%**	1.2%
***D*-class**		[-]	low	moderate	**low**	
approximation curves	F_{max}	[kN]	8.70	9.00		
	v_{max}	[mm]	1.80	2.30		
	K_{ini}	[kN/mm]	11.60	15.00		
	F_A	[kN]	6.70	6.80		
	v_B	[mm]	3.00	4.10		
	K_B	[kN/mm]	-1.90	-1.20		

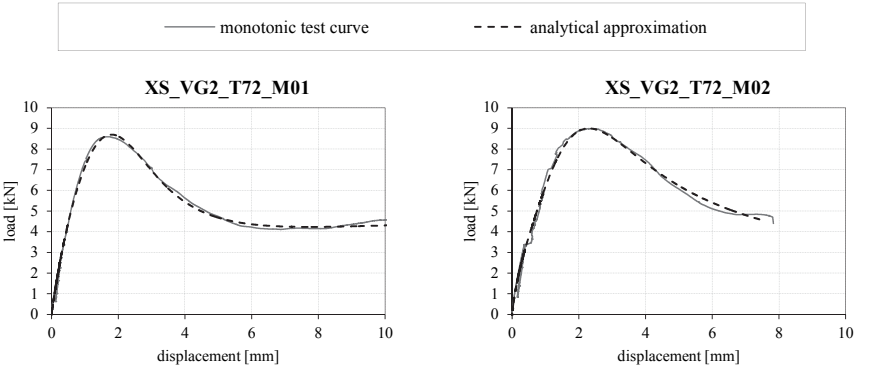

Figure B.29: actual and approximated load-displacement curves of monotonic tests on configuration XS_VG2_T72

Table B.30: results of cyclic tests on configuration XS_VG2_T72

notations		units	Z01	Z02	Z03	Z04	mean	*CoV*
ρ_{mean}		[kg/m³]	439	444	453	431	**442**	2.1%
F_{max}		[kN]	7.65	10.24	8.01	7.38	**8.32**	15.6%
v_{max}		[mm]	1.4	1.9	1.5	1.3	**1.5**	16.8%
$K_{ser,EN}$		[kN/mm]	7.903	9.250	8.062	8.404	**8.405**	7.1%
$F_{y,EN}$		[kN]	6.89	8.71	7.19	6.64	**7.36**	12.6%
$v_{y,EN}$		[mm]	0.8	0.9	0.8	0.7	**0.8**	7.4%
F_u		[kN]	6.12	8.19	6.41	5.91	**6.66**	15.6%
v_u		[mm]	4.2	3.5	2.4	3.1	**3.3**	21.9%
D_{EN}		[-]	4.9	3.9	2.9	4.2	**4.0**	20.8%
***D*-class**		[-]	moderate	low	low	moderate	**moderate**	
K_{SLS}		[kN/mm]	8.982	13.210	10.507	10.827	**10.882**	16.1%
K_{ULS}		[kN/mm]	8.314	10.997	9.012	9.221	**9.386**	12.2%
v_{ip}		[mm]	3.4	2.8	1.8	2.5	**2.6**	25.6%
Φ_{ip}		[-]	63%	59%	47%	59%	**57%**	12.2%
***D*-class**		[-]	moderate	low	low	low	**low**	
appr. envelope curves 1	F_{max}	[kN]	7.70	10.30	8.00	7.50		
	v_{max}	[mm]	1.70	2.00	1.50	1.65		
	K_{ini}	[kN/mm]	10.00	15.00	10.00	11.00		
	F_A	[kN]	6.00	8.00	5.80	5.90		
	v_B	[mm]	4.20	3.40	2.60	3.10		
	K_B	[kN/mm]	-0.50	-2.05	-1.75	-1.30		
appr. envelope curves 2	F_{max}	[kN]	7.10	9.50	7.40	6.90		
	v_{max}	[mm]	1.70	2.00	1.50	1.55		
	K_{ini}	[kN/mm]	9.00	15.00	10.00	12.00		
	F_A	[kN]	5.50	7.80	5.50	5.50		
	v_B	[mm]	4.20	3.40	2.50	3.00		
	K_B	[kN/mm]	-0.39	-2.08	-1.90	-1.20		
appr. envelope curves 3	F_{max}	[kN]	6.80	9.10	7.10	6.55		
	v_{max}	[mm]	1.60	1.90	1.45	1.45		
	K_{ini}	[kN/mm]	9.00	15.00	14.00	12.00		
	F_A	[kN]	5.60	7.50	5.40	5.30		
	v_B	[mm]	4.30	3.30	2.33	2.85		
	K_B	[kN/mm]	-0.40	-1.96	-2.12	-1.15		

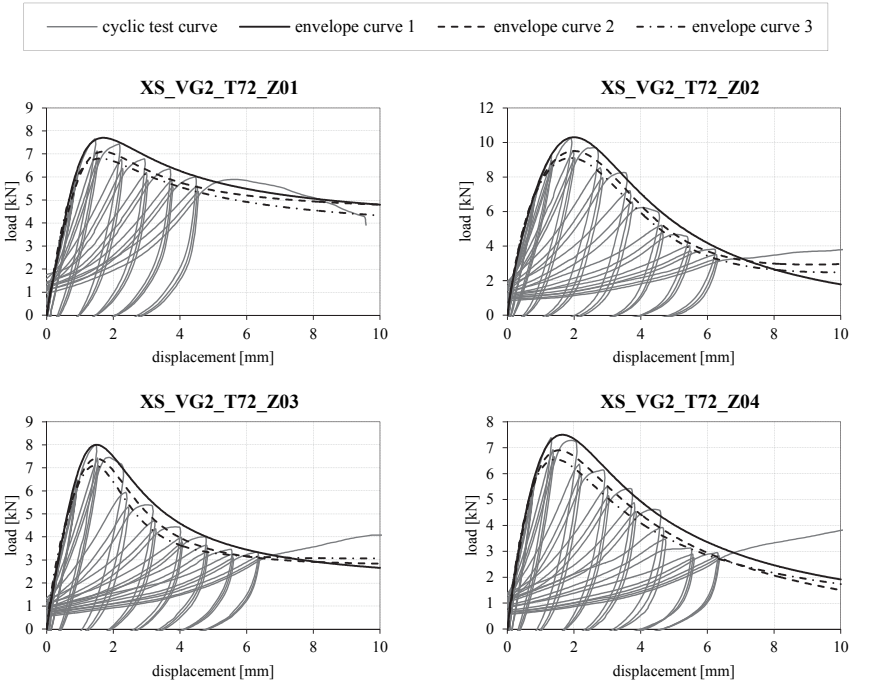

Figure B.30: actual and approximated load-displacement curves of cyclic tests on configuration XS_VG2_T72

B-2 Wall tests Graz

B-2.1 Overview general test set-up

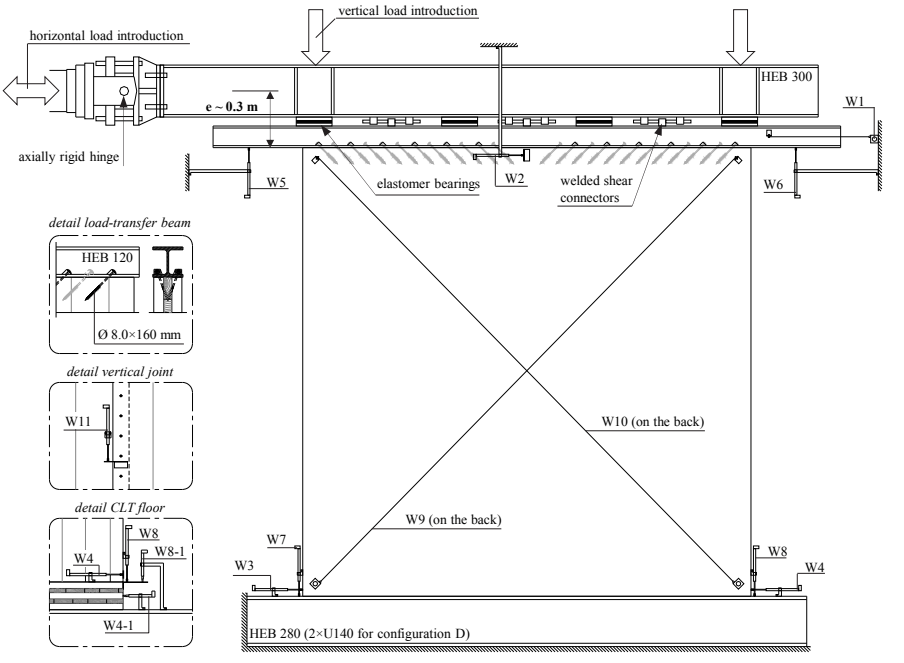

Figure B.31: overview test set-up for TU Graz wall tests

B-2.2 Configuration A

Table B.31: basic information for configuration A

parts	materials	specifications
wall segment	CLT	C24 | 112 mm (40-32-40)
foundation	steel girder	HEB 280
connection bottom joint	4×angle bracket	AE116

Table B.32: vertical loads and loading rates for configuration A

ID	vertical load	loading rate	note
WA_A_M01	20.8 kN/m	0.5 | 1.0 mm/s	-
WA_A_M02	20.8 kN/m	0.033 | 0.067 mm/s	-
WA_A_Z01	20.8 kN/m	2.0 mm/s	test interrupted by testing machine
WA_A_Z02	0 kN/m	2.0 mm/s	-
WA_A_Z03	20.8 kN/m	2.0 mm/s	-

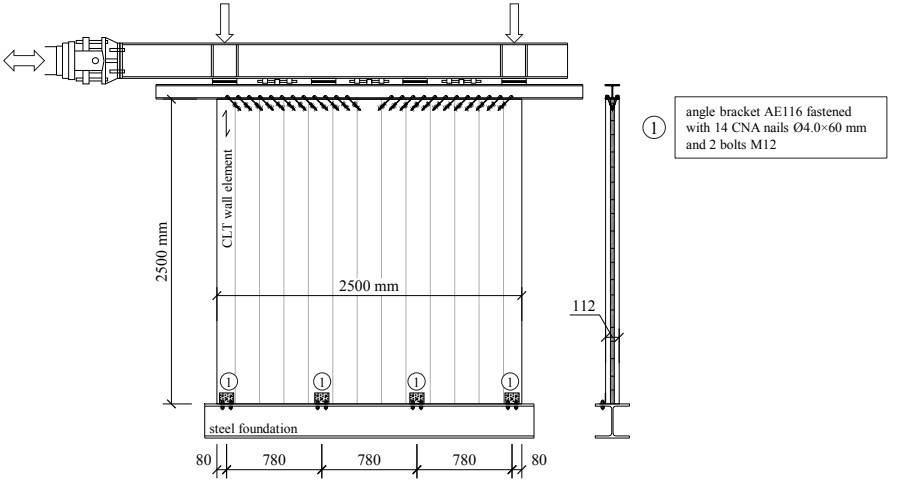

Figure B.32: test set-up for wall configuration A

Table B.33: results of monotonic and cyclic tests on configuration A

notations		units	M01	M02	Z01	Z02	Z03
F_{max}		[kN]	74.30	62.77	62.98	53.86	61.18
v_{max}		[mm]	33.7	30.6	26.3	29.9	25.4
$K_{ser,EN}$		[kN/mm]	8.414	11.349	10.943	3.452	9.745
$F_{y,EN}$		[kN]	40.36	30.97	31.63	43.04	31.25
$v_{y,EN}$		[mm]	4.2	2.2	2.5	11.4	2.6
F_u		[kN]	71.90	50.22	61.28	46.58	54.37
v_u		[mm]	42.7	48.4	40.6	51.9	43.2
D_{EN}		[-]	10.2	22.5	16.0	4.6	16.5
***D*-class**		[-]	high	high	high	moderate	high
K_{SLS}		[kN/mm]	18.484	63.020	21.816	6.846	21.613
K_{ULS}		[kN/mm]	10.256	15.365	12.906	4.196	12.727
v_{ip}		[mm]	33.4	40.2	33.4	41.1	35.8
Φ_{ip}		[-]	56%	66%	64%	58%	66%
***D*-class**		[-]	moderate	high	high	moderate	high
appr. envelope curves 1	F_{max}	[kN]	73.10	62.30	64.00	55.50	62.00
	v_{max}	[mm]	35.00	30.70	32.00	37.50	30.50
	K_{ini}	[kN/mm]	21.20	48.40	45.00	30.00	35.00
	F_A	[kN]	58.70	50.80	52.00	43.00	51.30
	v_B	[mm]	64.50	52.60	53.00	58.00	46.50
	K_B	[kN/mm]	-0.53	-0.70	-0.80	-0.90	-1.50
appr. envelope curves 2	F_{max}	[kN]			56.00	47.00	57.00
	v_{max}	[mm]			30.00	34.30	29.00
	K_{ini}	[kN/mm]			40.00	25.00	35.00
	F_A	[kN]			48.50	37.50	47.00
	v_B	[mm]			65.00	53.00	46.00
	K_B	[kN/mm]			-0.30	-0.88	-1.00
appr. envelope curves 3	F_{max}	[kN]			52.00	43.00	53.50
	v_{max}	[mm]			30.00	34.30	27.00
	K_{ini}	[kN/mm]			40.00	25.00	50.00
	F_A	[kN]			46.00	35.50	45.00
	v_B	[mm]			55.00	53.00	46.00
	K_B	[kN/mm]			-0.50	-0.88	-0.80

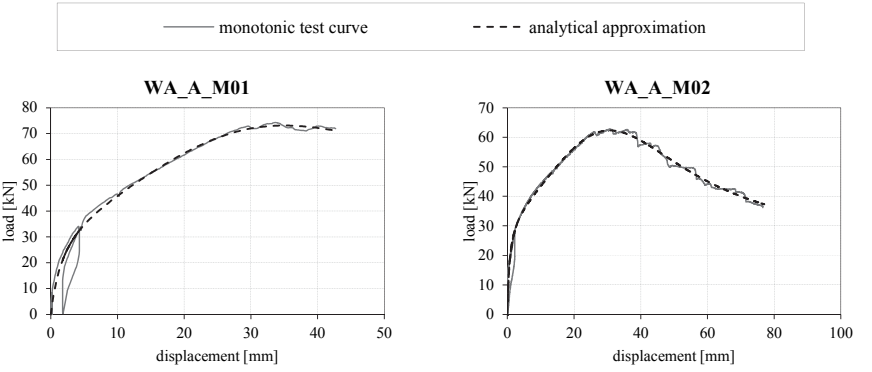

Figure B.33: actual and approximated load-displacement curves of monotonic tests on configuration A

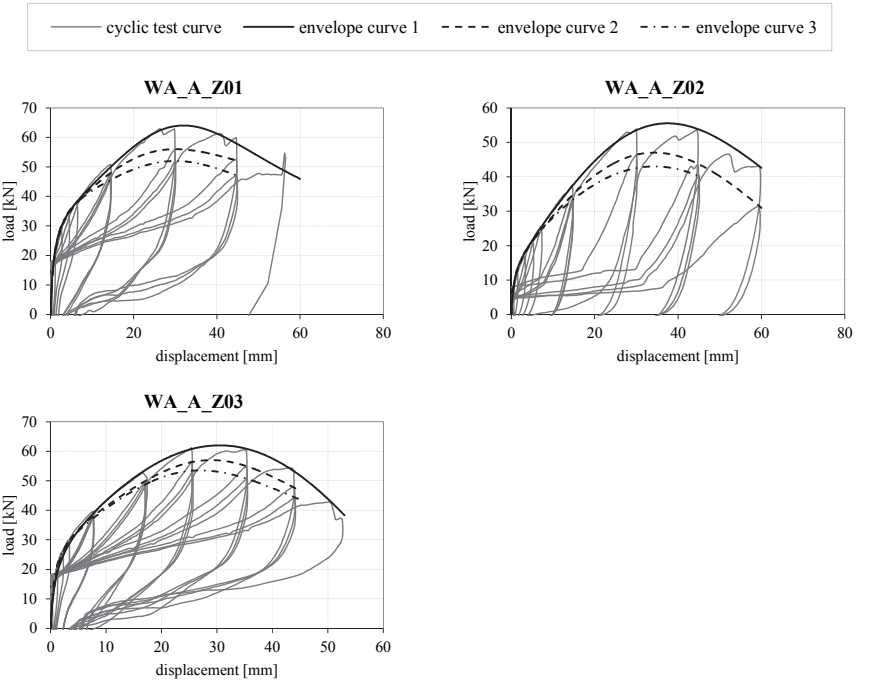

Figure B.34: actual and approximated load-displacement curves of cyclic tests on configuration A

B-2.3 Configuration B

Table B.34: basic information for configuration B

parts	materials	specifications
wall segment	CLT	C24 | 112 mm (40-32-40)
foundation	steel girder	HEB 280
connection bottom joint	2×hold-down | 2×angle bracket	HTT22 | AE116

Table B.35: vertical loads and loading rates for configuration B

ID	vertical load	loading rate	note
WA_B_M01	20.8 kN/m	0.033 | 0.067 mm/s	-
WA_B_Z01	20.8 kN/m	2.0 mm/s	-
WA_B_Z02	5.0 kN/m	2.0 mm/s	-

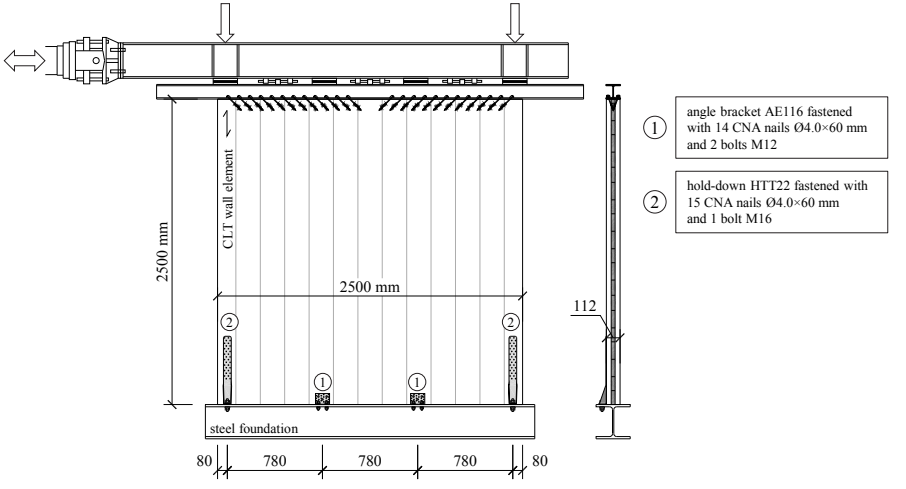

Figure B.35: test set-up for wall configuration B

Table B.36: results of monotonic and cyclic tests on configuration B

notations		units	M01	Z01	Z02
F_{max}		[kN]	77.36	71.73	69.98
v_{max}		[mm]	34.6	42.4	40.8
$K_{ser,EN}$		[kN/mm]	6.052	4.688	3.064
$F_{y,EN}$		[kN]	50.78	52.89	57.60
$v_{y,EN}$		[mm]	7.1	10.1	16.8
F_u		[kN]	62.00	57.38	64.53
v_u		[mm]	39.0	49.6	47.7
D_{EN}		[-]	5.5	4.9	2.8
D-class		[-]	moderate	moderate	low
K_{SLS}		[kN/mm]	24.481	12.491	7.481
K_{ULS}		[kN/mm]	8.000	5.817	3.900
v_{ip}		[mm]	29.0	38.3	33.2
Φ_{ip}		[-]	49%	54%	39%
D-class		[-]	moderate	moderate	low
appr. envelope curves 1	F_{max}	[kN]	76.30	72.50	69.00
	v_{max}	[mm]	35.23	39.00	41.30
	K_{ini}	[kN/mm]	172.00	20.00	12.00
	F_A	[kN]	59.80	57.00	48.00
	v_B	[mm]	39.15	49.50	54.00
	K_B	[kN/mm]	-26.00	-4.00	-1.80
appr. envelope curves 2	F_{max}	[kN]		66.00	61.50
	v_{max}	[mm]		36.00	41.00
	K_{ini}	[kN/mm]		20.00	25.00
	F_A	[kN]		51.50	45.00
	v_B	[mm]		48.00	55.00
	K_B	[kN/mm]		-2.50	-1.80
appr. envelope curves 3	F_{max}	[kN]		62.00	59.00
	v_{max}	[mm]		32.80	38.00
	K_{ini}	[kN/mm]		18.00	15.00
	F_A	[kN]		48.50	42.00
	v_B	[mm]		45.50	55.00
	K_B	[kN/mm]		-1.80	-1.00

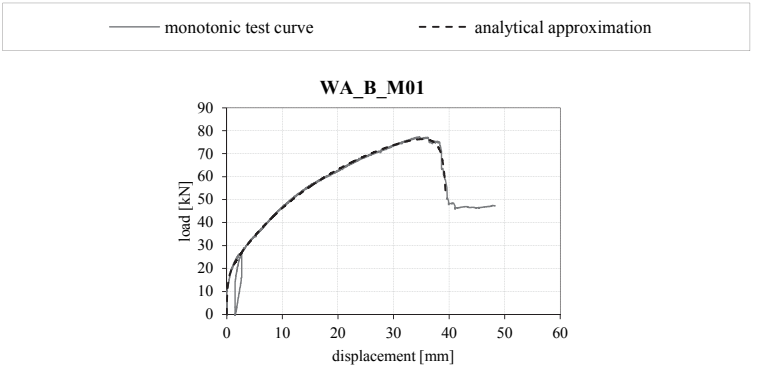

Figure B.36: actual and approximated load-displacement curve of monotonic test on configuration B

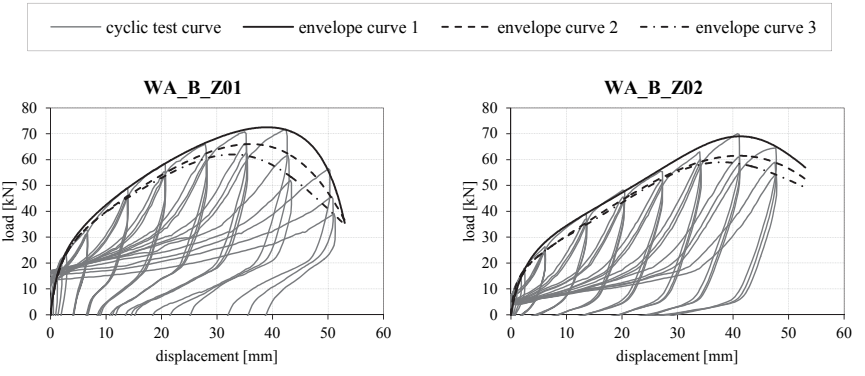

Figure B.37: actual and approximated load-displacement curves of cyclic tests on configuration B

B-2.4 Configuration C

Table B.37: basic information for configuration C

parts	materials	specifications
wall segment	CLT	C24 | 112 mm (40-32-40)
foundation	steel girder	HEB 280
connection bottom joint	4×angle brackets	AE116
connection vertical joint	half-lap joint with 24 screws	ASSY PLUS VG

Table B.38: vertical loads and loading rates for configuration C

ID	vertical load	loading rate	note
WA_C_M01	20.8 kN/m	0.5 | 1.0 mm/s	-
WA_C_M02	20.8 kN/m	0.033 | 0.067 mm/s	-
WA_C_Z01	20.8 kN/m	2.0 mm/s	-

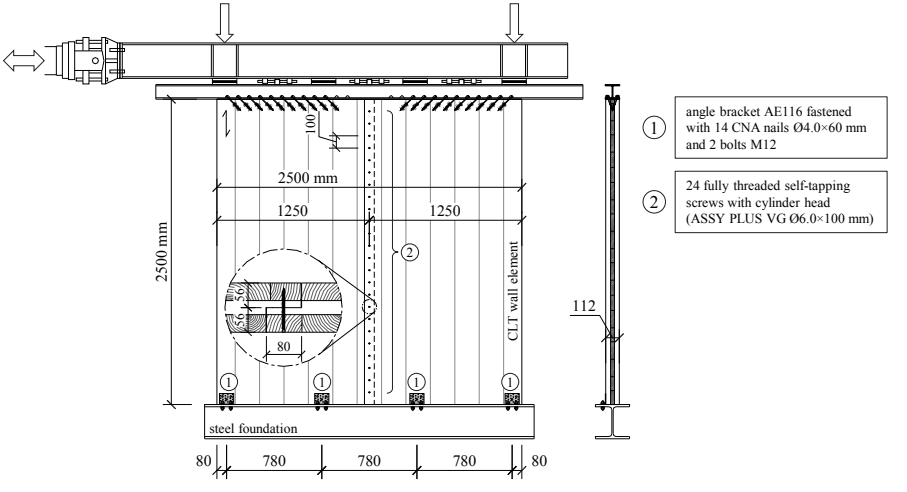

Figure B.38: test set-up for wall configuration C

Table B.39: results of monotonic and cyclic tests on configuration C

notations		units	M01	M02	Z01
F_{max}		[kN]	71.82	64.80	62.75
v_{max}		[mm]	39.2	34.1	28.7
$K_{ser,EN}$		[kN/mm]	8.779	8.265	14.465
$F_{y,EN}$		[kN]	37.88	34.80	29.76
$v_{y,EN}$		[mm]	3.9	3.5	1.8
F_u		[kN]	70.66	51.86	53.15
v_u		[mm]	46.0	52.8	44.2
D_{EN}		[-]	11.8	15.1	25.0
D-class		[-]	high	high	high
K_{SLS}		[kN/mm]	13.480	21.571	28.893
K_{ULS}		[kN/mm]	10.648	10.460	17.363
v_{ip}		[mm]	36.7	43.4	36.4
Φ_{ip}		[-]	60%	65%	65%
D-class		[-]	high	high	high
appr. envelope curves 1	F_{max}	[kN]	71.80	64.10	62.50
	v_{max}	[mm]	37.00	35.40	31.50
	K_{ini}	[kN/mm]	18.00	50.00	45.00
	F_A	[kN]	57.80	53.60	51.50
	v_B	[mm]	55.00	55.00	50.00
	K_B	[kN/mm]	-1.00	-1.28	-1.00
appr. envelope curve 2	F_{max}	[kN]			59.00
	v_{max}	[mm]			32.00
	K_{ini}	[kN/mm]			45.00
	F_A	[kN]			48.50
	v_B	[mm]			47.00
	K_B	[kN/mm]			-1.20
appr. envelope curve 3	F_{max}	[kN]			55.00
	v_{max}	[mm]			30.00
	K_{ini}	[kN/mm]			45.00
	F_A	[kN]			46.50
	v_B	[mm]			46.50
	K_B	[kN/mm]			-1.00

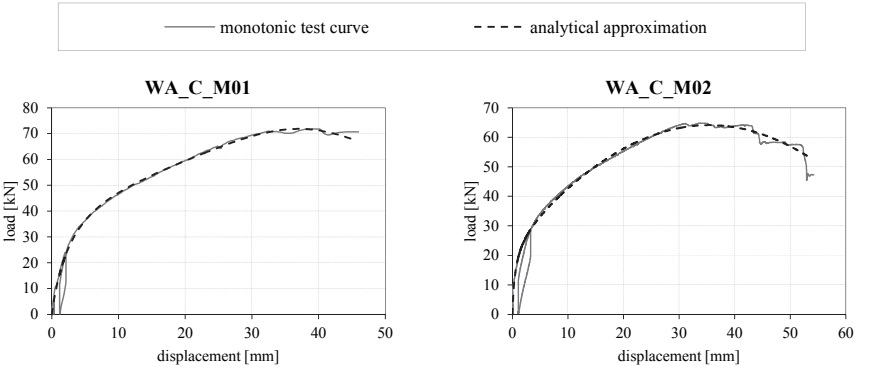

Figure B.39: actual and approximated load-displacement curves of monotonic tests on configuration C

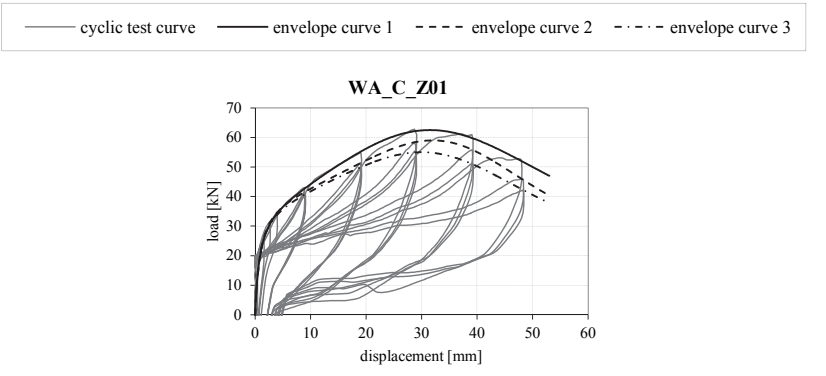

Figure B.40: actual and approximated load-displacement curve of cyclic test on configuration C

B-2.5 Configuration D

Table B.40: basic information for configuration D

parts	materials	specifications
wall segment	CLT	C24 | 112 mm (40-32-40)
foundation	CLT	C24 | 138 mm (32-21-32-21-32)
connection bottom joint	12×screws	Stardrive

Table B.41: vertical loads and loading rates for configuration D

ID	vertical load	loading rate	note
WA_D_M01	20.8 kN/m	0.033 | 0.067 mm/s	-
WA_D_Z01	20.8 kN/m	2.0 mm/s	-
WA_D_Z02	5.0 kN/m	2.0 mm/s	-

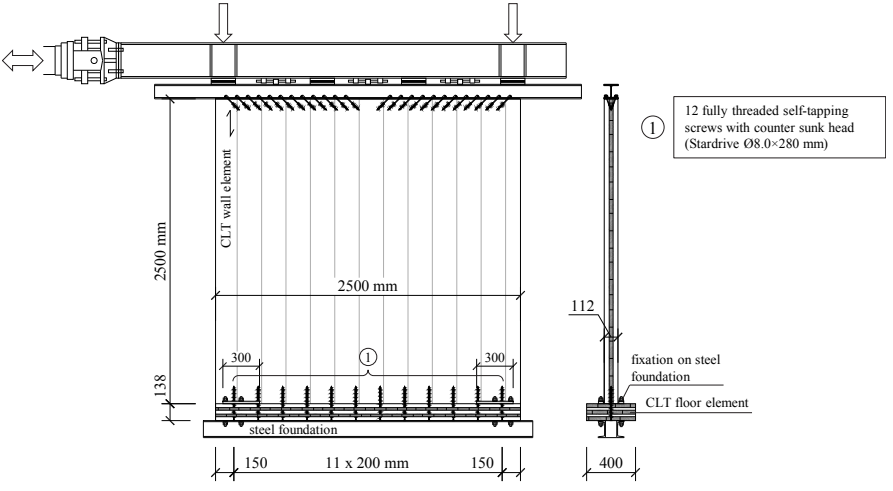

Figure B.41: test set-up for wall configuration D

Table B.42: results of monotonic and cyclic tests on configuration D

notations		units	M01	Z01	Z02
F_{max}		[kN]	51.07	60.42	46.80
v_{max}		[mm]	9.7	11.3	11.8
$K_{ser,EN}$		[kN/mm]	17.778	14.573	8.208
$F_{y,EN}$		[kN]	37.15	39.29	36.41
$v_{y,EN}$		[mm]	1.8	2.2	4.0
F_u		[kN]	40.88	48.33	37.44
v_u		[mm]	37.3	32.9	27.7
D_{EN}		[-]	20.7	15.1	7.0
D-class		[-]	high	high	high
K_{SLS}		[kN/mm]	110.069	31.026	13.820
K_{ULS}		[kN/mm]	23.672	21.169	10.390
v_{ip}		[mm]	33.2	27.9	22.8
Φ_{ip}		[-]	78%	70%	64%
D-class		[-]	high	high	high
appr. envelope curves 1	F_{max}	[kN]	51.60	60.50	47.20
	v_{max}	[mm]	12.90	13.50	15.30
	K_{ini}	[kN/mm]	180.00	100.00	15.00
	F_A	[kN]	47.30	53.90	41.30
	v_B	[mm]	35.50	32.00	29.60
	K_B	[kN/mm]	-0.54	-0.82	-1.09
appr. envelope curves 2	F_{max}	[kN]		54.90	45.00
	v_{max}	[mm]		15.80	17.00
	K_{ini}	[kN/mm]		100.00	15.00
	F_A	[kN]		51.10	40.00
	v_B	[mm]		35.20	30.30
	K_B	[kN/mm]		-1.10	-1.37
appr. envelope curves 3	F_{max}	[kN]		53.30	44.00
	v_{max}	[mm]		16.00	17.00
	K_{ini}	[kN/mm]		40.00	15.00
	F_A	[kN]		50.50	39.00
	v_B	[mm]		35.00	30.00
	K_B	[kN/mm]		-1.20	-1.33

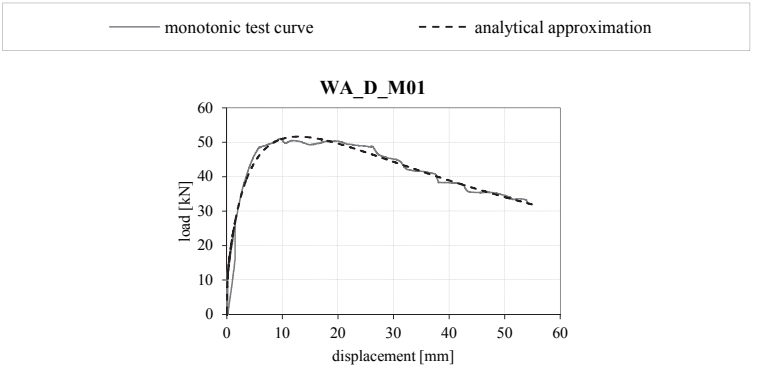

Figure B.42: actual and approximated load-displacement curve of monotonic test on configuration D

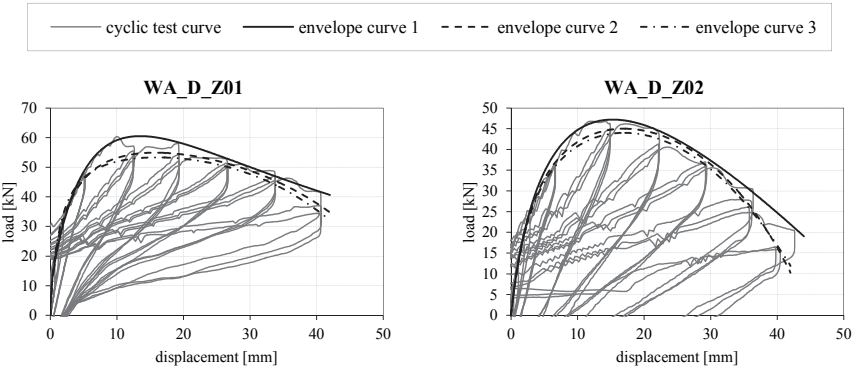

Figure B.43: actual and approximated load-displacement curves of cyclic tests on configuration D

B-2.6 Configuration E

Table B.43: basic information for configuration E

parts	materials	specifications
wall segment	CLT (opening (0.9/2.1 m)	C24 | 112 mm (40-32-40)
foundation	steel girder	HEB 280
connection bottom joint	2×hold-down | 2×angle bracket	HTT22 | AE116

Table B.44: vertical loads and loading rates for configuration E

ID	vertical load	loading rate	note
WA_D_M01	20.8 kN/m	0.033 | 0.067 mm/s	-
WA_D_Z01	20.8 kN/m	2.0 mm/s	-
WA_D_Z02	5.0 kN/m	2.0 mm/s	-

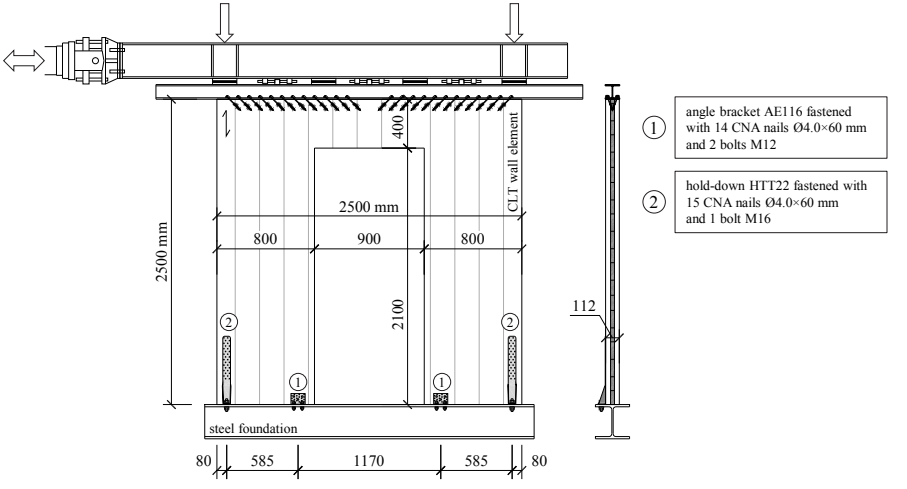

Figure B.44: test set-up for wall configuration E

Table B.45: results of monotonic and cyclic tests on configuration E

notations		units	M01	Z01	Z02
F_{max}		[kN]	74.62	75.76	57.79
v_{max}		[mm]	47.3	51.1	40.2
$K_{ser,EN}$		[kN/mm]	3.917	3.813	2.678
$F_{y,EN}$		[kN]	51.79	54.65	47.25
$v_{y,EN}$		[mm]	11.9	12.8	16.2
F_u		[kN]	59.89	60.61	56.94
v_u		[mm]	56.0	63.6	50.2
D_{EN}		[-]	4.7	5.0	3.1
***D*-class**		[-]	moderate	moderate	low
K_{SLS}		[kN/mm]	7.935	8.508	4.870
K_{ULS}		[kN/mm]	4.714	4.705	3.195
v_{ip}		[mm]	40.8	48.1	36.3
Φ_{ip}		[-]	46%	51%	45%
***D*-class**		[-]	moderate	moderate	moderate
appr. envelope curves 1	F_{max}	[kN]	73.80	75.00	58.00
	v_{max}	[mm]	46.90	48.80	46.00
	K_{ini}	[kN/mm]	10.00	18.00	10.00
	F_A	[kN]	54.10	56.40	43.20
	v_B	[mm]	56.20	64.00	65.00
	K_B	[kN/mm]	-3.80	-2.10	-1.10
appr. envelope curves 2	F_{max}	[kN]		69.00	54.00
	v_{max}	[mm]		45.00	43.00
	K_{ini}	[kN/mm]		18.00	10.00
	F_A	[kN]		53.00	41.00
	v_B	[mm]		61.00	60.00
	K_B	[kN/mm]		-1.70	-1.30
appr. envelope curves 3	F_{max}	[kN]		67.00	51.30
	v_{max}	[mm]		42.80	40.50
	K_{ini}	[kN/mm]		18.00	8.00
	F_A	[kN]		50.50	38.50
	v_B	[mm]		56.00	54.00
	K_B	[kN/mm]		-2.00	-1.40

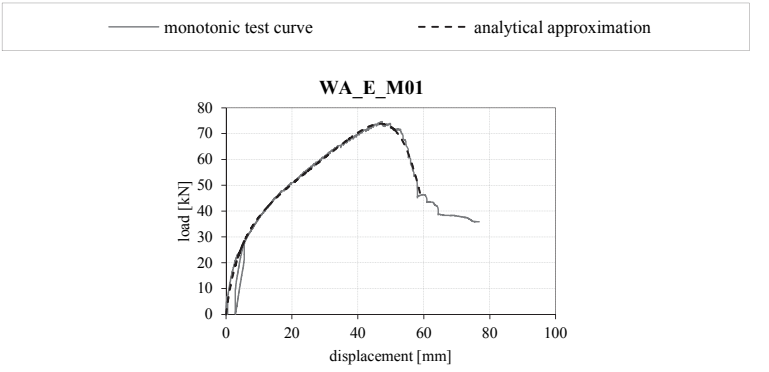

Figure B.45: actual and approximated load-displacement curve of monotonic test on configuration E

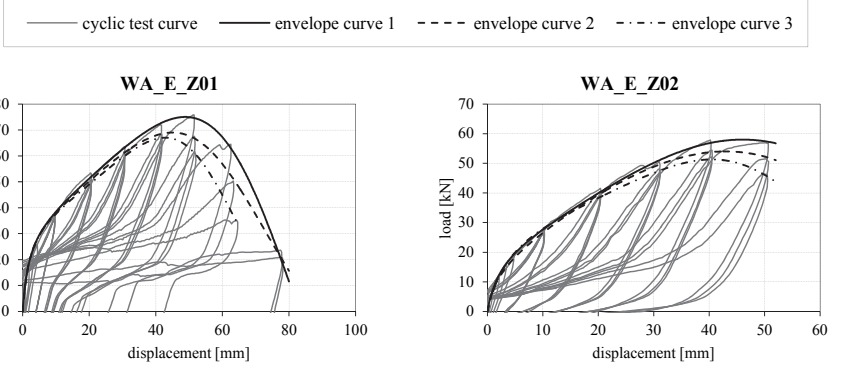

Figure B.46: actual and approximated load-displacement curves of cyclic tests on configuration E

ANNEX C MODEL VALIDATION

C-1 Wall tests Graz

C-1.1 Overview

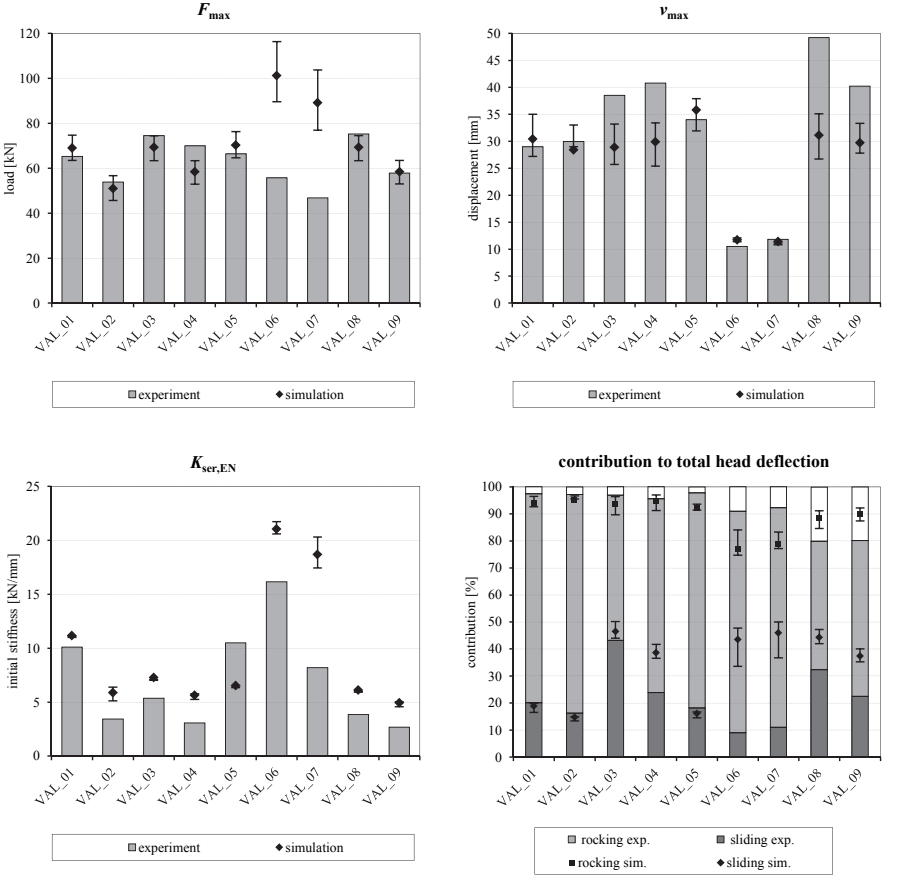

Figure C.1: model validation on tests conducted by TU Graz – overview of selected parameters

C-1.2 Validation 01

Table C.1: summarised results of validation 01

ID	considered tests	results	F_{max} [kN]	v_{max} [mm]	$K_{ser,EN}$ [kN/mm]	$v_{sl,max}$ [%]	$v_{rg,max}$ [%]	$v_{CLT,max}$ [%]
VAL_01	WA_A_M01 WA_A_M02 WA_A_Z01 WA_A_Z03	mean tests	65.31	29.0	10.113	20.1	77.4	2.6
		average simulation	68.96	30.4	11.174	18.8	75.1	6.1
		maximum simulation	74.71	35.0	11.004	16.5	77.7	5.7
		minimum simulation	63.46	27.2	11.122	19.8	73.9	6.3

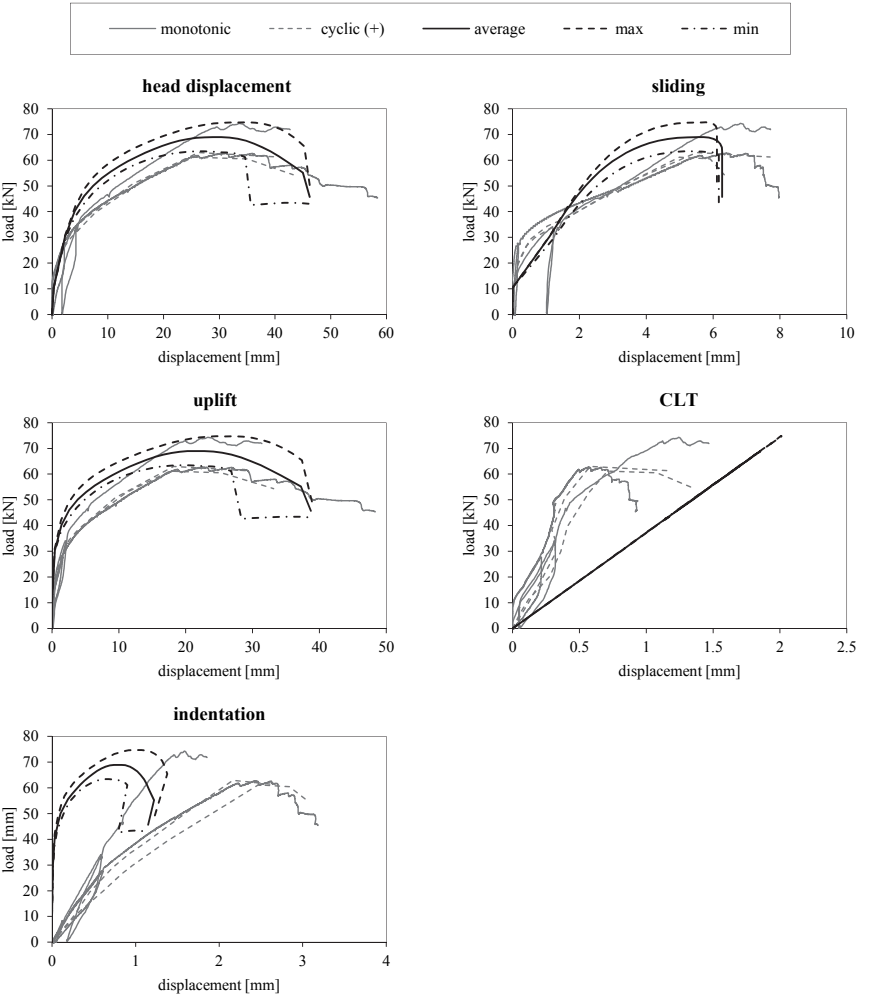

Figure C.2: comparison of experimental and simulated load-displacement curves for validation 01

C-1.3 Validation 02

Table C.2: summarised results of validation 02

ID	considered tests	results	F_{max} [kN]	v_{max} [mm]	$K_{ser,EN}$ [kN/mm]	$v_{sl,max}$ [%]	$v_{rg,max}$ [%]	$v_{CLT,max}$ [%]
VAL_02	WA_A_Z02	mean test	53.86	29.9	3.452	16.3	80.9	2.8
		average simulation	50.93	28.4	5.886	14.7	80.4	4.8
		maximum simulation	56.63	33.0	6.394	13.4	82.0	4.6
		minimum simulation	45.67	29.0	5.131	14.9	80.8	4.2

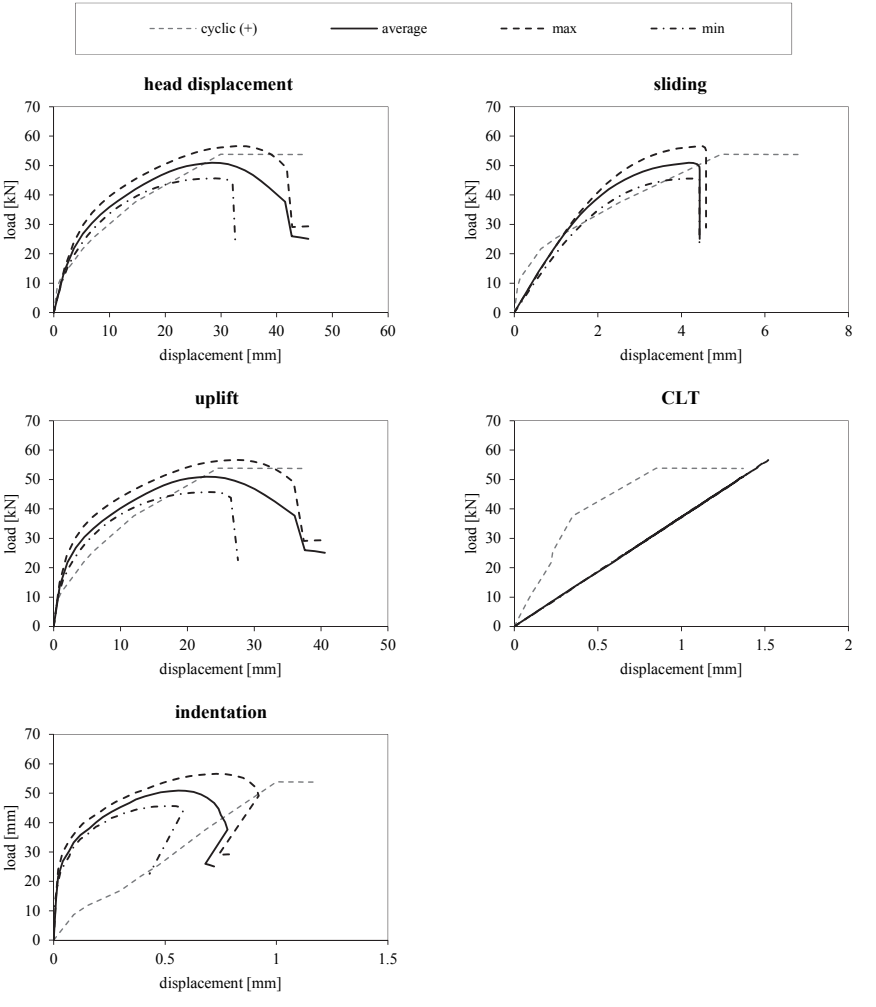

Figure C.3: comparison of experimental and simulated load-displacement curves for validation 02

C-1.4 Validation 03

Table C.3: summarised results of validation 03

ID	considered tests	results	F_{max} [kN]	v_{max} [mm]	$K_{ser,EN}$ [kN/mm]	$v_{sl,max}$ [%]	$v_{rg,max}$ [%]	$v_{CLT,max}$ [%]
VAL_03	WA_B_M01 WA_B_Z01	mean tests	74.54	38.5	5.370	43.2	53.7	3.2
		average simulation	69.35	28.9	7.270	46.5	47.1	6.4
		maximum simulation	74.44	33.2	7.075	44.0	49.9	6.0
		minimum simulation	63.37	25.7	7.040	50.2	43.2	6.6

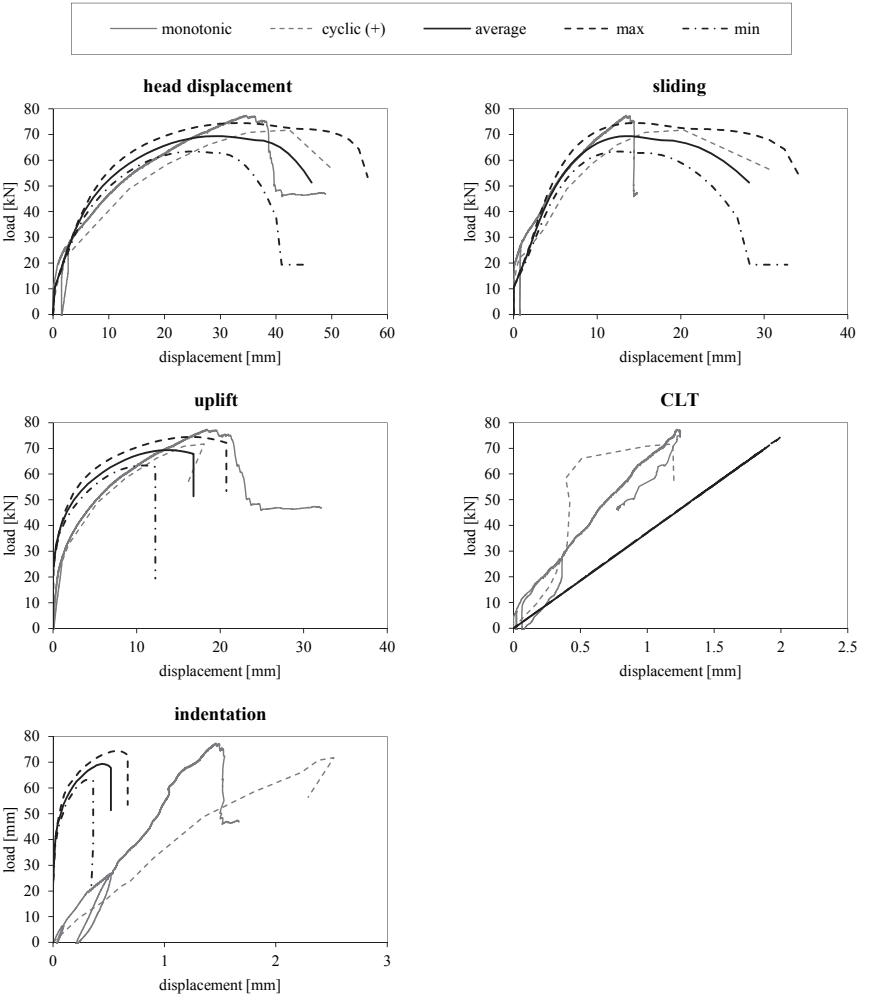

Figure C.4: comparison of experimental and simulated load-displacement curves for validation 03

C-1.5 Validation 04

Table C.4: summarised results of validation 04

ID	considered tests	results	F_{max} [kN]	v_{max} [mm]	$K_{ser,EN}$ [kN/mm]	$v_{sl,max}$ [%]	$v_{rg,max}$ [%]	$v_{CLT,max}$ [%]
VAL_04	WA_B_Z02	mean test	69.98	40.8	3.064	23.9	71.7	4.5
		average simulation	58.43	29.9	5.631	38.6	56.2	5.3
		maximum simulation	63.44	33.4	5.774	36.5	58.4	5.1
		minimum simulation	52.95	25.4	5.253	41.7	52.7	5.6

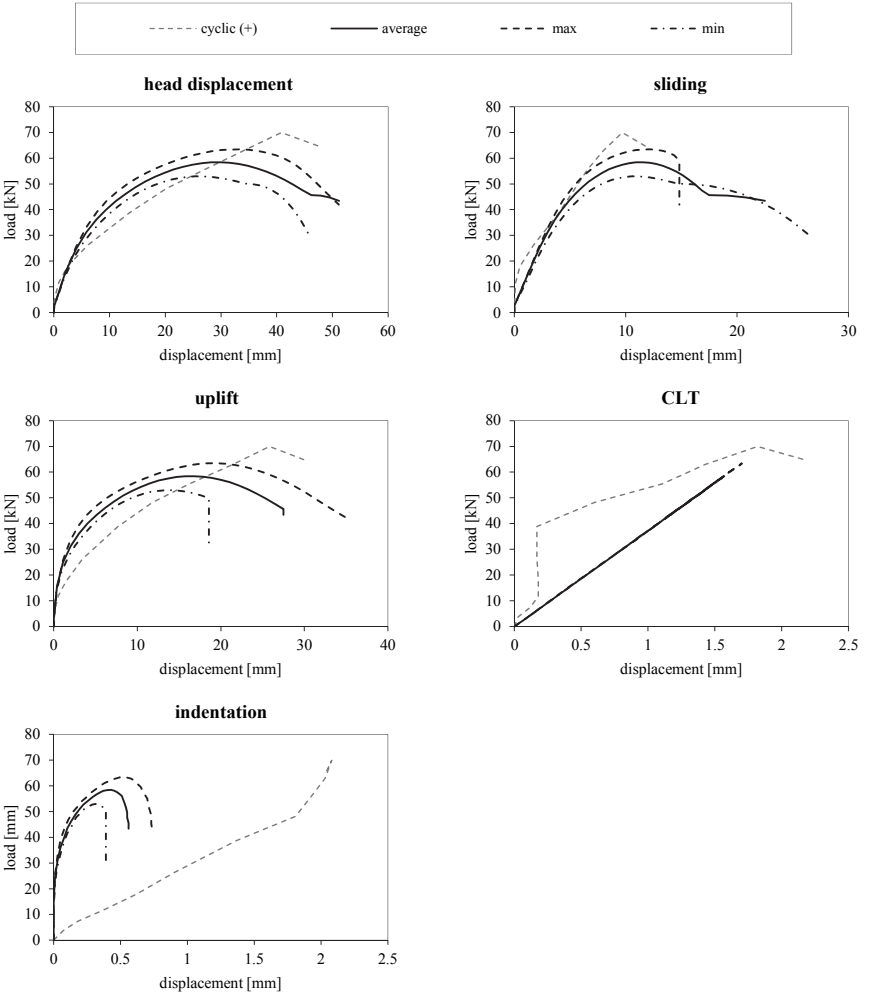

Figure C.5: comparison of experimental and simulated load-displacement curves for validation 04

C-1.6 Validation 05

Table C.5: summarised results of validation 05

ID	considered tests	results	F_{max} [kN]	v_{max} [mm]	$K_{ser,EN}$ [kN/mm]	$v_{sl,max}$ [%]	$v_{rg,max}$ [%]	$v_{CLT,max}$ [%]
VAL_05	WA_C_M01 WA_C_M02 WA_C_Z01	mean tests	66.46	34.0	10.503	18.2	79.6	2.2
		average simulation	70.30	35.8	6.523	16.1	76.1	7.8
		maximum simulation	76.31	37.9	6.514	14.5	77.5	8.0
		minimum simulation	64.67	31.9	6.356	16.7	75.3	8.1

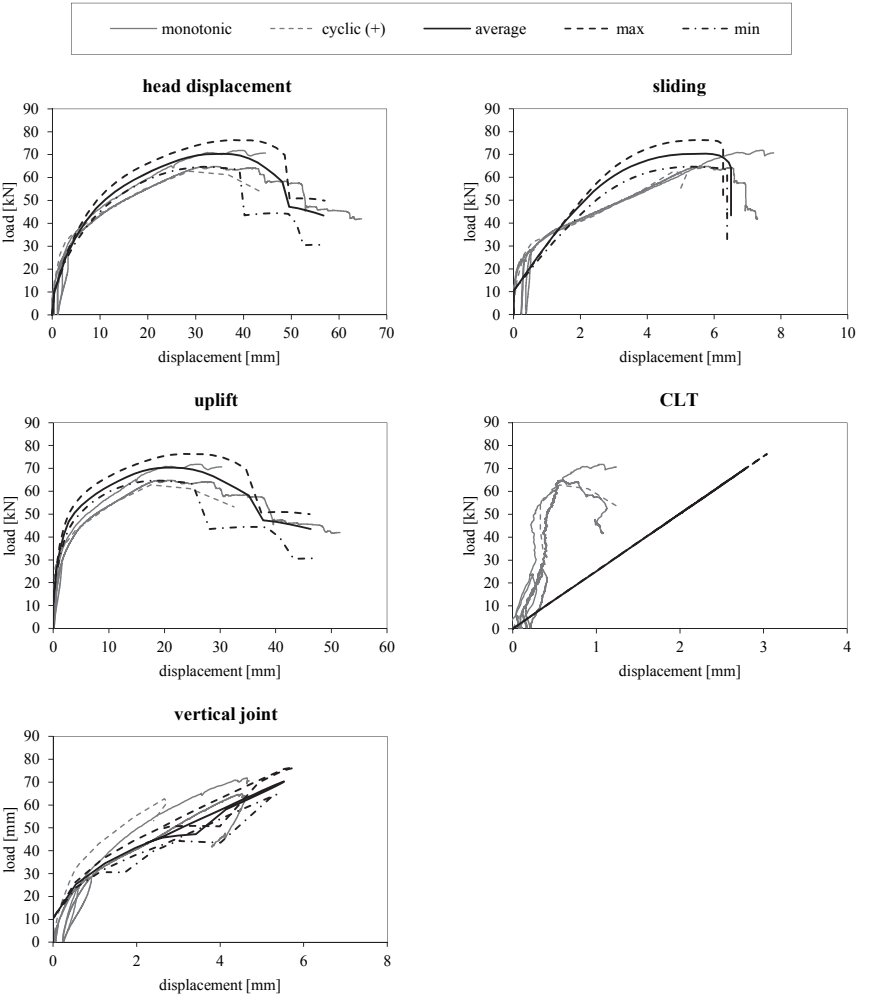

Figure C.6: comparison of experimental and simulated load-displacement curves for validation 05

C-1.7 Validation 06

Table C.6: summarised results of validation 06

ID	considered tests	results	F_{max} [kN]	v_{max} [mm]	$K_{ser,EN}$ [kN/mm]	$v_{sl,max}$ [%]	$v_{rg,max}$ [%]	$v_{CLT,max}$ [%]
VAL_06	WA_D_M01 WA_D_Z01	mean tests	55.74	10.5	16.167	9.0	82.0	9.1
		average simulation	101.17	11.7	21.049	43.5	33.3	23.2
		maximum simulation	116.33	12.1	21.738	33.6	40.6	25.8
		minimum simulation	89.59	11.4	20.601	47.7	31.2	21.1

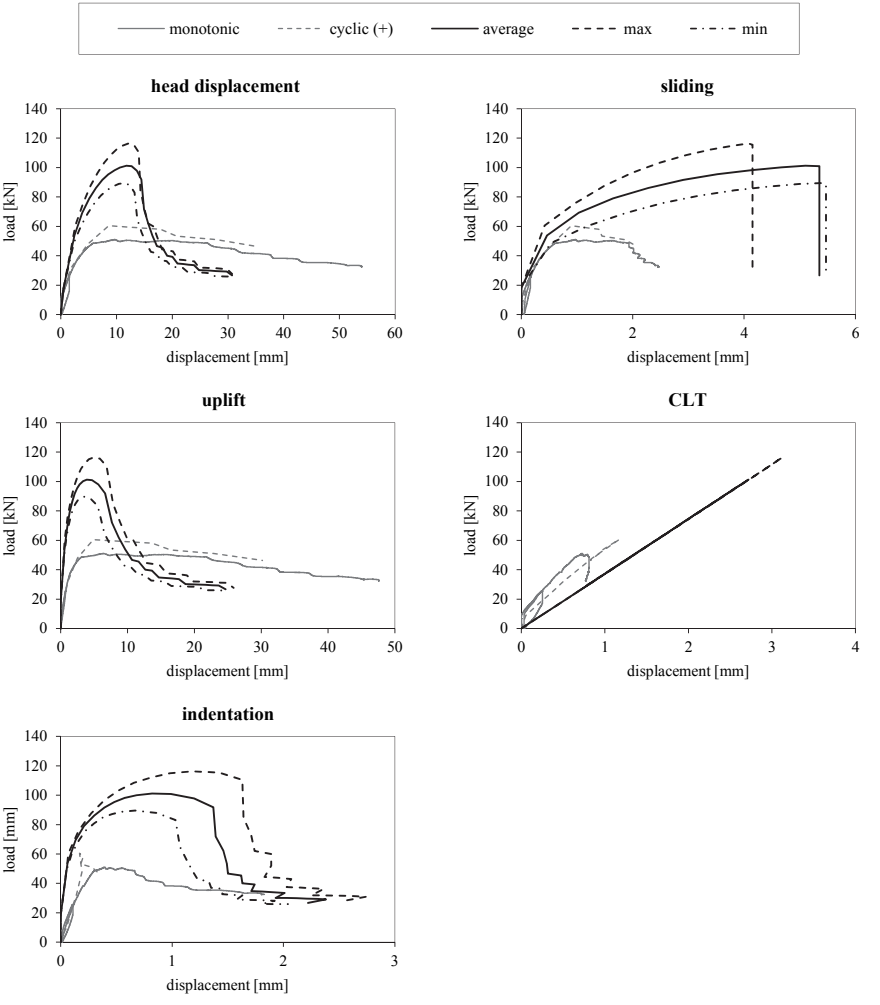

Figure C.7: comparison of experimental and simulated load-displacement curves for validation 06

C-1.8 Validation 07

Table C.7: summarised results of validation 07

ID	considered tests	results	F_{max} [kN]	v_{max} [mm]	$K_{ser,EN}$ [kN/mm]	$v_{sl,max}$ [%]	$v_{rg,max}$ [%]	$v_{CLT,max}$ [%]
VAL_07	WA_D_Z02	mean test	46.80	11.8	8.208	11.0	81.3	7.8
		average simulation	89.19	11.4	18.677	45.9	33.1	21.1
		maximum simulation	103.73	10.8	20.309	36.7	37.4	25.9
		minimum simulation	76.89	11.1	17.439	50.0	31.3	18.7

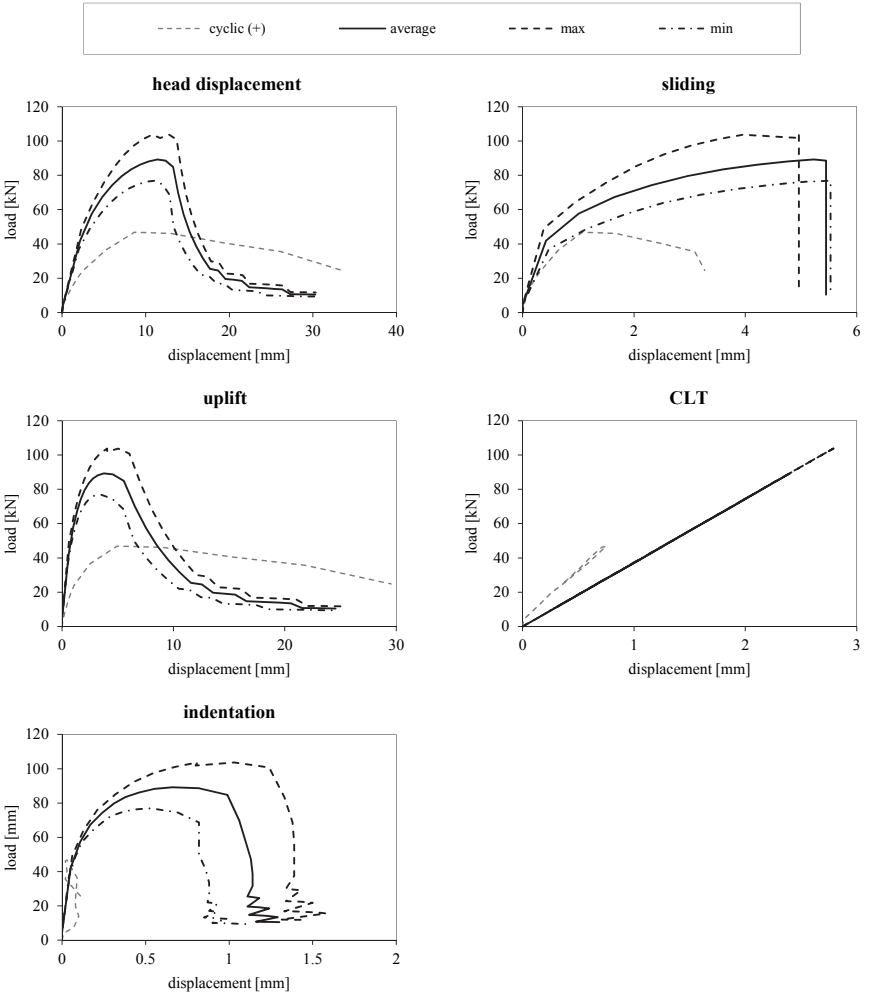

Figure C.8: comparison of experimental and simulated load-displacement curves for validation 07

C-1.9 Validation 08

Table C.8: summarised results of validation 08

ID	considered tests	results	F_{max} [kN]	v_{max} [mm]	$K_{ser,EN}$ [kN/mm]	$v_{sl,max}$ [%]	$v_{rg,max}$ [%]	$v_{CLT,max}$ [%]
VAL_08	WA_E_M01 WA_E_Z01	mean tests	75.19	49.2	3.865	32.3	47.6	20.1
		average simulation	69.31	31.1	6.115	44.3	44.1	11.6
		maximum simulation	74.49	35.1	5.989	42.0	46.9	11.1
		minimum simulation	63.41	26.7	5.934	47.2	40.3	12.4

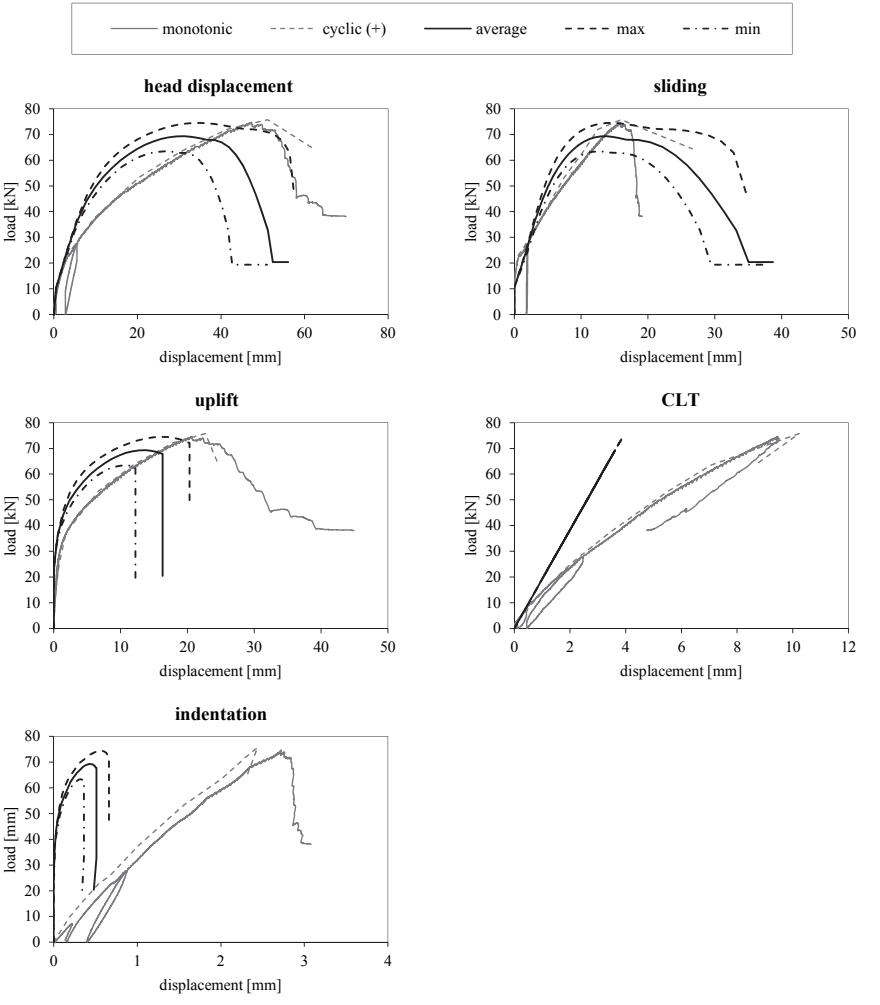

Figure C.9: comparison of experimental and simulated load-displacement curves for validation 08

C-1.10 Validation 09

Table C.9: summarised results of validation 09

ID	considered tests	results	F_{max} [kN]	v_{max} [mm]	$K_{ser,EN}$ [kN/mm]	$v_{sl,max}$ [%]	$v_{rg,max}$ [%]	$v_{CLT,max}$ [%]
VAL_09	WA_E_Z02	mean test	57.79	40.2	2.678	22.5	57.7	19.8
		average simulation	58.39	29.7	4.939	37.4	52.3	10.3
		maximum simulation	63.46	33.3	5.034	35.2	54.8	10.0
		minimum simulation	53.03	27.8	4.577	40.0	50.0	10.0

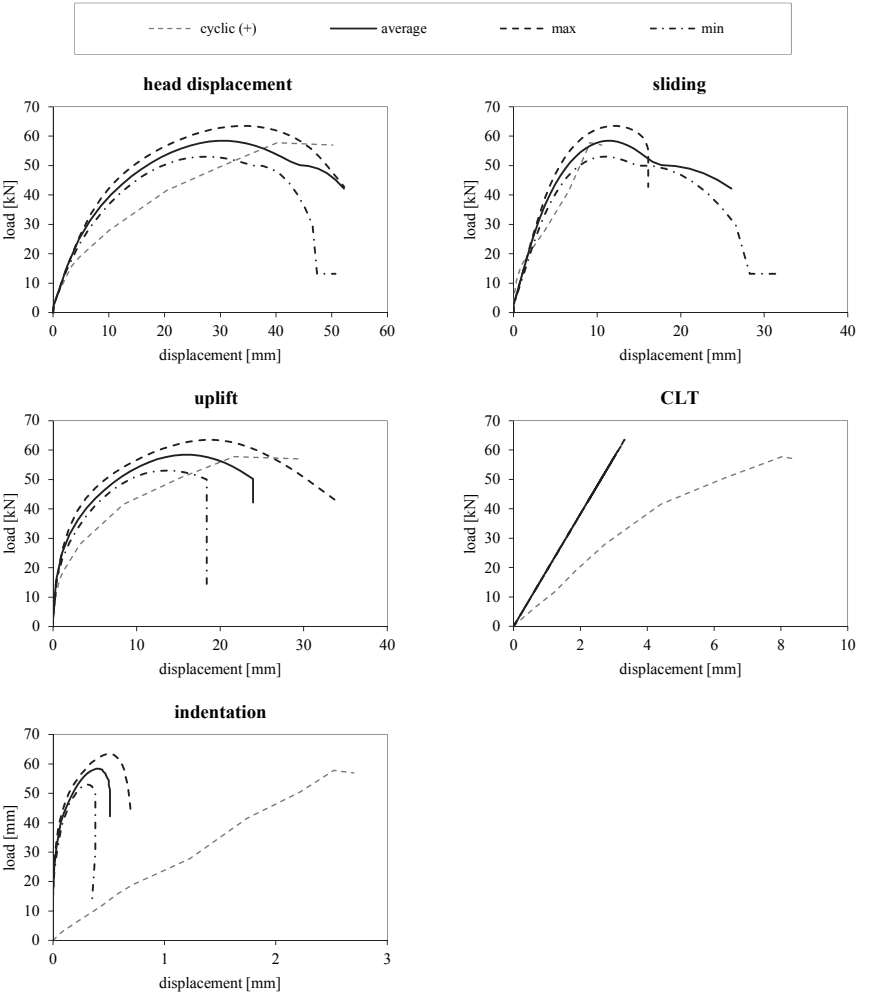

Figure C.10: comparison of experimental and simulated load-displacement curves for validation 09

C-2 Wall tests University of Trieste | IVALSA

C-2.1 Overview

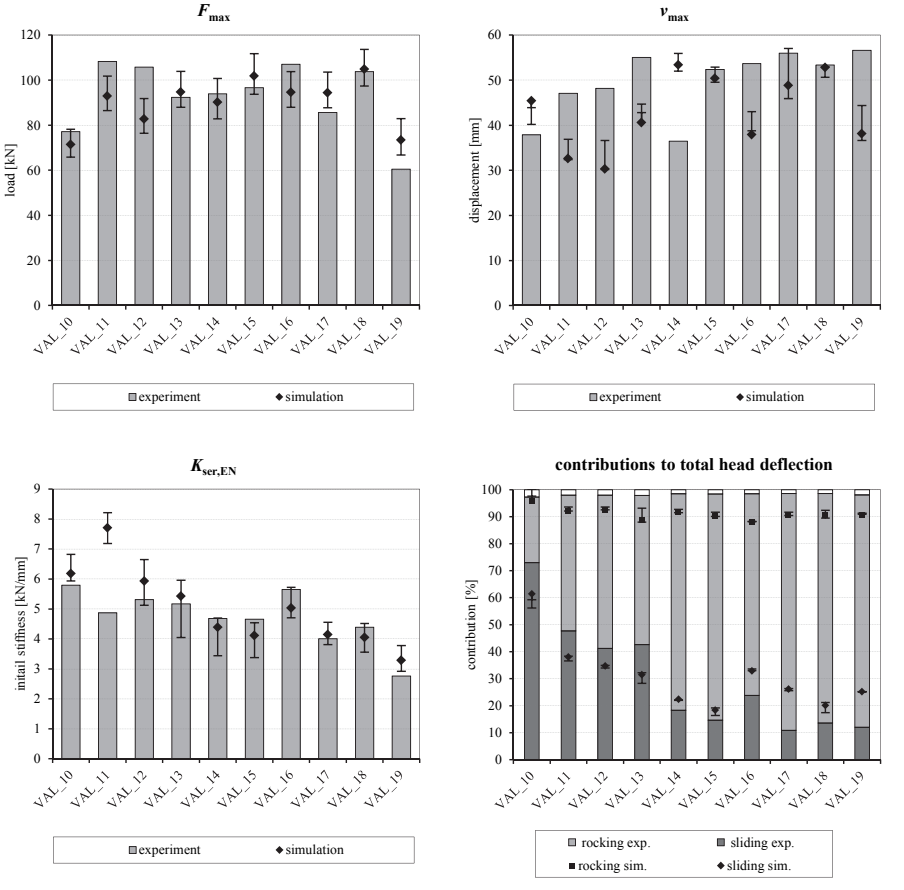

Figure C.11: model validation on tests conducted at IVALSA – overview of selected parameters

Note: The contributions to total head deflection are taken from Gavric et al. (2015a).

C-2.2 Validation 10

Table C.10: summarised results of validation 10

ID	considered tests	results	F_{max} [kN]	v_{max} [mm]	$K_{ser,EN}$ [kN/mm]	$v_{sl,max}$ [%]	$v_{rg,max}$ [%]	$v_{CLT,max}$ [%]
VAL_10	1.1	mean test	77.08	37.9	5.795	73.0	24.3	2.7
		average simulation	71.38	45.4	6.182	61.4	34.2	4.4
		maximum simulation	78.21	43.9	6.820	56.2	38.8	5.0
		minimum simulation	65.81	40.2	5.934	59.2	36.2	4.6

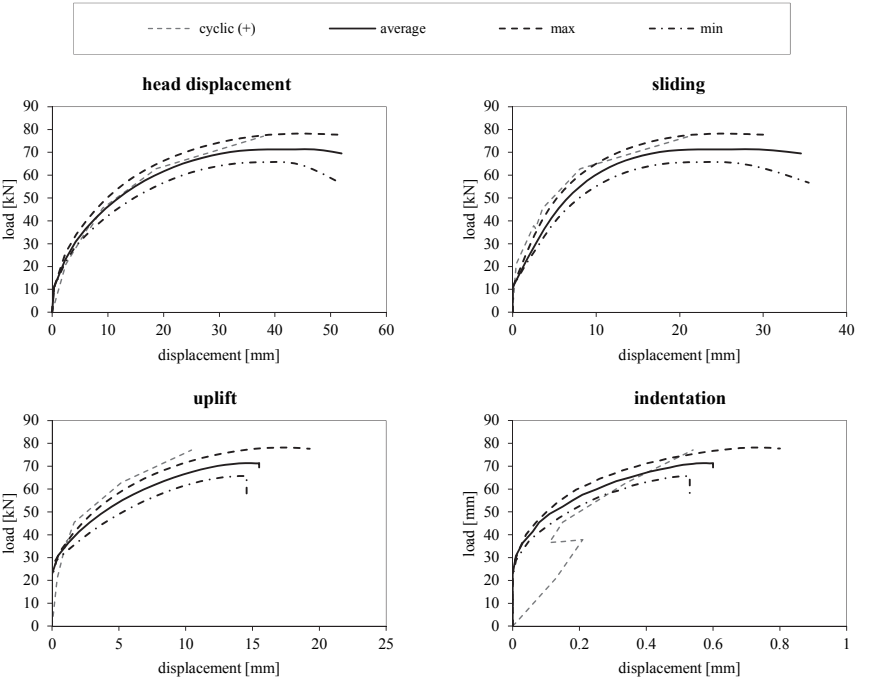

Figure C.12: comparison of experimental and simulated load-displacement curves for validation 10

C-2.3 Validation 11

Table C.11: summarised results of validation 11

ID	considered tests	results	F_{max} [kN]	v_{max} [mm]	$K_{ser,EN}$ [kN/mm]	$v_{sl,max}$ [%]	$v_{rg,max}$ [%]	$v_{CLT,max}$ [%]
VAL_11	1.2 1.4	mean test	108.25	47.1	4.876	47.7	50.3	2.0
		average simulation	92.90	32.6	7.707	38.0	54.0	8.0
		maximum simulation	101.79	36.9	8.213	36.6	55.6	7.8
		minimum simulation	86.49	32.4	7.187	38.3	54.1	7.5

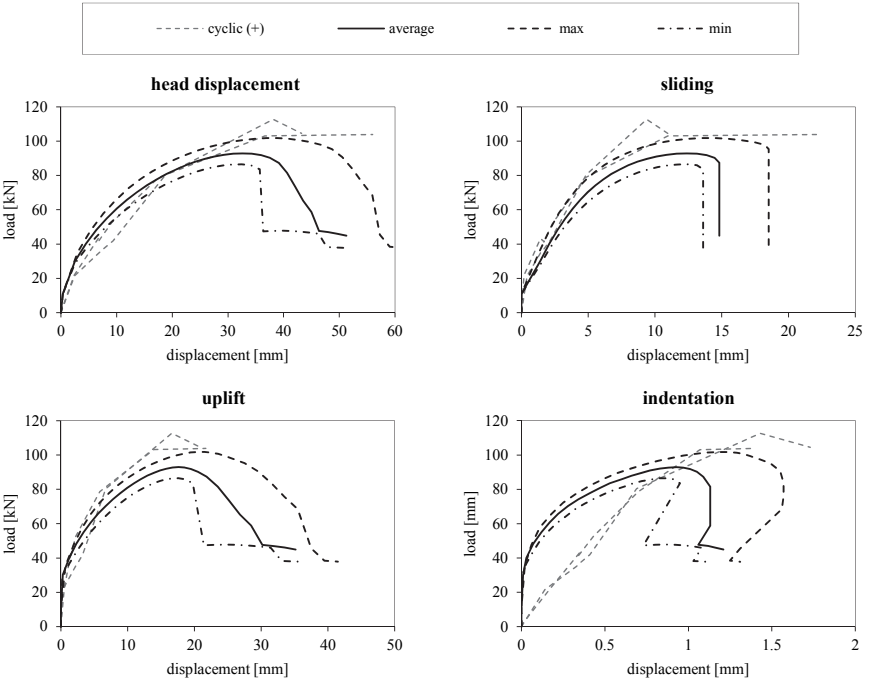

Figure C.13: comparison of experimental and simulated load-displacement curves for validation 11

C-2.4 Validation 12

Table C.12: summarised results of validation 12

ID	considered tests	results	F_{max} [kN]	v_{max} [mm]	$K_{ser,EN}$ [kN/mm]	$v_{sl,max}$ [%]	$v_{rg,max}$ [%]	$v_{CLT,max}$ [%]
VAL_12	1.3	mean test	105.74	48.2	5.311	41.2	56.8	2.0
		average simulation	82.73	30.3	5.934	34.7	57.6	7.7
		maximum simulation	91.78	36.6	6.650	34.0	58.9	7.1
		minimum simulation	76.40	30.2	5.127	34.9	57.9	7.2

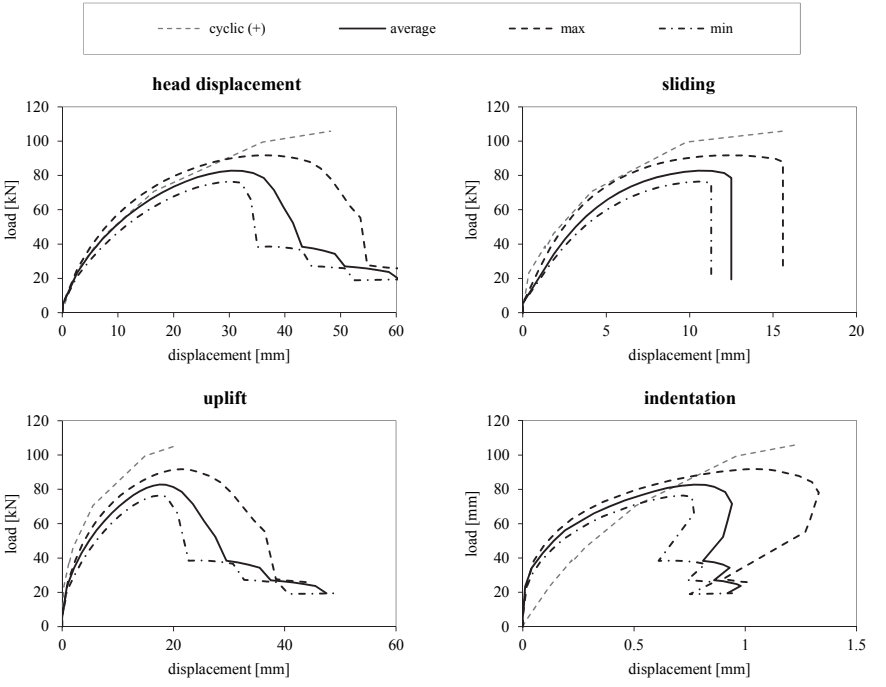

Figure C.14: comparison of experimental and simulated load-displacement curves for validation 12

C-2.5 Validation 13

Table C.13: summarised results of validation 13

ID	considered tests	results	F_{max} [kN]	v_{max} [mm]	$K_{ser,EN}$ [kN/mm]	$v_{sl,max}$ [%]	$v_{rg,max}$ [%]	$v_{CLT,max}$ [%]
VAL_13	2.1 2.2	mean test	92.37	55.1	5.174	42.6	55.3	2.2
		average simulation	94.73	40.6	5.425	31.5	57.3	11.3
		maximum simulation	103.84	44.7	5.954	32.2	56.5	11.3
		minimum simulation	87.88	42.8	4.048	28.3	61.7	10.0

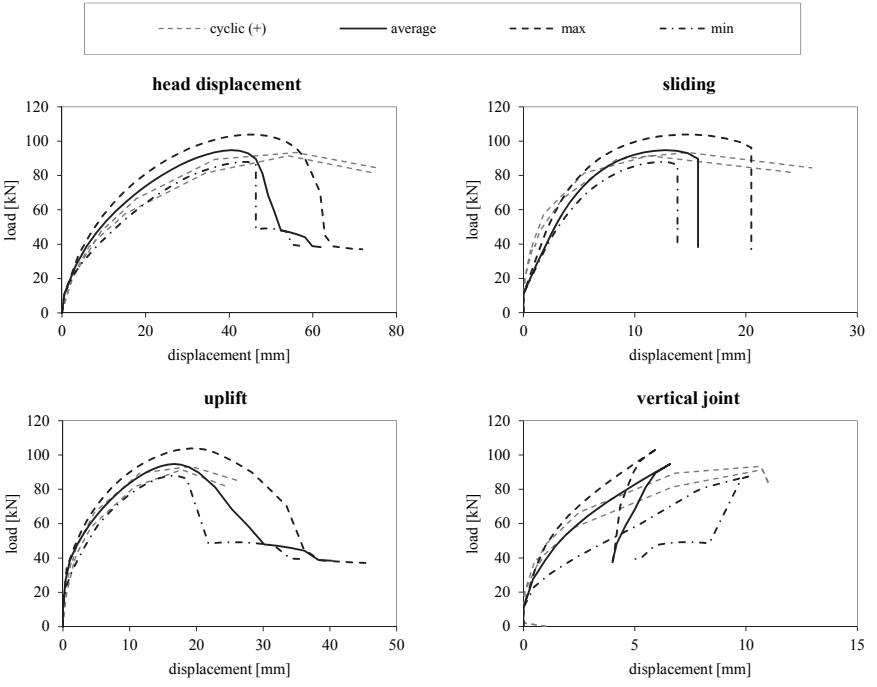

Figure C.15: comparison of experimental and simulated load-displacement curves for validation 13

C-2.6 Validation 14

Table C.14: summarised results of validation 14

ID	considered tests	results	F_{max} [kN]	v_{max} [mm]	$K_{ser,EN}$ [kN/mm]	$v_{sl,max}$ [%]	$v_{rg,max}$ [%]	$v_{CLT,max}$ [%]
VAL_14	2.3	mean test	93.88	36.5	4.682	18.3	80.2	1.5
		average simulation	90.16	53.4	4.389	22.4	69.4	8.2
		maximum simulation	100.70	55.9	4.703	22.1	69.1	8.7
		minimum simulation	82.83	52.0	3.443	22.0	70.3	7.7

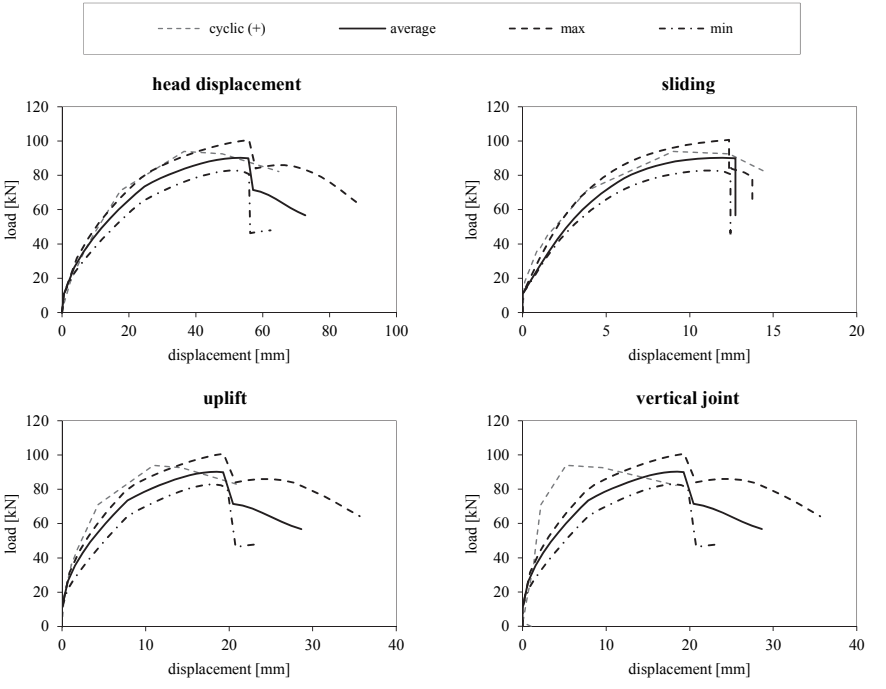

Figure C.16: comparison of experimental and simulated load-displacement curves for validation 14

C-2.7 Validation 15

Table C.15: summarised results of validation 15

ID	considered tests	results	F_{max} [kN]	v_{max} [mm]	$K_{ser,EN}$ [kN/mm]	$v_{sl,max}$ [%]	$v_{rg,max}$ [%]	$v_{CLT,max}$ [%]
VAL_15	2.4	mean test	96.66	52.3	4.661	14.6	83.8	1.6
		average simulation	101.82	50.4	4.117	18.4	71.8	9.8
		maximum simulation	111.76	52.9	4.543	16.4	73.3	10.2
		minimum simulation	93.70	49.5	3.379	19.2	71.7	9.2

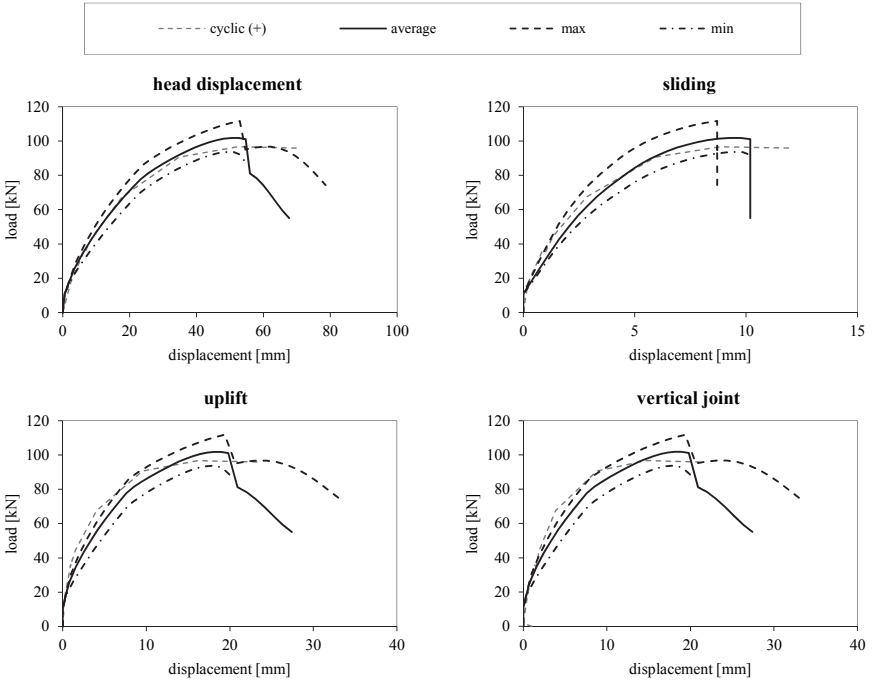

Figure C.17: comparison of experimental and simulated load-displacement curves for validation 15

C-2.8 Validation 16

Table C.16: summarised results of validation 16

ID	considered tests	results	F_{max} [kN]	v_{max} [mm]	$K_{ser,EN}$ [kN/mm]	$v_{sl,max}$ [%]	$v_{rg,max}$ [%]	$v_{CLT,max}$ [%]
VAL_16	3.1	mean test	107.04	53.6	5.654	23.8	74.7	1.5
		average simulation	94.64	37.9	5.034	32.9	55.0	12.1
		maximum simulation	103.78	43.0	5.722	33.0	55.3	11.7
		minimum simulation	87.94	38.8	4.706	33.6	55.4	11.0

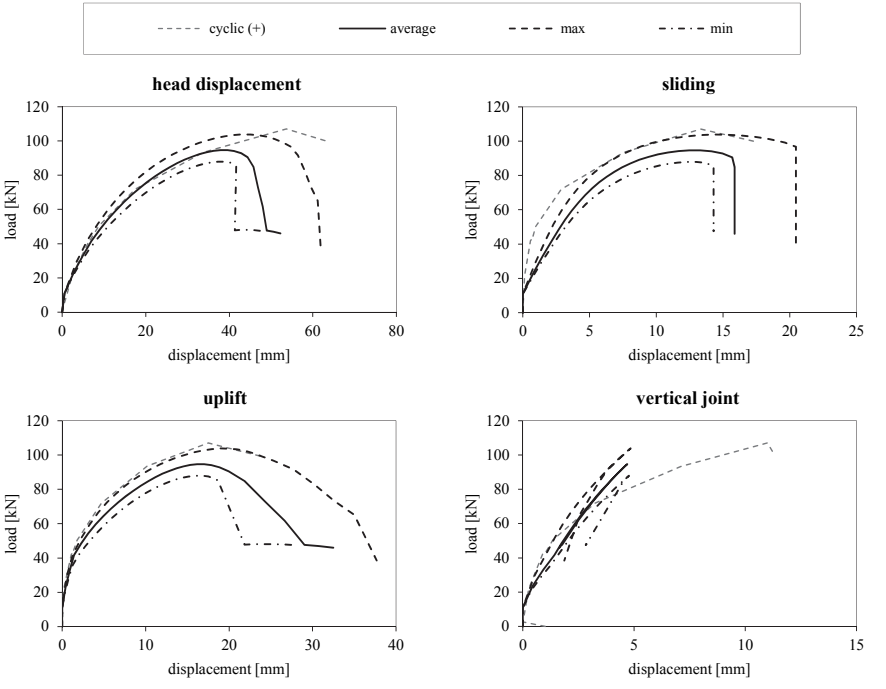

Figure C.18: comparison of experimental and simulated load-displacement curves for validation 16

C-2.9 Validation 17

Table C.17: summarised results of validation 17

ID	considered tests	results	F_{max} [kN]	v_{max} [mm]	$K_{ser,EN}$ [kN/mm]	$v_{sl,max}$ [%]	$v_{rg,max}$ [%]	$v_{CLT,max}$ [%]
VAL_17	3.2	mean test	85.63	56.0	4.005	10.8	87.7	1.4
	3.4 3.5 4.1	average simulation	94.43	48.8	4.142	26.1	64.5	9.4
		maximum simulation	103.56	57.0	4.557	25.6	65.6	8.8
	4.2	minimum simulation	87.74	45.9	3.808	26.4	64.4	9.3

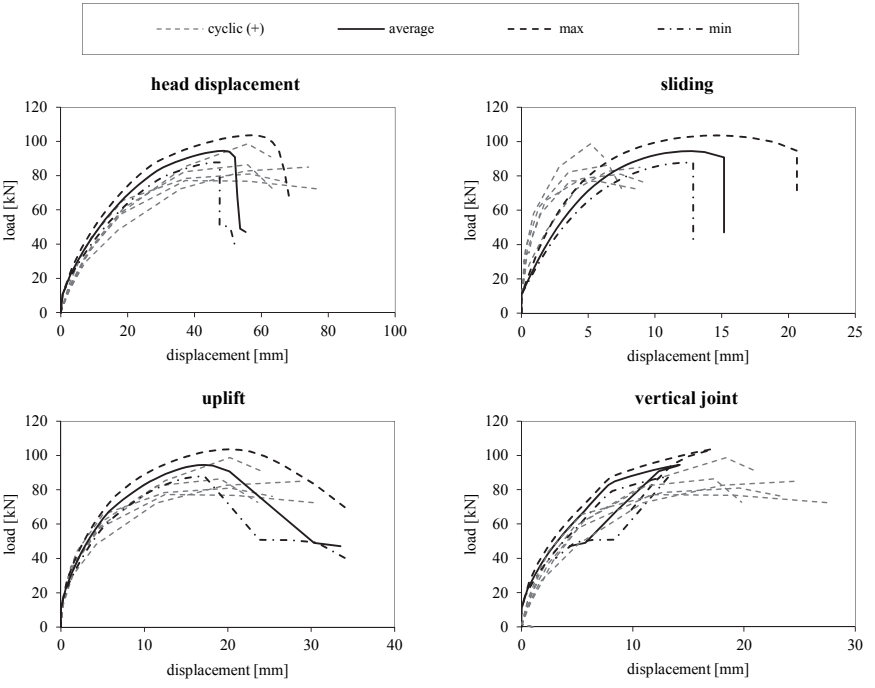

Figure C.19: comparison of experimental and simulated load-displacement curves for validation 17

C-2.10 Validation 18

Table C.18: summarised results of validation 18

ID	considered tests	results	F_{max} [kN]	v_{max} [mm]	$K_{ser,EN}$ [kN/mm]	$v_{sl,max}$ [%]	$v_{rg,max}$ [%]	$v_{CLT,max}$ [%]
VAL_18	3.3	mean test	103.72	53.4	4.395	13.6	85.0	1.4
		average simulation	104.91	52.7	4.047	20.1	70.3	9.7
		maximum simulation	115.82	61.6	4.479	18.5	72.4	9.1
		minimum simulation	97.40	50.6	3.555	21.2	69.4	9.3

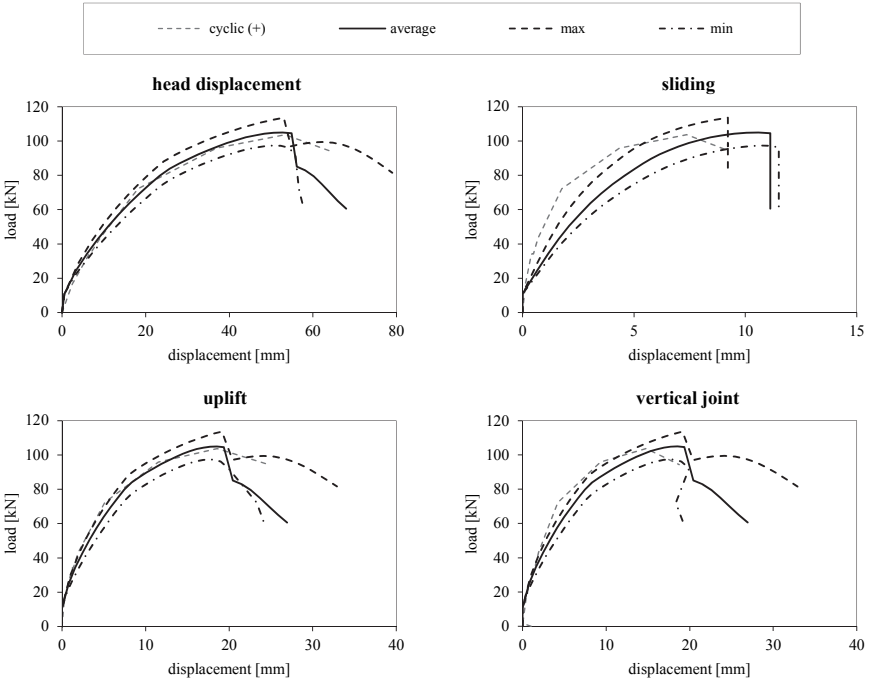

Figure C.20: comparison of experimental and simulated load-displacement curves for validation 18

C-2.11 Validation 19

Table C.19: summarised results of validation 19

ID	considered tests	results	F_{max} [kN]	v_{max} [mm]	$K_{ser,EN}$ [kN/mm]	$v_{sl,max}$ [%]	$v_{rg,max}$ [%]	$v_{CLT,max}$ [%]
VAL_19	3.6	mean test	60.46	56.6	2.765	12.0	86.1	1.9
		average simulation	73.44	38.1	3.291	25.2	65.4	9.4
		maximum simulation	82.94	44.4	3.782	25.2	65.7	9.1
		minimum simulation	66.72	36.6	2.921	25.1	66.1	8.9

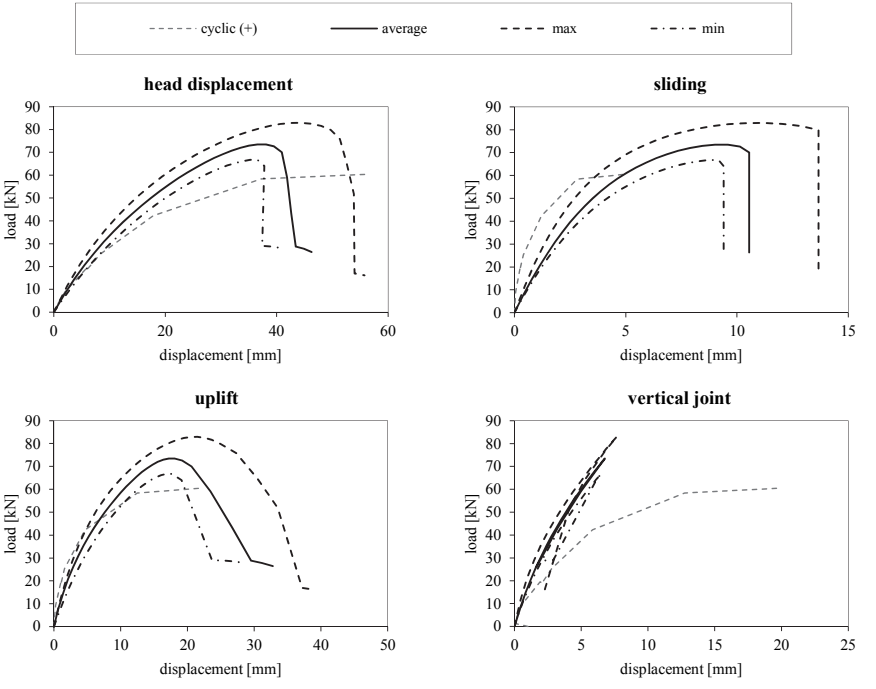

Figure C.21: comparison of experimental and simulated load-displacement curves for validation 19

Note: As documented in Gavric et al. (2015a), coupled behaviour was observed for this test; however, in the simulation single-coupled behaviour occurs.

C-3 Wall tests University of Kassel

C-3.1 Overview

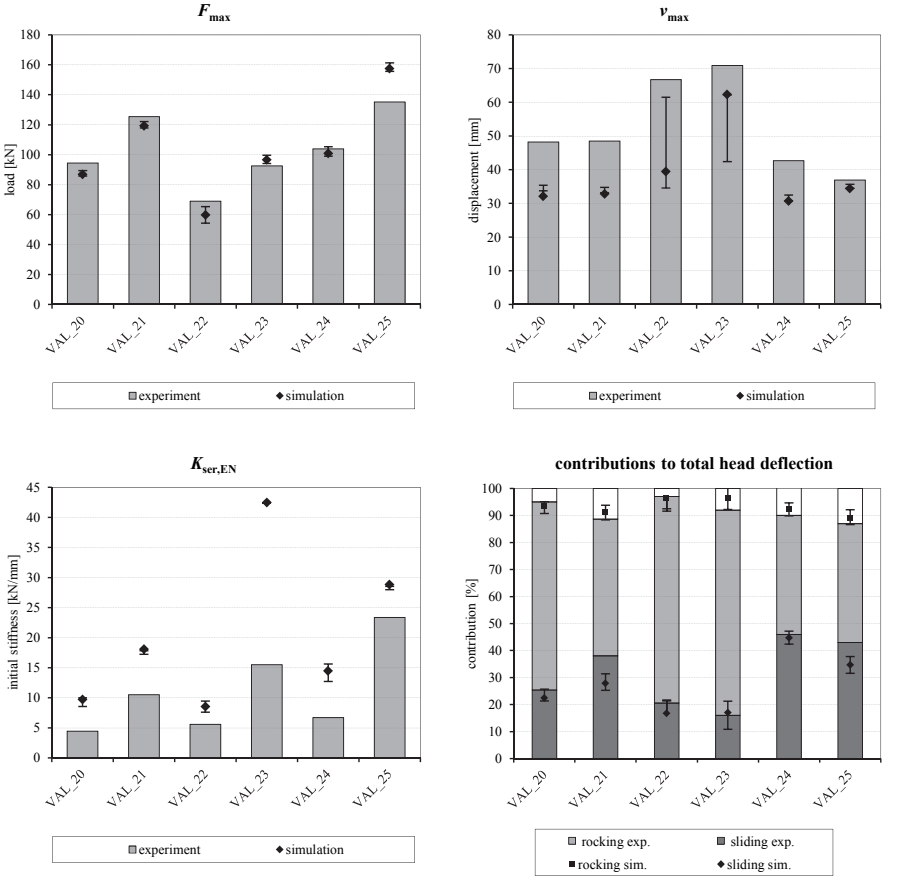

Figure C.22: model validation on tests conducted at the University of Kassel – overview of selected parameters

Note: The contributions to total head deflection are taken from Seim and Hummel (2013).

C-3.2 Validation 20

Table C.20: summarised results of validation 20

ID	considered tests	results	F_{max} [kN]	v_{max} [mm]	$K_{ser,EN}$ [kN/mm]	$v_{sl,max}$ [%]	$v_{rg,max}$ [%]	$v_{CLT,max}$ [%]
VAL_20	W-CLT-1.1 W-CLT-1.2 W-CLT-1.3	mean test	94.47	48.2	4.472	25.3	69.7	5.0
		average simulation	86.76	32.1	9.730	22.4	71.2	6.4
		maximum simulation	89.35	35.4	10.025	21.3	72.7	6.0
		minimum simulation	85.76	33.7	8.536	25.7	68.3	6.0

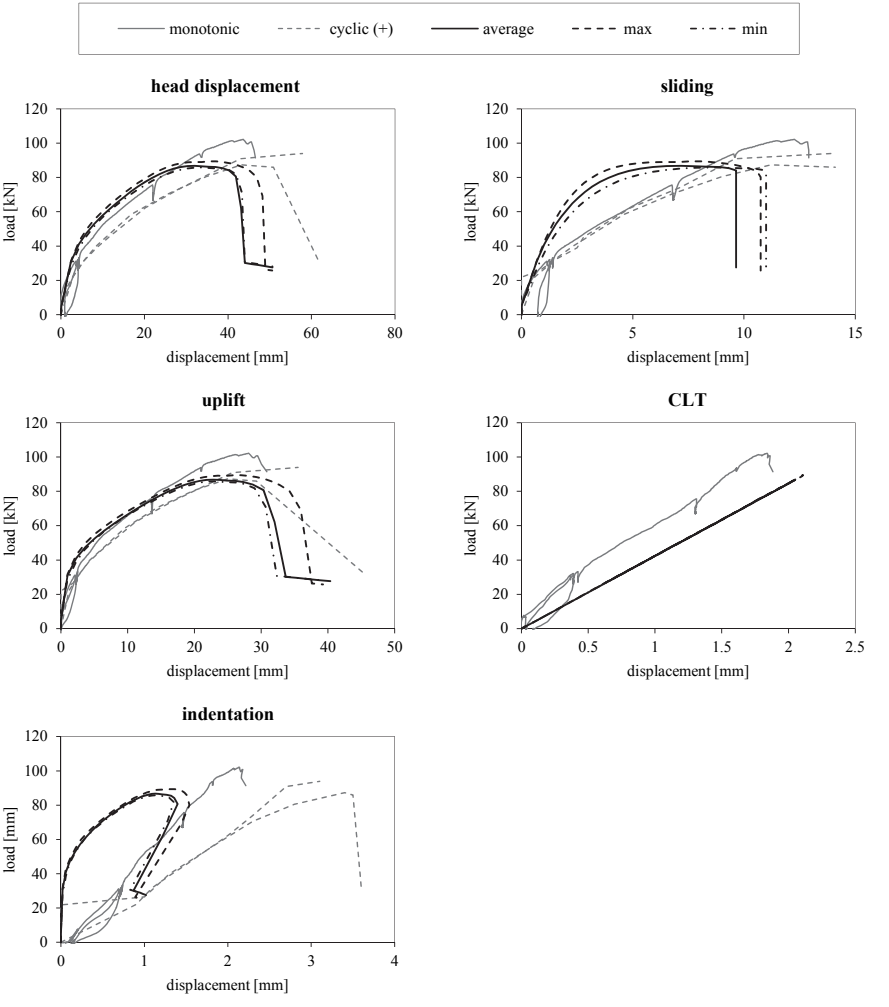

Figure C.23: comparison of experimental and simulated load-displacement curves for validation 20

C-3.3 Validation 21

Table C.21: summarised results of validation 21

ID	considered tests	results	F_{max} [kN]	v_{max} [mm]	$K_{ser,EN}$ [kN/mm]	$v_{sl,max}$ [%]	$v_{rg,max}$ [%]	$v_{CLT,max}$ [%]
VAL_21	W-CLT-2.1 W-CLT-2.2 W-CLT-2.3	mean test	125.46	48.5	10.520	38.0	50.7	11.3
		average simulation	119.25	32.8	18.086	27.8	63.6	8.6
		maximum simulation	122.09	33.2	17.837	25.3	66.0	8.7
		minimum simulation	117.87	34.8	17.232	31.4	60.6	8.0

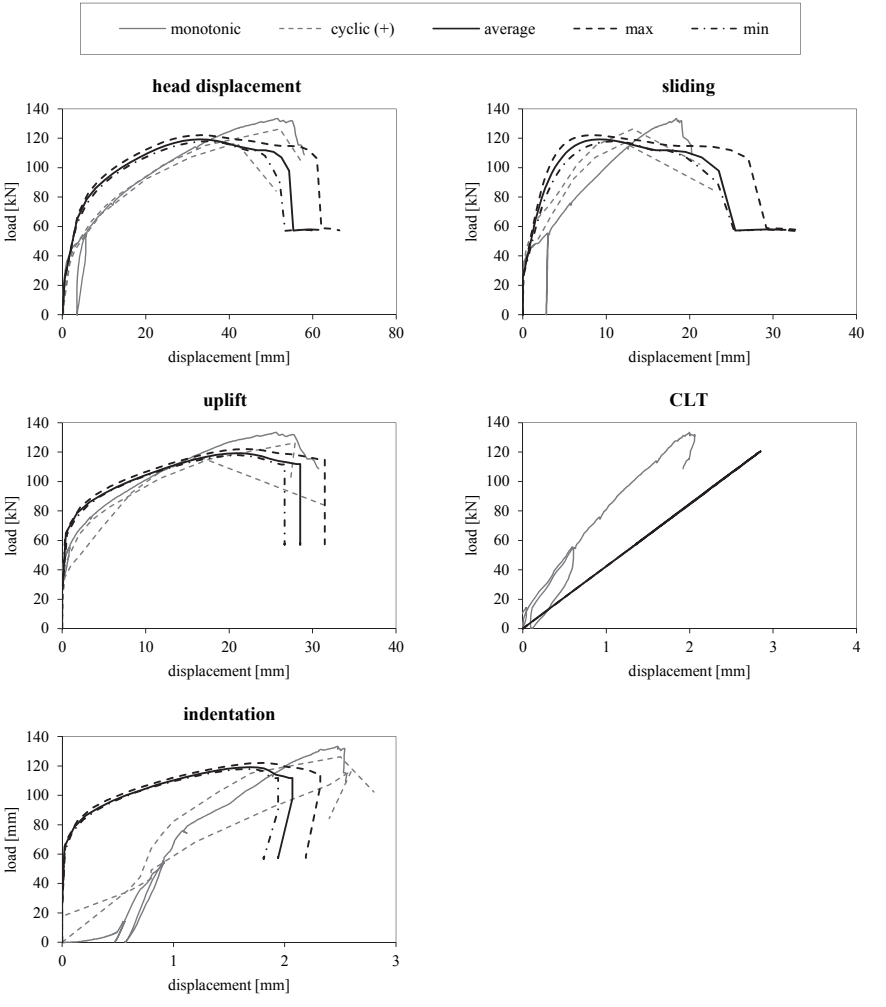

Figure C.24: comparison of experimental and simulated load-displacement curves for validation 21

C-3.4 Validation 22

Table C.22: summarised results of validation 22

ID	considered tests	results	F_{max} [kN]	v_{max} [mm]	$K_{ser,EN}$ [kN/mm]	$v_{sl,max}$ [%]	$v_{rg,max}$ [%]	$v_{CLT,max}$ [%]
VAL_22	W-CLT-3.1 W-CLT-3.2	mean test	68.94	66.8	5.605	20.5	76.5	3.0
		average simulation	59.85	39.4	8.545	16.7	79.8	3.6
		maximum simulation	65.33	61.5	9.458	21.7	75.8	2.5
		minimum simulation	54.35	34.6	7.591	21.3	74.9	3.7

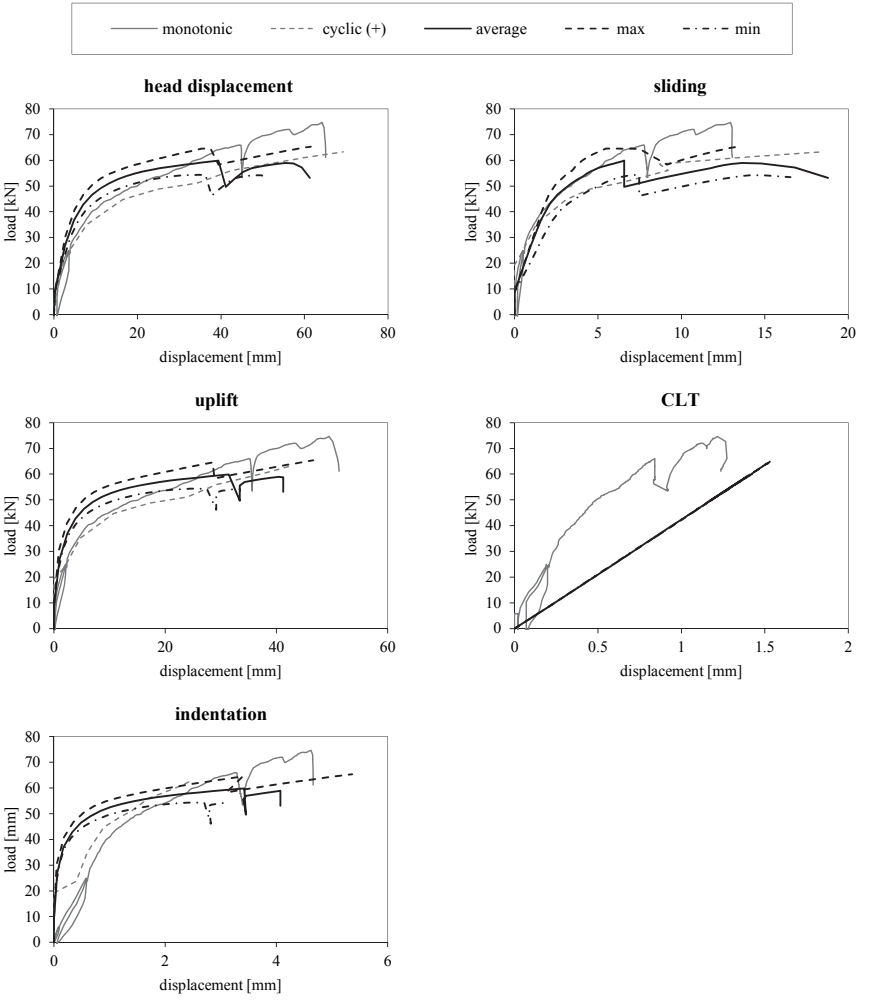

Figure C.25: comparison of experimental and simulated load-displacement curves for validation 22

C-3.5 Validation 23

Table C.23: summarised results of validation 23

ID	considered tests	results	F_{max} [kN]	v_{max} [mm]	$K_{ser,EN}$ [kN/mm]	$v_{sl,max}$ [%]	$v_{rg,max}$ [%]	$v_{CLT,max}$ [%]
VAL_23	W-CLT-3.3	mean test	92.53	70.9	15.505	16.0	76.0	8.0
		average simulation	96.56	62.3	42.476	17.0	79.4	3.7
		maximum simulation	99.63	42.4	42.476	10.8	83.7	5.5
		minimum simulation	94.11	62.2	42.476	21.2	75.2	3.6

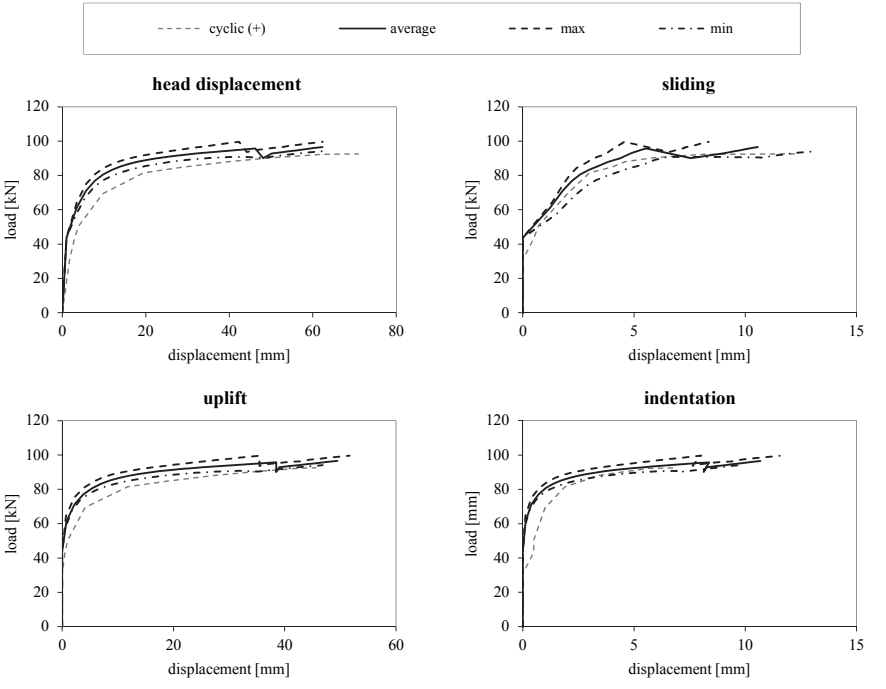

Figure C.26: comparison of experimental and simulated load-displacement curves for validation 23

C-3.6 Validation 24

Table C.24: summarised results of validation 24

ID	considered tests	results	F_{max} [kN]	v_{max} [mm]	$K_{ser,EN}$ [kN/mm]	$v_{sl,max}$ [%]	$v_{rg,max}$ [%]	$v_{CLT,max}$ [%]
VAL_24	W-CLT-3.5	mean test	103.87	42.7	6.714	46.0	44.0	11.0
		average simulation	100.86	30.7	14.478	44.7	47.6	7.7
		maximum simulation	105.32	32.5	15.643	42.4	50.0	7.7
		minimum simulation	98.96	30.7	12.724	47.2	45.2	7.6

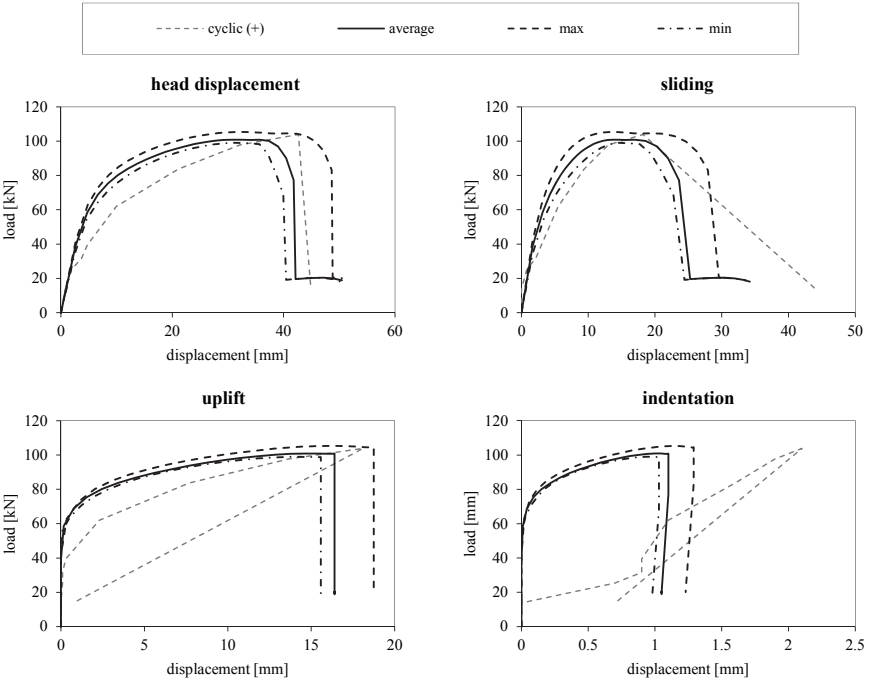

Figure C.27: comparison of experimental and simulated load-displacement curves for validation 24

C-3.7 Validation 25

Table C.25: summarised results of validation 25

ID	considered tests	results	F_{max} [kN]	v_{max} [mm]	$K_{ser,EN}$ [kN/mm]	$v_{sl,max}$ [%]	$v_{rg,max}$ [%]	$v_{CLT,max}$ [%]
VAL_25	W-CLT-4.3	mean test	135.20	37.0	23.398	43.0	44.0	13.0
		average simulation	157.46	34.4	28.824	34.7	54.4	10.8
		maximum simulation	161.38	34.5	28.525	31.6	57.4	11.0
		minimum simulation	155.60	35.7	27.975	37.8	51.9	10.3

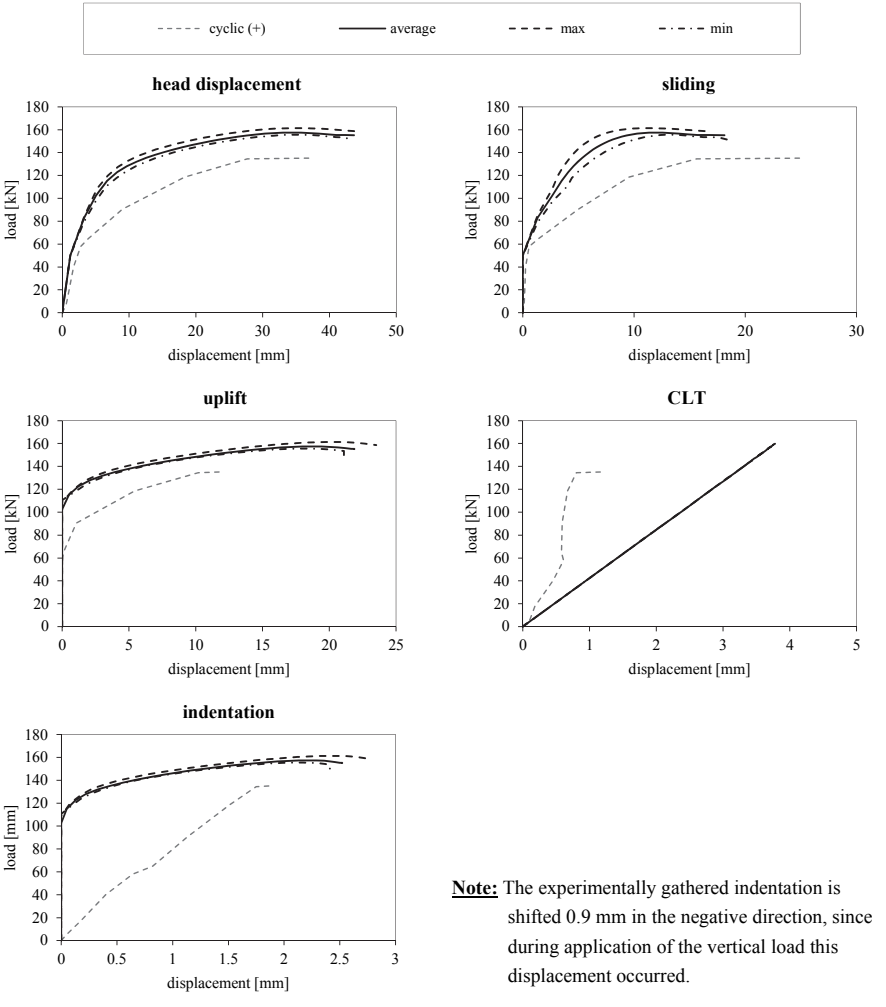

Note: The experimentally gathered indentation is shifted 0.9 mm in the negative direction, since during application of the vertical load this displacement occurred.

Figure C.28: comparison of experimental and simulated load-displacement curves for validation 25

C-4 FE wall simulation

C-4.1 Overview

Material properties and layup are chosen equal to the assumptions described in section 5-5.1.1. Moreover, only angle brackets (AB) basing on TU Graz tests are used as connections (compare section 5-2.2). Figure C.29 illustrates the geometric boundary conditions and lists the applied vertical loads.

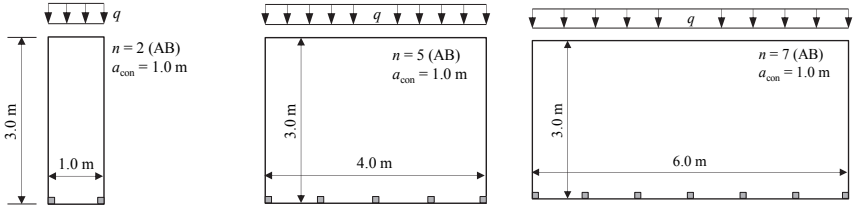

VAL_26: q = 10 kN/m
VAL_27: q = 25 kN/m
VAL_28: q = 50 kN/m

VAL_29: q = 10 kN/m
VAL_30: q = 25 kN/m
VAL_31: q = 50 kN/m

VAL_32: q = 10 kN/m
VAL_33: q = 25 kN/m
VAL_34: q = 50 kN/m

Figure C.29: overview for FE based model validation

C-4.2 Validations 26, 27 and 28

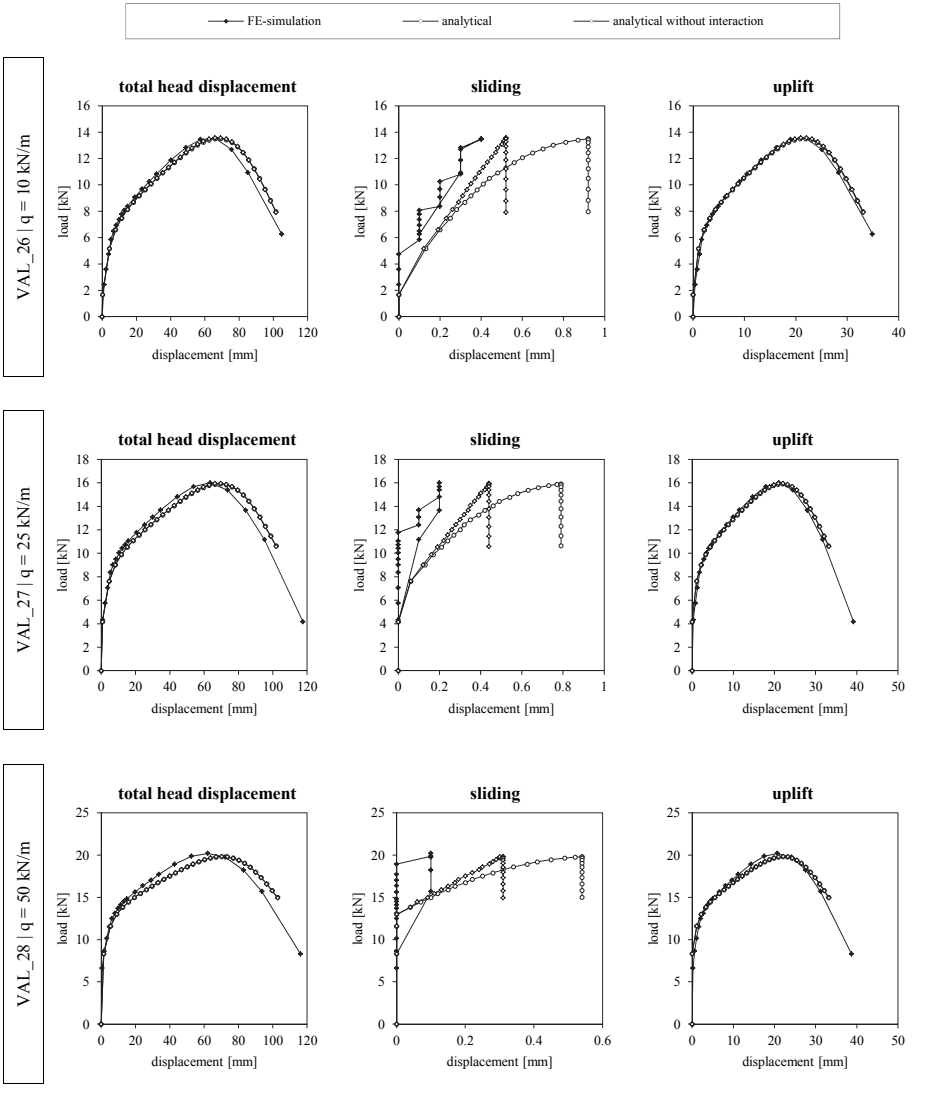

Figure C.30: FE based validation for a CLT wall with 1.0 m in length and varying vertical loads

C-4.3 Validations 29, 30 and 31

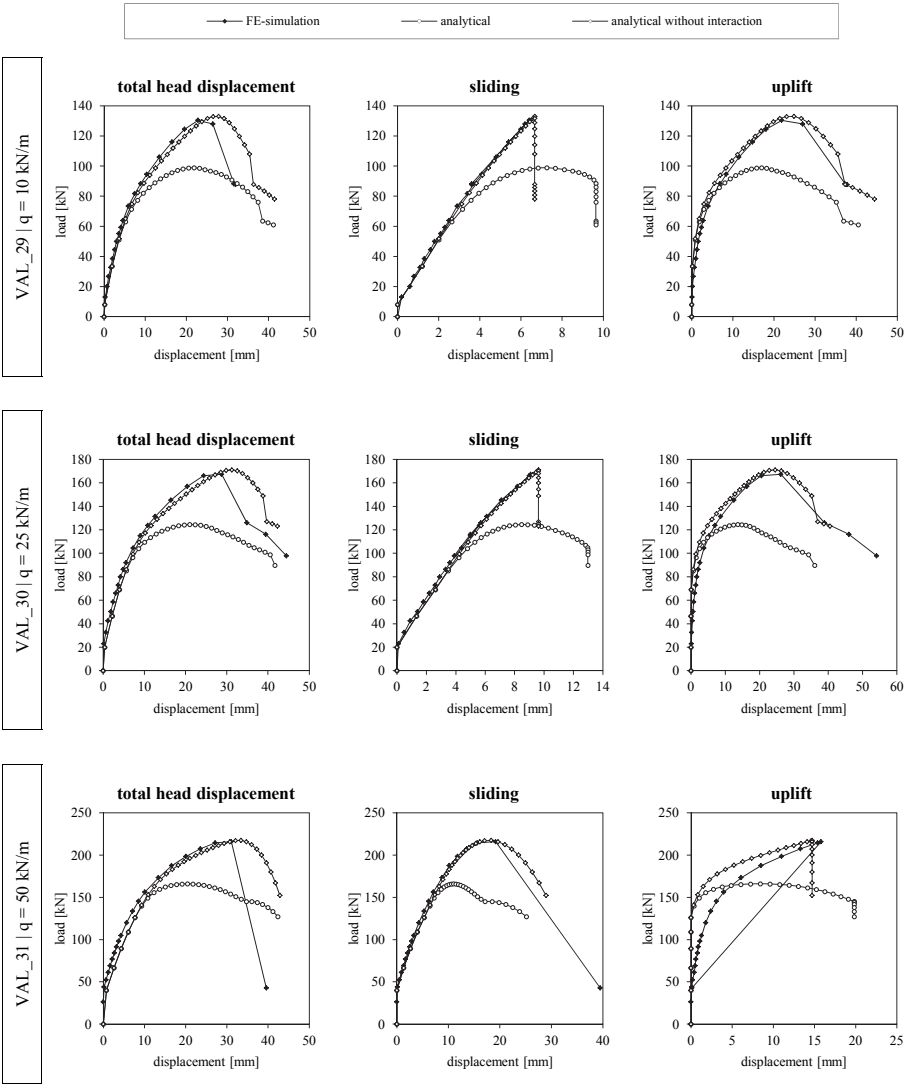

Figure C.31: FE based validation for a CLT wall with 4.0 m in length and varying vertical loads

C-4.4 Validations 32, 33 and 34

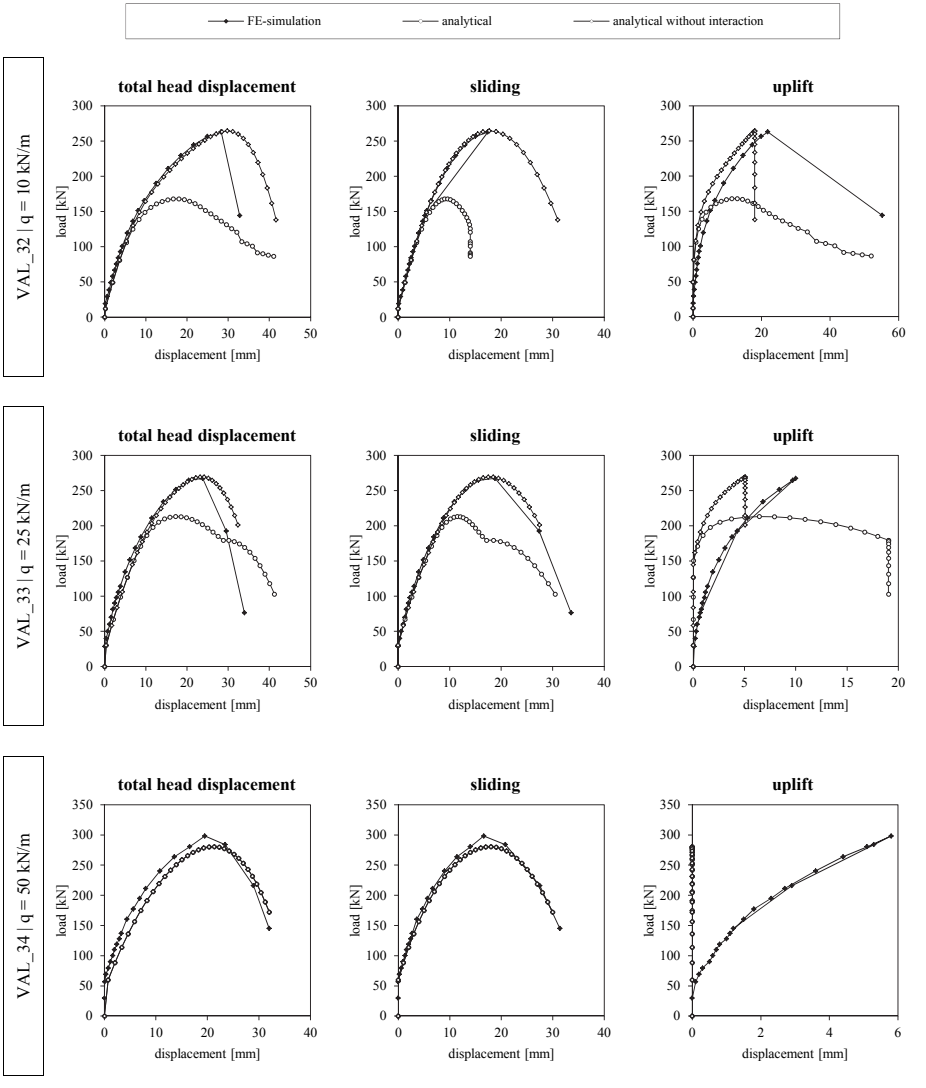

Figure C.32: FE based validation for a CLT wall with 6.0 m in length and varying vertical loads

ANNEX D MISCELLANEOUS

D-1 Formulas

Equations according to the model of Christensen (2008)

$$K_{\mathrm{T}}(v)=\frac{\mathrm{d}F}{\mathrm{d}v}=\frac{1}{\frac{\mathrm{d}v}{\mathrm{d}F}}=\frac{1}{\frac{1}{K_{\mathrm{ini}}}+\frac{a\cdot\left(\frac{F}{F_{\max}}\right)^{-1+m}\cdot m}{\left(1-\left(\frac{F}{F_{\max}}\right)^{m}\right)\cdot F_{\max}}} \tag{D.1}$$

$$\Delta K_{\mathrm{T}}(v)=\frac{\mathrm{d}^2F}{\mathrm{d}v^2}=-\left(\frac{\mathrm{d}^2v}{\mathrm{d}F^2}\right)\Big/\left(\frac{\mathrm{d}v}{\mathrm{d}F}\right)^3= \\ =\frac{-\frac{a\cdot\left(\frac{F}{F_{\max}}\right)^{-2+m}\cdot(-1+m)\cdot m}{\left(1-\left(\frac{F}{F_{\max}}\right)^{m}\right)\cdot F_{\max}^2}-\frac{a\cdot\left(\frac{F}{F_{\max}}\right)^{-2+2\cdot m}\cdot m^2}{\left(1-\left(\frac{F}{F_{\max}}\right)^{m}\right)^2\cdot F_{\max}^2}}{\left(\frac{1}{K_{\mathrm{ini}}}+\frac{a\cdot\left(\frac{F}{F_{\max}}\right)^{-1+m}\cdot m}{\left(1-\left(\frac{F}{F_{\max}}\right)^{m}\right)\cdot F_{\max}}\right)^3} \tag{D.2}$$

Determining the constant values fort the model of Glos (1978)

$$C_1=\frac{F_{\mathrm{a}}}{(C_5-1)\cdot K_{\mathrm{ini}}\cdot v_{\max}^{C_5}\cdot\left(1-\frac{F_{\mathrm{a}}}{F_{\max}}\right)} \tag{D.3}$$

$$C_2=\frac{1}{K_{\mathrm{ini}}} \tag{D.4}$$

$$C_3=\frac{1}{F_{\max}}-\frac{C_5}{K_{\mathrm{ini}}\cdot v_{\max}\cdot(C_5-1)} \tag{D.5}$$

$$C_4=\frac{1}{(C_5-1)\cdot K_{\mathrm{ini}}\cdot v_{\max}^{C_5}\cdot\left(1-\frac{F_{\mathrm{a}}}{F_{\max}}\right)} \tag{D.6}$$

Determining the constant values for the model of Brandner et al. (2017)

$$C_1 = \frac{1}{K_{\text{ini}}} \tag{D.7}$$

$$C_2 = \frac{1}{F_{\max} - K_{\text{ini}}\left(v_{\text{lin}} - v_{\text{in}}\right)} - \frac{C_4}{K_{\text{ini}} \cdot \left(v_{\max} - v_{\text{lin}}\right) \cdot \left(C_4 - 1\right)} \tag{D.8}$$

$$C_3 = \frac{1}{(C_4 - 1) \cdot K_{\text{ini}} \cdot \left(v_{\max} - v_{\text{lin}}\right)^{C_4}} \tag{D.9}$$

D-2 Tables

Table D.1 to Table D.4 show the input parameters for the four approximation models compared in section 3-5 after a least-squares fit (excluding the parameters F_{max} and v_{max}; here the original data points, gathered from the experimental tests are used)

Table D.1: input parameters for Y-M-U model

parameter	[T1]	[T2]	[S1]	[S2]	[M1]	[M2]
F_{max} [kN]	21.52	13.07	7.81	4.59	14.32	3.10
v_{max} [mm]	1.91	4.19	33.35	13.43	17.22	15.70
F_y [kN]	9.592	7.621	4.387	2.679	2.413	1.630
v_y [mm]	0.474	0.392	5.166	3.158	0.291	1.288
F_u [kN]	17.207	10.327	6.389	4.018	11.529	2.505
v_u [mm]	3.206	16.127	56.667	17.032	18.025	22.358

Table D.2: input parameters for the Yee and Melchers (1986) model

parameter	[T1]	[T2]	[S1]	[S2]	[M1]	[M2]
K_{ini} [kN/m]	25.616	18.919	0.940	1.390	11.344	1.618
F_t [kN]	24.946	12.947	8.300	2.514	2.134	2.075
K_p [kN/m]	4.319	-0.133	0.019	0.199	0.745	0.062
C [-]	-6.498	-0.956	-0.014	-0.069	-0.598	-0.068

Table D.3: input parameters for the Glos (1978) model

parameter	[T1]	[T2]	[S1]	[S2]	[M1]	[M2]
F_{max} [kN]	21.52	13.07	7.81	4.59	14.32	3.10
v_{max} [mm]	1.91	4.19	33.35	13.43	17.22	15.70
K_{ini} [kN/m]	25.128	24.841	1.029	1.201	11.048	1.394
F_a [kN]	18.007	11.151	6.320	4.318	-20.000	2.617
C [-]	11.722	6.888	9.150	40.487	1.044	22.302

Table D.4: input parameters for the model of Brandner et al. (2017)

parameter	[T1]	[T2]	[S1]	[S2]	[M1]	[M2]
F_{max} [kN]	21.52	13.07	7.81	4.59	14.32	3.10
v_{max} [mm]	1.91	4.19	33.35	13.43	17.22	15.70
K_{ini} [kN/m]	16.728	11.424	0.731	0.941	0.908	0.711
v_{in} [mm]	-0.079	-0.145	-0.697	-0.257	-1.530	-0.586
v_{lin} [mm]	0.142	0.012	0.305	0.060	0.004	0.032
C_4 [-]	3.415	1.596	4.466	10.964	17.666	9.071

D-3 Analytical curve model – solutions for C_1 to C_6

D-3.1 Resulting coefficients

```
Simplify[C1]
```

$$
\begin{aligned}
&(Fmax\ (-Fmax\ KB\ Kini\ vB\ (vA^{n}\ vB - vA\ vB^{n})\ ((-1+m)\ vB^{n}\ vmax^{1+m} - (-1+n)\ vB^{m}\ vmax^{1+n} - (m-n)\ vB\ vmax^{m+n}) -\\
&\quad FB\ Fmax\ Kini\ (-1+n)\ (-(m-n)\ vA\ vB^{n}\ vmax^{n}\ (-vB^{m}\ vmax + vB\ vmax^{m}) +\\
&\quad\quad (-1+m)\ vA^{n}\ vB\ vmax\ (vB^{n}\ vmax^{m} - vB^{m}\ vmax^{n})) + FB^{2}\ (Kini\ (-1+n)\\
&\quad\quad (-(m-n)\ vA\ vB^{n}\ vmax^{n}\ (-vB^{m}\ vmax + vB\ vmax^{m}) + (-1+m)\ vA^{n}\ vB\ vmax\ (vB^{n}\ vmax^{m} - vB^{m}\ vmax^{n})) +\\
&\quad\quad Fmax\ vA^{n}\ (-n\ (vB^{m} - vmax^{m})\ (-vB^{n}\ vmax + vB\ vmax^{n}) + m\ (-vB^{m+n}\ vmax - (-1+n)\ vB^{1+n}\\
&\quad\quad\quad vmax^{m} + n\ vB^{n}\ vmax^{1+m} + n\ vB^{1+m}\ vmax^{n} - (-1+n)\ vB^{m}\ vmax^{1+n} - vB\ vmax^{m+n})))) +\\
&\quad FA\ (-FB^{2}\ vmax^{n}\ (-Kini\ (-1+n)\ ((-1+m)\ vA^{n}\ vB^{1+m} - (-1+n)\ vA^{m}\ vB^{1+n} - (m-n)\ vA\ vB^{m+n})\ vmax +\\
&\quad\quad Fmax\ (-m\ (vA^{n} - vB^{n})\ (-vB^{m}\ vmax + vB\ vmax^{m}) + n^{2}\ vB^{n}\ (-vB^{m}\ vmax + vB\ vmax^{m} + vA^{m}\ (-vB + vmax) + vA\\
&\quad\quad\quad (vB^{m} - vmax^{m})) + n\ (vA^{m}\ vB^{n}\ (vB - vmax) - m\ vA\ vB^{n}\ (vB^{m} - vmax^{m}) - (1+m)\ vB^{n}\\
&\quad\quad\quad (-vB^{m}\ vmax + vB\ vmax^{m}) + vA^{n}\ ((-1+m)\ vB^{1+m} - m\ vB^{m}\ vmax + vB\ vmax^{m})))) +\\
&\quad FB\ Fmax\ (-Kini\ (-1+n)\ (-2\ (-1+n)\ vA^{m}\ vB^{1+n}\ vmax^{1+n} - (m-n)\ vA\ vB^{n}\ vmax^{n}\\
&\quad\quad\quad (vB^{m}\ vmax + vB\ vmax^{m}) + (-1+m)\ vA^{n}\ vB\ vmax\ (vB^{n}\ vmax^{m} + vB^{m}\ vmax^{n})) +\\
&\quad\quad Fmax\ vB^{n}\ (n\ (-(-1+n)\ vA^{m}\ (vB - vmax)\ vmax^{n} - vA^{n}\ vmax\ (vB^{m} - vmax^{m}) + n\ vA\ vmax^{n}\\
&\quad\quad\quad (vB^{m} - vmax^{m}) + (-1+n)\ vmax^{n}\ (-vB^{m}\ vmax + vB\ vmax^{m})) + m\ (-n\ vA\ vmax^{n}\ (vB^{m} - vmax^{m}) +\\
&\quad\quad\quad (-1+n)\ vmax^{n}\ (vB^{m}\ vmax - vB\ vmax^{m}) + vA^{n}\ (vB^{m}\ vmax + (-1+n)\ vB\ vmax^{m} - n\ vmax^{1+m})))) -\\
&\quad Fmax\ vB\ (KB\ Kini\ (-vA^{n}\ vB + vA\ vB^{n})\ ((-1+m)\ vB^{n}\ vmax^{1+m} - (-1+n)\ vB^{m}\ vmax^{1+n} - (m-n)\ vB\ vmax^{m+n}) +\\
&\quad\quad Fmax\ vB^{n}\ (-Kini\ (-1+n)\ ((-1+m)\ vA^{n}\ vmax^{1+m} - (-1+n)\ vA^{m}\ vmax^{1+n} - (m-n)\ vA\ vmax^{m+n}) +\\
&\quad\quad\quad KB\ ((-1+m)\ vB^{n}\ vmax^{1+m} - (-1+n)\ vB^{m}\ vmax^{1+n} - (m-n)\ vB\ vmax^{m+n} + vA^{n}\\
&\quad\quad\quad (-vB^{m}\ vmax + m\ vB\ vmax^{m} - (-1+m)\ vmax^{1+m}) + vA^{m}\ (vB^{n}\ vmax - n\ vB\ vmax^{n} +\\
&\quad\quad\quad (-1+n)\ vmax^{1+n}) + vA\ (n\ vmax^{n}\ (vB^{m} - vmax^{m}) - m\ vmax^{m}\ (vB^{n} - vmax^{n}))))))))\ /\\
&(Kini\ (Fmax\ (Fmax\ KB\ vB\ (-vA^{n}\ vB^{m} + vA^{m}\ vB^{n})\ (-(-1+m)\ vB^{n}\ vmax^{1+m} + (-1+n)\ vB^{m}\ vmax^{1+n} +\\
&\quad\quad (m-n)\ vB\ vmax^{m+n}) - FB^{2}\ (m-n)\ (-(-1+n)\ vA^{m}\ vB^{n}\ vmax^{n}\ (-vB^{m}\ vmax + vB\ vmax^{m}) +\\
&\quad\quad (-1+m)\ vA^{n}\ vB^{m}\ vmax^{m}\ (-vB^{n}\ vmax + vB\ vmax^{n})) +\\
&\quad FB\ Fmax\ (m-n)\ (-(-1+n)\ vA^{m}\ vB^{n}\ vmax^{n}\ (-vB^{m}\ vmax + vB\ vmax^{m}) +\\
&\quad\quad (-1+m)\ vA^{n}\ vB^{m}\ vmax^{m}\ (-vB^{n}\ vmax + vB\ vmax^{n}))) +\\
&\quad FA\ (-FB^{2}\ (m-n)\ (-(-1+m)\ vA^{n}\ vB^{1+m} + (-1+n)\ vA^{m}\ vB^{1+n} + (m-n)\ vA\ vB^{m+n})\ vmax^{m+n} +\\
&\quad FB\ Fmax\ (m-n)\ (2\ (m-n)\ vA\ vB^{m+n}\ vmax^{m+n} + (-1+n)\ vA^{m}\ vB^{n}\ vmax^{n}\ (vB^{m}\ vmax + vB\ vmax^{m}) -\\
&\quad\quad (-1+m)\ vA^{n}\ vB^{m}\ vmax^{m}\ (vB^{n}\ vmax + vB\ vmax^{n})) -\\
&\quad Fmax\ (Fmax\ (m-n)\ vB^{m+n}\ (-(-1+m)\ vA^{n}\ vmax^{1+m} + (-1+n)\ vA^{m}\ vmax^{1+n} + (m-n)\ vA\ vmax^{m+n}) -\\
&\quad\quad KB\ vB\ (vA^{n}\ vB^{m} - vA^{m}\ vB^{n})\ (-(-1+m)\ vB^{n}\ vmax^{1+m} + (-1+n)\ vB^{m}\ vmax^{1+n} + (m-n)\ vB\ vmax^{m+n})))))
\end{aligned}
$$

Simplify[C2]

$$\Big(\mathrm{Fmax}\,\Big(-\mathrm{Fmax}\,\mathrm{KB}\,\mathrm{Kini}\,\mathrm{vB}\,(\mathrm{vA}^{m}\,\mathrm{vB}-\mathrm{vA}\,\mathrm{vB}^{m})\Big(-(-1+m)\,\mathrm{vB}^{n}\,\mathrm{vmax}^{1+m}+(-1+n)\,\mathrm{vB}^{m}\,\mathrm{vmax}^{1+n}+(m-n)\,\mathrm{vB}\,\mathrm{vmax}^{m+n}\Big)-\mathrm{FB}\,\mathrm{Fmax}\,\mathrm{Kini}\,(-1+m)\,((m-n)\,\mathrm{vA}\,\mathrm{vB}^{m}\,\mathrm{vmax}^{m}\,(-\mathrm{vB}^{n}\,\mathrm{vmax}+\mathrm{vB}\,\mathrm{vmax}^{n})-(-1+n)\,\mathrm{vA}^{m}\,\mathrm{vB}\,\mathrm{vmax}\,(\mathrm{vB}^{n}\,\mathrm{vmax}^{m}-\mathrm{vB}^{m}\,\mathrm{vmax}^{n}))+\mathrm{FB}^{2}\,\Big(\mathrm{Kini}\,(-1+m)\,((m-n)\,\mathrm{vA}\,\mathrm{vB}^{m}\,\mathrm{vmax}^{m}\,(-\mathrm{vB}^{n}\,\mathrm{vmax}+\mathrm{vB}\,\mathrm{vmax}^{n})-(-1+n)\,\mathrm{vA}^{m}\,\mathrm{vB}\,\mathrm{vmax}\,(\mathrm{vB}^{n}\,\mathrm{vmax}^{m}-\mathrm{vB}^{m}\,\mathrm{vmax}^{n}))+\mathrm{Fmax}\,\mathrm{vA}^{m}\,\Big(n\,(\mathrm{vB}^{m}-\mathrm{vmax}^{m})\,(-\mathrm{vB}^{n}\,\mathrm{vmax}+\mathrm{vB}\,\mathrm{vmax}^{n})+m\,\Big(\mathrm{vB}^{m+n}\,\mathrm{vmax}+(-1+n)\,\mathrm{vB}^{1+n}\,\mathrm{vmax}^{m}-n\,\mathrm{vB}^{n}\,\mathrm{vmax}^{1+m}-n\,\mathrm{vB}^{1+m}\,\mathrm{vmax}^{n}+(-1+n)\,\mathrm{vB}^{m}\,\mathrm{vmax}^{1+n}+\mathrm{vB}\,\mathrm{vmax}^{m+n}\Big)\Big)\Big)\Big)+\mathrm{FA}\,\Big(\mathrm{FB}^{2}\,\mathrm{Kini}\,(-1+m)\,\Big(-(-1+m)\,\mathrm{vA}^{n}\,\mathrm{vB}^{1+m}+(-1+n)\,\mathrm{vA}^{m}\,\mathrm{vB}^{1+n}+(m-n)\,\mathrm{vA}\,\mathrm{vB}^{m+n}\Big)\,\mathrm{vmax}^{1+m}+\mathrm{Fmax}\,\Big(\mathrm{KB}\,\mathrm{Kini}\,\mathrm{vB}\,(\mathrm{vA}^{m}\,\mathrm{vB}-\mathrm{vA}\,\mathrm{vB}^{m})\,\Big(-(-1+m)\,\mathrm{vB}^{n}\,\mathrm{vmax}^{1+m}+(-1+n)\,\mathrm{vB}^{m}\,\mathrm{vmax}^{1+n}+(m-n)\,\mathrm{vB}\,\mathrm{vmax}^{m+n}\Big)+\mathrm{FB}\,\mathrm{Kini}\,(-1+m)\,\Big(2\,(-1+m)\,\mathrm{vA}^{n}\,\mathrm{vB}^{1+m}\,\mathrm{vmax}^{1+m}-(m-n)\,\mathrm{vA}\,\mathrm{vB}^{m}\,\mathrm{vmax}^{m}\,(\mathrm{vB}^{n}\,\mathrm{vmax}+\mathrm{vB}\,\mathrm{vmax}^{n})-(-1+n)\,\mathrm{vA}^{m}\,\mathrm{vB}\,\mathrm{vmax}\,(\mathrm{vB}^{n}\,\mathrm{vmax}^{m}+\mathrm{vB}^{m}\,\mathrm{vmax}^{n})\Big)+\mathrm{FB}^{2}\,\mathrm{vmax}^{m}\,\Big(n\,(\mathrm{vA}^{m}-\mathrm{vB}^{m})\,(-\mathrm{vB}^{n}\,\mathrm{vmax}+\mathrm{vB}\,\mathrm{vmax}^{n})+m^{2}\,\mathrm{vB}^{m}\,(\mathrm{vA}^{n}\,(\mathrm{vB}-\mathrm{vmax})+\mathrm{vB}^{n}\,\mathrm{vmax}-\mathrm{vB}\,\mathrm{vmax}^{n}+\mathrm{vA}\,(-\mathrm{vB}^{n}+\mathrm{vmax}^{n}))+m\,\Big(\mathrm{vA}^{n}\,\mathrm{vB}^{m}\,(-\mathrm{vB}+\mathrm{vmax})+n\,\mathrm{vA}\,\mathrm{vB}^{m}\,(\mathrm{vB}^{n}-\mathrm{vmax}^{n})+\mathrm{vA}^{m}\,\Big(-(-1+n)\,\mathrm{vB}^{1+n}+n\,\mathrm{vB}^{n}\,\mathrm{vmax}-\mathrm{vB}\,\mathrm{vmax}^{n}\Big)+(1+n)\,\mathrm{vB}^{m}\,(-\mathrm{vB}^{n}\,\mathrm{vmax}+\mathrm{vB}\,\mathrm{vmax}^{n})\Big)\Big)-\mathrm{Fmax}^{2}\,\mathrm{vB}^{m}\,\Big(\mathrm{Kini}\,(-1+m)\,\mathrm{vB}\,\Big((-1+m)\,\mathrm{vA}^{n}\,\mathrm{vmax}^{1+m}-(-1+n)\,\mathrm{vA}^{m}\,\mathrm{vmax}^{1+n}-(m-n)\,\mathrm{vA}\,\mathrm{vmax}^{m+n}\Big)+\mathrm{KB}\,\mathrm{vB}\,\Big(-(-1+m)\,\mathrm{vB}^{n}\,\mathrm{vmax}^{1+m}+(-1+n)\,\mathrm{vB}^{m}\,\mathrm{vmax}^{1+n}+(m-n)\,\mathrm{vB}\,\mathrm{vmax}^{m+n}+\mathrm{vA}^{n}\,\Big(\mathrm{vB}^{m}\,\mathrm{vmax}-m\,\mathrm{vB}\,\mathrm{vmax}^{m}+(-1+m)\,\mathrm{vmax}^{1+m}\Big)+\mathrm{vA}^{m}\,\Big(-\mathrm{vB}^{n}\,\mathrm{vmax}+n\,\mathrm{vB}\,\mathrm{vmax}^{n}-(-1+n)\,\mathrm{vmax}^{1+n}\Big)+\mathrm{vA}\,(-n\,\mathrm{vmax}^{n}\,(\mathrm{vB}^{m}-\mathrm{vmax}^{m})+m\,\mathrm{vmax}^{m}\,(\mathrm{vB}^{n}-\mathrm{vmax}^{n}))\Big)+\mathrm{FB}\,\Big(n\,(\mathrm{vA}^{m}-\mathrm{vmax}^{m})\,(-\mathrm{vB}^{n}\,\mathrm{vmax}+\mathrm{vB}\,\mathrm{vmax}^{n})+m^{2}\,\mathrm{vmax}^{m}\,(\mathrm{vA}^{n}\,(\mathrm{vB}-\mathrm{vmax})+\mathrm{vB}^{n}\,\mathrm{vmax}-\mathrm{vB}\,\mathrm{vmax}^{n}+\mathrm{vA}\,(-\mathrm{vB}^{n}+\mathrm{vmax}^{n}))+m\,\Big(\mathrm{vA}^{n}\,\mathrm{vmax}^{m}\,(-\mathrm{vB}+\mathrm{vmax})+n\,\mathrm{vA}\,\mathrm{vmax}^{m}\,(\mathrm{vB}^{n}-\mathrm{vmax}^{n})+(1+n)\,\mathrm{vmax}^{m}\,(-\mathrm{vB}^{n}\,\mathrm{vmax}+\mathrm{vB}\,\mathrm{vmax}^{n})+\mathrm{vA}^{m}\,\Big(\mathrm{vB}^{n}\,\mathrm{vmax}-n\,\mathrm{vB}\,\mathrm{vmax}^{n}+(-1+n)\,\mathrm{vmax}^{1+n}\Big)\Big)\Big)\Big)\Big)\Big)\Big/\Big(\mathrm{Kini}\,\Big(\mathrm{Fmax}\,\Big(\mathrm{Fmax}\,\mathrm{KB}\,\mathrm{vB}\,(-\mathrm{vA}^{n}\,\mathrm{vB}^{m}+\mathrm{vA}^{m}\,\mathrm{vB}^{n})\,\Big(-(-1+m)\,\mathrm{vB}^{n}\,\mathrm{vmax}^{1+m}+(-1+n)\,\mathrm{vB}^{m}\,\mathrm{vmax}^{1+n}+(m-n)\,\mathrm{vB}\,\mathrm{vmax}^{m+n}\Big)-\mathrm{FB}^{2}\,(m-n)\,(-(-1+n)\,\mathrm{vA}^{m}\,\mathrm{vB}^{n}\,\mathrm{vmax}^{n}\,(-\mathrm{vB}^{m}\,\mathrm{vmax}+\mathrm{vB}\,\mathrm{vmax}^{m})+(-1+m)\,\mathrm{vA}^{n}\,\mathrm{vB}^{m}\,\mathrm{vmax}^{m}\,(-\mathrm{vB}^{n}\,\mathrm{vmax}+\mathrm{vB}\,\mathrm{vmax}^{n}))+\mathrm{FB}\,\mathrm{Fmax}\,(m-n)\,(-(-1+n)\,\mathrm{vA}^{m}\,\mathrm{vB}^{n}\,\mathrm{vmax}^{n}\,(-\mathrm{vB}^{m}\,\mathrm{vmax}+\mathrm{vB}\,\mathrm{vmax}^{m})+(-1+m)\,\mathrm{vA}^{n}\,\mathrm{vB}^{m}\,\mathrm{vmax}^{m}\,(-\mathrm{vB}^{n}\,\mathrm{vmax}+\mathrm{vB}\,\mathrm{vmax}^{n}))+\mathrm{FA}\,\Big(-\mathrm{FB}^{2}\,(m-n)\,\Big(-(-1+m)\,\mathrm{vA}^{n}\,\mathrm{vB}^{1+m}+(-1+n)\,\mathrm{vA}^{m}\,\mathrm{vB}^{1+n}+(m-n)\,\mathrm{vA}\,\mathrm{vB}^{m+n}\Big)\,\mathrm{vmax}^{m+n}+\mathrm{FB}\,\mathrm{Fmax}\,(m-n)\,(2\,(m-n)\,\mathrm{vA}\,\mathrm{vB}^{m+n}\,\mathrm{vmax}^{m+n}+(-1+n)\,\mathrm{vA}^{m}\,\mathrm{vB}^{n}\,\mathrm{vmax}^{n}\,(\mathrm{vB}^{m}\,\mathrm{vmax}+\mathrm{vB}\,\mathrm{vmax}^{m})-(-1+m)\,\mathrm{vA}^{n}\,\mathrm{vB}^{m}\,\mathrm{vmax}^{m}\,(\mathrm{vB}^{n}\,\mathrm{vmax}+\mathrm{vB}\,\mathrm{vmax}^{n}))-\mathrm{Fmax}\,\Big(\mathrm{Fmax}\,(m-n)\,\mathrm{vB}^{m+n}\,\Big(-(-1+m)\,\mathrm{vA}^{n}\,\mathrm{vmax}^{1+m}+(-1+n)\,\mathrm{vA}^{m}\,\mathrm{vmax}^{1+n}+(m-n)\,\mathrm{vA}\,\mathrm{vmax}^{m+n}\Big)-\mathrm{KB}\,\mathrm{vB}\,(\mathrm{vA}^{n}\,\mathrm{vB}^{m}-\mathrm{vA}^{m}\,\mathrm{vB}^{n})\,\Big(-(-1+m)\,\mathrm{vB}^{n}\,\mathrm{vmax}^{1+m}+(-1+n)\,\mathrm{vB}^{m}\,\mathrm{vmax}^{1+n}+(m-n)\,\mathrm{vB}\,\mathrm{vmax}^{m+n}\Big)\Big)\Big)\Big)\Big)$$

Simplify[C3]

$$\frac{1}{\mathrm{Kini}}$$

Simplify[C4]

$$\begin{aligned}
&\Big(-FB^2\,(m-n)\,\Big(Kini\;vB^{m+n}\,\Big(-(-1+m)\;vA^n\;vmax^{1+m}+(-1+n)\;vA^m\;vmax^{1+n}+(m-n)\;vA\;vmax^{m+n}\Big)+\\
&\quad Fmax\,(-n\;vA^n\;vB^n\;vmax^n\,(vB^m-vmax^m)+m\;vA^n\;vB^m\;vmax^m\,(vB^n-vmax^n))\Big)+\\
&\quad FB\;Fmax\,(m-n)\,(Fmax\,(-n\;vA^m\;vB^n\;vmax^n\,(vB^m-vmax^m)+m\;vA^n\;vB^m\;vmax^m\,(vB^n-vmax^n))-\\
&\qquad Kini\,(-2\,(m-n)\;vA\;vB^{m+n}\;vmax^{m+n}-(-1+n)\;vA^m\;vB^n\;vmax^n\,(vB^m\;vmax+vB\;vmax^m)+\\
&\qquad\quad(-1+m)\;vA^n\;vB^m\;vmax^m\,(vB^n\;vmax+vB\;vmax^n)))-\\
&\quad Fmax\,\Big(KB\;Kini\;vB\,(vA^n\;vB^m-vA^m\;vB^n)\,\Big(-(-1+m)\;vB^n\;vmax^{1+m}+(-1+n)\;vB^m\;vmax^{1+n}+(m-n)\;vB\;vmax^{m+n}\Big)+\\
&\qquad Fmax\,\Big(Kini\,(m-n)\,\Big(-(-1+m)\;vA^n\;vB^{1+m}+(-1+n)\;vA^m\;vB^{1+n}+(m-n)\;vA\;vB^{m+n}\Big)\;vmax^{m+n}+\\
&\qquad\quad KB\;vB\,(vA^n\;vB^m-vA^m\;vB^n)\,(-n\;vmax^n\,(vB^m-vmax^m)+m\;vmax^m\,(vB^n-vmax^n))\Big)\Big)+\\
&\quad FA\,\Big(FB^2\,(m-n)\,(n\;vB^n\,(vA^m-vB^m)-m\;vB^m\,(vA^n-vB^n))\;vmax^{m+n}+KB\;Kini\;vB\,(vA^n\;vB^m-vA^m\;vB^n)\\
&\qquad\Big(-(-1+m)\;vB^n\;vmax^{1+m}+(-1+n)\;vB^m\;vmax^{1+n}+(m-n)\;vB\;vmax^{m+n}\Big)+\\
&\qquad Fmax^2\,(m-n)\;vB^{m+n}\,(n\;vmax^n\,(vA^m-vmax^m)-m\;vmax^m\,(vA^n-vmax^n))+Fmax\\
&\qquad\quad(KB\;vB\,(vA^n\;vB^m-vA^m\;vB^n)\,(-n\;vmax^n\,(vB^m-vmax^m)+m\;vmax^m\,(vB^n-vmax^n))-Kini\,(m-n)\,(-(-1+n)\\
&\qquad\qquad vA^m\;vB^n\;vmax^n\,(-vB^m\;vmax+vB\;vmax^m)+(-1+m)\;vA^n\;vB^m\;vmax^m\,(-vB^n\;vmax+vB\;vmax^n)))+\\
&\qquad FB\,(m-n)\,(Kini\,(-(-1+n)\;vA^m\;vB^n\;vmax^n\,(-vB^m\;vmax+vB\;vmax^m)+(-1+m)\;vA^n\;vB^m\;vmax^m\\
&\qquad\qquad(-vB^n\;vmax+vB\;vmax^n))+Fmax\,(-n\;vB^n\;vmax^n\,(-2\;vB^m\;vmax^m+vA^m\,(vB^m+vmax^m))+\\
&\qquad\quad m\;vB^m\;vmax^m\,(-2\;vB^n\;vmax^n+vA^n\,(vB^n+vmax^n)))))\Big)\Big/\Big(Kini\\
&\Big(Fmax\,\Big(Fmax\,KB\;vB\,(-vA^n\;vB^m+vA^m\;vB^n)\,\Big(-(-1+m)\;vB^n\;vmax^{1+m}+(-1+n)\;vB^m\;vmax^{1+n}+(m-n)\;vB\;vmax^{m+n}\Big)-\\
&\qquad FB^2\,(m-n)\,(-(-1+n)\;vA^m\;vB^n\;vmax^n\,(-vB^m\;vmax+vB\;vmax^m)+\\
&\qquad\quad(-1+m)\;vA^n\;vB^m\;vmax^m\,(-vB^n\;vmax+vB\;vmax^n))+FB\;Fmax\,(m-n)\,(-(-1+n)\;vA^m\;vB^n\\
&\qquad\quad vmax^n\,(-vB^m\;vmax+vB\;vmax^m)+(-1+m)\;vA^n\;vB^m\;vmax^m\,(-vB^n\;vmax+vB\;vmax^n))\Big)+\\
&\quad FA\,\Big(-FB^2\,(m-n)\,\Big(-(-1+m)\;vA^n\;vB^{1+m}+(-1+n)\;vA^m\;vB^{1+n}+(m-n)\;vA\;vB^{m+n}\Big)\;vmax^{m+n}+\\
&\qquad FB\;Fmax\,(m-n)\,(2\,(m-n)\;vA\;vB^{m+n}\;vmax^{m+n}+(-1+n)\;vA^m\;vB^n\;vmax^n\,(vB^m\;vmax+vB\;vmax^m)-\\
&\qquad\quad(-1+m)\;vA^n\;vB^m\;vmax^m\,(vB^n\;vmax+vB\;vmax^n))-\\
&\qquad Fmax\,\Big(Fmax\,(m-n)\;vB^{m+n}\,\Big(-(-1+m)\;vA^n\;vmax^{1+m}+(-1+n)\;vA^m\;vmax^{1+n}+(m-n)\;vA\;vmax^{m+n}\Big)-\\
&\qquad\quad KB\;vB\,(vA^n\;vB^m-vA^m\;vB^n)\,\Big(-(-1+m)\;vB^n\;vmax^{1+m}+(-1+n)\;vB^m\;vmax^{1+n}+(m-n)\;vB\;vmax^{m+n}\Big)\Big)\Big)\Big)
\end{aligned}$$

Simplify[C5]

$$\begin{aligned}
&\Big(-Fmax\,\Big(KB\;Kini\;vB\,(vA^n\;vB-vA\;vB^n)\,\Big((-1+m)\;vB^n\;vmax^{1+m}-(-1+n)\;vB^m\;vmax^{1+n}-(m-n)\;vB\;vmax^{m+n}\Big)+\\
&\quad Fmax\,\Big(-Kini\,(-1+n)\,\Big((-1+m)\;vA^n\;vB^{1+m}-(-1+n)\;vA^m\;vB^{1+n}-(m-n)\;vA\;vB^{m+n}\Big)\;vmax^{1+n}+\\
&\qquad KB\;vB\,(vA^n\;vB^m-vA^m\;vB^n)\,\Big(-vB^n\;vmax+n\;vB\;vmax^n-(-1+n)\;vmax^{1+n}\Big)\Big)\Big)+\\
&\quad FB\;Fmax\,\Big(-Kini\,(-1+n)\,\Big(-2\,(-1+n)\;vA^n\;vB^{1+n}\;vmax^{1+n}-(m-n)\;vA\;vB^n\;vmax^n\,(vB^m\;vmax+vB\;vmax^m)+\\
&\qquad(-1+m)\;vA^n\;vB\;vmax\,(vB^n\;vmax^m+vB^m\;vmax^n)\Big)+\\
&\qquad Fmax\,\Big(m\;vA^n\;vB^m\,\Big(-vB^n\;vmax+n\;vB\;vmax^n-(-1+n)\;vmax^{1+n}\Big)-\\
&\qquad\quad n\,((-1+n)\;vA^m\;vB^n\,(vB-vmax)\;vmax^n+vA^n\;vB^m\,(-vB^n\;vmax+vB\;vmax^n))\Big)\Big)-\\
&\quad FB^2\,\Big(-Kini\,(-1+n)\;vB^{1+n}\,\Big((-1+m)\;vA^n\;vmax^{1+m}-(-1+n)\;vA^m\;vmax^{1+n}-(m-n)\;vA\;vmax^{m+n}\Big)+\\
&\qquad Fmax\,\Big(m\;vA^n\;vmax^m\,\Big((-1+n)\;vB^{1+n}-n\;vB^n\;vmax+vB\;vmax^n\Big)-\\
&\qquad\quad n\,((-1+n)\;vA^m\;vB^n\,(vB-vmax)\;vmax^n+vA^n\;vmax^m\,(-vB^n\;vmax+vB\;vmax^n))\Big)\Big)+\\
&\quad FA\,\Big(-FB^2\,(m-n)\,\Big(-vA^n\;vB+n\;vA\;vB^n-(-1+n)\;vB^{1+n}\Big)\;vmax^{m+n}-\\
&\qquad Fmax^2\,(m-n)\;vB^{m+n}\,\Big(-vA^n\;vmax+n\;vA\;vmax^n-(-1+n)\;vmax^{1+n}\Big)+\\
&\qquad KB\;Kini\;vB\,(vA^n\;vB-vA\;vB^n)\,\Big((-1+m)\;vB^n\;vmax^{1+m}-(-1+n)\;vB^m\;vmax^{1+n}-(m-n)\;vB\;vmax^{m+n}\Big)-\\
&\qquad FB\;Kini\,(-1+n)\,(-(m-n)\;vA\;vB^n\;vmax^n\,(-vB^m\;vmax+vB\;vmax^m)+\\
&\qquad\quad(-1+m)\;vA^n\;vB\;vmax\,(vB^n\;vmax^m-vB^m\;vmax^n))+Fmax\,\Big(Kini\,(-1+n)\\
&\qquad\quad(-(m-n)\;vA\;vB^n\;vmax^n\,(-vB^m\;vmax+vB\;vmax^m)+(-1+m)\;vA^n\;vB\;vmax\,(vB^n\;vmax^m-vB^m\;vmax^n))+\\
&\qquad\quad KB\;vB\,\Big(-n\;vA\;vB^n\;vmax^n\,(vB^m-vmax^m)+vA^n\,\Big(-vB^n\;vmax^{1+m}+n\;vB^{1+m}\;vmax^n-(-1+n)\;vB^m\;vmax^{1+n}\Big)+\\
&\qquad\qquad vB^n\,\Big(vB^n\;vmax^{1+m}+(-1+n)\;vB^m\;vmax^{1+n}-n\;vB\;vmax^{m+n}\Big)+m\;vB^n\;vmax^m\\
&\qquad\qquad\quad(-vB^n\;vmax+vB\;vmax^n+vA^n\,(-vB+vmax)+vA\,(vB^n-vmax^n))\Big)+FB\,\Big(-n\,\Big(n\;vA\;vB^n\;vmax^n\,(vB^m+\\
&\qquad\qquad\qquad vmax^m\Big)-(-1+n)\;vB^n\;vmax^n\,(vB^m\;vmax+vB\;vmax^m)-vA^n\,\Big(vB^n\;vmax^{1+m}+vB^{1+m}\;vmax^n\Big)\Big)+\\
&\qquad\qquad m\,\Big(n\;vA\;vB^n\;vmax^n\,(vB^m+vmax^m)-(-1+n)\;vB^n\;vmax^n\,(vB^m\;vmax+vB\;vmax^m)+vA^n\\
&\qquad\qquad\quad\Big((-1+n)\;vB^{1+n}\;vmax^m-n\;vB^n\;vmax^{1+m}-n\;vB^{1+m}\;vmax^n+(-1+n)\;vB^m\;vmax^{1+n}\Big)\Big)\Big)\Big)\Big)\Big)\Big/\\
&\Big(Kini\,\Big(Fmax\,\Big(Fmax\,KB\;vB\,(-vA^n\;vB^m+vA^m\;vB^n)\,\Big(-(-1+m)\;vB^n\;vmax^{1+m}+(-1+n)\;vB^m\;vmax^{1+n}+\\
&\qquad(m-n)\;vB\;vmax^{m+n}\Big)-FB^2\,(m-n)\,(-(-1+n)\;vA^m\;vB^n\;vmax^n\,(-vB^m\;vmax+vB\;vmax^m)+\\
&\qquad(-1+m)\;vA^n\;vB^m\;vmax^m\,(-vB^n\;vmax+vB\;vmax^n))+FB\;Fmax\,(m-n)\,(-(-1+n)\;vA^m\;vB^n\\
&\qquad\quad vmax^n\,(-vB^m\;vmax+vB\;vmax^m)+(-1+m)\;vA^n\;vB^m\;vmax^m\,(-vB^n\;vmax+vB\;vmax^n))\Big)+\\
&\quad FA\,\Big(-FB^2\,(m-n)\,\Big(-(-1+m)\;vA^n\;vB^{1+m}+(-1+n)\;vA^m\;vB^{1+n}+(m-n)\;vA\;vB^{m+n}\Big)\;vmax^{m+n}+\\
&\qquad FB\;Fmax\,(m-n)\,(2\,(m-n)\;vA\;vB^{m+n}\;vmax^{m+n}+(-1+n)\;vA^m\;vB^n\;vmax^n\,(vB^m\;vmax+vB\;vmax^m)-\\
&\qquad\quad(-1+m)\;vA^n\;vB^m\;vmax^m\,(vB^n\;vmax+vB\;vmax^n))-\\
&\qquad Fmax\,\Big(Fmax\,(m-n)\;vB^{m+n}\,\Big(-(-1+m)\;vA^n\;vmax^{1+m}+(-1+n)\;vA^m\;vmax^{1+n}+(m-n)\;vA\;vmax^{m+n}\Big)-\\
&\qquad\quad KB\;vB\,(vA^n\;vB^m-vA^m\;vB^n)\,\Big(-(-1+m)\;vB^n\;vmax^{1+m}+(-1+n)\;vB^m\;vmax^{1+n}+(m-n)\;vB\;vmax^{m+n}\Big)\Big)\Big)\Big)
\end{aligned}$$

Simplify[C6]

$$
\begin{aligned}
&\Big(-FA\,KB\,Kini\,vB\,\left(vA^m\,vB-vA\,vB^m\right)\,\left(-(-1+m)\,vB^n\,vmax^{1+m}+(-1+n)\,vB^m\,vmax^{1+n}+(m-n)\,vB\,vmax^{m+n}\right)+\\
&\quad Fmax^2\,\left(-FB\,m\,vA^m\,vB^{m+n}\,vmax+FB\,n\,vA^m\,vB^{m+n}\,vmax-FB\,m\,vA^n\,vB^{1+m}\,vmax^m+FB\,m^2\,vA^n\,vB^{1+m}\,vmax^m+\right.\\
&\qquad FB\,m\,vA^m\,vB^{1+n}\,vmax^m-FB\,m\,n\,vA^m\,vB^{1+n}\,vmax^m+FB\,m\,vA^n\,vB^m\,vmax^{1+m}-FB\,m^2\,vA^n\,vB^m\,vmax^{1+m}+\\
&\qquad Kini\,vA^n\,vB^{1+m}\,vmax^{1+m}-2\,Kini\,m\,vA^n\,vB^{1+m}\,vmax^{1+m}+Kini\,m^2\,vA^n\,vB^{1+m}\,vmax^{1+m}-FB\,n\,vA^m\,vB^n\,vmax^{1+m}+\\
&\qquad FB\,m\,n\,vA^m\,vB^n\,vmax^{1+m}-Kini\,vA^m\,vB^{1+n}\,vmax^{1+m}+Kini\,m\,vA^m\,vB^{1+n}\,vmax^{1+m}+Kini\,n\,vA^m\,vB^{1+n}\,vmax^{1+m}-\\
&\qquad Kini\,m\,n\,vA^m\,vB^{1+n}\,vmax^{1+m}+Kini\,m\,vA\,vB^{m+n}\,vmax^{1+m}-Kini\,m^2\,vA\,vB^{m+n}\,vmax^{1+m}-Kini\,n\,vA\,vB^{m+n}\,vmax^{1+m}+\\
&\qquad Kini\,m\,n\,vA\,vB^{m+n}\,vmax^{1+m}-FA\,(m-n)\,vB^{m+n}\,\left(-vA^m\,vmax+m\,vA\,vmax^m-(-1+m)\,vmax^{1+m}\right)+\\
&\qquad KB\,vB\,\left(vA^n\,vB^m-vA^m\,vB^n\right)\,\left(vB^m\,vmax-m\,vB\,vmax^m+(-1+m)\,vmax^{1+m}\right)\Big)+FA\,FB\,Kini\,(-1+m)\\
&\quad ((m-n)\,vA\,vB^m\,vmax^m\,(-vB^n\,vmax+vB\,vmax^n)-(-1+n)\,vA^m\,vB\,vmax\,(vB^n\,vmax^m-vB^m\,vmax^n))+\\
&\quad FB^2\,\left(-FA\,(m-n)\,\left(-vA^m\,vB+m\,vA\,vB^m-(-1+m)\,vB^{1+m}\right)\,vmax^{m+n}+\right.\\
&\qquad Kini\,(-1+m)\,vB^{1+m}\,\left((-1+m)\,vA^n\,vmax^{1+m}-(-1+n)\,vA^m\,vmax^{1+n}-(m-n)\,vA\,vmax^{m+n}\right)\Big)+\\
&\quad Fmax\,\left(KB\,Kini\,vB\,\left(vA^m\,vB-vA\,vB^m\right)\,\left(-(-1+m)\,vB^n\,vmax^{1+m}+(-1+n)\,vB^m\,vmax^{1+n}+(m-n)\,vB\,vmax^{m+n}\right)+\right.\\
&\qquad FB^2\,\left(-m^2\,vA^n\,vB^m\,(vB-vmax)\,vmax^m-n\,vA^m\,vB\,vmax^n\,(vB^m-vmax^m)+\right.\\
&\qquad\quad m\,(vA^n\,vB^m\,(vB-vmax)\,vmax^m+vA^m\,vmax^n\,(n\,vB^m\,(vB-vmax)+vB^m\,vmax-vB\,vmax^m))\Big)+\\
&\qquad FA\,\left(-Kini\,(-1+m)\,((m-n)\,vA\,vB^m\,vmax^m\,(-vB^n\,vmax+vB\,vmax^n)-(-1+n)\,vA^m\,vB\,vmax\right.\\
&\qquad\qquad (vB^n\,vmax^m-vB^m\,vmax^n))+KB\,vB\,\left(-n\,vA\,vB^m\,vmax^n\,(vB^m-vmax^m)+vA^m\,\left(-vB^n\,vmax^{1+m}+n\,vB^{1+m}\right.\right.\\
&\qquad\qquad\quad vmax^n-(-1+n)\,vB^m\,vmax^{1+n}\Big)+vB^m\,\left(vB^n\,vmax^{1+m}+(-1+n)\,vB^m\,vmax^{1+n}-n\,vB\,vmax^{m+n}\right)+\\
&\qquad\qquad m\,vmax^m\,(vA^n\,vB^m\,(-vB+vmax)+vA\,vB^m\,(vB^n-vmax^n)+vB^m\,(-vB^n\,vmax+vB\,vmax^n))\Big)\Big)+\\
&\qquad FB\,\left(Kini\,(-1+m)\,\left(-2\,(-1+m)\,vA^n\,vB^{1+m}\,vmax^{1+m}+(m-n)\,vA\,vB^m\,vmax^m\,(vB^n\,vmax+vB\,vmax^n)+\right.\right.\\
&\qquad\quad (-1+n)\,vA^m\,vB\,vmax\,(vB^n\,vmax^m+vB^m\,vmax^n)\Big)+FA\,\left(m^2\,vB^m\,vmax^m\,(-vB^n\,vmax-vB\,vmax^n+vA\right.\\
&\qquad\quad\quad (vB^n+vmax^n))+n\,\left(-vB^m\,vmax^m\,(vB^n\,vmax+vB\,vmax^n)+vA^m\,\left(vB^n\,vmax^{1+m}+vB^{1+m}\,vmax^n\right)\right)+\\
&\qquad\quad m\,\left(-n\,vA\,vB^m\,vmax^m\,(vB^n+vmax^n)+(1+n)\,vB^m\,vmax^m\,(vB^n\,vmax+vB\,vmax^n)+vA^n\right.\\
&\qquad\quad\quad \left.\left.\left.\left.\left.\left((-1+n)\,vB^{1+n}\,vmax^m-n\,vB^n\,vmax^{1+m}-n\,vB^{1+n}\,vmax^n+(-1+n)\,vB^m\,vmax^{1+n}\right)\right)\right)\right)\right)\Big/\Big(Kini\\
&\Big(Fmax\,\left(Fmax\,KB\,vB\,\left(vA^n\,vB^m-vA^m\,vB^n\right)\,\left(-(-1+m)\,vB^n\,vmax^{1+m}+(-1+n)\,vB^m\,vmax^{1+n}+(m-n)\,vB\,vmax^{m+n}\right)+\right.\\
&\qquad FB^2\,(m-n)\,(-(-1+n)\,vA^m\,vB^n\,vmax^n\,(-vB^m\,vmax+vB\,vmax^m)+\\
&\qquad\quad (-1+m)\,vA^n\,vB^m\,vmax^m\,(-vB^n\,vmax+vB\,vmax^n))-FB\,Fmax\,(m-n)\,(-(-1+n)\,vA^n\,vB^n\\
&\qquad\quad vmax^n\,(-vB^m\,vmax+vB\,vmax^m)+(-1+m)\,vA^n\,vB^m\,vmax^m\,(-vB^n\,vmax+vB\,vmax^n))\Big)+\\
&\quad FA\,\left(FB^2\,(m-n)\,\left(-(-1+m)\,vA^n\,vB^{1+m}+(-1+n)\,vA^m\,vB^{1+n}+(m-n)\,vA\,vB^{m+n}\right)\,vmax^{m+n}-\right.\\
&\qquad FB\,Fmax\,(m-n)\,(2\,(m-n)\,vA\,vB^{m+n}\,vmax^{m+n}+(-1+n)\,vA^m\,vB^n\,vmax^n\,(vB^m\,vmax+vB\,vmax^m)-\\
&\qquad\quad (-1+m)\,vA^n\,vB^m\,vmax^m\,(vB^n\,vmax+vB\,vmax^n))+\\
&\qquad Fmax\,\left(Fmax\,(m-n)\,vB^{m+n}\,\left(-(-1+m)\,vA^n\,vmax^{1+m}+(-1+n)\,vA^m\,vmax^{1+n}+(m-n)\,vA\,vmax^{m+n}\right)-\right.\\
&\qquad\quad KB\,vB\,\left(vA^n\,vB^m-vA^m\,vB^n\right)\,\left(-(-1+m)\,vB^n\,vmax^{1+m}+(-1+n)\,vB^m\,vmax^{1+n}+(m-n)\,vB\,vmax^{m+n}\right)\Big)\Big)\Big)\Big)
\end{aligned}
$$

D-3.2 Simplified coefficients

Simplify[C1]

$$\begin{aligned}&\left(\text{Fmax}\,(\text{vB}-\text{vmax})\,\text{vmax}\,\left(16\,\text{Fmax}^2\,(\text{vB}-\text{vmax})^3+\right.\right.\\&\quad 8\,\text{Fmax}\,\text{Kini}\,\text{vB}^2\,(4\,\text{vB}-\text{vmax})\,\text{vmax}+25\,\text{KB}\,\text{Kini}\,\text{vB}^2\left(4\,\text{vB}^3-4\,\text{vB}^2\,\text{vmax}-\text{vB}\,\text{vmax}^2+\text{vmax}^3\right)\Big)-\\&\quad \text{FA}\left(25\,\text{KB}\,\text{Kini}\,\text{vB}^2\,(\text{vB}-\text{vmax})^2\,\text{vmax}\left(4\,\text{vB}^2-\text{vmax}^2\right)+\right.\\&\quad 4\,\text{Fmax}^2\,\text{vmax}\left(9\,\text{vB}^4-24\,\text{vB}^3\,\text{vmax}+27\,\text{vB}^2\,\text{vmax}^2-16\,\text{vB}\,\text{vmax}^3+4\,\text{vmax}^4\right)+\\&\quad \left.\text{Fmax}\,\text{vB}^2\left(25\,\text{KB}\,\text{vB}\,(\text{vB}-\text{vmax})^2\,(2\,\text{vB}-\text{vmax})+2\,\text{Kini}\,\text{vmax}^2\left(16\,\text{vB}^2-21\,\text{vB}\,\text{vmax}+4\,\text{vmax}^2\right)\right)\right)\Big)\Big/\\&\left(\text{Kini}\,\text{vB}^2\,\text{vmax}^2\left(-\text{Fmax}\,(\text{vB}-\text{vmax})\left(4\,\text{Fmax}\,(3\,\text{vB}-\text{vmax})\,\text{vmax}+25\,\text{KB}\,\text{vB}\left(2\,\text{vB}^2-3\,\text{vB}\,\text{vmax}+\text{vmax}^2\right)\right)+\right.\right.\\&\quad \left.\left.\text{FA}\left(25\,\text{KB}\,\text{vB}\,(\text{vB}-\text{vmax})^2\,(2\,\text{vB}-\text{vmax})+\text{Fmax}\,\text{vmax}\left(11\,\text{vB}^2-16\,\text{vB}\,\text{vmax}+4\,\text{vmax}^2\right)\right)\right)\right)\end{aligned}$$

Simplify[C2]

$$\begin{aligned}&\left(-2\,\text{Fmax}\,(\text{vB}-\text{vmax})\right.\\&\quad \left(16\,\text{Fmax}^2\,(\text{vB}-\text{vmax})^3+8\,\text{Fmax}\,\text{Kini}\,\text{vB}^3\,\text{vmax}+25\,\text{KB}\,\text{Kini}\,\text{vB}^2\,\text{vmax}\left(2\,\text{vB}^2-3\,\text{vB}\,\text{vmax}+\text{vmax}^2\right)\right)+\\&\quad \text{FA}\left(50\,\text{KB}\,\text{Kini}\,\text{vB}^2\,(\text{vB}-\text{vmax})^2\,(2\,\text{vB}-\text{vmax})\,\text{vmax}+\right.\\&\quad 8\,\text{Fmax}^2\left(5\,\text{vB}^4-16\,\text{vB}^3\,\text{vmax}+22\,\text{vB}^2\,\text{vmax}^2-15\,\text{vB}\,\text{vmax}^3+4\,\text{vmax}^4\right)+\\&\quad \left.\text{Fmax}\,\text{vB}^2\left(25\,\text{KB}\,(\text{vB}-\text{vmax})^2\,(2\,\text{vB}-\text{vmax})-\text{Kini}\,\text{vmax}\left(-16\,\text{vB}^2+16\,\text{vB}\,\text{vmax}+\text{vmax}^2\right)\right)\right)\Big)\Big/\\&\left(\text{Kini}\,\text{vB}^2\,\text{vmax}^2\left(-\text{Fmax}\,(\text{vB}-\text{vmax})\left(4\,\text{Fmax}\,(3\,\text{vB}-\text{vmax})\,\text{vmax}+25\,\text{KB}\,\text{vB}\left(2\,\text{vB}^2-3\,\text{vB}\,\text{vmax}+\text{vmax}^2\right)\right)+\right.\right.\\&\quad \left.\left.\text{FA}\left(25\,\text{KB}\,\text{vB}\,(\text{vB}-\text{vmax})^2\,(2\,\text{vB}-\text{vmax})+\text{Fmax}\,\text{vmax}\left(11\,\text{vB}^2-16\,\text{vB}\,\text{vmax}+4\,\text{vmax}^2\right)\right)\right)\right)\end{aligned}$$

Simplify[C3]

$$\frac{1}{\text{Kini}}$$

Simplify[C4]

$$\begin{aligned}&\left(\text{Fmax}\left(25\,\text{KB}\,\text{Kini}\,\text{vB}^2\,(\text{vB}-\text{vmax})^2\,(2\,\text{vB}-\text{vmax})\,\text{vmax}-8\,\text{Fmax}^2\left(2\,\text{vB}^3\,\text{vmax}-3\,\text{vB}\,\text{vmax}^3+\text{vmax}^4\right)+\right.\right.\\&\quad \left.\text{Fmax}\,\text{vB}\left(-25\,\text{KB}\,(\text{vB}-\text{vmax})^2\left(4\,\text{vB}^2-\text{vmax}^2\right)+\text{Kini}\,\text{vmax}^2\left(16\,\text{vB}^2-20\,\text{vB}\,\text{vmax}+5\,\text{vmax}^2\right)\right)\right)+\\&\quad \text{FA}\left(-25\,\text{KB}\,\text{Kini}\,\text{vB}^2\,(\text{vB}-\text{vmax})^2\,(2\,\text{vB}-\text{vmax})\,\text{vmax}+4\,\text{Fmax}^2\left(3\,\text{vB}^3\,\text{vmax}-6\,\text{vB}\,\text{vmax}^3+2\,\text{vmax}^4\right)+\right.\\&\quad \left.\left.5\,\text{Fmax}\,\text{vB}\,(\text{vB}-\text{vmax})\left(\text{Kini}\,\text{vmax}^2\left(-3\,\text{vB}+\text{vmax}\right)+5\,\text{KB}\left(4\,\text{vB}^3-4\,\text{vB}^2\,\text{vmax}-\text{vB}\,\text{vmax}^2+\text{vmax}^3\right)\right)\right)\Big)\Big/\\&\left(\text{Fmax}\,\text{Kini}\,\text{vB}\,\text{vmax}\left(\text{FA}\left(-25\,\text{KB}\,\text{vB}\,(\text{vB}-\text{vmax})^2\,(2\,\text{vB}-\text{vmax})+\text{Fmax}\,\text{vmax}\left(-11\,\text{vB}^2+16\,\text{vB}\,\text{vmax}-4\,\text{vmax}^2\right)\right)+\right.\right.\\&\quad \left.\left.\text{Fmax}\,(\text{vB}-\text{vmax})\left(4\,\text{Fmax}\,(3\,\text{vB}-\text{vmax})\,\text{vmax}+25\,\text{KB}\,\text{vB}\left(2\,\text{vB}^2-3\,\text{vB}\,\text{vmax}+\text{vmax}^2\right)\right)\right)\right)\end{aligned}$$

Simplify[C5]

$$\begin{aligned}&\left(-25\,\text{FA}\,\text{KB}\,\text{Kini}\,\text{vB}^2\,(\text{vB}-\text{vmax})^2\,\text{vmax}\left(4\,\text{vB}^2-\text{vmax}^2\right)+\right.\\&\quad 4\,\text{Fmax}^3\,\text{vmax}\left(5\,\text{vB}^4-28\,\text{vB}^3\,\text{vmax}+39\,\text{vB}^2\,\text{vmax}^2-20\,\text{vB}\,\text{vmax}^3+4\,\text{vmax}^4\right)+\\&\quad 5\,\text{Fmax}\,\text{vB}^2\,(\text{vB}-\text{vmax})\,\text{vmax}\left(5\,\text{KB}\,\text{Kini}\left(4\,\text{vB}^3-4\,\text{vB}^2\,\text{vmax}-\text{vB}\,\text{vmax}^2+\text{vmax}^3\right)+\right.\\&\quad \left.2\,\text{FA}\left(\text{Kini}\,\text{vmax}\left(-4\,\text{vB}+\text{vmax}\right)+5\,\text{KB}\left(2\,\text{vB}^2-3\,\text{vB}\,\text{vmax}+\text{vmax}^2\right)\right)\right)+\\&\quad \text{Fmax}^2\left(-25\,\text{KB}\,\text{vB}^2\,(\text{vB}-\text{vmax})^2\left(2\,\text{vB}^2+3\,\text{vB}\,\text{vmax}-2\,\text{vmax}^2\right)+\right.\\&\quad \text{vmax}\left(2\,\text{Kini}\,\text{vB}^2\,\text{vmax}\left(20\,\text{vB}^2-24\,\text{vB}\,\text{vmax}+5\,\text{vmax}^2\right)+\right.\\&\quad \left.\left.\left.\text{FA}\left(-45\,\text{vB}^4+144\,\text{vB}^3\,\text{vmax}-168\,\text{vB}^2\,\text{vmax}^2+80\,\text{vB}\,\text{vmax}^3-16\,\text{vmax}^4\right)\right)\right)\Big)\Big/\\&\left(\text{Fmax}\,\text{Kini}\,\text{vB}^2\,\text{vmax}^2\left(-\text{Fmax}\,(\text{vB}-\text{vmax})\left(4\,\text{Fmax}\,(3\,\text{vB}-\text{vmax})\,\text{vmax}+25\,\text{KB}\,\text{vB}\left(2\,\text{vB}^2-3\,\text{vB}\,\text{vmax}+\text{vmax}^2\right)\right)+\right.\right.\\&\quad \left.\left.\text{FA}\left(25\,\text{KB}\,\text{vB}\,(\text{vB}-\text{vmax})^2\,(2\,\text{vB}-\text{vmax})+\text{Fmax}\,\text{vmax}\left(11\,\text{vB}^2-16\,\text{vB}\,\text{vmax}+4\,\text{vmax}^2\right)\right)\right)\right)\end{aligned}$$

Simplify[C6]

$$\begin{aligned}&\left(-2\,\text{FA}\left(10\,\text{Fmax}\,\text{Kini}\,\text{vB}^3\,(\text{vB}-\text{vmax})\,\text{vmax}+25\,\text{KB}\,\text{Kini}\,\text{vB}^2\,(\text{vB}-\text{vmax})^2\,(2\,\text{vB}-\text{vmax})\,\text{vmax}+\right.\right.\\&\quad \left.\text{Fmax}^2\left(5\,\text{vB}^2-8\,\text{vB}\,\text{vmax}+4\,\text{vmax}^2\right)^2\right)+\text{Fmax}\left(50\,\text{KB}\,\text{Kini}\,\text{vB}^2\,(\text{vB}-\text{vmax})^2\,(2\,\text{vB}-\text{vmax})\,\text{vmax}+\right.\\&\quad 8\,\text{Fmax}^2\left(5\,\text{vB}^4-20\,\text{vB}^3\,\text{vmax}+28\,\text{vB}^2\,\text{vmax}^2-17\,\text{vB}\,\text{vmax}^3+4\,\text{vmax}^4\right)+\\&\quad \left.\left.\text{Fmax}\,\text{vB}^2\left(-25\,\text{KB}\,(\text{vB}-\text{vmax})^2\,(2\,\text{vB}-\text{vmax})+\text{Kini}\,\text{vmax}\left(20\,\text{vB}^2-20\,\text{vB}\,\text{vmax}+\text{vmax}^2\right)\right)\right)\right)\Big/\left(\text{Fmax}\right.\\&\quad \text{Kini}\,\text{vB}^2\,\text{vmax}^2\left(\text{FA}\left(-25\,\text{KB}\,\text{vB}\,(\text{vB}-\text{vmax})^2\,(2\,\text{vB}-\text{vmax})+\text{Fmax}\,\text{vmax}\left(-11\,\text{vB}^2+16\,\text{vB}\,\text{vmax}-4\,\text{vmax}^2\right)\right)+\right.\\&\quad \left.\left.\text{Fmax}\,(\text{vB}-\text{vmax})\left(4\,\text{Fmax}\,(3\,\text{vB}-\text{vmax})\,\text{vmax}+25\,\text{KB}\,\text{vB}\left(2\,\text{vB}^2-3\,\text{vB}\,\text{vmax}+\text{vmax}^2\right)\right)\right)\right)\end{aligned}$$

D-4 Inputs for RFEM 5 simulations

D-4.1 Stiffness matrix for CLT surface elements

Equation (D.10) depicts the stiffness matrix with the 21 modifiable parameters as given in RFEM 5 (2015). However, due to the existing gaps/cracks, a Poisson ratio equal to zero may be assumed for considering the orthotropic behaviour of CLT. As a consequence, solely the values in the main diagonal (D_{11} to D_{88}) remain; compare Silly (2010) and Bogensperger and Silly (2014). Equations (D.11) to (D.18) illustrate how these values are determined in the present thesis. More detailed information, especially regarding the torsional stiffness (D_{33}) and the shear correction factor for CLT, can be found in Schickhofer et al. (2010), Silly (2010), Bogensperger and Silly (2014) and ON B 1995-1-1 (2015).

$$D_{\text{stiffness}} = \begin{bmatrix} D_{11} & D_{12} & D_{13} & 0 & 0 & D_{16} & D_{17} & D_{18} \\ & D_{22} & D_{23} & 0 & 0 & \text{sym.} & D_{27} & D_{28} \\ & & D_{33} & 0 & 0 & \text{sym.} & \text{sym.} & D_{38} \\ & & & D_{44} & D_{45} & 0 & 0 & 0 \\ & & & & D_{55} & 0 & 0 & 0 \\ & & \text{sym.} & & & D_{66} & D_{67} & D_{68} \\ & & & & & & D_{77} & D_{78} \\ & & & & & & & D_{88} \end{bmatrix} \tag{D.10}$$

$$D_{11} = E_0 \cdot I_{\text{x,eff}} = E_0 \cdot \left(\sum I_{\text{x,i}} + \sum A_{\text{x,i}} \cdot e_{\text{x,i}} \right) \tag{D.11}$$

$$D_{22} = E_0 \cdot I_{\text{y,eff}} = E_0 \cdot \left(\sum I_{\text{y,i}} + \sum A_{\text{y,i}} \cdot e_{\text{y,i}} \right) \tag{D.12}$$

$$D_{33} = \frac{G_{\text{mean}} \cdot t_{\text{CLT}}^3}{12 \cdot \left(1 + 6 \cdot p_{\text{D}} \cdot \left(\frac{t_{\max}}{a} \right)^{q_{\text{D}}} \right)} \tag{D.13}$$

$$D_{44} = \frac{\left(G_{\text{mean}} \cdot \sum t_{\text{x,i}} + G_{\text{R,mean}} \cdot \sum t_{\text{y,i}} \right)}{\kappa_{\text{x}}} \tag{D.14}$$

$$D_{55} = \frac{\left(G_{\text{R,mean}} \cdot \sum t_{\text{x,i}} + G_{\text{mean}} \cdot \sum t_{\text{y,i}} \right)}{\kappa_{\text{y}}} \tag{D.15}$$

$$D_{66} = E_0 \cdot \sum t_{\text{x,i}} \tag{D.16}$$

$$D_{77} = E_0 \cdot \sum t_{\text{y,i}} \tag{D.17}$$

$$D_{88} = \frac{t_{\text{CLT}} \cdot G_{\text{mean}}}{1 + 6 \cdot p_{\text{s}} \left(\frac{t_{\max}}{a} \right)^{q_{\text{s}}}} \tag{D.18}$$

with

$D_{stiffness}$ ..... stiffness matrix for RFEM 5 (2015) input

D_{11}-D_{88} ..... elements of stiffness matrix

$I_{x|y,eff}$ ..... effective moment of inertia for the CLT element in $x|y$-direction

$I_{x|y,i}$ ..... moment of inertia of i-th single layer in $x|y$-direction

$A_{x|y,i}$ ..... area of i-th single layer in $x|y$-direction

$e_{x|y,i}$ ..... distance between i-th single layers' centre and the balance point of CLT element

$t_{x|y,i}$ ..... thickness of i-th single layer in $x|y$-direction

p_D, q_D ..... parameters according to Table D.5

$\kappa_{x|y}$ ..... shear correction factors

Note: For determining elements D_{11}, D_{22}, D_{66} and D_{77}, the MOE perpendicular to the grain (E_{90}) is assumed to be zero. Furthermore, for determining the moments of inertia and areas for the single layers, a so called 'one meter strip' is used (elements' width = 1.0 m). Finally, it is important to mention that application of these formulas lead to surface elements where the x-direction is equal to the direction of outer (deck) layers.

Table D.5 shows the parameters applied for determining the shear and torsional stiffness values; compare ON B 1995-1-1 (2015). For determining the shear correction factors, Equations (D.19) and (D.20) are used. Assuming an equal layer thickness and a G/G_R ratio of 1/10, lead to the respective values given in Table D.5; see also Bogensperger and Silly (2014).

Table D.5: required parameters for determining the elements of the stiffness matrix according to ON B 1995-1-1 (2015) and Bogensperger and Silly (2014); shown shear correction factors are valid for an equal layer thickness and a G/G_R ratio of 1/10

parameter	3 layers	5 layers	7 and more layers
p_S	0.53	0.43	
q_S		1.21	
p_D	0.89	0.67	0.55
q_D	1.33	1.26	1.23
$\kappa_{x\|y}$	4.85 | 1.44	4.11 | 5.32	3.87 | 4.36

$$\kappa_x = \frac{\sum\left(G_{x,i} \cdot t_i\right)}{\left(E_0 \cdot I_{x,eff}\right)^2} \cdot \int_{z=-\frac{t_{CLT}}{2}}^{z=\frac{t_{CLT}}{2}} \left[\int_{s=-\frac{t_{CLT}}{2}}^{s=z} E_x(s) \cdot s \cdot ds \right]^2 \cdot \frac{dz}{G_x(z)} \qquad \text{(D.19)}$$

$$\kappa_y = \frac{\sum\left(G_{y,i} \cdot t_i\right)}{\left(E_0 \cdot I_{y,eff}\right)^2} \cdot \int_{z=-\frac{t_{CLT}}{2}}^{z=\frac{t_{CLT}}{2}} \left[\int_{s=-\frac{t_{CLT}}{2}}^{s=z} E_y(s) \cdot s \cdot ds \right]^2 \cdot \frac{dz}{G_y(z)} \qquad \text{(D.20)}$$

Table D.6 lists the resulting parameters, used for defining the CLT elements; required input parameters are taken from Table 5.32.

Table D.6: input data for CLT surface elements

	D_{11} [kNm]	D_{22} [kNm]	D_{33} [kNm]	D_{44} [kN/m]	D_{55} [kN/m]	D_{66} [kN/m]	D_{77} [kN/m]	D_{88} [kN/m]
wall TU Graz tests	1326.4	31.7	39.6	11548.7	17333.3	928000	371200	44323.6
wall IVALSA tests	470.2	123.5	26.4	8340.2	2702.3	591600	197200	46620.8
wall parameter study	765.6	201.1	41.1	10128.5	5624.7	696000	464000	53047.5
floor parameter study	2583.9	678.6	119.6	15192.8	8437.0	1044000	696000	71271.1

Note: applied mesh size for all elements: 50 mm

D-4.2 Simulating connections

The parameters, defining the piecewise linear load-displacement diagram for considering the nonlinear behaviour of the connections, are computed by applying the average approximations documented in Chapter 5, i.e., section 5-2; the resulting coordinates are documented in Table D.7. The parameters applied for simulating top joint fasteners are listed in Table D.8.

Table D.7: FE input data for applied connections (basing on respective average approximation parameters)

	AE 116 (shear)		AE 116 (uplift)		HTT 22 (uplift)		step joint (parallel screws)	
	v [mm]	$F(v)$ [kN]	v [mm]	$F(v)$ [kN]	v [mm]	$F(v)$ [kN]	v [mm]	$F(v)$ [kN]
1	0.00	0.00	0.00	0.00	0.00	0.00	0.00	0.00
2	1.84	7.12	1.84	14.05	1.84	19.36	1.32	1.06
3	3.68	12.92	3.68	18.59	3.68	26.19	2.63	1.38
4	5.53	17.68	5.53	21.57	5.53	31.58	3.95	1.60
5	7.37	21.60	7.37	24.06	7.37	36.22	5.26	1.79
6	9.21	24.79	9.21	26.36	9.21	40.22	6.58	1.97
7	11.05	27.34	11.05	28.57	11.05	43.59	7.89	2.15
8	12.89	29.28	12.89	30.69	12.89	46.27	9.21	2.32
9	14.74	30.62	14.74	32.66	14.74	48.24	10.53	2.49
10	16.58	31.36	16.58	34.36	16.58	49.43	11.84	2.64
11	18.42	31.46	18.42	35.63	18.42	49.80	13.16	2.77
12	20.26	30.90	20.26	36.26	20.26	49.31	14.47	2.84
13	22.11	29.63	22.11	36.07	22.11	47.92	15.79	2.86
14	23.95	27.63	23.95	34.89	23.95	45.63	17.11	2.79
15	25.79	24.88	25.79	32.68	25.79	42.43	18.42	2.63
16	27.63	21.42	27.63	29.56	27.63	38.34	19.74	2.40
17	29.47	17.30	29.47	25.76	29.47	33.37	21.05	2.11
18	31.32	12.66	31.32	21.60	31.32	27.57	22.37	1.78
19	33.16	7.67	33.16	17.41	33.16	21.01	23.68	1.45
20	35.00	2.56	35.00	13.45	35.00	13.73	25.00	1.14

Table D.8: FE input data for estimating the top-joint effect

	Ø8.0×160 mm crosswise HEB 120 – CLT		Ø8.0×160 mm parallel UPN – CLT		Ø8.0×280 mm parallel CLT – CLT FT		Ø10.0×260 mm parallel CLT – CLT PT	
	v [mm]	$F(v)$ [kN]	v [mm]	$F(v)$ [kN]	v [mm]	$F(v)$ [kN]	v [mm]	$F(v)$ [kN]
1	0.00	0.00	0.00	0.00	0.00	0.00	0.00	0.00
2	0.32	2.16	0.26	3.53	0.26	5.92	1.84	4.49
3	0.63	3.74	0.53	6.35	0.53	10.63	3.68	5.59
4	0.95	4.95	0.79	8.54	0.79	14.31	5.53	6.15
5	1.26	5.91	1.05	10.21	1.05	17.10	7.37	6.54
6	1.58	6.69	1.32	11.43	1.32	19.15	9.21	6.86
7	1.89	7.32	1.58	12.27	1.58	20.56	11.05	7.16
8	2.21	7.82	1.84	12.80	1.84	21.44	12.89	7.44
9	2.53	8.19	2.11	13.06	2.11	21.87	14.74	7.70
10	2.84	8.44	2.37	13.09	2.37	21.93	16.58	7.90
11	3.16	8.54	2.63	12.94	2.63	21.67	18.42	7.99
12	3.47	8.47	2.89	12.63	2.89	21.15	20.26	7.95
13	3.79	8.21	3.16	12.18	3.16	20.40	22.11	7.79
14	4.11	7.76	3.42	11.62	3.42	19.47	23.95	7.56
15	4.42	7.14	3.68	10.97	3.68	18.37	25.79	7.31
16	4.74	6.41	3.95	10.23	3.95	17.14	27.63	7.09
17	5.05	5.65	4.21	9.43	4.21	15.79	29.47	6.90
18	5.37	4.95	4.47	8.57	4.47	14.35	31.32	6.75
19	5.68	4.39	4.74	7.66	4.74	12.83	33.16	6.63
20	6.00	4.00	5.00	6.71	5.00	11.24	35.00	6.55

Notes: HEB 120 – CLT: behaviour of one partially threaded screw Ø8.0×160 mm (effective length = 100 mm | inclined)

UPN 100 – CLT: axial behaviour of one partially threaded screw Ø8.0×160 mm (effective length = 100 mm)

CLT – CLT FT: axial behaviour of one fully threaded screw Ø8.0×280 mm (effective length = 134 mm); compare section 5-2.4.2

CLT – CLT PT: axial behaviour of partially threaded screw Ø10.0×260 mm (effective length = 100 mm | counter sunk head); compare Test 18 in Gavric (2013)

Monographic Series TU Graz

Timber Engineering & Technology

Volume 1 Gerhard Schickhofer
Starrer und nachgiebiger Verbund bei geschichteten, flächenhaften Holzstrukturen
2013; ISBN 978-3-85125-262-0

Volume 2 Reinhard Brandner
Stochastic System Actions and Effects in Engineered Timber Products and Structures
2013; ISBN 978-3-85125-263-7

Volume 3 Ulrich Hübner
Mechanische Kenngrößen von Buchen-, Eschen- und Robinienholz für lastabtragende Bauteile
2014; ISBN 978-3-85125-314-6

Volume 4 Andreas Meisel
Historische Dachwerke - Beurteilung, realitätsnahe statische Analyse und Instandsetzung
2015; ISBN 978-3-85125-433-4

Volume 5 Andreas Ringhofer
Axially Loaded Self-Tapping Screws in Solid Timber and Laminated Timber Products
2017; ISBN 978-3-85125-555-3

Volume 6 Georg Flatscher
Evaluation and approximation of timber connection properties for displacement-based analysis of CLT wall systems
2017; ISBN 978-3-85125-557-7